Crystallography Reports, Vol. 50, No. 5, 2005, pp. 715–720. Translated from Kristallografiya, Vol. 50, No. 5, 2005, pp. 775–781.

CRYSTALLOGRAPHIC SYMMETRY

Electrons of *l* Shells of Free Atoms As a Regular System of Points on a Sphere: III. Factors of Self-Organization of Electrons in the Periodic Table

T. F. Veremeĭchik

Shubnikov Institute of Crystallography, Russian Academy of Sciences, Leninskiĭ pr. 59, Moscow, 119333 Russia

e-mail: tomver@online.ru

Received March 23, 2005

Abstract—The factors determining the self-organization of the electron system of an atom at different levels of the periodic table are considered. Specifically, these factors are the isotropy and three-dimensional nature of space and the indistinguishability of electrons. The concept of a simplex is used, whose vertices correspond to a regular system of particles (minimum in number for a given space) in the state of the global minimum of the system's potential. These factors implement the principle of simplicity (small number of particles) and hierarchy in the periodic table of elements. The global minimum of the potential of *s*, *p*, *d*, and *f* shells is reached in odd-dimensional spaces. In a three-dimensional space, such a minimum is reached for *d* and *f* shells, in contrast to *s* and *p* shells, through shell mixing. © *2005 Pleiades Publishing, Inc.*

STATEMENT OF THE PROBLEM

In was shown in [1] that the maxima of the electron-density probability in the *l* shells of an atom (*s*, *p*, *d*, and *f* shells, well-known in quantum mechanics) are modeled by vertices of antiprisms. This result made it possible to explain a number of structural and physical properties of crystals [2]. Furthermore, we will use for brevity the term "electron" instead of "maximum of electron-density probability." In this study, we consider the factors implementing in the periodic table the principle of simplicity (minimum number of particles) and hierarchy in self-organization of electrons at different levels of the periodic table: *l* shells, periods, and the number of periods of different types. The specific features of antiprisms are analyzed in the context of the principle of simplicity and the existence of a global minimum in the most stable systems of particles (which are listed in the periodic table). To describe the crystallographic model of electron shells in more detail, we compare it with the quantum model and the structures of coordination polyhedra and clusters.

STABLE SYSTEMS OF COULOMB PARTICLES IN THE PERIODIC TABLE

The difference in the numbers of elements in the periods of the periodic table indicates the existence of stable groups of discrete particles and gives their numbers in groups. The first period contains two elements. The difference between the first and second (third) periods is eight elements. The difference between the second (third) and fourth (fifth) periods is ten elements. The difference between the fourth (fifth) and sixth (seventh) periods is 14 elements. The number of elements in the first period suggests that the formation of groups of particles begins with the simplest group consisting of two particles.

In the three-dimensional (3D) isotropic space, the centrosymmetrical potential $U(r)$, invariant with respect to all rotations around fixed axes and inversion, is the most symmetrical. From regular closed systems $\{A_i, N\}$, where N is the number of indistinguishable Coulomb particles, the simplest stable system in the field of the potential $U(r)$ is apparently a dimer $\{A_1, N = 2\}$, where N is exactly the number of elements in the first period. Groups with a small number of particles remain in the attractive field at larger radii r than the groups with a large number of particles. Therefore, the systems $\{A_i\}$ with different N will be spatially separated.

The equivalent vertices of a regular simplex—the simplest polyhedron in space [3]—correspond to the simplest regular system of particles and the global minimum of its potential. The number of points equal to the number of simplex fix a sphere in this space. Therefore, the number of particles in the system $\{A_{i+1}\}$ will be equal to the number of particles in the system $\{A_i\}$ plus four particles fixing a new sphere. The sequence of values of N in these systems forms an infinite series: 2, 6, 10, 14, …. The periodic table limits this series to the first four terms.

1063-7745/05/5005-0715$26.00 © 2005 Pleiades Publishing, Inc.

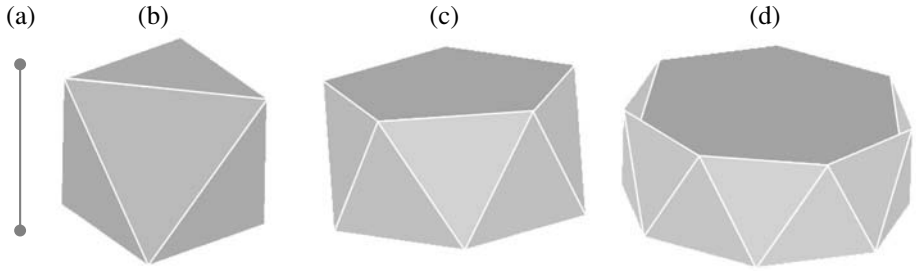

Fig. 1. Antiprisms in 3D space (octahedra in (a) 1-, (b) 3-, (c) 5-, and (d) 7-dimensional spaces), whose vertices model stable systems of 2, 6, 10, and 14 equivalent electrons of *l* shells in the periodic table.

We can suggest that the limitation of the number of the most stable systems $\{A_i\}$ to four is also related to the dimension factor. The ends of the radii of the spheres of the *l* shells in this set in 3D space fix the total sphere of 32 particles—the simplest and the most stable sum of the *l* shells. The number of shells limits also the number of types of periods in the periodic table: the first period corresponds to the filling of the *s* shell; the second and third periods correspond to the filling of the *s* and *p* shells; the fourth and fifth periods correspond to the filling of the *s*, *p*, and *d* shells; and the sixth and seventh periods correspond to the filling of the *s*, *p*, *d*, and *f* shells.

Owing to the central symmetry of the potential $U(r)$ and the correspondence of the minimum of repulsion of identical Coulomb particles to inversion (the latter generally leads to larger distances between particles than a reflection in plane or a rotation around a twofold axis), the systems $\{A_i\}$ should be centrosymmetric.

From the bodies whose vertices correspond to stable systems $\{A_i\}$ on a sphere, i.e., 5 regular Platonic bodies (all faces, edges, and vertices are identical) and three groups of semiregular bodies (equivalent vertices and edges but not all faces identical), specifically, a set of 14 Archimedean bodies and 2 infinite series of prisms and antiprisms [4, 5], it is the series of antiprisms that exhibit central symmetry and satisfy the conditions $\{A_1, N = 2\}$, $\{A_{i+1}, N_{i+1} = N_i + 4\}$ [1] (Fig. 1).

If the arrangement of particles somewhere corresponds to the lowest energy, they will be arranged in the same way in another place [6]. Thus, $\{A_i\}$ systems and their sequence will be repeated with an increase in the number of particles *N* and the radius *r*.

The arrangement of particles in a regular system of points is related to the optimization of their potential and implemented under the action of the potential gradient since the gradient becomes zero only at points of a regular system [7].

In the quantum model of atom, the potential of its many-electron system is constructed in the $2(2l + 1)$-dimensional space since each value of the potential corresponds to a certain distribution of electrons over $2l + 1$ vectors of coordinate space and two vectors $(\pm 1/2)$ of spin space. Here, *l* is the orbital momentum of an electron, which is an integer in *h* units. Therefore, a definite value of the projection of *l* on an isolated axis $m_1 = 2l + 1$ is juxtaposed to each vertex of the antiprism base. One of the antiprism bases is juxtaposed to the spin-up space and the other base is juxtaposed to the spin-down space [1]. The antiprisms are composed of *N*/2 dimers, which are transformed into each other in inversion, rotation, and inversion rotation operations. Therefore, another analogy can be used: as well as a dimer, an electron pair with a compensated spin serves as a forming pair (closed or ESR pair in quantum theory [8, 9]).

EQUIVALENCE OF PARTICLES IN *l* SHELLS AND OCTAHEDRA OF ODD-DIMENSIONAL SPACES

The bases of a dimer and of trigonal, pentagonal, and heptagonal antiprisms are regular simplices of zero-, two-, four-, and six-dimensional spaces. Antiprisms, as pairs of regular simplices sharing an inversion center, are at the same time octahedra of odd-dimensional spaces with dimensions of 1, 3, 5, and 7.

The odd dimensionality of the octahedra is caused by the fact that inversion performed *k* times is equivalent to unit operation at even *k* and single inversion at odd *k*. Therefore, if a straight line is an odd-fold inversion axis, it is simultaneously a rotary axis of the same order and its singularity is an inversion center. For example, the presence of a fivefold axis and a center of symmetry in a pentagonal antiprism is a necessary and sufficient condition for the existence of a fivefold inversion axis. However, the reverse statement is valid only for odd-fold axes [10]. Thus, absolute indistinguishability of all particles occurs when the number of vertices in antiprism bases is odd.

In the quantum model *l* shells, the coordinate space is odd-dimensional since at integer *l* the value of $m_1 = 2l + 1$ is odd. Even dimension of m_1 corresponds to the *j* coupling, at which the spin–orbit interaction in a particle is stronger than the interaction of the particle with the centrosymmetric field. Then, the total momentum of the particle $j = l + 1/2$ and the number of equivalent particles $N = 2j + 1$ acquire the values of the entire series of even numbers. It can be seen easily that the

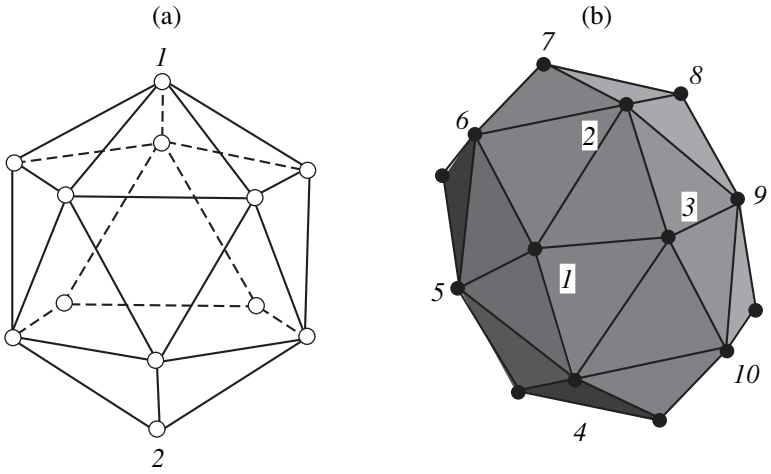

Fig. 2. Examples of combinations of antiprisms: (a) icosahedron—a combination of a dimer (points *1*, *2*) and a pentagonal antiprism (other points)—and (b) 20-vertex polyhedron—a combination of a trigonal antiprism (points *1–3*, vertices of the same base) and a heptagonal antiprism (points *4–10*, vertices of the same base).

momentum j and the momenta l and s can be transformed differently in symmetry operations. For example, a given value of j may arise from the states with $l = j - 1/2$ or $l = j + 1/2$. However, the states with these values of l, differing in parity $(-1)^l$, are differently transformed at inversion.

Pure j coupling is not implemented in an unexcited atom. However, upon strong excitation and filling of nl shells with high values n and l, which are located at large distances from the atomic core [11], a j electron retains its momentum in such a shell. This type of j coupling characterizes the relationship between interactions in the nucleons of an atom. Indeed, some nuclear shells are composed of 8, 12, 32, … nucleons. Such states (for example, $1f_{7/2}$, which contains 8 nucleons) are singled out into a separate stable group [12]. Owing to the different signs of the forces acting between particles of different types (attraction between nucleons and repulsion between electrons), their shells model different polyhedra: prisms and antiprisms in the first and second cases, respectively. Note that the projections of the prisms on the plane coincide with the orbits of nucleons in the semiclassical theory [13].

OPTIMAL POLYHEDRA OF *d* AND *f* SHELLS IN 3D SPACE

Let us consider the arrangement of particles in the vertices of the regular and semiregular polyhedra listed above. Obviously, the locations in the vertices of regular Platonic bodies correspond to the deepest minima of the potential of $\{A_i\}$ systems in 3D space. For example, the vertices of antiprisms in general satisfy the condition of global minimum. This condition is necessary but not sufficient since the edges of antiprisms are not necessarily equal to each other. However, a dimer and a trigonal antiprism coincide with regular octahedra of one-dimensional (1D) and 3D spaces, respectively, and the potential minimum has a global character in plane and in the volume of 3D space. In contrast, pentagonal and heptagonal antiprisms are only projections of the octahedra of five- and seven-dimensional spaces onto this space.

Thus, according to the crystallographic model, the minimum of the potential of *d* and *f* shells in 3D space is less stable than that of *s* and *p* shells, which provides an opportunity for additional minimization of the potential in this space [14]. The electrons of *d* and *f* shells can be included into a system of points of higher symmetry that is common with another shell—the system of vertices of one of centrosymmetrical Platonic bodies. Another possible way is to include these electrons into the system of vertices of a polyhedron with a large number of stabilizing bonds but only similar to a sphere in shape, as in the case of cluster structures [15]. Indeed, inclusion of ten electrons of the *d* shell into the system of vertices of an icosahedron, which is common with two electrons of the *s* shell (Fig. 2a), will increase the stability of the *d* shell in 3D space. Note that the icosahedron itself is a combination of a dimer and a pentagonal antiprism [2]. An example of a stabilizing polyhedron in the case of *d* and *f* shells is a convex polyhedron with 24 vertices, which is constructed in the same way as the polyhedron 20*A* in [15] (Fig. 2b), i.e., by aligning the $N/2$-fold rotary axes of pentagonal and heptagonal antiprisms.

According to the periodic table, the smaller depth of the potential minimum of *d* shells is explained by the fact that not only the *np* shell but also the $(n + 1)s$ shell are filled before the *nd* shell, where n is the principal quantum number. Similarly, the *np* and $(n + 1)s$ shells are filled before the $(n - 1)f$ shell. The optimization of the potential of *d* and *f* shells is confirmed by the equality or close values of the energies of *s* and *d* shells in the

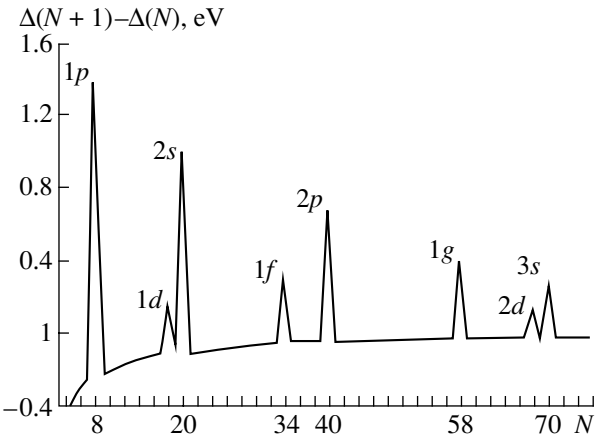

Fig. 3. Changes in the differences in the energy of electrons in clusters with $N + 1$ and N particles, depending on the number of particles (the mass-spectrometry data on clusters of Na ions [17]).

fourth and fifth periods and *d* and *f* shells in the sixth and seventh periods. For example, instead of the sequence of $d^N s^2$ configurations, we have the $d^{N+1}s$ or d^{N+2} configurations with a transition of an electron from an *s* to a *d* shell. Generally, the experimental spectra of atoms suggest that the energies of the nd^N, $nd^{N-1}(n + 1)s$, and $nd^{N-2}(n + 1)s^2$ configurations are close to each other and, in the case of some groups of elements or the spectra of singly ionized atoms, almost degenerate; furthermore, these groups of states can be assigned to the same shell: $n(d + s)^N$. The same violations of the filling regularity, as well as an electron transition, occur also in the case of $(n + 1)d$ and nf shells [12, 16]. Thus, the stability of *d* and *f* shells in the electron layer increases by the shell mixing. This mixing also facilitates the stabilization of the *s* shell, whose potential has a minimum only in a plane of 3D space.

The gradient of the potential, which results in mixing, is related to the weak noncentrosymmetric perturbation of the potential [16]. Note that this effect occurs in half-filled (d^5, f^7), filled (d^{10}, f^{14}), and related shells, for which the fivefold and sevenfold symmetries are maximally pronounced [2]. The approximate equality of the energies of *s* and *d* shells is clearly demonstrated in Fig. 3. This equality suggests that the above relationship can be retained in clusters at another type of pair interaction and the density of the medium.

STABILITY OF OCTAHEDRA

Only the vertices of a regular simplex, as the simplest polyhedron of $2l$-dimensional space, correspond to the simplest regular system and the global minimum of its potential. Therefore, the octahedron composed of a pair of simplices sharing an inversion center corresponds to the same characteristics in the centrosymmetric field of $(2l + 1)$-dimensional space.

For example, the simplex of two-dimensional (2D) space is a triangle, and, in the case of a three-atom cluster, the planar triangular structure with the D_{3h} symmetry is the most stable [18]. In 3D space, the octahedron—the simplest polyhedron of the centrosymmetric nonprimitive Platonic bodies, that is, the octahedron and icosahedron—is characterized by stability at a change in the parameters of the potential. The average number of bonds $K = E/N$, where E is the number of bonds (edges) converging to the same vertex (pairwise compensated for the octahedron), is maximum for nonprimitive polyhedra, that is, antiprisms ($K = 2$) and icosahedron ($K = 2.5$), and minimum for primitive polyhedra, that is, tetrahedron, cube, and dodecahedron ($K = 1.5$).

The fact that the potential minimum in the case of the octahedron is deeper than, for example, that in the case of the cube (next in N, centrosymmetrical but primitive polyhedron), is confirmed by theoretical and experimental data on the coordination polyhedra in crystals and structures of clusters of metals and inert gases [5, 15, 17–20]. The octahedral structure is so stable that a change in the parameters of the potential does not lead to isomerization. However, even at $N = 7$, the structure of the optimal isomer exhibits this dependence. Note that the global minimum of the potential in the case of the octahedron is implemented in two components of the potential. For *l* electrons, the main component is the summary field formed by the charge of the nucleus and the distributed charge of other electrons. In the next approximation, the potential is determined also by the repulsion between electrons. The existence of the global minimum of the first component follows, for example, from the relationship between the quantities *Dq*—the crystal-field components formed by octahedrally, cubically, or tetrahedrally coordinated ligands at the center of the polyhedron: $|Dq_{oct}| > |Dq_{cub}| > |Dq_{tet}|$. The existence of the global repulsion minimum follows from the fact that the distances between the vertices of a polyhedron inscribed in a sphere are maximum when all polyhedron faces are triangular. For example, the repulsion potential for particles located in the vertices of a cube is so high that cubic polyhedra (in contrast to octahedral ones) rarely occur in coordination compounds [5, 21].

DISCUSSION

Obviously, other discrete systems should have a shell structure in a centrosymmetric potential field. They include conglomerates in the intermediate state between individual atoms and crystals. The shell structure of these conglomerates manifests itself in the periodicity of their stability: clusters, containing a small number of particles, are followed by nanoparticles (large aggregates of atoms). Moreover, attempts have

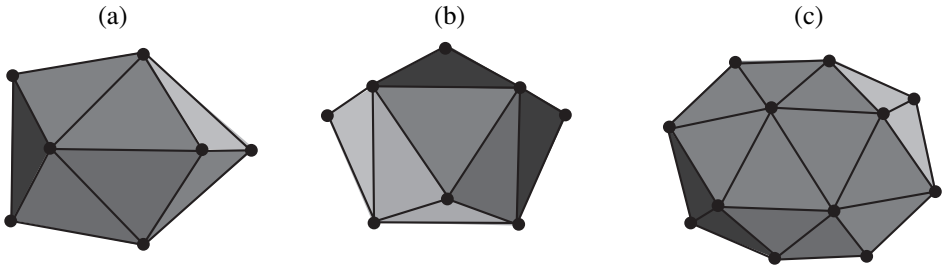

Fig. 4. Examples of structures of clusters composed of (a) 8, (b) 9, and (c) 18 particles [15].

been made to construct electronic and structural tables of clusters and nanoparticles of chemical elements by analogy with the periodic table [13]. However, the 3D nature of space maximally manifests itself in the sublevels of the periodic table, including the shell structure, since in this case particles are not localized at the center of polyhedra and the medium has zero viscosity. In these characteristics, an electron cloud corresponds to an electron gas in a spherical cavity with rigid walls, whereas a nucleus corresponds to a liquid. Clusters and nanoparticles correspond to systems of particles in a jellylike medium [13]. The limited length of the particle–particle attraction and the high density of space filling leads in the case of clusters or nanoparticles to the localization of particles not only in the vertices and the center but also on the faces and edges of polyhedra [22]. This arrangement does not correspond to the simplest systems $\{A\}$ related to space simplices. Moreover, the same numbers of particles can form different shells of clusters, corresponding to the vertices of different polyhedra [23]. For these reasons, the properties of our real 3D space do not manifest themselves in the structures of clusters and nanoparticles as clearly as in the case of *l* shells of atoms.

The crystallographic model of *l* shells supplemented the quantum model for explanation of a number of structural and physical properties of crystals and noncrystalline media [2, 14]. A striking example is the efficiency of laser crystals activated by *d* and *f* ions. The existence of long-lived metastable states and the similarity of the absorption spectra of unexcited and excited crystals activated by d^2, d^3, and f^3 ions was explained by the fact that the ground state of an activator and its excited states with spin flip of one electron are spatially equivalent in the crystal field [14]. High-quality crystals with these activators can be more easily obtained since the shells of the activators are also characterized by the maximum matching between the intrinsic "noncrystallographic" symmetry (five- and sevenfold axes) and the translational symmetry of a crystal. Indeed, the first crystals in which tunable narrow-band lasing was obtained were activated by only such ions [14].

Apparently, the results of this study are not only of methodological interest. As an example, we can point to the structures of clusters and nanocrystals. The structures of small clusters cannot be investigated directly and are thus calculated. The presence of 1D, 2D, and 3D octahedra in the calculated optimal structures of small clusters and combinations of these octahedra with pentagonal and heptagonal antiprisms in larger clusters (Figs. 2, 4) results from the fact that antiprisms correspond to the most stable groups with small numbers of particles. The occurrence of noncentrosymmetric and centrosymmetric forms of nanocrystals of copper and other metals (Fig. 5) [24, 25] can be explained by the manifestation of different relationships between the interaction in the $Cu^{2+}(d^9)$–$Cu^{+}(d^{10})$ pair (for Cu nanocrystals) and the interaction with the self-consistent field. This difference is due to different crystallization conditions.

Note, for structural units sharing an oriented bond, the spatial factor manifests itself in repeated orbitals in the form of a helical structure, as in protein macromolecules (filamentary, rodlike, tubular). In addition, the principle of hierarchy and small number of elements is also valid in living systems. Molecular biostructures are also characterized by four levels of structural organization [25]. This number is equal to the number of periods of different types in the periodic table. The structures of protomolecules (the first level) form only two types (biological "dimer"). In the structures of the first type (amino acids), a carbon atom is tetrahedrally coordinated (over four vertices of the simplex of 3D space) by hydrogen atoms and hydrogen-containing groups. In the structures of the second type (nucleotides), the same "magic" number is the number of types of pyrimidine or purine bases entering nucleotides.

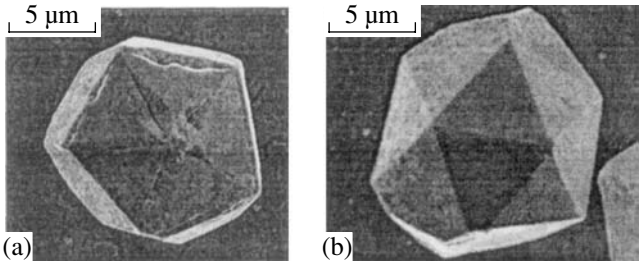

Fig. 5. Copper nanocrystals shaped as (a) a double-capped pentagonal prism and (b) an icosahedron [25].

CONCLUSIONS

In the crystallographic model, the dimension and isotropy of real 3D space and the indistinguishability of electrons manifest themselves in the formation of sublevels of the periodic table (in particular, in the minimum number of components in each sublevel) and in the principle of hierarchy. These manifestations follow from the properties of a simplex—the simplest space polyhedron. The number of simplex vertices also fixes a sphere in space.

In 3D space, the spherical surface is fixed by four points. Owing to this circumstance, the number of electrons in each member of the series of l shells is equal to their number in the previous shell plus four electrons fixing a new sphere. Thus, the dimension of real 3D space determines the increment in the number of electrons in l shells, which is equal to four electrons. Apparently, the dimension factor limits the number of l shells in the periodic table to four. This number of l shells also limits the number of types of periods in the periodic table to four.

A series of simplices of $2l$-dimensional spaces (i.e., with dimensions of 0, 2, 4, and 6) is juxtaposed to the series of l shells. Since simplices correspond to the simplest systems of equivalent particles in $2l$-dimensional spaces and the global minimum of their potential, octahedra, as well as pairs of simplices sharing an inversion center, have the same properties in $(2l + 1)$-dimensional spaces. Owing to the central symmetry of the potential, the simplest and initially stable system is a dimer. For shells with a large number of electrons, owing to the periodicity of four electrons, only odd-dimensional octahedra are implemented. Thus, finally, the odd dimensionality of octahedra is also the result of the isotropy and three-dimensional nature of space and the indistinguishability of electrons.

In contrast to octahedra of s and p shells, whose vertices correspond to the global minima of the potential of particles in plane and volume of 3D space, d and f shells are modeled by octahedra of high-dimensional spaces. Optimization of the spatial arrangement of electrons of d and f shells in 3D space occurs through shell mixing.

Thus, the beginning of each period corresponds to the global minimum of the potential of the regular system of electrons in the plane of 3D space (s shells), the middle of the period corresponds to the expansion of the potential minimum to the volume of 3D space (d and f shells), and the end of the period corresponds to the global minimum in the volume of 3D space (p shells). These features manifest themselves in the properties of chemical elements.

The dimension of our space also manifests itself in the organization of molecular biostructures.

ACKNOWLEDGMENTS

I am grateful to R.V. Galiulin for helpful discussions.

REFERENCES

1. T. F. Veremeĭchik and R. V. Galiulin, Kristallografiya **49** (5), 935 (2004) [Crystallogr. Rep. **49**, 847 (2004)].
2. T. F. Veremeĭchik and R. V. Galiulin, Kristallografiya **49** (6), 983 (2004) [Crystallogr. Rep. **49**, 887 (2004)].
3. N. N. Medvedev, *Voronoi–Delone Method in Investigation of the Structure of Noncrystalline Systems* (Sib. Otd. Ross. Akad. Nauk, Novosibirsk, 2000) [in Russian].
4. R. V. Galiulin, Usp. Fiz. Nauk **172** (2), 229 (2002) [Phys. Usp. **45**, 221 (2002)].
5. L. A. Aslanov, *Structure of Atoms, Molecules, Crystals* (Mosk. Gos. Univ., Moscow, 1985) [in Russian].
6. R. P. Feynman, R. B. Leighton, and M. Sands, *The Feynman Lectures on Physics* (Addison-Wesley, Reading, Mass., 1966; Mir, Moscow, 1966), Vol. 7.
7. R. V. Galiulin and S. E. Sigarev, Dokl. Akad. Nauk SSSR **293** (1), 99 (1987) [Sov. Phys. Dokl. **32**, 173 (1987)].
8. D. T. Sviridov and Yu. F. Smirnov, *Theory of Optical Spectra of Transition-Metal Ions* (Nauka, Moscow, 1977) [in Russian].
9. I. V. Bargatin, B. A. Grishanin, and V. N. Zadkov, Usp. Fiz. Nauk **171** (6), 625 (2001) [Phys. Usp. **44**, 597 (2001)].
10. P. M. Zorkiĭ, *Symmetry of Molecules and Crystal Structure* (Mosk. Gos. Univ., Moscow, 1986) [in Russian].
11. G. V. Golubkov and G. K. Ivanov, *Rydberg States of Atoms and Molecules and Elementary Processes with Their Participation* (Éditorial URSS, Moscow, 2001) [in Russian].
12. L. D. Landau and E. M. Lifshitz, *Course of Theoretical Physics*, Vol. 3: *Quantum Mechanics: Non-Relativistic Theory*, 3rd ed. (Nauka, Moscow, 1974; Pergamon, New York, 1977).
13. S. Bjornholm, Contemp. Phys. **31** (5), 39 (1990).
14. T. F. Veremeĭchik, in *Applied Geometry, Construction of Calculation Grids, and High-Efficiency Calculations* (Izd. Vych. Tsentra RAN, Moscow, 2004), p. 197 [in Russian].
15. J. P. K. Doye and D. J. Wales, J. Chem. Phys. **103** (10), 4234 (1995).
16. I. I. Sobel'man, *Introduction into Theory of Atomic Spectra* (GIFML, Moscow, 1963; Oxford University Press, Oxford, 1972).
17. W. D. Knight, K. Clemenger, W. A. Heer, *et al.*, Phys. Rev. Lett. **52** (24), 2141 (1984).
18. G. B. Sergeev, *Nanochemistry* (Mosk. Gos. Univ., Moscow, 2003) [in Russian].
19. K. Sudzuki, H. Fudzimori, and K. Hasimoto, *Amorphous Metals* (Metallurgiya, Moscow, 1987) [in Russian].
20. M. S. Stave and A. E. DePristo, J. Chem. Phys. **97** (5), 3386 (1992).
21. L. A. Aslanov, *Structures of Materials* (Mosk. Gos. Univ., Moscow, 1989) [in Russian].
22. B. M. Smirnov, Usp. Fiz. Nauk **171** (12), 129 (2001).
23. U. Naher, U. Zimmermann, and T. R. Martin, J. Chem. Phys. **99** (3), 2256 (1993).
24. A. Di. Cicco, A. Tarapanant, S. Faggiony, *et al.*, Phys. Rev. Lett. **91** (135), 505 (2003).
25. A. M. Glezer, private communication.
26. B. K. Vaĭnshteĭn, *Problems of Crystallography* (Nauka, Moscow, 1987) [in Russian].

Translated by Yu. Sin'kov

Crystallography Reports, Vol. 50, No. 5, 2005, pp. 721–726. Translated from Kristallografiya, Vol. 50, No. 5, 2005, pp. 782–787.

THEORY OF CRYSTAL STRUCTURES

Sublattices in Crystals

A. S. Poplavnoĭ and A. V. Silinin

Kemerovo State University, ul. Krasnaya 6, Kemerovo, 650043 Russia

e-mail: popl@kemsu.ru

Received March 30, 2004

Abstract—A method of representation of a crystal structure as a set of its constituent Bravais sublattices is developed. The conditions for compatibility of sublattices related to the same or different systems are formulated and the connection matrices for primitive parallel-translation vectors of the crystal lattice and the sublattices are determined. A method of alignment of the first Brillouin zones of the sublattices with the first Brillouin zone of the crystal is described. It is shown that alignment may lead to quasi-degeneration of the energy levels in the case of weak hybridization of the sublattice states. A relationship between the sublattice method and the method of an extended unit cell is established. © *2005 Pleiades Publishing, Inc.*

1. INTRODUCTION

In any complex crystalline compound, parallel-translation sublattices corresponding to the Bravais lattices can be selected. Each of these sublattices contains equivalent atoms of the same chemical element in its sites. It is expedient to select sublattices with minimum periods. It is obvious that in this case the number of sublattices will not be smaller than the number of chemical elements entering the crystal composition, since identical atoms may occupy symmetrically nonequivalent positions and enter different sublattices. Selection of sublattices is reasonable because their number and combination determine the physicochemical properties of crystals. For example, the donor and acceptor conductivities are related to different sublattices. The ionic conduction, chemical reactions, and many other processes are often due to a particular sublattice, whereas the other sublattices play the role of a framework or a catalyst.

In [1, 2], a new approach to the study of chemical bonding and electronic structure in predominantly ionic and ionic–molecular crystals was developed on the basis of the sublattice method and radically new features of chemical bonding related to the translational and point symmetry of sublattices were established. If the same Bravais lattice corresponds to the cation and anion sublattices, the chemical bonding between them is formed via the ionic mechanism. If Bravais lattices of different types correspond to the cation and anion sublattices, their alignment of the sublattices leads to the occurrence of maxima of valence electron density in interstitial sites and, as a result, to the formation of a covalently bonded anionic framework [3]. The role of the sublattices of noble metals in the formation of chemical bonding has also been established. In particular, it was shown that the charge transferred by a cation to an anionic plane in silver nitrite is so high that it manifests itself as an individual maximum. This circumstance allows us to speak about the formation of the anionic framework due to the cationic states [4]. To study the hybridization of sublattices, the concept of difference density (the result of the subtraction of the valence electron densities of the sublattices from the valence electron density of the crystal) was introduced. It was shown that the difference density is qualitatively similar to the traditionally used deformation density [4].

This study is organized as follows. In Section 2, the rules of the representation of crystal structures by parallel-translation sublattices corresponding to Bravais lattices are formulated. The conditions for the translational compatibility of the sublattices with the crystal lattice and the connection matrices for the primitive parallel-translation vectors of the crystal and those of the sublattices are found. The spatial arrangement of sublattices satisfies the requirements of invariance with respect to the crystallographic symmetry elements. In Section 3, the conditions for alignment of the first Brillouin zone of the crystal with the first Brillouin zones of the sublattices and the physical consequences caused by the difference between these Brillouin zones are discussed. In Section 4, the method developed is applied to crystals with the fluorite structure.

2. CONSTRUCTION OF CRYSTALS FROM SUBLATTICES

Let us denote the sets of primitive parallel-translation vectors of the crystal lattice Γ_L and the sublattice related to the Bravais lattice Γ_S, $\mathbf{a}_i(\Gamma_L)$ ($i = 1, 2, 3$) and $\mathbf{b}_j(\Gamma_S)$ ($j = 1, 2, 3$), respectively. These vectors can be related to each other as follows:

$$\mathbf{a}_i(\Gamma_L) = \sum_{j=1}^{3} (\Gamma_L|\Gamma_S)_{ij}\mathbf{b}_j(\Gamma_S). \quad (1)$$

We will refer to the matrix $(\Gamma_L|\Gamma_S)$ as the connection matrix for the primitive parallel-translation vectors of the lattice Γ_L and those of the sublattice Γ_S. For a sublattice to be invariant with respect to all elements of the group of parallel lattice translations, it is necessary and sufficient that all elements of the matrix $(\Gamma_L|\Gamma_S)$ be integers. Only in this case will a parallel lattice translation by any vector **n** equal to an integer linear combination of primitive parallel-translation vectors of the lattice, $\mathbf{a}_i(\Gamma_L)$, lead to the parallel translation of the sublattice by the same vector **n** (now equal to an integer linear combination of primitive parallel-translation vectors of the sublattice, $\mathbf{b}_j(\Gamma_S)$). This circumstance actually has the meaning of the invariance of the sublattice with respect to all elements of groups of parallel translations of both the lattice and sublattices.

Each type of Bravais lattices has its own set of primitive parallel-translation vectors. It is necessary to analyze all types of Bravais lattices in order to reveal all possible sublattices satisfying the translational symmetry of a given lattice. Note that the sublattices and the crystal lattice may belong either to the same or to different systems.

Let us introduce the matrices $\hat{a}(\Gamma_L)$ and $\hat{b}(\Gamma_S)$ consisting of the components of the primitive parallel-translation vectors of the lattice and sublattice, respectively. The first and second indices denote the number of the vector and the component of this vector, respectively:

$$\hat{a}(\Gamma_L) = \begin{pmatrix} a_{1x} & a_{1y} & a_{1z} \\ a_{2x} & a_{2y} & a_{2z} \\ a_{3x} & a_{3y} & a_{3z} \end{pmatrix}, \quad \hat{b}(\Gamma_S) = \begin{pmatrix} b_{1x} & b_{1y} & b_{1z} \\ b_{2x} & b_{2y} & b_{2z} \\ b_{3x} & b_{3y} & b_{3z} \end{pmatrix}. \quad (2)$$

Using these matrices, we can rewrite relation (1) in the form

$$\hat{a}(\Gamma_L) = (\Gamma_L|\Gamma_S)\hat{b}(\Gamma_S) \quad (3)$$

to obtain the expression for the matrix $(\Gamma_L|\Gamma_S)$:

$$(\Gamma_L|\Gamma_S) = \hat{a}(\Gamma_L)\hat{b}^{-1}(\Gamma_S), \quad (4)$$

where $\hat{b}^{-1}(\Gamma_S)$ is the matrix inverse to the matrix $\hat{b}(\Gamma_S)$.

Thus, to solve the problem stated, we have to specify sets of primitive parallel-translation vectors of the lattice and the sublattice, write matrices (2), and derive the matrix $(\Gamma_L|\Gamma_S)$ from (4). Then, all elements of the matrix $(\Gamma_L|\Gamma_S)$ should be integers, which will impose limitations on the components of the primitive parallel-translation vectors $\mathbf{b}_j(\Gamma_S)$ of the sublattice. Thus, we will find the sublattices compatible with the translational symmetry of the given lattice.

A set of constituent sublattices of the crystal should also satisfy the requirements of point symmetry. The reference point of each sublattice is shifted by vector $\mathbf{c}(\Gamma_S)$ from the common center of the crystal. Under the action of the elements of the symmetry space group of the crystal, these vectors should pass to equivalent positions:

$$\hat{h}_\alpha \mathbf{c}(\Gamma_S) + \boldsymbol{\tau}_\alpha = \mathbf{c}'(\Gamma_S) + \sum_{j=1}^{3} n_j^{(\alpha)} \mathbf{b}_j(\Gamma_S), \quad \alpha = 1, 2, \ldots, N, \quad (5)$$

where $\hat{h}_\alpha$ is the αth point element of the symmetry space group of the crystal, which is composed of N elements; $\boldsymbol{\tau}_\alpha$ is the corresponding fractional parallel translation for a nonsymmorphic group; and $n_j^{(\alpha)}$ is a set of integers corresponding to each αth element. The term $\mathbf{c}'(\Gamma_S)$ coincides with either $\mathbf{c}(\Gamma_S)$ or the reference point of a symmetrically equivalent sublattice. Successively analyzing all elements of the symmetry group of the crystal in relation (5), we determine the spatial arrangement of the sublattices that is compatible with this symmetry. The technique described makes it possible to find for any crystallographic symmetry group a set of compatible sublattices and determine their spatial arrangement.

When finding the matrices $(\Gamma_L|\Gamma_S)$, one has to take into account the symmetry hierarchy of the systems. A system G_0' is referred to as subordinated to the system G_0 ($G_0 \longrightarrow G_0'$) if the symmetry group G_0' is a subgroup of the group G_0 ($G_0' \subset G_0$) and any (of all possible) lattices of the system G_0 can be transformed by a small distortion into one of the lattices of the system G_0'. The hierarchy of systems can be schematically written as [5]

$$\begin{array}{ccccccc} & & & & D_{6h} & & \\ & & & & \downarrow & & \\ O_h & \longrightarrow & D_{4h} & \longrightarrow & D_{2h} & \longrightarrow & C_{2h} \longrightarrow S_2. \\ \downarrow & & & & & & \uparrow \\ \multicolumn{5}{c}{\longrightarrow D_{3d}} & & \end{array} \quad (6)$$

Actually, the conditions for the translational compatibility of sublattices imply the multiplicity of their periods to the periods of a given lattice. The formally written connection matrixes, with limitations imposed on the sublattice parameters, include, in particular, cases of transfer of a sublattice to a higher system in scheme (6). Analysis of all situations, according to the hierarchical scheme (6), is somewhat cumbersome and is the subject of another of our papers, which is being prepared for deposition.

In the Appendix, we give as an example the connection matrices providing the translational compatibility of crystals having simple and body-centered tetragonal lattices with sublattices of other systems. The designations of the Bravais lattices and the primitive parallel-

translation vectors used to calculate the matrices are chosen according to [6]. The quantities a and a_z are the spatial lattice periods; b, b_x, b_y, b_z, and β are the geometric parameters of the sublattices; and n, m, l, and k are integers.

3. FIRST BRILLOUIN ZONES OF THE CRYSTAL LATTICE AND SUBLATTICES

The Wigner–Seitz cell of a crystal lattice includes the Wigner–Seitz cells of all sublattices; therefore, the volume of its first Brillouin zone of the crystal lattice is either smaller or equal to the total volume of the first Brillouin zones of all sublattices. In this case, the largest is the first Brillouin zone of the sublattice with the smallest volume of the Wigner–Seitz cell. Let us denote the sets of primitive parallel-translation vectors of the crystal and the sublattices as $\mathbf{A}_i(\Gamma_L)$ (i = 1, 2, 3) and $\mathbf{B}_j(\Gamma_S)$ (j = 1, 2, 3), respectively. The vectors of these sets are related to each other by the expressions of type (1). Since the reciprocal lattices are represented by the same 14 Bravais lattices, the connection matrices for $\mathbf{A}_i(\Gamma_L)$ and $\mathbf{B}_j(\Gamma_S)$ turn out to be similar to $(\Gamma_L|\Gamma_S)$. The only thing that should be taken into account is the correspondence between the direct and reciprocal lattices (for example, for a fcc lattice, the Wigner–Seitz cell is a rhombododecahedron and the first Brillouin zone is a Fedorov cuboctahedron). Since all sublattices are translationally compatible with the crystal lattice, their first Brillouin zones can be transformed into the first Brillouin zone of the crystal. The wave vectors $\mathbf{k}_j(\Gamma_S)$, lying in the first Brillouin zones of the sublattices, are transformed into the vectors $\mathbf{k}_j(\Gamma_L)$ of the first Brillouin zone of the crystal according to the relation

$$\mathbf{k}(\Gamma_L) = \mathbf{k}(\Gamma_S) + \sum_{i=1}^{3} n_i(\Gamma_L, \Gamma_S)\mathbf{A}_i(\Gamma_L), \qquad (7)$$

where $n_i(\Gamma_L,\Gamma_S)$ are integers.

When the first Brillouin zones of the sublattices are transformed into the first Brillouin zone of the crystal, one has to take into account the point symmetry, which may be higher for a sublattice than for the crystal. In this case, the combinatorial symmetry classification of the first Brillouin zones [7] turns out to be very useful. Furthermore, the irreducible representations of the sublattice symmetry groups are expanded in irreducible representations of the crystal symmetry group. The starting point in this procedure is the establishment (using relation (7)) of the correspondence between the irreducible stars of the lattice and sublattice representations. Then, the irreducible representations of the groups of wave vectors are expanded. If the method developed here is applied to the band theory, the calculated energy spectrum of a sublattice is assigned to the first Brillouin zone of the crystal. In this case, the following situations may occur. When the point symmetry group of a sublattice is higher than that of the crystal, the energy spectrum of the sublattice may contain degeneracies that are absent in the crystal lattice. Allowance for the hybridization between sublattices removes all these degeneracies. However, if the sublattice hybridization is small, the splittings are also small and we can speak about quasi-degeneration caused by the highest point symmetry of a particular sublattice. Quasi-degeneration may also occur when the crystal and a sublattice have identical point but different translational symmetries. Since the group of parallel translations of the crystal lattice is generally a subgroup of the group of parallel sublattice translations, the reconstruction of the first Brillouin zones leads to the convolution of the sublattice energy spectrum to the first Brillouin zone of the crystal. This circumstance leads to degeneracies, which are also removed owing to the sublattice hybridization.

Let us compare the sublattice method formulated by us with the method of an extended unit cell [8], which is used to simulate periodic point defects. The analogy between these methods is that the construction of an extended unit cell is in fact similar to the method of construction of a crystal from sublattices. However, there is a significant difference: extended unit cells are constructed only within one system, whereas sublattices may belong to different systems. A method of generation of special points, based on the method of an extended unit cell, was developed in [8]. Note that such a procedure can also be used within the sublattice method, not only to generate sets of special points but also to determine the relations between special points of different systems.

4. CRYSTALS WITH THE FLUORITE STRUCTURE

In the simplest cases, crystals can be constructed from identical Bravais sublattices. Examples are the well known crystals diamond and sphalerite, which are composed of two fcc sublattices shifted with respect to each other by a quarter of the body diagonal of the cube; crystals with the NaCl structure, composed of two fcc sublattices shifted by a half edge of the cube; and crystals with the CsCl structure, formed by two primitive cubic sublattices, one of which has a sublattice coinciding with the centers of cubes of the other sublattice.

A more complicated situation occurs in AB_2 crystals, for example, in compounds with the fluorite and antifluorite structures. For example, a crystal with the fluorite structure has an fcc lattice. In this case, cations occupy sites of the fcc sublattice with the parameter a: $\mathbf{a}_1$ = (0, a/2, a/2), $\mathbf{a}_2$ = (a/2, 0, a/2), and $\mathbf{a}_3$ = (a/2, a/2, 0). Anions are located in the sites $\mathbf{b}_1$ = (a/2, 0, 0), $\mathbf{b}_2$ = (0, a/2, 0), and $\mathbf{b}_3$ = (0, 0, a/2) of the primitive cubic sublattice with the parameter a/2, which is shifted with respect to the cation sublattice by a quarter of the body

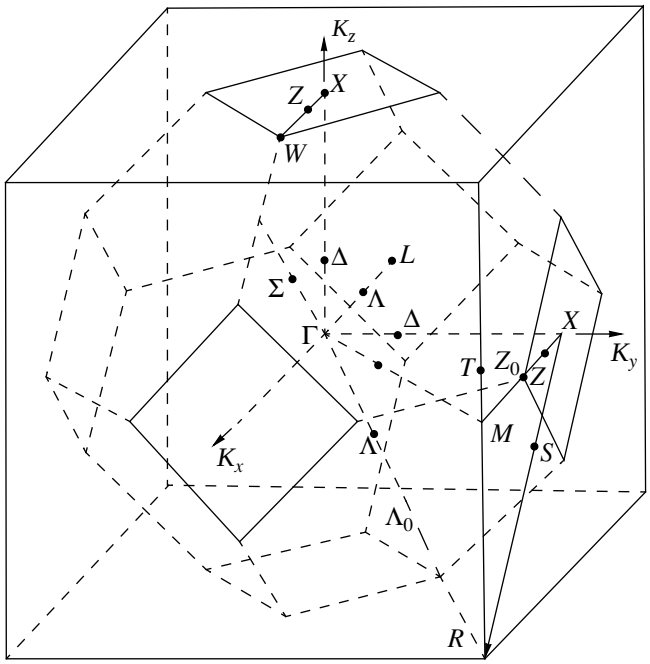

The first Brillouin zone of a crystal with the fluorite structure, located in the first Brillouin zone of the anion sublattice.

diagonal of the cube: **c** = (*a*/4, *a*/4, *a*/4). Thus, a crystal with this structure can be considered to be constructed from two different Bravais sublattices: fcc and primitive cubic sublattices.

The connection matrix for the primitive parallel-translation vectors of the sublattices has the form

$$(\Gamma_c^f \big| \Gamma_c) = \begin{pmatrix} 0 & 1 & 1 \\ 1 & 0 & 1 \\ 1 & 1 & 0 \end{pmatrix}. \quad (8)$$

The anion sublattice can also be represented by two fcc sublattices, similar to the cation sublattice, with reference points shifted by 1/4 and 3/4 of the body diagonal. Thus, it can be seen that the choice of sublattices in crystals is not always an unambiguous procedure. A particular representation can be convenient, depending on the problem to be solved. On the basis of the principle of the minimum number of sublattices, it is expedient to consider the lattice of a crystal with the fluorite structure as composed of an fcc cation sublattice and a primitive cubic anion sublattice.

Let us now consider the first Brillouin zones of the cation and anion sublattices of the crystals under consideration. The primitive parallel-translation vectors of the lattice reciprocal to the crystal lattice (in $2\pi/a$) units) will be written as $\mathbf{A}_1 = (-1, 1, 1)$, $\mathbf{A}_2 = (1, -1, 1)$, and $\mathbf{A}_3 = (1, 1, -1)$. The primitive parallel-translation vectors of the lattice reciprocal to the anion sublattice (in the same units) have the form $\mathbf{B}_1 = (2, 0, 0)$, $\mathbf{B}_2 = (0, 2, 0)$, and $\mathbf{B}_3 = (0, 0, 2)$. The volume of the first Brillouin zone of a crystal with the fluorite structure is smaller by a factor of 2 than the volume of first Brillouin zone of the anion sublattice. Figure shows both

Expansion of irreducible stars of the anion sublattice in irreducible stars of a crystal with the fluorite structure

Crystal lattice		Anion sublattice	
type of star	vectors of the star (in $2\pi/a$)	type of star	vectors of the star (in $2\pi/a$)
Γ	(0, 0, 0)	Γ R	(0, 0, 0) (1, 1, 1)
X	(0, 1, 0)	X M	(0, 1, 0) (1, 1, 0)
L	(1/2, 1/2, 1/2)	Λ_0	(1/2, 1/2, 1/2)
W	(1/2, 1, 0)	Z_0	(1/2, 1, 0)
Z	(2μ, 1, 0), –1/4 < μ < 1/4	Z	(2μ, 1, 0), –1/4 < μ < 1/4 (–1 + 2μ, 0, 1), 1/4 < μ < 1/2 (1 + 2μ, 0, 1), –1/2 < μ < –1/4
Δ	(0, 2μ, 0), –1/2 < μ < 1/2	Δ T	(0, 2μ, 0), –1/2 < μ < 1/2 (1, 1, 2μ), –1/2 < μ < 1/2
Λ	(μ, μ, μ), –1/2 < μ < 1/2	Λ	(2μ, 2μ, 2μ), –1/4 < μ < 1/4 (–1 + 2μ, –1 + 2μ, –1 + 2μ), 1/4 < μ < 1/2 (1 + 2μ, 1 + 2μ, 1 + 2μ), –1/2 < μ < –1/4
Σ	(2μ, 2μ, 0), –3/8 < μ < 3/8	Σ	(2μ, 2μ, 0), –3/8 < μ < 3/8 (–1 + 2μ, –1 + 2μ, 1), 3/8 < μ < 1/2 (1 + 2μ, 1 + 2μ, 1), –1/2 < μ < –3/8
		S	(2μ, 1, 2μ), –1/8 < μ < 1/8 (–1 + 2μ, 0, –1 + 2μ), 1/8 < μ < 1/2 (1 + 2μ, 0, 1 + 2μ), –1/2 < μ < –1/8

these Brillouin zones with the symmetric points and lines denoted according to [6]. Now we have to transfer the vectors of the Brillouin zone of the anion sublattice to the first Brillouin zone of the crystal using formula (7) or expand the irreducible stars of the wave vectors of the anion sublattice in irreducible stars of the wave vectors of the crystal. The results of this expansion are listed in the table.

It can be seen from the table that translational degeneracies, caused by the convolution of the band-energy spectrum of the anion sublattice, arise at the symmetric points and lines of the first Brillouin zone of the crystal. Indeed, the calculated valence-band energy spectrum of fluorite [9] consists of two closely located *s* bands and six weakly split *p* bands of fluorine, which were formed owing to the convolution of the valence states of fluorine from the Brillouin zone of the primitive cubic sublattice to the Brillouin zone of the fcc lattice.

APPENDIX

Connection matrices for the tetragonal lattices and sublattices of other systems:

Simple tetragonal lattice (Γ_q)

$$(\Gamma_q|\Gamma_c) = \begin{pmatrix} n & 0 & 0 \\ 0 & n & 0 \\ 0 & 0 & m \end{pmatrix}, \quad (\Gamma_q|\Gamma_c^f) = \begin{pmatrix} -n & n & n \\ n & -n & n \\ m & m & -m \end{pmatrix},$$

$$(\Gamma_q|\Gamma_c^v) = \begin{pmatrix} 0 & n & n \\ n & 0 & n \\ m & m & 0 \end{pmatrix}, \quad \begin{cases} n = a/b \\ m = a_z/b. \end{cases}$$

$$(\Gamma_q|\Gamma_q) = \begin{pmatrix} n & 0 & 0 \\ 0 & n & 0 \\ 0 & 0 & m \end{pmatrix},$$

$$(\Gamma_q|\Gamma_q^v) = \begin{pmatrix} 0 & n & n \\ n & 0 & n \\ m & m & 0 \end{pmatrix}, \quad \begin{cases} n = a/b \\ m = a_z/b_z. \end{cases}$$

$$(\Gamma_q|\Gamma_0) = \begin{pmatrix} n & 0 & 0 \\ 0 & m & 0 \\ 0 & 0 & l \end{pmatrix}, \quad (\Gamma_q|\Gamma_0^b) = \begin{pmatrix} n & -n & 0 \\ m & m & 0 \\ 0 & 0 & l \end{pmatrix},$$

$$(\Gamma_q|\Gamma_0^f) = \begin{pmatrix} -n & n & n \\ m & -m & m \\ l & l & -l \end{pmatrix},$$

$$(\Gamma_q|\Gamma_0^v) = \begin{pmatrix} 0 & n & n \\ m & 0 & m \\ l & l & 0 \end{pmatrix}, \quad \begin{cases} n = a/b_x \\ m = a/b_y \\ l = a_z/b_z. \end{cases}$$

$$(\Gamma_q|\Gamma_m) = \begin{pmatrix} n & -k & 0 \\ 0 & m & 0 \\ 0 & 0 & l \end{pmatrix},$$

$$(\Gamma_q|\Gamma_m^b) = \begin{pmatrix} n & -k & -k \\ 0 & m & m \\ 0 & -l & l \end{pmatrix}, \quad \begin{cases} n = a/(b_x\cos\beta) \\ m = a/b_y \\ l = a_z/b_z \\ k = a\tan\beta/b_y. \end{cases}$$

Body-centered tetragonal lattice (Γ_q^v)

$$(\Gamma_q^v|\Gamma_c) = \begin{pmatrix} -n & n & m \\ n & -n & m \\ n & n & -m \end{pmatrix}, \quad \begin{cases} n = a/(2b) \\ m = a_z/(2b). \end{cases}$$

$$(\Gamma_q^v|\Gamma_c^f) = \begin{pmatrix} n+m & m-n & -m \\ m-n & n+m & -m \\ -m & -m & n+m \end{pmatrix}, \quad \begin{cases} n = a/b \\ m = a_z/(2b). \end{cases}$$

$$(\Gamma_q^v|\Gamma_c^v) = \begin{pmatrix} m & m-n & 0 \\ m-n & m & 0 \\ n-m & n-m & n \end{pmatrix}, \quad \begin{cases} n = a/b \\ m = (a+a_z)/(2b). \end{cases}$$

$$(\Gamma_q^v|\Gamma_q) = \begin{pmatrix} -n & n & m \\ n & -n & m \\ n & n & -m \end{pmatrix}, \quad \begin{cases} n = a/(2b) \\ m = a_z/(2b_z). \end{cases}$$

$$(\Gamma_q^v|\Gamma_q^v) = \begin{pmatrix} m & m-n & 0 \\ m-n & m & 0 \\ n-m & n-m & n \end{pmatrix},$$

$$\begin{cases} n = a/b \\ m = a/(2b) + a_z/(2b_z). \end{cases}$$

$$(\Gamma_q^v|\Gamma_0) = \begin{pmatrix} -n & m & l \\ n & -m & l \\ n & m & -l \end{pmatrix}, \quad \begin{cases} n = a/(2b_x) \\ m = a/(2b_y) \\ l = a_z/(2b_z). \end{cases}$$

$$(\Gamma_q^v|\Gamma_0^b) = \begin{pmatrix} -n+m & m & l \\ n-m & -m & l \\ m & -n+m & -l \end{pmatrix},$$

$$\begin{cases} n = a/b_x \\ m = a/(2b_x) + a/(2b_y) \\ l = a_z/(2b_z). \end{cases}$$

$$(\Gamma_q^v|\Gamma_0^f) = \begin{pmatrix} l & l-n-m & m-l \\ l-n-m & l & n-l \\ m-l & n-l & l \end{pmatrix},$$

$$\begin{cases} n = a/b_x \\ m = a/b_y \\ l = a/(2b_x) + a/(2b_y) + a_z/(2b_z). \end{cases}$$

$$(\Gamma_q^v|\Gamma_0^v) = \begin{pmatrix} l & l-m & m-n \\ n-2m+l & n-m+l & n-m \\ 2m-n-l & m-l & m \end{pmatrix},$$

$$\begin{cases} n = a/b_x \\ m = a/(2b_x) + a/(2b_y) \\ l = a/(2b_y) + a_z/(2b_z). \end{cases}$$

$$(\Gamma_q^v|\Gamma_m) = \begin{pmatrix} -n & k & l \\ n & -k & l \\ n & m-k & -l \end{pmatrix},$$

$$\begin{cases} n = a/(2b_x\cos\beta) \\ m = a/b_y \\ l = a_z/(2b_z) \\ k = a(1+\tan\beta)/(2b_y). \end{cases}$$

$$(\Gamma_q^v|\Gamma_m^b) = \begin{pmatrix} -n & -l+k & k \\ n & -k & l-k \\ n & m+l-k & m-k \end{pmatrix},$$

$$\begin{cases} n = a/(2b_x\cos\beta) \\ m = a/b_y \\ l = a_z/b_z \\ k = a(1+\tan\beta)/(2b_y) + a_z/(2b_z). \end{cases}$$

REFERENCES

1. Yu. N. Zhuravlev and A. S. Poplavnoĭ, Zh. Strukt. Khim. **42** (5), 860 (2001).
2. Yu. N. Zhuravlev and A. S. Poplavnoĭ, Zh. Strukt. Khim. **42** (6), 1056 (2001).
3. Yu. N. Zhuravlev and A. S. Poplavnoĭ, Fiz. Tverd. Tela (St. Petersburg) **45** (1), 37 (2003) [Phys. Solid State **45**, 36 (2003)].
4. Yu. N. Zhuravlev and A. S. Poplavnoĭ, Kristallografiya **47** (5), 810 (2002) [Crystallogr. Rep. **47**, 744 (2002)].
5. R. A. Évarestov and V. P. Smirnov, *Methods of Group Theory in Quantum Chemistry of Solids* (Leningr. Gos. Univ., Leningrad, 1987) [in Russian].
6. O. V. Kovalev, *Irreducible and Induced Representations and Corepresentations of Fedorov Groups* (Nauka, Moscow, 1986) [in Russian].
7. R. V. Galiulin, Kristallografiya **29** (4), 638 (1984) [Sov. Phys. Crystallogr. **29**, 378 (1984)].
8. R. A. Evarestov and V. P. Smirnov, J. Phys.: Condens. Matter **9**, 3023 (1997).
9. F. Gan, Y.-N. Xu, M.-Z. Huang, *et al.*, Phys. Rev. B **45** (15), 8248 (1992).

Translated by Yu. Sin'kov

Crystallography Reports, Vol. 50, No. 5, 2005, pp. 727–734. Translated from Kristallografiya, Vol. 50, No. 5, 2005, pp. 788–796.

THEORY OF CRYSTAL STRUCTURES

Generation of Crystal Structures of Heteromolecular Compounds by the Method of Discrete Modeling of Packings

A. V. Maleev, I. K. Zhitkov, and V. G. Rau

Vladimir State Pedagogical University, pr. Stroiteleĭ 11, Vladimir, 600024 Russia

e-mail: andr_mal@mail.ru

Received June 30, 2004

Abstract—Within the method of discrete modeling of packings, an algorithm of generation of possible crystal structures of heteromolecular compounds containing two or three molecules in the primitive unit cell, one of which has an arbitrary shape and the other (two others) has a shape close to spherical, is proposed. On the basis of this algorithm, a software package for personal computers is developed. This package has been approved for a number of compounds, investigated previously by X-ray diffraction analysis. The results of generation of structures of five compounds—four organic salts (with one or two spherical anions) and one solvate—are represented. © *2005 Pleiades Publishing, Inc.*

Much attention has been given to the problem of predicting (generation) of structures of molecular crystals. The reasons for this are as follows. First, the interest in such phenomena as crystalline polymorphism [1] and phase transitions [2, 3], whose occurrence directly depends on the possibility of existence of different crystal structures of the same chemical compound, is constantly increasing. Second, powder methods for studying crystal structures, which have been intensively developed in recent years [4], impose specific requirements on the methods of their interpretation, a phenomenon which is related to limited experimental data and, as a result, insufficient efficiency of the conventional methods for determining structures (the direct and Patterson methods). Among the actively developed new interpretation techniques, the methods of a priori search of possible crystal structures take a particular position.

Conventional algorithms for predicting crystal structures include three main stages: (i) generation of a large number of initial structures, (ii) rough rejection of unlikely structures, and (iii) final refinement of the remaining ones. The first stage is generally reduced to the introduction of some hypothetical space, each point of which determines a particular crystal structure. Then this space is either passed through with some step or is randomly and more or less uniformly filled; for example, by the Monte Carlo method. In this case, the main problems are as follows: first, determination of the independent region of this hypothetical space and, second, the development of rules for the most uniform filling of this region. The second stage is based either on the estimation of the energy of intermolecular interaction (the structures with energies exceeding some critical value are rejected) or on geometric analysis of the mutual arrangement of molecules (the structures with overly short intermolecular contacts are rejected). In the third stage, the energy refinement of the lattice parameters and of the position and orientation of molecules in the structure is performed (as rule, by the method of atom–atom potentials).

Previously, we proposed a new approach to the implementation of the two first stages of generation of crystal structures, which is based on the use of the method of discrete modeling of packings [5]. Within this approach, the algorithm of generation and initial rejection of models of crystal structures contains only integer calculations and does not consume much memory, which makes it possible to reduce the computational time at the first two stages significantly. In addition, this approach does not imply a priori setting of the unit-cell parameter and the symmetry space group. On the basis of this approach, algorithms of generation of homomolecular Bravais structures, containing molecules of the same orientation, and the structures with molecules of two orientations, linked by an inversion center, were considered in [6, 7].

However, many molecular crystals are heteromolecular, i.e., contain two or more symmetrically independent (not necessarily chemically identical) molecules. In this study, we propose an algorithm of generation of heteromolecular compounds containing two or three molecules in the primitive unit cell, one of which has an arbitrary shape, while the other molecule (two other molecules) has a shape close to spherical. The requirement for an approximately spherical shape of one or two molecules is related to the fact that the orientation of this molecule (these molecules) remains uncertain in the algorithm proposed. We can assign to such structures, for example, cation–anion and cation–dianion complexes with halogen, tetrafluoroborate, and hexafluoroborate anions (or solvate compounds with one or two solvent molecules) with a shape close to spherical, in the structural classes of types $P1$, $Z_C =$

1(1), $Z_A = 1(1)$; $P\bar{1}$, $Z_C = 1(\bar{1})$, $Z_A = 1(\bar{1})$; $P\bar{1}$, $Z_C = 1(\bar{1})$, $Z_A = 2(1)$; and $P1$, $Z_C = 1(1)$, $Z_A = 2(1,1)$. Here, Z_C and Z_A are, respectively, the numbers of cations and anions (for solvates, of main solvate molecules and solvent molecules) in the unit cell. The position occupied by an ion (molecule) is indicated in parenthesis. In what follows, describing the generation algorithm, we will refer to the main solvate molecule and the solvent molecule as a cation and an anion, respectively.

The algorithm proposed includes four main stages: (i) approximation of organic cations and anions by discrete models—polycubes; (ii) calculation of all possible translational packings of polycubes of the cation and the anion (anions) with a given packing factor; (iii) reduction of the cell parameters to the conventional form and calculation of the atomic coordinates from the obtained packings of polycubes; and (iv) optimization of the translational-lattice parameters, the orientation of the cation, and the position of the anion (anions).

Let us consider each of these stages in more detail.

APPROXIMATION OF A MOLECULAR CATION AND ANION BY DISCRETE MODELS

According to the close-packing principle, the distance between two atoms of neighboring molecules in molecular crystals [8] cannot be smaller than some value (for example, equal to the sum of van der Waals radii of these atoms), which is determined by the geometric characteristics of the atoms. On the basis of this principle, the geometric model of a molecule consisting of n atoms is a geometric figure $M = \bigcup_{j=1}^{n} S_j$, where S_j is a sphere of radius R_j (the van der Waals radius of the jth atom) with a center at the point $\mathbf{r}_j$ (the coordinates of the jth atom in some basis). A polycube of a molecular cation, which consists of p cubes, can be set by integer coordinates of the centers of these cubes $\{\mathbf{l}_i, i = 1, 2, \ldots, p\}$ in the basis whose vectors have the same length and are parallel to the three perpendicular edges of a cube. Then, the cation polycube is a geometric figure $P = \bigcup_{i=1}^{p} C_i$, where C_i is a cube with a center at the point with coordinates $\mathbf{l}_i$. If an anion is a single atom, it should be considered as a sphere of radius R, where R is the ionic or van der Waals radius of the atom. In the case of a molecular anion (or a solvent molecule), in the first-order approximation, it can also be assumed to be a sphere, whose radius is determined as the shortest possible distance from the center of the molecule to the geometric models approximating the neighboring molecules. The anion polycube composed of q cubes can be specified by the set $\{\mathbf{m}_f, f = 1, 2, \ldots, q\}$; in this case, the size of the cube of the anion polycube is the same as that of the cube of the cation polycube. The discrete model of the anion is a geometric figure $Q = \bigcup_{f=1}^{q} C_f$, where C_f is a cube with a center at the point $\mathbf{m}_f$.

CALCULATION OF ALL POSSIBLE TRANSLATIONAL PACKINGS OF CATION AND ANION POLYCUBES WITH A SPECIFIED PACKING FACTOR

The necessary and sufficient criterion for the possibility of translational packing of polyminos (polycubes in the three-dimensional case) composed of p cubes, with the packing factor $k = p/N$, where N is the packing-space order, was reported in [9]. The criterion for the possibility of translational packing of two polycubes linked by an inversion center, with the packing factor $k = 2p/N$, was given in [7]. Similarly to the above-mentioned criteria, let us formulate the criterion for packing of two independent polycubes.

The packing space is a lattice whose every site is denoted by a weight (index, number) in such a way that any sets of lattice sites with identical weights form identical (accurate to shift) sublattices of the initial lattice [5, 9]. The coordinate columns of the vectors of one of the bases of such a sublattice form the integer matrix (in the basis of the initial lattice)

$$Y = \begin{pmatrix} x_1 & x_2 & x_3 \\ 0 & y_2 & y_3 \\ 0 & 0 & z_3 \end{pmatrix},$$

where $0 \le x_2 < x_1$, $0 \le x_3 < x_1$, $0 \le y_3 < y_2$, and $z_3 > 0$. The matrix Y is referred to as the packing-space matrix. The packing-space order is equal to the product of the diagonal elements of the matrix Y: $N = x_1 y_2 z_3$.

To provide the existence of the translational packing of two polycubes $\{\mathbf{l}_i, i = 1, 2, \ldots, p\}$ and $\{\mathbf{m}_f, f = 1, 2, \ldots, q\}$ with the packing factor $k = (p + q)/N$, it is necessary and sufficient that all points $\{\mathbf{l}_i, i = 1, 2, \ldots, p\} \cup \{\mathbf{r} + \mathbf{m}_f, f = 1, 2, \ldots, q\}$ of at least one Nth-order packing space have pairwise different weights. The vector $\mathbf{r}$ is one of the vectors of the fundamental region of the sublattice of translations, specified by the packing space; for example, the vector in the form $\begin{pmatrix} u \\ v \\ w \end{pmatrix}$, where u, v, and w are integers in the ranges $0 \le u < x_1$, $0 \le v < y_2$, and $0 \le w < z_3$.

Assuming the cation and anion polycubes and the packing factor k to be specified, we first calculate the packing-space order N as the simple natural number nearest to the fraction $(p + q)/k$. The choice of a simple packing-space order makes it possible to significantly reduce the time of calculation of the weight of a pack-

ing-space point and decrease the number of packing spaces.

For each packing space, the criterion is checked in two stages. First, the criterion for the cation polycube is checked and, if this criterion is satisfied, the criterion for the anion polycube is checked for all possible values of the vector **r**.

The criterion for packing of the cation polycube and the two anion polycubes is formulated similarly. In this case, for each packing space, the criterion for packing of polycubes is first checked for the cation polycube and, if the criterion is satisfied, the criteria for the polycubes of the first and second anion are checked successively.

CALCULATION OF THE CRYSTAL STRUCTURES CORRESPONDING TO THE OBTAINED PACKINGS OF POLYCUBES

Each obtained packing of polycubes of the cation and the anion (anions) is described by the packing-space matrix Y and one or two displacement vectors of the anion polycubes with respect to the origin of coordinates. The packing space determines the lattice of translations of the polycube packing; the column vectors of the packing-space matrix Y set the basis of this lattice of translations:

$$\mathbf{a} = s\begin{pmatrix} N \\ 0 \\ 0 \end{pmatrix}, \quad \mathbf{b} = s\begin{pmatrix} x_1 \\ 1 \\ 0 \end{pmatrix}, \quad \mathbf{c} = s\begin{pmatrix} x_1 \\ 0 \\ 1 \end{pmatrix},$$

where s is the approximation step. In addition, we can assume that the coordinates of the cation atoms $\{\mathbf{r}_{Kj}, j = 1, 2, \ldots, n\}$, where n is the number of cation atoms, are known in the orthonormal basis used. When the anion polycube is calculated, its position is taken arbitrarily, for example, at the origin of coordinates. Then, the coordinates of the anion (anions) in the structure corresponding to the packing will be determined by the vector **r** (vectors $\mathbf{r}_1$ and $\mathbf{r}_2$). Since in a packing prime-order space the fundamental region is covered by the vectors $\begin{pmatrix} u \\ 0 \\ 0 \end{pmatrix}$, where $u = 0, 1, \ldots, N-1$, the coordinates of the anion (anions) in the basis **a**, **b**, **c** will be equal to $s\begin{pmatrix} u_1 \\ 0 \\ 0 \end{pmatrix}$ (and $s\begin{pmatrix} u_2 \\ 0 \\ 0 \end{pmatrix}$). For convenience of further calculations, this basis should be reduced to the conventional crystallographic basis $\mathbf{a}_n$, $\mathbf{b}_n$, $\mathbf{c}_n$ (for example, using the Delone algorithm), in which for all atoms of the structure, the coordinates are written in fractions of the unit-cell vectors:

$$\mathbf{r}_j' = Y_n^{-1}\mathbf{r}_j,$$

where Y_n is the matrix of the column vectors $\mathbf{a}_n$, $\mathbf{b}_n$, $\mathbf{c}_n$ in the basis **a**, **b**, **c**.

In the algorithm considered here, the coordinates of individual atoms of molecular anions are not determined. For further optimization and comparative analysis, the coordinates of the geometric center (centers) of the anion (anions) are calculated by the above formulas. The determination of possible orientations of molecular anions in the crystal is a separate problem. Possible approaches to its solution will be published elsewhere.

OPTIMIZATION OF THE PARAMETERS OF THE LATTICE OF TRANSLATIONS, OF THE ORIENTATION OF THE CATION, AND OF THE POSITION OF THE ANION (ANIONS)

The models of crystal structures obtained in the previous stage are fairly rough. This roughness creates additional difficulties in further comparative analysis of the structures obtained. Therefore, if possible, these models should be refined. One of the refinement procedures that can be used here is the minimization of the intermolecular-interaction energy, for example, using the method of atom–atom potentials.

If molecules are assumed to be rigid, in the case of a crystalline salt, composed of one molecular cation and a spherical anion, the intermolecular-interaction energy is a function of the following parameters: six geometric values determining the lattice of translations of the crystal (for example, the unit cell parameters a, b, c, α, β, and γ); the parameters determining the cation orientation in the lattice (three Euler angles θ, φ, and ψ); and the anion coordinates x_A, y_A, and z_A.

When the unit cell contains one molecular cation and two spherical anions, the number of variable parameters increases, and the function of the energy of the crystal structure takes the form $U(a, b, c, \alpha, \beta, \gamma, \theta, \varphi, \psi, x_{A1}, y_{A1}, z_{A1}, x_{A2}, y_{A2}, z_{A2})$, where x_{A1}, y_{A1}, and z_{A1} are the coordinates of first anion and x_{A2}, y_{A2}, and z_{A2} are the coordinates of the second anion in the unit cell.

In the algorithm proposed, when anions (or solvent molecules) consist of several atoms, only the positions of their geometric centers are determined. Therefore, in the energy refinement, anions were replaced with virtual atoms, whose parameters were determined from minimum possible intermolecular contacts of these anions.

APPROVAL OF THE ALGORITHM AND VERIFICATION OF ITS ADEQUACY

On the basis of the algorithm considered here, a software package for IBM PCs has been developed.

Table 1. Basic crystallographic data on the crystal structures investigated by XRD and some parameters of their generation by the discrete modeling method

Name in the CSD classification, reference	SIVZIG, [11]	AZSTBG, [12]	FIDYIA, [13]	ACIDIZ, [14]	ECIZAR, [15]
Gross formula	$C_{18}H_{27}N_2O_3S^+ \cdot Cl^-$	$C_{14}H_{16}N_2^{2+} \cdot 2I^-$	$C_{19}H_{27}N_2S^+ \cdot 2CH_3SO_3^-$	$C_{34}H_{28}N_4O_4 \cdot C_4H_8O_2$	$C_{48}H_{50}N_4^{2+} \cdot 2(BF_4^-)$
Structural class	$P1$, $Z_C = 1(1)$, $Z_A = 1(1)$	$P\bar{1}$, $Z_C = 1(\bar{1})$, $Z_A = 2(1)$	$P1$, $Z_C = 1(1)$, $Z_A = 1(1)$	$P\bar{1}$, $Z_C = 1(\bar{1})$, $Z_A = 1(1)$	$P\bar{1}$, $Z_C = 1(\bar{1})$, $Z_A = 2(1)$
Anion or solvent	chlorine, Cl^-	iodine, I^-	methanesulfonate, $CH_3SO_3^-$	1,4-dioxane, $C_4H_8O_2$	tetrafluoroborate, BF_4^-
Effective anion radius R, Å	1.8	2.0	2.5	2.5	2.0
Criterion of noncoincidence between molecular structures σ, Å	0.32	0.13	0.08	0.25	0.30
Approximation step s, Å	0.37–0.72	0.43–0.73	0.38–0.69	0.41–0.79	0.42–0.75
Packing factor of polycubes k	0.58–0.64	0.67–0.72	0.60–0.64	0.56–0.60	0.56–0.61
Number of calculated structures	249	318	347	223	1002
Number of structures corresponding to the XRD data	30	17	123	11	16
Criterion for difference between structures Δ, Å	30	20	27	19	15

This package was approved for a number of crystal structures investigated previously by X-ray diffraction (XRD). The crystallographic data on these structures were taken from the Cambridge Structural Database (CSD) [10]. The table contains some results of the generation of crystal structures of five heteromolecular compounds, differing by the number or shape of anions or the structural class.

The first four rows contain brief data on the crystal structures: the CSD name of a structure and a reference to the source of the XRD data, the gross formula, the structural class with indication of the symmetry of the cation and anion positions, and the name and the gross formula of the anion or the solvent molecule. The SIVZIG and AZSTBG compounds contain one-atom halogen anions, which, from the point of view of molecular packing, can be assumed to be ideally spherical. The three other compounds contain molecular anions and solvent molecules composed of several atoms; therefore, their shape can be considered spherical only in the first-order approximation. The AZSTBG and ECIZAR structures contain two anions per unit cell; the other structures contain one anion per unit cell.

Next, the anion effective radius is indicated. For single-atom anions, this is equal to the van der Waals radius of the corresponding atom. For molecular anions and solvent molecules, the effective radius is determined by the intermolecular contacts of the anion. For example, it can be estimated as the minimum difference between the distance from the anion center to an atom of the neighboring molecule and the van der Waals radius of this atom. Estimation was performed on the basis of the analysis of several (previously investigated by XRD) structures containing the same anion or solvent molecule as the generated structure. The value of the effective radius was used to calculate the anion polycube and fit the energy parameters of the virtual atom, which was placed in the structure instead of the molecular anion or the solvent molecule during the optimization.

The coordinates of the cation atoms were calculated by the molecular-mechanics method [16]. The degree of the difference between the calculated model of the cation and the experimentally determined model was estimated using the Zorkiĭ criterion $\sigma = ((1/n)\sum_{i=1}^{n}(\mathbf{r}_i - \mathbf{r}_i')^2)^{1/2}$, where $\mathbf{r}_i$ and $\mathbf{r}_i'$ are the radius vectors of the ith atoms of the molecules under comparison [17]. The value of σ was minimized by the steepest descent method, while varying the orientation of one of the molecules with aligned geometric centers. The simulation quality is much better for cations of the FIDYIA and AZSTBG compounds; for cations of the SIVZIG and ESIZAR compounds, the results are poorer.

Table 2. Lattice parameters of the experimental and related model crystal structures

Name in the CSD classification	*a*, Å		*b*, Å		*c*, Å		α, deg		β, deg		γ, deg	
	XRD	DMM*	XRD	DMM	XRD	DMM	XRD	DMM	XRD	DMM	XRD	DMM
SIVZIG	6.059	5.94	7.970	8.73	11.134	11.01	109.31	110.4	93.90	94.2	107.89	110.2
AZSTBG	8.190	8.26	7.017	7.32	7.743	7.67	84.19	80.3	61.56	63.0	80.26	76.4
FIDYIA	6.841	7.12	9.319	9.42	9.678	9.10	64.42	68.2	69.67	68.8	76.74	79.3
ACIDIZ	5.995	5.98	10.242	10.46	14.292	13.94	93.370	94.1	90.595	91.2	103.557	99.8
ECIZAR	9.0324	9.11	10.5874	10.78	12.5495	13.00	93.64	92.7	106.299	109.1	110.788	109.7

* Discrete modeling method.

For each structure, discrete models (polycubes) of the cation were calculated for nine random orientations of the molecule with the approximation steps (side of a cube in the polycube) s = 0.35, 0.36, …, 0.80 Å. In accordance with the approximation-quality criterion described in [6], five to eight polycubes were selected in each case. The minimum and maximum approximation steps for the selected polycubes, for which possible packings were then calculated, are listed in the 7th row of Table 1. Note that approximation steps exceeding 0.8 Å should not be used because the error in the calculations of generated crystal structures is unwarrantedly high in this case. There is also no point in using approximation steps much smaller than 0.3 Å, since the computational time significantly increases in this case without a radical decrease in error.

For each selected polycube of the cation and polycube (polycubes) of the anion (anions), we calculated all possible packings with different packing factors in the intervals indicated in the 8th row of Table 1. The upper limit of the interval is determined by the value of the packing factor at which there are no possible packing for the polycubes under consideration. The lower limit was chosen so that the number of calculated packings would not exceed several hundred.

The next row of Table 1 contains the total number of found packings of polycubes, and, therefore, the number of crystal structures calculated for each compound on the basis of these packings. After optimization of the structures, comparative analysis of the crystal lattices and molecular packings was performed. This analysis allowed us to separate the entire set of model crystal structures into nonintersecting classes, in which the geometry of the lattices of translations and the mutual arrangement of the molecules turned out to be almost identical. Each of such classes determines a structure that can be a polymorphic modification of this compound. One of the criteria of the adequacy of the calculations performed is that, for each compound, the structure of one of such polymorphs turned out to be similar to a crystal structure investigated by XRD and taken by us from the CSD. The numbers of calculated crystal structures entering the classes corresponding to the structures investigated by XRD are listed in the 10th row of Table 1 for each compound.

To quantitatively estimate the degree of difference between similar crystal structures, a special criterion Δ was proposed in the form of the convergent series

$$\Delta = \left(\sum_{m=-\infty}^{+\infty} \sum_{p=-\infty}^{+\infty} \sum_{q=-\infty}^{+\infty} \sum_{i=1}^{n} (\mathbf{r}_{impq} - \mathbf{r}'_{impq})^2 f(R) \right)^{1/2},$$

where $\mathbf{r}_{impq}$ and $\mathbf{r}'_{impq}$ are the radius vectors of the ith atoms of the structures under comparison, obtained from the initial atoms by the translations (m, p, q), and $f(R)$ is a function of the distance R from the origin of coordinates to the middle of the segment connecting these atoms: $R = 0.5|\mathbf{r}_{impq} + \mathbf{r}'_{impq}|$. Minimization of the criterion Δ is performed by varying the spatial orientation of one of the structures using the steepest descent method. In our calculations, we used the function $f(R) = \exp(-R/\lambda)$, where λ is the constant determining how rapidly the series converges. Since the series is convergent, its summation should be terminated at a certain value of R. (We used λ = 7 Å and R = 70 Å.)

Our estimation shows that the values of the criterion Δ in the range 1–2 Å correspond to identical (within the conventional XRD error) crystal structures; the values from 2 to 20 Å correspond to models fairly close to each other; in the range 20–40 Å, the coincidence between structures is satisfactory; and the values above 40 Å generally indicate significant differences in the crystal structures under comparison. The values of the criterion Δ characterizing the difference between an experimental model and a similar model of crystal structures for each compound are listed in the last row of Table 1.

Figures 1–5 show the projections of the crystal structures of all compounds under study along one of the principal crystallographic directions. Atoms of molecular anions or solvent molecules in the experimental structures are shown as spheres with radii corresponding to the van der Waals radii. The positions of the anions and solvent molecules in the model structures are shown by dotted lines. (Molecular anions are replaced by spheres with corresponding effective radii.)

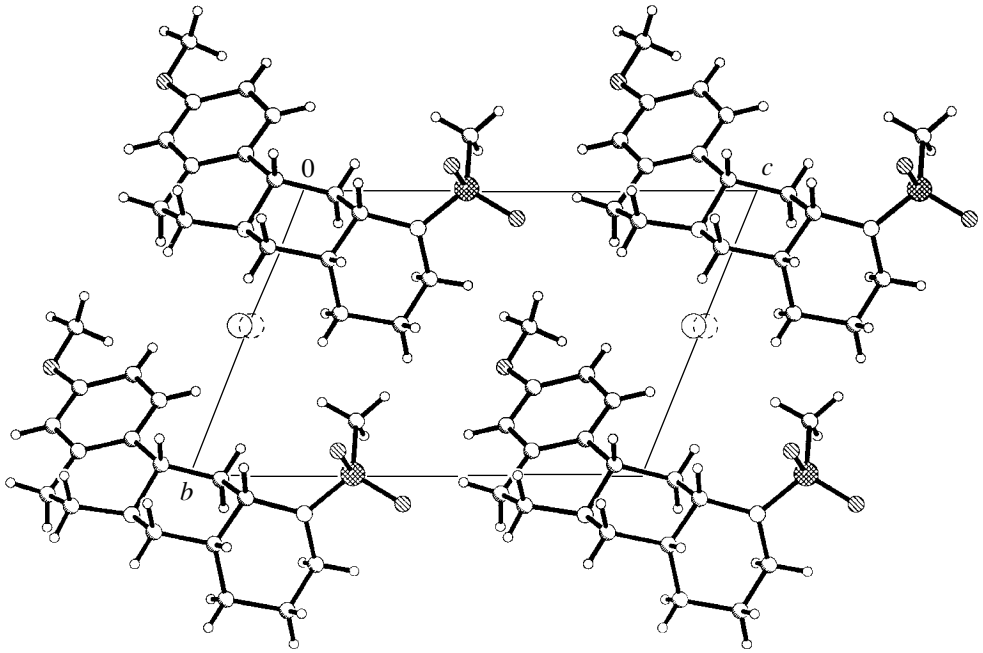

Fig. 1. Structure of the hydrochloride of (8aR,12aS,13aS)-5,8,8a,9,10,11,12,12a,13,13a-decahydro-3-methoxy-12-methylsulfonyl-6H-isoquino(2,1-g)(1,6)naphthyridine (SIVZIG). Projection along the *a* axis.

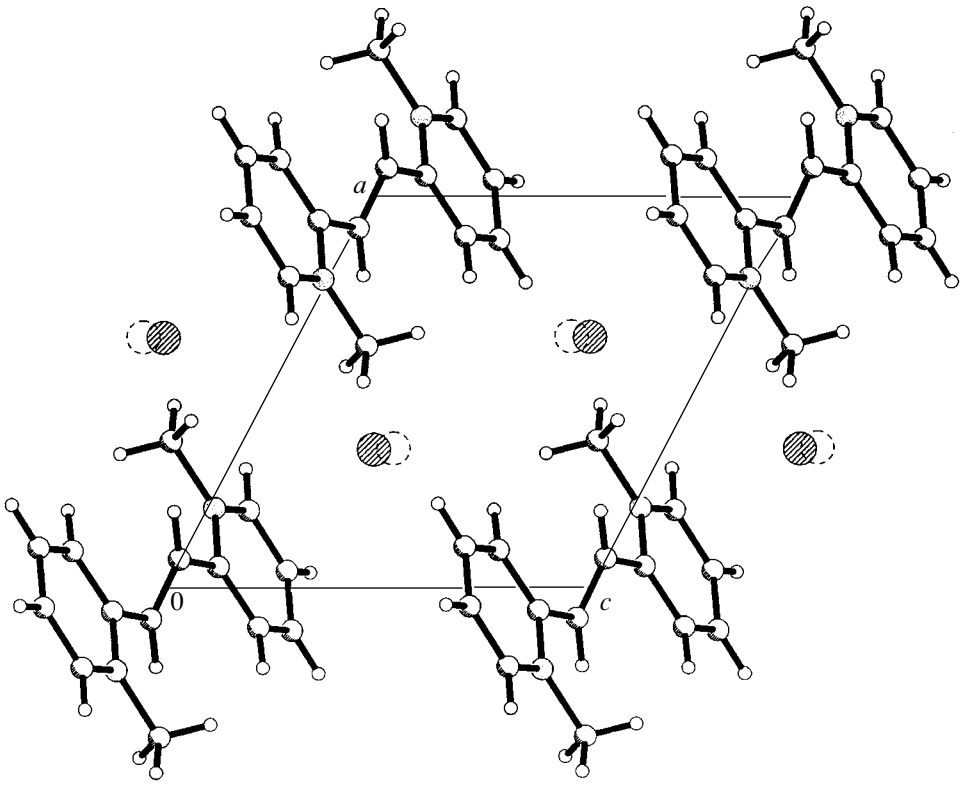

Fig. 2. Structure of the diiodide of (*E*)-6,6'-dimethyl-6,6'-diazoniastilbene (AZSTBG). Projection along the *b* axis.

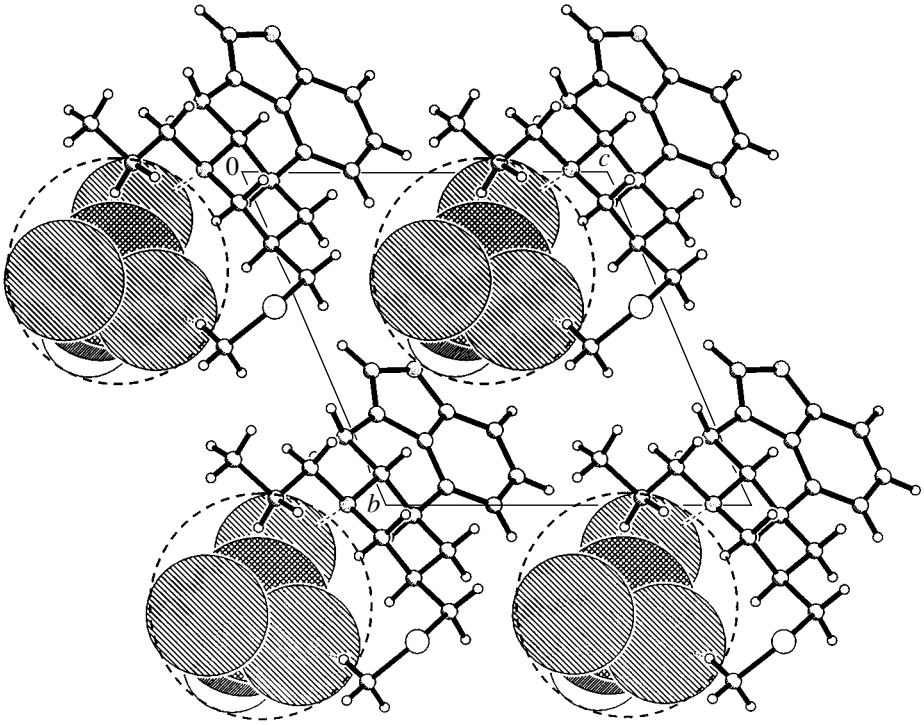

Fig. 3. Structure of the methanesulfonate of (8β)-8-((methylthio)methyl)-6-propylergoline (FIDYIA). Projection along the *a* axis.

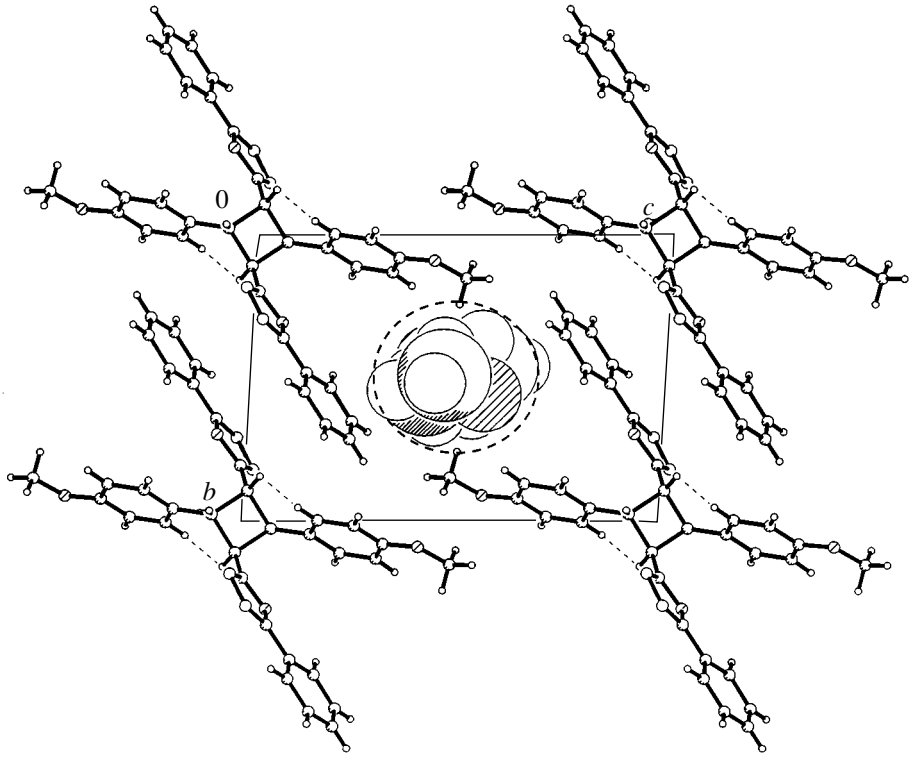

Fig. 4. Structure of the 1,4-dioxane solvate of 1,3-bis(4-methoxyphenyl)-2,4-bis(5-phenyl-1,3,4-oxadiazole-2-yl)cyclobutane (ACIDIZ). Projection along the *a* axis.

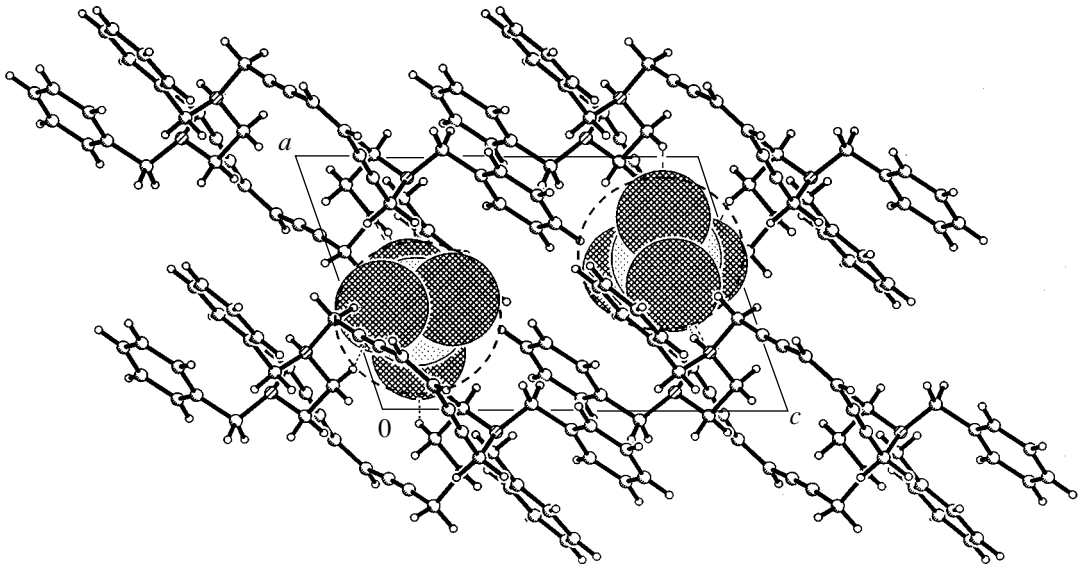

Fig. 5. Structure of bis(tetrafluoroborate) of (1,4,13,16-tetrabenzyl-1,4,13,16-tetra-aza-cyclotetracosa-8,20-dien-6,10,18,22-tetrain) (ECIZAR). Projection along the *b* axis.

The position and orientation of the main molecules of the model and experimental structures are almost the same; for this reason, Figs. 1–5 show only the main molecules of the experimental structures. Table 2 contains the lattice parameters of the experimental and model (similar to experimental) crystal structures.

Thus, we believe that the main result of the investigation carried out here is that the algorithm of generation of crystal structures developed within the method of discrete modeling makes it possible to calculate all possible crystal structures of heteromolecular compounds whose primitive unit cell contains one molecule with an arbitrary shape and one or two molecules with a shape similar to spherical.

ACKNOWLEDGMENTS

We are grateful to K.A. Potekhin for fruitful discussion of the results.

This study was supported by the Russian Foundation for Basic Research, project no. 04-01-16835, and the Ministry of Education of the Russian Federation, project no. A03-2.9-873.

REFERENCES

1. L. N. Kuleshova and M. Yu. Antipin, Kristallografiya **46** (1), 19 (2001) [Crystallogr. Rep. **46**, 13 (2001)].
2. I. I. Vorontsov, K. A. Potekhin, M. Yu. Antipin, and I. E. Zanin, Kristallografiya **45** (2), 266 (2000) [Crystallogr. Rep. **45**, 234 (2000)].
3. I. I. Vorontsov, K. A. Potekhin, M. Yu. Antipin, *et al.*, Kristallografiya **46** (5), 833 (2001) [Crystallogr. Rep. **46**, 758 (2001)].
4. V. B. Zlokazov and V. V. Chernyshev, J. Appl. Crystallogr. **25**, 447 (1992).
5. A. V. Maleev, V. G. Rau, K. A. Potekhin, *et al.*, Dokl. Akad. Nauk SSSR **315** (4–6), 1382 (1990) [Sov. Phys. Dokl. **35**, 997 (1990)].
6. A. V. Maleev, Kristallografiya **46** (1), 19 (2001) [Crystallogr. Rep. **46**, 13 (2001)].
7. A. V. Maleev, Kristallografiya **47** (5), 797 (2002) [Crystallogr. Rep. **47**, 731 (2002)].
8. A. I. Kitaigorodsky, *Molecular Crystals* (Nauka, Moscow, 1971) [in Russian].
9. A. V. Maleev, Kristallografiya **40** (3), 394 (1995) [Crystallogr. Rep. **40**, 354 (1995)].
10. CSD version 5.25 (November 2003).
11. R. D. Clark, D. B. Repke, J. Berger, *et al.*, J. Med. Chem. **34**, 705 (1991).
12. J. Vansant, G. Smets, J. P. Declercq, *et al.*, J. Org. Chem. **45**, 1557 (1980).
13. L. Y. Y. Ma, N. Camerman, J. K. Swartzendruber, *et al.*, Can. J. Chem. **65**, 256 (1987).
14. Y. Zheng, J.-P. Zhuang, W.-Q. Zhang, *et al.*, Acta Crystallogr. E **57**, 1029 (2001).
15. T. Chandra, M. Pink, and J. M. Zaleski, Inorg. Chem. **40**, 5878 (2001).
16. U. Burkert and N. Allinger, *Molecular Mechanics* (American Chemical Society, Washington, 1982; Mir, Moscow, 1986).
17. A. E. Razumaeva and P. M. Zorkiĭ, Vestn. Mosk. Univ. **21** (1), 27 (1980).

Translated by Yu. Sin'kov

Crystallography Reports, Vol. 50, No. 5, 2005, pp. 735–738. Translated from Kristallografiya, Vol. 50, No. 5, 2005, pp. 797–800.

DIFFRACTION AND SCATTERING OF IONIZING RADIATIONS

Structurization of a Solvent Interacting with Fullerene C_{60}

B. M. Ginzburg*, Sh. Tuĭchiev, S. Kh. Tabarov**, and A. A. Shepelevskiĭ***

** Institute of Problems of Mechanical Engineering, Russian Academy of Sciences, Vasil'evskiĭ ostrov, Bol'shoĭ pr. 61, St. Petersburg, 199178 Russia*

e-mail: ginzburg@tribol.ipme.ru

*** Tajik State University, ul. Rudaki 17, Dushanbe, 734016 Tajikistan*

Received December 14, 2004

Abstract—Solutions of fullerene C_{60} in toluene and *p*-xylene were investigated by small-angle X-ray diffraction. In all small-angle scattering curves, the scattering intensity decreases to constant value I_C with an increase in the scattering angle. The value of I_C nonmonotonically depends on the fullerene concentration. The radii of gyration of scattering elements were determined by constructing small-angle X-ray diffraction patterns in Guinier coordinates. © *2005 Pleiades Publishing, Inc.*

Toluene, xylenes, and other benzene derivatives are good solvents for fullerenes [1]. In this paper, we report the results of the investigation of solutions of fullerene C_{60} in toluene and *p*-xylene by small-angle X-ray scattering.

The intensity of small-angle scattering curves was measured on a KRM-1 setup with slit collimation of a primary X-ray beam; the beam half-width was 2.5 min. The investigated scattering angles were in the range from 15′ to 2°. The error in measuring the intensity did not exceed ±0.2 pulse/s in the entire range of scattering angles.

Rectangular cells were made of a thin (7.5–10 μm) polymer film. The thickness of the cells containing samples was 1.0–1.5 mm. The cells were filled with the solutions studied and hermetically sealed. Measurements in transmission were performed: a cell with a solution was installed at the center of a goniometer perpendicular to the primary beam and a scattering curve (*1*) was recorded; then the sample was placed in front of the first slit and the profile of the primary beam (*2*) was measured taking into account its absorption in the sample. Furthermore, curve *2* was subtracted from curve *1*; the thus obtained difference diffraction patterns are given below as the experimental curves $I(s)$, where $s = 4\pi\theta/\lambda$, 2θ is the scattering angle, and λ is the X-ray wavelength. Note that the scattering intensity in curves *2* at the minimum angle, from which the measurement began, was the same for a solvent and the solutions of C_{60} in the entire concentration range within the experimental error. Therefore, the curves were not normalized to the same intensity of the primary beam. All measurements were performed at 25°C using Ni-filtered Cu_{K_α} radiation.

Fullerene C_{60} with a purity level of 99.7%, obtained by the Huffman–Krätschmer method, was used to prepare solutions of C_{60} in toluene with concentrations of 0.001, 0.01, 0.1, and 0.2% and in *p*-xylene with concentrations of 0.001, 0.01, 0.1, and 0.5%. Reagent grade solvents were used.

Figure 1 shows the small-angle diffraction patterns of the samples. In all curves, the scattering intensity monotonically decreases with an increase in the scattering angle, then reaches constant value I_C at angles of ~70′ for toluene (Fig. 1a) and ~80′ for *p*-xylene (Fig. 1b).

According to the data in the literature, the tendency of small-angle scattering intensity toward a constant value is characteristic of homogeneous liquids and glasses [2]. The value of I_C generally increases with an increase in temperature. Thermal density fluctuations are considered the main reason for scattering.

In the case of fullerene solutions, the dependence of I_C on the concentration of fullerene C_{60} is nonmonotonic. At a concentration of 0.001%, the scattering curves are almost the same for both solvents; their shape is similar to that of the scattering curve for a pure solvent, but the intensity is somewhat higher.

Radical changes are observed at a concentration of 0.01% (curves *3* in Figs. 1a, 1b): almost the entire small-angle scattering curve of the solution in toluene and the entire curve of the solution in *p*-xylene lie below the scattering curve of the solvent. Such changes in I_C can be explained by the structurization of the solvent under the action of fullerene. (The structurization

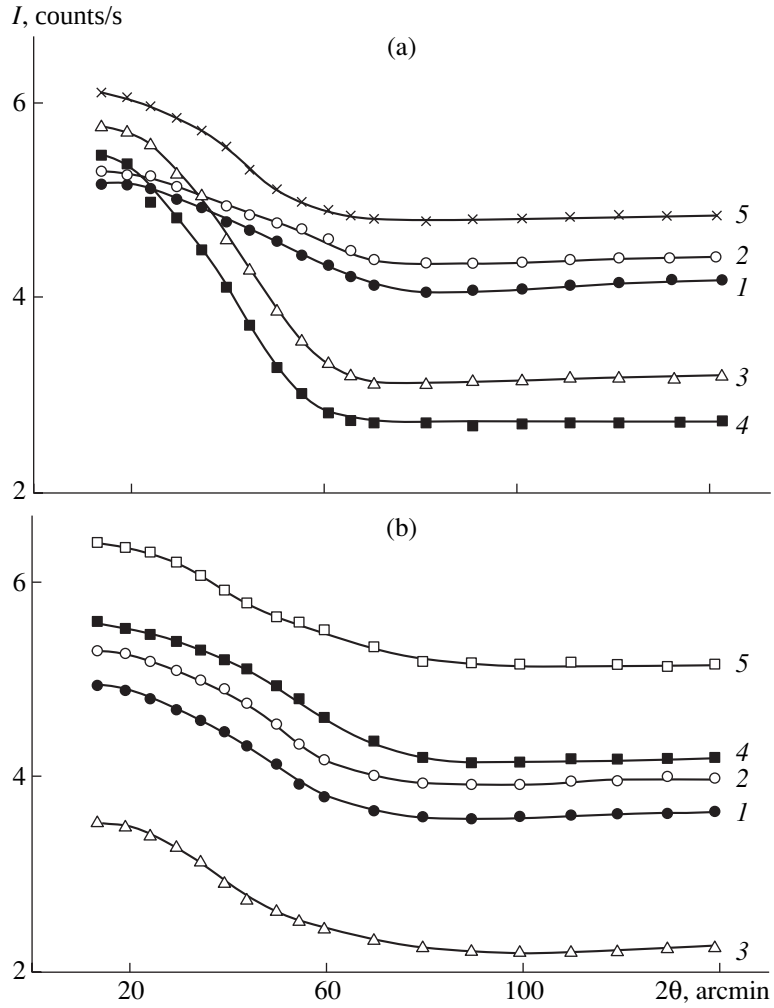

Fig. 1. Small-angle scattering curves (Cu_{K_α} radiation) for solutions of fullerene C_{60} (a) in toluene with fullerene concentrations of (*1*) 0 (pure toluene), (*2*) 0.001, (*3*) 0.01, (*4*) 0.1, and (*5*) 0.2% and (b) in *p*-xylene with fullerene concentrations of (*1*) 0 (pure *p*-xylene), (*2*) 0.001, (*3*) 0.01, (*4*) 0.1, and (*5*) 0.5%.

is meant to suppress thermal density fluctuations.) Apparently, this process is accompanied by an increase in the density and the degree of solvent ordering.

Indeed, there are data in the literature indicating that the density of a C_{60} solution in toluene nonmonotonically changes with an increase in the fullerene concentration: it first decreases to reach a minimum and then increases again [3]; i.e., the dependence observed is qualitatively similar to that for I_C.

Solvent structurization may result in heat release and a negative entropy decrement, which was observed by calorimetric methods during the dissolution of the fullerene in toluene [4].

After I_C reaches its minimum value (at concentrations C_{FR} = 0.1% for toluene and 0.01% for *p*-xylene), a further increase in the fullerene concentration leads to an increase in I_C. The reasons for this phenomenon are still unclear. A possible reason is that the value of the fullerene concentration approaches that for a saturated solution [1].

Figure 2 shows the small-angle diffraction patterns reconstructed in Guinier coordinates [5]. The values of I_C and the radii of gyration R_g for the systems under study are listed in the table.

Let us compare the obtained radii of gyration with the sizes of the C_{60} molecule. According to the calculated and experimental data, the C_{60} fullerene molecule is a truncated icosahedron with an internal cavity with zero electron density [6]; the cavity diameter is 0.4 nm. The external diameter of the C_{60} molecule is 0.714 nm [7]. Taking into account these sizes, one can model the C_{60} molecule in the first-order approximation by a spherical shell with a uniform density distribution. The

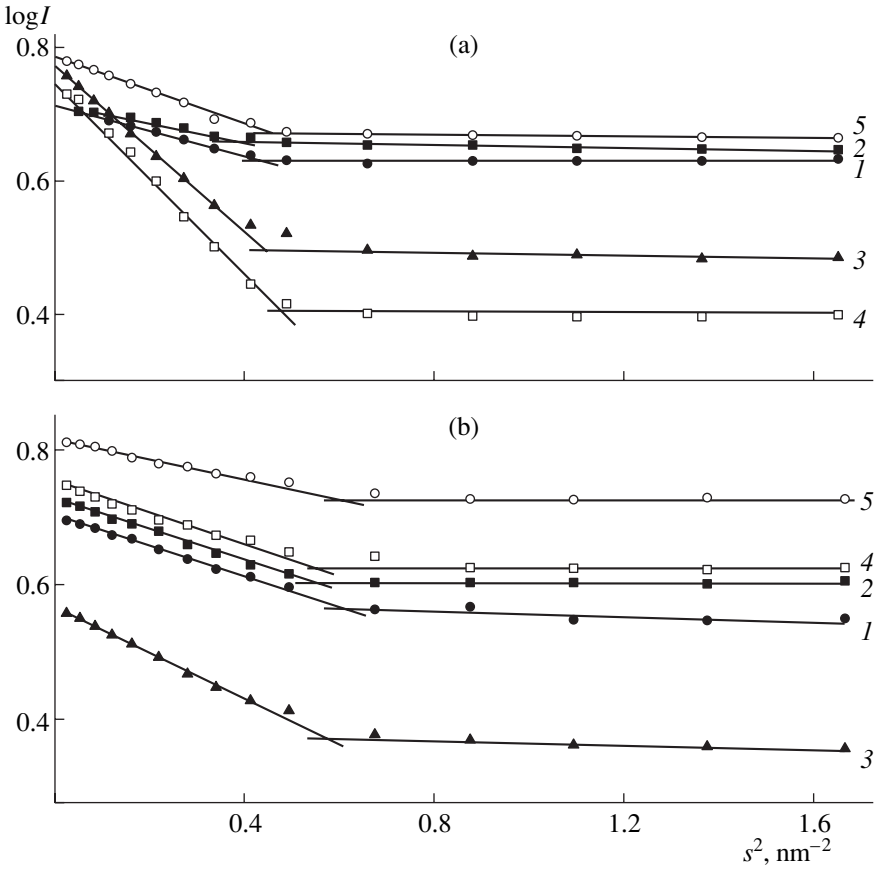

Fig. 2. The same X-ray diffraction patterns as in Fig. 1, reconstructed in Guinier coordinates.

radius of gyration for this shell can be written as

$$R_g = (3/5)^{1/2} R_e [(1 - C^5)/(1 - C^3)]^{1/2},$$

where $C = R_i/R_e$. Then, the radius of gyration of the C_{60} molecule is 0.30 nm, which is much smaller than even the smallest experimentally obtained radius.

Different models of the supramolecular structure can be proposed to explain this difference in the radii of gyration. The simplest model considers associates of fullerene molecules. The table contains the sizes of associates calculated within the model of spheres with homogeneous density for the experimental radii of gyration. The largest sphere, with a radius of 2.8 nm, can contain ~90C_{60} molecules (in the case of hexagonal close packing). In fact, this value should be somewhat smaller because the packing is unlikely to be similar to crystalline.

It was noted in [1] that fractal clusters (with dimensions close to that of associates in sample 2) are formed in solutions of fullerenes. Apparently, it is the formation of fractal structures, along with the long-range effect of fullerene on the solvent structure, that leads to the suppression of thermal fluctuations in solutions.

Sizes of scattering elements in the samples

Sample no.	Solvents and solutions	R_g, nm	R_0, nm
1	toluene	1.2	1.5
2	toluene + 0.001% C_{60}	1.0	1.3
3	toluene + 0.01% C_{60}	2.1	2.7
4	toluene + 0.1% C_{60}	2.2	2.8
5	toluene+ 0.2% C_{60}	1.3	1.7
6	*p*-xylene	1.25	1.6
7	*p*-xylene + 0.001% C_{60}	1.25	1.6
8	*p*-xylene + 0.01% C_{60}	1.55	2.0
9	*p*-xylene + 0.1% C_{60}	1.25	1.6
10	*p*-xylene + 0.5% C_{60}	1.0	1.3

Note: R_g is the radius of gyration and R_0 is the radius of a homogeneous sphere.

REFERENCES

1. V. N. Bezmel'nitsyn, A. V. Eletskiĭ, and M. V. Okun', Usp. Fiz. Nauk **168** (11), 1195 (1998).
2. D. I. Svergun and L. A. Fĭgin, *X-ray and Neutron Small-Angle Scattering* (Nauka, Moscow, 1986; Plenum, New York, 1987).
3. N. V. Mekalova, *Fullerenes in Solutions* (UGNTU, Ufa, 2001) [in Russian].
4. M. H. Herbst, G. H. M. Dias, J. G. Magalhaes, *et al.*, J. Mol. Liq. (2004) (in press).
5. A. Guinier, *Theórie et Technique de la Radiocristallographie* (Dunod, Paris, 1956; Fizmatgiz, Moscow, 1961).
6. S. V. Kozyrev and V. V. Rotkin, Fiz. Tekh. Poluprovodn. (St. Petersburg) **27** (9), 1409 (1993) [Semiconductors **27** (9), 777 (1993)].
7. A. V. Eletskiĭ and B. M. Smirnov, Usp. Fiz. Nauk **165** (9), 977 (1995) [Phys. Usp. **165** (9), 935 (1995)].

Translated by Yu. Sin'kov

Crystallography Reports, Vol. 50, No. 5, 2005, pp. 739–750. Translated from Kristallografiya, Vol. 50, No. 5, 2005, pp. 801–812.

DIFFRACTION AND SCATTERING OF IONIZING RADIATIONS

Structural Characterization of Interfaces in the $Al_xGa_{1-x}As/GaAs/Al_xGa_{1-x}As$ Heterostructures by High-Resolution X-ray Reflectometry and Diffractometry

A. A. Lomov*, A. G. Sutyrin*, D. Yu. Prokhorov*, G. B. Galiev, Yu. V. Khabarov**, M. A. Chuev***, and R. M. Imamov***

** Shubnikov Institute of Crystallography, Russian Academy of Sciences, Leninskiĭ pr. 59, Moscow, 119333 Russia*

e-mail: imamov@ns.crys.ras.ru

*** Institute of Ultrahigh-Frequency Semiconductor Electronics, Russian Academy of Sciences, Nagornaya ul. 7–8, Moscow, 117105 Russia*

**** Institute of Physics and Technology, Russian Academy of Sciences, Nakhimovskiĭ pr. 36, Moscow, 117218 Russia*

Received December 27, 2004

Abstract—The structural properties of multilayer $Al_xGa_{1-x}As/GaAs/Al_xGa_{1-x}As$ systems ($x \approx 0.2$) grown on GaAs(001) substrates are studied by the methods of double-crystal X-ray diffractometry and reflectometry. The depth profiles of deformation, amorphization, and density of the layers are obtained. It is shown that despite small differences (5–7%) in the densities of the $Al_xGa_{1-x}As$ layers and the substrate and the small thickness of the AlAs layer (1–2 nm) separating the GaAs quantum well, it is possible to reconstruct the heterostructure model by the method of X-ray reflectometry and to determine the thickness of the transitional layers at a resolution of 0.1–0.2 nm. It is also established that the reflectometry data obtained complement the X-ray diffraction data considerably and allow one to estimate the roughness and the character of the aluminum distribution at the interfaces. © *2005 Pleiades Publishing, Inc.*

INTRODUCTION

The method of double-crystal X-ray diffractometry [1–4] holds a firm place in modern diagnostics of low-dimensional semiconductor heterostructures because it allows one to evaluate parameters of individual layers and their interfaces by solving the inverse problem. Although the solution of this problem is far from trivial, the recent development of computational methods made the restoration of the thickness, deformation, composition, and static Debye–Waller factor of epitaxial layers from double-crystal diffractometry curves a routine procedure [3, 5]. However, the nonuniqueness of the solution obtained does not allow one to determine these parameters with the necessary accuracy and depth resolution. Therefore, the most important problem here is the selection of an adequate model of the structure from all the possible variants. The solution of this problem is associated, first and foremost, with the development of high technologies in modern micro- and optoelectronics such that they would allow one to obtain sufficiently narrow and deep quantum wells [6]. The quantum-dimensional effects in such structures associated with the limitations imposed on the electron gas are strongly dependent on the structural details of the quantum wells and their boundaries. The precision analysis of the structure of such objects can be solved only on the basis of mathematically justified processing of the precise experimental data. In fact, simultaneous processing of the double-crystal diffractometry curves obtained from different crystallographic planes of the structure solves the problem of nonuniqueness of the structure model [7]. However, despite a high sensitivity, the method of double-crystal X-ray diffractometry (as any other method) fails to give exhaustive detailed information on the structure. For example, analysis of buried thin (about an angstrom thick) layers allows one to determine only the phase increment of the reflected wave, $\Delta\Phi_h = K_h \times \Delta u$ [8], where K_h is the magnitude of the reciprocal-lattice vector and Δu is the displacement introduced by a thin layer. In this case, the layer thickness l_i and its deformation $\Delta d_i/d$ are related. Moreover, X-ray diffraction methods based on the analysis of the hth Fourier component of crystal polarizability have a low sensitivity to the strongly amorphized layers formed, e.g., as a result of oxidation processes at the surface. These layers considerably influence the electrophysical characteristics of the heterostructures.

The above circumstances dictate the use of some other methods such as photoluminescence [9] and reflection spectroscopy [10], secondary-ion mass spectrometry [11], total external reflection fluorescence spectroscopy [12], etc. One of such methods is high-resolution X-ray reflectometry (HRXR) [13]. This method allows one to independently determine the dis-

(a)

GaAs protective cap layer, $l_1 \sim 8$ nm
$Al_xGa_{1-x}As$ barrier layer, $x = 0.22$, $l_2 \sim 16.5$ nm
$Al_xGa_{1-x}As$ barrier layer, $x = 0.22$, $l_3 \sim 16.5$ nm
GaAs quantum well, $l_4 \sim 13$ nm
GaAs separating layer, $l_5 \sim 1.8$ nm
GaAs quantum well, $l_6 \sim 13$ nm
$Al_xGa_{1-x}As$ barrier layer, $x = 0.22$, $l_7 \sim 16.5$ nm
$Al_xGa_{1-x}As$ barrier layer, $x = 0.22$, $l_8 \sim 16.5$ nm
GaAs buffer layer, $l_9 \sim 0.5$ μm
GaAs (001) substrate, $l_{10} \sim 500$ μm

(b)

n-GaAs protective cap layer, $l_1 \sim 4$–8 nm
First *n*-type $Al_xGa_{1-x}As$ barrier layer with $c(Si) = 10^{18}$ cm^{-3}, $l_2 = 65$ nm
Second *n*-type $Al_xGa_{1-x}As$ barrier layer with $c(Si) = 10^{18}$ cm^{-3}, $l_3 = 150$ nm
GaAs buffer layer, $l_4 = 0.2$ μm
GaAs (001) substrate, $l_5 = 500$ μm

Fig. 1. Structure of the (a) 46*m* and 5*p* and (b) *G*24 and *G*681 samples set by the growth technology.

tribution of electron density over the crystal depth and also distortion and roughness of surfaces and interfaces [14, 15]. The use of the density data and the data on thin layers obtained by double-crystal X-ray diffractometry provides additional possibilities for thorough analysis of layers, e.g., allows one to check the validity of Vegard's law in these layers. High-resolution X-ray reflectometry has some advantages in comparison with many other methods because it allows one to use the same equipment as in double-crystal X-ray diffractometry experiments.

Recently, the interest in multilayer $Al_xGa_{1-x}As/GaAs/Al_xGa_{1-x}As$ systems has increased considerably because of their widespread use in optoelectronics and powerful UHF transistors. These systems consist of a GaAs quantum well enclosed between two $Al_xGa_{1-x}As$ barrier layers. It should be noted that doping of the external sides of the barrier layers considerably increases the power of transistors prepared on their basis and the introduction of a thin separating AlAs layer into the quantum changes the phonon and energy spectra of electrons. Then, it is assumed that the velocity of the intrasubband scattering would considerably decrease and, therefore, the mobility of electrons would increase [16]. The state and the sharpness of the interfaces in this model play an essential role. Thus, the study of such structures is of great scientific and applied importance.

The present work is dedicated to the study of quantum-well boundaries and separating AlAs layer depending on the doping of the external parts of the $Al_xGa_{1-x}As$ barrier layers of $Al_xGa_{1-x}As/GaAs/Al_xGa_{1-x}As/GaAs(001)$ heterostructure and analysis of possible structural distortions of the barrier layers with and without a protective GaAs subsurface layer. The data obtained are compared with the corresponding atomic-force-microscopy (AFM) and photoluminescence data.

SAMPLE PREPARATION AND MEASUREMENT METHODS

Two groups of samples were grown by molecular-beam epitaxy (MBE) on semi-insulating GaAs(001) substrates misoriented along the [110] direction by 3° on a TsNA-24 setup. The technological structures of the samples 46*m* and 5*p* (group I) and *G*24 and *G*681 (group II) are schematically shown in Figs. 1a and 1b, respectively. To prevent spreading of substrate defects into the heterostructure, the substrates were preliminarily coated with ~0.5-μm-thick GaAs buffer layers in the samples of both groups.

Next, the samples of group I were obtained in the following sequence: first, an $Al_xGa_{1-x}As$ barrier layer with a thickness of $l_7 + l_8 = 16.5 \times 2$ nm; then, a GaAs quantum well (QW) with a thickness of $l_4 + l_6 = 13 \times 2$ nm and a thin ($l_5 \approx 1.8$ nm) separating layer in the middle of the quantum layer; and, finally, the upper $Al_xGa_{1-x}As$ barrier layer with the thickness $l_2 + l_3 = 16.5 \times 2$ nm. The process was completed with overgrowth of a GaAs protective cap layer with the thickness $l_1 \sim 8$ nm. The aluminum concentration in the barrier layers was $x \sim 0.22$. The specific growth characteristic of the sample 5*p* in comparison with the growth characteristic of the sample 46*m* was Si doping of the external parts ($l_8 = 16.5$ nm) of the $Al_xGa_{1-x}As$ barrier layers to a Si concentration of $n = 10^{18}$ cm^{-3}. The total thickness of the $Al_xGa_{1-x}As$ barriers was the same in all the structures and was equal to 33 nm. The growth temperature was 600°C for the GaAs and AlAs layers and 640°C for the $Al_xGa_{1-x}As$ layers. The ratio of the arsenic and gallium fluxes in the growth zone was equal to 30.

Figure 1b schematically shows a sample of group II. The internal structure of all the samples was the same with only one exception—sample G681 had no protective cap layer. The $Al_xGa_{1-x}As$ barrier layers ($x \approx 0.22$) were doped with Si to concentrations of ~10^{18} and ~6×10^{17} cm^{-3} for the layers with the thicknesses l_2 and l_3, respectively, with the total layer thickness being $L =$

$l_2 + l_3 \approx 0.2$–0.3 μm. The growth conditions were as follows: the ratio of the arsenic and gallium fluxes in the growth zone was 30 and 60 for *G*24 and *G*681 samples, respectively. The growth temperatures of the GaAs and $Al_xGa_{1-x}As$ layers were 600 and 630°C for sample *G*681 and 585 and 615°C for sample *G*24.

X-ray diffraction and X-ray reflectometry measurements were performed on a TRS-1 triple-crystal X-ray spectrometer. The incident X-ray radiation from a 1.2 kW tube with a copper anode was formed by a slit Ge(001) monochromator (thrice reflected 004 reflection). The double-crystal X-ray diffractometry curves were recorded in the quasidispersionless (*n*, –*m*) crystal geometry. We studied the 004 reflection for all the samples. The double-crystal X-ray diffractometry curves were recorded in the mode of the set statistics (5–10%). The step of angular scanning was 10 arc sec far from the exact Bragg angle and 1 arc sec in the vicinity of this angle. To decrease the contribution of the diffuse and background components to the recorded signal, we used a horizontal slit with a width of 5 arc min placed in front of the detector. The reflectometry curves were recorded in the θ/2θ and θ modes with the use of a slit with a width of 2 arc min placed in front of the detector. The scanning step ranged within 10″–20″. Depending on the signal intensity, the measurement time at each point ranged from 2 to 100 s with the average statistics being equal to 5%.

Photoluminescence spectra were measured by the standard method. Photoluminescence was excited by a continuous argon laser with a wavelength of 488 nm. The excitation density varied within 10–10^2 W/cm^2. A sample was placed into an optical cryostat, which allowed us to vary the sample temperature from liquid nitrogen temperatures to room temperature.

EFFECT OF BARRIER-LAYER DOPING ON THE STRUCTURES OF THE SEPARATING LAYER AND THE QUANTUM-WELL BOUNDARIES

Diffractometry. The double-crystal X-ray diffractometry curves of samples 46*m* and 5*p* are shown by vertical bars in Figs. 2a and 2b with due regard for the statistical errors. The curves calculated for the final models are shown by solid lines. Figure 2b also shows the double-crystal X-ray diffractometry curves calculated on the basis of the growth model shown in Fig. 1a (*1*) with an AlAs separating layer and (*2*) without such a layer. It is seen that the tails of all the curves for all the samples show characteristic oscillations, with their number on the right from the Bragg maximum being considerably larger than on the left of it. This effect is associated with the influence of the main Bragg maximum from the substrate on interference. For simple models of layers (single layers on the surface of crystalline substrates, superlattices, etc.), the oscillation period allows one to calculate the layer thickness and the average deformation is determined from the position of the central Bragg maximum of the layer [17]. The double-crystal diffractometry curve from heterostructures with layers of different thicknesses and compositions has a more complicated shape. Therefore, in this case, the reconstruction of the parameters of multilayer heterostructures is possible only by mathematical fitting of the experimental data [2–5, 17] with due regard for the diffuse-scattering contribution to the recorded intensity.

Double-crystal X-ray diffractometry curves were analyzed on the basis of the χ^2 criterion within the framework of the dynamical theory of X-ray scattering using the following procedure [2]:

$$\chi^2 = \frac{1}{m-N}\sum_{i=1}^{m}(I_i^t - I_i^{ex})^2/s_i^2. \quad (1)$$

Here, m is the number of points on the experimental curves, N is the number of parameters to be determined (thickness, deformation, static Debye–Waller factor for each layer, diffuse-scattering intensity), I_i^t and I_i^{ex} are the theoretically calculated and experimentally measured intensities, and s_i are the measurement errors at each point.

For all the structures studied, as an initial approximation, we used the models with the parameters corresponding to the growth conditions (Fig. 1). In fact, we assumed that the layers were uniform over the whole thickness and had sharp interfaces. A curve calculated for the sample 5*p* is shown in Fig. 2b (curve *1*). It is seen that the positions and the amplitudes of the calculated oscillations differ considerably from the experimentally observed positions and amplitudes. In order to obtain the reliable structure parameters we fitted the theoretically calculated double-crystal diffractometry curves to the experimentally measured ones. We varied the following parameters: layer thickness l_j in the heterostructure (j is the layer number); the perpendicular components of the relative change in the crystal-lattice parameter, $\Delta a_{j\perp}/a$ (depending, in particular, on the Al concentration in the $Al_xGa_{1-x}As$ layers); and the static Debye–Waller factors f_j ($0 \le f \le 1$), which describe the degree of disorder and imperfection in the layers. Diffraction scattering from a thin AlAs separating layer was very weak. Therefore, we assumed in fitting that the thickness of this layer was equal to the technologically set one and, thus, varied only the crystal-lattice parameter $\Delta a_\perp/a$ (corresponding to the average aluminum concentration in this layer) and the static Debye–Waller factor f. When analyzing the double-crystal X-ray diffractometry curves, we took into account diffuse scattering, which, unlike diffractive scattering, in the general case, is incoherent and has an angular dependence that shows no oscillations. It should also be noted that, in the case of multilayer superlattices, the roughness replication at the interfaces or the formation of a

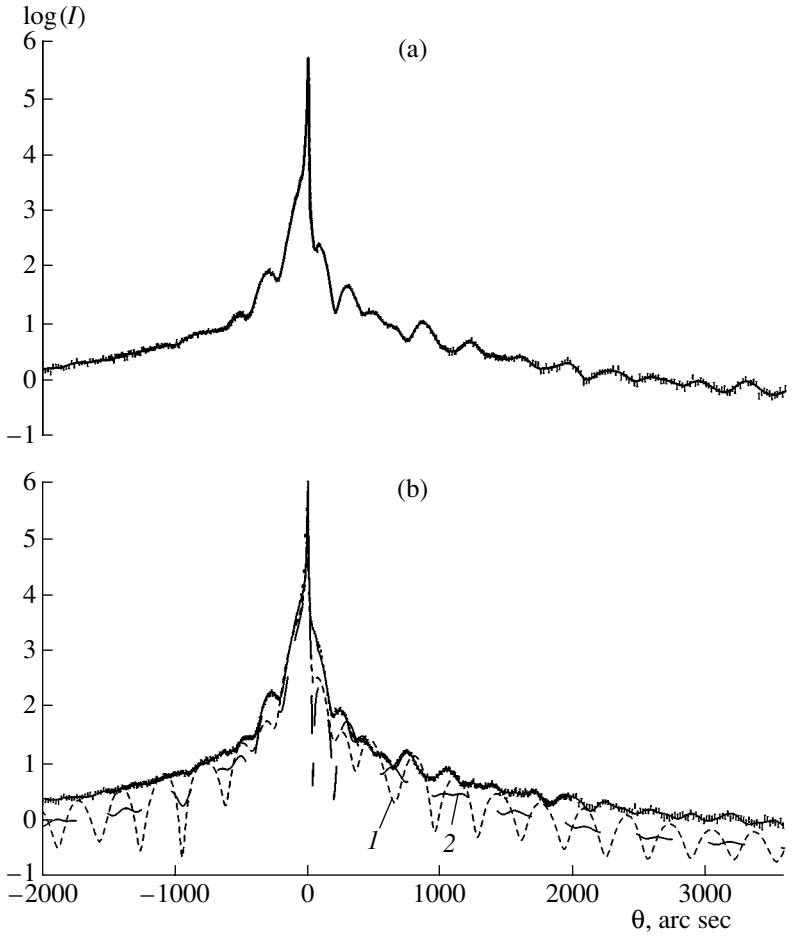

Fig. 2. Double-crystal X-ray diffractometry curves (vertical bars) and theoretically calculated curves (solid lines) for two samples: (a) 46*m* and (b) 5*p*. Curve *1* is calculated by the parameters set by technology for the sample 5*p*. Curve *2* is similar but calculated without the AlAs layer.

long-range order of scatterers along the surface can give rise to partly coherent diffuse scattering [18, 19]. However, in our case, this effect was practically absent and the diffuse scattering could be described by a piecewise smooth function [20]. In our case, the validity of this approach was confirmed by additional experimental measurements with the use of slits having various angular widths and different scanning modes $(\theta + \theta_0)/(1 + \beta)\theta$, where β is the factor of reflection asymmetry and θ_0 is the constant angular displacement of the sample.

The double-crystal X-ray diffractometry curves calculated for the final models are shown by solid lines in Figs. 2a and 2b for the samples 46*m* (undoped) and 5*p* (doped with silicon), respectively. For a more detailed description of the experimental double-crystal X-ray diffractometry curves we introduced into the initial models two additional transitional layers above and below the GaAs quantum well (sublayers Sl_1 and Sl_4) (Fig. 1a) (see table). The introduction of these sublayers at the fixed thickness of the separating layer did not give rise to any new physical result. The calculations showed that even thin sublayers have parameters close to those of the barrier layers in both doped and undoped samples. An increase in the sublayer thickness is equivalent to the division of the barrier layers into sublayers with the same characteristics and, therefore, cannot give any new physical solution. However, the data obtained indicate the formation of sharp interfaces (with thickness not exceeding 1–2 nm) between the $Al_xGa_{1-x}As$ barrier layers and the separated GaAs quantum well (Fig. 1a).

The layer parameters (thickness; relative density $\nu = \rho(x)/\rho_0$, where ρ_0 is the density of the single-crystal substrate; and the static Debye–Waller factor *f*) reconstructed from the diffraction data are indicated in the table. The calculations show that the fitting curves for all the samples ($\chi^2 \le 1.5$) describe the experimental curves well. Thus, Figs. 2a and 2b show that the number of oscillations, their angular positions, and the intensity values on the experimental and resulting curves practically completely coincide. The static Debye–Waller factor for all the layers is close to unity, which indicates a very high perfection of the layers. The value of the

Layer parameters obtained by double-crystal X-ray diffractometry (DCXD) and high-resolution X-ray reflectometry (HRXR)

Layer	Parameters	*G*46*m*		*G*5*p*	
		DCXD	HRXR	DCXD	HRXR
GaAs, GaAs cap layer l_1	l, nm	2.8(3)	9.5	9.4(4)	13.0
	ρ/ρ_0	1.000(1)	1.00(4)	1.000(1)	1.03(7)
	f	0.65(5)	–	0.80(2)	–
$Al_xGa_{1-x}As$ $l_2 + l_3$	l, nm	35.5(4)	31.9	35.5(2)	35.2
	ρ/ρ_0	0.94(1)	0.93(3)	0.96(1)	0.98(8)
	f	0.90(2)	–	0.99(1)	–
Sl_1, sublayer	l, nm	1.5(5)	~1.5	1.5(5)	~1.5
	ρ/ρ_0	0.8(1)	0.96(4)	0.92(4)	0.9(1)
	f	0.79(3)	–	0.95(1)	–
GaAs, GaAs quantum well l_4	l, nm	16.2(2)	14.2	15.6(3)	14.8
	ρ/ρ_0	0.993(3)	0.98(4)	0.996(2)	1.0(1)
	f	0.91(1)	–	1.00(0)	–
Sl_2, sublayer	l, nm	–	~0.2	–	~0.8
	ρ/ρ_0	–	0.94(7)	–	1.0(1)
AlAs, l_5	l, nm	1.8	1.4	1.8	1.6
	ρ/ρ_0	0.66(5)	0.68(6)	0.76(4)	0.81(9)
	f	0.61(2)	–	0.85(1)	–
Sl_3, sublayer	l, nm	–	~0.2	–	~1.2
	ρ/ρ_0	–	0.94(9)	–	0.88(8)
GaAs, GaAs quantum well l_6	l, nm	15.3(9)	17.9	15.4(8)	17.5
	ρ/ρ_0	0.994(2)	0.97(5)	0.971(2)	0.98(8)
	f	0.90(1)	–	0.932(9)	–
Sl_4, sublayer	l, nm	1.5(5)	~1.5	1.5(5)	~1.5
	ρ/ρ_0	0.93(2)	0.96(4)	0.90(1)	0.95(8)
	f	0.84(4)	–	0.87(4)	–
$Al_xGa_{1-x}As$ $l_7 + l_8$	l, nm	30.3(9)	29.0	34.5(8)	31.9
	ρ/ρ_0	0.91(2)	0.95(2)	0.90(2)	0.96(8)
	f	0.829(7)	–	0.81(1)	–
GaAs, buffer layer l_9	l, nm	494(2)	–	521(4)	–
	ρ/ρ_0	0.997(1)	–	0.999(1)	–
	f	0.919(8)	–	0.89(1)	–
GaAs, GaAs substrate l_{10}	l, nm	500	–	500	–
	ρ/ρ_0	1.000(1)	–	1.000(1)	–
	f	0.906(9)	–	0.89(1)	–

parameter f for a thin AlAs separating layer ranges within ~0.6–0.8. Therefore, this layer may also be considered a single-crystal one. However, the diffractometric data do not allow one to establish the cause of the lower reflectivity of the AlAs layer. It may be associated with a large number of lattice defects and inhomogeneity or spreading of the layer boundaries. It is necessary to indicate that any X-ray diffraction experiments is undertaken, first of all, with the aim to determine the lattice parameters, the changes in the interplanar spacings, etc. The data on impurity concentration, composition of solid solutions, and their continuity or porosity are determined on the basis of chosen model representations. The relative density ν was calculated with due regard for possible tetragonal distortions in thin deformed layers under the assumption that Vegard's law is fulfilled [1]. To confirm the adequacy of the layer models, determine the thickness of the separating layer, and refine the interface structure, we recorded the respective high-resolution X-ray reflectometry curves.

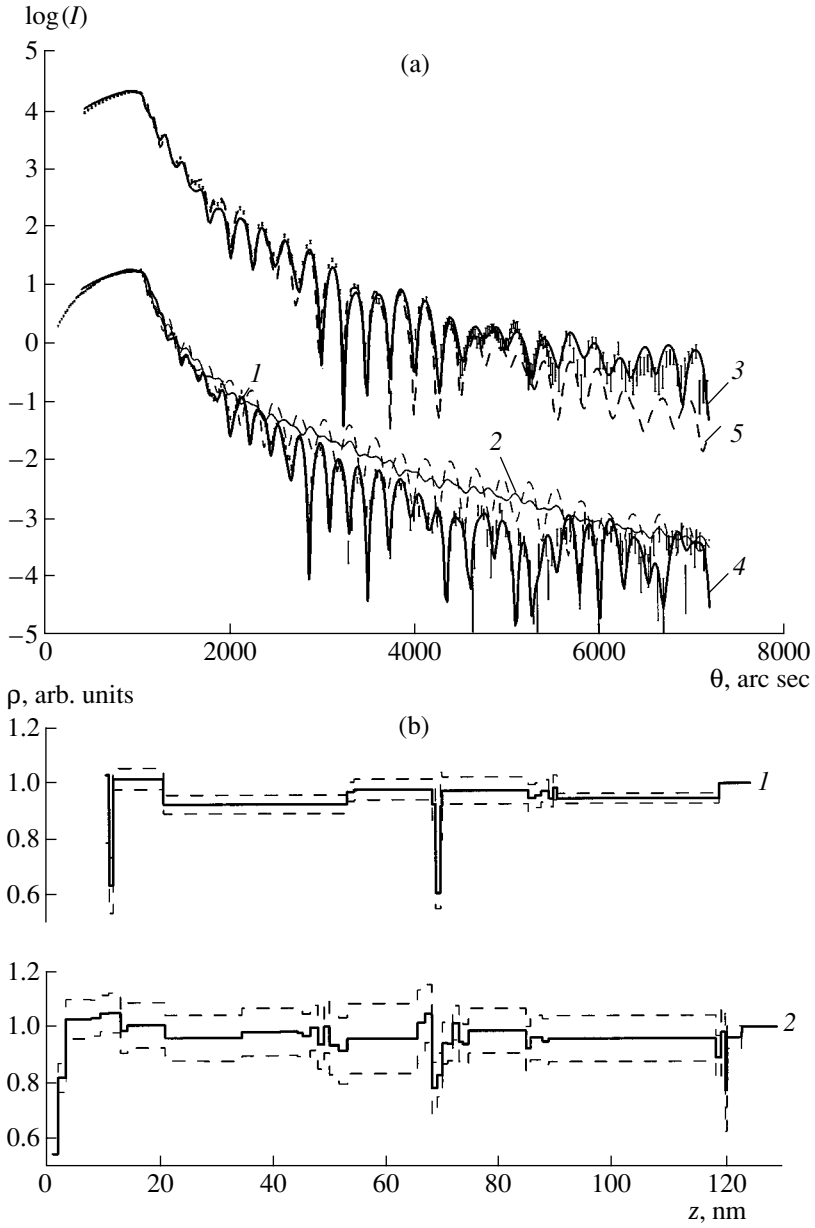

Fig. 3. Specular reflection curves (vertical bars) for two samples 46*m* (above) and 5*p* (below; $\times 10^{-3}$). (a) curve *1* is calculated by the parameters set by technology for the sample 5*p*; *2* is the analogous curve *1* calculated without the AlAs layer; curves *3* and *4* illustrate fitting to the multilayer model for samples 46*m* and 5*p*, respectively; curve *5* is analogous to curve *3* but for the case of rough boundaries around the AlAs layer (the roughness parameter $\sigma = 0.5$ nm). (b) Density-distribution profiles for a multilayer model and the error intervals for the parameters of the samples 46*m* (curve *1*) and 5*p* (curve *2*), respectively.

Reflectometry. The experimental curves for the samples 46*m* (above) and 5*p* (below, $\times 10^{-3}$) are indicated by vertical bars in Fig. 3a. One can see a large number of pronounced oscillations at large grazing angles. It should be noted that we managed to measure the intensity of specular reflection in a considerably larger angular range (0″–7200″) than in the double-crystal X-ray diffractometry experiment despite a lower (by an order of magnitude) intensity of the incident radiation and a small difference in the layer densities in the heterostructure studied (Fig. 1a).

The model was reconstructed by the method described in [15]. The initial model consisted of six independent layers (Fig. 1a) with rough interfaces. The correspondent model curve for the sample 5*p* is shown by a dashed line (*1*) in Fig. 3a. The oscillations on this curve are quite similar to those observed on the experimental curve. Despite a relatively good agreement of the angular positions, the amplitudes of the oscillations on the model curve differ from the experimentally measured amplitudes considerably. Thus, high-resolution X-ray reflectometry data show that, on the whole, the

grown structure corresponds to the structure set by the growth technology. However, the density distributions along the layer depth are different. These smallest deviations are established quite reliably because of the high sensitivity of the method of high-resolution X-ray reflectometry. The intensity measurements in the range exceeding the range of recording of double-crystal X-ray diffractometry curves allow one to determine the structure parameters with a higher depth resolution and refine the diffractometric data.

One of the main tasks of the present study was to determine the structure of the AlAs separating layer. It was shown [15] that high-resolution X-ray reflectometry is very sensitive to the presence of thin layers at the structure interfaces with slight density variations. Curve *2* in Fig. 3a corresponds to the model of the sample 5*p* without the separating AlAs layer. It is seen that the oscillation amplitude considerably decreases. The curve is inconsistent with the experimental results, which shows that the model having no thin layers inside the structures is inadequate. Different experimental curves from samples 46*m* and 5*p* indicate different internal compositions of the layers forming the heterostructure (Fig. 1a).

High-resolution X-ray reflectometry curves were fitted on the basis of the model of an arbitrary number of sublayers with independent densities. Fitting of the reflectometry curves on the basis of the χ^2 criterion (1) is associated with a much larger number of experimental factors than in the diffractometric curves and is difficult to take into account. This model can lead to physically unjustified solutions, e.g., the solution with pronounced density beatings in neighboring thin sublayers. Therefore, the most appropriate solution was selected under certain constraints: the density variation in neighboring sublayers of each layer and in the interlayer boundaries were limited to 5–10%. Layer thicknesses were also varied. The calculated X-ray reflectometry curves for the resulting model of the samples 46*m* (curve *3*) and 5*p* (curve *4*) are shown in Fig. 3a. We managed to attain the minimum χ^2 values for the samples 46*m* and 5*p* equal to 9 and 15, respectively. For the sample 46*m*, the solution was determined on the basis of the model consisting of 19 layers, whereas for the sample 5*p*, the number *N* of the sublayers in the fitting procedure was increased to 52. The introduction of a large number of parameters yields better fitting results, but, at the same time, increases the errors of their determination (20%) considerably. This general problem is associated with the limited volume of the experimental information contained in the experimentally measured curve. The reduction of the number of sublayers to 41 allows one to reduce the errors to the ≤12% (Fig. 3b, dashed lines around curve *2*). The worse quality of fitting of the X-ray reflectometry curve for the sample 5*p* than of that for the undoped sample 46*m* is explained by its complex morphology, primarily, in the vicinity of the quantum well.

The fitted models of the density profiles $\nu(z)$ (curves *1* and *2*) for the samples 46*m* and 5*p*, respectively, are shown in Fig. 3b. It is seen that the layer structure is consistent with the diffractometry data. The qualitative and quantitative differences revealed are associated mainly with the thickness and the boundaries Sl_2 and Sl_3 of the AlAs separating layer and the boundaries between the $Al_xGa_{1-x}As$ barrier layers and GaAs quantum well. For the sample 46*m*, the thickness of the AlAs layer is ~1.4 nm along the interlayer boundary width Sl_2 and Sl_3 ranging within 0.1–0.2 nm (see table). The corresponding thicknesses for the sample 5*p* are 1.6 and ≈0.8–1.2 nm. In order to control the model sensitivity to the thickness of the boundaries Sl_2 and Sl_3 of the sample 46*m*, we performed the calculations at boundary thicknesses ranging within 0.3–0.5 nm. Curve *5* corresponding to these calculations is shown in Fig. 3a. The behavior of the curve tails show that, at large grazing angles, the discrepancy between curves *3* and *5* considerably exceeds the measurement error.

The thicknesses and densities of the layers determined by the method of X-ray reflectometry after averaging over thicknesses of the layers forming the heterostructure (Fig. 1a) and with due regard for the error intervals (Fig. 3b) are indicated in the table. It is seen from the table that the average densities in the layers and sublayers Sl_{1-4} obtained on the basis of the X-ray reflectometry data agree satisfactorily with the results obtained by the double-crystal X-ray diffractometry with due regard for Vegard's law. The thicknesses of the barrier layers, quantum wells, and sublayers are within the experimental accuracy and agree with the double-crystal X-ray diffractometry data. Analysis of the table leads to the following conclusions. The X-ray reflectometry confirms the formation of the interface between the barrier-layer and the quantum well with a thickness ranging within 1–2 nm for both doped and undoped samples. Second, the structure of the barrier layers and quantum-well layers after doping become less homogeneous. Third, doping also results in an increase in the thickness of the boundaries separating the AlAs $Sl_{2,3}$ layer up to ~1 nm. Finally, the X-ray reflectometry data confirm the existence of a thin protective cap layer at the heterostructure surface revealed by double-crystal X-ray diffractometry. The two methods give somewhat different (by a factor of 1.5–3.0) thickness of the cap layer, which seems to be associated with the existence on the surface of an additional strongly amorphized layer making no contribution to the diffraction scattering and, therefore, revealed only by high-resolution X-ray reflectometry. This result confirms the necessity of combined use of high-resolution X-ray reflectometry and double-crystal X-ray diffractometry for more detailed characterization of multilayer heterostructures.

It is also important to note that because of the lack of experimental data it is very difficult to extract similar detailed information on the thin-layer boundaries from double-crystal X-ray diffractometry data alone under

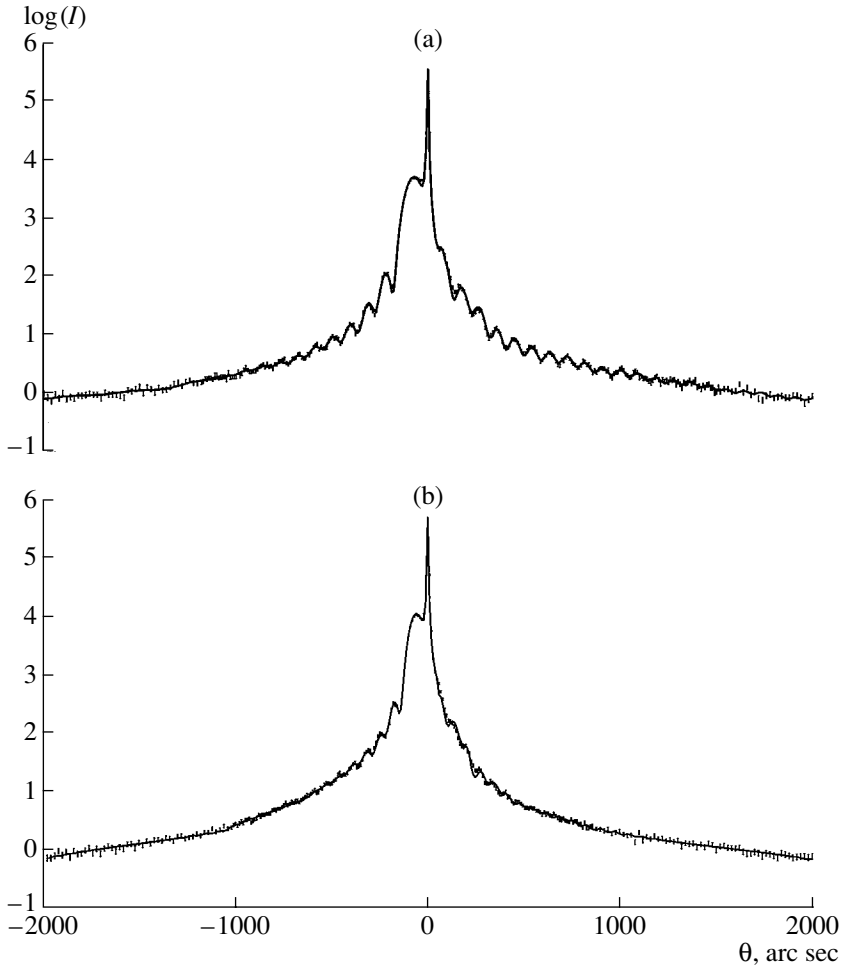

Fig. 4. Double-crystal X-ray diffractometry curves (vertical bars) and the corresponding theoretically calculated curves (solid lines) for the samples (a) *G*24 and (b) *G*681.

laboratory conditions. This is explained by the fact that 1- to 2-nm-thick layers influence mainly the tails of double-crystal X-ray diffractometry curves [2, 3]. It is difficult to record these curves in a large angular range because of an increasing contribution of diffuse scattering from heterostructure and substrate defects. Diffuse scattering is distributed around the reciprocal-lattice point *hkl* and a considerable part of diffuse scattering is recorded together with the useful signal. Conversely, when measuring high-resolution X-ray reflectometry curves, diffuse scattering, an analogue of small angle scattering, is concentrated in close to the incident but not the reflected beam. The use of narrow slits in front of the detector in high-resolution X-ray reflectometry experiments makes it possible to considerably reduce the diffuse-scattering contribution to the recorded intensity. Note also that the use of a crystal analyzer instead of the slit may help to suppress diffuse scattering also in the double-crystal X-ray diffractometry experiments. However, the use of a crystal analyzer makes the experiment and the subsequent processing of the results much more difficult. Moreover, the use of small grazing angles increases the contribution of scattering from thin layers with respect to the total scattering. For example, in the experiment illustrated by Fig. 2, at deviation angles of 2000 arc sec, the intensity of Bragg scattering decreases by more than five orders of magnitude, whereas in the high-resolution X-ray reflectometry method, such a decrease in intensity is observed at angles exceeding 7200 arc sec.

INFLUENCE OF THE PROTECTIVE CAP LAYER ON THE STABILITY OF THE STRUCTURE OF ALUMINUM-CONTAINING BARRIER LAYERS

Diffractometry. Experimental double-crystal X-ray diffractometry curves from samples *G*24 and *G*681 after their keeping for a year under laboratory conditions are shown in Fig. 4a and Fig. 4b, respectively. Despite some obvious differences, on the whole, the curves are similar and indicate the formation of heterostructures (Fig. 1b) in both samples. The absence of a cap layer on sample *G*681 practically does not affect

the shape of the respective double-crystal X-ray diffractometry curve. The "classical shape" of double-crystal X-ray diffractometry curves corresponds to the curves obtained from the samples coated with a thin epitaxial film [17]. It is seen that, in addition to the main diffraction maximum at $\Delta\theta = 0$, the tails of the double-crystal X-ray diffractometry curves have an additional maximum at $\Delta\theta \approx -90''$ and small oscillations on both sides of the main Bragg maximum. The estimates based on the kinematical theory show that the surface of each sample is coated with a 0.2- to 0.3-μm-thick single-crystal layer with a lattice parameter somewhat larger than the lattice parameter of the GaAs substrate ($\Delta a_\perp/a \approx 6.7 \times 10^{-4}$). In accordance with Vegard's law and with due regard for possible tetragonal distortions, the average content of Al in the $Al_xGa_{1-x}As$ layers (Fig. 1b) amounts to $x \sim 0.25$ in both samples. These data show that, on the whole, the layers grown on the surface of *G*24 and *G*681 samples correspond to the heterostructure set by technology. Note also that the additional oscillations on double-crystal X-ray diffractometry curves from sample *G*681 are somewhat weaker. Taking into account the total thickness of the heterostructure, we see that this phenomenon cannot be explained by the absence of a ~4–8-nm-thick protective layer on sample *G*681 (Fig. 1b). Later, it will be shown that this indicates the presence of some local structural distortions of the subsurface layers of this sample. The theoretical treatment of the experimental curves based on the χ^2 model showed the following. The heterostructure of sample *G*681 ($\chi^2 = 1.56$) consists of two layers; counted from the buffer layer: the $Al_{0.22}Ga_{0.78}As$ (l = 236.7(1) nm layer, f = 0.98(1)) and the GaAs, layer (l = 6.2(1) nm, f = 0.474). The heterostructure of sample *G*24 ($\chi^2 = 2.7$) consists of three layers: $Al_{0.22}Ga_{0.78}As$ (l = 149.6(1) nm, f = 0.92(1)), $Al_{0.22}Ga_{0.78}As$ (l = 53.7(1) nm, f = 0.95(1), and GaAs (l = 5.0(1) nm, f = 0.80(2)). These data show that both samples are coated with weakly reflecting layers with thicknesses ranging within 5–6 nm and not containing Al. Under these layers, the perfect barrier layers are located.

Reflectometry. Figure 5a shows high-resolution X-ray reflectometry curves (vertical bars) for samples *G*24 (up to 3600 arc sec) and *G*681 (up to 1500″) obtained by θ/2θ scanning. It is seen that these curves differ from one another considerably, whereas the experimental double-crystal X-ray diffractometry curves recorded from the same samples are similar (Fig. 4). Thus, for the sample *G*24, considerable specular reflection with weak oscillations is observed in the whole angular range studied. The theoretical treatment of this curve by the method suggested in [15] yielded a model curve with $\chi^2 = 3$ shown in Fig. 5a (curve *1*). The corresponding theoretical density-distribution profile over depth is shown in Fig. 5b (curve *1*, dashed lines show the error interval for density). It is seen that the structure consists of three layers with a total thickness of ~220 nm, which is also confirmed by the double-crystal X-ray diffractometry data and is consistent with the growth model (Fig. 1b). The absence of the sharp upper boundary of the protective cap layer indicates, in particular, its degradation during sample storage and also presence of some adsorbed atoms.

Conversely, for the sample *G*681, no specular reflection is observed immediately after the attainment of the critical angle of total external reflection, $\theta_c = 1080''$. This result shows that, in this case, the heterostructure of the sample *G*681 has no protective cap layer and, after storage under the laboratory conditions, the sample surface is strongly distorted. The respective calculation was performed on the basis of the Gaussian model [15] of the transitional layer of thickness t = 9 nm on the sample surface (curve *2* in Fig. 5a). The corresponding density profile is shown by curve *2* in Fig. 5b.

To confirm the pronounced surface roughness of the sample *G*681 (in comparison with the surface of the sample *G*24) we recorded the diffuse-scattering distribution in the vicinity of the 000 reciprocal-lattice point by θ scanning. Analysis of its sections showed that the *G*24 sample shows only specular reflection without any noticeable diffuse maximum. At the same time, the diffuse-scattering sections of the sample *G*681 showed no specular-reflection maximum immediately after the attainment of scattering angles exceeding θ_c. At the same time, these sections show only an intense Yoneda peak, which indicates the considerable surface roughness and density inhomogeneities in the main layers [21]. The reflectometry data confirm the formation of heterosystems in both *G*24 and *G*681 samples and show that the subsurface layers of these samples differ both quantitatively and qualitatively. This difference is caused by considerable structural changes in the subsurface layers of the sample *G*681 in the process of its storage. As a result, the surface morphology and the parameters of the subsurface layers of the samples of group II are considerably different. In order to confirm the conclusion about the surface distortion, these samples were studied by atomic force microscopy. The surface images of the samples *G*24 and *G*681 are shown in Figs. 6a and 6b, respectively. Their analysis shows that the surface roughness of the samples *G*24 and *G*681 attains the values ~3 and ~10 nm, respectively. These results are consistent with the models of vacuum/crystal interfaces illustrated for samples of group II in Fig. 5b.

Photoluminescence. The experimental photoluminescence spectra of the samples *G*24 and *G*681 measured at T = 77 K are shown in Figs. 6c and 6d, respectively. The spectra of as-grown samples have an intense band at λ = 735 nm corresponding to the transitions between the ground states of electrons and holes in the quantum well. The higher intensity of the main band on the photoluminescence spectrum of the as-grown sample *G*681 in comparison with the analogous intensity of the spectrum from the *G*24 sample is explained by a strong dependence of the increase in the photolumines-

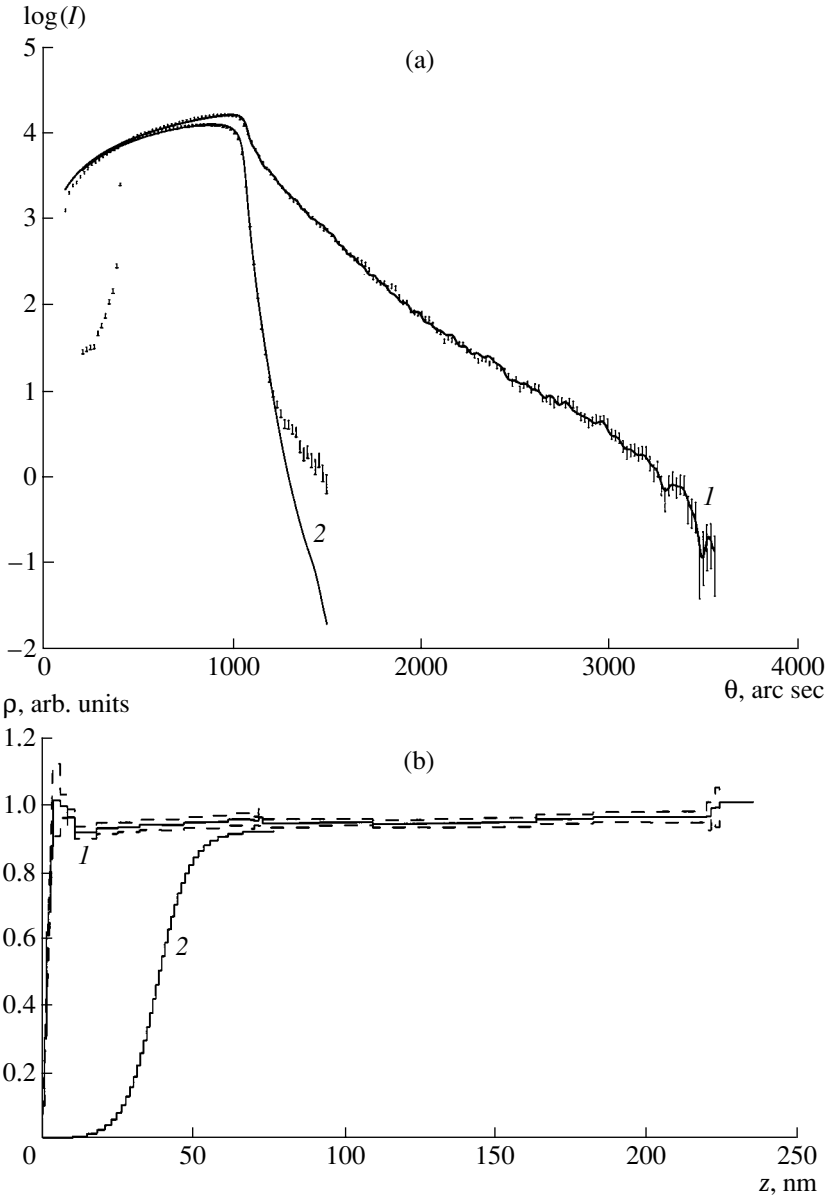

Fig. 5. (a) Specular reflection curves (vertical bars) from the samples *G*24 (on the right) and *G*681 (on the left) and the calculated curves for the sample *G*24 (curve *1* for the multilayer model) and *G*681 (curve *2* with due regard for the transitional layer) and (b) density-distribution profiles for the samples *G*24 (curve *1* with the error interval) and *G*681 (curve *2*).

cence yield on the temperature of growth of the GaAs and AlGaAs layers in the *G*681 sample [22]. To verify the sensitivity of the double-crystal X-ray diffractometry to the presence of a protective cap layer on the surface and stability of the structure of the barrier layers of samples *G*24 and *G*681, we recorded the spectra of the same samples after one year of storage in air (open circles in Figs. 6c and 6d). It is seen that the intensities of photoluminescence bands of the sample *G*24 (Fig. 6c) remained unchanged, whereas the intensity of the main band of the sample *G*681 (Fig. 6d) having no GaAs protective cap layer decreased by more than an order of magnitude. This result shows that the surface distortion seems to be associated with the high chemical activity of aluminum atoms. This is confirmed by pronounced surface roughness of the sample *G*681. The residual photoluminescence of the sample *G*681 becomes clear after comparative analysis of the photoluminescence spectra and the double-crystal X-ray diffractometry and high-resolution X-ray reflectometry data.

Indeed, the high-resolution X-ray reflectometry data show that degradation of the sharp vacuum/crystal interface on the surface of the *G*881 sample resulted in the formation of ~9-nm-high roughness. The roughness and other structural defects in the subsurface layers of this sample became the centers of photoluminescence

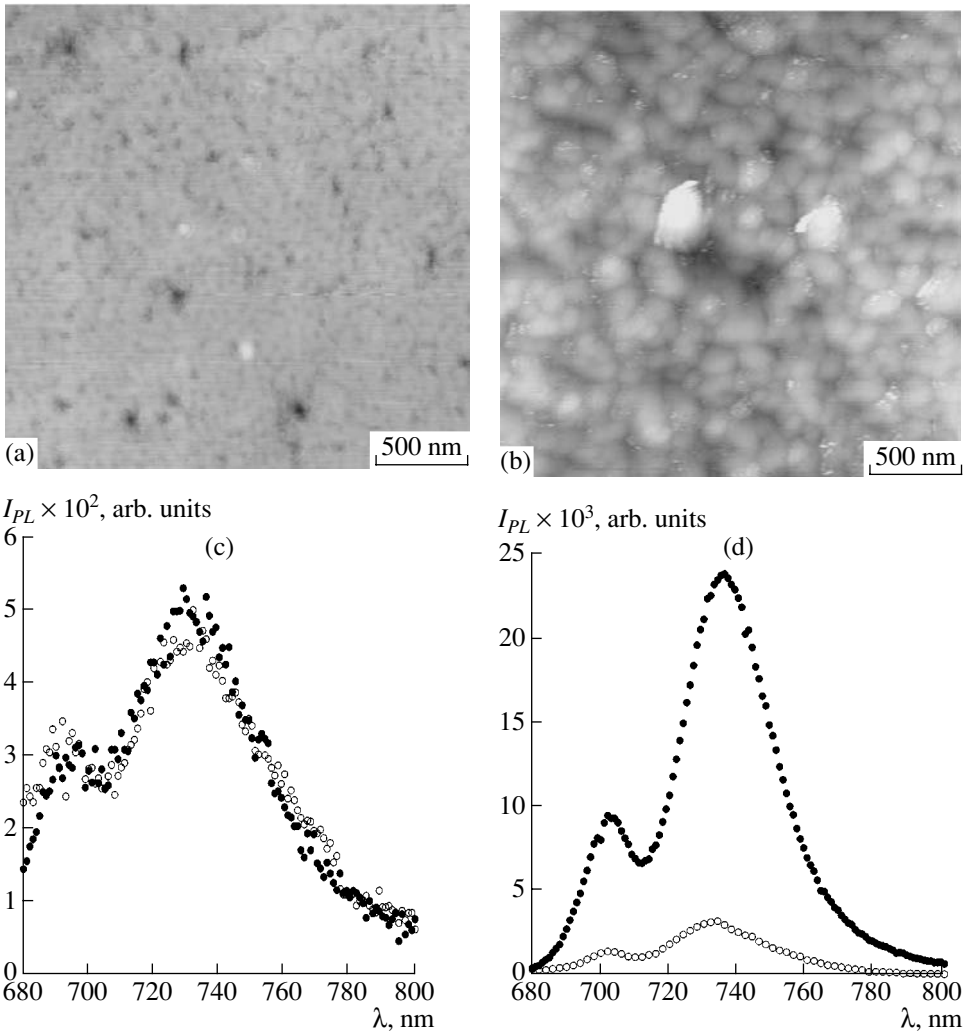

Fig. 6. (a, b) AFM images of the surfaces and (c, d) the photoluminescence spectra of the samples *G*24 and *G*681. Closed circles are the data obtained for as-grown samples; open circles, for samples kept in air for a year.

quenching and disappearance of the photoluminescence yield. At the same time, the diffraction data show that the heterostructure of the sample *G*681 was preserved despite surface degradation during sample storage and that the individual layers of this heterostructure may be considered as single crystal layers with volume defects in the subsurface layer, whereas the remaining crystalline parts determined the photoluminescence yield observed.

CONCLUSIONS

Our study showed that the exhaustive characterization of a multilayer heterosystem with thin (several nanometers) deeply located layers requires the use of the high-resolution X-ray reflectometry method along with double-crystal X-ray diffractometry. The use of the former is especially important for the determination of the thickness and composition of the layers with the lattice parameters that only slightly differ from the lattice parameter of the substrate.

The combined use of double-crystal X-ray diffractometry and high-resolution X-ray reflectometry in the studies of the nanodimensional $Al_xGa_{1-x}As/GaAs/Al_xGa_{1-x}As$ system allowed us to determine the thickness and the composition of the AlAs layer separating the quantum well at a resolution ranging within 0.1–1.2 nm and also to evaluate the widths of its interfaces. Analysis of the density-distribution profiles of these structures allowed us to establish the influence of doping of the barrier layers on their homogeneity, determine the size of the quantum wells, and confirm and refine the data obtained by double-crystal X-ray diffractometry.

A higher depth resolution in the high-resolution X-ray reflectometry (in comparison with the double-crystal X-ray diffractometry) was attained by using small grazing angles and considerably reducing the

intensity of the background component in the total signal. This also allowed us to record high-resolution X-ray reflectometry curves in a wider angular interval, 0°–2°, in comparison with the angular interval of 0.5° in double-crystal X-ray diffractometry.

Comparison of the densities of binary layers of the known chemical compositions obtained by the X-ray diffraction method with the data obtained by X-ray reflectometry allowed us not only to verify the validity of Vegard's law for very thin elastically stressed layers but showed that a similar approach may also be applied to ternary and quaternary solid solutions.

Finally, it should be noted that the insufficient sensitivity of the double-crystal X-ray diffractometry to roughness and surface morphology of the samples made the combined use of double-crystal X-ray diffractometry and high-resolution X-ray reflectometry necessary for the successful construction of adequate models of individual layers, especially in the studies of their aging.

ACKNOWLEDGMENTS

We are grateful to V. A. Bushuev for his interest in our study and useful remarks. The study was supported by the Federal Agency on Science, project nos. 37.029.1.1.034, 40.072.1.1.1177, and 40.072.1.1.1178 and the Russian Foundation for Basic Research, project no. NSh-14.04.2003.2.

REFERENCES

1. L. Tapfer and K. Ploog, Phys. Rev. B **40**, 9802 (1989).
2. A. M. Afanas'ev, M. A. Chuev, R. M. Imamov, *et al.*, Kristallografiya **42** (3), 514 (1997) [Crystallogr. Rep. **42** (3), 467 (1997)].
3. A. M. Afanas'ev and R. M. Imamov, Kristallografiya **48** (5), 786 (2003) [Crystallogr. Rep. **48** (5), 728 (2003)].
4. V. Holy, U. Pietsch, and T. Baumbach, *High-Resolution X-ray Scattering from Thin Films and Multilayers* (Springer, Berlin, 1999).
5. M. Wormington, Ch. Panaccione, and K. Matney, Philos. Trans. R. Soc. London, Ser. A **357**, 2827 (1996).
6. Zh. I. Alferov, Fiz. Tekh. Poluprovodn. (St. Petersburg) **32** (1), 3 (1990).
7. A. A. Lomov, M. A. Chuev, and G. V. Ganin, Tech. Phys. Lett. **30** (5), 441 (2004).
8. A. M. Afanas'ev, M. A. Chuev, R. M. Imamov, *et al.*, Pis'ma Zh. Éksp. Teor. Fiz. **74** (10), 560 (2001) [JETP Lett. **74** (10), 498 (2001)].
9. S. V. Evstigneev, R. M. Imamov, and A. A. Lomov, Fiz. Tekh. Poluprovodn. (St. Petersburg) **34** (6), 719 (2000).
10. L. P. Avakyants, P. Yu. Bokov, G. B. Galiev, *et al.*, Opt. Spektrosk. **93** (6), 929 (2002) [Opt. Spectrosc. **93** (6), 857 (2002)].
11. A.-M. Lanzilloto, M. Santos, and M. Shayegan, Appl. Phys. Lett. **55** (14), 1445 (1989).
12. H. Schwenke, P. A. Beaven, and J. Knoth, J. Anal. Chem. **365**, 19 (1999).
13. R. A. Cowley and T. W. Ryan, J. Phys. D **20**, 61 (1987).
14. W. M. Plotz and K. Lischka, J. Phys. III (France) **4**, 1503 (1994).
15. V. A. Bushuev, A. A. Lomov, and A. G. Sutyrin, Kristallografiya **47** (4), 741 (2002) [Crystallogr. Rep. **47** (4), 683 (2002)].
16. Yu. Pozhela, K. Pozhela, and V. Yutsene, Fiz. Tekh. Poluprovodn. (St. Petersburg) **34** (9), 1053 (2000).
17. D. K. Bouén and B. K. Tanner, *High-Resolution X-ray Diffractometry and Topography* (Nauka, St. Petersburg, 2002) [in Russian].
18. V. Holy and T. Baumbach, Phys. Rev. B **49** (15), 10668 (1994).
19. A. Bruson, C. Dufour, B. George, *et al.*, Solid State Commun. **71** (12), 11045 (1989).
20. A. M. Afanas'ev, R. M. Imamov, A. A. Lomov, *et al.*, Mikroélektronika **32** (2), 83 (2003).
21. A. A. Lomov, V. A. Karavanskiĭ, R. M. Imamov, *et al.*, Kristallografiya **47** (6), 1122 (2002) [Crystallogr. Rep. **47** (6), 1051 (2002)].
22. *Molecular Beam Epitaxy and Heterostructures*, Ed. by L. L. Chang and K. Ploog (Martimus Nishoff, Amsterdam, 1985; Mir, Moscow, 1989).

Translated by L. Man

Crystallography Reports, Vol. 50, No. 5, 2005, pp. 751–758. Translated from Kristallografiya, Vol. 50, No. 5, 2005, pp. 813–819.

STRUCTURE OF INORGANIC COMPOUNDS

Absolute Structure of $La_3Ga_5SiO_{14}$ Langasite Crystals

B. A. Maksimov*, V. N. Molchanov*, B. V. Mill, E. L. Belokoneva**, M. Kh. Rabadanov*, A. A. Pugacheva**, Yu. V. Pisarevskiĭ*, and V. I. Simonov***

** Shubnikov Institute of Crystallography, Russian Academy of Sciences, Leninskiĭ pr. 59, Moscow, 119333 Russia*

e-mail: vladimol@ns.crys.ras.ru

*** Moscow State University, Leninskie gory, Moscow, 119992 Russia*

e-mail: mill@plms.phys.msu.ru

Received November 5, 2004

Abstract—The absolute structure of $La_3Ga_5SiO_{14}$ piezoelectric crystals (a = 8.1746(6) Å, c = 5.1022(4) Å, space group $P321$, Z = 1) with the positive sense of rotation of the plane of polarization is refined using X-ray diffraction analysis (R = 1.37%, R_w = 1.71%, 2413 unique reflections, $\max \sin\theta/\lambda = 1.15$ Å^{-1}). The contributions from the anharmonicity of thermal vibrations of lanthanum atoms are calculated with the use of the components of the third- and fourth-rank tensors. It is demonstrated that these contributions can have a significant effect. © *2005 Pleiades Publishing, Inc.*

INTRODUCTION

Crystals of the $La_3Ga_5SiO_{14}$ langasite family ($Ca_3Ga_2Ge_4O_{14}$ structural type, space group $P321$) are promising piezoelectric materials. In this respect, large-sized crystals of $La_3Ga_5SiO_{14}$, $La_3Nb_{0.5}Ga_{5.5}O_{14}$, and $La_3Ta_{0.5}Ga_{5.5}O_{14}$, which are of great practical interest, have been industrially produced by the Czochralski method in a number of countries [1–3]. Moreover, a rather large number of other crystals of related compositions, including solid solutions, have been grown and their elastic, dielectric, electromechanical [1], spectroscopic [4], and crystal optical (in particular, gyrotropic) characteristics [5, 6] have been investigated.

As regards the gyrotropic characteristics, it should be noted that, in the symmetry class 32 involving the space group $P321$, there can exist two chiral modifications that differ from each other as an image differs from its centrosymmetrical mapping. Specifically, such chiral modifications differ in the sense of rotation of the plane of light polarization. Knowing the sense of rotation of the plane of light polarization, it is possible to determine the elastic constants of the crystals under investigation. Depending on the sign, the so-called oblique cut in the yz plane is chosen with a clockwise or counterclockwise rotation with respect to the optic axis 3. Ignoring this circumstance can lead to incorrect determination of some important physical constants of the crystals. As a rule, the sense of rotation of the plane of polarization is determined using polarization-optical methods. The sense is considered as clockwise (positive optical activity) and counterclockwise (negative optical activity) for dextrorotation and levorotation, respectively [7].

Sil'vestrova *et al.* [8, 9] were the first to determine the sign of the optical activity of the $La_3Ga_5SiO_{14}$ and $La_3Nb_{0.5}Ga_{5.5}O_{14}$ crystals, which turned out to be right-handed crystals. Heimann *et al.* [6] also established that the $La_3Ga_5SiO_{14}$, $La_3Nb_{0.5}Ga_{5.5}O_{14}$, $La_3Ta_{0.5}Ga_{5.5}O_{14}$, and $Si_3NbGa_3Si_2O_{14}$ crystals have the positive sign of the optical activity. As far as we know, data for crystals of the langasite family with the experimentally found negative sign of the optical activity are not available in the literature. The rotatory powers (but without signs of the optical activity) for the $La_3Ga_5SiO_{14}$, $La_3Nb_{0.5}Ga_{5.5}O_{14}$, $La_3Ga_5GeO_{14}$, $Ca_3Ga_2Ge_4O_{14}$, and $Sr_3Ga_2Ge_4O_{14}$ crystals were reported by Baturina *et al.* [5]. Two enantiomorphic forms in crystals of the langasite family were first compared during determination of the absolute structures of the $Sr_3Ga_2Ge_4O_{14}$ and $La_3Nb_{0.5}Ga_{5.5}O_{14}$ crystals [10].

The refinement of the structure of $La_3Ga_5SiO_{14}$ crystals was described in four papers [11–14]. Kuz'micheva *et al.* [14] determined the absolute structure and confirmed its correctness in accordance with the universally accepted criteria [15]. Since the studied crystals had a different origin and their structures differed as an image [11–13] and its centrosymmetrical mapping [14], we once again determined the absolute structure of the langasite crystal, which is "genetically" identical to the crystal studied in [11, 12].

The purpose of this study was to refine precisely the structural parameters of the $La_3Ga_5SiO_{14}$ compound, to determine the absolute structure, and to investigate specific features of the electron density and thermal vibrations of the atoms involved.

1063-7745/05/5005-0751$26.00 © 2005 Pleiades Publishing, Inc.

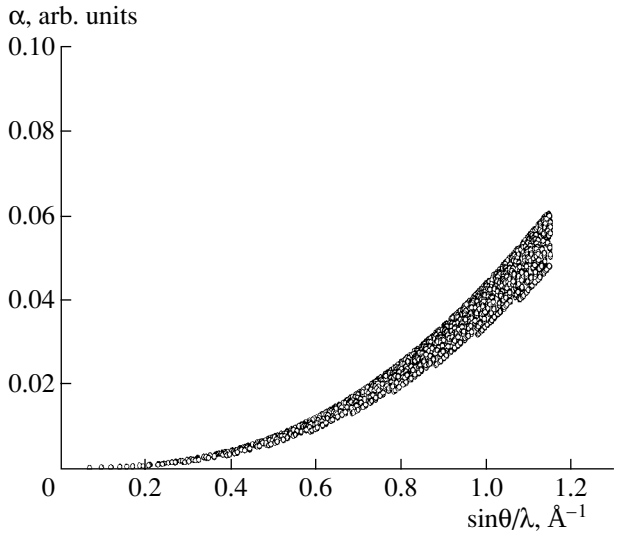

Fig. 1. Correction for thermal diffuse scattering as a function of the parameter $\sin\theta/\lambda$.

SAMPLE PREPARATION AND EXPERIMENTAL TECHNIQUE

The sample to be studied was prepared from an $La_3Ga_5SiO_{14}$ single crystal grown by the Czochralski method from a melt of stoichiometric composition. The crystal weighing as much as 265 g was characterized by constant lattice parameters over the bulk in contrast to the crystal described in [14], whose lattice parameters varied significantly (up to 0.075 and 0.05 Å for the unit cell parameters *a* and *c*, respectively).

A spherical crystal 0.16 mm in diameter was used in X-ray diffraction analysis. The measurements were performed on a CAD-4F diffractometer (filtered MoK_α radiation). The diffraction reflections obtained during automatic searching and their subsequent indexing confirmed the hexagonal type of the lattice previously known for langasite with lattice parameters close to those determined in [12]. A total of 15777 diffraction reflections with $\max \sin\theta/\lambda = 1.15$ Å^{-1} were collected within a full sphere of the reciprocal lattice. The stability of the primary beam was controlled periodically (every three hours) by measuring the intensities of three noncoplanar reflections. The maximum deviations of the intensities of the control reflections did not exceed 0.7% of their mean intensities (the total time of the experiment was approximately equal to 240 h). The intensities were corrected for the Lorentz and polarization factors. Correction for absorption was also introduced. After selecting the reflections with $I > 3\sigma(I)$ and averaging the symmetry-equivalent reflections, a total of 2413 unique reflections $F^2(hkl)$ were obtained for crystallographic calculations. Note that the Friedel equivalent reflections were not averaged. This was necessary for determining the absolute structure. The experimental reflections $F^2(hkl)$ were corrected for thermal diffusion scattering with the use of the elastic constants (taken from [16]) according to the procedure described in [17]. The dependence of the correction for thermal diffuse scattering on the parameter $\sin\theta/\lambda$ is plotted in Fig. 1. The main crystal data, data collection, and refinement parameters for the structure under investigation are presented in Table 1. The processing of the experimental data and all crystallographic calculations were performed with the JANA-2000 software package [18].

CRYSTAL STRUCTURE REFINEMENT

The $Ca_3Ga_2Ge_4O_{14}$ structure can be described as a mixed framework consisting of oxygen tetrahedra of two types, namely, small-sized tetrahedra in the positions 2*d* (cation positions with symmetry 3) and large-sized tetrahedra in the positions 3*f* (symmetry 2), and octahedra in the positions 1*a* (symmetry 32). The coordination polyhedron of large-sized cations occupying holes (the positions 3*e* with symmetry 2) in the framework has eight oxygen vertices and can be represented as a distorted dodecahedron with trigonal faces [19]. The structure is layered: along the *c* axis, tetrahedral layers alternate with layers composed of octahedra and dodecahedra.

In the $La_3Ga_5SiO_{14}$ crystal structure, La^{3+} ions occupy the positions 3*e*, Ga^{3+} ions are located in the positions 1*a* and 3*f*, and Ga^{3+} and Si^{4+} ions (in a ratio of 1 : 1) are situated at the positions 2*d*. This cation distribution with positional parameters taken from [12] and transformed using the matrix (1, 0, 0/0, 1, 0/0, 0, –1) served as the initial model for the structure under investigation. The above transformation corresponds to rotation about the [001] direction through 180° and to the changeover to the structural model inverted with respect to the model described in [11, 12]: (1, 0, 0/0, 1, 0/0, 0, –1) = (–1, 0, 0/0, –1, 0/0, 0, 1) · (–1, 0, 0/0, –1, 0/0, 0, –1).

The transformation (–1, 0, 0/0, –1, 0/0, 0, 1) eliminates the differences associated with the choice of the coordinate axes in the diffraction experiments described in [11–14] and in our work. The axis orientation and chirality chosen correspond to the absolute structure of the $La_3Nb_{0.5}Ga_{5.5}O_{14}$ compound [10]. As in [12], we note that the published structural data for crystals of the langasite family should be analyzed with due regard for the ambiguity in the choice of the reciprocal lattice axes, which, in the (001) basal plane, can be rotated with respect to each other through an angle of $60° \cdot (2n + 1)$.

The structure was refined by the least-squares method using the atomic curves for neutral atoms with allowance made for the dispersion corrections. The analysis of different extinction models on the basis of the Becker–Coppens formalism led to approximately identical results. Preference (with a minimum advantage) was given to the second type of extinction model

Table 1. Main crystal data, data collection, and refinement parameters for the structure of the $La_3Ga_5SiO_{14}$ compound

Chemical formula	$La_3Ga_5SiO_{14}$
Space group, Z	$P321$, 1
a, Å	8.1746(6)
c, Å	5.1022(4)
V, Å^3	295.27(5)
ρ_{calcd}, g/cm^3	5.720(1)
Crystal radius, mm	0.08
μ_{Mo}, mm^{-1}	21.99
Diffractometer	CAD-4F
Radiation, Å	MoK_α, 0.71073
Monochromator	Graphite
Index ranges	$-18 \le (h, k) \le 18; -11 \le l \le 11$
Scan mode	$\omega/2\theta$
$(\sin\theta/\lambda)_{max}$, Å^{-1}	1.15
Number of reflections measured	15777
Number of unique reflections	2520
$R(I)_{av}$, %	3.14
Number of reflections in the refinement with $I > 3\sigma(I)$	2413
Number of parameters refined	53
Weighting scheme	$1/[\sigma(F)^2 + 0.0002F^2]$
Extinction coefficient	$0.60(1) \times 10^4$
$\Delta\rho$, e/Å^3	$-0.65 \le \Delta\rho \le 0.60$
R/R_w	1.37/1.71
S	1.21
Flack parameter	0.043

characterized by a Lorentzian distribution of mosaic blocks over sizes.

When thermal motion of atoms is taken into account in the isotropic approximation (R/R_w = 4.54/5.61%, S = 3.64), the residual electron densities $\Delta\rho$ in the vicinity of the lanthanum atom in the $x0z$ plane considerably exceed the background densities and can be as high as ±10 e/Å^3 at a distance of ~0.4 Å (Fig. 2a). The inclusion of thermal vibrations of all atoms in the structure in the anisotropic approximation results in a substantial decrease both in the reliability factors R to 1.51% and R_w to 2.04% (S = 1.28) and in the extreme values of the residual electron densities. However, the difference distribution $\Delta\rho$ in the vicinity of the lanthanum atom involves the region that has a positive density with an extreme value of ~2 e/Å^3 and is shifted along the twofold axis 2 to the right of the subtracted lanthanum atom by a distance of ~0.4 Å (Fig. 2b). We believe that this effect is associated with the anharmonicity of thermal vibrations of the lanthanum atom. The inclusion of the anharmonicity with the use of the components of the tensors up to the fourth-rank tensor almost completely eliminates the residual electron density in the vicinity of the lanthanum atom in the difference synthesis (Fig. 2c) and leads to a decrease in the factors R to 1.37%, R_w to 1.71%, and S to 1.21. The advisability of accounting for the anharmonicity of thermal vibrations of the lanthanum atom was checked against to the Hamilton criterion [20], which yields a high significance level (99.5%) of the decrease in the factor R. In this case, peaks exceeding the background values are virtually absent in the three-dimensional distribution of the residual electron density. For the other atoms, the anharmonic contributions from the thermal motion are less significant. Although the use of the tensors up to the fourth-rank tensor for all the atoms in the structure decreases the factors R to 1.24%, R_w to 1.53%, and S to 1.1, it virtually does not affect the residual electron density map. Therefore, only the anharmonicity of thermal motion of the lanthanum atom was taken into account in the final refinement. The thermal motion of the other

Table 2. Fractional coordinates and thermal parameters of the basis atoms

Atom	Wyckoff position	x/a	y/b	z/c	B_{eq}, Å^2
La	3*e*	0.41895(3)	0	0	0.76(1)
Ga(1)	1*a*	0	0	0	0.90(1)
Ga(2), Si*	2*d*	1/3	2/3	0.53207(7)	0.61(1)
Ga(3)	3*f*	0.76526(3)	0	1/2	0.72(1)
O(1)	2*d*	1/3	2/3	0.1951(5)	1.18(3)
O(2)	6*g*	0.4649(2)	0.3110(2)	0.3157(3)	1.48(3)
O(3)	6*g*	0.2221(2)	0.0812(3)	0.7643(3)	1.69(4)

* Site occupation: 0.5Ga + 0.5Si.

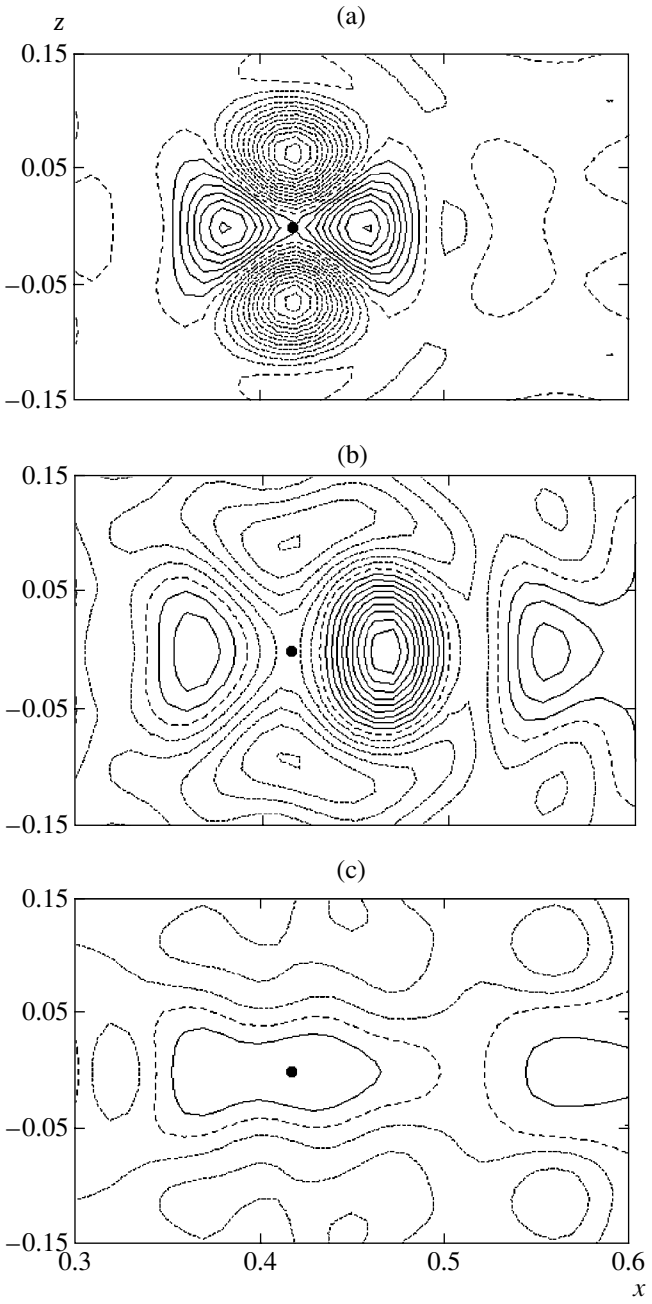

Fig. 2. Sections *x*0*z* of the residual electron density Δρ through the La basis atom at different stages of the refinement of the $La_3Ga_5SiO_{14}$ structure. The closed circle indicates the position of the subtracted La atom. Numbers along the horizontal and vertical axes are the fractional coordinates. The positive and negative regions are shown by solid and dotted lines, respectively. The zero contour is depicted by dashed lines. Contour interval: (a) 1.0 and (b, c) 0.2 e/Å^3.

atoms was refined in the anisotropic harmonic approximation.

At the final stage, we attempted to refine the quantitative composition of atoms in the unit cell of the $La_3Ga_5SiO_{14}$ crystal by the step-scan method [21]. This procedure did not reveal noticeable deviations from the $La_3Ga_5SiO_{14}$ stoichiometric composition for completely occupied crystallographic positions.

The initial choice of the absolute structure was made reasoning from the relative volume of the inverted twin component that was determined in the course of the refinement and corresponded to the Flack parameter in terms of the concept developed in [15]. The final choice was based on a comparison of the results obtained by the least-squares calculations in the anisotropic harmonic approximation of thermal vibrations of all atoms for two possible modifications that differ as an image (initial model, $R = 1.51\%$, $R_w = 2.04\%$, $S = 1.28$) and its centrosymmetrical mapping ($R = 2.95\%$, $R_w = 4.09\%$, $S = 2.15$). Therefore, it was shown that the absolute structure of the $La_3Ga_5SiO_{14}$ crystal under investigation differs from the initial model [12] and corresponds to the structure determined in [14].

The coordinates and thermal parameters of the basis atoms are presented in Table 2. The parameters of the thermal vibrations in the anisotropic harmonic (U_{ij}) and anharmonic (C_{ijk}, D_{ijkl}) approximations are listed in Tables 3 and 4, respectively. The sizes and orientation of thermal ellipsoids are given in Table 5. The selected interatomic distances are presented in Table 6.

RESULTS AND DISCUSSION

The parameters of the anharmonic thermal vibrations can be interpreted using the probability density functions for atomic displacements from equilibrium positions. In order to analyze the possible displacements of the lanthanum atom along the 2 axis coinciding with the principal axis of its thermal ellipsoid (Table 5), we constructed the *x*0*z* sections of the probability density functions (Fig. 3). The total probability density function calculated with the use of the components of the second-, third-, and fourth-rank tensors (Fig. 3a) is slightly increased in the direction of dominant vibrations of the lanthanum atom (along the 2 axis). Figure 3b illustrates the combined contribution made by the anharmonicity of thermal vibrations with the inclusion of the components of the third- and fourth-rank tensors. The anharmonic contributions associated with the fourth-rank tensor most strongly affect the probability density function and lead to its increase in the central part (Fig. 3d). The anharmonic terms determined by the components of the third-rank tensor also make a considerable contribution (Fig. 3c). As a result, an increase in the total probability density function along the direction of dominant vibrations is equal in magnitude to its decrease in the opposite direction. A comparison of Figs. 3c and 3d shows that the inclusion of the anharmonicity governed by the third-rank tensor results in an increase in the probability density function in the antibonding direction.

Table 3. Anisotropic thermal parameters of atoms (U_{ij}, Å^2)

Atom	U_{11}	U_{22}	U_{33}	U_{12}	U_{13}	U_{23}
La	0.00997(3)	0.00913(3)	0.00674(3)	0.00457(2)	0.00022(1)	0.00043(2)
Ga(1)	0.01435(8)	0.01435(8)	0.0055(1)	0.00718(4)	0	0
Ga(2), Si*	0.00851(9)	0.00851(9)	0.0061(1)	0.00425(4)	0	0
Ga(3)	0.00880(5)	0.01001(6)	0.00881(6)	0.00500(3)	0.00172(2)	0.00345(5)
O(1)	0.0123(4)	0.0123(4)	0.0202(8)	0.0062(2)	0	0
O(2)	0.0161(4)	0.0214(5)	0.0206(5)	0.0106(4)	0.0098(4)	0.0094(4)
O(3)	0.0215(5)	0.0338(7)	0.0163(4)	0.0194(5)	0.0088(4)	0.0165(5)

* Site occupation: 0.5Ga + 0.5Si.

Table 4. Anharmonic parameters of the thermal motion of lanthanum atoms ($C \times 10^3$, Å; $D \times 10^4$, Å)

C_{111} 0.00037(2)	C_{112} −0.000003(9)	C_{113} 0.00004(1)	C_{122} −0.000003(9)	C_{123} 0.00004(1)	C_{133} 0.00019(2)
D_{1111} 0.00023(2)	D_{1112} 0.00011(1)	D_{1113} 0.00006(1)	D_{1122} 0.00012(1)	D_{1123} 0.00003(1)	D_{1133} 0.00006(1)
D_{1222} 0.00013(2)	D_{1223} −0.00002(4)	D_{1233} 0.000037(8)	D_{1333} 0.000005(9)	D_{2222} 0.00027(8)	D_{2223} −0.00005(7)
D_{2233} 0.00007(2)	D_{2333} 0.00003(3)	D_{3333} −0.00034(7)			

Note: $C_{222} = C_{223} = C_{233} = C_{333} = 0$.
$C_{122} = C_{112}$.
$C_{123} = C_{113}$.
$D_{1222} = 3*D_{1122} - 2*D_{1112}$.
$D_{1223} = 3*D_{1123} - 2*D_{1113}$.
$D_{2222} = 6*D_{1122} - 4*D_{1112}$.
$D_{2223} = 6*D_{1123} - 4*D_{1113}$.
$D_{2233} = 2*D_{1233}$.
$D_{2333} = 2*D_{1333}$.

Table 5. Sizes and orientation of the thermal ellipsoids of the basis atoms

Atom and point symmetry of the atomic position	Semiaxis length, Å	Angles between the thermal ellipsoid axes and the crystallographic axes, deg		
		a	*b*	*c*
La	0.07890	90	134.95	54.66
2	0.08185	90	120.06	144.66
	0.09609	0	120	90
Ga(1)	0.08876	90	90	0
32	0.09070	150	90	90
	0.09073	30	90	90
Ga(2), Si	0.07570	90	90	0
3	0.08626	141.16	98.84	90
	0.08626	141.16	98.84	90
Ga(3)	0.07802	90	43.85	56.38
2	0.08931	180	60	90
	0.11463	90	118.65	33.62
O(1)	0.07398	90	90	0
3	0.10317	142.21	97.79	90
	0.10317	142.21	97.79	90
O(2)	0.08579	128.35	93.80	49.25
1	0.10374	138.25	64.27	131.46
	0.12408	103.99	26.05	68.40
O(3)	0.07713	98.43	118.22	40.34
1	0.09236	171.57	55.08	96.66
	0.15094	90.26	47.94	50.44

Table 6. Interatomic distances (Å) in the crystal structure of the $La_3Ga_5SiO_{14}$ compound

La polyhedron		Ga(1) octahedron		Ga(2), Si tetrahedron		Ga(3) tetrahedron	
La–O(1) × 2	2.646(1)	Ga(1)–O(3) × 6	1.994(2)	Ga(2), Si–O(1)	1.719(3)	Ga(3)–O(2) × 2	1.908(1)
O(2) × 2	2.506(2)	O(3)–O(3') × 6	2.756(3)	O(2') × 3	1.748(2)	O(3') × 2	1.810(2)
O(2') × 2	2.870(2)	O(3") × 3	3.124(3)	O(1)–O(2) × 3	2.947(3)	O(2)–O(2')	2.879(3)
O(3) × 2	2.352(2)	O(3"') × 3	2.665(2)	O(2)–O(2') × 3	2.712(3)	O(3) × 2	2.873(2)
						O(2')–O(3') × 2	2.995(2)
						O(3)–O(3')	3.355(3)

In [11, 12], the structural model of the $La_3Ga_5SiO_{14}$ crystal was refined without determining the absolute structure. The analysis of the experimental data obtained in [12] allows us to make the inference that they can be used to determine the absolute structure. The structural model was refined according to the JANA-2000 software package without regard for the twin component inverted with respect to the initial

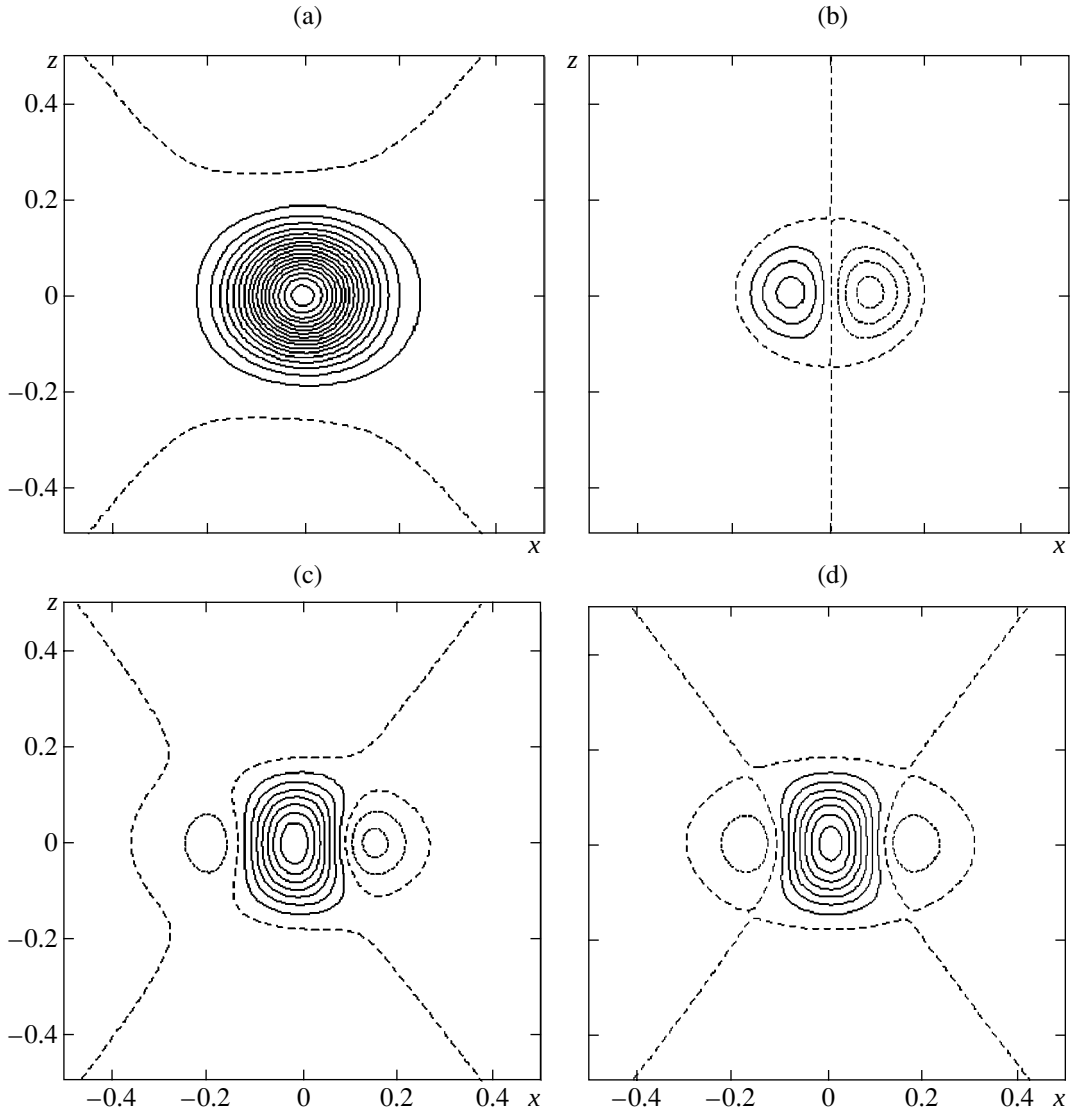

Fig. 3. Anharmonic contributions of the thermal motion to the probability density function for the La atom in the *x*0*z* sections. The length of the section edge is 1.0 Å. The section centers coincide with the position of the La atom. The positive and negative regions are shown by solid and dotted lines, respectively. The zero contour is depicted by dashed lines. Contour interval: (a) five relative units (total probability density function), (b) two relative units (anharmonic contributions of the third- and fourth-rank tensors), (d) two relative units (anharmonic contribution of the fourth-rank tensor), and (c) one relative unit (anharmonic contribution of the third-rank tensor).

component (R = 3.32%, R_w = 3.51%, S = 3.33). The inclusion of the inverted component demonstrated that the relative volume of this component is equal to 96% at R = 2.53%, R_w = 2.91%, and S = 2.79. The results obtained suggest that the crystals studied in this work and in [11, 12] have identical absolute structures. This confirms our assumption that the $La_3Ga_5SiO_{14}$ crystals grown from related seed materials have the same absolute structure.

Therefore, the crystals studied in [11, 12, 14] and in this work are identical in the absolute structure. The structural model proposed in [13] is inverted with respect to the other model. The authors of [13] (like the authors of [11, 12]) did not seek to determine the absolute structure. As a consequence, the data obtained in [13] do not provide a way to make a conclusive inference regarding the chirality of the crystal under investigation.

Considering the configuration of the absolute structures, we should note that, in 1980, we grew the crystals of the langasite family from two different seed crystals. The $Ca_3Ga_2Ge_4O_{14}$ crystal was grown by the Czochralski method through crystallization of a melt of the corresponding composition on a platinum wire. The first crystals of $Sr_3Ga_2Ge_4O_{14}$ and $Na_2CaGe_6O_{14}$ were grown from $Ca_3Ga_2Ge_4O_{14}$ seeds. Single crystals of this group should belong to the same enantiomorphic form. Crystals of the second group were grown from langasite. The $La_3Ga_5SiO_{14}$ seeds were used to grow the first crystals of $La_3Nb_{0.5}Ga_{5.5}O_{14}$, $La_3Ta_{0.5}Ga_{5.5}O_{14}$, $La_3Ga_5GeO_{14}$, $Nd_3Ga_5SiO_{14}$, $Pr_3Ga_5SiO_{14}$, $Sr_3TaGa_3Si_2O_{14}$, $Ca_3TaGa_3SiO_{14}$, $Ca_3Ga_2Ge_4O_{14}$, and $Sr_3Ga_2Ge_4O_{14}$, which, according to our concept, belong to another enantiomorphic form.

The existence of crystals of the langasite family with different senses of rotation of the plane of polarization is confirmed by the results obtained in the study of the optical activity for a number of crystals prepared from two different seed materials. These data demonstrate that crystals of the langasite family can be grown in a controlled fashion with a required sense of rotation of the plane of polarization. The enantiomorphic forms with different senses of rotation of the plane of polarization can coexist in crystals with grown twins.

The results of the precise refinement of the positional and thermal parameters of atoms and the determined absolute structure of the $La_3Ga_5SiO_{14}$ crystal with the positive sign of the optical activity can be useful for in-depth understanding of the structure–property relationships for crystals of the langasite family.

ACKNOWLEDGMENTS

We are grateful to Yu.A. Durasov and E.N. Il'ichev (Faculty of Physics, Moscow State University) for their assistance in the determination of the sense of rotation of the plane of polarization.

This work was supported by the Russian Foundation for Basic Research (project nos. 03-02-17075, 04-05-64630) and the State Program of Support for Leading Scientific Schools of the Russian Federation (project no. NSh-1642.2003.5).

REFERENCES

1. B. V. Mill and Yu. V. Pisarevsky, in *Proceedings of the IEEE/EIA International Frequency Control Symposium, Kansas City, USA, 2000* (Kansas City, 2000), p. 133.
2. M. Honal, R. Fachberger, T. Holzheu, *et al.*, in *Proceedings of the IEEE/EIA International Frequency Control Symposium, Kansas City, USA, 2000* (Kansas City, 2000), p. 113.
3. D. Puccio, N. Saldanho, D. C. Malocha, and M. Pereira da Cunha, in *Proceedings of the IEEE International Frequency Control Symposium, New Orleans, USA, 2002* (New Orleans, 2002), p. 324.
4. A. A. Kaminskiĭ, B. V. Mill, and S. É. Sarkisov, *Physics and Spectroscopy of Laser Crystals* (Nauka, Moscow, 1986) [in Russian].
5. O. A. Baturina, B. N. Grechushnikov, A. A. Kaminskiĭ, *et al.*, Kristallografiya **32** (2), 406 (1987) [Sov. Phys. Crystallogr. **32** (2), 236 (1987)].
6. R. B. Heimann, M. Hengst, M. Rosenberg, and J. Bohm, Phys. Status Solidi A **195** (2), 468 (2003).
7. *ANSI/IEEE Standard 176-1987: IEEE Standard on Piezoelectricity* (IEEE, New York, 1988), p. 1.
8. I. M. Sil'vestrova, Yu. V. Pisarevskiĭ, P. A. Senyushenkov, and A. I. Krupnyĭ, Fiz. Tverd. Tela (Leningrad) **28** (9), 2875 (1986) [Sov. Phys. Solid State **28** (9), 1613 (1986)].
9. I. M. Sil'vestrova, Yu. V. Pisarevskiĭ, A. A. Kaminskiĭ, and B. V. Mill', Fiz. Tverd. Tela (Leningrad) **29** (5), 1520 (1987) [Sov. Phys. Solid State **29** (5), 870 (1987)].
10. V. N. Molchanov, B. A. Maksimov, A. F. Kondakov, *et al.*, Pis'ma Zh. Éksp. Teor. Fiz. **74** (4), 244 (2001) [JETP Lett. **74** (4), 222 (2001)].
11. B. V. Mill', A. V. Butashin, G. G. Khodzhabagyan, *et al.*, Dokl. Akad. Nauk SSSR **264** (6), 1385 (1982) [Sov. Phys. Dokl. **27** (6), 434 (1982)].
12. E. L. Belokoneva, S. Yu. Stefanovich, Yu. V. Pisarevskiĭ, and A. V. Mosunov, Zh. Neorg. Khim. **45** (11), 1786 (2000).
13. T. Iwataki, H. Ohsato, K. Tanaka, *et al.*, J. Alloys Compd. **290**, 279 (2001).

14. G. M. Kuz'micheva, V. B. Rybakov, E. N. Domoroshchina, and A. B. Dubovskiĭ, Neorg. Mater. **38** (10), 1234 (2002).
15. H. D. Flack and G. Bernardinell, Acta Crystallogr., Sect. A: Fundam. Crystallogr. **55**, 908 (1999).
16. A. P. Dudka, M. Kh. Rabadanov, and A. A. Loshmanov, Kristallografiya **34** (4), 818 (1989) [Sov. Phys. Crystallogr. **34** (4), 490 (1989)].
17. P. A. Senyushchenkov, Candidate's Dissertation in Physics and Mathematics (Moscow, 1998).
18. V. Petriček and M. Dusek, *JANA 2000* (Inst. of Physics, Praha, 2000).
19. E. L. Belokoneva and B. V. Mill, in *Crystal Chemistry Classification of Minerals* (Mosk. Gos. Univ., Moscow, 1985), p. 140 [in Russian].
20. W. C. Hamilton, Acta Crystallogr., Sect. A: Cryst. Phys., Diffr., Theor. Gen. Crystallogr. **38**, 729 (1965).
21. L. A. Muradyan, S. F. Radaev, and V. I. Simonov, in *Methods of Structural Analysis* (Nauka, Moscow, 1989), p. 5 [in Russian].

Translated by O. Borovik-Romanova

Crystallography Reports, Vol. 50, No. 5, 2005, pp. 759–765. Translated from Kristallografiya, Vol. 50, No. 5, 2005, pp. 820–826.

STRUCTURE OF INORGANIC COMPOUNDS

Synthesis and Structural Study of Phosphates $K_2Mg_{0.5}Zr_{1.5}(PO_4)_3$, $Rb_2Mg_{0.5}Zr_{1.5}(PO_4)_3$, and $Cs_2Mg_{0.5}Zr_{1.5}(PO_4)_3$ with Langbeinite Structure

A. I. Orlova*, V. A. Orlova*, A. I. Beskrovnyĭ, I. G. Trubach*, and V. S. Kurazhkovskaya*****

** Department of Chemistry, Nizhni Novgorod State University, pr. Gagarina 23, Nizhni Novgorod, 603950 Russia*

e-mail: oai@uic.nnov.ru

*** Joint Institute for Nuclear Research, ul. Zholio-Kyuri 6, Dubna, Moscow oblast, 141980 Russia*

**** Faculty of Geology, Moscow State University, Leninskie gory, Moscow, 119992 Russia*

Received April 17, 2004

Abstract—New orthophosphates $K_2Mg_{0.5}Zr_{1.5}(PO_4)_3$, $Rb_2Mg_{0.5}Zr_{1.5}(PO_4)_3$, and $Cs_2Mg_{0.5}Zr_{1.5}(PO_4)_3$ are synthesized and characterized by X-ray powder diffraction and IR spectroscopy. These orthophosphates crystallize in the structure type of the mineral langbeinite (cubic system, sp. gr. $P2_13$, $Z = 4$). The structure of phosphate $Cs_2Mg_{0.5}Zr_{1.5}(PO_4)_3$ is refined by the Rietveld method using neutron powder diffraction data (a DN-2 time-of-flight diffractometer, the Joint Institute for Nuclear Research, Dubna, Russia) in the temperature range 15–600°C. The structure of this compound is characterized by the mixed $[Mg_{0.5}Zr_{1.5}(PO_4)_3]^{2-}$ framework, whose large cavities are occupied by cesium atoms. Mg^{2+} and Zr^{4+} cations randomly occupy two crystallographically independent positions. The influence of the temperature factor on distortions of the framework polyhedra is analyzed. © *2005 Pleiades Publishing, Inc.*

INTRODUCTION

Phosphates, which are characterized by framework structures containing mixed $[T_2(PO_4)_3]^{n-}$ anionic groups, where n is the framework charge varying from 0 to 4 and T are elements in oxidation states from +1 to +5, form a large group of inorganic compounds. All possible formula types of the frameworks of such compounds were described in [1]. Calculations revealed 24 possible types. Such frameworks can exist in several structural modifications [2], one of which is the langbeinite structure type. This, like the $NaZr_2(PO_4)_3$ (NZP) structure type, contains the topological unit $[T_2(PO_4)_3]$ consisting of two TO_6 octahedra and three PO_4 tetrahedra linked to each other by shared oxygen atoms. Large cavities in the langbeinite structure can be occupied (two positions) by charge-compensating cations. For the langbeinite framework, $2 \le n \le 4$. The extraframework positions can be occupied by cations in oxidation states of +1 and +1 if $n = 2$, +1 and +2 if $n = 3$, and +1 and +3 or +2 and +2 if $n = 4$. Phosphates with the $[T_2(PO_4)_3]^{2-}$ framework have been studied in most detail and are well described in the literature. In these compounds, $T_2 = RM$, where R are trivalent Ti, V, Cr, Fe, Ga, Y, Er, Yb, and Bi cations, and M are tetravalent Ti, Zr, Sn, and Hf cations. Sodium and potassium ions serve as cations compensating for the framework charge $n = 2$. These compounds are $Na_2RTi(PO_4)_3$, R = Fe or Cr [3]; $K_2RTi(PO_4)_3$, R = Ti [4], V [5], Y, Er, or Yb [6]; $K_2RZr(PO_4)_3$, R = Fe [7], Y, or Gd [8]; $K_2RHf(PO_4)_3$, R = Ga, Fe, Cr [9], or Bi [10]; and $K_2RSn(PO_4)_3$, R = Ga, Fe, or Cr [9]. All these compounds crystallize in the cubic system within the sp. gr. $P2_13$.

It should be noted that most of these compounds contain potassium in cavities. At the same time, no compounds with NZP-type frameworks of the composition $[RM(PO_4)_3]^{2-}$ containing either potassium or larger alkali cations are known. Presumably, the cavities in the framework of the langbeinite modification are more favorable to be occupied by larger charge-compensating cations as compared to the NZP-type modification.

The aim of this study was to verify the validity of the prediction [1] of the possible existence of phosphates having $[B_{0.5}M_{1.5}(PO_4)_3]^{2-}$-type frameworks with $n = 2$, where B is an element in the oxidation state of +2. We also examined whether it is possible to crystallize compounds that are characterized by this framework; have the langbeinite structure; and contain potassium, rubidium, or cesium cations in cavities. To this end, we synthesized and characterized phosphates $K_2Mg_{0.5}Zr_{1.5}(PO_4)_3$, $Rb_2Mg_{0.5}Zr_{1.5}(PO_4)_3$, and $Cs_2Mg_{0.5}Zr_{1.5}(PO_4)_3$.

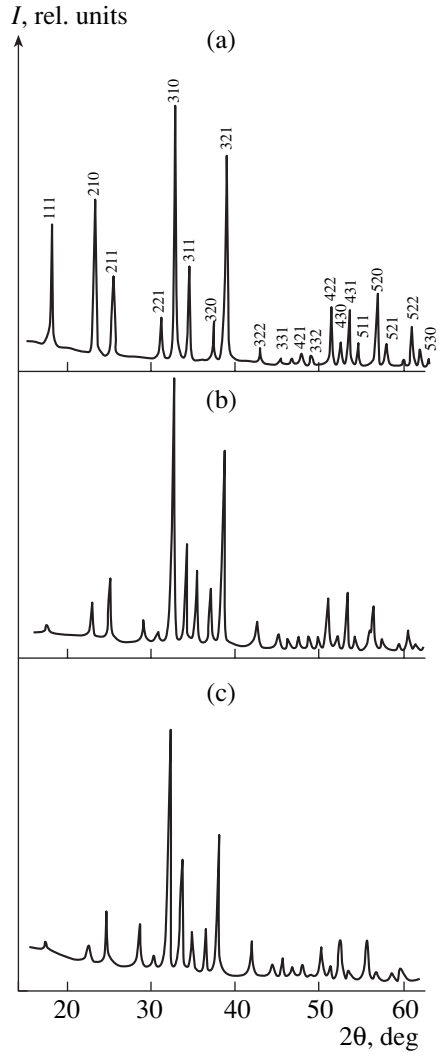

Fig. 1. X-ray diffraction patterns of the phosphates (a) $K_2Mg_{0.5}Zr_{1.5}(PO_4)_3$, (b) $Rb_2Mg_{0.5}Zr_{1.5}(PO_4)_3$, and (c) $Cs_2Mg_{0.5}Zr_{1.5}(PO_4)_3$.

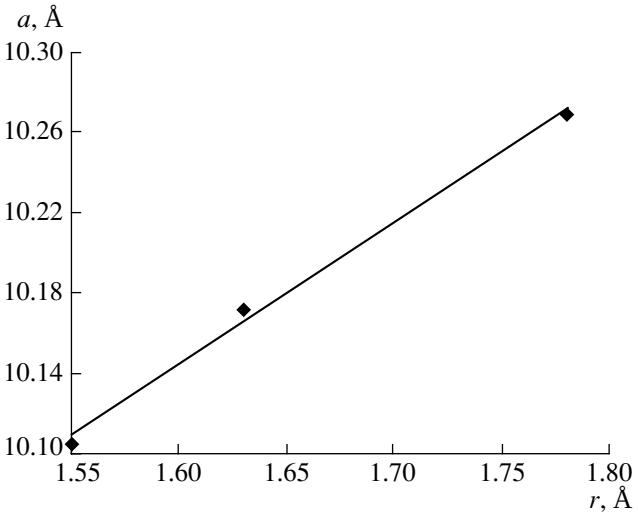

Fig. 2. Dependence of the unit-cell parameter a on the radius of the alkali cation.

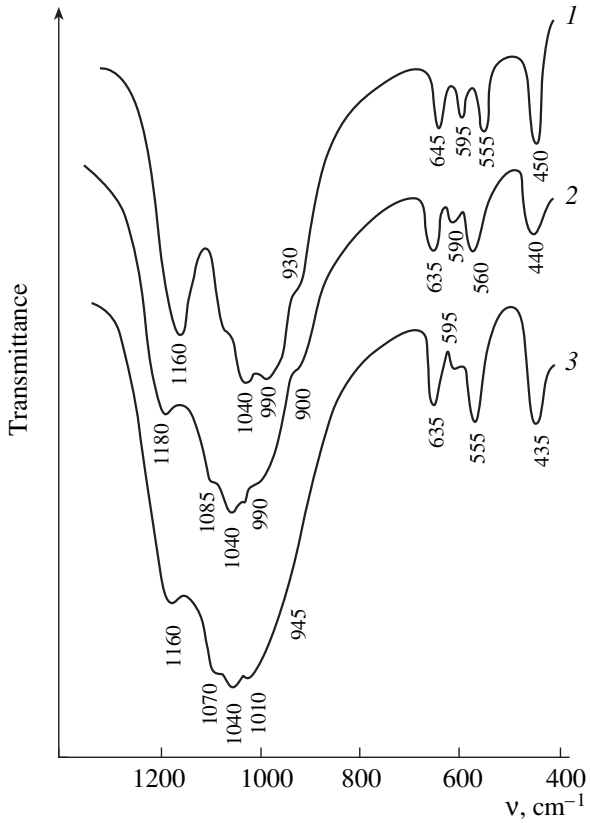

Fig. 3. IR spectra of the phosphates (*1*) $K_2Mg_{0.5}Zr_{1.5}(PO_4)_3$, (*2*) $Rb_2Mg_{0.5}Zr_{1.5}(PO_4)_3$, and (*3*) $Cs_2Mg_{0.5}Zr_{1.5}(PO_4)_3$.

In addition to scientific interest, these compounds have drawn attention for solving certain practical problems, in particular, in nuclear technologies producing wastes containing alkali elements (Na, K, Rb, Cs) with high concentrations. Framework phosphates hold promise for developing procedures for isolation of these elements from the biosphere. The presence of cesium in wastes excludes the possibility of extracting radioactive cesium from them. Owing to the geometric restrictions on the diffusion of extraframework cations, the langbeinite structure can trap these cations and prevent hazardous radionuclides from contaminating the environment.

EXPERIMENTAL

Samples were synthesized by the sol-gel method using 1-M aqueous solutions of the alkali chlorides $MgCl_2$ and $ZrOCl_2$ and H_3PO_4 as the starting reagents. A 1-M H_3PO_4 solution was added with stirring to aqueous solutions of the starting salts taken in a stoichiometric ratio. The resulting gel was dried at 90°C for one to two days and then successively heated at 600, 800, and

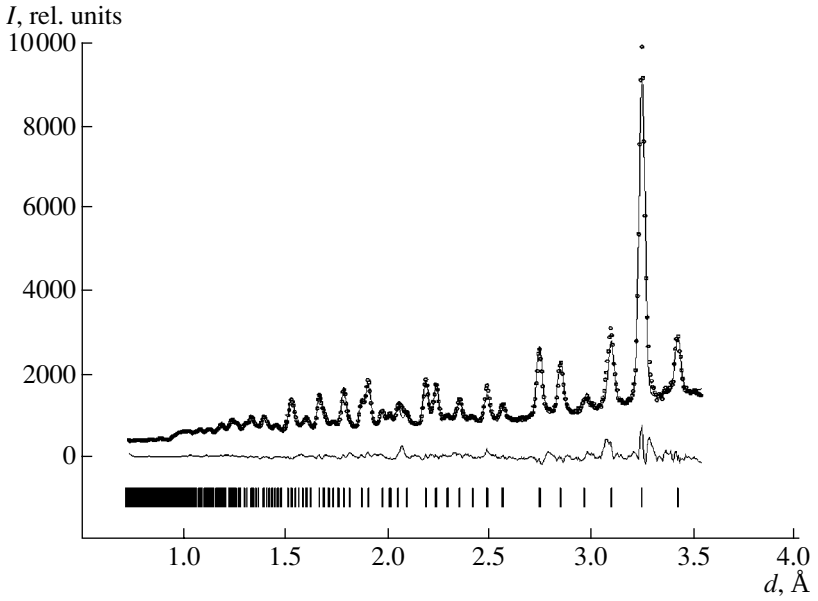

Fig. 4. Experimental (□) and theoretical (solid line) neutron-diffraction profiles of $Cs_2Mg_{0.5}Zr_{1.5}(PO_4)_3$ and the difference curve (experiment minus calculation) normalized to the rms deviation at a point. The calculated positions of the diffraction peaks are indicated by vertical bars.

1000°C for one day at each temperature, the heating being alternated with fine grinding in an agate mortar.

Samples were studied by X-ray powder diffraction, IR spectroscopy, and neutron powder diffraction. X-ray diffraction study was carried out on a DRON-3M diffractometer using filtered CuK_α radiation (Ni filter, λ = 1.54056 Å) in the 2θ-angle range from 14° to 60°. The IR spectra were recorded on a SPECORD 75IR spectrophotometer in the wavenumber range from 1400 to 400 cm^{-1} (samples were prepared as thin films on KBr substrates).

The neutron diffraction patterns of the phosphate $Cs_2Mg_{0.5}Zr_{1.5}(PO_4)_3$, which was placed in a cylindrical container (d = 10 mm), were recorded at 15, 150, 300,

Table 1. Results of refinement of the crystal structure of $Cs_2Mg_{0.5}Zr_{1.5}(PO_4)_3$

Characteristic	t, °C				
	15	150	300	450	600
Space group	$P2_13$				
a, Å	10.2624(5)	10.2657(9)	10.2735(9)	10.2835(9)	10.2886(9)
V, Å^3	1080.804	1081.847	1084.315	1087.484	1089.103
Z	4				
Color	white				
d spacing, Å	0.73–3.53				
Number of reflections	303	322	315	323	317
R_{exp}	1.69	2.62	2.58	2.56	2.37
R_{wp}	3.75	4.89	4.52	4.45	4.39
R_p	4.17	5.65	5.38	5.21	4.89
χ^2	6.94	5.78	4.02	3.58	5.03
Number of parameters in refinement	39				

Table 2. Occupancies of positions (w), atomic coordinates, and temperature factors B_{iso} in the $Cs_2Mg_{0.5}Zr_{1.5}(PO_4)_3$ structure

Atom	Position	w	t = 15°C				t = 600°C			
			x	y	z	B_{iso}	x	y	z	B_{iso}
Cs(1)	4*a*	1	0.0638(5)	0.0638(5)	0.0638(5)	3.5	0.0668(6)	0.0668(6)	0.0668(6)	3.0
Cs(2)	4*a*	1	0.2872(4)	0.2872(4)	0.2872(4)	2.3	0.2939(6)	0.2939(6)	0.2939(6)	3.1
(Mg/Zr)(1)	4*a*	0.50(5)	0.8579(3)	0.8579(3)	0.8579(3)	1.6	0.8500(5)	0.8500(5)	0.8500(5)	3.0
Zr(2)	4*a*	1.00(5)	0.5829(3)	0.5829(3)	0.5829(3)	3.0	0.5853(6)	0.5853(6)	0.5853(6)	3.2
P	12*b*	1	0.6250(3)	0.4607(3)	0.2753(4)	0.5	0.6266(6)	0.4511(5)	0.2717(6)	1.8
O(1)	12*b*	1	0.6364(4)	0.5003(3)	0.4163(4)	2.4	0.6329(6)	0.5040(5)	0.4237(5)	2.6
O(2)	12*b*	1	0.7462(4)	0.4767(3)	0.2001(4)	1.3	0.7463(5)	0.4817(4)	0.2043(4)	1.2
O(3)	12*b*	1	0.5880(4)	0.3168(3)	0.2715(3)	1.5	0.5975(4)	0.3081(4)	0.2775(5)	1.5
O(4)	12*b*	1	0.5258(4)	0.5364(4)	0.1944(4)	3.3	0.5167(6)	0.5216(6)	0.1900(6)	3.2

450, and 600°C on a DN-2 time-of-flight diffractometer installed on an IBR-2 fast pulsed reactor (Joint Institute for Nuclear Research, Dubna, Russia) [11]. The structure was refined by the Rietveld method using the MRIA program [12].

Table 3. Selected interatomic distances (Å) and bond angles (deg) in the structure of phosphate $Cs_2Mg_{0.5}Zr_{1.5}(PO_4)_3$

Temperature, °C	15	600
	$Cs(1)O_9$ polyhedron	
Cs(1)–O(2)	3.16(5)	3.18(6)
Cs(1)–O(3)	3.06(6)	3.08(5)
Cs(1)–O(4)	2.83(5)	3.36(5)
	$Cs(2)O_9$ polyhedron	
Cs(2)–O(1)	3.11(6)	3.11(4)
Cs(2)–O(2)	3.19(5)	3.11(6)
Cs(2)–O(4)	2.83(5)	2.79(5)
	MO_6 octahedron	
Zr–O(1)	1.95(5)	1.89(5)
Zr–O(2)	2.18(5)	2.19(5)
Mg/Zr–O(3)	2.05(5)	1.84(5)
Mg/Zr–O(4)	2.07(6)	2.17(5)
	PO_4 tetrahedron	
P–O(1)	1.48(5)	1.63(4)
P–O(2)	1.45(5)	1.42(5)
P–O(3)	1.50(4)	1.48(5)
P–O(4)	1.50(6)	1.56(6)
O(1)–P–O(2)	113.9(4)	110.3(5)
O(1)–P–O(3)	107.7(5)	107.0(5)
O(1)–P–O(4)	115.9(5)	112.2(5)
O(2)–P–O(3)	107.8(4)	113.7(4)
O(2)–P–O(4)	102.8(5)	104.7(4)
O(3)–P–O(4)	108.3(5)	109.0(4)

RESULTS AND DISCUSSION

The X-ray diffraction patterns of the $K_2Mg_{0.5}Zr_{1.5}(PO_4)_3$, $Rb_2Mg_{0.5}Zr_{1.5}(PO_4)_3$, and $Cs_2Mg_{0.5}Zr_{1.5}(PO_4)_3$ samples (Fig. 1) show reflections with the *hkl* Miller indices 111, 210, 211, 300, 310, 311, 320, 321, etc., of the cubic lattice. Such reflections are characteristic of phosphates of the langbeinite structure type. The X-ray patterns were indexed in the langbeinite structure type ($K_2Mg_2(SO_4)_3$ is the synthetic analog, sp. gr. $P2_13$). The calculated unit-cell parameters of the cubic lattice for the phosphates studied are a = 10.105(2), 10.172(2), and 10.270(2) Å and V = 1047.4(5), 1051.4(5), and 1083.6(5) Å^3, respectively. The unit-cell parameter a linearly depends on the radius of the alkali cation (Fig. 2). The picnometric density ρ_{exp} of phosphate $K_2Mg_{0.5}Zr_{1.5}(PO_4)_3$ was determined to be 3.26 g/cm^3, which is close to the X-ray density (ρ_{calcd} = 3.27 g/cm^3).

The IR spectra of the phosphates are shown in Fig. 3. The local symmetry of the PO_4 tetrahedron in the langbeinite structure is C_1. The factor-group analysis of internal vibrations of the phosphorus tetrahedron allowed us to determine the following normal-vibration modes in the crystal field (crystal symmetry $P2_13$, factor group T):

$$\nu_1 \longrightarrow A_1 \longrightarrow A(C_1) \longrightarrow F(T),$$
$$\nu_2 \longrightarrow E \longrightarrow 2A(C_1) \longrightarrow 2F(T),$$
$$\nu_3, \nu_4 \longrightarrow F_2 \longrightarrow 3A(C_1) \longrightarrow 3F(T).$$

The IR spectra of the phosphates $A_2Mg_{0.5}Zr_{1.5}(PO_4)_3$ show bands predicted by the group theory. Three bands at 990, 1040, and 1080 (sh) cm^{-1} are due to P–O asymmetric stretching vibrations ν_3, and the band at 930 cm^{-1} is due to asymmetric stretching vibrations ν_1. The range 640–550 cm^{-1} contains bands due to three of the predicted vibrations corresponding to the bending vibrations ν_4 at 645, 595, and 555 cm^{-1} and ν_2 at 450 cm^{-1}. The bands show a general tendency to shift to

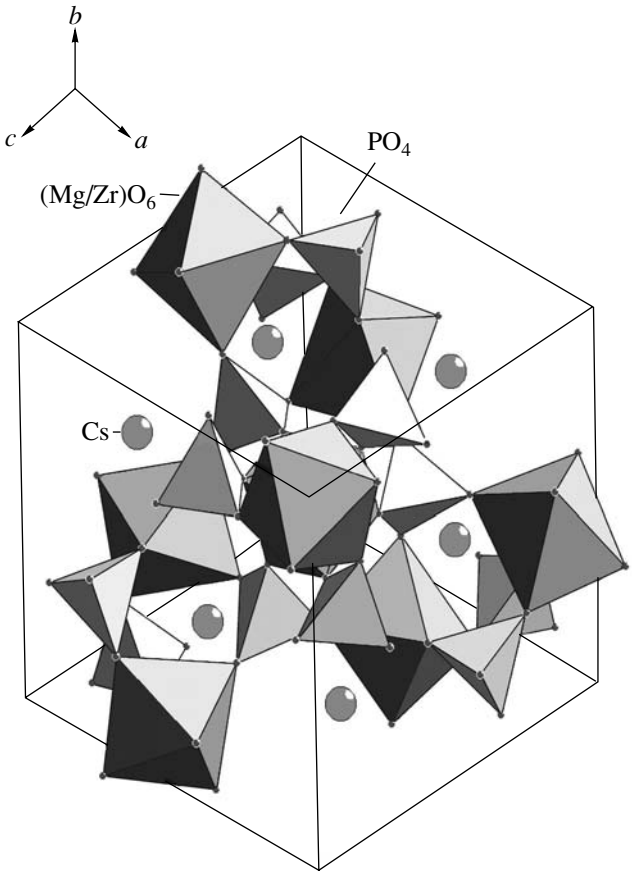

Fig. 5. Fragment of the $Cs_2Mg_{0.5}Zr_{1.5}(PO_4)_3$ structure.

low frequencies with an increase in the weight of the alkali cation.

We used the atomic coordinates of phosphate $K_2YZr(PO_4)_3$ [8] as the starting model for the refinement of the $Cs_2Mg_{0.5}Zr_{1.5}(PO_4)_3$ structure. The results of the refinement are listed in Table 1. The experimental and theoretical neutron-diffraction profiles of the sample (t = 15°C) and the difference curve (experiment minus calculation) normalized to the rms deviation at a point are shown in Fig. 4. The calculated positional and thermal parameters (t = 15 and 600°C) are given in Table 2. The corresponding interatomic distances and bond angles are listed in Table 3.

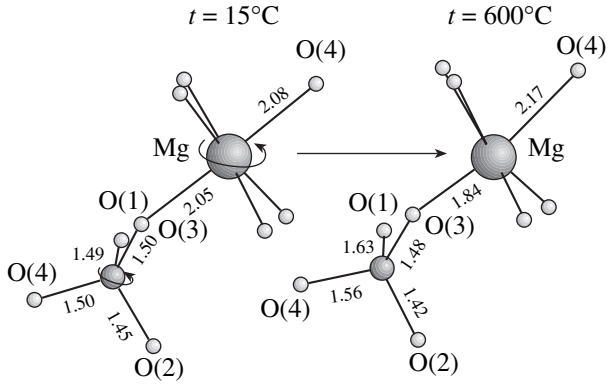

Fig. 6. Distortions of the framework polyhedra upon heating.

A fragment of the structure of the phosphate $Cs_2Mg_{0.5}Zr_{1.5}(PO_4)_3$ is shown in Fig. 5. This structure is based on the mixed anionic framework $[Mg_{0.5}Zr_{1.5}(PO_4)_3]^{2-}$ composed of discrete MgO_6, ZrO_6, and PO_4 polyhedra. The group (dimer) consisting of two octahedra and three tetrahedra linked to each other by shared oxygen atoms is a characteristic fragment of this framework.

In the $Cs_2Mg_{0.5}Zr_{1.5}(PO_4)_3$ compound, zirconium and magnesium cations are randomly distributed over two nonequivalent 4*a* positions in the anionic framework. This result can be attributed to the fact that these elements have equal ionic radii (r = 0.72 Å).

Distortions of the framework polyhedra characterized by the maximum dispersion Δ of the bond lengths vary with temperature. At 15°C, phosphorus tetrahedra are only slightly distorted (Δ = 0.05 Å), and the O–P–O bond angles are close to the calculated value for the ideal tetrahedron (109.5°). The bond lengths vary with

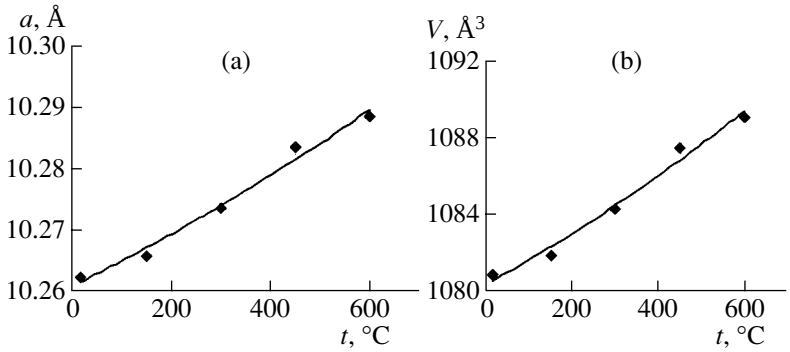

Fig. 7. Temperature dependences of the (a) unit-cell parameter a ($p = 1 \times 10^{-8}T^2 + 4 \times 10^{-5}T + 10.261$) and (b) the unit-cell volume V ($p = 4 \times 10^{-6}T^2 + 1 \times 10^{-2}T + 1080.3$).

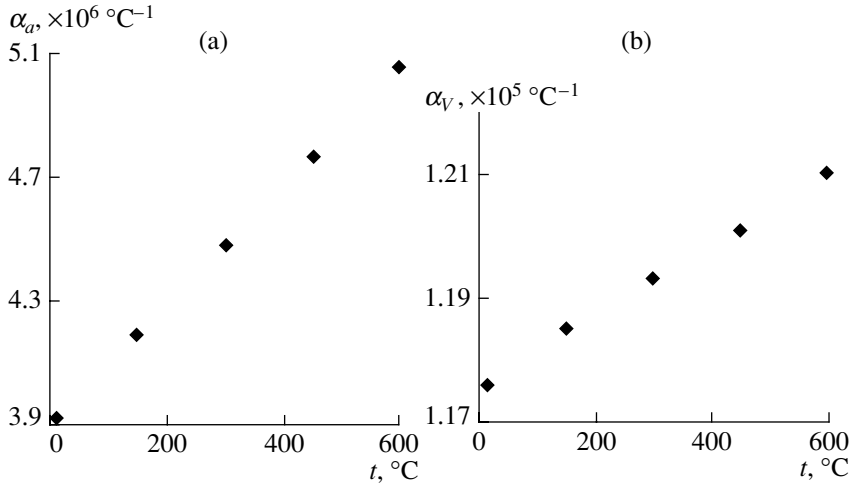

Fig. 8. Temperature dependences of the thermal-expansion coefficients (a) α_a and (b) α_V.

temperature. At 600°C, Δ for the phosphorus tetrahedron is 0.21 Å. Somewhat smaller distortions are observed in the metal–oxygen MgO_6 and ZrO_6 octahedra (Δ = 0.23 and 0.35 Å at 15 and 600°C, respectively). In addition, the polyhedra are rotated with an increase in temperature (see Fig. 6).

The temperature dependences of the of the unit-cell parameters *a* and *V* shown in Fig. 7 are described by the second-degree polynomial. The polynomial parameters of thermal expansion were calculated using Eqs. (1) and (2):

$$p = p_2T^2 + p_1T + p_0, \quad (1)$$

$$\alpha = (p_1 + 2p_2T)/p. \quad (2)$$

Here, α is the thermal-expansion coefficient: $\alpha = 1/p \times dp/dT$.

Table 4. Experimental polynomial parameters

Unit-cell parameters	Polynomial parameters		
	p_2	p_1	p_0
a	1×10^{-8}	4×10^{-5}	10.261
V	4×10^{-6}	1×10^{-2}	1080.3

Table 5. Thermal expansion coefficients for the phosphate $Cs_2Mg_{0.5}Zr_{1.5}(PO_4)_3$

t, °C	α_a, ×10^6 °C^–1	α_V, ×10^6 °C^–1
15	3.93	11.76
150	4.18	11.85
300	4.48	11.93
450	4.76	11.20
600	5.05	12.10

The polynomial parameters p_2, p_1, and p_0 are given in Table 4. The thermal-expansion coefficients α_a and α_V are listed in Table 5.

The temperature dependences of the thermal-expansion coefficients are shown in Fig. 8. It can be seen that α_a and α_V increase with an increase in temperature. At t = 600°C, α_a and α_V are 5.05×10^{-6} and 12.10×10^{-6} °C^{-1}, respectively.

CONCLUSIONS

In this study, we confirmed the prediction of the existence of phosphates with the $[B_{0.5}M_{1.5}(PO_4)_3]^{2-}$ frameworks. The new compounds $K_2Mg_{0.5}Zr_{1.5}(PO_4)_3$, $Rb_2Mg_{0.5}Zr_{1.5}(PO_4)_3$, and $Cs_2Mg_{0.5}Zr_{1.5}(PO_4)_3$ were synthesized and characterized. We demonstrated for the first time that rubidium and cesium cations are involved in phosphates with the $[T_2(PO_4)_3]^{2-}$ frameworks. These phosphates were found to crystallize in the structure type of the mineral langbeinite. Therefore, we confirmed the hypothesis that phosphates having the $[T_2(PO_4)_3]^{2-}$ frameworks and containing large alkali cations in cavities crystallize in the langbeinite structure type (cubic system, sp. gr. $P2_13$). The influence of the temperature factor on the unit-cell parameters and distortions of the framework polyhedra was analyzed.

ACKNOWLEDGMENTS

This study was supported by a grant of the President of the Russian Federation, project no. NSh-1415.2003.2 and the grant "Development of the Scientific Potential of the Higher School," the subprogram "Development of the Infrastructure of the Scientific, Technical, and Innovation Activity of the Higher School and Its Personnel" (no. 3, 2005), section

"Development of the Research of Young Teachers, Scientists, Postgraduates, and Students" (no. 33).

REFERENCES

1. A. I. Orlova, Radiokhimiya **44** (5), 385 (2002).
2. R. G. Sizova, V. A. Blinov, A. A. Voronkov, *et al.*, Kristallografiya **26** (2), 293 (1981) [Sov. Phys. Crystallogr. **26**, 165 (1981)].
3. J. Isasi and A. Daidouh, Solid State Ionics **133**, 303 (2000).
4. A. Leclaire, A. Benmoussa, M. M. Borel, and A. Grandin, J. Solid State Chem. **78**, 227 (1989).
5. Rangan K. Kasthuri and J. Gopalakrishnan, J. Solid State Chem. **109**, 116 (1994).
6. T. Norberg Stefan, Acta Crystallogr. **58**, 743 (2002).
7. A. I. Orlova, I. G. Trubach, V. S. Kurazhkovskaya, *et al.*, J. Solid State Chem. **173**, 314 (2003).
8. H. Wulff, U. Guth, and B. Loescher, Powder Diffraction **7** (2), 103 (1992).
9. R. Perret, J. Less-Common Met. **144**, 195 (1988).
10. E. R. Losilla, S. Bruque, M. A. G. Aranda, *et al.*, Solid State Ionics **112**, 53 (1998).
11. http://nf8.jinr.ru/userguide-97/dn-2.htm
12. V. B. Zlokazov and V. V. Chernyshev, J. Appl. Crystallogr. **25**, 447 (1992).

Translated by T. Safonova

Crystallography Reports, Vol. 50, No. 5, 2005, pp. 766–772. Translated from Kristallografiya, Vol. 50, No. 5, 2005, pp. 827–833.

STRUCTURE OF INORGANIC COMPOUNDS

Refined Crystal Structure of $Ca[B_8O_{11}(OH)_4]$—A Synthetic Calcium Analog of Strontioborite

N. A. Yamnova, Yu. K. Egorov-Tismenko, N. V. Zubkova, O. V. Dimitrova, and A. P. Kantor

Faculty of Geology, Moscow State University, Leninskie gory, Moscow, 119992 Russia

e-mail: natalia_yamnova@mail.ru

Received September 24, 2004

Abstract—A calcium analog of strontioborite, namely, $Ca[B_8O_{11}(OH)_4]$, is synthesized under hydrothermal conditions (T = 270°C, P = 20 atm) within the framework of the study of the phase formation in the $CaCl_2 \cdot Rb_2CO_3 \cdot B_2O_3$ system. The crystal structure of the synthetic calcium borate [a = 7.4480(5) Å, b = 8.2627(5) Å, c = 9.8102(6) Å, β = 108.331(1)°, V = 573.09(6) Å^3, space group $P2_1$, Z = 2, ρ_{calcd} = 2.15 g/cm^3; Brucker SMART CCD automated diffractometer, 5506 reflections, λMoK_α] is refined by the least-squares procedure in the anisotropic approximation of thermal atomic vibrations to R_1 = 0.050. The calcium borate studied has a crystal structure identical to the structure of the natural strontium borate (strontioborite) $Sr[B_8O_{11}(OH)_4]$ and its calcium analog synthesized earlier. The crystal structure is built up of stacks consisting of skeleton layers (formed by boron–oxygen polyanions) and isolated strontium (calcium) polyhedra located in trigonal holes of the skeleton layers. Through channels that can contain H_2O molecules are formed between the stacks. The structure refinement and analysis of the IR spectrum of the synthetic calcium analog of strontioborite do not confirm the previously proposed hypothesis that water molecules are involved in the channels of the structure. A comparative crystal chemical analysis of the calcium borate under investigation and its formula analog, namely, the lead borate $Pb[B_8O_{11}(OH)_4]$, is performed. © *2005 Pleiades Publishing, Inc.*

INTRODUCTION

When studying the phase formation in the $CaCl_2$: Rb_2CO_3 : B_2O_3 system, colorless transparent crystals with a planar prismatic habit were synthesized under hydrothermal conditions at a 1 : 1 : 2 ratio of the components. Crystallization was performed with an excess of boron at temperature T = 270°C and pressure P = 20 atm. The crystals grown were examined using qualitative X-ray microanalysis on a CamScan 4DV scanning electron microscope equipped with a Link energy-dispersive spectrometer (analyst E.V. Guseva). It was found that, among the metal atoms, only calcium atoms enter into the composition of the crystal sample. The identification of the X-ray powder diffraction pattern of the sample synthesized revealed that this compound is structurally similar to the natural strontium borate (strontioborite) $Sr[B_8O_{11}(OH)_4]$ (a = 9.909 Å, b = 8.130 Å, c = 7.623 Å, β = 108.4°, space group $P2_1$, Z = 2) and the synthetic calcium borate $Ca[B_8O_{11}(OH)_4]$ (a = 9.814 Å, b = 8.261 Å, c = 7.619 Å, β = 108.5°, space group $P2_1$, Z = 2). In 1960, Lobanova [1] was the first to describe strontioborite as an Mg,Sr borate of the composition $4(Sr_{0.75}Ca_{0.25})O \cdot 2MgO \cdot 12B_2O_3 \cdot 9H_2O$. More recent investigations of strontioborite [2] and a synthetic calcium borate [3] established that these compounds have identical crystal structures. The structures of both compounds are built up of stacks consisting of skeleton layers (formed by boron–oxygen polyanions) and isolated strontium (calcium) polyhedra located in trigonal holes of these skeleton layers. Through channels that can contain H_2O molecules are formed between the stacks. It should be noted that, by that time, only the O^{2-} ions and $(OH)^-$ groups were revealed in the anionic moieties of the structures of strontioborite and its calcium analog. However, the investigation into the thermal properties and the analysis of the IR spectra of the synthetic calcium borate [4, 5] demonstrated that the composition of this compound involves one water molecule of the zeolite type. This water molecule can be desorbed upon heating of the compound from 70 to 500°C and absorbed upon cooling in an atmosphere saturated with water vapor. On this basis, it was assumed that the composition of the synthetic calcium borate corresponds to the formula $Ca[B_4O_6(OH)]_2 \cdot H_2O$. Zayakina and Brovkin [3] compared the results of chemical, thermal, and X-ray diffraction analyses and suggested that channels in the structure of the borate under investigation can contain water molecules. In this case, the composition of the synthetic calcium borate should correspond to the formula $Ca[B_8O_{11}(OH)_4] \cdot nH_2O$, where n varies from 0 to 1 depending on the synthesis conditions. Since the structural investigations of strontioborite and its calcium analog (the structural models of both compounds were refined to large values of the discrepancy factors R_{hkl} = 11 and 12%, respectively) failed to answer the question as to what is the form of water incorporation into the structure, it was expedient

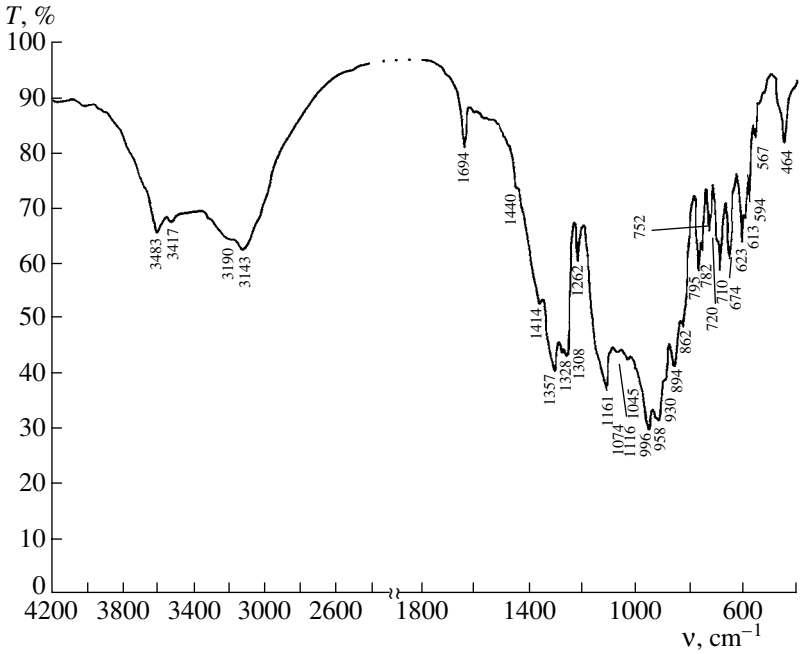

Fig. 1. IR spectrum of the $Sr[B_8O_{11}(OH)_4]$ strontioborite.

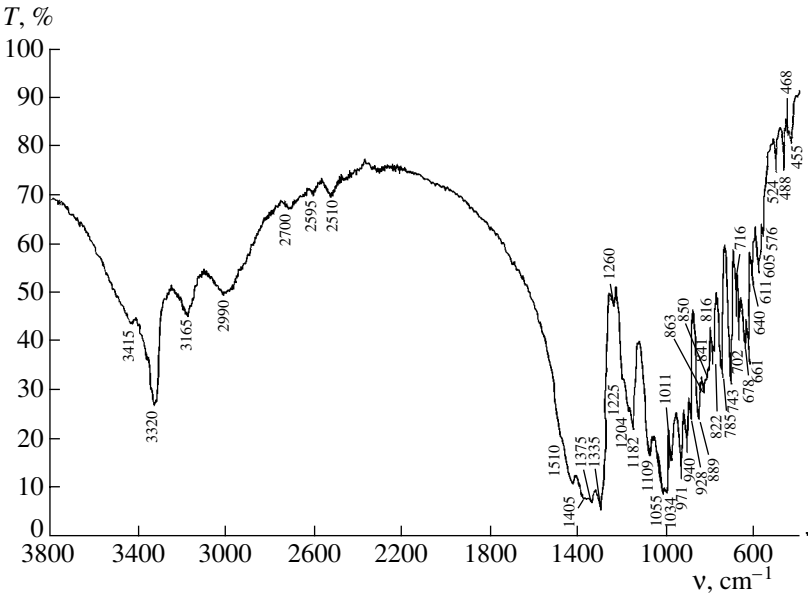

Fig. 2. IR spectrum of the $Ca[B_8O_{11}(OH)_4]$ synthetic calcium borate.

to refine the crystal structure of the synthetic calcium analog of strontioborite.

At the first stage, the synthetic crystals and the strontioborite samples (Chelkar deposit, North Caspian Region), which were kindly supplied by I.V. Pekov, were studied using IR spectroscopy on a Specord 75 IR spectrophotometer by N.V. Chukanov at the Institute of Problems of Chemical Physics (Chernogolovka, Moscow oblast, Russia). The analysis of the absorption bands in the IR spectrum of the strontioborite sample (Fig. 1) revealed that the structure contains molecular water (the absorption bands observed at frequencies of 3483 and 3417 cm^{-1} are attributed to the stretching vibrations of water molecules, whereas the band observed at a frequency of 1694 cm^{-1} corresponds to the bending vibrations of water molecules). However, the IR spectrum of the synthetic calcium borate (Fig. 2) does not exhibit bands associated with stretching or

Table 1. Main crystal data, data collection, and refinement parameters for the structure of the $Ca[B_8O_{11}(OH)_4]$ compound

Characteristics	Parameters
Crystal system	Monoclinic
Space group, Z	$P2_1$, 2
Unit cell parameters	
a, Å	7.4480 (5)
b, Å	8.2627 (5)
c, Å	9.8102 (6)
β, deg	108.331 (1)
V, Å^3	573.09(6)
ρ_{calcd}, g/cm^3	2.15
μ, mm^{-1}	0.64
Crystal size, mm	$0.50 \times 0.30 \times 0.05$
$\sin\theta/\lambda_{max}$	0.768
Index ranges	$-11 \le h \le 11$, $-12 \le k \le 9$, $-14 \le l \le 15$
Number of reflections measured	5506
Number of unique reflections with $I \ge 2\sigma(I)$ [R_{int}]	2663 [0.043]
Final discrepancy factors R_1/wR_2 [$I \ge 2\sigma(I)$]	0.050/0.091
S	0.860
$\Delta\rho_{max}/\Delta\rho_{min}$, e Å^{-3}	1.36/–0.79
Number of parameters refined	229
Flack parameter	0.07(4)

bending vibrations of water molecules. In the frequency range 3800–3200 cm^{-1}, the IR spectra of the strontioborite and synthetic calcium borate samples also differ from each other. The IR spectrum of the former compound (Fig. 1) does not contain three bands of the OH vibrations (at frequencies of 3320, 3165, and 2990 cm^{-1}), which manifest themselves in the spectrum of the latter compound (Fig. 2). A comparison of the two spectra showed that these spectra are similar to each other in the frequency range 1440–1260 cm^{-1}, which corresponds to the BO_3 vibrations. Furthermore, the IR spectrum of the strontioborite sample exhibits bands at frequencies of 1160–930 cm^{-1}, which are attributed to the stretching vibrations of BO_4 tetrahedra, whereas the IR spectrum of the synthetic calcium borate involves a medium-intensity band at a frequency of 1180 cm^{-1}, which is assigned to the bending vibrations of B–OH bonds.

EXPERIMENTAL TECHNIQUE. THE MODEL AND REFINEMENT OF THE STRUCTURE

The experimental intensities of X-ray diffraction reflections for the calcium borate synthesized were collected on a Brucker SMART CCD automated single-crystal diffractometer (λMoK_α) (Laboratory of Crystal Chemistry and X-ray Diffraction Analysis, China University of Geosciences, Beijing, China). The main crystal data, data collection, and refinement parameters for the structure of the $Ca[B_8O_{11}(OH)_4]$ compound are presented in Table 1. According to the analysis of the X-ray diffraction pattern, the crystal structure of the synthetic calcium borate has space group $P2_1$.

The crystal structure was solved by direct methods with the SHELX97 program package [6]. The structural model proposed was refined in the full-matrix anisotropic approximation for the non-hydrogen atoms. The hydrogen atoms were located from the difference electron-density map. The absence of significant additional maxima in the difference electron-density map confirmed the validity of the structural model. The compound with the formula $Ca[B_8O_{11}(OH)_4]$ (Z = 2, ρ_{calcd} = 2.15 g/cm^3) corresponds to the final discrepancy factor (Table 1). The anionic moiety of the structure was separated into O^{2-} ions and $(OH)^-$ groups on the basis of the calculated local balance of the bond valences at the anions with allowance made for both the cation–oxygen distances (according to [7]) and the contributions of hydrogen atoms (according to [8]) (Table 2). The geometric parameters of hydrogen bonds in the structure of the $Ca[B_8O_{11}(OH)_4]$ compound are listed in Table 3. The crystallographic data for the structure studied (CIF file) have been deposited with the Inorganic Crystal Structure Database ICSD (deposit no. 415082).

DESCRIPTION OF THE STRUCTURE AND DISCUSSION OF THE RESULTS

The solution of the structure confirmed the assumption that the compound under investigation is isostructural to both the strontioborite mineral and the calcium borate synthesized earlier. The structural framework is formed by layers of polymerized boron–oxygen polyanions and isolated calcium cations. A polyanion of the composition $[B_8O_{11}(OH)_4]^{2-}$ involves a $[B_3^tB_3^\Delta O_{10}(OH)]^{3-}$ ring group and a dimer bonded to the ring and composed of $[B_2^\Delta O(OH)_3]^{1+}$ boron triangles (Fig. 3). The ring hexaborate radical, which was first found in the structure of the natural tunellite $Sr[B_6O_9(OH)_2] \cdot 3H_2O$ [9] and then revealed in the structures of more than ten natural and synthetic borates, is built up of three vertex-shared tetrahedra and three triangles completed through two free vertices of the tetrahedra. The dimer composed of boron triangles (a suanite-like radical) and the hexaborate radical are

Table 2. Local balance of the bond valences at anions in the structure of the $Ca[B_8O_{11}(OH)_4]$ compound

Cation / Anion	Ca	B(1)	B(2)	B(3)	B(4)	B(5)	B(6)	B(7)	B(8)	H(1)	H(2)	H(3)	H(4)	ΣV_{ij}
O(1)	0.20	0.80				1.04								2.04
O(2)	0.23		0.81	1.02										2.06
O(3)		0.69	0.68		0.65									2.02
O(4)	0.25			1.04	0.80									2.09
O(5)	0.17				0.80	1.04								2.01
O(6)	0.18	0.81				1.05								2.04
O(7)*	0.17								1.00		0.83			2.00
O(8)					0.80		1.05						0.15	2.00
O(9)	0.18		0.81	1.02										2.01
O(10)			0.77					1.06				0.22		2.05
O(11)		0.80						1.04		0.26				2.10
O(12)							1.02		1.03					2.05
O(13)*	0.23						1.01					0.78		2.02
O(14)*								1.00			0.17		0.85	2.02
O(15)*	0.18								1.02	0.74				1.94

Note: Oxygen atoms of the $(OH)^{-1}$ groups are marked with an asterisk.

linked together through a free oxygen vertex of one of the tetrahedra. The mean boron–anion distances in the boron tetrahedra and in the boron triangles involved in the hexaborate radical and those in the trigonal dimer fall in the standard ranges and are equal to 1.466, 1.469, and 1.473 Å in the tetrahedra; 1.361, 1.356, and 1.359 Å in the triangles; and 1.362 and 1.365 Å in the dimer. As in the other borates with tunellite-like radicals, the B–O distances for the oxygen atom bonded to three boron tetrahedra are somewhat larger than the mean distances (1.508, 1.513, and 1.533 Å). The $[B_3^tB_3^\Delta O_{10}(OH)] \cdot [B_2^\Delta O(OH)_3]$ polyanions related by the 2_1 screw axes are joined together into layers perpendicular to the *a* axis of the unit cell (Fig. 3a). The congruent layers, which are adjacent to each other along the *a* axis, are also related by the 2_1 screw axes. This configuration specifies the unit cell parameter $a \sim 7.4$ Å, which is commensurate to the thickness of one layer (Fig. 4a). The calcium cations located at the centers of the trigonal holes formed by the boron–oxygen radicals (Fig. 3a) are surrounded by nine nearest neighbor ligands, which, in turn, form isolated polyhedra. The $Ca[B_8O_{11}(OH)_4]$ neutral layers are linked into a single structure through nine-vertex calcium polyhedra in which six oxygen vertices lie in the layer, one OH vertex belongs to the boron triangle of the dimer in the same layer, and the other two vertices belong to the dimer of the adjacent layer (Fig. 4a). Moreover, the layers are also linked by the hydrogen bonds between the $(OH)^-$ groups and the O^{2-} ions of the adjacent layers (Fig. 4a).

Similar boron–oxygen polyanions joined together into layers form the framework of the structure of the synthetic lead borate $Pb[B_6O_{10}(OH) \cdot B_2O(OH)_3]$ (a = 7.911 Å, b = 9.979 Å, c = 14.03 Å, γ = 90.36°, space group $P2_1/n$) [10], which is a formula analog of the synthetic calcium borate and, correspondingly, strontioborite. The differences lie both in the configuration of the layer as a whole and in the mutual arrangement of individual layers. In the structure of the synthetic lead borate, the boron–oxygen layers are also composed of the tunellite-like radicals $[B_3^tB_3^\Delta O_{10}(OH)]^{3-}$ and suanite dimers $[B_2^\Delta O(OH)_3]^{1+}$. However, in the structures of the synthetic calcium borate and stron-

Table 3. Geometric parameters of hydrogen bonds in the structure of the $Ca[B_8O_{11}(OH)_4]$ compound

D–H···*A*	*D*–H, Å	H···*A*, Å	*D*–*A*, Å	*DHA* angle, deg
O(15)–H(1)···O(11)	0.89(3)	1.70(3)	2.582(4)	171.1(2)
O(7)–H(2)···O(14^{i})	0.83(3)	1.98(3)	2.805(4)	171.1(3)
O(13)–H(3)···O(10)	0.85(3)	1.85(3)	2.685(4)	170.2(2)
O(14)–H(4)···O(8^{ii})	0.81(3)	2.13(4)	2.917(4)	163.5(3)

Note: Symmetry codes: (i) (x, y, z – 1), (ii) ($-x$, 1/2 + y, $-z$).

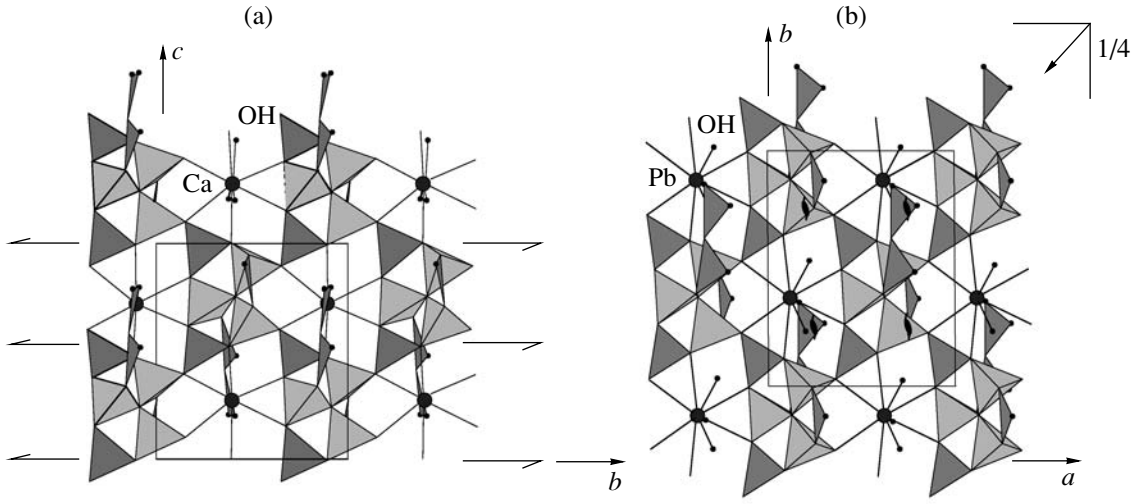

Fig. 3. Boron–oxygen layers in the structures of (a) the $Ca[B_8O_{11}(OH)_4]$ calcium borate and (b) the $Pb[B_8O_{11}(OH)_4]$ lead borate. Solid lines indicate the cation–anion bonds.

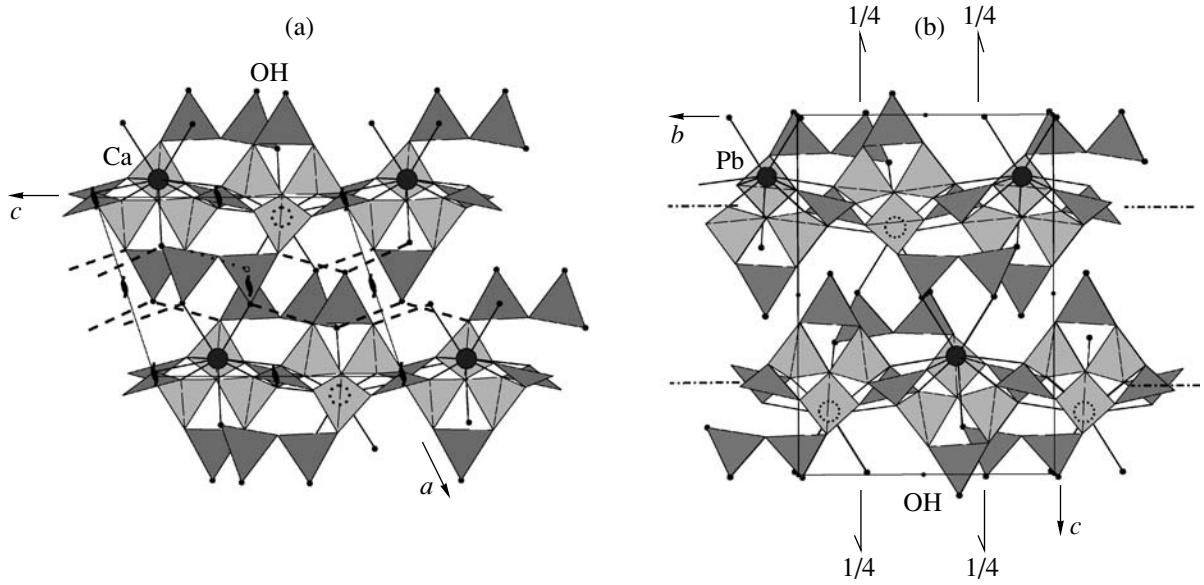

Fig. 4. Projections of the structures of (a) the $Ca[B_8O_{11}(OH)_4]$ calcium borate and (b) the $Pb[B_8O_{11}(OH)_4]$ lead borate onto the *xz* and *yz* planes, respectively. Solid lines indicate the cation–anion bonds, and dashed lines represent the hydrogen bonds.

tioborite, the dimers are oriented in opposite directions along the *c* axis of the unit cell (Figs. 3a, 4a), because they are related by the 2_1 screw axis lying in the layer plane. By contrast, in the structure of the synthetic lead borate, the $[B_2O(OH)_3]^{1+}$ dimers are oriented in the same direction along the *b* axis of the unit cell, because the neighboring polyanions are related by the inclined plane lying in the layer plane *n* (Figs. 3b, 4b). Furthermore, in the structure of the synthetic lead borate, the boron–oxygen layers adjacent to each other along the *c* axis are related through the center of inversion and, hence, are enantiomorphic (Fig. 4b), whereas the corresponding layers in the structures of the synthetic calcium borate and strontioborite are congruent. This circumstance accounts for the fact that the unit cell parameter *c* for the lead borate ($c \sim 14$ Å) is approximately two times larger than the unit cell parameter $a \sim 7.4$ Å for the calcium borate. The central part of the layer in the structure of the synthetic calcium borate consists of hexaborate groups and is similar to the corresponding layer in the structure of the $Sr[B_6O_9(OH)_2] \cdot 3H_2O$ tunellite. In both structures, the hexaborate polyanions are related by the 2_1 screw axes in the layers and the doubling of the unit cell parameter $a \sim 14$ Å in the tunellite structure as compared to the corresponding unit cell parameter in the calcium borate structure (as is the case

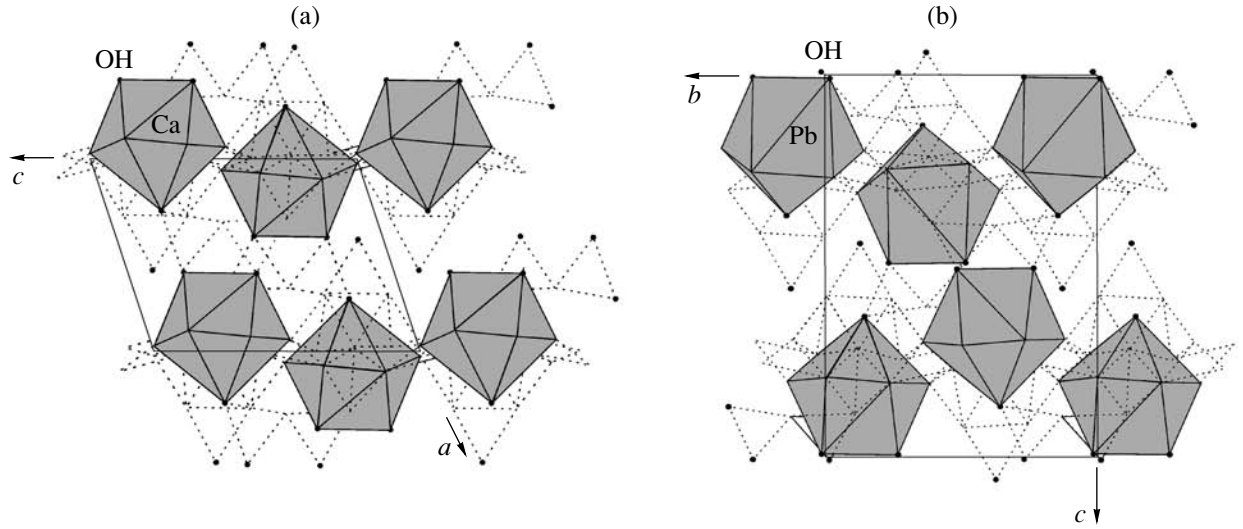

Fig. 5. Arrangement of the polyhedra around the calcium and lead cations in the structures of (a) the $Ca[B_8O_{11}(OH)_4]$ calcium borate and (b) the $Pb[B_8O_{11}(OH)_4]$ lead borate. Dashed lines indicate edges of the boron tetrahedra and boron triangles in the boron–oxygen polyanions.

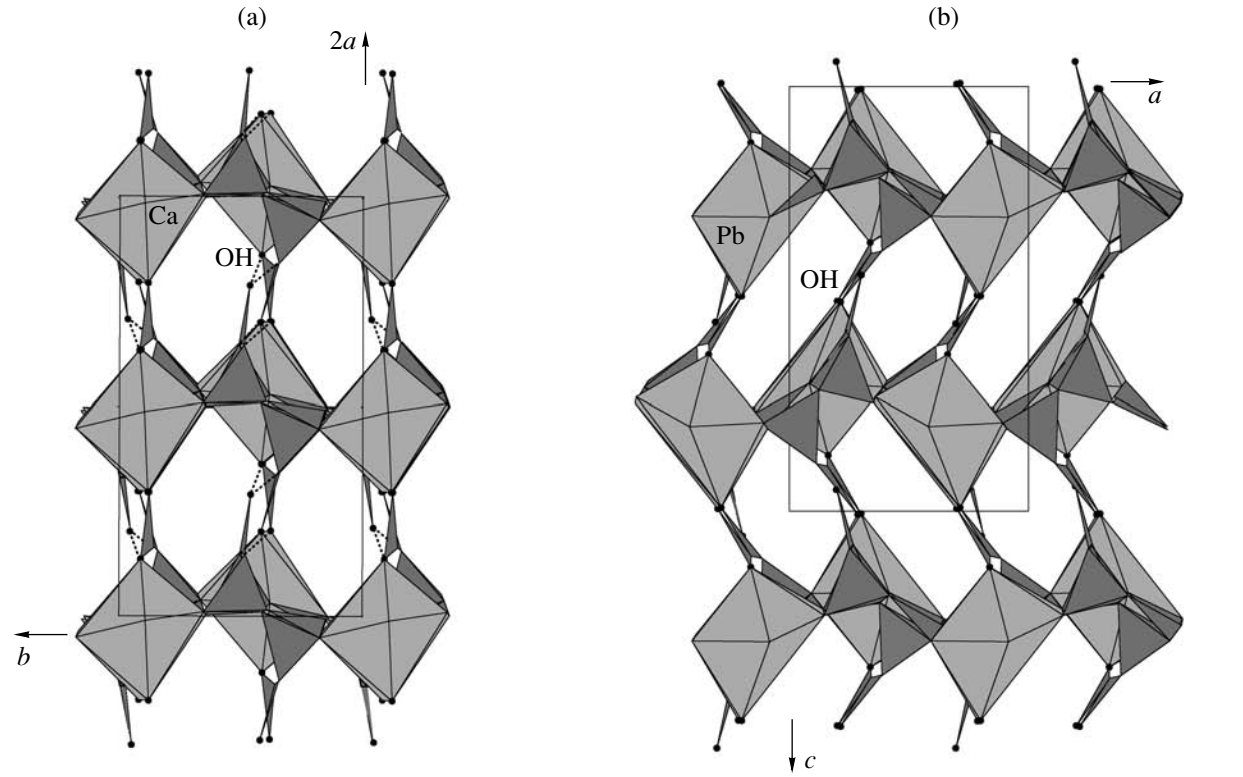

Fig. 6. Projections of the structures of (a) the $Ca[B_8O_{11}(OH)_4]$ calcium borate and (b) the $Pb[B_8O_{11}(OH)_4]$ lead borate onto the *xy* and *xz* planes, respectively.

in the lead borate structure) is caused by the presence of the center of inversion between the adjacent layers.

Although the structural motifs in the arrangement of large-sized cations in trigonal holes of the boron–oxygen skeleton layer in the structures of the synthetic calcium borate and synthetic lead borate are similar to each other (Figs. 3a, 3b), the isolated nine-vertex polyhedra around the calcium cations in the adjacent layers turn out to be congruent, whereas the corresponding polyhedra around the lead cations are enantiomorphic (Figs. 5a, 5b). Moreover, the Ca–O and O–O distances

in the calcium polyhedra lie in the standard ranges and are equal to 2.478–2.630 Å (mean distance, 2.572 Å) and 2.267–4.480 Å (mean distance, 3.130 Å), respectively. In the lead polyhedra, there is a larger spread in Pb–O and O–O distances, which are equal to 2.540–2.939 Å (mean distance, 2.726 Å) and 2.295–5.310 Å (mean distance, 3.306 Å), respectively. Such an asymmetric coordination, which is characteristic of many divalent lead compounds, arises from the specific features in the configuration of the electron shell of divalent lead, for example, with the manifestation of a lone pair of 6*s* electrons.

As was noted above, the zeolite properties exhibited by the calcium analog of strontioborite are associated with the presence of through channels in the structure (Fig. 6a). Similar channels also exist in the structure of the synthetic lead borate (Fig. 6b). However, the synthetic calcium borate is characterized by channels with identical cross sections. By contrast, in the structure of the lead borate, the channels with different shapes of the cross sections alternate in a staggered order along the *a* and *c* axes of the unit cell. This can be explained both by the asymmetry of the lead polyhedra (the lengths of the edges bounding the channels fall in the range 3.122–5.130 Å in the lead borate and in the range 3.106–4.480 Å in the calcium borate) and by the fact that, in the lead borate, the suanite groups belonging to the same boron–oxygen layer have different orientations along the diagonals of the (010) face of the unit cell (Fig. 6b). In the structure of the synthetic calcium borate (Fig. 6a), the suanite groups are oriented along the *a* axis of the unit cell. These differences are also responsible for the approximately twofold increase in the unit cell parameter *c* in the lead borate structure as compared to the corresponding unit cell parameter in the calcium borate structure.

According to Belokoneva *et al.* [10], the structures of strontioborite $Sr[B_8O_{11}(OH)_4]$, synthetic lead borate $Pb[B_8O_{11}(OH)_4]$, tunellite $Sr[B_6O_9(OH)_2] \cdot 3H_2O$, strontioginorite $SrCa[B_{14}O_{20}(OH)_6] \cdot 5H_2O$, aristarainite $Na_2Mg[B_6O_8(OH)_4]_2 \cdot 4H_2O$, and macallisterite $Mg_2[B_6O_7(OH)_6]_2 \cdot 9H_2O$ belong to the OD family in which all the representatives are formed by identical fragments, i.e., hexaborate blocks. The structural diversity of this family can be explained by the symmetry of the ribbons and layers composed of hexaborate blocks, on the one hand, and by the presence of different symmetry elements relating the adjacent layers in the structures considered in [10], on the other hand.

The structure refinement and the analysis of the IR spectrum of the synthetic calcium analog of strontioborite did not confirm the assumption made earlier by Zayakina and Brovkin [3], according to which the structural channels can contain water molecules. However, the results of the IR spectroscopic investigations indicate that this possibility must not be ruled out in natural strontioborite. The validity of the hypothesis proposed by those authors can be verified by refining the mineral structure.

ACKNOWLEDGMENTS

We would like to thank Ma Zhesheng, Shi Nicheng, Ye Danian, and Xiong Ming (Laboratory of Crystal Chemistry and X-ray Diffraction Analysis, China University of Geosciences, Beijing, China) for their assistance in performing the experiments.

REFERENCES

1. V. V. Lobanova, Dokl. Akad. Nauk SSSR **135** (4), 173 (1960).
2. A. A. Brovkin, N. V. Zayakina, and V. S. Brovkina, Kristallografiya **20** (5), 911 (1975) [Sov. Phys. Crystallogr. **20** (5), 563 (1975)].
3. N. V. Zayakina and A. A. Brovkin, Kristallografiya **23** (6), 1167 (1978) [Sov. Phys. Crystallogr. **23** (6), 659 (1978)].
4. I. Ya. Nekrasov, A. P. Grigor'ev, T. A. Grigor'eva, *et al.*, *Investigation of High-Temperature Borates* (Nedra, Moscow, 1970) [in Russian].
5. I. Ya. Nekrasov and E. V. Vlasova, Rentgenogr. Min. Syr'ya, No. 8, 111 (1971).
6. G. M. Sheldrick, *SHELX97: Program for the Solution and Refinement of Crystal Structures* (Siemens Energy and Automation, Madison, Wisconsin, 1997).
7. N. E. Brese and M. O'Keeffe, Acta Crystallogr., Sect. B: Struct. Sci. **47**, 192 (1991).
8. G. Ferraris and G. Ivaldi, Acta Crystallogr., Sect. B: Struct. Sci. **44**, 341 (1988).
9. J. R. Clark, Am. Mineral. **49**, 1549 (1964).
10. E. L. Belokoneva, T. A. Korchemkina, and O. V. Dimitrova, Zh. Neorg. Khim. **44** (6), 951 (1999).

Translated by O. Borovik-Romanova

Crystallography Reports, Vol. 50, No. 5, 2005, pp. 773–778. Translated from Kristallografiya, Vol. 50, No. 5, 2005, pp. 834–839.

STRUCTURE OF INORGANIC COMPOUNDS

Crystal Structure Refinement of Bifluorides MHF_2 (M = Na, NH_4, Rb). Crystal Structures of $Rb_5F_4(HF_2) \cdot 2H_2O$ and $RbF \cdot H_2O$

S. I. Troyanov

Faculty of Chemistry, Moscow State University, Leninskie gory, Moscow, 119992 Russia
e-mail: troyanov@thermo.chem.msu.ru

Received January 11, 2005

Abstract—The crystal structures of alkali metal and ammonium bifluorides MHF_2 (M = Na, NH_4, or Rb) are refined using single-crystal X-ray diffraction. In all the crystals of acid fluorides studied, HF_2^- anions have a linear structure with F···F distances ranging from 2.277 to 2.281 Å. The crystal structures of the $Rb_5F_4(HF_2) \cdot 2H_2O$ and $RbF \cdot H_2O$ compounds are determined. It is established that, in these structures, the O–H···F hydrogen bonds whose lengths are equal to 2.55–2.57 and 2.63 Å participate in the formation of trinuclear bent anions and zigzag anionic chains, respectively. © *2005 Pleiades Publishing, Inc.*

INTRODUCTION

Monoacid salts of hydrofluoric acid are important inorganic compounds that have found extensive use in laboratory inorganic synthesis and engineering, for example, in the production of fluorine and hydrogen fluoride [1]. These compounds contain HF_2^- bifluoride anions, which are characterized by the shortest hydrogen bond known to date. Investigation into the crystal structure of bifluorides and other salts with $H_nF_{n+1}^-$ anions is of particular importance in elucidating the nature of strong hydrogen bonding. In this respect, the structures of acid fluorides of the general formula MH_nF_{n+1} have been studied using X-ray and neutron diffraction analyses. It should be noted that the structures of acid fluorides of potassium (n = 1–4) [2–4] and ammonium (n = 1, 3, 4, 7) [5, 6] are best understood. However, data on the crystal structure of lithium, rubidium, and cesium bifluorides were obtained more than forty years ago with the use of insufficiently reliable experimental techniques. For some of these structures, the data available in the literature on the length of F···F hydrogen bonds have been given without experimental errors and discrepancy factors (R_1). Kruh *et al.* [7] determined the crystal structure of the $RbHF_2$ compound with a large value of the final R factor (0.12, X-ray powder diffraction analysis). McDonald [5] examined the electron density distribution for NH_4HF_2 crystals and simultaneously refined the scattering curves for fluorine and sodium atoms. As a result, the author of [5] obtained very flattened maxima in the electron density distribution for positions of hydrogen atoms in the bifluoride anions and, moreover, revealed an additional uninterpretable maximum in the difference Fourier synthesis. (The data presented for the NH_4HF_2 compound in the Inorganic Crystal Structure Database (ICSD no. 14140) contain substantial mistakes: the errors in the determination of the atomic coordinates are ten times overestimated; furthermore, the discrepancy factors are given as 0.03(!), whereas the R factors obtained in [5] amount to 0.050 and 0.077.) McGaw and Ibers [8] carried out X-ray and neutron diffraction investigations of sodium bifluoride single crystals. However, the X-ray diffraction intensities were estimated by the photomethod and the number of reflections collected in neutron diffraction experiments was relatively small, which somewhat limited the accuracy of the results obtained using the least-squares procedure.

In the present study, we obtained reliable crystal data for three bifluorides, namely, $NaHF_2$, NH_4HF_2, and $RbHF_2$, and determined the crystal structures of a rubidium fluoride monohydrate and a mixed rubidium "fluoride–bifluoride" hydrate. Moreover, the data obtained for the structure of the bifluoride anions were compared with those available in the literature.

SAMPLE PREPARATION AND EXPERIMENTAL TECHNIQUE

The simplest procedure for preparing crystalline bifluorides involves the reaction of the relevant fluorides (or carbonates) with hydrofluoric acid and the subsequent concentration of the resultant solutions. This procedure was used for synthesizing the $RbHF_2$ salt. The ammonium and sodium bifluorides studied in this work were prepared in the course of crystallization from solutions of other salts, for example, sodium selenate or

Table 1. Crystal data, data collection, and refinement parameters of the structures under investigation

Empirical formula	$NaHF_2$	NH_4HF_2	$RbHF_2$	$Rb_5F_4(HF_2) \cdot 2H_2O$	$RbF \cdot H_2O$
Molecular weight M	62.00	57.05	124.48	578.39	122.49
Crystal system	Trigonal	Orthorhombic	Tetragonal	Orthorhombic	Orthorhombic
Space group, Z	$R\bar{3}m$, 3	*Pmna*, 4	*I*4/*mcm*, 4	*Pccn*, 4	*Pnma*, 4
a, Å	3.444(1)	8.396(2)	5.875(1)	11.978(3)	8.045(3)
b, Å	3.444(1)	3.630(1)	5.875(1)	13.484(4)	4.187(1)
c, Å	13.767(4)	8.172(2)	7.184(1)	7.084(2)	8.328(3)
V, Å^3	141.42(7)	249.1(1)	246.44(7)	1144.1(5)	280.5(2)
ρ_{calcd}, g/cm^3	2.184	1.521	3.355	3.358	2.900
Crystal size, mm	$0.7 \times 0.4 \times 0.3$	$0.9 \times 0.9 \times 0.15$	$0.5 \times 0.4 \times 0.05$	$0.6 \times 0.18 \times 0.16$	$0.4 \times 0.32 \times 0.1$
$\mu(MoK_\alpha)$, cm^{-1}; T_{min}/T_{max}	4.7; 0.782/0.846	2.0; 0.743/0.970	198.1; 0.077/0.997	212.8; 0.019/0.105	173.8; 0.031/0.280
Temperature, K	140	160	150	170	170
θ_{max}, deg	34.6	29.9	32.3	26.4	26.7
Number of reflections measured/Number of unique reflections	296/100	1397/393	1528/137	4643/1157	1637/340
Number of reflections with $F^2 > 2\sigma(F^2)$	86	354	105	608	248
Number of reflections in the refinement/Number of parameters refined in the least-squares procedure	88/8	373/28	112/10	1147/68	333/24
R_1/wR_2	0.016/0.039	0.023/0.059	0.016/0.031	0.042/0.080	0.033/0.067
$\Delta\rho_{max}/\Delta\rho_{min}$, e/Å^3	0.12/–0.21	0.27/–0.14	0.58/–0.56	0.99/–1.07	1.08/–1.14

Table 2. Selected interatomic distances in the crystal structures of the MHF_2, $Rb_5F_4(HF_2) \cdot 2H_2O$, and $RbF \cdot H_2O$ compounds

Structure	$\langle M$–F(O)$\rangle$	F···H···F	F···H	N(O)–H···F
$NaHF_2$	2.3001(6)	2.277(1)	1.1383(5)	
NH_4HF_2		2.281(1)	1.1404(5)	2.8094(7)*
		2.278(1)	1.1388(5)	2.7964(6)*
$RbHF_2$	2.8949(7)	2.280(4)	0.7(1)	
$Rb_5F_4(HF_2) \cdot 2H_2O$	2.898	2.280(15)	1.15(2)	2.567(10)**
	3.066***			2.549(11)**
$RbF \cdot H_2O$	2.858			2.627(5)**
	3.123***			

* Hydrogen bond N–H···F.
** Hydrogen bond O–H···F.
*** Averaged Rb–O distance.

ammonium sulfate. Prior to crystallization, hydrofluoric acid was added to these solutions and then they were evaporated at temperatures of 70–90°C. In the reaction mixture used to prepare rubidium bifluoride crystals, other salts precipitated in the form of platelike and needle-shaped crystals after hydrofluoric acid was partially removed. According to the X-ray diffraction analysis, the salts obtained correspond to the compositions $Rb_5F_4(HF_2) \cdot 2H_2O$ and $RbF \cdot H_2O$.

The experimental intensities of X-ray diffraction reflections were collected at low temperatures on a Stoe STADI4 four-circle diffractometer for MHF_2 crystals or on a Stoe IPDS diffractometer equipped with an area detector for crystals of rubidium salt hydrates with the use of MoK_α monochromatic radiation (λ = 0.71073 Å). The unit cell parameters were additionally refined with a large number of high-angle reflections scanned at positive and negative θ angles. This made it possible to

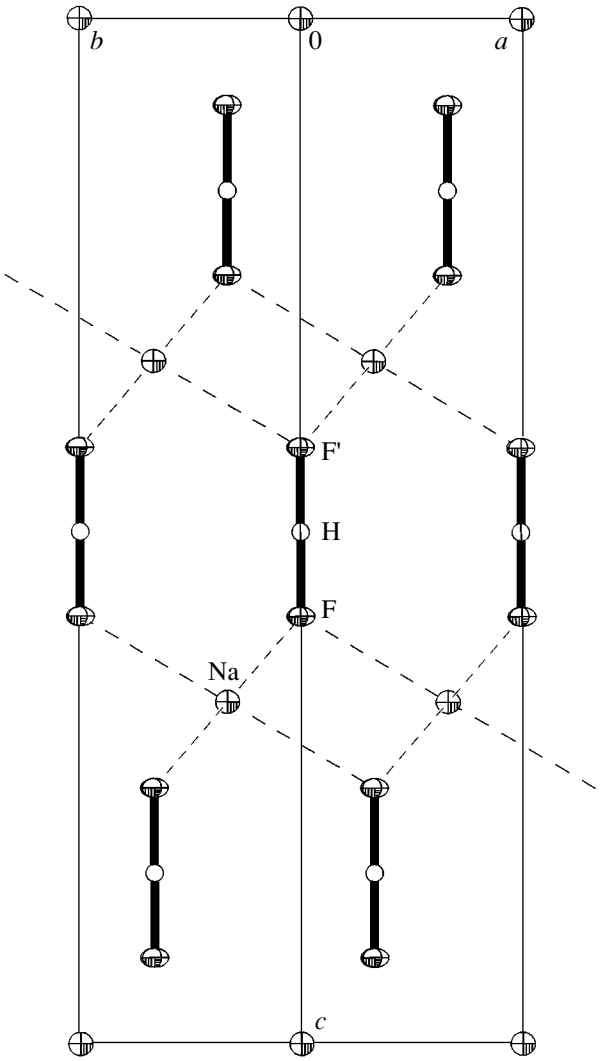

Fig. 1. Projection of the crystal structure of the $NaHF_2$ compound along the [110] direction. Thermal ellipsoids of non-hydrogen atoms are drawn at the 50% probability level.

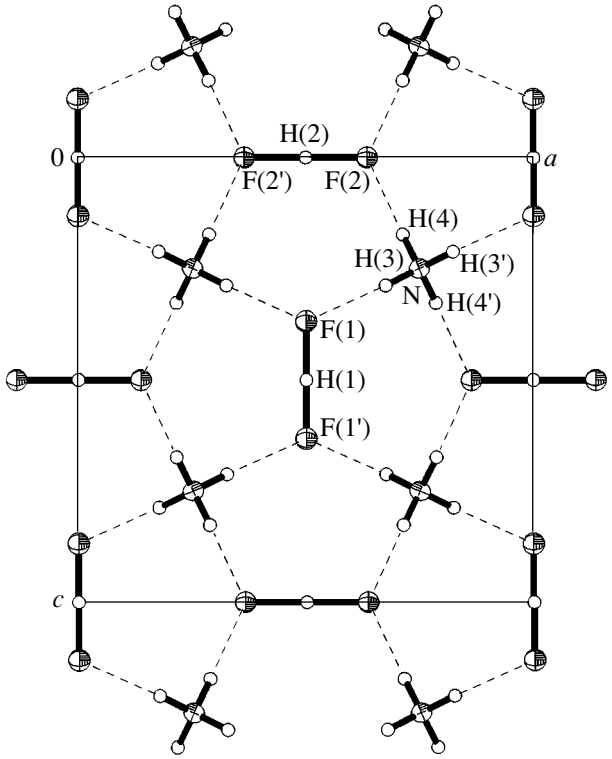

Fig. 2. Projection of the crystal structure of the NH_4HF_2 compound along the *x* axis. Thermal ellipsoids of non-hydrogen atoms are drawn at the 50% probability level.

eliminate the errors introduced by both the absorption and the inaccuracy of the crystal alignment. The intensities of reflections measured were corrected for adsorption by using either the empirical method on the basis of ψ scans of several reflections or the numerical method with allowance made for the real crystal shape. The absorption correction was particularly important for the crystals of rubidium salts, which are characterized by very large linear absorption coefficients. In this case, the crystal shape was additionally refined with the X-SHAPE program package [9]. The crystallographic parameters and details of the structure refinement are summarized in Table 1.

The crystal structures were solved by direct methods with the SHELXS97 program package [10] and the subsequent Fourier syntheses. All the non-hydrogen atoms were refined in the anisotropic approximation, whereas the hydrogen atoms were refined in the isotropic approximation with the SHELXL97 program package [11]. The complete list of crystallographic data for the structures of the five compounds studied in this work have been deposited with the Inorganic Crystal Structure Database (FIZ, Karlsruhe, CSD nos. 415006–415010). The selected interatomic distances in the crystal structures of the rubidium salt hydrates are given in Table 2.

RESULTS AND DISCUSSION

The crystal structures of the $NaHF_2$, NH_4HF_2, and $RbHF_2$ compounds, on the whole, were determined with a high accuracy. This allowed us to obtain the reliable data on the structure of hydrogen bifluoride anions HF_2^- in these crystals. Crystalline bifluorides of alkali metals and ammonium differ in their structural types depending on the nature and size of the cations. Crystals with small-sized cations, for example, Li^+ [12] and Na^+ [7], have a trigonal structure (space group $R\bar{3}m$), whereas crystals with large-sized cations, for example, K^+ [2], Rb^+ [8], and Cs^+ [8], have a tetragonal structure (space group *I*4/*mcm*). The ammonium bifluoride crystals are characterized by a specific structural type [5] due to the formation of hydrogen bonds between cations and anions.

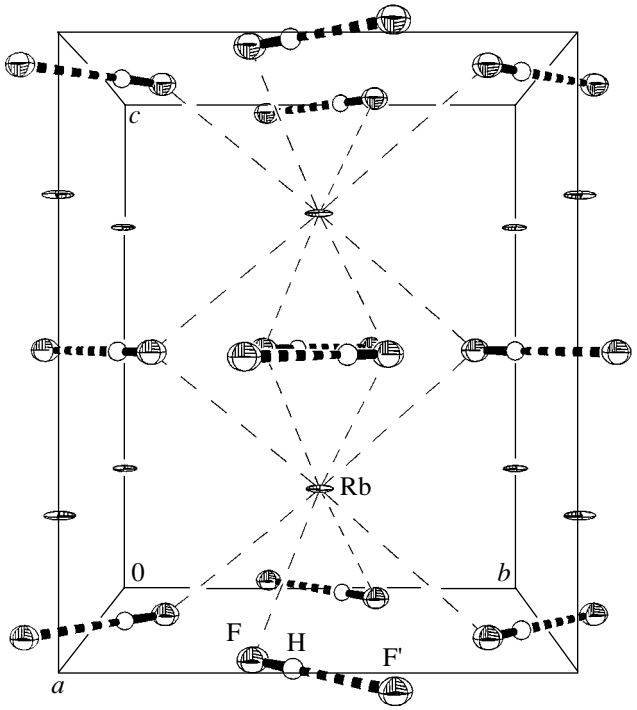

Fig. 3. A general view of the crystal structure of the $RbHF_2$ compound along the *x* axis. Thermal ellipsoids of non-hydrogen atoms are drawn at the 50% probability level. Disordered hydrogen atoms are shown in only one of the two positions.

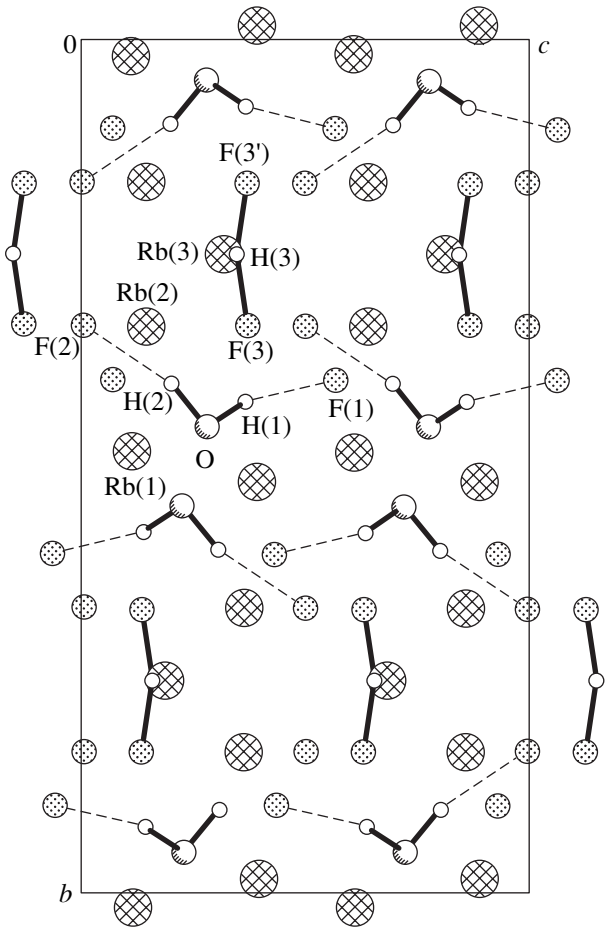

Fig. 4. Projection of the crystal structure of the $Rb_5F_4(HF_2) \cdot 2H_2O$ compound along the *x* axis.

Our structural data for the $NaHF_2$ compound made it possible to refine the results obtained in the X-ray and neutron diffraction experiments performed earlier by McGaw and Ibers [8] for sodium bifluoride single crystals. The F···H···F distance is equal to 2.277(1) Å, and the hydrogen atom is located at the center of inversion. This corresponds to a single-minimum symmetric hydrogen bond. According to [8], the hydrogen bond is also symmetric in shape but the F···H···F distance is somewhat shorter (2.264–2.266 Å) in both the protonated and deuterated compounds. It is interesting to note that the F···F distance determined in the present work coincides with the F···F distance found in the structures of bifluorides of both potassium [2] and lithium [12], even though Frevel and Rinn [12] used the intensities obtained from the photometric measurements of the X-ray powder diffraction pattern (*R* factors are not reported in their paper).

In the structure of the $NaHF_2$ compound, the sodium atoms are located in a trigonally distorted octahedral environment in which the Na–F bond lengths are equal to 2.300 Å. These distances are somewhat shorter than the Na–F bond lengths (2.318 Å) determined in [8]. Since the sodium atoms occupy positions with fixed coordinates, this insignificant discrepancy is most likely associated with the fact that the temperatures of the diffraction measurements in our work and in [8] differ by 150 K. Figure 1 shows the packing in the crystal structure of the sodium bifluoride in the projection along the [110] direction. All the HF_2^- anions with a linear structure are aligned parallel to each other. The sodium atoms are involved in the coordination of the fluorine atoms of six different anions, whereas each fluorine atom is bonded not only to the hydrogen atom but also to six sodium atoms.

In this work, the crystal structure of the ammonium bifluoride was determined with a considerably higher accuracy as compared to the results published earlier in [5]. In our case, the standard deviations of the atomic coordinates decreased by a factor of four or five. The structure contains linear symmetric bifluoride anions of two types, whose axes are perpendicular to each other (Fig. 2). The F(1)···H(1)···F(1') anions are somewhat inclined with respect to the *x*0*z* plane, whereas all the F(2)···H(2)···F(2') anions are aligned parallel to the *a* axis. The F···H···F distances are actually equal to each other [2.281(1) and 2.278(1) Å]. Each fluorine atom is involved in the hydrogen bond in the bifluoride anion and, moreover, acts as an acceptor in two hydrogen

bonds of the N–H···F type with distances of 2.809 and 2.796 Å. The directionality of the four hydrogen bonds with the participation of the nitrogen atom leads to a substantial difference between the topologies of this crystal structure and the structures of the bifluorides containing singly charged metal cations with approximately identical sizes (K, Rb). However, this specific feature virtually does not affect the length of the hydrogen bond in the bifluoride anion.

According to the X-ray powder diffraction data obtained by Kruh *et al.* [7], the crystal structure of the $RbHF_2$ compound belongs to the structural type of potassium bifluoride. Note that cesium bifluoride also crystallizes in the same structural type. In these structures, the cation is located in a square–antiprismatic environment of eight fluorine atoms, each involved in one of the eight different HF_2^- anions (Fig. 3). By virtue of the structural similarity of the bifluorides under investigation, it would be reasonable to assume that, in the structure of the rubidium bifluoride, the bifluoride anion should also have a single-minimum linear symmetric structure. However, the refinement of the structure with a hydrogen atom at the center of inversion (i.e., at the midpoint of the F···F hydrogen bond) led to a very large isotropic thermal parameter $U_H = 0.15$ Å^2. Furthermore, the difference Fourier syntheses always revealed a peak shifted from the center. The refinement of the symmetrically disordered hydrogen atom gave a reasonable value of the thermal parameter (U_H = 0.04 Å^2). In this case, the hydrogen atom appears to be at a short distance (0.7 Å) from one of the fluorine atoms, even though it lies on the F···F line. In both variants of the hydrogen atom position, the F···F distance remains unchanged [2.280(4) Å] and is actually equal to that in the structure of the KHF_2 compound [2.277(6) Å] [2] and other bifluorides. The revealed disordering of the hydrogen atom in the structure of the rubidium bifluoride cannot be considered the final result, because the small final *R* factor was obtained only after the very large correction for absorption in the crystal was introduced in the calculation. The existence of asymmetric bifluoride anions was reliably established by the neutron diffraction method for a number of salts, for example, *p*-toluidinium bifluoride [13]. Therefore, in order to reliably determine the proton location in the structure of the $RbHF_2$ bifluoride, it is necessary to use neutron diffraction methods.

Crystals of the mixed rubidium fluoride–bifluoride hydrate $Rb_5F_4(HF_2) \cdot 2H_2O$ and rubidium fluoride monohydrate $RbF \cdot H_2O$ were revealed together with $RbHF_2$ bifluoride crystals in the reaction mixture a few months after the synthesis of the rubidium bifluoride. It seems likely that these hydrates formed in the course of gradual removal of the hydrogen fluoride from the system. Both these compounds had not been known earlier. Apart from rubidium cations, the crystal structure of the $Rb_5F_4(HF_2) \cdot 2H_2O$ hydrate contains bifluoride anions and hydrated fluoride anions F···H–O–H···F (Fig. 4). The bifluoride anions with a F···F distance of 2.280(15) Å are somewhat bent. However, the positions of the hydrogen atoms in this structure are determined highly unreliably. The hydrated trinuclear anions have a bent structure (owing to the directionality of the bonds in the water molecule) with relatively strong hydrogen bonds O–H···F, whose length lies in the range 2.55–2.57 Å (Table 2).

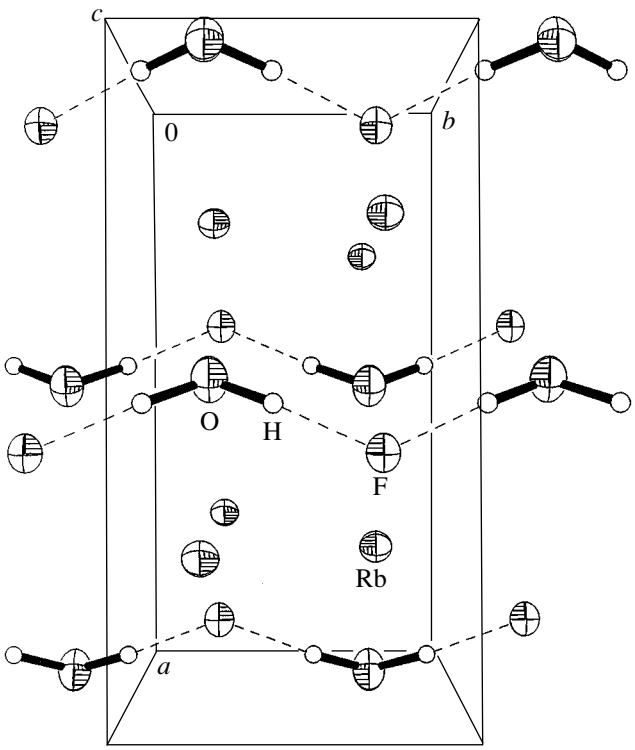

Fig. 5. A general view of the crystal structure of the $RbF \cdot H_2O$ compound along the *z* axis. Thermal ellipsoids of nonhydrogen atoms are drawn at the 50% probability level.

The crystal structure of the rubidium fluoride monohydrate has no analogs among the alkali metal fluoride hydrates known to date, because only potassium fluoride dihydrate and potassium fluoride tetrahydrate have hitherto been characterized structurally. The O–H···F hydrogen bonds [2.627(5) Å] in this structure are longer than those in the rubidium fluoride–bifluoride hydrate. This difference is explained by the fact that the fluorine atom acts as an acceptor not in one but in two hydrogen bonds, which, in turn, leads to the formation of infinite zigzag chains aligned parallel to the *b* axis in the structure (Fig. 5).

CONCLUSIONS

Thus, we refined three crystal structures of the previously studied bifluorides. The result obtained for the structure of the $RbHF_2$ bifluoride was rather unexpected because the hydrogen atom involved in the

hydrogen bond turned out to be disordered. It was demonstrated that, in all the studied crystal structures with bifluoride anions, the hydrogen bond length lies in the range 2.277–2.281 Å. In the crystal structures of the rubidium fluoride hydrates, the O–H···F hydrogen bonds lead to the formation of trinuclear bent anions or zigzag anionic chains.

REFERENCES

1. A. K. Opalovskiĭ and T. D. Fedotova, *Hydrofluorides* (Nauka, Novosibirsk, 1973) [in Russian].
2. J. A. Ibers, J. Chem. Phys. **40**, 402 (1964).
3. D. Mootz and D. Boenigk, J. Am. Chem. Soc. **108**, 6634 (1986).
4. B. A. Coyle, L. W. Schroeder, and J. A. Ibers, J. Solid State Chem. **1**, 386 (1970).
5. T. R. R. McDonald, Acta Crystallogr. **13**, 113 (1960).
6. D. Mootz and W. Poll, Z. Naturforsch., B: Chem. Sci. **39**, 290 (1984).
7. R. Kruh, K. Fuwa, and T. E. McEver, J. Am. Chem. Soc. **78**, 4256 (1956).
8. B. L. McGaw and J. A. Ibers, J. Chem. Phys. **39**, 2677 (1963).
9. *X-SHAPE: Crystal Optimization for Numerical Absorption Correction, Version 1.01* (Stoe and Cie, Darmstadt, 1996).
10. G. M. Sheldrick, *SHELXS97: Program for Solution of Crystal Structures from Diffraction Data* (Univ. of Göttingen, Germany, 1997).
11. G. M. Sheldrick, *SHELXL97: Program for the Refinement of Crystal Structures* (Univ. of Göttingen, Germany, 1997).
12. L. K. Frevel and H. W. Rinn, Acta Crystallogr. **15**, 286 (1962).
13. J. M. Williams and L. F. Schneemeyer, J. Am. Chem. Soc. **95**, 5780 (1973).

Translated by O. Borovik-Romanova

Crystallography Reports, Vol. 50, No. 5, 2005, pp. 779–784. Translated from Kristallografiya, Vol. 50, No. 5, 2005, pp. 840–845.

STRUCTURE OF INORGANIC COMPOUNDS

Specific Features of the Crystal Structure and Magnetic Properties of $KTaO_3$ Produced by Electrolysis of Melts

V. F. Shamraĭ, A. V. Arakcheeva, V. V. Grinevich, and A. B. Mikhaĭlova

Baikov Institute of Metallurgy and Materials Science, Russian Academy of Sciences, Leninskiĭ pr. 49, Moscow, 119991 Russia

e-mail: shamray@ultra.imet.ac.ru

Received August 5, 2004

Abstract—The magnetic susceptibility $\chi(T)$ at 4.2 K < T < 293 K; the dependence of the magnetic moment on the magnetic field strength, $M(H)$, at 4.2, 77, and 293 K; and the electrical resistivity $\rho(T)$ at 4.2 K < T < 293 K are studied for samples of perovskite-phase $KTaO_3$ obtained by both solid-phase synthesis ($KTaO_3^s$) and deposition on a cathode during electrolysis of melts ($KTaO_3^e$). Yellowish white $KTaO_3^s$ powders are diamagnetic and reveal dielectric properties. Dark polycrystalline $KTaO_3^e$ samples with metallic luster are characterized by the dependence $\rho(T)$ typical of metals and additional paramagnetic contribution to the paramagnetic susceptibility as compared with $KTaO_3^e$. Changes in the properties of $KTaO_3$ during electrocrystallization are attributed to partial reduction of tantalum. They are revealed in the structural features of $KTaO_3^e$ (excess of tantalum as compared to the stoichiometric composition of $KTaO_3^e$, deficiency of the oxygen sublattice, and clearly pronounced anharmonicity of atomic vibrations). A change of the cation–anion–cation interactions, occurring owing to the overlapping of oxygen p orbitals with tantalum t_{2g} orbitals and the formation of impurity levels near the conduction band, leads to the generation of free carriers, which make a paramagnetic contribution to the magnetic susceptibility. © *2005 Pleiades Publishing, Inc.*

INTRODUCTION

It was reported previously that the properties of complex tantalum and niobium oxides obtained by deposition on a cathode during electrolysis of melts differ significantly from those of their analogs produced by conventional synthesis [1, 2]. These crystals are nontransparent and have intense black color with metallic luster and semiconductor or metallic conductivity. Their physical properties and structural motif are similar to those of oxide bronzes formed by other transition metals.

Interest in oxide bronzes is mainly due to their metallic properties, which are uncommon for oxides [3, 4]. The crystal structures of bronzes are formed by $B(O, F)_6$ octahedra, where B are atoms of the transition metals W, V, Ti, Nb, and Ta. These octahedra are linked by shared vertices into frameworks of different types, within which atoms of alkali and alkaline earth metals (A atoms) are located. The transition metals in bronzes are in a reduced oxidation state, and their complete oxidation with retention of the structural type leads to the loss of the properties characteristic of bronzes. Thus, the $K_{0.5}W^{5.5+}O_3$ compound with perovskite structure is a bronze in its properties but the isostructural $K_{0.5}W^{6+}_{0.5}Ta^{5+}_{0.5}O_3$ compound does not belong to this group.

The perovskite-like structure ABO_3, to which $KTaO_3$ also belongs, is one of the most widely spread types among oxide bronzes, which are being intensively studied in view of the need for new ferroelectric materials [5]. The perovskite structure can be regarded as a framework formed by BO_6 octahedra with shared vertices. Cavities between cotahedra are occupied by A atoms in the cubooctahedral environment of oxygen atoms. It is assumed in some studies considering the ferroelectrical properties of bronzes with perovskite structure that B cations can occupy positions displaced from the center of the oxygen octahedron [5, 6]. Thus, there is a nonequivalence of B–O bonds, which results in the occurrence of permanent pseudodipoles.

The $KTaO_3$ compound is a dielectric retaining its cubic structure up to liquid-helium temperatures. Distinguishing features of the $KTaO_3$ crystal structure obtained by electrocrystallization on a cathode are as follows: K cations are partially replaced by Ta–Ta dumbbells, the anharmonicity of vibrations of Ta atoms is more clearly pronounced, and there is a deficiency of the oxygen sublattice [7]. The structural for-

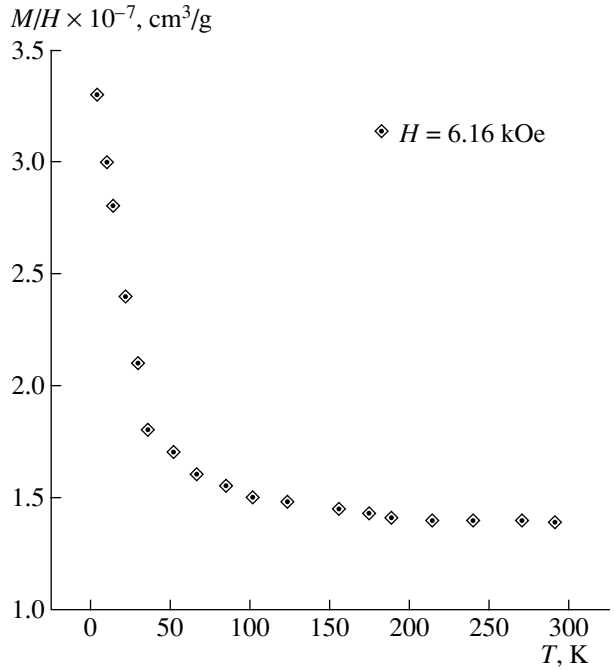

Fig. 1. Temperature dependence of the magnetic susceptibility of the $KTaO_3^e$ sample.

mula, reflecting these specific features, can be written as $KTa_{1+z}O_3$, where $z \simeq 0.11$.

In this work, we compared the magnetic properties of polycrystalline samples of the perovskite phase of $KTaO_3$ obtained by electrolysis from melts with polycrystalline $KTaO_3$ samples obtained by solid-phase synthesis.

EXPERIMENTAL

Dark polycrystalline $KTaO_3$ samples with metallic luster were obtained by electrolysis using the ternary eutectic LiF–NaF–KF as a solvent and K_2TaF_7 or K_2TaOF_5 as tantalum-containing components. Electrolysis was carried out at temperatures 900 K < T < 1200 K with the cathode current density J_c in the range from 0.1 to 0.3 A/cm^2. The electrolysis product on the cathode, apart from the main component $KTaO_3$ (hereafter, $KTaO_3^e$), contained inclusions of α Ta and the tetragonal phase of $K_{0.4}TaO_{2.4}F_{0.6}$.

Transparent yellowish white polycrystalline samples of the stoichiometric compound $KTaO_3$ (hereafter, $KTaO_3^s$) were obtained by solid-phase synthesis with repeated sintering in the temperature range 800 K < T < 1100 K.

The presence of ferromagnetic impurities (Fe, Co, Ni) in the samples was checked by the atomic-emission method with induction plasma. No impurities were found accurate to 0.002 wt %.

X-ray diffraction analysis was performed on a URD6 diffractometer (CuK_α radiation, scan in the range 15° < 2θ < 100°, an exposure time at each point of 10 s). $K_{0.4}TaO_{2.4}F_{0.6}$ and α-Ta were present in the $KTaO_3^e$ sample as the main impurities. The $KTaO_3^s$ sample contained an impurity phase of $K_{0.4}TaO_3$. The total content of impurity phases did not exceed 10% in both cases. The $KTaO_3$ phase was identified using the SIMREF program [8]; the atomic parameters from [7] were not refined. The Bragg reliability factor R_B was 9.6 and 6.4% for $KTaO_3^e$ and $KTaO_3^s$, respectively, and the corresponding lattice periods were 3.992 and 3.987 Å.

The magnetic properties were measured in the range 4.2 K < T < 293 K by the Faraday method on a magnetic balance with a sensitivity of 0.03 dyn in magnetic fields up to 6.25 kOe. During the measurements, the temperature was measured with an accuracy of 1 K.

The electrical resistivity ρ of pressed samples 8 mm long was measured in the temperature range 4.2 K < T < 293 K by the four-probe method. The distance between the voltage probes was ~5 mm. The current–voltage characteristics of the samples were linear within experimental error as the measured current density changed by two orders of magnitude (from 0.5 to 50 A/cm^2).

RESULTS

The dependence χ(T) for $KTaO_3^e$ samples at temperatures decreasing from room to liquid-helium temperature is characteristic of paramagnets (Fig. 1). The dependence of the magnetic moment on the magnetic field strength, $M(H)$, significantly differs from linear at liquid-helium temperature, as well as at liquid-nitrogen and room temperatures (Fig. 2). The magnetic properties of the $KTaO_3^s$ compound are typical of diamagnets (Figs. 3, 4). The magnetic susceptibility χ of the $KTaO_3^s$ sample is negative and almost constant in the temperature range 77 K < T < 273 K (Fig. 3). At these temperatures, the diamagnetic signal increases almost linearly with an increase in the magnetic field H (Fig. 4b). The magnetic susceptibility increases abruptly with a decrease in temperature in the range 4.2 K < T < 77 K for both $KTaO_3^s$ and $KTaO_3^e$ samples. (Figs. 1, 3). At the same time, the character of the dependence $M(H)$ at liquid-helium temperature is significantly different for these two samples (Figs. 2a, 4a).

The unusually sharp dependence χ(T) in the range 4.2 K < T < 20 K observed for $KTaO_3^s$ (Fig. 3) is characteristic of ferromagnetic impurities present in the

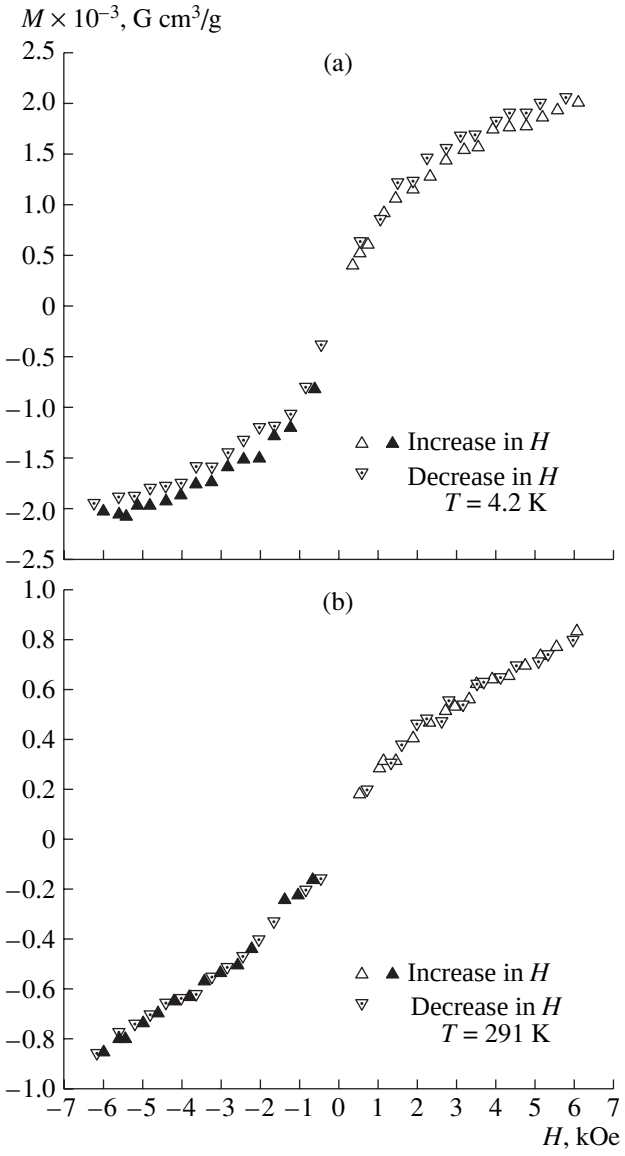

Fig. 2. Dependences of the magnetic moment on the magnetic field strength, $M(H)$, for the $KTaO_3^e$ sample at T = (a) 4.2 and (b) 291 K.

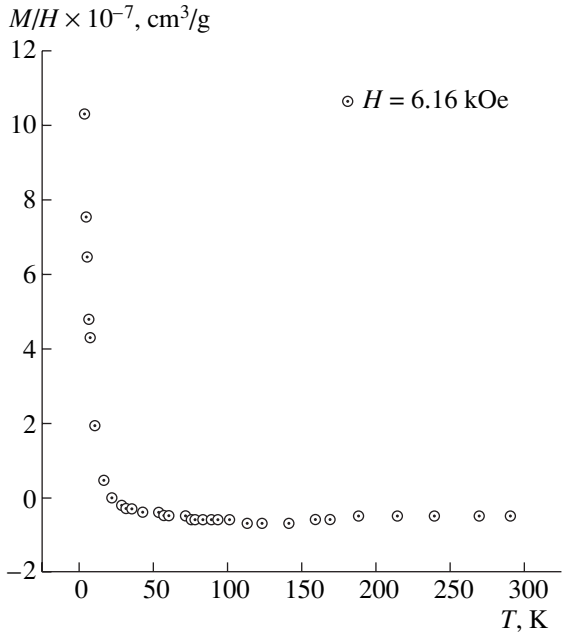

Fig. 3. Temperature dependence of the magnetic susceptibility of the $KTaO_3^s$ sample.

material. In this context, the dependence $M(H)$ for the $KTaO_3^s$ compound (Fig. 4a) was approximated by the Brillouin equation on the assumption that the paramagnetic contribution caused by the presence of iron impurity is nonzero:

$$M = NnJg\beta\left[\frac{2J+1}{2J}\coth\left(\frac{[2J+1]x}{2J}\right) - \frac{1}{2J}\coth\left(\frac{x}{2J}\right)\right]; \quad (1)$$

$$x = \frac{gJ\beta H}{k_B T},$$

where N is Avogadro's number, n is the parameter determining the number of magnetic moments, J is the cation magnetic moment, g is the Lande factor, β is the Bohr magneton, and k_B is the Boltzmann constant.

The calculations were performed for the Fe^{3+} and Fe^{2+} ions. (Their electronic configurations are $^6S_{3/2}$ and $^5D_4$, respectively.) The obtained values of n are 0.00117 and 0.00109, respectively. Recalculation to the atomic concentration yields ~0.02 at %, which greatly exceeds the sensitivity of chemical analysis showing no iron impurities.

Approximation of the dependence $M(H)$, which was obtained by measuring the magnetic moment of the $KTaO_3^e$ sample at 4.2 K (Fig. 2a), by the Langevin equation,

$$M = Nnm\beta\left[\coth\left(\frac{mH\beta}{k_B T}\right) - \frac{k_B T}{mH\beta}\right], \quad (2)$$

where N, n, and β are the same parameters as in (1) and m is the magnetic moment, gives $n = 2 \times 10^{-6}$ and m = 55. This result suggests a possibility of forming rather large clusters with localized magnetic moments $m \cong 50\ \mu_B$.

The temperature dependence of the electrical resistivity for the $KTaO_3^e$ samples has a clearly pronounced metallic character (Fig. 5). At the same time, it is noteworthy that the resistivity is high: evaluation of its value at liquid-helium temperature gives $\rho \simeq 0.28\ \Omega$ cm; i.e.,

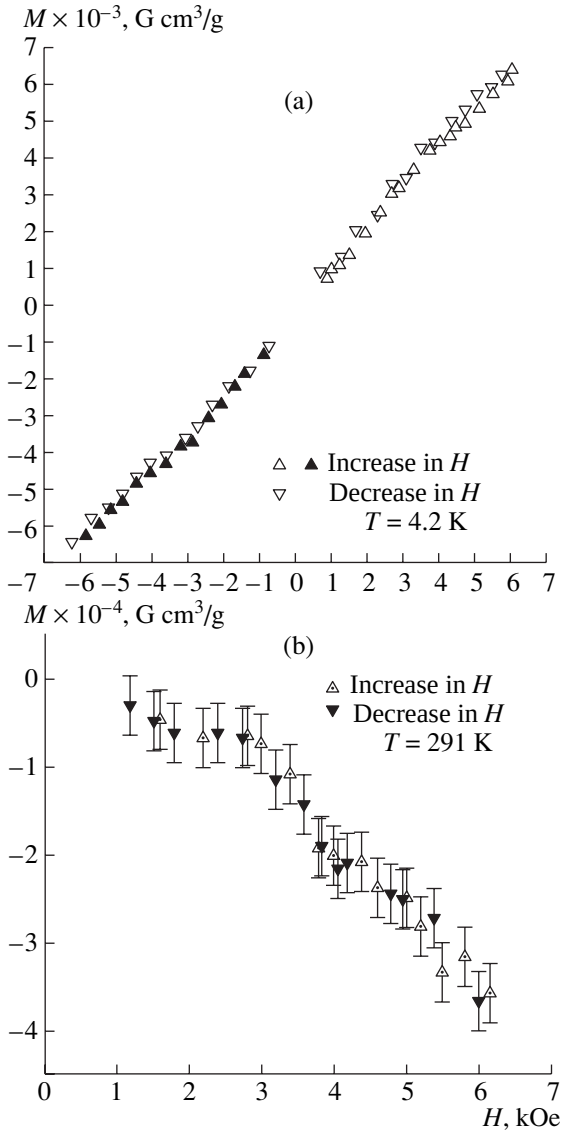

Fig. 4. Dependences of the magnetic moment on the magnetic field strength, $M(H)$, for the $KTaO_3^s$ sample at T = (a) 4.2 and (b) 291 K.

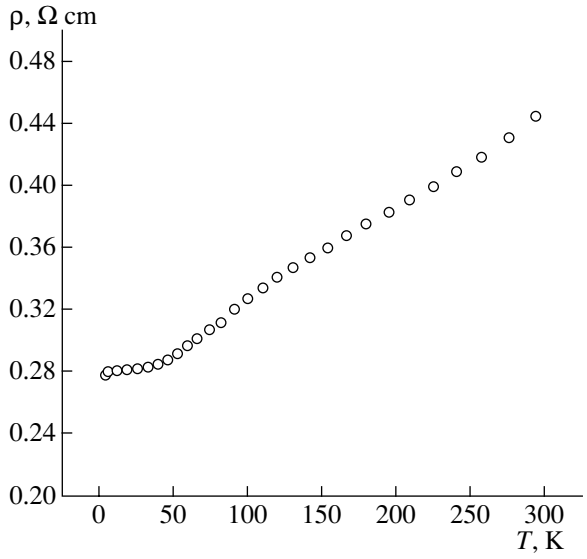

Fig. 5. Temperature dependence of the resistivity of the $KTaO_{3-\rho}^e$ sample.

the electrical conductivity $\sigma \simeq 3.6\ \Omega^{-1}\,\text{cm}^{-1}$. The $KTaO_3^s$ samples revealed dielectric properties.

DISCUSSION

The main difference between the $KTaO_3^e$ crystals obtained by electrolysis of melts and conventional $KTaO_3^s$ crystals is in the existence of electrical conductivity and additional paramagnetic contribution to the susceptibility of $KTaO_3^e$ samples. Evidently, this difference is primarily related to the degree of oxidation of tantalum and the defects in the structure of the perovskite phase of $KTaO_3^e$.

According to the data of [7], the central potassium atom in many unit cells in the $KTaO_3^e$ lattice is replaced by Ta–Ta dumbbells with extremely short distances d_{Ta-Ta} = 2.72 Å. The presence of Ta–Ta dumbbells with short distances is a characteristic feature of crystal structures of tantalum-containing oxides crystallized by electrolysis of melts on the cathode [9, 10]. These dumbbells are statistically distributed over the $KTaO_3^e$ lattice. Moreover, the oxygen sublattice in $KTaO_3^e$ is deficient (the occupation number of the (1/2, 0, 0) position p = 0.95) and the anharmonicity of vibrations of Ta atoms located at the unit cell vertices is much more pronounced than in $KTaO_3^s$ [7, 11]. The question of distribution of vacancies in the oxygen sublattice and Ta–Ta dumbbells remains open. In the first approximation, two situations are possible: either oxygen vacancies are distributed randomly or their distribution is correlated with Ta–Ta dumbbells. In the case of the correlated distribution, it can be suggested that there are some unit cells whose positions are occupied by only Ta atoms (Fig. 6). With due regard to the structure refinement carried out in [7], the formula of such a compound can be written as $K_{1-x}Ta_zO_{3(1-x)}$, where $x = z/2$ and $z \simeq 0.11$. Evidently, these specific features of the crystal structure may significantly noticeably affect the cation–anion–cation interactions in the lattice; the band structure; and, correspondingly, the magnetic properties and the electrical conductivity of $KTaO_3^e$.

The kinetic and magnetic properties of transition metal oxides with perovskite structure are often considered assuming that the cation–anion–cation interactions via oxygen ions are the decisive factor for these compounds. In undistorted cubic perovskites, such as $KTaO_3$, where the angle of the *B*–O–*B* bond is 180°C, the overlapping of e_g orbitals of *B* cations with oxygen *p* orbitals and the oxygen *p* orbitals with t_{2g} orbitals of *B* cations with the formation of σ and π bonds, respectively, is energetically favorable. Oxygen *p* orbitals forming π bonds with t_{2g} orbitals of *B* cations are p_σ orbitals with respect to *A* cations. Thus, *A*–O σ bonds compete with *B*–O π bonds.

In $KTaO_3^e$, the *B* cation is tantalum, whose outer electronic configuration does not contain e_g electrons, and the *A* component is an alkali metal. Therefore, the main cation–anion–cation interactions are realized in the *B*–O–*B* chain via π bonds. According to [12], the cation–anion–cation interactions between cations via $t_{2g}^3 e_g^0$ electronsare considered to be weak and the behavior of such electrons is described in the close-coupling approximation. The Fermi level in the band structure of $KTaO_3$ is located between the occupied bonding π band and the antibonding π* band; as a consequence, electronic conductivity and the Pauli contribution to the magnetic susceptibility are absent in this compound.

As one would expect, the conventional $KTaO_3^s$ samples are diamagnetic insulators. A specific feature of their magnetic behavior is the abrupt increase in the magnetic susceptibility with a decrease in temperature in the liquid-helium temperature range, a phenomenon which indicates the presence of paramagnetic centers. According to the above evaluations, this contribution to the magnetic susceptibility cannot be attributed to iron impurities. It is most likely that this contribution is related to paramagnetic centers formed at the lattice defects. Vacancies in the oxygen or potassium sublattices, as well as extended defects, such as dislocations and stacking faults, may serve as such centers in polycrystalline $KTaO_3^s$. Similar dependences $\chi(T)$, controlled by the paramagnetic contribution of lattice defects, obtained previously by measuring magnetic susceptibility of ZnO crystals, were discussed in [13].

As noted above, the $KTaO_3^e$ crystals have both an oxygen deficit relative to the ABO_3 stoichiometry (deficiency of the 1/2,0,0 positions) and an excess of tantalum, whose atoms form dumbbells replacing potassium and are randomly distributed over the structure. It is well known that Ta^{3+} cations located near oxygen vacancies in the perovskite structure can form impurity levels near the conduction band [14]. Small distances between Ta atoms belonging to dumbbells and Ta atoms located in the (000) positions, whose length is close to the shortest Ta–Ta distances in bcc tantalum, $d_{Ta–Ta} = 2.86$ Å, indicate a possibility of strong interactions of dumbbells with the main lattice, which weaken the main cation–anion–cation *B*–O–*B* interactions. This means that for $KTaO_3^e$, along with the formation of impurity levels, one would expect diffusion of the π band and a change in its occupancy. This should result in the generation of free carriers and, hence, occurrence of electrical conductivity and the Pauli contribution to the magnetic susceptibility.

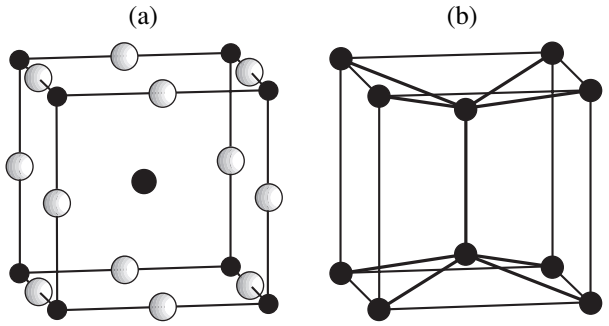

Fig. 6. (a) Unit cell of $KTaO_3$. (b) Model of a tantalum cluster formed at the replacement of K atoms with Ta–Ta dumbbells and oxygen elimination.

The measurements of the magnetic properties of the $KTaO_3^e$ samples indicate the existence of rather extensive regions of cluster type, which are characterized by a large magnetic moment (~50 μ_B) and, apparently, an excess electron concentration. The occurrence of these regions may be related to the existence of regions depleted and enriched with oxygen, a condition which seems to be highly probable in the case of the formation of cells centered by Ta–Ta dumbbells and free of oxygen (Fig. 6). This phenomenon is related to the reduction processes at the cathode during the $KTaO_3^e$ crystallization, which result in different degrees of oxidation of tantalum. It is likely that tantalum atoms are completely reduced in randomly isolated clusters (Fig. 6). This assumption is confirmed by the fact that each such cluster is similar to the unit cell of bcc α-tantalum. The difference is in the splitting of the central position in the *bcc* unit cell, which is caused by the retention of interatomic Ta–Ta distances (2.86 Å) from both positions of the center to the cell vertices when the cell edge increases (3.30 Å in α Ta and 3.98 Å in a cluster). The behavior of the electrical conductivity becomes clear within this concept.

Apparently, the presence of vacancies in the oxygen sublattice of $KTaO_3^e$ violates the symmetry of the crystal field in the TaO_6 octahedra, thus leading to the nonequivalence of Ta–O bonds within the octahedron. This is confirmed by large values of the components of the thermal vibration tensor, which determine the anhar-

monicity of thermal vibrations. (The values of $F112233 \times 10^6$ and $F111122 \times 10^6$ for tantalum and oxygen are –0.0002, –0.0003 and 0.0005, 0.0003, respectively.) Since the anharmonicity of thermal vibrations in perovskites is often considered in the context of their ferroelectrical properties [15], it seems reasonable to study them in the $KTaO_3^e$ samples.

In conclusion, it should be noted that there are difficulties in evaluation of the contributions to the magnetic susceptibility of the materials studied, which are related not only to the ambiguity of their separation (evaluation of the diamagnetic contribution χ_{dia} and the Van Vleck contribution χ_{vv}). The measurements were carried out on polycrystalline samples. Therefore, the state of the substructure of a material, second phase inclusions, and other factors may affect the results. Nevertheless, the results obtained here allow us to attribute the occurrence of electrical conductivity in $KTaO_3^e$ and the larger values of its magnetic susceptibility as compared to $KTaO_3^s$, synthesized by conventional methods, to the generation of free carriers due to the partial reduction of tantalum at the cathode.

ACKNOWLEDGMENTS

We are grateful to A.V. Mitin for measuring the properties of the samples.

This study was supported by the Russian Foundation for Basic Research (project no. 02-03-32982).

REFERENCES

1. A. V. Arakcheeva, G. Chapuis, V. V. Grinevich, and V. F. Shamraĭ, Kristallografiya **49** (1), 75 (2004) [Crystallogr. Rep. **49** (1), 70 (2004)].
2. A. V. Arakcheeva, V. V. Grinevich, G. Chapuis, and V. F. Shamraĭ, Kristallografiya **47** (2), 272 (2002) [Crystallogr. Rep. **47** (2), 237 (2002)].
3. *Oxide Bronzes*, Ed. by V. I. Spitsyn (Nauka, Moscow, 1982) [in Russian].
4. A. Wells, *Structural Inorganic Chemistry* (Clarendon Press, Oxford, 1984; Mir, Moscow, 1987).
5. E. G. Fesenko, *Perovskite Family and Ferroelectricity* (Atomizdat, Moscow, 1972) [in Russian].
6. W. P. Mason and B. T. Matthias, Phys. Rev. **74**, 1622 (1948).
7. A. V. Arakcheeva, G. Chapui, V. Grinevitch, *et al.*, Acta Crystallogr. B **57**, 157 (2001).
8. H. Ritler, G. Thringer, G. K. Maichle, and W. Randl, SIMREF 2.5 (Inst. für Kristallogr. Univ. Tubingen, 1998).
9. A. V. Arakcheeva, V. V. Grinevich, A. V. Mitin, *et al.*, Kristallografiya **46** (2), 221 (2001) [Crystallogr. Rep. **46** (2), 182 (2001)].
10. V. F. Shamraĭ, J. K. Warhulska, A. V. Arakcheeva, and V. V. Grinevich, Kristallografiya **49** (6), 1025 (2004) [Crystallogr. Rep. **49** (6), 930 (2004)].
11. E. A. Zhurova, V. E. Zavodnik, and V. G. Tsirel'son, Kristallografiya **40** (5), 18 (1995) [Crystallogr. Rep. **40** (5), 14 (1995)].
12. J. B. Goodenough, *Magnetism and Chemical Bond* (Interscience, New York, 1963; Metallurgiya, Moscow, 1968).
13. Yu. V. Shaldin and J. K. Warhulska, Neorg. Mater. **39** (10), 1218 (2003).
14. D. M. Hannon, Phys. Rev. **164** (1), 164 (1967).
15. J. H. Barret, Phys. Rev. **86**, 118 (1952).

Translated by T. Dmitrieva

Crystallography Reports, Vol. 50, No. 5, 2005, pp. 785–788. Translated from Kristallografiya, Vol. 50, No. 5, 2005, pp. 846–849.

STRUCTURE OF ORGANIC COMPOUNDS

Crystal Structure of Calcium Bis(Nitrilotriacetato)di(μ-hydroxo)dichromate(III) Hexahydrate, $Ca[(Nta)Cr(\mu\text{-}OH)_2Cr(Nta)] \cdot 6H_2O$

I. N. Polyakova*, A. L. Poznyak, and V. S. Sergienko***

** Kurnakov Institute of General and Inorganic Chemistry, Russian Academy of Sciences, Leninskiĭ pr. 31, Moscow, 119991 Russia*

e-mail: sokol@igic.ras.ru

*** Institute of Molecular and Atomic Physics, National Academy of Sciences of Belarus, pr. Franziska Skaryny 70, Minsk, 220072 Belarus*

Received January 10, 2005

Abstract—The compound $Ca[(Nta)Cr(\mu\text{-}OH)_2Cr(Nta)] \cdot 6H_2O$ is synthesized, and its X-ray structure analysis is performed [$R_1 = 0.0285$, $wR_2 = 0.0766$ for 4330 reflections with $I > 2\sigma(I)$]. The crystals are built of centrosymmetric dimeric anionic complexes $\{[Cr(Nta)(\mu\text{-}OH)]_2\}^{2-}$, cationic $[Ca(H_2O)_3]^{2+}$ fragments, and crystallization water molecules, which are linked into a three-dimensional framework. Two independent anionic complexes have similar structures but differ in the mode of binding with Ca atoms, water molecules, and adjacent anions. Distorted octahedral environments of the Cr atoms are formed by four atoms (N + 3O) of the Nta^{3-} tetradentate chelate ligand and two oxygen atoms of the bridging OH^- ligands. The Cr–O–Cr bridges have symmetric structures [Cr–O, 1.944–1.961(2) Å]. The Ca environment includes seven oxygen atoms of three water molecules and four anionic complexes [Ca–O, 2.397–2.430(3) Å]. © *2005 Pleiades Publishing, Inc.*

INTRODUCTION

As a part of our systematic structural investigations of transition metal complexes with aminopolycarboxylicic acids, a compound of Cr(III) with nitrilotriacetic acid (H_3Nta), $Ca[Cr_2(OH)_2(Nta)_2] \cdot 6H_2O$ (**I**), was synthesized and its crystal structure was determined by X-ray diffraction.

The first Cr(III) complexes with H_3Nta and related ligands were obtained almost forty years ago on the rise of interest in complexonates [1–4]. In the first study [1], it was found that the ammonium salt of the chromium complex with *Nta* (presumably, having the $[Cr(Nta)(OH)(H_2O)_2]^-$ composition) is isolated in the form of dark violet and green crystals, whose aqueous solutions are characterized by identical absorption spectra. As far as we know, this fact has not been explained to date. In a subsequent ^2H NMR study of a similar deuterated solution, the composition and structure of the complex were corrected [5]. It was established that bridging OH groups link Cr*Nta* complexes into $[(Nta)Cr(\mu\text{-}OH)_2Cr(Nta)]^{2-}$ dimers. The dimeric structure of the anionic complex in the crystal state was confirmed recently by the examples of the tetragonal (**II**) and monoclinic (**III**) modifications of the cesium salt $Cs_2[Cr_2(OH)_2(Nta)_2] \cdot 4H_2O$ [6] and the potassium salt $K_2[Cr_2(OH)_2(Nta)_2] \cdot 6H_2O$ (**IV**) [7]. Crystals **II**–**IV** refer to the dark violet form. This study shows that black crystals **I** obtained by us are also related to the dark violet form.

EXPERIMENTAL

Synthesis

An aqueous solution containing equivalent amounts of $CrCl_3 \cdot 6H_2O$ and H_3Nta was neutralized with an excess of calcium carbonate upon prolonged heating on a boiling water bath. The hot solution was filtered off and allowed to stand in a Dewar vessel for crystallization. Black prismatic crystals **I** precipitated during slow cooling.

X-ray Diffraction Study

Crystals **I** ($C_{12}H_{26}CaCr_2N_2O_{20}$) are triclinic; a = 9.699(3) Å, b = 10.562(3) Å, c = 13.064(4) Å, α = 88.66(3)°, β = 75.17(3)°, γ = 64.26(2)°, V = 1159.4(6) Å^3, Z = 2, M = 662.43, ρ_{calcd} = 1.898 g/cm^3, μ = 1.258 mm^{-1}, $F(000)$ = 680, and space group $P\bar{1}$.

The experimental data were obtained at room temperature on an Enraf–Nonius CAD4 diffractometer from a single crystal 0.24 × 0.30 × 0.36 mm in size (λMoK_α, graphite monochromator, θ_{max} = 28°, ω scan mode). A total of 5833 reflections were collected, of which 5532 were unique reflections (R_{int} = 0.0123) used

Table 1. Selected bond lengths *d* (Å) and angles ω (deg) in structure **I**

Bond	*d*	Bond	*d*
Cr(1)–O(13)	1.9462(16)	Ca(1)–O(2*w*)	2.419(2)
Cr(1)–O(13)^{i}	1.9612(18)	Ca(1)–O(2)	2.4203(19)
Cr(1)–O(3)	1.9845(17)	Ca(1)–O(10)^{iv}	2.4299(19)
Cr(1)–O(5)	1.9853(18)	O(1)–C(2)	1.279(3)
Cr(1)–O(1)	1.9875(16)	O(2)–C(2)	1.235(3)
Cr(1)–N(1)	2.0623(18)	O(3)–C(4)	1.278(3)
Cr(2)–O(14)	1.9443(18)	O(4)–C(4)	1.229(3)
Cr(2)–O(14)^{ii}	1.9509(19)	O(5)–C(6)	1.274(3)
Cr(2)–O(7)	1.9622(16)	O(6)–C(6)	1.239(3)
Cr(2)–O(11)	1.992(2)	O(7)–C(8)	1.283(3)
Cr(2)–O(9)	2.0165(19)	O(8)–C(8)	1.230(3)
Cr(2)–N(2)	2.0667(19)	O(9)–C(10)	1.279(3)
Ca(1)–O(4)^{iii}	2.397(2)	O(10)–C(10)	1.241(3)
Ca(1)–O(1*w*)	2.407(2)	O(11)–C(12)	1.295(3)
Ca(1)–O(3*w*)	2.408(3)	O(12)–C(12)	1.226(3)
Ca(1)–O(8)	2.4126(18)		
Angle	ω	Angle	ω
O(13)–Cr(1)–O(13)^{i}	82.61(7)	O(14)–Cr(2)–O(14)^{ii}	78.73(8)
O(13)–Cr(1)–O(3)	98.03(7)	O(14)–Cr(2)–O(7)	95.97(7)
O(13)^{i}–Cr(1)–O(3)	88.91(8)	O(14)^{ii}–Cr(2)–O(7)	174.55(7)
O(13)–Cr(1)–O(5)	95.91(7)	O(14)–Cr(2)–O(11)	97.01(8)
O(13)^{i}–Cr(1)–O(5)	178.15(7)	O(14)^{ii}–Cr(2)–O(11)	91.52(9)
O(3)–Cr(1)–O(5)	90.18(8)	O(7)–Cr(2)–O(11)	90.38(8)
O(13)–Cr(1)–O(1)	98.30(7)	O(14)–Cr(2)–O(9)	101.63(8)
O(13)^{i}–Cr(1)–O(1)	91.72(8)	O(14)^{ii}–Cr(2)–O(9)	91.54(8)
O(3)–Cr(1)–O(1)	163.61(7)	O(7)–Cr(2)–O(9)	88.27(8)
O(5)–Cr(1)–O(1)	89.60(8)	O(11)–Cr(2)–O(9)	161.35(7)
O(13)–Cr(1)–N(1)	179.75(7)	O(14)–Cr(2)–N(2)	177.55(8)
O(13)*–Cr(1)–N(1)	97.16(7)	O(14)^{ii}–Cr(2)–N(2)	100.59(7)
O(3)–Cr(1)–N(1)	82.07(7)	O(7)–Cr(2)–N(2)	84.76(7)
O(5)–Cr(1)–N(1)	84.32(7)	O(11)–Cr(2)–N(2)	80.64(8)
O(1)–Cr(1)–N(1)	81.59(7)	O(9)–Cr(2)–N(2)	80.71(7)

Symmetry transformations: (i) –*x*, –*y* + 1, –*z* + 2; (ii) –*x* – 2, –*y* + 2, –*z* + 1; (iii) *x* – 1, *y* + 1, *z*; (iv) *x* + 1, *y*, *z*.

in the calculations. The data were corrected for absorption by the azimuthal-scan method [8].

The structure was solved by the direct method (SHELXS97 [9]). The hydrogen atoms were located from difference Fourier maps. The structure was refined by the least-squares procedure on F^2 in the approximation of anisotropic thermal vibrations of the non-hydrogen atoms and isotropic vibrations of the hydrogen atoms (SHELXL97 [9]). The H atoms of the *w*(5) and *w*(6) water molecules were refined within a riding model with $U_{iso} = 1.2U_{eq}$ for the O(5*w*) and O(6*w*) atoms. The refinement converged to the following estimates: $R_1 = 0.0285$ and $wR_2 = 0.0766$ for 4330 reflections with $I > 2\sigma(I)$; $R_1 = 0.0477$ and $wR_2 = 0.0842$ for all the unique reflections; *GOOF* = 1.054; $\Delta\rho_{min}/\Delta\rho_{max} = -0.612/0.754$ e/Å^3.

The selected bond lengths and angles are listed in Table 1. A fragment of structure **I** is shown in the figure.

The crystal data for compound **I** have been deposited with the Cambridge Structural Database (CCDC no. 260719).

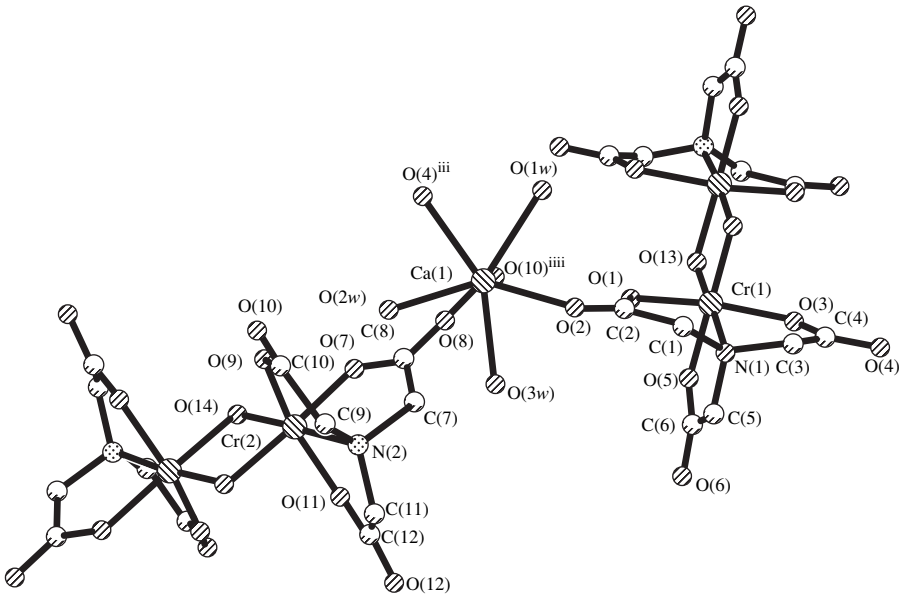

Fragment of structure **I**.

RESULTS AND DISCUSSION

Crystal **I** is built of $\{[Cr(Nta)(\mu\text{-}OH)]_2\}^{2-}$ centrosymmetric dimeric anionic complexes, $[Ca(H_2O)_3]^{2+}$ cationic fragments, and crystallization water molecules. The unit cell contains two independent anionic complexes, which have similar structures and close geometric parameters but differ in the mode of binding with Ca atoms. The coordination polyhedra of the Cr(1) and Cr(2) atoms in complexes *A* and *B*, respectively, are distorted octahedra with four atoms (N + 3O) of the Nta^{3-} tetradentate chelate ligand and two oxygen atoms of the bridging hydroxo ligands at the vertices. The Cr–N bond lengths in complexes *A* and *B* are almost identical [1.962(2), 1.967(2) Å]. The lengths of three Cr–O(*Nta*) bonds are identical in complex *A* [1.985–1.988(2) Å] but differ significantly in complex *B* [1.962–2.017(2) Å]. In both complexes, the lengths of the bridging Cr–O bonds have close values [1.944–1.961(2) Å] and the Cr–O–Cr bridges have symmetric structures. The central planar four-membered Cr_2O_2 rings in the two complexes somewhat differ in shape. Compared to complex *A*, the ring in complex *B* is elongated along the Cr···Cr axis [3.012, 2.935(1) Å] and contracted along the O···O axis [2.471(3), 2.579(2) Å], which is reflected also in the endocyclic CrOCr and OCrO angles [97.39(7)° and 82.61(7)° in *A*; 101.27(8)° and 78.73(8)° in *B*]. One of the glycine cycles closed by the Nta^{3-} ligand is substantially flattened and approximately coplanar to the central fragment. The mean atomic deviations (Δ_{av}) from the planes of the Cr(1)N(1)C(5)C(6)O(5) and Cr(2)N(2)C(7)C(8)O(7) rings are 0.003 and 0.029 Å and the dihedral angles formed with the corresponding Cr_2O_2 planes are 1.1° and 3.8°, respectively. Two other glycine cycles are corrugated to an identical degree (Δ_{av} = 0.148–0.157 Å), and their mean planes are approximately perpendicular to the planes of the central fragments.

In the previously studied compounds **II**–**IV** with alkali metal cations, the structure of the $\{[Cr(Nta)(\mu\text{-}OH)]_2\}^{2-}$ anionic complex is the same as in **I**. The anionic complex can exist in two isomer forms with the *cis* or *trans* position of the N atoms relative to the Cr···Cr axis. In compounds**I**–**IV**, the *trans* isomers are formed. In an analogous cobalt(III) compound, $Cs_2[Co(Nta)(\mu\text{-}OH)]_2 \cdot 4H_2O$ [10], the anionic complex has a similar structure. The closeness of the geometric parameters of the $\{[Cr(Nta)(\mu\text{-}OH]_2\}^{2-}$ anionic complex in different compounds is quite natural, and the observed differences apparently result from the interaction of the anion with the outer sphere, that is, cations, water molecules, and ligands of the neighboring complexes. Each of compounds **I**–**IV** is characterized by its own model of these interactions. In compound **I**, the environment of Ca^{2+} cations includes two carbonyl O atoms of each Nta^{3-} ligand. In complex *A*, these are the O(2) and O(4) atoms of the two glycine groups located perpendicular to the central fragment. In complex *B*, these are the O(10) and O(8) atoms of the glycine groups, of which one is perpendicular and the other is coplanar to the central fragment.

Six independent water molecules and two hydroxide ions in the unit cell of crystal **I** form an extended hydrogen bond system (Table 2). The hydroxo groups form strong linear O(13)–H(13)···O(4*w*) and O(14)–H(14)···O(6) hydrogen bonds. Complexes*A* and *B* are involved in the hydrogen bonds as proton acceptors to a different degree. Of six oxygen atoms of the Nta^{3-} ligand, three and five atoms participate in hydrogen

Table 2. Characteristics of the hydrogen bonds in structure **I**

X–H···*Y* bond	Symmetry transformation for atom *Y*	Distance, Å		*XHY* angle, deg
		H···*Y*	*X*···*Y*	
O(13)–H(13)···O(4*w*)	*x*, *y*, *z*	1.93(3)	2.635(3)	178(4)
O(14)–H(14)···O(6)	*x* – 1, *y* + 1, *z*	2.14(4)	2.767(3)	179(5)
O(1*w*)–H(1*w*1)···O(10)	–*x* – 2, –*y* + 2, –*z* + 2	2.42(5)	3.144(3)	165(5)
O(1*w*)–H(2*w*1)···O(3)	–*x*, –*y* + 1, –*z* + 2	2.18(5)	2.959(3)	170(4)
O(2*w*)–H(1*w*2)···O(5*w*)	*x* – 1, *y* + 1, *z*	2.04(4)	2.831(4)	160(4)
O(2*w*)–H(2*w*2)···O(7)	*x*, *y*, *z*	2.51(4)	2.930(3)	118(4)
O(2*w*)–H(2*w*2)···O(6*w*)	–*x*, –*y* + 1, –*z* + 1	2.55(4)	3.154(6)	142(4)
O(3*w*)–H(1*w*3)···O(12)	–*x* – 1, –*y* + 1, –*z* + 1	1.95(4)	2.761(3)	174(4)
O(3*w*)–H(2*w*3)···O(6*w*)	–*x*, –*y* + 1, –*z* + 1	1.97(3)	2.697(5)	175(3)
O(4*w*)–H(1*w*4)···O(5*w*)	*x*, *y*, *z*	1.91(3)	2.738(4)	172(3)
O(4*w*)–H(2*w*4)···O(2)	*x* + 1, *y*, *z*	2.21(5)	2.832(3)	145(5)
O(5*w*)–H(1*w*5)*···O(9)	*x* + 2, *y* – 1, *z*	1.94	2.999(4)	148
O(5*w*)–H(1*w*5)*···O(10)	*x* + 2, *y* – 1, *z*	2.05	3.011(4)	136
O(5*w*)–H(2*w*5)*···O(11)	–*x*, –*y* + 1, –*z* + 1	1.80	2.806(3)	174
O(6*w*)–H(1*w*6)*···O(6)	*x*, *y*, *z*	1.78	2.840(5)	166

Note: The asterisked H atoms were refined within the riding model.

bonding in complexes *A* and *B*, respectively. The carbonyl O(6) and O(12) atoms, which are not bound to the Ca^{2+} cation, serve as acceptors of two and one hydrogen bonds, respectively.

The Ca^{2+} environment is formed by seven oxygen atoms belonging to three water molecules [O(1*w*), O(2*w*), O(3*w*)] and four Nta^{3-} ligands [O(2), O(4), O(8), O(10)], two atoms of complexes *A* and *B* each. The $\{[Cr(Nta)(\mu\text{-}OH)]_2\}^{2-}$ anionic complexes and hydrated Ca^{2+} cations form a three-dimensional framework. Hydrogen bonds involving water molecules additionally stabilize the framework.

ACKNOWLEDGMENTS

We are grateful to the Russian Foundation for Basic Research for the support in the payment of the license for using the Cambridge Structural Database, project no. 02-07-90322.

REFERENCES

1. A. Uehara, E. Kyuno, and R. Tsuchiya, Bull. Chem. Soc. Jpn. **40** (10), 2317 (1967).
2. A. Uehara, E. Kyuno, and R. Tsuchiya, Bull. Chem. Soc. Jpn. **40** (10), 2322 (1967).
3. A. Uehara, E. Kyuno, and R. Tsuchiya, Bull. Chem. Soc. Jpn. **41** (10), 2385 (1968).
4. M. G. Voronkov and S. V. Mikhaĭlova, Khim. Geterotsikl. Soedin., No. 9, 1174 (1972).
5. N. Koine, R. J. Bianchini, and J. I. Legg, Inorg. Chem. **25** (16), 2835 (1986).
6. H. G. Visser, W. Purcell, and S. S. Basson, Polyhedron **18** (21), 2795 (1999).
7. J.-H. Choi, T. Suzuki, and S. Kaizaki, Acta Crystallogr., Sect. E **59** (9), 812 (2003).
8. A. C. T. North, D. C. Phillips, and F. S. Mathews, Acta Crystallogr., Sect. A: Cryst. Phys., Diffr., Theor. Gen. Crystallogr. **24** (3), 351 (1968).
9. G. M. Sheldrick, *SHELXS97 and SHELXL97: Program for the Solution and Refinement of Crystal Structures* (Univ. of Göottingen, Göottingen, 1997).
10. H. G. Visser, W. Purcell, S. S. Basson, and Q. Claassen, Polyhedron **15** (22), 2851 (1996).

Translated by I. Polyakova

Crystallography Reports, Vol. 50, No. 5, 2005, pp. 789–795. Translated from Kristallografiya, Vol. 50, No. 5, 2005, pp. 850–856.

STRUCTURE OF MACROMOLECULAR COMPOUNDS

Deuterated Hen Egg-White Lysozyme Crystals: Optimization of the Growth Conditions and Morphology

A. V. Svanidze*, S. G. Lushnikov*, and L. A. Shuvalov†**

** Ioffe Physicotechnical Institute, Russian Academy of Sciences, Politekhnicheskaya ul. 26, St. Petersburg, 194021 Russia*

e-mail: svanidze@mail.ioffe.ru

*** Shubnikov Institute of Crystallography, Russian Academy of Sciences, Leninskiĭ pr. 59, Moscow, 119333 Russia*

Received October 27, 2004

Abstract—Deuterated and protonated tetragonal lysozyme crystals are grown using the hanging-drop vapor-diffusion method. The size of the lysozyme crystals grown is determined as a function of the concentration of sodium chloride used as a precipitant. It is found that crystallization leads to the formation of lysozyme crystals with three different habits. Morphological and X-ray diffraction analyses of the deuterated and protonated lysozyme crystals demonstrate that, despite the different habits, all the crystals grown belong to the tetragonal crystal system. The simple forms of lysozyme crystals are revealed. It is shown that the habits of the lysozyme crystals are determined by the specific combinations of simple forms. The mechanisms responsible for the formation of lysozyme crystals with different habits are discussed. © *2005 Pleiades Publishing, Inc.*

INTRODUCTION

Since the mid-1950s, the structure of protein molecules has been investigated using X-ray diffraction methods [1], as just this structure that may offer a clue to the understanding of the protein functions. The possibility of preparing proteins in the crystalline form has been widely used for performing X-ray diffraction analysis. Hen egg-white lysozyme is one of the proteins whose crystals can be grown in the simplest way. That is the reason why lysozyme crystals have served as convenient model objects for studying both the crystallization of macromolecules and the physical properties of proteins.

The influence of different factors on the growth of lysozyme crystals has been thoroughly investigated over the last thirty years (see [2] and references therein). It has been demonstrated that the temperature, the pH, and the ionic strength of the solution used for growing crystals, as well as the concentrations of the protein and the precipitant in the crystallization solution, are the controlling factors in crystallization of lysozyme [3]. A change in the acidity of the crystallization solution leads to a variation in the charge of the protein molecule due to the protonation or deprotonation of amino acid residues in a polypeptide chain of the lysozyme molecule. This brings about a change in the intermolecular interaction forces and, consequently, affects the product of protein crystallization [4]. Moreover, magnetic and electric fields can also exert an effect on the protein crystallization; in particular, strong magnetic fields with a strength of approximately 10 T are favorable for the growth of high-quality large-sized lysozyme crystals [5–7]. There exist other factors (such as the earth gravity, ultrasonic wave fields, etc.) that also affect the growth of protein crystals and, therefore, must be taken into account in the preparation of special-purity large-sized protein crystals.

A large number of works concerned with the study of lysozyme crystallization have dealt with analyzing the conditions of crystal growth from solutions prepared with ordinary water. However, the question as to how the isotopic exchange of hydrogen with deuterium affects the growth and physical properties of lysozyme crystals remains an open question. The purpose of this work was to prepare deuterated crystals of hen egg-white lysozyme and to analyze the crystallization conditions.

SAMPLE PREPARATION AND EXPERIMENTAL TECHNIQUE

Deuterated crystals of lysozyme (Fluka, United States) were grown using the hanging-drop vapor-diffusion method at a temperature of 18°C. The crystallization solution (pH 4.6) was prepared with heavy water (D_2O) and contained the protein (20 mg/ml), sodium acetate (0.1 M; Ékros, Russia), and sodium azide (0.01 M; Fluka, United States). Sodium chloride (Ékros, Russia) was used as a precipitant. The sodium chloride concentration in the crystallization solution was varied from 2 to 4%. The counter solution (pH 4.6), which was also prepared with heavy water, contained sodium acetate (0.1 M) and sodium azide (0.01 M). The

† Deceased.

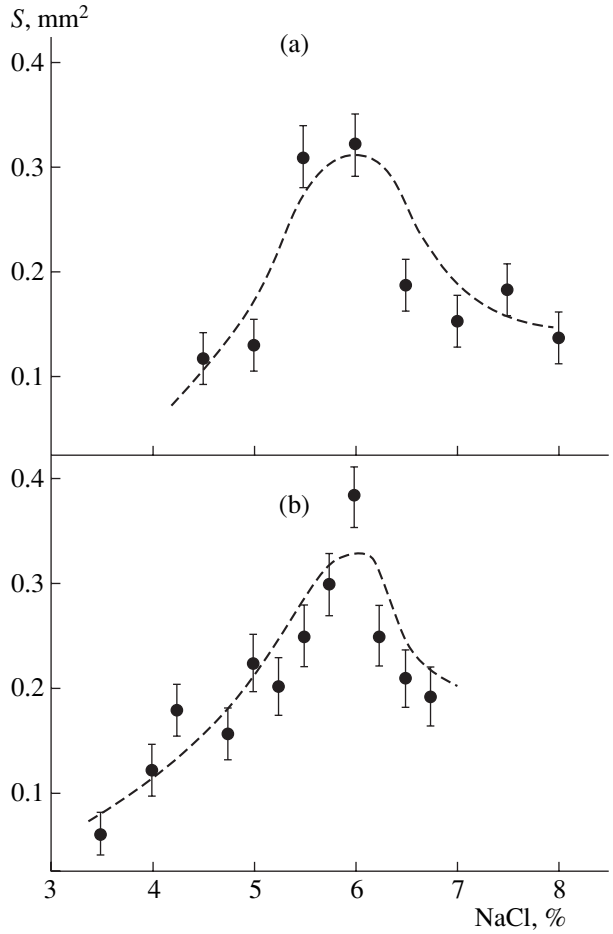

Fig. 1. Dependences of the size of (a) deuterated and (b) protonated tetragonal lysozyme crystals (grown by the hanging-drop vapor-diffusion method) on the sodium chloride concentration. The crystals were grown in a 0.1 M CH_3CO_2Na solution containing the protein (20 mg/ml) at pH 4.6. Designation: S (mm^2) is the surface area visible under a microscope for the largest crystal.

sodium chloride concentration in the counter solution was twice as high as that in the crystallization solution.

A similar procedure was used to grow lysozyme crystals from solutions prepared with ordinary water. The growth temperature was equal to 10°C. The crystallization solution (pH 4.6) contained the protein (20 mg/ml), sodium acetate (0.1 M), and sodium azide (0.01 M). The sodium chloride concentration in the crystallization solution was varied from 0.5 to 3.5%. The counter solution (pH 4.6) contained sodium acetate (0.1 M), sodium azide (0.01 M), and sodium chloride whose concentration was twice as high as that in the crystallization solution. The aforementioned crystallization conditions were chosen from analyzing the data available in the literature. It was assumed that these conditions are optimum for growing lysozyme crystals.

The deuterated and protonated lysozyme crystals were subjected to morphological analysis. The angles between the crystal faces and the crystal sizes were determined using an MP-3 polarizing microscope. In what follows, the crystals grown from the solutions prepared with ordinary water and those grown from the solutions prepared with heavy water (D_2O) will be referred to as the protonated and deuterated crystals, respectively.

The crystal structure was determined by X-ray diffraction analysis on a MAR 345 diffractometer (Shubnikov Institute of Crystallography, Russian Academy of Sciences, Moscow, Russia) at a wavelength λ = 1.5417 Å. It was established that the protonated and deuterated lysozyme crystals belong to space group $P4_32_12$. The unit cell parameters are as follows: $a = b$ = 79.535 Å and c = 38.118 Å for the protonated crystals and $a = b$ = 79.551 Å and c = 38.017 Å for the deuterated crystals. The degree of deuteration of the lysozyme crystals grown from the solutions prepared with heavy water was not determined.

EXPERIMENTAL RESULTS AND DISCUSSION

Dependences of the Size and Amount of Deuterated Lysozyme Crystals on the Precipitant Concentration

The preparation of deuterated analogs of the lysozyme crystals and the investigation into their properties involve an analysis of the influence of different factors on the growth of lysozyme crystals from solutions prepared with heavy water (D_2O). We assumed that the isotopic exchange of hydrogen with deuterium should not lead to substantial changes in the growth conditions, except for a decrease in the solubility of lysozyme [8]. Therefore, the optimum conditions for growing deuterated lysozyme crystals can be chosen from analyzing the data available in the literature on the growth of protonated lysozyme crystals.

During growth of deuterated lysozyme crystals, we varied only one parameter, namely, the concentration of the precipitant (sodium chloride) in the crystallization solution. The other growth conditions described in the preceding section were not varied under the assumption that they are optimum for growing tetragonal lysozyme crystals. As a result, we obtained the dependences of the size of deuterated crystals on the precipitant concentration (Fig. 1a). A similar procedure was used to determine the dependence of the size of protonated crystals on the precipitant concentration (Fig. 1b). As is clearly seen from Fig. 1, the dependences of the sizes of deuterated and protonated lysozyme crystals on the concentration of sodium chloride in the crystallization solution are similar to each other and exhibit a maximum. At a low precipitant concentration, the crystallization leads to the formation of small-sized lysozyme crystals due to the low supersaturation of the solution. An increase in the salt concentration brings about the formation of relatively large-sized lysozyme crystals of good quality. The sizes of these crystals reach a maximum at a sodium chloride concentration of 6% (Fig. 1).

This made it possible to obtain deuterated tetragonal lysozyme crystals whose sizes (i.e., distances between the opposite {110} faces) could be as large as 0.62 ± 0.01 mm. It should be noted that an excess content of the precipitant exerts an adverse effect on the crystallization due to the formation of a great number of small-sized crystals and the appearance of crystalline aggregates and twins.

The results of the experiments performed in this work demonstrate that the conditions used for growing lysozyme crystals from the solutions prepared with heavy and ordinary water differ from each other only slightly. However, the sizes of the deuterated lysozyme crystals, on the average, are smaller than those of the lysozyme crystals grown from the solutions prepared with ordinary water. Most probably, this can be associated with the changes in both the strength of intermolecular hydrogen bonds and the permittivity of the solution in the case when the crystals are grown from the solutions prepared with heavy water.

The influence of quite different factors on the nucleation of protein crystals in the crystallization solution and on their subsequent growth considerably complicates the precise reproducibility of the results obtained. Changes in the temperature, the protein and salt concentrations, and the pH of the solutions from experiment to experiment lead to variations in the growth conditions. Consequently, the experimental dependence of the surface area of the lysozyme crystals on the precipitant concentration $S(C_{NaCl})$ (Fig. 1) can vary significantly; however, the general trend of this dependence remains unaltered.

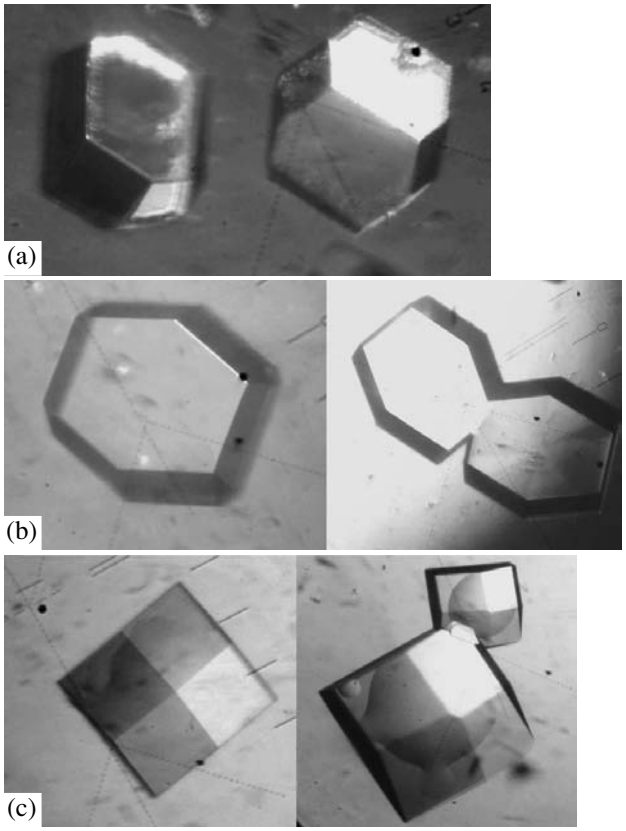

Fig. 2. Micrographs of (a) bulk, (b) platelike, and (c) pyramidal deuterated lysozyme crystals (Carl Zeiss NU 2F microscope).

Morphology of Tetragonal Lysozyme Crystals

In the course of optimizing the growth conditions of lysozyme crystals, it was found that crystals with different habits can be grown under the same initial conditions. Moreover, it is possible to distinguish three repetitive habits of lysozyme crystals, which radically differ from each other. These habits are represented by "bulk" crystals (Fig. 2a); "platelike" crystals (Fig. 2b), which are well known from previous investigations; and "pyramidal" crystals (Fig. 2c). Since crystals with these three habits have rather often formed in our experiments, it can be assumed that we are dealing here with regularities of the lysozyme crystal growth. Reasoning from the data available in the literature, we can argue that the given conditions (see the section Sample Preparation and Experimental Technique) provide the growth of tetragonal lysozyme crystals. However, the natural question arises as to whether crystals with different habits have the same symmetry, or, to put it differently, whether lysozyme crystals with all the three habits belong to the tetragonal crystal system.

The study of any crystal primarily involves X-ray diffraction and (or) morphological analyses. In the early stage of crystallography, morphological analysis was an efficient tool for determining the crystal symmetry. However, this approach lost its initial significance due to the development of X-ray diffraction analysis. The determination of the symmetry from the habit of a protein crystal is extremely important because this method permits one to avoid destruction of the sample in the course of X-ray diffraction measurements. In our case, we used the potentialities of the classical crystallography for analyzing the crystal structure and then refined the results with the use of X-ray diffraction analysis.

The experiments performed in this work revealed that the crystallization leads to the formation of deuterated (and protonated) lysozyme crystals characterized by three different habits. The micrographs of the crystals and the schematic drawings of the structures, including all the crystal faces and all the angles between the edges, are given for each habit in Figs. 2 and 3. Since the crystal habit corresponds to a particular crystal structure, the morphological analysis enables us to judge the symmetry of the lysozyme crystals. It is clearly seen from Fig. 3 that the lysozyme crystals belong to the tetragonal crystal system, because the projection of each of the three crystal structures onto the *ab* plane is a tetragon and the angles between the corresponding crystal edges for all the three habits are equal to each other.

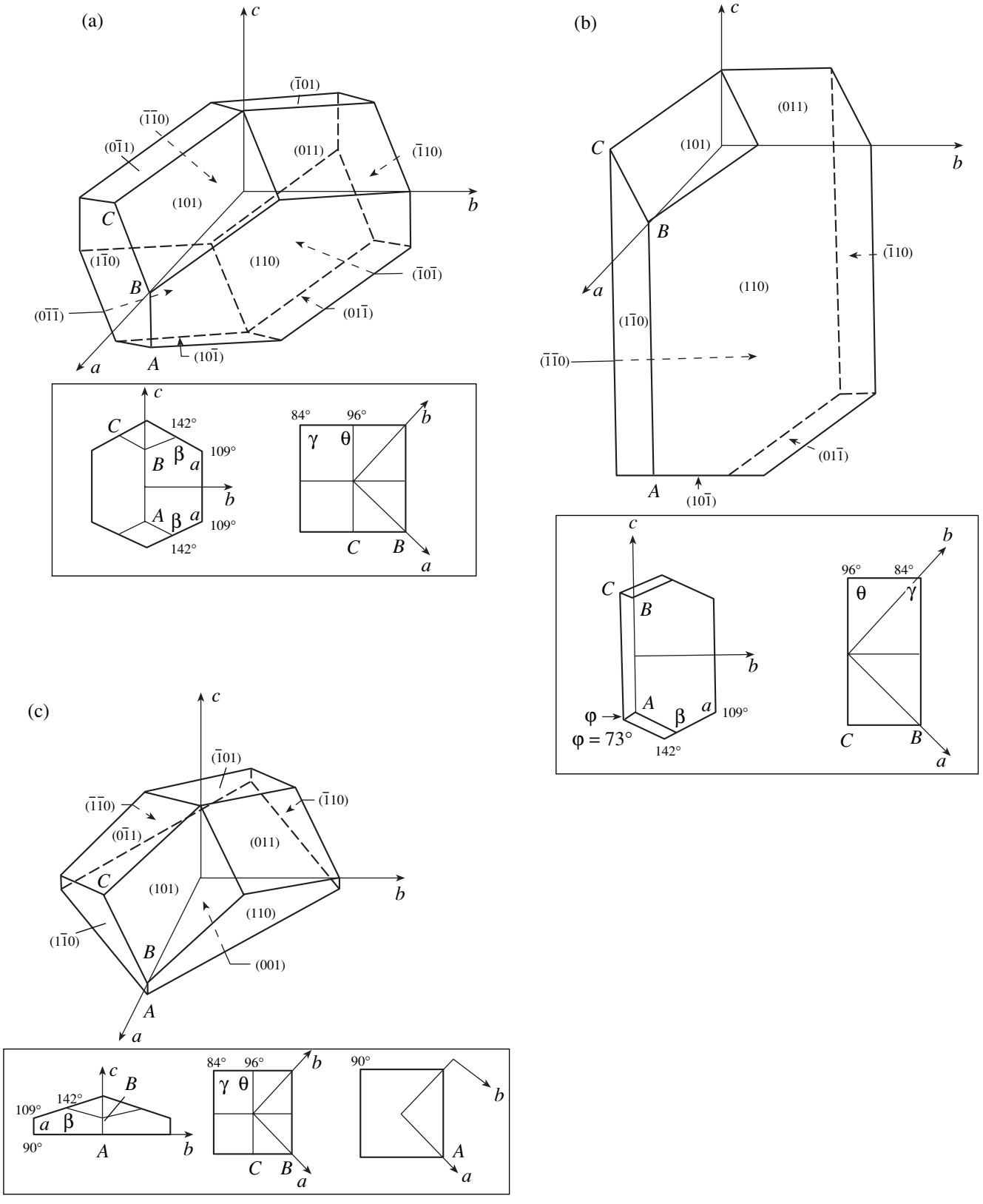

Fig. 3. Habits of (a) bulk, (b) platelike, and (c) pyramidal deuterated lysozyme crystals. The insets show (a–c) the projections of the crystal structure onto the *bc* (at the left) and *ab* planes and (c) the bottom view of the projection of the crystal structure onto the *ab* plane (at the right).

The analysis of the habit of the deuterated lysozyme crystals demonstrated that the faces of these crystals belong to three simple forms, namely, a tetragonal prism, a tetragonal bipyramid, and a tetragonal pyramid. Examination of the crystal habits revealed that, for deuterated lysozyme crystals, the first habit, i.e., bulk crystals (Figs. 2a, 3a), can be represented as a convex polyhedron formed by a combination of two simple forms, such as a tetragonal prism and a tetragonal bipyramid. The intersection of these simple forms determines the general view of the polyhedron corresponding to this habit (Fig. 4a). The second habit, i.e., platelike crystals (Figs. 2b, 3b), can be described as a polyhedron formed by a combination of the same simple forms as the first habit, but, in this case, the tetragonal bipyramid is truncated along the diagonal (Fig. 4b). The third habit, i.e., pyramidal crystals (Figs. 2c, 3c), is a polyhedron formed by a combination of the tetragonal prism and the tetragonal pyramid (Fig. 4c). It is worth noting that all three habits can transform into each other through the truncation of particular faces with a change in the linear dimensions of the simple forms in the combination.

The formation of lysozyme crystals with three different habits is associated with the manifestation of particular faces on the crystal surface. In turn, the appearance of a specific face on the crystal surface depends on its growth rate: the crystal surface has faces with the lowest growth rates [9]. Therefore, the lysozyme crystals grown under different conditions can have different habits. The opposite statement also holds true: different crystal habits suggest different conditions of the crystal growth.

The possible mechanisms of the growth of different tetragonal lysozyme crystal faces were considered in detail in [10, 11]. There are no grounds to believe that the mechanisms responsible for the growth of the lysozyme crystals, which are formed from solutions prepared with heavy water, and those for the growth of conventional lysozyme crystals studied in [10, 11] can substantially differ from each other. The maximum growth rates of the {110} and {101} faces correspond to different protein concentrations in the crystallization solution [10, 11]. This is associated with the different growth mechanisms of these faces. The (110) face is formed through the sequential attachment of octamers consisting of eight lysozyme molecules, whereas the (101) face grows via the attachment of tetramers. At higher protein concentrations, there arise conditions favorable for the growth of the (110) face. However, during crystallization, the protein concentration in a drop of the crystallization solution progressively decreases because the lysozyme molecules are adsorbed on the surface of growing crystals. This leads to the predominant formation of tetramers in the solution and, hence, to an increase in the growth rate of the {101} face. Therefore, at different protein concentrations in the crystallization solution, there arise conditions favorable for the growth of different faces and responsible for the formation of lysozyme crystals with three different habits in the same drop.

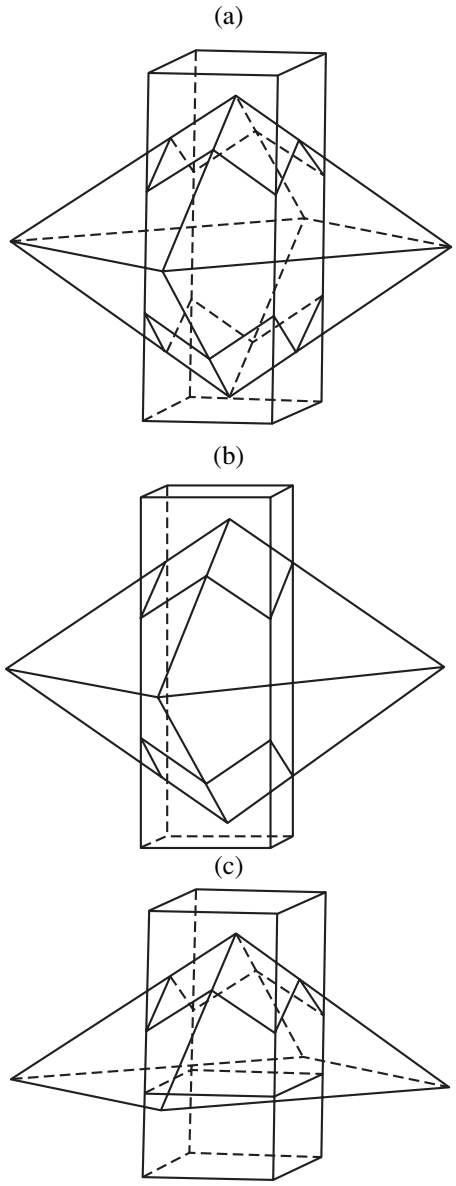

Fig. 4. Schematic diagram illustrating the formation of combinations of the following simple forms: (a) a tetragonal prism and a tetragonal bipyramid, (b) a tetragonal prism and a tetragonal bipyramid truncated along the diagonal, and (c) a tetragonal prism and a tetragonal pyramid.

The X-ray diffraction data indicate that all deuterated lysozyme crystals with three different habits have space group $P4_32_12$ and are characterized by the unit cell parameters $a = b = 79.551$ Å and $c = 38.017$ Å.

On the Problem of Structural Phase Transitions in Lysozyme Crystals

In the mid-1970s, there appeared publications [12, 13] which argued that orthorhombic lysozyme

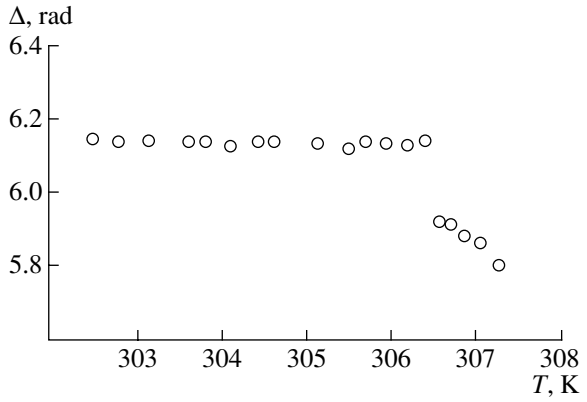

Fig. 5. Temperature dependence of the index of birefringence for the lysozyme crystal [15].

crystals (space group $P2_12_12_1$) grown at a temperature of 313 K undergo a phase transition. It was shown that, upon cooling of orthorhombic lysozyme crystals, their symmetry at a temperature of 298 K becomes tetragonal with space group $P4_32_12$. At present, these papers have been cited in discussions of the physical properties of lysozyme crystals and the possible structural transformations in them.

However, more recently, Kobayashi *et al.* [14] investigated optical properties (such as the optical activity and birefringence) of tetragonal lysozyme crystals and determined the gyration tensor components for these crystals. In [14], the authors obtained a temperature dependence of the phase difference Δ between two elliptically polarized components into which a linearly polarized wave incident on a plane-parallel crystal plate is decomposed. For these components, the normal to the crystal plate coincides with the wave normal. The phase difference between these two waves after they have traveled a distance d in the crystal is given by the relationship $\Delta = (2\pi/\lambda) * \Delta n * d$, where Δn is the difference between the refractive indices for the elliptically polarized components. With knowledge of the phase difference Δ, it is possible to judge the birefringence of the lysozyme crystal. The dependence obtained in [14] is plotted in Fig. 5. It can be seen from this figure that the phase difference Δ exhibits a steplike anomaly at a temperature of 306.5 K. In [14], this feature was explained by the denaturation of the sample. However, the anomaly observed in the aforementioned temperature dependence most likely indicates a first-order structural transition.

Although the above results are obviously inconsistent with each other, their analysis leads us to the inference that the structural phase transition actually occurs in tetragonal lysozyme crystals at a temperature of 306.5 K. The observed contradiction calls for further investigation into the physical properties and structure of lysozyme crystals at temperatures close to the hypothetical phase transition.

CONCLUSIONS

Thus, we elucidated the influence of the growth conditions of lysozyme crystals on their sizes and analyzed the morphology of deuterated crystals of hen egg-white lysozyme.

The main conclusions drawn in this study can be summarized as follows:

(i) The growth of tetragonal lysozyme crystals from solutions prepared with heavy and ordinary water obeys the same regularities.

(ii) During growth of lysozyme crystals through the hanging-drop vapor diffusion, the crystallization conditions change in such a way that the crystals grown exhibit three different habits corresponding to tetragonal symmetry.

(iii) Each of the three crystal habits is determined by a specific combination of the simplest forms.

The performed analysis of the data available in the literature revealed a number of contradictions regarding the problem of the structural phase transition in lysozyme crystals. The inference was made that lysozyme crystals undergo a first-order structural phase transition at a temperature of 306.5 K.

ACKNOWLEDGMENTS

We would like to thank I.P. Kuranova and N.I. Sosfenov for their assistance in performing this study.

This work was supported by the Russian Foundation for Basic Research (project no. 02-02-17330), the Council on Grants from the President of the Russian Federation within the State Program in Support of Leading Scientific Schools (project nos. NSh-1415.2003.2, NSh-2168.2003.2), and the Physical Science Division of the Russian Academy of Sciences.

REFERENCES

1. *Modern Crystallography*, Vol. 2: *Structure of Crystals*, Ed. by B. K. Vainshtein, V. M. Fridkin, and V. L. Indenbom (Nauka, Moscow, 1979; Springer, Berlin, 1982).
2. *Protein Structure, Stability, and Folding*, Ed. by P. Murphy (Humana, Totowa, NJ, 2001), p. 261.
3. E. Cacioppo and M. L. Pusey, J. Cryst. Growth **114**, 286 (1991).
4. J. K. Baird, S. C. Scott, and Yeong Woo Kim, J. Cryst. Growth **232**, 50 (2001).
5. C. N. Nanev and A. Penkova, J. Cryst. Growth **232**, 285 (2001).
6. G. Sazaki, E. Yoshida, H. Komatsu, *et al.*, J. Cryst. Growth **173**, 231 (1997).
7. D. C. Yin, Y. Oda, N. I. Wakayama, and M. Ataka, J. Cryst. Growth **252**, 618 (2003).

8. M. Budayova-Spano, F. Dauvergne, and D. Myles, in *Proceedings of the Fourteenth International Conference on Crystal Growth in Conjunction with the Twelfth International Conference on Vapor Growth and Epitaxy, Grenoble, France, 2004* (Grenoble, 2004), p. 343.
9. *Modern Crystallography*, Vol. 1: *Fundamentals of Crystals: Symmetry and Methods of Structural Crystallography*, Ed. by B. K. Vainshtein, 2nd ed. (Nauka, Moscow, 1979; Springer, Berlin, 1994).
10. A. Nadarajah and M. L. Pusey, Acta Crystallogr., Sect. D: Biol. Crystallogr. **52**, 983 (1996).
11. A. Nadarajah, M. Li, and M. L. Pusey, Acta Crystallogr., Sect. D: Biol. Crystallogr. **53**, 524 (1997).
12. P. Jolles and J. Berthou, FEBS Lett. **23** (1), 21 (1972).
13. J. Berthou and P. Jolles, Biochim. Biophys. Acta **336**, 222 (1974).
14. J. Kobayashi, T. Asahi, M. Sakurai, *et al.*, Acta Crystallogr., Sect. A: Found. Crystallogr. **54**, 581 (1998).

Translated by O. Borovik-Romanova

Crystallography Reports, Vol. 50, No. 5, 2005, pp. 796–800. Translated from Kristallografiya, Vol. 50, No. 5, 2005, pp. 857–861.

STRUCTURE OF MACROMOLECULAR COMPOUNDS

Structure of a New Crystal Modification of the Bacterial NAD-Dependent Formate Dehydrogenase with a Resolution of 2.1 Å

E. V. Filippova*, K. M. Polyakov*, T. V. Tikhonova, T. N. Stekhanova**, K. M. Boĭko**, and V. O. Popov****

** Engelhardt Institute of Molecular Biology, Russian Academy of Sciences, ul. Vavilova 32, Moscow, 119991 Russia*

e-mail: kostya@eimb.relarn.ru

*** Bach Institute of Biochemistry, Russian Academy of Sciences, Leninskiĭ pr. 33, Moscow, 119071 Russia*

Received February 16, 2005

Abstract—Formate dehydrogenase (FDG) from methylotrophic bacteria *Pseudomonas sp.* 101 catalyzes the reaction of oxidation of the formate ion to carbon dioxide, which is accompanied by the reduction of nicotinamid adenine dinucleotide (NAD^+). The structures of the apo and holo (enzyme-NAD-azide triple complex) forms of the enzyme were determined earlier. In an attempt to prepare a complex of FDG with the product of the enzymatic reaction (NADH), a new crystal modification of FDG is obtained (space group $P4_22_12$, $a = b =$ 93.3 Å, $c =$ 103.05 Å). The FDG structure is solved by the molecular replacement method and refined to $R =$ 20.7%. The asymmetric part of the unit cell contains one FDG molecule. In contrast to the previously studied FDG structures, the biologically active dimer is formed by the crystallographic rotation axis. A comparative structural analysis of the studied form with the apo and holo forms of the enzyme is performed. The influence of the molecular structure on the environment in the crystal is investigated. © *2005 Pleiades Publishing, Inc.*

INTRODUCTION

Formate dehydrogenase (FDG) from methylotrophic bacteria *Pseudomonas sp.* 101 catalyzes the reaction of oxidation of the formate ion to carbon dioxide, which is accompanied by the reduction of NAD^+ to NADH. The NAD-dependent formate dehydrogenase belongs to the family of *D*-specific dehydrogenases of 2-hydroxy acids [1]. Enzymes of this family form the class of α/β proteins and have a similar structure of the peptide chain. By now, three-dimensional structures of the following representatives of this family have been determined: formate dehydrogenase [2], *D*-3-glycerophosphate dehydrogenase [3], *D*-glycerate dehydrogenase [4], *D*-lactate dehydrogenase and its complex with NADH [5, 6], and dehydrogenase of 2-hydroxyisocaproic acid [7]. For FDG from the *Pseudomonas sp.* 101 bacterium, the structures of the apo (native protein) and holo (FDG-NAD-azide triple complex) forms of the enzyme have been determined with resolutions of 1.8 and 2.05 Å, respectively [2]. The asymmetric parts of the unit cells of both structures contain similar dimers in which the protein subunits are related by the noncrystallographic twofold rotation axis. The FDG molecule consists of two domains, namely, the coenzyme-binding and catalytic domains. The structures of the apo and holo forms of FDG differ in the position of the catalytic domain. The apo form of FDG has an open conformation, whereas the holo form of FDG has a closed conformation [2]. In this paper, we report the structure of a new crystal modification of FDG from *Pseudomonas sp.* 101 with a resolution of 2.1 Å, which was determined in an attempt to obtain crystals of the FDG complex with the product of the enzymatic reaction NADH. The conformational changes in the molecule were analyzed, and the structure were compared with those of the apo and holo forms of the enzyme.

EXPERIMENTAL

Crystals were prepared by diffusion through a gaseous phase in hanging and sessile drops at a temperature of 16–17°C. A reservoir (1 ml) contained a solution of ammonium sulfate (48% saturated) and 2-methyl-2,4-pentanediol (MPD, 8 vol %) in a 0.1 M HEPES buffer (pH 7.3). Drops (10 μl) contained a protein solution (9.6 mg/ml), ammonium sulfate (24% saturated), 4% MPD, and NADH (2 mM) in a 0.1 M HEPES buffer (pH 7.3). The crystals belong to space group $P4_22_12$ with the unit cell parameters $a = b =$ 93.3 Å and $c =$ 103.05 Å. The diffraction data were obtained with a resolution of 2.1 Å at 20°C from one crystal with the use of a CCD detector installed on a DORIS XII storage ring of the DEZY synchrotron (Hamburg) at a wavelength of 1.009 Å. The data were processed with the DENZO and SCALEPACK program packages [8]. The

1063-7745/05/5005-0796$26.00 © 2005 Pleiades Publishing, Inc.

statistical characteristics of the diffraction data set are listed in Table 1.

The FDG structure was solved by the molecular replacement method with the MOLREP program package [9]. The structure of a subunit of the molecule of the apo form of the enzyme (the PDB code is 2NAC) served as the starting model. The molecular replacement based on the data at 3.5 Å resolution allowed us to obtain a model corresponding to $R = 34.8\%$ with a correlation coefficient of 0.682. The asymmetric part of the unit cell contains one protein molecule. The crystallographic refinement of the structure was performed with the REFMAC program package [10]. The O program [11] was used to exercise visual control over the refinement process, to introduce significant changes into the atomic model of the structure, and to localize water molecules. The statistical characteristics of the structural refinement and the atomic model are listed in Table 1. The NADH molecule was not found in the crystal structure of FDG.

Table 1. Diffraction data set, structural refinement, and atomic-model statistics (data for a layer with a resolution of 2.13–2.10 Å are given in parentheses)

Resolution, Å	69.01–2.10
Total number of reflections measured	115593
Number of unique reflections	29590
Recurrence	3.9
Completeness, %	94.3(91.3)
R_{merge}, %	7.8(49.5)
Temperature factor from the Wilson plot, Å^2	38.2
R factor, %	20.7
R_{free}, %	25.0
rms deviations of bond lengths, Å	0.020
rms deviations of bond angles, deg	1.881
Number of atoms in the protein molecule	2923
Number of sulfate ions	1
Number of water molecules	181
Average B factor, Å^2	32.6
Number of residues in the most favorable regions of the Ramachandran plot*	277
Number of residues in the allowed regions of the Ramachandran plot*	42
Number of residues outside the allowed regions of the Ramachandran plot*	1

* Except for the *Gly* and *Pro* residues.

RESULTS AND DISCUSSION

The schematic drawing of the polypeptide chain of the FDG molecule is given in Fig. 1. The polypeptide chain of the molecule has a globular two-domain structure. The first domain, which is responsible for the NAD^+ binding, is formed by residues 147–333, and the second domain, which determines the catalytic properties of the enzyme, is formed by the residues 1–147 and 333–374. Both domains in FDG have a similar structure [12] and consist of a parallel left-twisted β-sheet surrounded by α-helices. The coenzyme-binding domain has a β-sheet of seven parallel β-chains (192–198, 216–220, 236–238, 249–254, 278–281, 304–307, 326–330), which are linked together by α-helices (146–163, 200–214, 226–234, 258–262, 266–273, 289–300, 319–324). The catalytic domain has a β-sheet consisting of five parallel β-chains (1–7, 69–73, 91–95, 115–120, 138–140), which are surrounded by four α-helices (59–67, 81–87, 104–111, 128–136), and a disordered loop (9–59). The C-terminal part of this domain is formed by an α-helix (337–258) and a β-hairpin (367–369, 372–374).

The atomic model of FDG obtained in this study contains 374 amino acid residues. Twenty six C-terminal residues were not located from the electron density maps. A sulfate ion was found in the model in a region corresponding to the region of binding of the pyrophosphate part of the NAD molecule in the structure of the FDG holo form. Similarly, the sulfate ion is bound in the structure of the apo form. In the studied structure, as well as in the structures of the apo and holo forms of FDG, the Ala198 residue is located outside the allowed region on the Ramachandran plot. An exhaustive explanation of the unusual conformation of this residue was offered in [2].

In contrast to the structures of the apo and holo forms, the asymmetric part of the unit cell of the studied structure contains one enzyme molecule. Two protein molecules related by the diagonal rotation axis (symmetry operation: $y, x, -z$) form a biologically active dimer. The packing of FDG molecules in the unit cell is shown in Fig. 2. The FDG molecule has six nearest

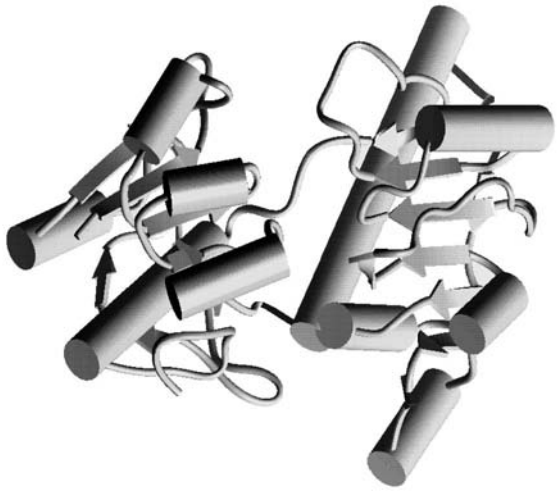

Fig. 1. Secondary structure of the FDG molecule.

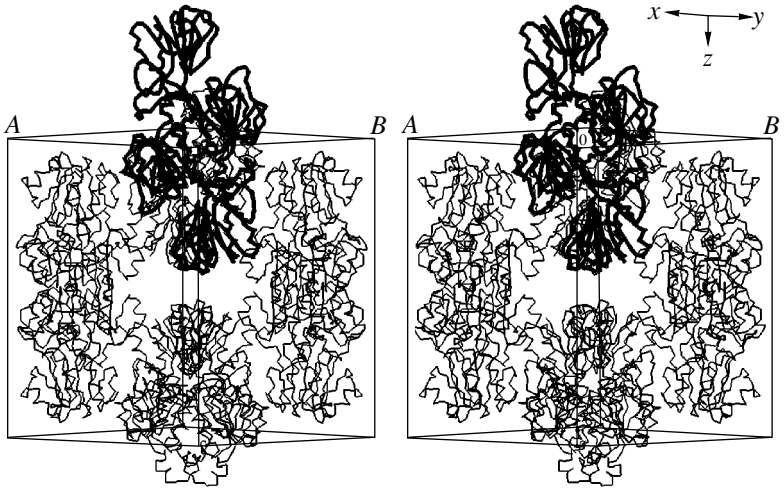

Fig. 2. Stereodiagram of the packing of FDG molecules in the unit cell.

neighbors. The areas of the contact zones between symmetry-related molecules are presented in Table 2. The contacts between the molecules within the dimer are substantially stronger than the other contacts. For this pair of molecules, the area of the contact surface is equal to 3891 Å^2 and the molecules in a dimer are linked by 27 hydrogen bonds. Similar dimer structures were found in the apo and holo forms of the enzyme [2], in which the dimers are formed between the molecules related by noncrystallographic twofold rotation axes. The interactions between the molecules in the dimer are predominantly due to the residues belonging to the coenzyme-binding domain (146–163, 165–175, 200–214, 319–324, 326–330).

The structure obtained was compared with the structures of the apo and holo forms of FDG with the use of the LSQCAB program package [13]. The root-mean-square (rms) deviations of the coordinates of all the Cα atoms in the studied structure from those in the molecules of the apo and holo forms of FDG are equal to 0.4 and 1.2 Å, respectively. A comparison of the individual domains of the studied molecule with the *A* and *B* subunits of the holo form of FDG showed that, for the Cα atoms, the root-mean-square deviation is equal to 0.6 Å. Thus, the studied structure has an open conformation and is similar to the structure of the apo form of the enzyme. The deviation of the positions of the corresponding Cα atoms in the studied structure upon the superposition with the *A* and *B* subunits of the apo form as a function of the residue number is plotted in Fig. 3 [the data for the C-terminal region of the molecule (residues 370–374) are omitted because the rms deviations of the corresponding Cα atoms exceed 10 Å]. The deviations larger than 0.7 Å were revealed in the following parts of the chain: 59–68, 76–87, 104–111, 128–134, 226–234, and 299–301. The differences between the structures can be explained as resulting from both the different environments in the crystal and the mobility of individual structural elements (large *B* factors). Note also that, similar to the structure of the apo form of FDG, in all these regions (except for 299–301) of the studied structure, the temperature factors have the largest values.

Analysis of the contacts and hydrogen bonds between the symmetrically equivalent molecules in this structure and the apo form of FDG was performed with

Table 2. Characteristics of the intermolecular contacts in the FDG structure

Symmetry operation	Translation	Area of the contact surface for molecules related by different symmetry operations, Å^2	Number of hydrogen bonds inside the contact zone
$-x + 1/2, y + 1/2, -z + 1/2$		299	5
$-x, -y, z$	$+a + b$	134	
$x + 1/2, -y + 1/2, -z + 1/2$	$-a$	188	1
$-x + 1/2, y + 1/2, -z + 1/2$	$-b$	315	5
$x + 1/2, -y + 1/2, -z + 1/2$		195	1
$y, x, -z$		3891	27

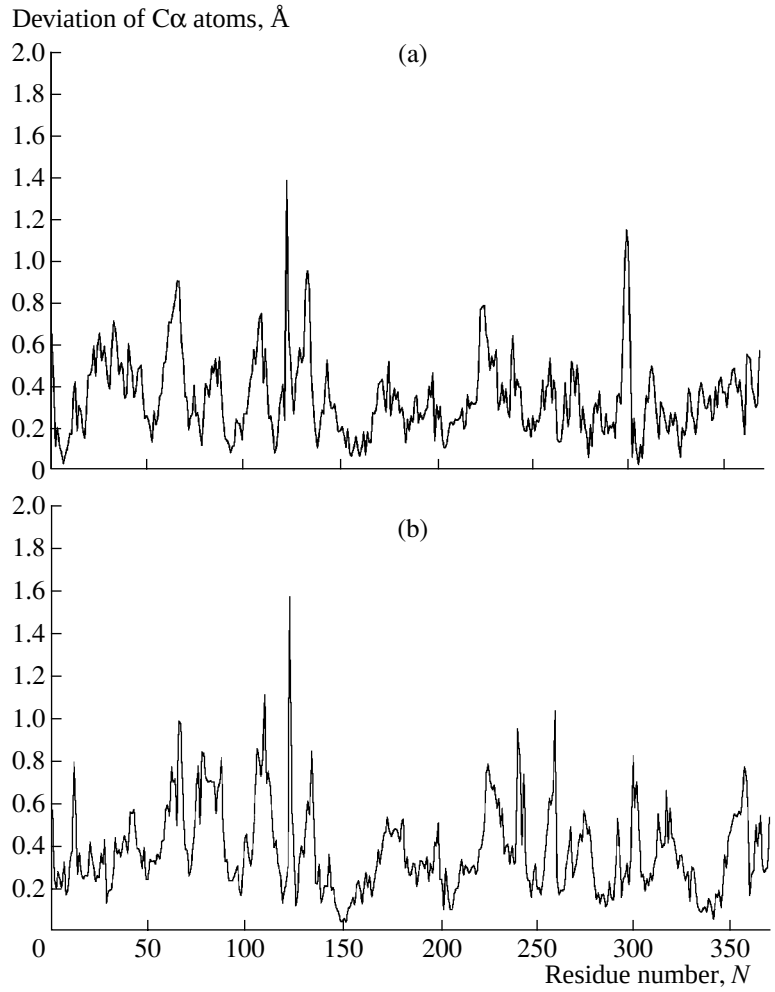

Fig. 3. Deviation of the coordinates of the Cα atoms in the studied structure from those of the apo form of FDG as a function of the residue number: (a) comparison of subunit *A* and (b) comparison of subunit *B*. The structures are compared by the superposition of the coordinates of the corresponding Cα atoms of residues 1–369.

the CONTACT program package [13]. The interatomic contacts shorter than 5.5 Å and the hydrogen bonds shorter than 3.3 Å were taken into account. None of the contacts between symmetrically equivalent molecules in the structure of the monomer (space group $P4_22_12$) were found to be similar to those in the apo form of the enzyme (space group $P2_1$).

The differences between the structures in the regions 128–134 and 299–301 are due to the contacts of the *A* and *B* subunits of the apo form with symmetrically equivalent molecules. In the studied structure, no contacts are found in this region. On the contrary, the structural differences in the region 226–234 are explained by the formation of intermolecular contacts only in the studied structure. In the region 76–87, the contacts are found in all the molecules. In the region 59–68, the intermolecular contacts are observed in the studied molecule and in the *B* subunit of the apo form of FDG.

The largest structural differences were revealed in the regions of residues 123 and 370–374. The atoms of the main chain of residues *Ile*122 and *Gly*123 participate in the binding of the formate ion by the enzyme [2]. In the studied structure, the conformation of the loop 122–125 changes with respect to that in the structures of the apo and holo forms because of the rotation of the carboxyl group of the *Gly*123 residue (Fig. 4). This conformation of the loop is stabilized as a result of the formation of the hydrogen bond between the atoms O *Gly*123 and O*G*1 *Thr*119. In the structures of the apo and holo forms, the position of the loop is stabilized by the hydrogen bond between the atoms O*G Ser*124 and O*G*1 *Thr*119. Stereodiagrams of the loop 122–125 in the studied structure and the structure of the apo form of the enzyme are shown in Fig. 4.

Large deviations of the Cα atoms of the C-terminal part (residues 370–374) in the studied structure from the corresponding positions in the structures of the apo and holo forms result from the rotation of these residues

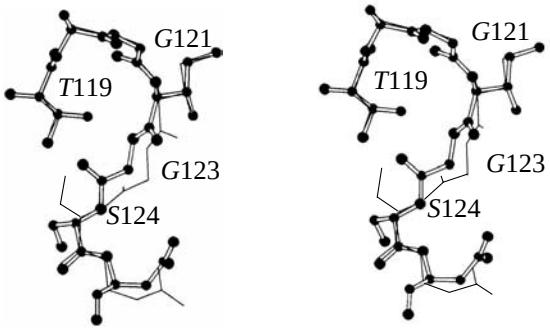

Fig. 4. Stereodiagram of the loop 122–125 in the studied structure (the ball-and-stick model) and in the apo form of FDG (thin lines).

in opposite directions. The position of the C-terminal part of the chain in the structures of the apo and holo forms of the enzyme is stabilized by the N *Glu*369··O *Ala*372 and O *Ile*367··N *Glu*374 hydrogen bonds between the atoms of the main chain. The C-terminal part of the chain is directed toward the interdomain cavity. In the holo form, residues 374–391 shield the active center from the solvent and additionally fix the position of the coenzyme at the active center by forming three hydrogen bonds with the NAD^+ molecule [2]. In the studied structure, the conformation of the 370–374 section of the chain is stabilized as a result of the formation of the N *Ile*361··O *Leu*373, O*G*1 *Thr*138··N *Gly*370, and O*E*1 *Glu*369··O *Ala*372 hydrogen bonds. In this case, the C-terminal part of the chain is oriented in the direction opposite to the interdomain cavity. It is this position of the C-terminal fragment that can be responsible for the failure in obtaining the complex of FDG with NADH in the crystal state.

ACKNOWLEDGMENTS

This study was supported by NATO, grant CLG no. 977839.

REFERENCES

1. K. Vinals, E. Depiereux, and E. Feytmans, Biochem. Biophys. Res. Commun. **192**, 182 (1993).
2. V. S. Lamzin, Z. Dauter, V. O. Popov, *et al.*, J. Mol. Biol. **236**, 759 (1994).
3. D. J. Schuller, G. A. Grant, and L. J. Banaszak, Nat. Struct. Biol. **2**, 69 (1995).
4. J. D. Goldberg, T. Yoshida, and P. Brick, J. Mol. Biol. **236**, 1123 (1994).
5. V. S. Stoll, M. S. Kimber, and E. Pai, Structure **4**, 437 (1996).
6. A. Rozeto, S. Kochhar, H. Hottinger, *et al.*, J. Mol. Biol. **318**, 109 (2002).
7. U. Dengler, K. Niefind, M. Kiess, and D. Schomburg, J. Mol. Biol. **267**, 640 (1997).
8. Z. Otwinowski and W. Minor, Methods Enzymol. **276**, 307 (1997).
9. A. A. Vagin and A. Teplyakov, J. Appl. Crystallogr. **30**, 1022 (1997).
10. G. N. Murshudov, A. A. Vagin, and E. J. Dodson, Acta Crystallogr., Sect. D: Biol. Crystallogr. **53**, 240 (1997).
11. T. A. Jones, J.-Y. Zou, S. W. Cowan, and M. Kjeldgaard, Acta Crystallogr., Sect. A: Found. Crystallogr. **47**, 110 (1991).
12. A. S. Kutzenko, V. S. Lamzin, and V. O. Popov, FEBS Lett. **423**, 105 (1998).
13. The SERC (UK) Collaborative Computing Project No. 4, Acta. Crystallogr., Sect. A: Found. Crystallogr. **46**, 585 (1994).

Translated by I. Polyakova

Crystallography Reports, Vol. 50, No. 5, 2005, pp. 801–807. Translated from Kristallografiya, Vol. 50, No. 5, 2005, pp. 862–868.

REAL STRUCTURE OF CRYSTALS

Fluctuations of Impurity Composition and Their Role in Dislocation Cross Slip in Crystals

B. V. Petukhov

Shubnikov Institute of Crystallography, Russian Academy of Sciences, Leninskiĭ pr. 59, Moscow, 119333 Russia

Received April 21, 2004

Abstract—The influence of impurities on the kinetics of split-dislocation cross slip caused by a change in the stacking-fault energy is studied theoretically. It is shown that the fluctuations in the impurity composition of a crystal make a considerable contribution to the kinetics of dislocation cross slip. The activation-energy spectrum and the average frequency of the processes of dislocation cross slip are calculated for a model of random impurity distribution in a crystal. The calculation shows that the fluctuations in impurity concentration, reducing the stacking-fault energy, play an important role in the low-temperature region. *© 2005 Pleiades Publishing, Inc.*

INTRODUCTION

Alloying of crystalline materials is an efficient method of improving their mechanical properties and, in particular, their plasticity. Therefore, the study of the mechanisms of the influence of impurities on the dislocation dynamics is very important. Plastic deformation of crystals proceeds via dislocation motion, usually, along certain slip planes dictated by the crystal structure. The role of slip planes is often played by closely packed planes of a crystal in which the dislocations are split into pairs of partial dislocation separated by a strip of a stacking fault. The configuration energy of a split dislocation is lower than the energy of a linear configuration. This planar structure ensures an easy motion of a dislocation in the main plane and hinders its transition into the transverse planes. However, in some particular cases, the effect of directional internal or external stresses can also stimulate the transition of a dislocation into a transverse plane.

The change of the slip plane or the so-called dislocation cross slip gives rise to a number of new interesting phenomena playing an important role in the processes of deformation hardening of materials, self-organization of dislocation ensembles, texture formation, etc. [1–3]. Dislocation cross slip in ordered alloys gives rise to an anomalous increase in deforming stresses with temperature [4, 5] and, thus, makes these alloys very promising materials for various high-temperature applications.

Prior to the dislocation incorporation into a transverse plane, it should acquire a constricted configuration at the site of the intersection of the main and transverse planes. The change in the dislocation configuration results in an increase of the dislocation energy and, therefore, is associated with overcoming a certain energy barrier. The barrier height or the activation energy of cross slip depends on the splitting width, which, in turn, is determined by the energy of a stacking fault located between the partial dislocations. As is well known, the stacking-fault energy may considerably be changed by alloying the material. This allows one to control the rate of cross-slip processes. Up to now, the effect of impurities has been discussed in terms of the changes in the average stacking-fault energy due to alloying. This effect is associated either with a decrease in the splitting width (which increases the probability of recombination of two partial dislocations) or with the changes in the average stacking-fault energies in the main and transverse planes (which modifies the driving force necessary for the change of the slip plane). However, the second factor takes place only in some particular mechanisms of cross slip. The cross-slip driving force depends on the state of the dislocation core in the secondary plane, which may lead to different scenarios of the process [3]. In particular, a dislocation built into a transverse plane can be split again in this plane if it is a closely packed plane or, otherwise, can be split again in the plane neighboring the initial one. The second variant of dislocation emergence into a new plane suggested in [6] is illustrated in Fig. 1.

Since a crystal is periodic, the change in the average energy of a split-dislocation configuration does not make any contribution to the driving force of the process of dislocation transition between the neighboring planes of a crystal. At first sight, this fact closes the most important channel of influence of alloying associated with the change in the stacking-fault energy. However, in actual fact, this is not true. Below, we suggest a new mechanism of such an influence. The main concept of this mechanism is based on the fact that a fluctuation in the impurity composition breaks the transnational periodicity of the crystal. This results in the formation of a fluctuating contribution to the difference between

1063-7745/05/5005-0801$26.00

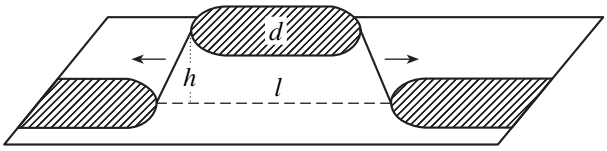

Fig. 1. Nucleus of cross slip of a split dislocation according to the jog-pair mechanism: d is the distance between the partial dislocations (stacking-fault width), h is the distance between the neighboring planes (cross-slip step), and l is the nucleus length approximately corresponding to the distance between jogs in the transverse plane.

the energies of the dislocation configurations in neighboring crystal planes, i.e., to random variations of the height of the barrier that should be overcome by a dislocation prior to cross slip. Statistical calculation has shown that this contribution has a strong influence on the whole scheme of the process.

First, let us consider in brief the kinetics of the scenario of dislocation cross slip in a pure crystal and then extend this consideration to a crystal with impurities. The split parts of a dislocation located in parallel planes are related in the transverse planes by so-called jogs. An increase in the length of the dislocation segment in a new plane (growth of a nucleus) proceeds via jog glide along the intersection line of the main and transverse planes. This type of dislocation cross slip is analogous to the dislocation motion in a periodic relief of the crystal lattice via formation of kink pairs and it is called the mechanism of jog pairs [3]. This mechanism plays an important role during dislocation immobilization in intermetallic compounds by way of the formation of so-called incomplete Kear–Wilsdorf locking [4] and in many other instances.

The activation energy E of cross slip of a dislocation segment of length l in a homogeneous material is the sum of the energies E_{2J} of two jogs, the energy of their elastic attraction (inversely proportional to the distance between these jogs the $-\alpha/l$, and the change in the energy of the segment displaced in the field of the stress τ, $-\tau bhl$:

$$E = E_{2J} - \alpha/l - \tau bhl. \quad (1)$$

Here, b is the length of the Burgers vector of a dislocation and h is the distance between the neighboring planes. It is assumed that the length l exceeds the jog size, so the jogs may be considered as point objects. The quantity $F_0 = \tau bh$ plays the part of the driving force of jogs which ensures their motion in the opposite directions and growth of the displaced segment. For ordered alloys during the formation of incomplete Kear–Wilsdorf locking induced by cross slip of the leading superpartial dislocation, the quantity F_0 contains a considerable contribution from the elastic interaction with the trailed superpartial dislocation [5, 7]. The barrier height is determined by the maximum potential in Eq. (1), $E = E_{2J} - 2\sqrt{\alpha F_0}$, attained at the critical nucleus length $l_0 = \sqrt{\alpha/F_0}$. The frequency of elementary cross-slip events per unit time is given by the Arrhenius equation

$$I = I_0 \exp(-E/kT), \quad (2)$$

where k is the Boltzmann constant, T is the temperature, and I_0 is a constant preexponential factor.

EFFECT OF ALLOYING ON RECOMBINATION ENERGY

Dislocation cross slip, being a thermally activated process, is very sensitive to relatively small variations in the sample composition. Impurities affect the cross-slip kinetics by modifying the barrier that should be overcome by dislocations. In principle, all three terms in Eq. (1) may be modified, but the mechanisms responsible for their modification are different and, to a certain extent, may be considered separately. This is caused by essentially different spatial scale of impurity interactions with dislocations corresponding to different terms in Eq. (1). Jogs are the localized objects and have small volumes. At a low impurity concentration (~1%), each individual jog interacts with rare impurity atoms. A stacking fault, being a two-dimensional object, has a larger space for interaction. In this case, the number of impurities participating in the interactions is proportional to the splitting width of a split dislocation, d, which often considerably exceeds the lattice period a (i.e., $d \gg a$) and the length l of the nucleus of the displaced portion (Fig. 1). In this case, the interaction of impurities with dislocation is of a collective nature. Therefore, the main channel of impurity influence is usually considered to be the modification of a stacking-fault energy and the corresponding change in the recombination energy ΔE_r. The present study considers low-doped crystals and diluted solid solutions with the slight variation of elastic moduli and the parameters determined by these moduli being ignored.

In a homogeneous material, the elastic-repulsion force of a partial dislocation per unit length, K_{el}/d, competes with the attraction force equal to the energy stacking fault per unit area, γ [1–3]. At equilibrium, $K_{el}/d = \gamma$, which allows one to determine the equilibrium splitting width as $d = K_{el}/\gamma$. The recombination energy per dislocation unit length is the integral of the force of dislocation interaction,

$$\Delta E_r = \int_{d_c}^{d} (K_{el}/x - \gamma)dx = K_{el}\ln\left(\frac{K_{el}}{\gamma d_c}\right) - \gamma(d - d_c). \quad (3)$$

Here, $d_c \ll d$ is the critical minimum distance, after the attainment of which the dislocation is said to be recombined back into a complete dislocation. If the number of impurities is small, the change in the stacking-fault energy density in comparison with its value in a pure

crystal, γ_0, can be considered as a linear function of concentration c; i.e., $\gamma \approx \gamma_0 + cu/S_0$. Here, S_0 is the stacking-fault area per unit cell; u is the energy of the interaction of this defect with one impurity atom, which is considered below as a phenomenological parameter; and γ_0 is the energy density of a stacking fault. Depending on the chemical nature of an impurity, both attraction ($u < 0$) and repulsion ($u > 0$) can take place. Impurities modify the width of dislocation splitting into partial dislocations in a pure crystal, d_0, as $d = d_0/[1 + cu/(\gamma_0 S_0)]$ and, thus, change the energy of partial-dislocation recombination, ΔE_r. We consider the case of a rather fast dislocation motion and, therefore, the mobility of impurities may be ignored so that they are considered to be "frozen" into a crystal.

Since the initial and final (with respect to dislocation motion) crystal-lattice planes are equivalent, the changes in the recombination energy in the uniform impurity distribution in these planes are also equivalent and make no contributions to the cross-slip driving force in the mechanism under study. However, since the impurity distribution is not rigorously uniform and has some fluctuations, the impurity concentrations in the neighboring planes can be different. This modifies the recombination energy of partial dislocations given by Eq. (3) in different planes. The difference in the recombination energies in different planes gives rise to an additional fluctuating contribution to the driving force of gliding jogs, which can be described as

$$F = F_0 + K_{el} \ln \frac{\gamma_0 + c_1 u/S_0}{\gamma_0 + c_2 u/S_0}. \quad (4)$$

Here, c_1 and c_2 are the impurity concentrations at the site of transition in the initial and secondary planes, respectively. Equation (4) shows that the conditions of cross slip may be different at different sites of the dislocation line. Although the spectrum of fluctuations is large, the fluctuations we are interested in are those whose characteristic size is not less than the splitting width d. We shall describe such fluctuations by Eq. (4) that is valid for a sufficiently smooth spatial variation of concentrations c_1 and c_2 averaged over the scale d.

If the impurities are randomly distributed over the material and give rise to the fluctuating contribution to the driving force described by Eq. (4), the nucleus energy of a moving dislocation is also a random quantity, which is determined by the equation

$$E\{c\} = E_{2J} - \int (F - \alpha/l^2) dl, \quad (5)$$

where F is set by Eq. (4) and the integral is calculated along the length of a displaced segment. The cross-slip rate in this situation is determined by the frequency of thermally activated transitions of a dislocation into the transverse plane averaged along the dislocation. At a sufficient dislocation length, averaging of frequencies along the dislocation is equivalent to averaging over the spectrum of all the impurity configurations in accordance with the equation

$$\begin{aligned} \langle I \rangle &= \langle I_0 \exp[-E\{c\}/kT] \rangle \\ &= \int I_0 \exp[-E\{c\}/kT] P\{c\} d\{c\}. \end{aligned} \quad (6)$$

Here, $P\{c\}$ symbolizes the probability density of the implementation of a random impurity distribution in a certain interval $d\{c\}$ of the configurational space. (Eq. (6) will be considered in detail later.) The quantity $P\{c\}$ decreases with the deviation of impurity concentrations from the average value c_0. At the same time, the frequency of thermally activated transitions dependent on the fluctuation form may either decrease or exponentially increase with an increase in the deviation of the concentration from its average value in the sample. This is associated with either a higher stacking-fault energy in the secondary plane and a negative contribution to the driving force given by Eq. (4) or a decrease in the stacking-fault energy and a positive contribution to the driving force. In the former case, the integrand in Eq. (6) decreases because of fluctuations which, thus, make no considerable contribution to the average frequency determined by Eq. (6). In the latter case, conversely, the integrand first increases with an increase in fluctuations, and then starts decreasing because of a more dramatic decrease in the probability of formation of more pronounced fluctuations. As a result, the integrand passes through the maximum at a certain impurity configuration $c = c_{opt} \neq c_0$ and, therefore, the average frequency given by Eq. (6) is determined mainly by a certain optimum fluctuation in the impurity distribution. It should be noted that a similar approach is widely used in the calculations of the characteristics of disordered systems (see, e.g., [8]). Earlier, this approach was also used to determine the impurity effect on the dislocation motion by the kink mechanism [9, 10].

To avoid any misunderstanding, we have to state that the optimum fluctuations are specific for each concrete problem and depend considerably on the conditions of each problem and, therefore, have nothing in common with the intuitively expected "typical" fluctuations. When considering the application of the theory to an ideal solution of impurities, we ignore possible limitations imposed onto the form of optimum fluctuations associated with the interaction of impurity atoms with one another. A favorable fluctuation, which increases the transition frequency, would have been the fluctuation increasing the energy of a dislocation segment in the initial plane and reducing it in the secondary plane. However, because a dislocation can travel in the initial plane and relax to the position with the energy minimum within the expectation time being located in front of the barrier, the fluctuations, which increase the dislocation energy in the initial plane, may be avoided and, therefore, may be ignored. Thus, we

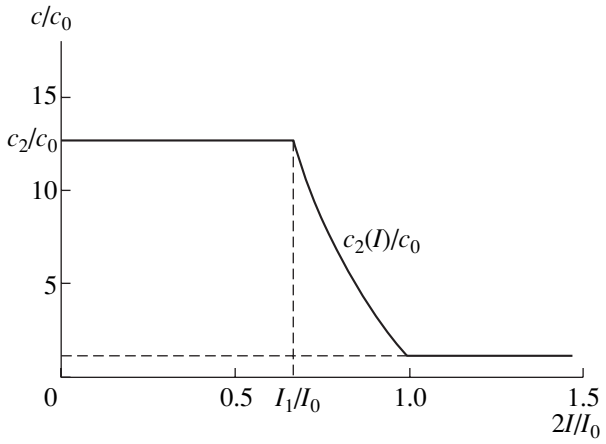

Fig. 2. Distribution of impurities in the optimum fluctuation at the parameter values $c_0u/\gamma_0S_0 = -0.01$ and $\varepsilon = 0.5$.

assume that $c_1 = c_0$. In the secondary plane, we are interested in the change of the impurity concentration within a distance equal to the critical nucleus size. i.e., within a strip of the width $d = K_{el}/(\gamma_0 + c_2u/S_0)$. Within such a width (which varies with the change in the impurity concentration and which should be determined by a self-consisted method), we assume that the impurity distribution is uniform. The characteristic size along the longitudinal direction is assumed to be much larger than d, and the optimum impurity distribution along the critical nucleus is sought for as a function of the longitudinal coordinate, $c_2 = c_2(l)$. Our next problem is the search for the most probable impurity fluctuation corresponding to the given activation energy of cross slip.

FUNCTION OF BARRIER-HEIGHT DISTRIBUTION

The height of a barrier that should be overcome by a dislocation in the vicinity of the impurity fluctuation is determined by the maximum potential in Eq. (5) and is evaluated from this equation at different impurity distributions along the nucleus. The solution of the corresponding variational problem shows that the optimum fluctuation corresponding to the required lowering of the barrier reduces to the uniform impurity distribution $c_2 = \text{const}$ along the central interval $(-l_1/2, l_1/2)$ and an nonuniform distribution resulting in the constant nucleus energy (plateau) at the peripheral intervals $(-l_0/2, -l_1/2)$ and $(l_1/2, l_0/2)$. The length l_1 is related to c_2 as $l_1 = \sqrt{\alpha/F(c_2)}$. This formula generalizes the analogous condition for the extremum potential in a pure material, $l_0 = \sqrt{\alpha/F_0}$. The impurity concentration at the central portion of the nucleus, c_2, is uniquely related to the barrier height by the following equation

$$E = E_{2j} - 2\sqrt{\alpha\left[F_0 + K_{el}\ln\left(\frac{\gamma_0 + c_0u/S_0}{\gamma_0 + c_2u/S_0}\right)\right]}. \quad (7)$$

The impurity distribution at the peripheral portion of $c_2(l)$ is determined from the condition of equal force of jog attraction $\alpha/4l^2$ and the driving force $F(c_2)$ which sets the potential constancy in Eq. (5):

$$c_2(l) = \frac{\gamma_0S_0}{u}\left\{\left(1 + \frac{c_0u}{\gamma_0S_0}\right)\exp\left[-\frac{F_0}{K_{el}}\left(\frac{l_0^2}{4l^2} - 1\right)\right] - 1\right\}. \quad (8)$$

Note that, because of the symmetry of the optimum function, we limited ourselves to the description only of its right-hand side at positive l.

Figure 2 illustrates the form of the optimum fluctuation at the following parameter values: $c_0u/\gamma_0S_0 = -0.01$ and $\varepsilon \equiv (E_0 - E)/(2\sqrt{\alpha F_0}) = 0.5$.

Now, let us determine the probability of encountering the impurity fluctuation that would lead to the required barrier height. In other words, let us determine the function of the barrier-height distribution. For this we have to determine the statistical weight of the impurity configurations of the given type. We consider a random impurity distribution over the sample or an ideal solid solution. Then, the probability we are interested in is the product of the probabilities of the uniform distribution along the central portion P_1 and an nonuniform distribution corresponding to the condition (8) at the peripheral portion P_2. In accordance with the Poisson ratio, the probability of encountering $N_1 = c_2dl_1/S_0$ impurities at the average value $N_0 = c_0dl_1/S_0$ is equal to $P_1 = N_0^{N_1}\exp(-N_0)/(N_1!)$. At $N_1 \gg 1$, we arrive at the approximate relationship $P_1 = \exp S_1$, where the entropy S_1 is

$$\begin{aligned} S_1 &= -N_1\ln\frac{N_1}{eN_0} - N_0 \\ &= -\frac{d_0l_1/S_0}{1 + c_2u/(\gamma_0S_0)}\left(c_2\ln\frac{c_2}{ec_0} + c_0\right). \end{aligned} \quad (9)$$

Here, e is the base of natural logarithms ($e = 2.72\ldots$).

In a similar way, the probability P_2 of impurity distribution $c_2(l)$ between l_1 and l_0 is written as $P_2 = \exp S_2$, where the entropy S_2 is given by the integral

$$S_2 = -\frac{2d_0}{S_0}\int_{l_1/2}^{l_0/2}\frac{1}{1 + c_2(l)u/(\gamma_0S_0)}\left[c_2(l)\ln\frac{c_2(l)}{ec_0} + c_0\right]dl, \quad (10)$$

which sums up the contributions of type (9) from small sections of length dl (which substitutes l_1 in Eq. (9)) within which the impurity concentration and the splitting width are taken to be constant.

Thus, the probability of encountering the required barrier height E is

$$P = \exp(S_1 + S_2), \tag{11}$$

where S_1 and S_2 are set by Eqs. (9) and (10) and the impurity concentrations c_2 and $c_2(l)$ at the center of the optimum fluctuation and at its periphery are determined by Eqs. (7) and (8), respectively.

In the important case of $c_2|u|/(\gamma_0 S_0) < 1$, the Eqs. (9)–(11) are simplified. The distribution function of the barrier-height is obtained as

$$P(E) = \exp\left\{\frac{2\sqrt{\alpha F_0}}{u}\left[(\varepsilon + 1 - \sqrt{1 + F_1/F_0}) \times \ln(1 - \varepsilon(\varepsilon + 2)F_0/F_1) - 2\varepsilon + 2\sqrt{1 + F_1/F_0}\ln\left(1 + \frac{\varepsilon}{1 + \sqrt{1 + F_1/F_0}}\right)\right]\right\}. \tag{12}$$

Here, $\varepsilon \equiv (E_0 - E)/(2\sqrt{\alpha F_0})$. We also introduce here a new parameter $F_1 = K_{el}c_0 u/(\gamma_0 S_0)$, which characterizes the average influence of impurities on the recombination energy of partial dislocations.

AVERAGE FREQUENCY OF DISLOCATION TRANSITIONS

By use of the data on the barrier-height distribution obtained, it is possible to calculate in an explicit form the average frequency of transitions, $\langle I\rangle$. Averaging can be performed either over the spectrum of barrier heights E or over any other parameter uniquely related to E. In particular, impurity fluctuations of the type we are interested in are uniquely characterized by the impurity concentration at the central part of the nucleus, c_2. The frequency of transitions in the vicinity of a concrete fluctuation is $I = I_0\exp\{-[E_{2J} - 2\sqrt{\alpha F(c_2)}]/kT\}$. The probability of encountering such a fluctuation is $P(E) = \exp[S_1(c_2) + S_2(c_2)]$. The weighted frequency of a transition is given by the equation

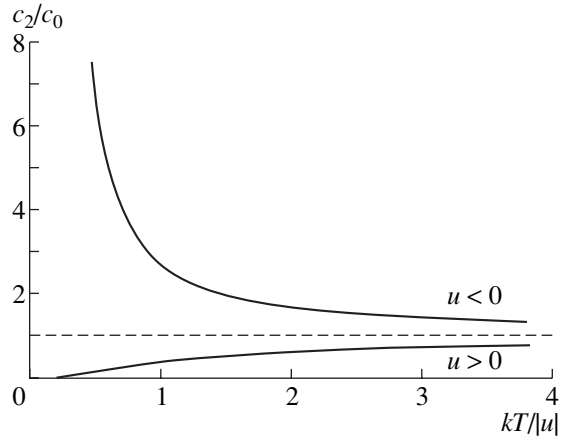

Fig. 3. Evolution of the impurity concentration at the center of the optimum fluctuation as a function of temperature in the case of their attraction to ($u < 0$) and repulsion from ($u > 0$) a stacking fault ($c_0|u|/(\gamma_0 S_0) = 0.01$ and $F_0/K_{el} = 0.1$).

$$I_p = I_0\exp\left[-\frac{E_{2J} - 2\sqrt{\alpha F(c_2)}}{kT} + S_1(c_2) + S_2(c_2)\right]. \tag{13}$$

The average frequency is obtained by summing up the particular contributions in Eq. (13), but the main contribution to the sum comes from the term with the maximum exponent. One can readily see when differentiating the exponent that the maximum value corresponds to c_2, which is related to temperature as

$$\frac{kT}{u} = -\frac{1 + c_2 u/\gamma_0 S_0}{\ln(c_2/c_0) + (c_2 - c_0)u/(\gamma_0 S_0)}. \tag{14}$$

Equation (14) is shown in the graphical form in Fig. 3. One can clearly see the evolution of the impurity fluctuations important for cross slip as a function of temperature. Determining the optimum c_2 value from Eq. (14) (usually by its numerical solution) and substituting the result into Eq. (13), we arrive at the estimate of the average transition frequency. In the limiting case $c_2|u|/(\gamma_0 S_0) < 1$, one can also obtain the analytical solution in the form

$$c_{2\,\mathrm{opt}} \approx c_0\exp\left[-\frac{u}{kT}\right]. \tag{15}$$

Substituting the above result into Eq. (13), we arrive at the average transition frequency in the explicit form

$$\langle I\rangle \approx I_0\exp\left\{-\frac{E_{2J} - 2\sqrt{\alpha(F_0 + F_1)}}{kT} - \frac{4\sqrt{\alpha F_0}}{u}\left(\sqrt{1 + \frac{F_1}{F_0}\left[1 - \exp\left(-\frac{u}{kT}\right)\right]} - 1 - \sqrt{1 + \frac{F_1}{F_0}}\ln\frac{\sqrt{1 - (F_1/F_0)(\exp(-u/kT) - 1)} + \sqrt{1 + F_1/F_0}}{1 + \sqrt{1 + F_1/F_0}}\right)\right\}. \tag{16}$$

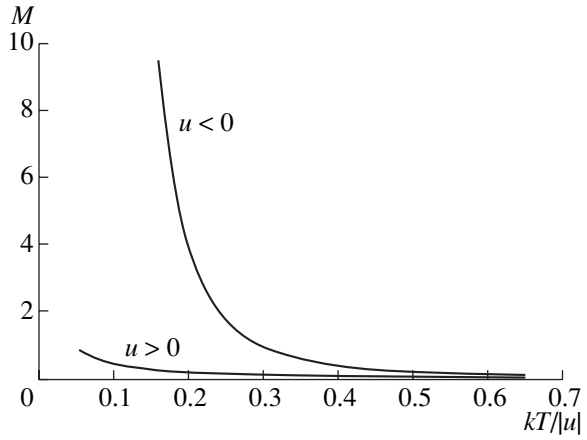

Fig. 4. Temperature dependence of the factor $M = \ln(\langle I\rangle/I)|u|/(4\sqrt{\alpha F_0})$ characterizing the change in the frequency of the cross-slip events. The parameter values are $c_0|u|/(\gamma_0 S_0) = 0.01$ and $F_0/K_{el} = 0.1$.

The effect of impurities strongly depends on the nature of impurity interactions with a stacking fault (the sign of the parameter u).

The impurities attracted to the stacking fault ($u < 0$) reduce the stacking-fault energy and, therefore, their elevated concentration in the secondary plane ensures dislocation cross slip, which is reflected in Eqs. (15) and (16). A dramatic increase in the concentration of impurities at considerable fluctuations with lowering of the temperature (Eq. (15)) results in the driving force of the fluctuation nature in the low-temperature region exceeding the driving force caused by external stresses. In the case of repulsive impurities ($u > 0$), characterized by strong repulsion ($u > kT$), Eq. (15) dictates their vanishing concentration at the secondary-plane sites favorable for the dislocation transition. Figure 4 illustrates the temperature dependence of the average transition frequency for various types of impurities.

CONCLUSIONS

The conventional discussion of the effect of material alloying on the kinetics of dislocation cross slip in terms of the change in the average stacking-fault energy is inapplicable to the case of the jog-pair mechanism. We suggested a somewhat modified model based on fluctuations in impurity composition. Because of a high sensitivity of thermally activated processes to the activation energy, the sites with locally reduced barrier height considerably increase the average frequency of elementary cross-slip events.

It should be emphasized that the effects of the homogeneous modification of the material parameter are proportionally to c_0, whereas the fluctuation effects are shown to be proportional to $c_0\exp(-u/kT)$. In other words, the fluctuation effects are anomalously high in the case of attracting impurities at $|u| > kT$. This makes the fluctuation mechanism of the effect of impurities in the low-temperature region more efficient than the conventionally considered homogeneous mechanisms. This qualitative conclusion is valid not only for jog pairs but also for other cross-slip scenarios.

One of the possible implementation of the jog-pair mechanism is, in particular, the formation of incomplete Kear–Wilsdorf locking in ordered alloys. As a result, dislocations lose their mobility. According to various observations [11, 12], the replacement of Ni atoms by Fe atoms in the $Ni_{3-x}Fe_xGe$ solid solutions in the low-temperature region (~77 K) results in a dramatic hardening of the initial Ni_3Ge. Analysis of the microscopic observations of dislocation structures shows that the frequency of the cross-slip events after the replacement of 15% of the Ni atoms by Fe increases considerably. This may cause hardening, which exceeds the hardening characteristic of direct dislocation deceleration by local impurity barriers considerably [12]. These experimental findings are consistent with the fluctuation mechanism of the influence of solution atoms on the cross-slip kinetics of dislocations suggested in the present study.

Finally, we would like to indicate the following. Recently, the cross-slip energy of dislocations in copper or nickel was obtained by direct computer simulation of the process at the atomic level [13, 14]. One of the important problems of such computer simulation is the choice of the minimum but sufficiently large computational cell. Such a cell in a homogeneous material sufficient for the consideration of a nucleus of an elementary cross-slip event consists of $l_0/a \sim 10^2$ crystal-lattice periods. In the solution of a similar problem for a solid solution, the minimum unit cell should exceed at least the repetition period L of pronounced impurity fluctuations, which is inversely proportional to the probability of encountering the optimum impurity fluctuation; i.e., $L \sim l_0\exp[-S_1(c_2) - S_2(c_2)]$, where c_2 is determined by Eqs. (14) or (15). Such fluctuations are rare, and the average distance between such fluctuations is large. Thus, the constraints imposed on the computational-cell size in simulation of dislocation cross slip in solid solutions are much more rigid, especially in the low-temperature region. This makes the analytical approaches to the problem similar to the one developed above much more valuable.

REFERENCES

1. J. Friedel, *Dislocations* (Pergamon Press, Oxford, 1964; Mir, Moscow, 1967).
2. B. I. Smirnov, *Dislocation Structure and Crystal Strengthening* (Nauka, Leningrad, 1981) [in Russian].
3. W. Püschl, Prog. Mater. Sci. **47**, 415 (2002).

4. P. Veyssiere and G. Saada, *Dislocations in Solids*, Ed. by F. R. N. Nabarro (Elsevier, North-Holland, Amsterdam, 1996), Vol. 10, p. 253.
5. B. A. Grinberg and M. A. Ivanov, *Ni_3Al and TiAl Intermetallic Compounds: Microstructure and Deformation Behaviour* (Nauka, Yekaterinburg, 2002) [in Russian].
6. H. Yoshinaga and R. Horiuchi, Trans. Jpn. Inst. Met. **5**, 14 (1963).
7. M. H. Yoo, Scr. Metall **20**, 915 (1986).
8. I. M. Lifshits, S. A. Gredeskul, and L. A. Pastur, Fiz. Nizk. Temp. (Kiev) **2**, 1093 (1976) [Sov. J. Low Temp. Phys. **2**, 533 (1976)].
9. B. V. Petukhov, Fiz. Tverd. Tela (Leningrad) **32**, 579 (1990) [Sov. Phys. Solid State **32**, 336 (1990)].
10. B. V. Petukhov, Fiz. Tverd. Tela (St. Petersburg) **35**, 1121 (1993) [Phys. Solid State **35**, 571 (1993)].
11. T. Suzuki, Y. Oya, and D. M. Wee, Acta Metall. **28**, 301 (1980).
12. T. J. Balk, M. Kumar, and K. J. Hemker, Acta Mater. **49**, 1725 (2001).
13. T. Rasmussen, K. W. Jacobsen, T. Leffers, *et al.*, Phys. Rev. Lett. **79**, 3676 (1997).
14. S. Rao, Philos. Mag. A **80**, 1293 (2000).

Translated by L. Man

Crystallography Reports, Vol. 50, No. 5, 2005, pp. 808–813. Translated from Kristallografiya, Vol. 50, No. 5, 2005, pp. 869–875.

LATTICE DYNAMICS AND PHASE TRANSITIONS

Propagation of Elastic Waves Near Acoustic Axes in Crystals under the Action of Extreme External Forces: I. Piezoelectric Crystal in an Electric Field

V. V. Alenkov, A. N. Zabelin, N. V. Perelomova, and S. I. Chizhikov

Moscow State Institute of Steel and Alloys, Leninskiĭ pr. 4, Moscow, 119049 Russia

e-mail: zabelin@fomos-t.ru

Received March 22, 2005

Abstract—The directions of an external electric field at which extreme changes occur in the difference in the velocities of elastic waves propagating along the initial acoustic axis in a piezoelectric medium of arbitrary symmetry are theoretically determined. The problem of degeneracy in an external electric field is considered for elastic waves propagating in a given direction from the vicinity of an initial acoustic axis. The extreme electric fields and corresponding changes in the characteristics of transverse waves are calculated by the example of the behavior of acoustic axes in $Bi_{12}GeO_{20}$, $Bi_{12}SiO_{20}$, $La_3Ga_5SiO_{14}$, and $LiNbO_3$ crystals. © *2005 Pleiades Publishing, Inc.*

INTRODUCTION

The effect of external electrical and mechanical forces on the properties of elastic waves propagating near acoustic axes in crystals has long attracted the attention of researchers. Classification of acoustic axes according to the type of the contact geometry of the velocity surfaces of elastic waves and the features of the polarization vector fields in the vicinity of degeneracy points was given for nonpiezoelectric crystals in [1–4] and generalized for piezoelectrics in [5]. Alshits *et al.* [3, 4] investigated the behavior of degeneracies of different types (shift, splitting, or disappearance) under small perturbations of the elastic properties of crystals, which are described by symmetric material tensors. In [6], on the basis of the perturbation theory, solutions for the phase velocities and polarization vectors of elastic waves in the vicinity of acoustic axes were found as functions of an arbitrarily oriented electric field. Analytical expressions were obtained, which make it possible to determine angles of shifts and splitting of acoustic axes directed along the crystal symmetry axes in the absence of external forces. Equations of acoustic axes were obtained in [7] for a centrosymmetric cubic crystal in an external electric field. It was shown that the electric field, as a result of the reduction of the crystal symmetry, causes splitting and shift of acoustic axes of an unperturbed crystal.

The behavior of acoustic axes in cubic crystals of $Bi_{12}SiO_{20}$ and $SrTiO_3$ and trigonal crystals of $LiNbO_3$ and $La_3Ga_5SiO_{14}$ in external electric fields of particular directions and under a uniaxial mechanical load was considered in [8–11]. It was shown in [8] that an electric field directed along the twofold symmetry axis, owing to the reduction of the crystal symmetry, splits the acoustic axis [001] in the cubic piezoelectric $Bi_{12}SiO_{20}$. The behavior of acoustic axes in mechanically pressed and mechanically free $LiNbO_3$ and $SrTiO_3$ crystals in an external static electric field was analyzed in [9]. It was shown that the numerically obtained dependences of the angles of splitting and shift of acoustic axes on the external electric field are in agreement with the results of [6] up to the fields $E \leq 10^7$ V/m, a result which is consistent with the corresponding data on $LiNbO_3$ [10]. The behavior of the acoustic axis directed along the threefold symmetry axis in a $La_3Ga_5SiO_{14}$ crystal under homogeneous static stresses was considered in [11].

At the same time, the following extreme problems are of both theoretical and practical interest: (i) determination of the directions of an external force at which either the initial direction $\mathbf{n}_0$ of the acoustic axis is retained or the difference in the elastic wave velocities is maximum for the $\mathbf{n}_0$ direction and (ii) determination of external forces inducing an acoustic axis[1] in a given direction n near the initial acoustic axis.

We plan to report the solution of the above-stated problems in a series of three papers. In the first paper, we consider extreme electric fields for acoustic axes in piezoelectric crystals. The second paper will deal with extreme electric fields for acoustic axes in centrosymmetric crystals. The third paper will be devoted to

[1] We will use the term "induced acoustic axis" for the direction along which the phase velocities of at least two elastic waves become degenerate under the action of an external force.

1063-7745/05/5005-0808$26.00 © 2005 Pleiades Publishing, Inc.

extreme mechanical forces for acoustic axes in crystals of arbitrary symmetry.

INITIAL EQUATIONS FOR ELASTIC WAVES PROPAGATING NEAR ACOUSTIC AXES IN A PIEZOELECTRIC CRYSTAL

The phase velocities v_α and the polarization vectors $\mathbf{U}^{(\alpha)}$ of elastic waves propagating in a piezoelectric crystal in a dc electric field $\mathbf{E}$ are described by the Green–Christoffel equation, linearized with respect to the magnitude of the external force [6, 12]:

$$(\Gamma_{ik}^{(0)} + \Gamma_{ik}^{(1)})U_k^{(\alpha)} = v_\alpha^2 U_i^{(\alpha)}, \quad \alpha = 1, 2, 3, \qquad (1)$$

where

$$\Gamma_{ik}^{(0)} = \frac{1}{\rho}\left(c_{ijkl}n_j n_l + \frac{1}{\varepsilon}e_i e_k\right),$$

$$\Gamma_{ik}^{(1)} = \frac{1}{\rho}(c^*_{ijklpq}d_{rpq} - e^*_{rijkl})n_j n_l E_r + 2\Gamma_{if}^{(0)}d_{rfk}E_r$$

for a mechanically free crystal and

$$\Gamma_{ik}^{(1)} = -\frac{1}{\rho}e^*_{rijkl}n_j n_l E_r$$

for a mechanically pressed crystal. Here, $\hat{\Gamma}^{(0)}$ is the Christoffel tensor of a piezoelectric medium at $E = 0$; $\hat{\Gamma}^{(1)}$ is the tensor describing the perturbation of the tensor $\hat{\Gamma}^{(0)}$ by the electric field; $e_i = e_{qir}n_q n_r$; $\varepsilon = \varepsilon_{qr}n_q n_r$;

$$c^*_{ijklpq} = c_{ijklpq} + \frac{1}{\varepsilon}\left[e_{tij}n_t e_{rklpq}n_r + e_{tkl}n_t e_{rijpq}n_r - \frac{1}{\varepsilon}(e_{tij}n_t e_{rkl}n_r f_{uvpq}n_u n_v)\right];$$

$$e^*_{rijkl} = e_{rijkl} - \frac{1}{\varepsilon}\left[e_{tij}n_t f_{rpkl}n_p + e_{tkl}n_t f_{rpij}n_p - \frac{1}{\varepsilon}(e_{tij}n_t e_{pkl}n_p \varepsilon_{uvr}n_u n_v)\right];$$

ρ is the density at $E = 0$; c_{ijkl}, c_{ijklpq}, d_{rpq}, e_{pkl}, e_{rijkl}, ε_{qr}, ε_{uvr}, and f_{rpij} are the linear and nonlinear elastic, piezoelectric, dielectric, and electrostriction tensors, determined according to [12, 13]; n_j are the components of the unit vector of the wave normal at $E = 0$; and E_r are the components of the vector of the external electric field.

The solution to Eq. (1) for the phase velocities of elastic waves propagating near an acoustic axis is the approximate expression[2] [6]

$$v_{1,2}(\mathbf{n}, \mathbf{E}) = v_{01} + [D_3 + (\Gamma_{11}^{(1)} + \Gamma_{22}^{(1)}) \mp \sqrt{(D_1 + (\Gamma_{11}^{(1)} - \Gamma_{22}^{(1)}))^2 + (D_2 + 2\Gamma_{12}^{(1)})^2}]/4v_{01}, \qquad (2)$$

where[3] $\Gamma_{\alpha\beta}^{(1)}(\mathbf{n}_0, \mathbf{E}) = U_i^{(0\alpha)}\Gamma_{ik}^{(1)}U_k^{(0\beta)}$ ($\alpha, \beta = 1, 2$) and $D_k(\Delta\mathbf{n})$ ($k = 1, 2, 3$) are the coefficients determined by the type of the initial acoustic axis [3, 5]. Here, we take as the zero-order approximation the solutions to Eq. (1) at $E = 0$ along $\mathbf{n}_0$: the phase velocities $v_\alpha(\mathbf{n}_0)|_{E=0} \equiv v_{0\alpha}$ ($v_{01} = v_{02} \neq v_{03}$) and the polarization vectors $\mathbf{U}^{(\alpha)}(\mathbf{n}_0)|_{E=0} \equiv \mathbf{U}^{(0\alpha)}$, where $\mathbf{U}^{(01)}$ and $\mathbf{U}^{(02)}$ are arbitrary unit vectors forming a right-handed triad with the vector $\mathbf{U}^{(03)}$. One of the perturbation parameters is the deviation of the wave normal $|\Delta\mathbf{n}| = |\mathbf{n} - \mathbf{n}_0| \ll 1$; the other parameter is the perturbation $|\Gamma_{\alpha\beta}^{(1)}/v_{01}^2| \ll 1$, introduced by the external force.

For a given propagation direction $\mathbf{n}$ of elastic waves, the components $\Gamma_{\alpha\beta}^{(1)}$ can be represented as [14]

$$\Gamma_{\alpha\beta}^{(1)} = U_i^{(0\alpha)}\Gamma_{ik}^{(1)}U_k^{(0\beta)} = (\mathbf{G}^{(\alpha\beta)} \times \mathbf{E}), \quad \alpha, \beta = 1, 2, 3, \qquad (3)$$

where

$$G_r^{(\alpha\beta)}(\mathbf{n}) = \left[\frac{1}{\rho}(c^*_{ijklpq}d_{rpq} - e^*_{rijkl})n_j n_l + 2v_{0\alpha}^2 d_{rik}\right]U_i^{(0\alpha)}U_k^{(0\beta)}$$

for a mechanically free crystal,

$$G_r^{(\alpha\beta)}(\mathbf{n}) = -\frac{1}{\rho}e^*_{rijkl}n_j n_l U_i^{(0\alpha)}U_k^{(0\beta)}$$

for a mechanically pressed crystal, and $v_{0\alpha} \equiv v_\alpha(\mathbf{n})|_{E=0}$ and $\mathbf{U}^{(0\alpha)} \equiv \mathbf{U}^{(\alpha)}(\mathbf{n})|_{E=0}$ are the solutions to Eq. (1) for the direction n at $E = 0$. Substituting (3) into (2), we obtain the following expression for the phase velocities of elastic waves propagating near an acoustic axis in a piezoelectric crystal in an external electric field:

$$v_{1,2}(\mathbf{n}, \mathbf{E}) = v_{01} + [D_3 + (\mathbf{h}^+ \times \mathbf{E}) \mp \sqrt{(D_1 + (\mathbf{h}^- \times \mathbf{E}))^2 + (D_2 + (\mathbf{f} \times \mathbf{E}))^2}]/4v_{01}.$$

[2] In what follows, we will speak about the twofold degeneracy of the phase velocities of elastic waves, while using the index $\alpha = 3$ for an nondegenerate wave, and assume that $v_1 \leq v_2$ and $\Delta v = v_2 - v_1 \geq 0$ for any $\mathbf{n}$.

[3] In this study, Latin indices are used to denote the components of vectors and tensors in an arbitrary basis and Greek indices are used in the basis $\{\mathbf{U}^{(01)}, \mathbf{U}^{(02)}, \mathbf{U}^{(03)}\}$.

Here, $\mathbf{h}^{\mp}(\mathbf{n}_0) = \mathbf{G}^{(11)} \mp \mathbf{G}^{(22)}$ and $\mathbf{f}(\mathbf{n}_0) = 2\mathbf{G}^{(12)} = 2\mathbf{G}^{(21)}$. Then, the difference in the phase velocities of elastic waves can be written as

$$\begin{aligned}\Delta v(\mathbf{n}, \mathbf{E}) &= v_2(\mathbf{n}, \mathbf{E}) - v_1(\mathbf{n}, \mathbf{E}) \\ &= \sqrt{(D_1 + (\mathbf{h}^- \times \mathbf{E}))^2 + (D_2 + (\mathbf{f} \times \mathbf{E}))^2}/2v_{01} \\ &= \sqrt{\mathbf{E}\hat{F}\mathbf{E} + 2(\mathbf{R}^+ \times \mathbf{E}) + D}/2v_{01},\end{aligned} \quad (4)$$

where $F_{ij}(\mathbf{n}_0) = h_i^- h_j^- + f_i f_j$, $\mathbf{R}^+(\Delta\mathbf{n}) = D_1\mathbf{h}^- + D_2\mathbf{f}$, and $D(\Delta\mathbf{n}) = D_1^2 + D_2^2$. Relation (4) is initial for solving the above-stated (see Introduction) extreme problems for a piezoelectric in an electric field.

EXTREME DIRECTIONS OF AN ELECTRIC FIELD FOR ELASTIC WAVES PROPAGATING IN THE DIRECTION OF THE INITIAL ACOUSTIC AXIS IN A PIEZOELECTRIC CRYSTAL

According to (4), the determination of the directions $\mathbf{m}$ of an external electric field (E = const) corresponding to the extreme difference in the velocities of elastic waves propagating along the initial acoustic axis at E = 0 is reduced to the problem[4] of determining the directions $\mathbf{m}$ at which the quadratic form $\mathbf{m}\hat{F}\mathbf{m}$ reaches extreme values. Solution of problems of this type is well known: the quadratic form $\mathbf{m}\hat{F}\mathbf{m}$, and, therefore, $\Delta v(\mathbf{m})|_{\mathbf{n}_0,\, E = \text{const}}$, reaches extreme values if the field $\mathbf{E}$ is directed along the eigenvectors of the tensor $\hat{F}$. Note that these extreme values are equal to the corresponding eigenvalues $\lambda \sim (\Delta v(\mathbf{m})|_{\mathbf{n}_0,\, E = \text{const}})^2$ of the tensor $\hat{F}$. Hence, the directions $\mathbf{m}$ of the external electric field that retain the initial acoustic axis will correspond to the eigenvalues $\lambda = 0$. It should be noted that the field $\mathbf{E}$, retaining the acoustic axis in the direction $\mathbf{n}_0$, changes the velocities of elastic waves by $\Delta v_{1,2} = (\mathbf{h}^+ \times \mathbf{E})/4v_{01}$ for all $\mathbf{n}$ near the degeneracy direction, including the direction $\mathbf{n}_0$.[5]

Let us find the extreme directions of the external electric field for different geometries of the vectors $\mathbf{h}^-$ and $\mathbf{f}$ in which they are not equal to zero simultaneously:[6]

(i) $\mathbf{f} \neq 0$, $\mathbf{h}^- = \mu\mathbf{f}$.[7] Let us introduce the Cartesian coordinate system with the unit vector $\mathbf{e}_3$ directed along the vector $\mathbf{f}$. In this system, $\mathbf{h}^- = \mu f_3 \mathbf{e}_3$, $\mathbf{f} = f_3\mathbf{e}_3$, and

$$\hat{F} = \begin{bmatrix} 0 & 0 & 0 \\ 0 & 0 & 0 \\ 0 & 0 & (1+\mu^2) f_3^2 \end{bmatrix}.$$

The tensor $\hat{F}$ has the eigenvalues $\lambda_1 = \lambda_2 = 0$, which corresponds to the eigenvector plane perpendicular to the vector $\mathbf{f}$, and $\lambda_3 > 0$, which corresponds to the eigenvector parallel to the vector $\mathbf{f}$. Thus, the field $\mathbf{E} \perp \mathbf{f}$ retains the initial acoustic axis. At $\mathbf{E} \parallel \mathbf{f}$, the value of $\Delta v(\mathbf{m})|_{\mathbf{n}_0,\, E = \text{const}}$, will be maximum.

(ii) $\boldsymbol{\omega} = [\mathbf{h}^- \times \mathbf{f}] \neq 0$. Let us introduce the Cartesian coordinate system with the unit vectors $\mathbf{e}_1$ and $\mathbf{e}_3$ directed along the vectors $\mathbf{h}^-$ and $\boldsymbol{\omega}$, respectively. In this system, $\mathbf{h}^- = h_1\mathbf{e}_1$, $\mathbf{f} = f_1\mathbf{e}_1 + f_2\mathbf{e}_2$, $\boldsymbol{\omega} = h_1 f_2 \mathbf{e}_3 = \omega_3\mathbf{e}_3$, and

$$\hat{F} = \begin{bmatrix} h_1^2 + f_1^2 & f_1 f_2 & 0 \\ f_1 f_2 & f_2^2 & 0 \\ 0 & 0 & 0 \end{bmatrix}.$$

One of the eigenvalues of the tensor $\hat{F}$ is $\lambda_3 = 0$ corresponding to the eigenvector parallel to the vector $\boldsymbol{\omega}$. Two other eigenvalues $\lambda_{1,2} > 0$ of the tensor $\hat{F}$ correspond to a pair of mutually orthogonal eigenvectors lying in the plane of the vectors $\mathbf{h}^-$ and $\mathbf{f}$. Thus, at $\mathbf{E} \parallel \boldsymbol{\omega}$, the acoustic axis in the direction $\mathbf{n}_0$ is retained. The value of $\Delta v(\mathbf{m})|_{\mathbf{n}_0,\, E = \text{const}}$ will be extreme when the field $\mathbf{E}$ coincides with one of the main directions of the tensor $\hat{F}$ in the plane of the vectors $\mathbf{h}^-$ and $\mathbf{f}$. In the case $\mathbf{h}^- \perp \mathbf{f}$, the quantity $\Delta v(\mathbf{m})|_{\mathbf{n}_0,\, E = \text{const}}$ reaches extreme values if the field $\mathbf{E}$ is directed along the vector $\mathbf{h}^-$ or $\mathbf{f}$. Under the additional condition $|\mathbf{h}^-| = |\mathbf{f}|$, the value of $\Delta v(\mathbf{m})|_{\mathbf{n}_0,\, E = \text{const}}$ is maximum at any $\mathbf{E} \perp \boldsymbol{\omega}$.

THE PROBLEM OF EXISTENCE OF AN INDUCED ACOUSTIC AXIS IN A GIVEN DIRECTION IN A PIEZOELECTRIC CRYSTAL

To determine the external electric field inducing an acoustic axis in a given direction $\mathbf{n}$ near the initial acoustic axis consists in finding the external force at which $\Delta v(\mathbf{E})|_{\mathbf{n} = \text{const}} = 0$. According to (4), this problem reduces to the solution of the following system of equations:

$$\begin{aligned} D_1 + (\mathbf{h}^- \times \mathbf{E}) &= 0, \\ D_2 + (\mathbf{f} \times \mathbf{E}) &= 0. \end{aligned} \quad (5)$$

Let us consider the solutions to this system of equations for different geometries of the vectors $\mathbf{h}^-$ and $\mathbf{f}$.

[4] For the direction of the initial acoustic axis, $D_1 = D_2 \equiv 0$.

[5] $\mathbf{h}^+ \equiv 0$ for the directions $\mathbf{n}_0$ with the types of symmetry 32, $\bar{4}$, $\bar{4}2m$, 422, $\bar{6}$, $\bar{6}m2$, 622, and 222 (class 23) at $E = 0$.

[6] $\mathbf{h}^- = \mathbf{f} \equiv 0$ for the directions $\mathbf{n}_0$ with the types of symmetry 4, 422, 4*mm*, 6, 622, 6*mm* at $E = 0$.

[7] It can be proved that, in this geometry of the vectors $\mathbf{h}^-$ and $\mathbf{f}$, there is always a pair of vectors $\mathbf{U}^{(01)}$, $\mathbf{U}^{(02)}$ for which $\mathbf{f} \neq 0$.

(i) $\mathbf{f} \neq 0$, $\mathbf{h}^- = \mu\mathbf{f}$. In the Cartesian coordinate system with the unit vector $\mathbf{e}_3$ directed along the vector $\mathbf{f}$, system of equations (5) takes the form

$$D_1 + \mu f_3 E_3 = 0,$$
$$D_2 + f_3 E_3 = 0.$$

This system has the solution

$$\mathbf{E} = -\frac{D_2}{f_3}\mathbf{e}_3, \quad (6)$$

provided that

$$D_1 - \mu D_2 = 0. \quad (7)$$

According to (4), the field $\mathbf{E} \perp \mathbf{f}$ does not affect the value of $\Delta v(\mathbf{E})|_{\mathbf{n}=\text{const}}$. Therefore, expression (6) determines the minimum electric field

$$\mathbf{E}_{\min} = -\frac{D_2}{|\mathbf{f}|^2}\mathbf{f},$$

inducing an acoustic axis in the direction $\mathbf{n}$, for which condition (7) is satisfied.

At $E > E_{\min}$, an acoustic axis will be induced in the direction $\mathbf{n}$ if the field $\mathbf{E}$ makes angles $\theta_E = \arccos(E_{\min}/E)$ with the vector $\mathbf{f}$ at $D_2 < 0$ and $\theta_E = \pi - \arccos(E_{\min}/E)$ at $D_2 > 0$. For a given E, the angle θ_E sets a cone of directions of the field $\mathbf{E}$.

(ii) $\boldsymbol{\omega} = [\mathbf{h}^- \times \mathbf{f}] \neq 0$. In the Cartesian coordinate system with the unit vectors $\mathbf{e}_1$ and $\mathbf{e}_3$ directed along the vectors $\mathbf{h}^-$ and $\boldsymbol{\omega}$, respectively, system of equations (5) takes the form

$$D_1 + h_1 E_1 = 0,$$
$$D_2 + f_1 E_1 + f_2 E_2 = 0.$$

The solution to this system is

$$\mathbf{E} = -\frac{D_1 f_2}{\omega_3}\mathbf{e}_1 + \frac{D_1 f_1 - D_2 h_1}{\omega_3}\mathbf{e}_2. \quad (8)$$

As follows from (4), the field $\mathbf{E} \parallel \boldsymbol{\omega}$ does not affect the value of $\Delta v(\mathbf{E})|_{\mathbf{n}=\text{const}}$. Therefore, expression (8) determines the minimum electric field inducing an acoustic axis in the given direction $\mathbf{n}$.

Formula (8) can be written as

$$\mathbf{E}_{\min} = -\hat{F}^{-1}\mathbf{R}^+, \quad (9)$$

where

$$\hat{F}^{-1} = \frac{1}{|\boldsymbol{\omega}|^2}\begin{bmatrix} f_2^2 & -f_1 f_2 & 0 \\ -f_1 f_2 & h_1^2 + f_1^2 & 0 \\ 0 & 0 & 0 \end{bmatrix}$$

or

$$\mathbf{E}_{\min} = [\mathbf{R}^- \times \boldsymbol{\omega}]/|\boldsymbol{\omega}|^2, \quad (10)$$

where $\mathbf{R}^- = D_2\mathbf{h}^- - D_1\mathbf{f}$. In particular, it follows from (9) that, when $\mathbf{h}^- \perp \mathbf{f}$ and $|\mathbf{h}^-| = |\mathbf{f}|$, an acoustic axis is induced in the given direction $\mathbf{n}$ at $\mathbf{E}_{\min} = -\mathbf{R}^+/|\mathbf{h}^-|^2$.

It can be proved that if the initial acoustic axis corresponds to conical or tangential degeneracy, the direction of the field $\mathbf{E}_{\min}$ depends only on the azimuthal angle of the direction $\mathbf{n}$.

With the consideration that $\mathbf{R}^\mp \neq 0$ for all $\mathbf{n}$ in the vicinity of the initial acoustic axis, it follows from (9) and (10) that an acoustic axis may be induced in any direction $\mathbf{n}$. Note that for all $\mathbf{n}$ the field $\mathbf{E}_{\min}$ will lie in the plane of the vectors $\mathbf{h}^-$ and $\mathbf{f}$.

For $E > E_{\min}$, an acoustic axis will be induced in the direction $\mathbf{n}$ at $\mathbf{E} = \mathbf{E}_{\min} \pm \sqrt{E^2 - E_{\min}^2}\,\boldsymbol{\omega}/|\boldsymbol{\omega}|$. For a given E, we will have a pair of directions of the field $\mathbf{E}$, symmetric with respect to the plane of the vectors $\mathbf{h}^-$ and $\mathbf{f}$.

ACOUSTIC AXES IN THE PIEZOELECTRIC CRYSTALS $Bi_{12}GeO_{20}$, $Bi_{12}SiO_{20}$, $La_3Gi_5SiO_{14}$, AND $LiNbO_3$ IN AN EXTERNAL ELECTRIC FIELD

The most complete experimental data on the nonlinear electromechanical properties were obtained for crystals of $Bi_{12}GeO_{20}$ and $Bi_{12}SiO_{20}$ (class 23) [13], $La_3Ga_5SiO_{14}$ (class 32) [15], and $LiNbO_3$ (class 3m) [16]. Let us consider the acoustic axes in these crystals. The vectors $\mathbf{n}$ and $\mathbf{E}$, unless otherwise noted, are set in the crystallophysical coordinate system X_i by the Cartesian coordinates n_i and E_i or spherical angles (φ, θ) and (φ_E, θ_E). (The angles θ and θ_E are counted from the X_3 axis.) All calculations were performed for the field $E = 10^7$ V/m. For convenience of comparison of the values of $\Delta v(\mathbf{n}_0, \mathbf{E})$ for different crystals, we introduced the coefficient $\alpha_{\Delta v} = \frac{1}{v_{01}}\left(\frac{\Delta v(\mathbf{n}_0, \mathbf{E})}{\Delta E}\right)_{\Delta\varepsilon \to 0}$.

Let us first consider the acoustic axis of tangential degeneracy with the Poincaré index $n = 1$, directed along the [001] axis in $Bi_{12}GeO_{20}$ and $Bi_{12}SiO_{20}$ crystals. For this acoustic axis, $\mathbf{h}^\mp = 0$ and $\mathbf{f} \parallel [001]$. The electric field $\mathbf{E} \perp [001]$ retains the initial acoustic axis; in this case, $\Delta v_{1,2} \equiv 0$. The difference in the velocities of transverse waves propagating along the [001] axis is maximum at $\mathbf{E} \parallel [001]$. The field $\mathbf{E} \parallel [001]$ leads to the splitting of the initial degeneracy into a pair of conical degeneracies with $n = 1/2$, whose azimuthal angles are $\varphi = \{\pm\}\,\pi/4 + \pi n$. The angle θ between the initial and induced acoustic axes is related to the field $\mathbf{E}_{\min}$ as follows: $\mathbf{E}_{\min} = (0, 0, \{\mp\}\,E_0 \sin^2\theta)$. The calculated values of E_0, of half-angle of splitting θ, and of coefficient $\alpha_{\Delta v}$

Table 1. Acoustic axes with the Poincaré index $n = 1$ in $Bi_{12}GeO_{20}$ and $Bi_{12}SiO_{20}$ crystals in an external electric field

Crystal	Mechanical state	E_0, 10^9 V/m	θ, deg	$\alpha_{\Delta v}$, 10^{-10} m/V
$Bi_{12}GeO_{20}$	mechanically free	4.14	5.64	1.76
	mechanically pressed	1.26	10.22	5.76
$Bi_{12}SiO_{20}$	mechanically free	3.15	6.46	2.58
	mechanically pressed	4.34	5.5	1.88

Table 2. Acoustic axes with the Poincaré index $n = -1/2$ in $LiNbO_3$, $La_3Ga_5SiO_{14}$, $Bi_{12}GeO_{20}$, and $Bi_{12}SiO_{20}$ crystals in an external electric field

Crystal	Mechanical state	E_0, 10^9 V/m	β, deg	θ, deg	$\lvert\Delta v_{1,2}\rvert$, m/V	$\alpha_{\Delta v}$, 10^{-10} m/V
$LiNbO_3$	mechanically free	1.38		0.41	2.08	2.17
	mechanically pressed	0.89		0.65	3.04	3.38
$La_3Ga_5SiO_{14}$	mechanically free	63.5		0.01	0	0.08
	mechanically pressed	16.6		0.03	0	0.32
$Bi_{12}SiO_{20}$	mechanically free	8.84	−76.16	0.06	0.02	0.65
	mechanically pressed	12.5	−86.33	0.05	0.64	0.46
$Bi_{12}GeO_{20}$	mechanically free	8.3	−67.44	0.07	0.28	0.66
	mechanically pressed	5.61	−27.1	0.1	0.87	0.97

are listed in Table 1. Note that the mechanical state of a $Bi_{12}GeO_{20}$ crystal significantly affects the behavior of the acoustic axes of tangential degeneracy in an external electric field.

Let us consider conically degenerate acoustic axes with the Poincaré index $n = -1/2$, directed at $E = 0$ along the axes 3 in $LiNbO_3$, $La_3Ga_5SiO_{14}$, $Bi_{12}GeO_{20}$, and $Bi_{12}SiO_{20}$ crystals. For these axes, the vectors $\mathbf{n}_0$, $\mathbf{h}^-$, and $\mathbf{f}$ are mutually orthogonal and $|\mathbf{h}^-| = |\mathbf{f}|$; note that $\mathbf{h}^+ \equiv 0$ in $La_3Ga_5SiO_{14}$ and $\mathbf{h}^+ \parallel 3$ in other crystals. The field $\mathbf{E} \parallel 3$ retains the initial acoustic axis; in this case, the difference $\Delta v_{1,2}$ in the velocities of transverse waves remains constant only in $La_3Ga_5SiO_{14}$. The difference in the velocities of transverse waves propagating along the axis 3 is maximum at $\mathbf{E} \perp 3$. The field $\mathbf{E} \perp 3$ also causes maximum deviation of the acoustic axis from its initial position. The direction of the field $\mathbf{E}_{\min}$ and the azimuthal angle of the induced acoustic axis are related as follows:[8] $\varphi_E = \varphi$ in $LiNbO_3$, $\varphi_E = \varphi + \pi/2$ in $La_3Ga_5SiO_{14}$, and $\varphi_E = \varphi + \beta + \pi$ in $Bi_{12}SiO_{20}$ and $Bi_{12}GeO_{20}$. The magnitude of the field $\mathbf{E}_{\min}$ is determined by the relation $E_{\min} = E_0 \sin\theta$ for all crystals. The calculated values of E_0, the angle β, the angle of displacement θ, the quantity $|\Delta v_{1,2}|$, and the coefficient $\alpha_{\Delta v}$ are listed in Table 2. It should be noted that the mechanical state of a $Bi_{12}GeO_{20}$ crystal affects the orientation of the field $\mathbf{E}_{\min}$. However, the displacement of acoustic axes is small in all crystals. The above calculations are in agreement with the data of [6, 8, 13].

Finally, let us consider the behavior of the conically degenerate acoustic axes with the Poincaré index $n = 1/2$ in $LiNbO_3$ crystals ($\mathbf{n}_0 \parallel m$: $\varphi = 90°$ and $\theta = 69.77°$) and $La_3Ga_5SiO_{14}$ crystals ($\mathbf{n}_0 \perp 2$: $\varphi = 90°$ and $\theta = 132.71°$). For these axes, $\mathbf{h}^- \perp \mathbf{f}$ and $|\mathbf{h}^-| \neq |\mathbf{f}|$; $\mathbf{h}^\mp \parallel m$ and $\mathbf{f} \perp m$ in $LiNbO_3$ and $\mathbf{h}^\mp \parallel 2$ and $\mathbf{f} \perp 2$ in $La_3Ga_5SiO_{14}$. The electric field $\mathbf{E} \parallel [\mathbf{h}^- \times \mathbf{f}]$ retains the initial acoustic axis, changing the velocities of transverse waves only in $LiNbO_3$, ($|\Delta v_{1,2}| = 2.04$ and 1.75 m/s in mechanically free and mechanically pressed crystals, respectively.) The maximum difference in the velocities of transverse waves propagating in the direction $\mathbf{n}_0$ is reached at $\mathbf{E} \parallel \mathbf{f}$ in both crystals. The field $\mathbf{E}_{\min}$ is described as follows:[9] $E_1 = E_{01}n_1$ and $E_2 = E_{02}n_2$ for $LiNbO_3$, $E_1 = E_{02}n_2$ and $E_2 = E_{01}n_1$ for $La_3Ga_5SiO_{14}$, and

$$E_{\min} = \sqrt{E_{01}^2 \cos^2\varphi + E_{02}^2 \sin^2\varphi}\sin\theta \qquad (11)$$

for both crystals. It follows from (11) that, for a given value of a external force, the extrema of the angle of displacement of the initial acoustic axis will be observed in the directions set by the azimuthal angles $\varphi = \pi n$ at $\mathbf{E} \parallel \mathbf{f}$ (the angle θ_1) and $\varphi = \pi/2 + \pi n$ at $\mathbf{E} \parallel \mathbf{h}^-$

[8] Here, the coordinate system $x_1 \parallel [110]$, $x_3 \parallel [111]$ ($x_3 \parallel \mathbf{n}_0$) is introduced for $Bi_{12}SiO_{20}$ and $Bi_{12}GeO_{20}$ crystals.

[9] Here, the coordinates of the vector $\mathbf{n}$ are set in the coordinate systems $x_1 \parallel X_1$, $x_3 \parallel \mathbf{n}_0$, whereas the coordinates of the vector $\mathbf{E}_{\min}$ are set in the two-dimensional coordinate systems $x_1' \parallel X_1$, $x_2' \parallel \mathbf{h}^-$ (in $LiNbO_3$) and $x_2' \parallel \mathbf{f}$ (in $La_3Ga_5SiO_{14}$).

Table 3. Acoustic axes with the Poincaré index $n = 1/2$ in $LiNbO_3$ and $La_3Ga_5SiO_{14}$ crystals in an external electric field

Crystal	Mechanical state	E_{01}, 10^9 V/m	E_{02}, 10^9 V/m	θ_1, deg	θ_2, deg	$\mathbf{h}^-$	$\mathbf{f}$	$\alpha_{\Delta v}$, 10^{-10} m/V
$LiNbO_3$	mechanically free	–1.13	4.86	0.51	0.12	$\varphi = 90°$ $\theta = 95.3°$		1.54
	mechanically pressed	–1.81	2.29	0.32	0.25	$\varphi = 90°$ $\theta = 90.55°$	$\varphi = 0°$ $\theta = 90°$	0.96
$La_3Ga_5SiO_{14}$	mechanically free	5.42	–118	0.11	~0	$\varphi = 0°$ $\theta = 90°$	$\varphi = -90°$ $\theta = 117.88°$	0.82
	mechanically pressed	4.67	87.2	0.12	0.01	$\varphi = 180°$ $\theta = 90°$	$\varphi = -90°$ $\theta = 113.72°$	0.95

(the angle θ_2). The calculated values of E_{01} and E_{02}, the directions of the vectors $\mathbf{h}^-$ and $\mathbf{f}$, the angles θ_1 and θ_2, and the coefficient $\alpha_{\Delta v}$ are listed in Table 3.

CONCLUSIONS

The approach developed here on the basis of separate description of nonlinear electromechanical properties of a piezoelectric medium in a specified direction and the external force made it possible to obtain a number of general results describing the behavior of an arbitrary acoustic axis in an external electric field.

Within an approximation that is linear in the magnitude of an external force, some directions of an external electric field retaining the initial acoustic axis always exist. The occurrence of an induced acoustic axis is possible in any direction near the initial acoustic axis if $[\mathbf{h}^- \times \mathbf{f}] \neq 0$ and in the directions satisfying condition (7) if $\mathbf{h}^- = \mu\mathbf{f}$. Note that the field $\mathbf{E}$ at which an acoustic axis is induced in a given direction has a single value provided that the external force (the field $\mathbf{E}_{min}$) is minimum.

It should also be noted that the geometry of the vectors $\mathbf{h}^-$ and $\mathbf{f}$ is independent of the type of the initial acoustic axis. For example, the geometry of the vectors $\mathbf{h}^-$ and $\mathbf{f}$ is the same for the axes 3 and $\bar{6}$; however, the initial acoustic axes are conically and tangentially degenerate in the former and latter cases, respectively. The geometry $\mathbf{h}^- = \mu\mathbf{f}$ is implemented for the acoustic axes having the symmetries of the direction 222 (class 23), $\bar{4}2m$, and $\bar{4}$ at $E = 0$.

The results of the calculations show (Tables 1–3) that the acoustic axes of tangential degeneracy are more sensitive to an electric field in comparison with the axes of conical degeneracy.

REFERENCES

1. V. I. Alshits and E. Lothe, Kristallografiya **24** (4), 672 (1979) [Sov. Phys. Crystallogr. **24**, 387 (1979)].
2. V. I. Alshits and E. Lothe, Kristallografiya **24** (4), 683 (1979) [Sov. Phys. Crystallogr. **24**, 393 (1979)].
3. V. I. Alshits and A. L. Shuvalov, Kristallografiya **29** (4), 629 (1984) [Sov. Phys. Crystallogr. **29**, 373 (1984)].
4. V. I. Alshits, A. V. Sarychev, and A. L. Shuvalov, Zh. Éksp. Teor. Fiz. **89** (3), 922 (1985) [Sov. Phys. JETP **62**, 531 (1985)].
5. V. I. Alshits and A. L. Shuvalov, Kristallografiya **33** (1), 7 (1988) [Sov. Phys. Crystallogr. **33**, 1 (1988)].
6. V. I. Alshits and A. L. Shuvalov, in *Physical Crystallography*, Ed. by B. K. Vaĭnshteĭn and L. A. Shuvalov (Nauka, Moscow, 1992) [in Russian].
7. V. N. Belyĭ, B. B. Sevruk, and A. G. Khatkevich, Kristallografiya **31** (1), 5 (1986) [Sov. Phys. Crystallogr. **31**, 1 (1986)].
8. B. P. Sorokin, Yu. I. Kokorin, S. I. Burkov, and K. S. Aleksandrov, Kristallografiya **31** (4), 706 (1986) [Sov. Phys. Crystallogr. **31**, 416 (1986)].
9. B. D. Zaĭtsev, I. E. Kuznetsova, and A. L. Shuvalov, Kristallografiya **41** (6), 1050 (1996) [Crystallogr. Rep. **41**, 997 (1996)].
10. A. E. Volotskiĭ, B. D. Zaĭtsev, V. I. Neĭman, *et al.*, Akust. Zh. **36** (5), 840 (1990) [Sov. Phys. Acoust. **36**, 470 (1990)].
11. B. P. Sorokin, P. P. Turchin, and D. A. Glushkov, Fiz. Tverd. Tela (St. Petersburg) **36** (10), 2907 (1994) [Phys. Solid State **36**, 1545 (1994)].
12. V. E. Lyamov, *Polarization Effects and Anisotropy Interaction of Acoustic Waves in Crystals* (Mosk. Gos. Univ., Moscow, 1983) [in Russian].
13. M. P. Zaĭtseva, Yu. I. Kokorin, Yu. M. Sandler, *et al.*, in *Nonlinear Electromechanical Properties of Acentric Crystals*, Ed. by K. S. Aleksandrov (Nauka, Novosibirsk, 1986) [in Russian].
14. A. N. Zabelin and N. V. Perelomova, Izv. Akad. Nauk **57** (6), 98 (1993).
15. K. S. Aleksandrov, B. P. Sorokin, P. P. Turchin, and D. A. Glushkov, Ferroelectr. Lett. Sect. **14** (5–6), 115 (1992).
16. Y. Cho and K. Yamanouchi, J. Appl. Phys. **61** (3), 875 (1987).

Translated by Yu. Sin'kov

Crystallography Reports, Vol. 50, No. 5, 2005, pp. 814–816. Translated from Kristallografiya, Vol. 50, No. 5, 2005, pp. 876–879.

LATTICE DYNAMICS AND PHASE TRANSITIONS

Improper Ferromagnetic Phase Transitions in Crystals

S. V. Grigor'ev and B. M. Darinskiĭ

Voronezh State Technical University,
Moskovskiĭ pr. 14, Voronezh, 394026 Russia
e-mail: darinskii@math.vsu.ru

Received November 19, 2004

Abstract—A complete set of possible improper phase transitions leading to polarization and magnetization of crystals is found from tensor bases of representations of the black-and-white point group of crystal symmetry by using the multiplication table of irreducible representations. The dependences of the secondary order parameter on the primary order parameter are presented for different classes of the symmetry group. © *2005 Pleiades Publishing, Inc.*

The concept of improper phase transitions was introduced in study of ferroelectric crystals. Indenbom was the first to point out to the possibility of occurrence of polarization as a result of a phase transition with enlargement of the crystal unit cell [1]. The term *improper phase transitions* was introduced in [2]. A great number of studies are devoted to the experimental and theoretical study of regularities of improper phase transitions (see, for example, [3–7]). As a result, in the 1970s, the physics of improper phase transitions became a kind of a narrow-range field in ferroelectricity.

In most crystals undergoing improper phase transitions, the amplitude of some optical mode of atomic vibrations serves as the primary order parameter. The secondary order parameter is the polarization vector. However, as shown in [8], there are crystal classes of the white group, in which macroscopic characteristics, such as components of the deformation tensor, the polarization vector, or the angles of rotation of atomic groups in a crystal cell, are the primary order parameters. Such improper phase transitions occur without changing the number of atoms in the unit cell. Possible directions of the vector of spontaneous polarization after such improper phase transitions were shown in [9]. To study the symmetry properties of the electrical and magnetic characteristics, it is necessary to use the black-and-white crystal group [10]. The crystallographic classes of black-and-white point groups, allowing the simultaneous occurrence of macroscopic magnetic and electrical moments, were noted by Shuvalov and Belov [11]. The question of possible improper phase transitions has not been raised because of the evident absence in the gray group of the invariant represented by the product of a component of the *t*-odd axial magnetization vector and the square of some other order parameter. As will be shown below, invariants of this type are possible in a black-and-white group. This fact suggests the existence of improper phase transitions in crystals. In this study, we will point to the crystal classes of the black-and-white group in which transitions leading to the occurrence of polarization and magnetization in crystals are possible.

We have considered all crystallographic classes of the black-and-white symmetry group. For each class, the tensor bases of representations are indicated and the representations with bases containing the components of the polar polarization vector and the axial magnetization vector are selected. Using the multiplication table of representations, we obtained the invariants responsible for the occurrence of improper phase transitions. The results are listed in the table.

The first column of the table contains the standard notation of groups and representations (in italics) in which magnetoelectric phase transitions are possible. In the second column, the components of the primary order parameter are listed. If this basis contains polarization components, one has to take into account that near the phase-transition point these components should obey the linear relations

$$P_i = C_{ij}M_j. \quad (1)$$

The coefficients C_{ij} in these relations are the tabular characteristics of a crystal, similar to the components of the dielectric permittivity or elastic moduli. In the third column, the invariants that make improper phase transitions possible are listed. The fourth column contains the components of the secondary order parameter. P_i and M_i are the components of the polarization and magnetization vectors, respectively.

The table shows that the vector of the primary order parameter in crystals belonging to the tetragonal system lies in the *xy* plane, and the secondary components of the order parameter are vectors directed along the fourfold axis. The primary order parameter contains electric and magnetic components for all classes of the tetragonal system, except for the $D_{4h}(D_{2h})$ group. The

Primary and secondary order parameters for improper phase transitions in crystals with the symmetry of the black-and-white point group

Group Representation	Primary order parameter	Invariants	Components of the secondary order parameter
		Tetragonal system	
$C_4(C_2)$ 4' E	(P_1, P_2), (M_1, M_2)	$M_3P_1P_2$, $M_3(P_1^2 - P_2^2)$	M_3
$S_4(C_2)$ $\bar{4}'$ E	(P_1, P_2), (M_1, M_2)	$M_3(P_1^2 - P_2^2)$, $P_3M_1^2 - M_2^2$	M_3, P_3
$C_{4h}(C_{2h})$ $4'/m$ E_u	(P_1, P_2), (M_1, M_2)	$M_3(P_1^2 - P_2^2)$	M_3
$D_4(D_2)$ 4'22' E	(P_1, P_2), (M_1, M_2)	$P_3P_1P_2$, $M_3M_1M_2$	P_3, M_3
$C_{4v}(C_{2v})$ 4'mm' E	(P_1, P_2), (M_1, M_2)	$M_3P_1P_2$	M_3
$D_{2d}(D_2)$ $\bar{4}'2m'$ E	(P_1, P_2), (M_1, M_2)	$M_3P_1P_2$, $P_3M_1M_2$	P_3, M_3
$D_{2d}(C_{2v})$ $\bar{4}'2'm$ E	(P_1, P_2), (M_1, M_2)	$M_3P_1P_2$, $P_3M_1M_2$	P_3, M_3
$D_{2d}(S_4)$ $\bar{4}2'm'$ E	(P_1, P_2), (M_1, M_2)	$P_3M_1M_2$	P_3
$D_{4h}(D_{2h})$ 4'/mmm' E_u	(P_1, P_2)	$M_3P_1P_2$	M_3
		Trigonal system	
$D_3(C_3)$ 32' E	(P_1, P_2), (M_1, M_2)	$P_3(M_1^3 - 3M_1M_2^2)$	P_3
		Hexagonal system	
$C_6(C_3)$ 6' E_1	(P_1, P_2)	$2M_1P_1P_2 + M_2(P_1^2 - P_2^2)$, $M_1(P_1^2 - P_2^2) - M_2P_1P_2$, $M_3(P_1^3 - 3P_1P_2^2)$, $M_3(3P_1^2P_2 - P_2^3)$	M_1, M_2, M_3
$D_6(D_3)$ 6'22' E_1	(P_1, P_2)	$M_3(3P_1^2P_2 - P_2^3)$	M_3
$D_6(D_3)$ 6'22' E_2	(M_1, M_2)	$M_1^3 - 3M_1M_2^2$, $P_3(3M_1^2M_2 - M_2^3)$	P_3
$C_{6v}(C_{3v})$ 6'mm' E_1	(P_1, P_2)	$M_3(P_1^3 - 3P_1P_2^2)$	M_3
		Cubic system	
$O(T)$ 4'32' T_1	(P_1, P_2, P_3)	$M_3P_1P_2 + M_2P_1P_3 + M_1P_2P_3$	M_1, M_2, M_3
$O_h(T_h)$ $m3m$' T_{1u}	(P_1, P_2, P_3)	$M_3P_1P_2 + M_2P_1P_3 + M_1P_2P_3$	M_1, M_2, M_3
$T_d(T)$ 4'3m' T_2	(P_1, P_2, P_3), (M_1, M_2, M_3)	$M_3P_1P_2 + M_2P_1P_3 + M_1P_2P_3$, $P_3M_1M_2 + P_2M_1M_3 + P_1M_2M_3$	M_1, M_2, M_3, P_1, P_2, P_3

secondary order parameter may be one- or two-component, depending on the crystallographic class. The symmetry limitations in crystals of the $D_{4h}(D_{2h})$ group lead to accompaniment of the purely ferroelectric phase transition by the occurrence of magnetization through the mechanism of improper phase transitions. For all groups of the tetragonal system, a usual quadratic dependence of the secondary order parameter on the components of the primary order parameter is fulfilled, which, as is well known, leads to the linear temperature dependence of the secondary order parameter.

In crystals of the hexagonal system, the third component of the secondary order parameter has a cubic dependence on the components of the primary order parameter. This circumstance leads to a power temperature dependence of the secondary order parameter with an exponent of 3/2. There is the $C_6(C_3)$ group, for which the magnetic components M_1 and M_2 of the secondary order parameter obey a quadratic dependence on similar components of the polarization vector, which is the primary order parameter. The third magnetic component in the same crystals has a cubic dependence on the same components. The phase transitions in the $D_6(D_3)$ and $C_{6v}(C_{3v})$ groups are ferroelectric with respect to the primary order parameter and magnetic with respect to the secondary order parameter. An opposite situation occurs in the other representation of the $D_6(D_3)$ group: the primary order parameter proves to be magnetic and the secondary order parameter is electrical.

There are three classes of crystals belonging to the cubic system, in which improper magnetic phase transitions are possible. The first two groups of this system, listed in the table, allow improper magnetic phase transitions, in which the primary and secondary order parameters are the components of the polarization and magnetization vectors, respectively. The secondary order parameter shows a usual quadratic dependence on the components of the primary order parameter. We should note a specific feature of these phase transitions. If a polarization vector directed along any crystallographic axis arises as a result of the main ferroelectric phase transition, the secondary component is zero. For other directions of the spontaneous-polarization vector, a magnetic effect occurs. Symmetry analysis shows that ferroelectric second-order phase transitions may lead to the occurrence of spontaneous-polarization vectors directed along the sides or body diagonals of the unit cell. In the first case, a crystal is not magnetized. In the second case, magnetization directed along the body diagonal occurs. If a crystal undergoes a first-order phase transition with the formation of a polarization vector directed along a cube face diagonal, the magnetization vector is directed along the edge normal to this face.

In conclusion, let us state the main results of this study. Crystals with the symmetry of the point black-and-white group allow improper phase transitions involving the components of the polarization and magnetization vectors as the primary and secondary order parameters. Improper phase transitions are allowable in all systems with high-order symmetry axes. In crystals belonging to the tetragonal symmetry, the dependence of the third component of the secondary order parameter on the components of the primary order parameter is quadratic. In crystals of the hexagonal and trigonal systems, this dependence is cubic. Evidently, the same dependence will be retained for the corresponding space groups. A similar dependence for the components in the *xy* plane is quadratic.

ACKNOWLEDGMENTS

This study was supported in part by the Civilian Research and Development Foundation (USA) and the Ministry of Education of the Russian Federation (grant no. VZ-010).

REFERENCES

1. B. L. Indenbom, Kristallografiya **5** (2), 115 (1960) [Sov. Phys. Crystallogr. **5**, 106 (1960)].
2. V. Dvorak and J. Petzelt, Phys. Lett. A **35**, 209 (1971).
3. K. Aizu, Phys. Rev. A **136**, 753 (1964).
4. Yu. M. Gufan and P. V. Sakhnenko, Fiz. Tverd. Tela (Leningrad) **14**, 1915 (1972) [Sov. Phys. Solid State **14**, 1660 (1972)].
5. F. P. Levanyuk and D. G. Sannikov, Usp. Fiz. Nauk **132**, 693 (1980) [Sov. Phys. Usp. **23**, 868 (1980)].
6. P. Toledano and J.-C. Toledano, Phys. Rev. B **14**, 3097 (1976).
7. P. Toledano and J.-C. Toledano, Phys. Rev. B **25**, 1946 (1982).
8. V. Janovec, V. Dvorac, and J. Petzelt, Czech. J. Phys. B **25**, 1362 (1975).
9. V. A. Adamov, B. M. Darinsky, A. A. D'jachenko, and L. A. Shuvalov, J. Korean Phys. Soc. **32**, S740 (1998).
10. I. S. Zheludev, Izv. Akad. Nauk SSSR **24** (11), 1437 (1960).
11. L. A. Shuvalov and N. V. Belov, Kristallografiya **7** (2), 192 (1962) [Sov. Phys. Crystallogr. **7**, 150 (1962)].

Translated by T. Dmitrieva

Crystallography Reports, Vol. 50, No. 5, 2005, pp. 817–822. Translated from Kristallografiya, Vol. 50, No. 5, 2005, pp. 880–886.

LATTICE DYNAMICS AND PHASE TRANSITIONS

Polymorphic Transformations in Alkali Halide Crystals at Temperatures Different from Absolute Zero

S. V. Karpenko*, A. Kh. Kyarov, and A. I. Temrokov***

** Research Institute of Applied Mathematics and Automation, Kabardino-Balkar Scientific Center, Russian Academy of Sciences, ul. Shortanova 89, Nalchik, 360000 Russia*
e-mail: sv_karpenko@mail333.com
*** Kabardino-Balkar State University, ul. Chernyshevskogo 173, Nalchik, 360004 Russia*
Received October 26, 2004

Abstract—The polymorphic transformations in alkali halide crystals at temperatures above absolute zero are numerically simulated using the proposed method. © *2005 Pleiades Publishing, Inc.*

INTRODUCTION

Under normal conditions, alkali halides have a crystal lattice of the NaCl type (structure *B*1). In all such compounds, an increase in the pressure leads to reconstructive first-order phase transitions to phases with the CsCl-type structure (structure *B*2) [1–3]. The relative simplicity of experimental investigations has made it possible to gain a deeper insight into the dynamics of these transitions and to reveal the origin of the cluster structures of both phases [4–6]. At present, investigation into the structural phase transitions (including the *B*1–*B*2 transitions) has been a very important problem. However, the majority of theoretical studies have been concerned with analyzing the properties of similar transformations in infinite crystals at absolute zero [7–10]. The validity of this approach is supported primarily by the small surface contribution to the thermodynamic potential of the crystal. However, the inclusion of the surface effects provides a means for revealing more subtle phenomena that accompany phase transitions between allotropic modifications of the compound. It is this size effect that manifests itself in *B*1–*B*2 transformations in ionic compounds of the composition M^+X^-. The *B*1–*B*2 transition in small-sized samples of alkali halide compounds was considered in detail in our earlier works [11, 12]. The purpose of this study was to examine the *B*1–*B*2 transformation in ionic crystals at temperatures different from 0 K. Special attention was focused on the construction of the temperature dependences of the phase transition pressure.

FORMULATION OF THE PROBLEM

Let us consider polymorphic transformations in ionic crystals at temperatures different from 0 K. In this case, the thermodynamic potential obtain in our previous study [11] for an infinite crystal,

$$G_{B_i} = \sum_{k=1}^{7} N_k^{(i)} U_k^{(i)}(a_k^{(i)} R^{(i)}) - V^{(i)} \frac{\partial}{\partial V^{(i)}} \left[\sum_{k=1}^{7} N_k^{(i)} U_k^{(i)}(a_k^{(i)} R^{(i)}) \right] - \frac{\alpha_\mu^{(i)}}{R^{(i)}},$$

should be complemented by the term $G_S = -TS$ describing the contribution of the configurational entropy. In the above expression, the index i numbers the phases *B*1 and *B*2. Note that the energy of the non-Coulomb interaction of ions with the pair potential $U(R)$ is virtually independent of the temperature, because the electron gas is degenerate at the temperatures $T < T_m$ under consideration. The temperature contributions to the thermodynamic potential can be taken into account through the replacement of the Madelung constant in the Coulomb energy of the lattice by the parameter K (hereafter, this parameter will be referred to as the temperature parameter of the Coulomb interaction) that characterizes the Coulomb energy and depends on the temperature: $K = K(T)$. Note that $K \longrightarrow \alpha_\mu$ at $T \longrightarrow 0$ K. Therefore, the Coulomb contribution to the thermodynamic potential of the crystal is governed by the Madelung constant of the structure $G^{(\text{Coulomb})} = -\dfrac{\alpha_\mu}{R}$ at $T =$ 0 K and $G^{(\text{Coulomb})} = -\dfrac{K_T(T)}{R}$ at temperatures different from absolute zero.

The temperature parameter of the Coulomb interaction as a function of the temperature is calculated by the molecular dynamics method. Now, we consider the specific features of the application of this method to the investigation of structural phase transformations in ionic crystals.

APPLICATION OF THE MOLECULAR DYNAMICS METHOD TO THE INVESTIGATION OF THE *B*1–*B*2 TRANSITION

The molecular dynamics method is based on the assumption that the atomic motion obeys the classical laws in condensed matter. This assumption is quite justified for describing liquids and solids, in which the de Broglie wavelength of atoms is considerably shorter than the characteristic interatomic distance in the system, and, hence, wave effects can be ignored. Moreover, the M^+X^- alkali halide crystals studied in the present work have filled electron shells, i.e., have an electronic structure characteristic of noble-gas crystals. This circumstance also confirms the validity of the classical approach to the description of the properties of similar systems.

By definition, the Madelung constant α_μ is represented by the formula [13]

$$\alpha_\mu = \sum_{j \neq i} \pm p_{ij}^{-1}, \quad (1)$$

where the quantities p are written as

$$r_{ij} = p_{ij} R_0, \quad (2)$$

R_0 is the distance between the nearest neighbors, and r_{ij} is the distance between the ith and jth ions. With due regard for relationship (2), formula (1) can be rewritten in the following form:

$$\frac{\alpha_\mu}{R_0} = \sum_{j \neq i} \frac{\pm 1}{r_{ij}}, \quad (3)$$

where r_{ij} is the distance between the jth ion and the ion chosen as a reference point. Note that, when the initial ion is negative, the plus and minus signs in expression (3) correspond to positive and negative ions, respectively. Generally speaking, the numerator of the right-hand side of expression (3) should involve the ion charge q_j; however, we have $|q_j| = 1$ for the M^+X^- alkali halide crystals under consideration.

Therefore, from expression (3) with the use of the Ewald method [14] for calculating lattice sums, we can determine the Madelung constant, which, in turn, determines the energy of the Coulomb interaction between ions in the lattice at 0 K. For crystal temperatures $T >$ 0 K, we can write the following relationship:

$$K_T = R_0^{(T)} \sum_{j \neq i} \frac{\pm 1}{r_{ij}}, \quad (4)$$

where $R_0^{(T)}$ is the interionic distance at a given temperature and K_T is the temperature parameter of the Coulomb interaction.

As a result, the problem is reduced to the summation of the reciprocals of the distances between the ion chosen as the reference point (the initial ion) and surrounding ions. The problem can be solved using the molecular dynamics method. At the first stage, a set of coordinates of ions located at sites of the crystal lattice at the initial instant of time is generated. Then, the system relaxes to an equilibrium state and the reciprocals of the ion coordinates are summed up with allowance made for ion signs. The calculated sum is used to determine the temperature parameter of the Coulomb interaction K_T at a temperature T. Then, the calculations are performed at different temperatures up to the melting point of the crystal. Let us consider in more detail the formulated problem in terms of the molecular dynamics method [15].

The Hamiltonian describing the interaction of N particles can be represented in the form

$$H = \sum_i \frac{p_i^2}{2m} + \sum_{i<j} U(\mathbf{r}_{ij}),$$

where $\mathbf{r}_{ij}$ is the distance between the ith and jth particles. We assume that the number of particles in the system is constant and their total momentum is equal to zero. The particle motion is described by the Newton equations

$$\frac{d^2\mathbf{r}_i(t)}{dt^2} = \frac{\sum_{i<j} \mathbf{F}_i(\mathbf{r}_{ij})}{m}. \quad (5)$$

The system of the second-order differential equations is analytically solved by double integration over the time from 0 to t. The first and second integrations give the velocities of particles and their coordinates, respectively. Integration requires the knowledge of the initial coordinates of particles and their initial velocities. Under specified initial conditions, the system moves along the trajectory with a constant energy in the phase space.

Equations (5) are numerically solved by discretizing the second-order differential operator on the left-hand side of these equations. This leads to the explicit equation in central differences; that is,

$$\frac{d^2\mathbf{r}_i}{dt^2} = h^{-2}[\mathbf{r}_i(t+h) - 2\mathbf{r}_i(t) + \mathbf{r}_i(t-h)] = \frac{\mathbf{F}_i(t)}{m}. \quad (6)$$

Equation (6) permits one to determine the particle coordinates at the time step $t + h$ through the coordinates at the preceding steps t and $t - h$ and the force acting on the particle at the step t. The coordinates at the time step $t + h$ are written in the form

$$\mathbf{r}_i(t+h) = 2\mathbf{r}_i(t) - \mathbf{r}_i(t-h) + \mathbf{F}_i(t)h^2/m. \quad (7)$$

It is assumed that $t_n = nh$, $\mathbf{r}_i(t_n) = \mathbf{r}_i^n$, and $\mathbf{F}_i^n = \mathbf{F}_i(t_n)$. Then, Eq. (7) takes the form

$$\mathbf{r}_i^{n+1} = 2\mathbf{r}_i^n - \mathbf{r}_i^{n-1} + \mathbf{F}_i^n h^2/m. \quad (8)$$

By specifying $\mathbf{r}_i^0$ and $\mathbf{r}_i^1$, all the subsequent positions of particles can be determined from the recursive relationship (8). The particle positions at the $(n + 1)$st time step are extrapolated from the particle positions at two preceding steps (two-step method).

In order to calculate the kinetic energy, it is necessary to know the particle velocities. The velocities are calculated in the following approximation:

$$\mathbf{v}_i^n = (2h)^{-1}(\mathbf{r}_i^{n+1} - \mathbf{r}_i^{n-1}).$$

Note that the velocities calculated at the $(n + 1)$st step are the velocities at the preceding step, i.e., at the nth step. This means that the kinetic energy is calculated with a one-step delay as compared to the potential energy.

Equations (6) and (8) with specified initial coordinates of particles correspond to the Verlet algorithm [16]. The advantage of this algorithm is the time reversibility: the calculation of the system reversed in time results in the same equations. This holds true only in principle. In view of the inevitable rounding errors upon arithmetic operations performed with a limited accuracy, the calculated trajectories of the particles do not coincide with true trajectories. The algorithm is not self-starting. In order to initiate this algorithm, it is necessary to specify a set of particle positions not only at the initial instant of time but also at the next step. It is considerably more convenient when the initial particle positions are specified at the lattice sites. If the positions and velocities of particles are specified by the initial conditions, the positions $\mathbf{r}_i^1$ can be calculated from the relationship

$$\mathbf{r}_i^1 = \mathbf{r}_i^0 + h\mathbf{v}_i^0 + (h^2/2m)\mathbf{F}_i^0. \quad (9)$$

Then, the algorithm starts with the second step.

We reformulated the Verlet algorithm in such a way as to obtain a more stable numerical scheme [15]. Let us introduce the designation

$$\mathbf{Z}_i^n = h^{-1}(\mathbf{r}_i^{n+1} - \mathbf{r}_i^n). \quad (10)$$

The equations

$$\mathbf{r}_i^n = \mathbf{r}_i^{n-1} + h\mathbf{Z}_i^{n-1}, \quad \mathbf{Z}_i^n = \mathbf{Z}_i^{n-1} + (h/m)\mathbf{F}_i^n \quad (11)$$

are mathematically equivalent to Eqs. (8) and are referred to as the additive equations. Further reformulation leads to the Verlet algorithm in the velocity form with

(i) specifying the positions $\mathbf{r}_i^1$ at the first step,

(ii) specifying the velocities $\mathbf{v}_i^1$ at the first step,

(iii) calculating the positions at the $(n + 1)$st time step and

$$\mathbf{r}_i^{n+1} = \mathbf{r}_i^n + h\mathbf{v}_i^n + (h^2/2m)\mathbf{F}_i^n,$$

(iv) calculating the velocities at the $(n + 1)$st time step

$$\mathbf{v}_i^{n+1} = \mathbf{v}_i^n + (h/2m)(\mathbf{F}_i^{n+1} + \mathbf{F}_i^n).$$

It is essential that the positions and velocities of particles are calculated at the same time step. Furthermore, an increase in the stability of the algorithm is extremely important when simulating the system for a long time.

In general, exact initial conditions corresponding to a given energy of the system are unknown. In order for the system to attain a required energy, reasonable initial conditions are specified. Then, the energy is either removed from the system or introduced into it. The procedure is performed until the system reaches the required state. For an equilibrium phase within the Verlet algorithm, this is provided by the normalization of particle velocities [16]. Such a normalization can lead to large changes in the particle velocities. In order to eliminate undesirable effects that can arise in this case, the system after normalization is again brought to equilibrium. The equilibrium phase can be obtained using the following algorithm:

(1) Integration of the equations of motion at a given time step.

(2) Calculation of the total energy of the system.

(3) Normalization of the particle velocities when the total energy differs from the required energy.

(4) Repetition of the procedure beginning with the first step until the system attains equilibrium.

The initial positions of particles in the crystal are specified at sites of a face-centered cubic or body-centered cubic lattice, and the particle velocities are specified by the corresponding Maxwell distribution at a given temperature. The time step is taken to be $h = 10^{-14}$ s, and the total time of the evolution of the system is $t = 10^{-8}$ s. The equations of motion enable one to calculate the behavior of the system only on the surface of a constant energy. However, in our case, it is necessary to calculate the properties of the system along an isotherm, i.e., it is necessary to modify the equations of motion. The modification should be such that the system is conceptually coupled to the thermal reservoir, which can introduce the energy fluctuations required for reaching the given temperature of the system [17].

One way of ensuring fluctuations at T = const consists in complementing the equations of motion by the coupling equation [17]. Such a coupling can be provided by fixing the kinetic energy in the course of the computer experiment. Note that the coupling can be nonholonomic. This leads to the so-called isokinetic molecular dynamics scheme

$$\Lambda = \frac{1}{2}\sum_i m v_i^2 = \text{const}. \quad (12)$$

When the system has a constant temperature, the total kinetic energy can be taken proportional to the time

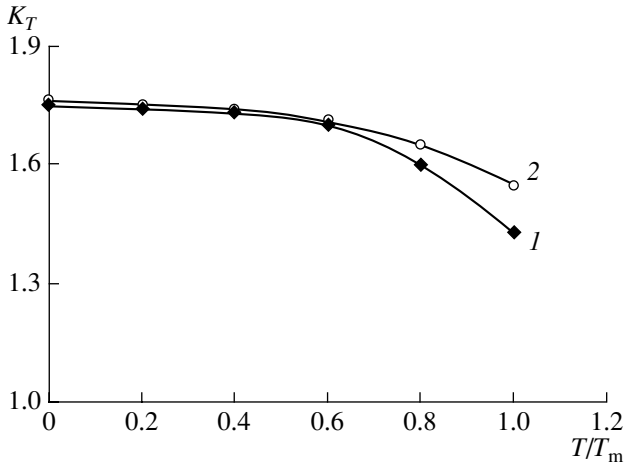

Fig. 1. Temperature dependences of the Coulomb interaction parameter for (*1*) the NaCl-type structure and (*2*) the CsCl-type structure.

with a very small proportionality factor (Gaussian isokinetic molecular dynamics) [17]; that is,

$$\frac{1}{2}\sum_i m v_i^2 = \alpha t.$$

Now, we formulate the algorithm of the isokinetic molecular dynamics. In this case, only the average temperature is fixed. The algorithm is as follows:

Start of the time cycle.

(1) Calculation of the forces.

(2) Calculation of the positions $\mathbf{r}^{n+1} = \mathbf{g}_1(\mathbf{r}^n, \mathbf{v}^n, \mathbf{F}^n)$.

(3) Calculation of the velocities $\mathbf{v}^{n+1} = \mathbf{g}_2(\mathbf{v}^n, \mathbf{F}^n, \mathbf{F}^{n+1})$.

(4) Calculation of the kinetic energy E_k.

(5) Normalization of the velocities $\mathbf{v}^{n+1} \longleftarrow \beta\mathbf{v}^{n+1}$.

End of the time cycle.

The functions $\mathbf{g}_1$ and $\mathbf{g}_2$ are represented by the recursive relationships. Note that the function $\mathbf{g}_2$ should provide an additional dependence on the force at the $(n+1)$st step. For this purpose, the first step of the cycle is introduced between the second and third steps. After attaining equilibrium of the system, the fifth step of the cycle is ignored.

The question arises as to the magnitude of the normalization factor β. The system has $3N$ degrees of freedom. However, since the total momentum of the system is equal to zero, the number of degrees of freedom becomes smaller by three. Moreover, the constancy of the kinetic energy results in a decrease in the number of degrees of freedom by unity. As a consequence, we have

$$\beta = \left[(3N-4)k_BT/\sum_i m v_i^2\right]^{1/2}. \qquad (13)$$

After normalization, we obtain the expression

$$\frac{1}{2}\sum_i m v_i^2 = \frac{1}{2}(3N-4)k_BT.$$

Therefore, the molecular dynamics algorithm for the *NVE* ensemble can be formulated in the following final form:

Start of the time cycle.

(1) Specification of the initial positions $\mathbf{r}_i^1$ at sites of the corresponding crystal lattice.

(2) Specification of the initial velocities $\mathbf{v}_i^1$ with the use of the Maxwell distribution.

(3) Calculations of the particle positions at the $(n+1)$st time step

$$\mathbf{r}_i^{n+1} = \mathbf{r}_i^n + h\mathbf{v}_i^n + \frac{h^2}{2m}\mathbf{F}_i^n.$$

(4) Calculations of the particle velocities at the $(n+1)$st time step

$$\mathbf{v}_i^{n+1} = \mathbf{v}_i^n + \frac{h}{2m}(\mathbf{F}_i^{n+1} + \mathbf{F}_i^n).$$

(5) Calculation of the sum $\sum_i m(v_i^n)^2$ and the normalization factor β.

(6) Normalization of all the velocities $\mathbf{v}_i^{n+1} \longleftarrow \beta\mathbf{v}_i^{n+1}$.

End of the time cycle.

As a result of the simulation, we obtain a set of coordinates of chosen particles $\mathbf{r}_i(t)$ as a function of the time.

TEMPERATURE DEPENDENCE OF THE PRESSURE OF THE POLYMORPHIC TRANSFORMATION

The calculated particle coordinates $\mathbf{r}_i(t)$ were used to calculate the sum in relationship (4) (with allowance made for the aforementioned sign rule) and then the temperature parameter of the Coulomb interaction K_T. Figure 1 depicts the dependences $K_T(T)$ for ionic crystals with the NaCl- and CsCl-type lattice structures. The analysis of the dependences $K_T(T)$ in Fig. 1 permits us to make a number of very important inferences. First, the parameter K_T for both the $B1$ (NaCl-type) and $B2$ (CsCl-type) structures only slightly and almost linearly varies up to temperatures of the order of $1/2T_m$. However, in the temperature range $0.7T_m$–T_m, the behavior of the dependence drastically changes and the temperature parameter of the Coulomb interaction $K_T^{\min}$ at temperatures of the order of the melting temperature appears to be considerably smaller than the

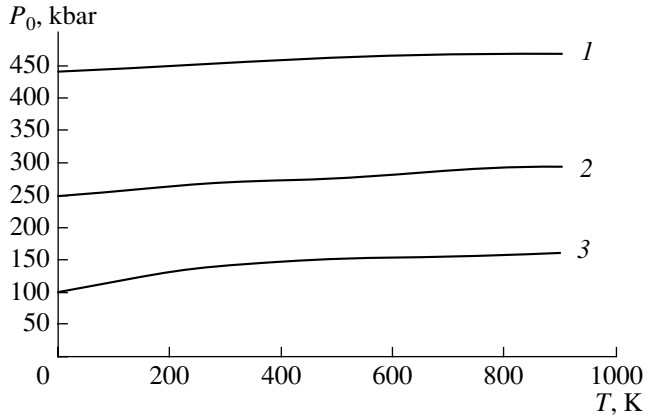

Fig. 2. Temperature dependences of the pressure of the polymorphic transformation for the lithium halide compounds (*1*) LiF, (*2*) LiCl, and (*3*) LiBr.

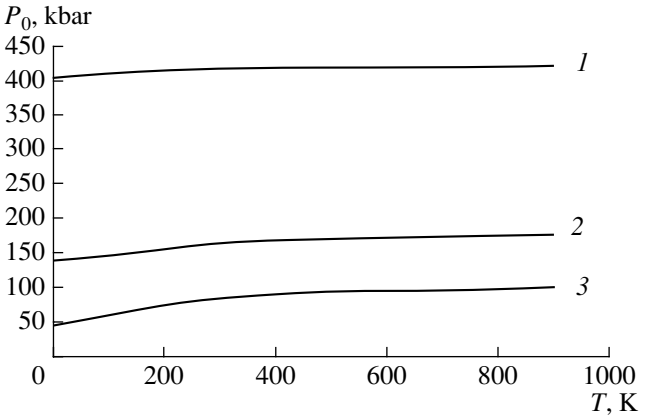

Fig. 3. Temperature dependences of the pressure of the polymorphic transformation for the sodium halide compounds (*1*) NaF, (*2*) NaCl, and (*3*) NaBr.

Madelung constant of the corresponding crystal structure. In this case, the change in the parameter K_T for crystals with the $B1$ structure turns out to be substantially larger than that for the $B2$ structure:

$$K_{\min}^{B1} = 1.432998, \quad K_{\min}^{B2} = 1.551149,$$

$$\alpha_{\mu}^{B1} = 1.747558, \quad \alpha_{\mu}^{B2} = 1.762670.$$

Therefore, the temperature parameter of the Coulomb interaction $K_T(T)$ at temperatures of the order of the melting temperature is smaller than the Madelung constant by 18% for crystals with the NaCl-type lattice and by 12% for crystals with the CsCl-type lattice:

$$\Delta(B1) = K_{\min}^{B1} - \alpha_{\mu}^{B1} = 0.31456,$$

$$\Delta(B2) = K_{\min}^{B2} - \alpha_{\mu}^{B2} = 0.211521.$$

It should be noted that the difference between the Madelung constants of the $B1$ and $B2$ structures at $T = 0$ K is approximately equal to 1%, whereas the difference between the parameters K_T^{B1} and K_T^{B2} at $T \sim T_m$ is approximately 7.5%. This suggests that the change in the energy of the Coulomb interaction of particles with an increase in the temperature for compounds with the CsCl-type structure is smaller than the corresponding change for compounds with the NaCl-type structure. Consequently, we can predict that the temperatures and heats of melting for ionic crystals with the $B2$-type lattice should be, on average, higher than those for ionic crystals with the $B1$-type lattice. The analysis of the data available in the literature on the heats of melting of alkali halide crystals [18] demonstrates that the above ratio is valid for all the compounds studied in the present work. Therefore, the proposed model qualitatively and quantitatively describes the temperature effects of the polymorphic transformations in ionic crystals.

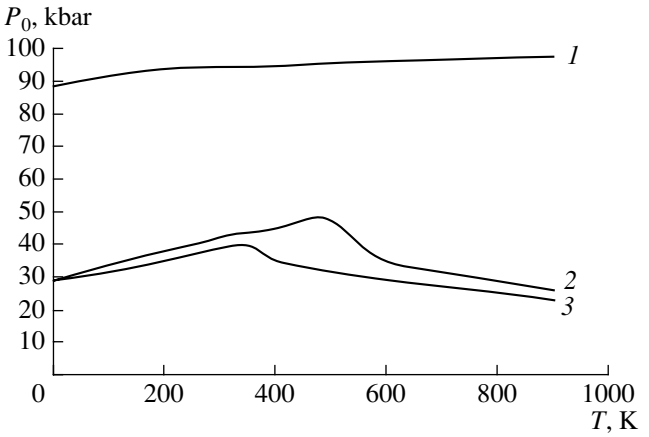

Fig. 4. Temperature dependences of the pressure of the polymorphic transformation for the potassium halide compounds (*1*) KF, (*2*) KCl, and (*3*) KBr.

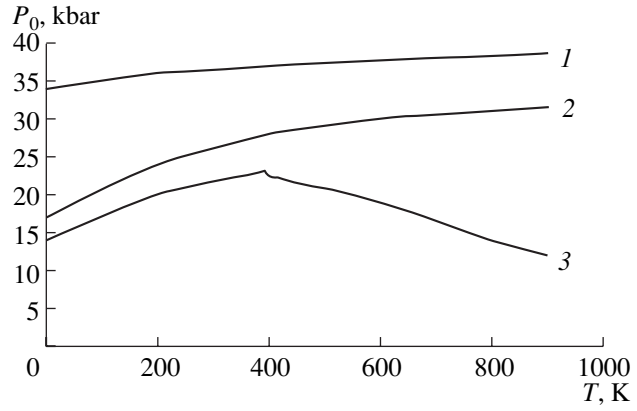

Fig. 5. Temperature dependences of the pressure of the polymorphic transformation for the rubidium halide compounds (*1*) RbF, (*2*) RbCl, and (*3*) RbBr.

The thermodynamic potential of a crystal at $T \neq 0$ K can be written in the form

$$G_{B_i} = \sum_{k=1}^{7} N_k^{(i)} U_k^{(i)}(a_k^{(i)} R^{(i)}) - V^{(i)} \frac{\partial}{\partial V^{(i)}} \left[\sum_{k=1}^{7} N_k^{(i)} U_k^{(i)}(a_k^{(i)} R^{(i)}) \right] - \frac{K_T^{(i)}}{R^{(i)}}. \quad (14)$$

The temperature T in expression (14) is a parameter. For chosen temperature T_f, the temperature parameter of the Coulomb interaction K_{T_f} is calculated for crystals with the $B1$ and $B2$ structures. Then, the pressure of the polymorphic transformation is calculated with the use of the thermodynamic potential (14) according to the procedure described above. The calculations are performed at different temperatures T_f' of the system up to temperatures of the order of the melting point of the crystal.

The temperature dependences of the pressure of the polymorphic transformation for lithium, sodium, potassium, and rubidium halides are plotted in Figs. 2–5, respectively. The pressure of the polymorphic transformation for the lithium and sodium compounds, potassium and rubidium fluorides, and rubidium chloride increases weakly with an increase in the temperature ($\Delta P/\Delta T > 0$), whereas the inequality $\Delta P/\Delta T < 0$ is observed for the KCl, KBr, and RbBr crystals over the entire range of temperatures under investigation. The theoretical calculations predicted that the dependences $P_0(T)$ for three compounds exhibit maxima at the following critical temperatures T_{cr}: T_{cr}(KCl) = 491 K, T_{cr}(KBr) = 337 K, and T_{cr}(RbBr) = 393 K. Consequently, we can make the inference that, at $T = T_{cr}$, the entropy jump is absent upon the $B1$–$B2$ phase transition: $\Delta S_{B1-B2}(T_{cr}) = 0$. Unfortunately, the experimental data on the pressure of the polymorphic transformation at high temperatures are very unreliable. However, these data do not exclude the possibility of maxima in the dependences $P(T)$ of the $B1$–$B2$ phase transition for the potassium chloride and potassium bromide in the temperature range $T \sim 150$–350 K [19]. This is in good agreement with the critical temperatures T_{cr} calculated in the present study. Therefore, for the KCl, KBr, and RbBr crystals, there can exist isotherms whose intersection leads to a change in the sign of the thermal effect accompanying the $B1$–$B2$ phase transformation.

REFERENCES

1. P. W. Bridgman, *The Physics of High Pressure* (Bell, London, 1949).
2. *Structural Phase Transitions in Crystals under High Pressure*, Ed. by K. S. Aleksandrov (Nauka, Novosibirsk, 1982) [in Russian].
3. *Shock Waves and Extreme States of Matter*, Ed. by V. E. Fortov, L. V. Al'tshuler, R. F. Trunin, and A. I. Funtikov (Nauka, Moscow, 2000) [in Russian].
4. R. Dashler, High Temp.–High Press. **20** (4), 324 (1988).
5. R. Dashler, High Temp.–High Press. **20** (6), 661 (1988).
6. Ya. Yu. Volkova, G. V. Babushkina, and A. N. Babushkin, in *Metastable States and Phase Transitions* (IT Ural. Otd. Ross. Akad. Nauk, Yekaterinburg, 2001), p. 198 [in Russian].
7. G. A. Rozman, Fiz. Tverd. Tela (St. Petersburg) **36** (7), 2139 (1994) [Phys. Solid State **36** (7), 1167 (1994)].
8. Yu. M. Gufan and I. V. Ternovskiĭ, Fiz. Tverd. Tela (St. Petersburg) **35** (9), 2352 (1993) [Phys. Solid State **35** (9), 1165 (1993)].
9. A. R. Rezai-Ford, J. Anwar, and S. M. Clarr, Mater. Sci. Forum **228**, 375 (1996).
10. É. I. Éstrin, Materialovedenie, No. 9, 11 (1999).
11. S. V. Karpenko, A. Kh. Kyarov, A. I. Temrokov, and D. L. Vinokurskiĭ, Kristallografiya **47** (2), 326 (2002) [Crystallogr. Rep. **47** (2), 291 (2002)].
12. S. V. Karpenko and A. I. Temrokov, Zh. Tekh. Fiz. **74** (11), 115 (2004) [Tech. Phys. **49** (11), 1509 (2004)].
13. D. W. Heermann, *Computer Simulation Methods in Theoretical Physics* (Springer-Verlag, New York, 1986; Nauka, Moscow, 1990).
14. C. Kittel, *Introduction to Solid State Physics*, 2nd ed. (Wiley, New York, 1956; Fizmatgiz, Moscow, 1963).
15. W. C. Swope, H. C. Andersen, P. H. Berence, and K. R. Wilson, J. Chem. Phys. **76**, 637 (1982).
16. W. G. Hoover, D. J. Evans, R. B. Hickman, *et al.*, Phys. Rev. A **22**, 1690 (1980).
17. A. J. Darnell and W. A. McCollum, J. Phys. Chem. Solids **31**, 805 (1970).
18. *Selected Values of Chemical Thermodynamic Properties* (National Bureau of Standards, Washington, 1952), Circular NBS No. 500.
19. I. P. Bazarov, I. V. Gevorkyan, and P. N. Nikolaev, *Nonequilibrium Thermodynamics and Physical Kinetics* (Mosk. Gos. Univ., Moscow, 1989) [in Russian].

Translated by O. Borovik-Romanova

Crystallography Reports, Vol. 50, No. 5, 2005, pp. 823–826. Translated from Kristallografiya, Vol. 50, No. 5, 2005, pp. 887–891.

PHYSICAL PROPERTIES OF CRYSTALS

Effect of Impurities on the Optical Properties of $PbWO_4$ Crystals

A. N. Annenkov*, A. A. Blistanov, A. O. Kustova**, V. A. Ligun*, and I. O. Yakimova****

** Bogoroditsk Plant of Technochemical Products, Bogoroditsk, Tula oblast, 301800 Russia*

*** Moscow State Institute of Steel and Alloys, Leninskiĭ pr. 4, Moscow, 119049 Russia*

e-mail: a-blistanov@e-mail.ru

Received November 17, 2004

Abstract—The effect of excess W and La^{3+}, Y^{3+}, and Mo^{6+} impurities on the luminescence spectra and the thermally stimulated luminescence of $PbWO_4$ crystals is studied. A high tungsten content (up to 1 at %) in the charge mixture results in a high luminescence intensity in the green spectral region. Lanthanum impurity decreases the transmission in the short-wavelength ($k > 29\,000$ cm^{-1}) spectral region. Lanthanum and yttrium impurities decrease the luminescence intensity. At low (10^2 ppm) concentrations, Mo impurity can somewhat increase the light yield. However, the presence of Mo in $PbWO_4$ shifts the absorption-band edge to longer wavelengths, while an increase in the Mo concentration above 10^2 ppm decreases the luminescence intensity. © *2005 Pleiades Publishing, Inc.*

INTRODUCTION

Doping of $PbWO_4$ (PWO) crystals was previously used [1–4] to eliminate coloration and increase the light yield and radiation resistance. A charge change occurring when a matrix ion is substituted by a heterovalent impurity ion leads to rearrangement of intrinsic point defects and affects the change in the optical properties of the crystals.

Hole centers (Pb^{3+}, O^-) negatively affect the optical properties of PWO [3, 4]. To compensate for these defects, trivalent impurities were used [1, 2, 5–7]. It was shown [2, 5, 7] that the trivalent impurities (La, Y, Lu), substituting lead, increase the transmission in the short-wavelength (320–420 nm) spectral region and the radiation resistance of PWO.

One of the most important problems is the effect of the Mo impurity, which is difficult to eliminate in tungstate crystals. There is evidence that molybdenum produces electron traps and negatively affects the scintillation properties of tungstate crystals, while suppressing the fast luminescence component [8–11].

EXPERIMENTAL RESULTS

In this study, we consider the effect of Y, La, and Mo impurities and an excess of W on the transmission and luminescence spectra and the integrated thermally stimulated luminescence (TSL) of PWO crystals. The transmission spectra of 10-mm-thick crystal plates were recorded on a SPECORD spectrophotometer. Luminescence was excited by X-ray CuK_α radiation. The luminescence spectra were measured in reflection on a DMR-23 spectrometer and registered in the photon counting mode by a FÉU-100 photomultiplier. The spectral sensitivity of the FÉU-100 is constant with an accuracy to a value within 10% in the wavelength range 250–650 nm.

Crystals 1–5 (Table 1) were grown in a nitrogen atmosphere at the Bogoroditsk Plant of Technochemical Products (BPTCP). Crystals 6 and 7 were grown at the same plant within the ALICE project. Molybdenum-doped crystals 8 and 9 were grown at the All-Russia Research Institute for the Synthesis of Materials (VNIISIMS).

The impurities were analyzed by spark mass spectrometry on a JEOL JMS-01-BM2 mass spectrometer (Japan). The molybdenum content was determined by X-ray fluorescent energy-dispersive spectrometry on a PHILIPS PW95000 system. The random error in determining the concentration is characterized by a relative

Table 1. Impurity content in PWO crystals

Crystal	Impurity	Impurity content, ppm
1	La	200
	Y	90
2	W excess	0.5% in charge mixture
3	W excess	0.5% in charge mixture
	Mo	500
4	La	400
5	Mo	9
6	Mo	20
7	Mo	100
8	Mo	700
9	Mo	5000

1063-7745/05/5005-0823$26.00 © 2005 Pleiades Publishing, Inc.

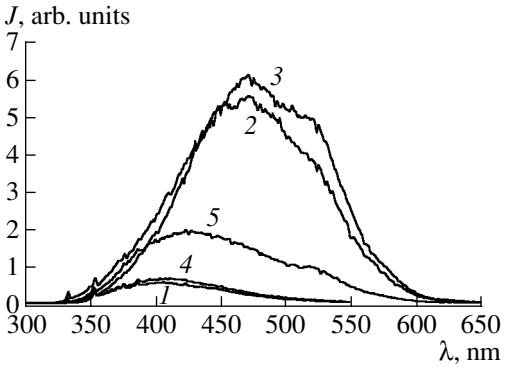

Fig. 1. Luminescence spectra of doped $PbWO_4$ crystals with impurity contents of (*1*) 200 ppm La and 90 ppm Y, (*2*) 0.5 at % of excess W, (*3*) 500 ppm Mo and 0.5 at % of excess W, and (*4*) 400 ppm La and for (*5*) an undoped crystal.

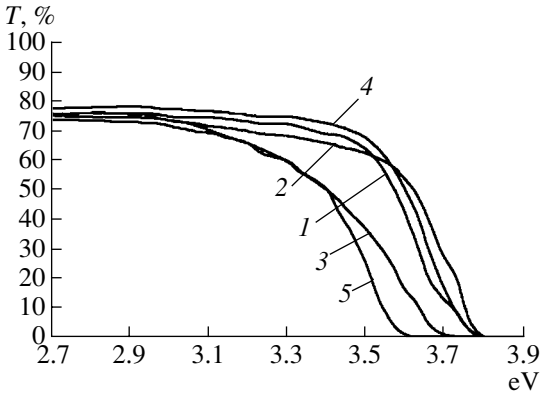

Fig. 2. Transmission spectra of doped $PbWO_4$ crystals with the impurity contents of (*1*) 200 ppm La and 90 ppm Y, (*2*) 0.5 at % of excess W, (*3*) 500 ppm Mo and 0.5 at % of excess W, and (*4*) 400 ppm La and for (*5*) an undoped crystal.

standard deviation. The latter ranged from 0.15 to 0.30 for the spark mass spectrometry and was 0.05 for X-ray fluorescent energy-dispersive spectrometry. The values obtained by the analysis are listed in Table 1 in particles per million (1 ppm = 0.0001 at %). Table 1 presents only the concentrations of basic impurities; the concentration of other impurities is no more than 10 ppm. Crystals 2 and 3 were grown with a higher (up to 1 at % in the charge mixture) tungsten content as compared with the stoichiometric composition. Since W is the main component in PWO crystals, its content was not analyzed.

A distinguishing feature of the crystals grown from a charge mixture with a higher tungsten content is a high luminescence intensity *J* in the green spectral region (Fig. 1, curves *2*, *3*). At the same time, the transmission spectra of these crystals (Fig. 2) are quite different. In crystal 3, containing molybdenum, the absorption band edge is shifted to longer wavelengths (curve *3*), while crystal 2 (with excess W but without Mo) exhibits the shortest-wavelength absorption-band edge (curve *2*).

The transmission *T* of La-doped crystals 1 and 4 is somewhat lower in the short-wavelength ($k >$ 29000 cm^{-1}) spectral region (Fig. 2, curves *1*, *4*). These crystals exhibit the lowest total luminescence intensity, which is especially low in the green spectral region (Fig. 1, curves *1*, *4*).

Crystal 5 was not intentionally doped and was considered nominally pure.

A general feature of the TSL curves for PWO is a peak at 100–120 K (Fig. 3). The presence of this peak in the crystals grown in a nitrogen atmosphere (BPTCP) and its enhancement as a result of vacuum annealing give grounds to relate it to oxygen vacancies [10, 11]. Other authors relate this peak to the presence of Pb^{3+}-type hole centers [12]. We believe that the TSL peak observed at 100–120 K can hardly be attributed to Pb^{3+}-type centers because this peak can be clearly seen in the spectra of pure crystals grown in a neutral medium (BPTCP) and annealed in vacuum.

The TSL spectrum of crystal 2 (with excess W) contains the most complete set of peaks. Therefore, it is reasonable to decompose the TSL spectrum of this crystal into Gaussian components and list their temperatures as most typical for PWO (Table 2).

The peak temperatures listed in Table 2 can be subdivided into three groups: (I) the low-temperature (100–115 K) group, (II) the medium-temperature (170–190 K) group, and (III) the high-temperature (210–240 K) group. It should be noted that, in the crystals with excess W grown in air (VNIISIMS), the deep trap levels, responsible for the peaks of type III, are most pronounced (Fig. 4, curve *1*). Annealing (in argon) results in a general decrease in the TSL light sum (Fig. 4, curve *2*) and in a relative decrease in the TSL intensity associated with deep trap centers.

In the Mo-doped crystals, the absorption-band edge is shifted to longer wavelengths. The luminescence spectra of the Mo-doped crystals that were at our disposal are shown in Fig. 5. The presence of Mo sup-

Table 2. Temperatures corresponding to the TSL peaks of a PWO crystal with W excess (1 at % in charge mixture)

TSL peak	Temperature, K	Trapping-center level, eV
1	110	0.22
2	172	0.34
3	190	0.38
4	208	0.40
5	220	0.44
6	242	0.48

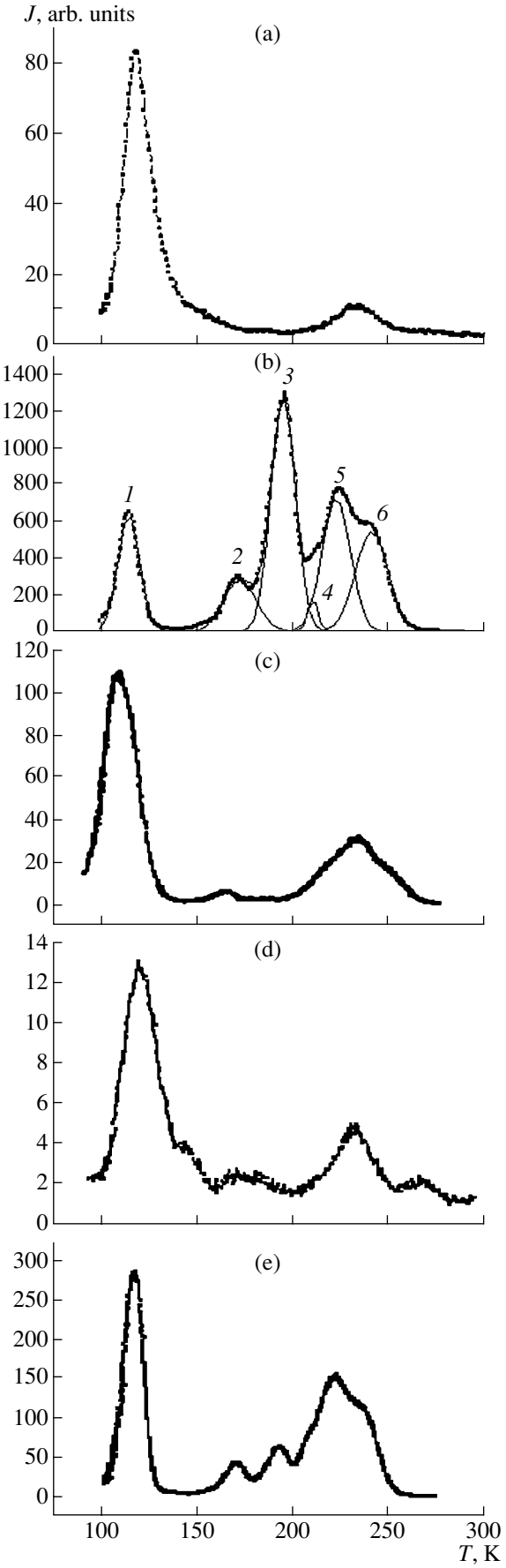

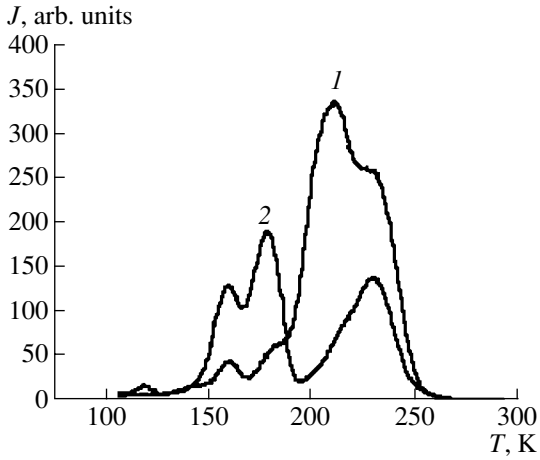

Fig. 4. TSL spectra of the $PbWO_4$ crystals with 0.5 at % of excess W: (*1*) the unannealed sample and (*2*) the sample annealed in argon at 800 K.

presses the blue luminescence. At low (up to 500 ppm) Mo concentrations, the intensity of the long-wavelength (green) luminescence increases with an increase in the concentration. However, with a further increase in the Mo concentration, the intensity of the green luminescence decreases. It should be noted that the construction of a joint concentration dependence by comparing curves *1*, *2*, and *3*, on the one hand, and curves *4* and *5*, on the other hand, is not quite correct, since samples 1, 2, and 3 were obtained at BPTCP, while samples 4 and 5, were prepared at VNIISIMS (i.e., under different conditions). However the shift of the luminescence peaks to the green region with an increase in the Mo concentration allows a qualitative comparison of the TSL intensity for all these crystals. It is likely that this comparison can explain the difference in the behavior of the luminescence intensity, depending on the Mo presence, for the crystals from different sources.

DISCUSSION

It is believed that a deficit of tungsten arises during the growth of PWO crystals. This deficit is compensated for by the appearance of the lead ions in the Pb^{3+} state. The addition of WO_3 to the charge mixture plays a positive role, increasing the transmission in the spectral region containing an absorption band at 420 nm (k = 24000 cm^{-1}), which is attributed to Pb^{3+} ions. An excess of tungsten facilitates the formation of lead vacancies [V_{Pb}^{2-}] and compensating oxygen vacancies

Fig. 3. TSL spectra of $PbWO_4$ crystals. The impurity contents are (a) 200 ppm La and 90 ppm Y, (b) 0.5 at % of excess W, (c) 500 ppm Mo and 0.5 at % of excess W, (d) 400 ppm La. The spectrum in panel (e) is for an undoped crystal. Curves (*1*–*6*) in panel (b) (crystal 2 in Table 1) demonstrate the decomposition of the TSL spectrum into Gaussian components.

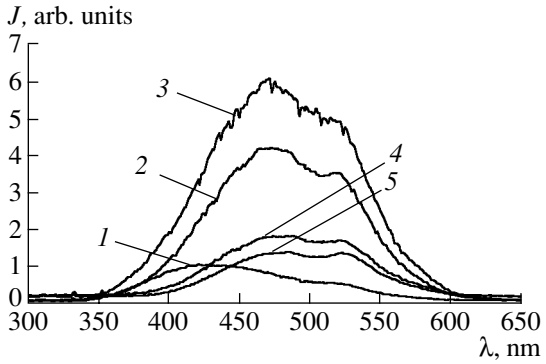

Fig. 5. Luminescence spectra of Mo-doped $PbWO_4$ crystals. The impurity contents are (*1*) 20, (*2*) 100, (*3*) 500, (*4*) 700, and (*5*) 5000 ppm.

$[V_O^{2+}]$. $[V_{Pb}^{2-}]$ defects may give rise to hole centers, which are responsible for the increase in the luminescence intensity. $[V_O^{2+}]$ defects and their associations can be related to the increase in the stored light sum and the formation of relatively deep trap centers responsible for the TSL peaks of group III.

The TSL light sum in PWO : La^{3+} crystals is two orders of magnitude lower than that in PWO:W crystals (compare Figs. 3a and 3d and Fig. 3b). The impurities (La^{3+}, Y^{3+}), which increase the positive charge by substituting Pb^{2+}, compete with $[V_O^{2+}]$-based centers and decrease the stored light sum. This fact again supports the assumption that the TSL peaks in the temperature range 200–250 K are due to $[V_O^{2+}]$-based centers.

The effect of Mo^{6+} on the PWO transmission spectrum is explained by a higher polarizability of $[MoO_4]^{2-}$ ions with respect to $[WO_4]^{2-}$ ions. Therefore, the substitution of W^{6+} by Mo^{6+} in the scheelite-type lattice leads to the formation of tetrahedra, in which O^{2-} is more easily ionized. It is possible that at low Mo^{6+} concentrations this phenomenon increases the number of excited states, thus enhancing the luminescence intensity, without significantly affecting the decrease in transmission. Such an effect can be observed if the dependence of the luminescence intensity on the Mo^{6+} concentration is linear, while absorption exponentially depends on the Mo^{6+} concentration.

A possible explanation of the luminescence suppression in highly doped PWO_4:Mo crystals is the significant increase in the light absorption in the short-wavelength spectral region associated with the shift of the absorption edge in the PWO:Mo crystals to the spectral region 350–360 nm, as compared to the beginning of the absorption band ($\lambda < 380$ nm), which is typical of blue-luminescent crystals. However, this shift is not so large that it directly suppresses the luminescence at $\lambda > 400$–420 nm. Apparently, the presence of Mo in high concentrations leads to additional quenching of blue luminescence due to the suppression of excitation processes at $\lambda < 350$–360 nm, which, owing to the Stokes shift, give rise to the luminescence in the range 400–420 nm.

CONCLUSIONS

An increase in the W concentration in PWO crystals leads to the suppression of Me^{3+}-type hole centers and enhances the luminescence intensity of these crystals. At the same time, an increase in the W concentration results in the increase in the number of relatively deep trap centers and the stored TSL light sum.

Doping of $PbWO_4$ by La^{3+} impurities decreases the TSL efficiency and the luminescence intensity. This effect can be related to a decrease in the efficiency of the formation of Pb^{3+} and O^- hole centers.

The presence of small amounts (10^2 ppm) of a Mo impurity in $PbWO_4$ crystals can somewhat increase the light yield. However, the presence of Mo results in the shift of the luminescence spectrum to longer wavelengths, and the luminescence intensity decreases as the Mo concentration increases.

ACKNOWLEDGMENTS

We are grateful to B.I. Zadneprovskii for supplying the Mo-doped $PbWO_4$ crystals.

REFERENCES

1. P. Lecoq, I. Dafinei, E. Auffrau, *et al.*, Nucl. Instrum. Methods Phys. Res. A **365**, 291 (1995).
2. A. N. Annenkov, M. Korzhik, and P. Lecoq, IEEE Trans., No. S-37, 10 (1999).
3. A. Fedorov, M. Korzhik, O. Missevitch, *et al.*, Rad. Instrum. **26** (1), 107 (1996).
4. A. N. Annenkov, A. Fedorov, Ph. Galez, *et al.*, Phys. Status Solidi A **151**, 1 (1996).
5. M. Kabayashi, Y. Usuki, M. Ishii, *et al.*, Nucl. Instrum. Methods Phys. Res. A **399**, 261 (1997).
6. S. Baccaro, P. Bohacek, and B. Borgia, Phys. Status Solidi A **160**, 5 (1997).
7. M. Kobayashi, Y. Usuki, M. Ishi, and M. Nikl, Nucl. Instrum. Methods Phys. Res. A **486**, 170 (2002).
8. A. Hofstaetter, R. Oeder, A. Scharmann, *et al.*, Phys. Status Solidi B **89**, 375 (1978).
9. M. Bohm, A. E. Borisevich, G. Yu. Drobychev, *et al.*, Phys. Status Solidi A **167**, 243 (1998).
10. A. A. Blistanov, A. N. Goryunova, B. I. Zadneprovskiĭ, *et al.*, Mater. Élektron. Tekh., No. 4, 41 (2001).
11. A. A. Blistanov, B. I. Zadneprovskiĭ, V. A. Nefedov, and V. S. Petrakov, Mater. Élektron. Tekh., No. 2, 39 (2002).
12. S. Burachas, A. Apanasenko, B. Grinev, *et al.*, Int. J. Inorg. Mater. **3**, 1101 (2001).

Translated by A. Zolot'ko

Crystallography Reports, Vol. 50, No. 5, 2005, pp. 827–835. Translated from Kristallografiya, Vol. 50, No. 5, 2005, pp. 892–899.

PHYSICAL PROPERTIES OF CRYSTALS

Specific Features of the Substitution of Fe^{3+} Impurity Ions for Zr^{4+} in $NaZr_2(PO_4)_3$ Single Crystals

G. R. Bulka*, V. M. Vinokurov*, A. A. Galeev*, G. A. Denisenko, N. M. Khasanova*, G. V. Kanunnikov**, N. M. Nizamutdinov*, S. V. Stefanovsky***, and A. Yu. Trul*****

** Kazan State University, Kremlevskaya ul. 18, Kazan, 420008 Tatarstan, Russia*
e-mail: Vladimir.Vinokurov@ksu.ru
*** Shubnikov Institute of Crystallography, Russian Academy of Sciences, Leninskiĭ pr. 59, Moscow, 119333 Russia*
**** NPO Radon, Sed'moĭ Rostovskiĭ per. 2/14, Moscow, 119121 Russia*
Received December 20, 2004

Abstract—The EPR spectra of Fe^{3+} impurity ions in $NaZr_2(PO_4)_3$ single crystals at 300 K are investigated, and the spin Hamiltonian of these ions is determined. A comparative analysis of the spin-Hamiltonian and crystal-field tensors is performed using the maximum invariant component method. It is demonstrated that Fe^{3+} impurity ions substitute for Zr^{4+} ions with local compensator ions located in cavities of the *B* type. It is revealed that the invariant of the spin-Hamiltonian tensor B_4 and the crystal-field tensor V_4^{44} depend substantially on the mutual arrangement of ions in the first and second coordination spheres. The corresponding dependences are analyzed. © *2005 Pleiades Publishing, Inc.*

INTRODUCTION

Sodium zirconium phosphate $NaZr_2(PO_4)_3$ has a mixed framework $M_2(TO_4)_3$ [1] of the rhombohedral type [2]. This material is promising for use as an ionic conductor [3] and a ceramic matrix for immobilization of radioactive wastes for their long-term storage [4]. The $NaZr_2(PO_4)_3$ compound is the end member of the continuous series of $Na_{1+x}Zr_2Si_xP_{3-x}O_{12}$ (x = 0–3) solid solutions, in which the heterovalent substitution of impurity ions for host ions leads to a redistribution of filling cations in the structure [5] and to a change in the crystal field in the substitution region. Structural investigations by the EPR method allow one to elucidate the influence of impurity ions on the distribution of mobile ions in the structure.

When studying the crystals by the EPR method, the location of an impurity ion in the ground state with spin $S \geq 5/2$ in the case of nonlocal charge compensation can be reliably determined from the topological parameters of the spin-Hamiltonian tensor B_4 and the irreducible quadratic tensor product $\{V_4 \otimes V_4\}_4 = V_4^{44}$ of the crystal-field tensor V_4 [6, 7]. A comparative analysis of the spin-Hamiltonian and crystal-field tensors is performed using the point-charge model by ignoring the disturbance of the field in the substitution region of the central ion. The presence of a charge compensator in the substitution region substantially changes the spin-Hamiltonian tensor B_2. Hence, the location of the compensator ion, as a rule, is determined from a comparative analysis of the tensor B_2 and the second-rank irreducible quadratic tensor product $\{V_4 \otimes V_4\}_2 = V_2^{44}$ of the crystal-field tensor V_4 [6, 7].

In order to justify the correctness of these approximations as applied to point defects in the crystal, it is necessary to extend the classes of objects and to analyze objects belonging to different classes. For this purpose, dielectric crystals with ionic conductivity seem to be appropriate systems in which the locations of filling cations are governed by the framework structure and have been determined by diffraction methods.

The purpose of this work was to investigate in detail the angular dependence of the Fe^{3+} EPR spectra of $NaZr_2(PO_4)_3$ single crystals and to calculate and analyze their spin-Hamiltonian and crystal-field tensors comparatively.[1]

The spin-Hamiltonian and crystal-field irreducible tensors A_L of rank L are analyzed using the maximum invariant component (MIC) method [8], which is based on the examination of the part $S_L(G_S)$ of the invariant S_L

[1] The preliminary results were reported at the International Conference "Spectroscopy, X-ray Diffraction, and Crystal Chemistry of Minerals" (Kazan, 1997); the International Conference on Growth and Physics of Crystals, Dedicated to the Memory of M.P. Shaskolskaya (Moscow, 1998); the France–Spain Conference on Chemistry and Physics of Solids (Carcans–Buisson, 2000); and the 4th National Conference on Application of X-ray, Synchrotron, Neutron, and Electron Radiation to Investigation of Materials (Shubnikov Institute of Crystallography, Russian Academy of Sciences, Moscow, 2003).

1063-7745/05/5005-0827$26.00 © 2005 Pleiades Publishing, Inc.

of the tensor A_L in the unitary group U upon rotation of the coordinate system. It should be noted that $S_L(G_S)$ is the invariant of the subgroup G_S of the group U. Unlike the conventional use of the invariant combinations of the internal-field parameters for describing low-symmetry activator centers in crystals and glasses [9], the invariants used in the MIC method are applied to the determination of the spatial orientation of the tensors. In order to elucidate the role played by the invariants in analyzing the intrinsic and orientational properties of the tensors, in this paper, we discuss an analogue of the MIC method and the method of the transformation of the quadratic forms and equations of second-order surfaces into their canonical forms. We also consider the dependence of the invariants of the spin-Hamiltonian and crystal-field tensors on the mutual arrangement of the first and second coordination spheres of a paramagnetic ion.

THE CANONICAL FORM OF THE SPIN HAMILTONIAN

The location of an impurity paramagnetic ion in a single crystal is determined by analyzing the tensors B_L of the spin Hamiltonian $\hat{H}$ with the MIC and topological methods [10]. The spin Hamiltonian $\hat{H}$ can be written in the form

$$\hat{H} = \beta\hat{S}g\overline{H} + \sum_L \hat{H}_L,$$

where

$$\hat{H}_L = \sum_{M=-L}^{L} T_{LM}(\hat{S})A_{LM} = \sum_{M=-L}^{L} B_{LM}T_{LM}(\hat{S}) \quad (1)$$

and L = even number.

By using the second-rank tensor B_2 as an example, we will demonstrate that these methods, as applied to the EPR method, are similar to the methods used to investigate polynomials and hypersurfaces in analytic geometry [11].

Let $X_0Y_0Z_0$ be the Cartesian coordinate system in which the tensors of the spin Hamiltonian (1) are defined. The indicating surface of the tensor of rank $L = 2$ [7, 10] can be expressed through the Euler angles (α, β, $\gamma = 0$): $B_{20}(\alpha\beta) = \sqrt{3/2}\,(B_{22}\cos 2\alpha - B_{2-2}\sin 2\alpha)\sin^2\beta - \sqrt{6}\,(B_{21}\cos\alpha - B_{2-1}\sin\alpha)\sin\beta\cos\beta + (1/2)B_{20}(3\cos^2\beta - 1)$. By using the designations $x = \sin\beta\cos\alpha$, $y = \sin\beta\sin\alpha$, and $z = \cos\beta$, this surface is rearranged into the form $B_{20}(x, y, z) = a_{11}x^2 + a_{22}y^2 + a_{33}z^2 + 2a_{12}xy + 2a_{13}xz + 2a_{23}yz + a_{44}$, where $a_{11} = \sqrt{3/2}\,B_{22}$, $a_{22} = -\sqrt{3/2}\,B_{22}$, $a_{33} = (3/2)B_{20}$, $a_{44} = -B_{20}/2$, $a_{12} = -\sqrt{3/2}\,B_{2-2}$, $a_{13} = -\sqrt{3/2}\,B_{21}$, and $a_{23} = \sqrt{3/2}\,B_{2-1}$. The surface $B_{20}(x, y, z)$ is defined on a unit sphere $x^2 + y^2 + z^2 = 1$.

By rotating the $X_0Y_0Z_0$ coordinate system, it is possible to find the $X'Y'Z'$ coordinate system in which the indicating surface $B_{20}(x, y, z)$ has the canonical form [11]: $B_{20}(x', y', z') = a'_{11}x'^2 + a'_{22}y'^2 + a'_{33}z'^2 + a'_{44}$, where $a'_{11} = \sqrt{3/2}B'_{22}$, $a'_{22} = -\sqrt{3/2}B'_{22}$, $a'_{33} = 3/2\,B'_{20}$, and $a'_{44} = -1/2\,B'_{20}$. Depending on the sign of the ratio B'_{22}/B'_{20}, the function $B_{20}(x', y', z')$ can be represented in the following form: $B_{20}(x', y', z') = 1/2\,B'_{20}\,(\pm x'^2/a^2 \mp y'^2/a^2 + z'^2/c^2 - 1)$, where $1/a^2 = \sqrt{6}\eta$, $\eta = |B'_{22}/B'_{20}|$, and $1/c^2 = 3$. It can be seen that the indicating surface of the tensor B_2 has the external symmetry group $D_{2h} = 3L_2 3PC$ [12], whose twofold axes are parallel to the axes of the $X'Y'Z'$ coordinate system and are principal.

The topology of the indicating surface of the tensor B_2 is determined by the characteristic equation $B_{20}(x, y, z) = 0$, which, in the $X'Y'Z'$ coordinate system, has the form $B_{20}(x', y', z') = 0$ or $\pm x'^2/a^2 \mp y'^2/a^2 + z'^2/c^2 = 1$. This equation coincides with the canonical equation for a one-sheeted hyperboloid. The indicating and characteristic surfaces have identical symmetries and principal axes. The intersection of a one-sheeted hyperboloid with a sphere of radius $R = 1$ separates the sphere into three parts: one part differs from the other parts by the sign of $B_{20}(x', y', z')$.

At $\eta = 0$, the zeros of the function $B_{20}(x', y', z')$ are represented by the circles $x'^2 + y'^2 = 2/3$ at the height $z' = \pm\sqrt{1/3}$. At $B'_{22}/B'_{20} > 0$ and $0 < \eta \le 1/\sqrt{6}$, we have $a^2 \ge 1$ and a throat ellipse ($y' = 0$) intersects the unit sphere at the points $x'^2 = 2a^2/(3a^2 - 1)$ and $z'^2 = (a^2 - 1)/(3a^2 - 1)$. In this case, the lines of the zero level are symmetrically located with respect to the plane $z' = 0$. At $\eta > 1/\sqrt{6}$, we have $a^2 < 1$ and the throat ellipse does not intersect the unit sphere; i.e., the intersection lines of the sphere and the hyperboloid are located on different sides of the plane $y' = 0$.

In order to determine the system of the principal axes of the tensor B_2 by the MIC method, the invariant $S_2 = (B_{20})^2 + 2\sum_{M=1}^{2}[(B_{2M})^2 + (B_{2-M})^2]$ in any coordinate system XYZ obtained through rotation of the coordinate system $X_0Y_0Z_0$ is represented as the sum $S_2 = S_2(D_{2h}) + S_{2r}$, where $S_2(D_{2h}) = (B_{20})^2 + 2(B_{22})^2$. The XYZ axes coincide with the $3L_2$ axes of the group D_{2h}. The coordinate system in which the quantity $S_2(D_{2h})$ takes the maximum value, $\max S_2(D_{2h}) = S_2 = (B'_{20})^2 + 2(B'_{22})^2$, represents the system of the principal axes. The system of the principal axes can also be determined by diagonalizing the corresponding second-rank Cartesian tensor.

However, there exist a number of problems that can be solved only using the MIC method. Let us determine the measure of deviation of the tensor B_2 from symmetry $D_{\infty h}$. When the tensor B_2 has symmetry $D_{\infty h}$, the Z'

axis of the $X'Y'Z'$ coordinate system in which $S_2 = (B_{20})^2$ is the axis ∞ of the group $D_{\infty h}$. If the symmetry is distorted with respect to the symmetry group $D_{\infty h}$, the invariant S_2 in the XYZ coordinate system is represented as the sum $S_2 = S_2(D_{\infty h}) + S_{2r}$, where $S_2(D_{\infty h}) = (B_{20})^2$. By rotating the XYZ coordinate system, we find the coordinate system (XYZ, $D_{\infty h}$) in which the term $S_2(D_{\infty h})$ takes the maximum value, $\max S_2(D_{\infty h})$. The quantity $d = [S_2 - \max S_2(D_{\infty h})]/S_2$ is the measure of deviation of the tensor B_2 from symmetry $D_{\infty h}$.

The MIC method appears to be indispensable in a comparative analysis of tensors B_L of rank $L \geq 4$ that are irreducible with respect to the group of continuous rotations. The characteristic equation $B_{L0}(\alpha, \beta) = 0$ at $L \geq 4$ that determines the zero level of the indicating surface corresponds to a more complex topology [7].

SAMPLE PREPARATION AND EXPERIMENTAL TECHNIQUE

Single crystals of $NaZr_2(PO_4)_3$ were grown by the solution–melt method with the use of the initial reagents Na_2CO_3, ZrO_2, $NH_4H_2PO_4$, NaF, and V_2O_5 taken in the ratio (mol %) $0.07Na_2O : 0.07ZrO_2 : 0.32P_2O_5 : 0.47NaF : 0.07V_2O_5$ [13]. Crystallization was performed by cooling the system at a rate of 0.5 K/h in the temperature range 950–800°C. After completing the process, the platinum bar was removed from the solution and cooled to room temperature at a rate of 50 K/h. The crystals grown had the form of individual rhombohedra. Moreover, the single crystals were grown with the use of the initial batch containing MoO_2.

The EPR spectra were recorded at a frequency ν = 9.4 GHz and a temperature of 300 K on a DX 70-02 EPR spectrometer (SKB Analitpribor, Belarussian State University, Minsk). The sensitivity of the spectrometer to impurities was equal to 10^{14} spins/G. In order to investigate the spectra of the single-crystal samples in detail, the spectrometer was equipped with a specially designed goniometer. The high-quality spectra were obtained by their prolonged accumulation.

ELECTRON PARAMAGNETIC RESONANCE OF Fe^{3+} IONS IN A $NaZr_2(PO_4)_3$ SINGLE CRYSTAL

The EPR study was performed using isometric crystals ~2 mm in size with rhombohedral faces of the $[11\bar{2}4]$ type. The samples grown from the melt containing the molybdenum dopant are characterized by the narrowest and most intense lines (Fig. 1). The EPR spectra involve lines of Cr^{3+}, Mn^{2+} (~10^{-5} wt %), and Fe^{3+} (~$n \times 10^{-4}$ wt %) impurities. In the present work, we thoroughly examined only the Fe^{3+} EPR spectra. The preliminary investigation into the angular dependence of the EPR spectra revealed that, at $H \parallel [0001]$, six symmetry-related Fe^{3+} EPR spectra (K_M = 6) are merged together (Fig. 1a). According to the space group $D_{3d}^6 - R\bar{3}c$ of the $NaZr_2(PO_4)_3$ structure [1], the multiplicity K_M = 6 corresponds to the position with the Laue symmetry group C_i. On this basis, the spin Hamiltonian (1) with symmetry C_i was chosen for describing one symmetry-related spectrum.

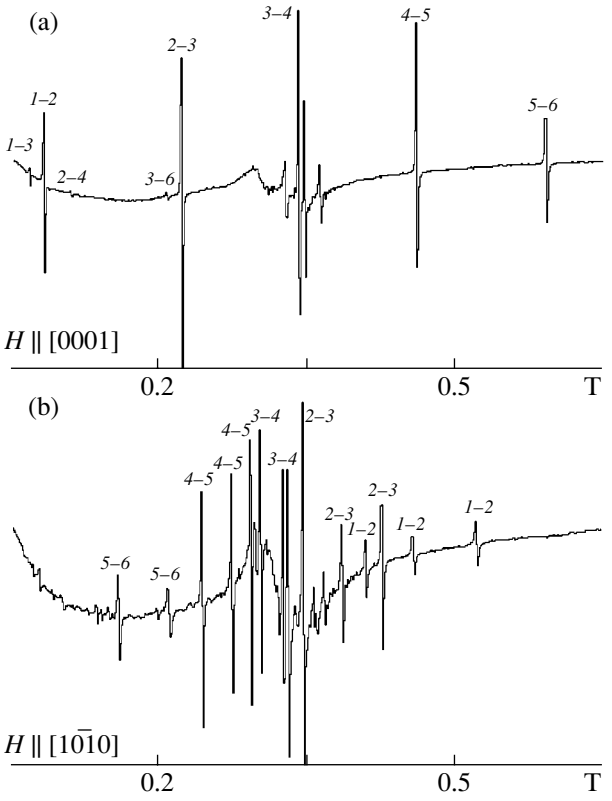

Fig. 1. Fe^{3+} EPR spectra of $NaZr_2(PO_4)_3$ crystals at a frequency ν = 9.4 GHz and at a temperature of 300 K in magnetic fields (a) $H \parallel [0001]$ and (b) $H \parallel [10\bar{1}0]$. The identification of the transitions corresponds to the energy-level diagram in Fig. 3.

The direction of the field **H** in the spin Hamiltonian (1) is described by the unit vector $\mathbf{n}[\sin\theta\cos\varphi, \sin\theta\sin\varphi, \cos\theta]$ in the coordinate system with the axes $X_0 \parallel L_2$, $Y_0 \parallel P$, and $Z_0 \parallel L_3$. The L_2 and L_3 axes and the P plane are the symmetry elements in the group D_{3d} of the crystal. The coordinate systems for each six symmetry-related positions of Fe^{3+} ions are related by the symmetry elements of the group $D_3 \subset D_{3d}$, which are represented by the Euler angles (α, β, γ): $E \longleftrightarrow (0, 0, 0)$, $3_1 \longleftrightarrow (2\pi/3, 0, 0)$, $3_2 \longleftrightarrow (-2\pi/3, 0, 0)$ $2_x \longleftrightarrow (0, \pi, \pi)$, $2_{xy} \longleftrightarrow (0, \pi, \pi/3)$, and $2_{\bar{x}y} \longleftrightarrow (-\pi/3, \pi, 0)$. In these local coordinate systems, the unit vector **n** has the coordinates $[\sin\theta\cos\varphi, \sin\theta\sin\varphi, \cos\theta]$, $[-\sin\theta\cos(\varphi + 60), -\sin\theta\sin(\varphi + 60), \cos\theta]$, $[-\sin\theta\cos(\varphi - 60), -\sin\theta\sin(\varphi - 60), \cos\theta]$, $[\sin\theta\cos\varphi, -\sin\theta\sin\varphi, -\cos\theta]$, $[-\sin\theta\cos(\varphi + 60), \sin\theta\sin(\varphi + 60), -\cos\theta]$,

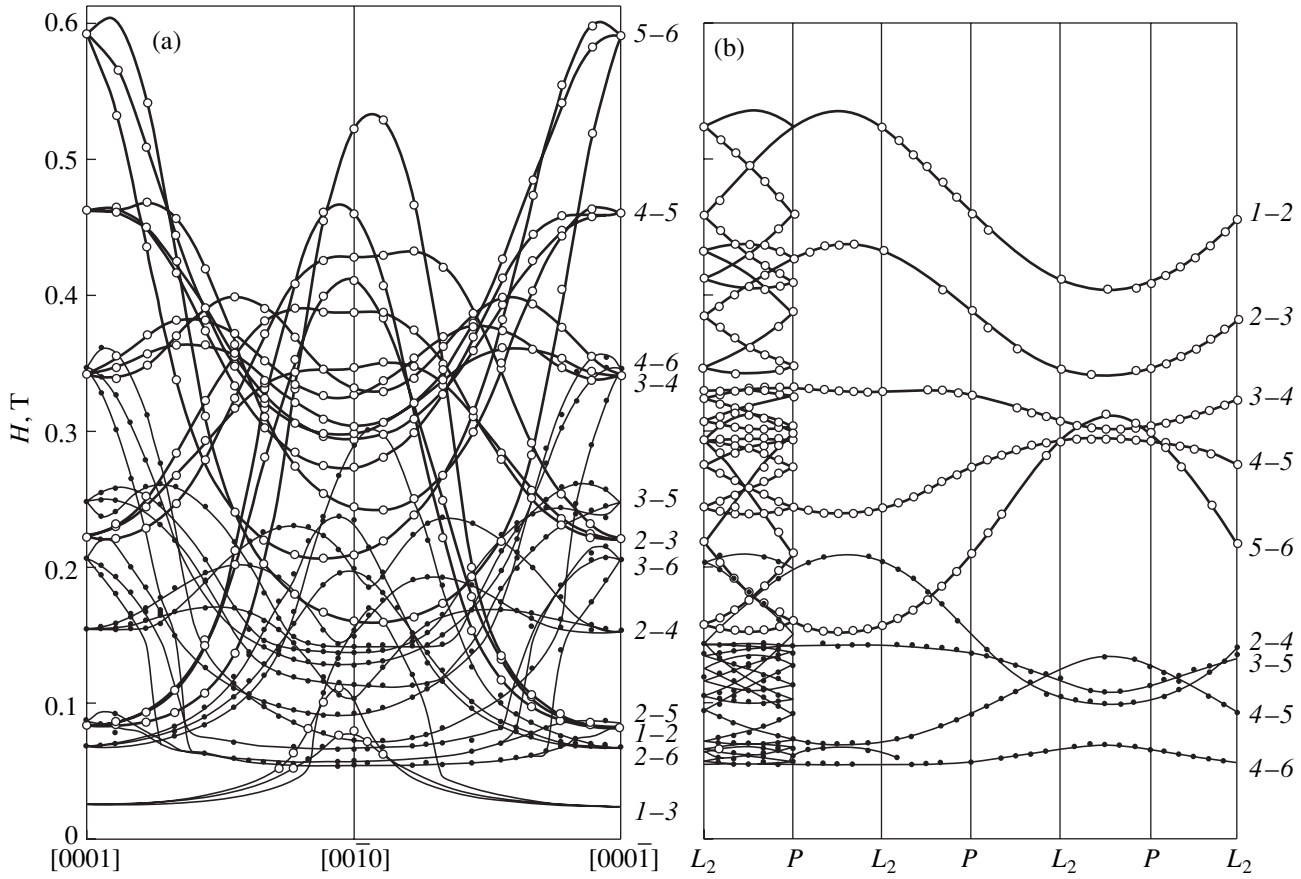

Fig. 2. Angular dependences of the Fe^{3+} EPR spectrum for the $NaZr_2(PO_4)_3$ crystal in the (a) (1210) and (b) (0001) crystallogarphic planes. Open and closed circles indicate the measured resonance fields H for the transitions at $\Delta M = 1$ and $\Delta M \neq 1$, respectively. Lines represent the resonance fields H calculated from the spin-Hamiltonian parameters. The identification of the transitions corresponds to the energy-level diagram in Fig. 3.

and $[-\sin\theta\cos(\varphi - 60), \sin\theta\sin(\varphi - 60), -\cos\theta]$, respectively.

In order to choose the planes for detailed measurements of the spectra, we analyzed the dependences of the tensors B_2 and B_4 of the spin Hamiltonian (1) on the Euler angles ($\alpha = \varphi$, $\beta = \theta$, $\gamma = 0$) [7] within the exact independent domain of the group D_{3d} [14]. In this domain, we restricted ourselves to two forms represented by the dihedral angle between the $(01\bar{1}0)$ and $(\bar{1}2\bar{1}0)$ planes [14] and the trihedral angle with the $(\bar{1}2\bar{1}0)$, $(\bar{2}110)$, and (0001) faces [15]. The boundaries of these forms can be set and controlled using the arrangement of the symmetry-related EPR spectra. When the Zeeman energy is comparable or larger than the initial splittings, the angular dependence of the EPR spectrum is predominantly governed by the diagonal elements $B_{20}(\varphi, \theta)$ and $B_{40}(\varphi, \theta)$ of the spin Hamiltonian, i.e., by indicating surfaces of the tensors. Consequently, with the aim of increasing the accuracy of the determination of the spin-Hamiltonian parameters, the planes for measurements of the spectra within the exact independent domain should be chosen so that all the tensor elements contribute to the dependences $B_{20}(\varphi, \theta)$ and $B_{40}(\varphi, \theta)$. In EPR studies, when the spin-Hamiltonian matrix is numerically diagonalized, the planes for measurements are chosen taking into account the requirements for the minimization of the time of spectrum recording. In our experiments, the angular dependences were measured in the $(\bar{1}2\bar{1}0)$ and (0001) planes (Figs. 2a, 2b). The angular dependence of three doubly degenerate symmetry-related EPR spectra in the $(\bar{1}2\bar{1}0)$ plane (Fig. 2a) permits us to determine reliably all the spin-Hamiltonian parameters, except the element B_{43}.

In order to determine the element B_{43}, we measured the angular dependence of all six symmetry-related EPR spectra in the (0001) plane at $0° \le \varphi \le 30°$ (Fig. 2). These data make it possible to construct the dependence of any symmetry-related EPR spectrum in the range $0° \le \varphi \le 180°$ in the (0001) plane.

By using the components of the vector **H** in the local coordinate systems, the spin-Hamiltonian parameters (table) were calculated according to a program similar to that described in [16]. The dependence of the energy

levels and their differences on the external magnetic field **H** is shown in Fig. 3.

ANALYSIS OF THE SPIN-HAMILTONIAN AND CRYSTAL-FIELD TENSORS

The structure of the $NaZr_2(PO_4)_3$ crystal [1] was analyzed in order to determine the location of Fe^{3+} impurity ions in this crystal. The $NaZr_2(PO_4)_3$ framework has the space group $R\bar{3}c - D_{3d}^6$ and can be represented as a rhombohedral unit cell whose vertices and center are occupied by lanterns. The structure of the central lantern turns out to be inverted with respect to the structure of the lanterns located at the vertices, and this lantern serves as a bridge between the latter lanterns [2]. The M_2T_3 lantern is composed of two *M* octahedra [ZrO_6] with a common triple axis and three *T* tetrahedra [PO_4] (Fig. 4). The parallel edges of this linking tetrahedra form an empty trigonal prism with symmetry D_3 between octahedra. In this framework, the M_2T_3 lanterns alternate along the triple axis and form octahedral cavities of the *A* type. Between columns, there are *B*-type cavities formed by ten O^{2-} ions (Fig. 4).

In the $NaZr_2(PO_4)_3$ structure, the ions of the framework occupy the following positions with the symmetry groups G_α: Zr^{4+}, 12*c* ($G_\alpha = C_3$); P^{5+}, 18*e* ($G_\alpha = C_2$); O_I, 36*f* ($G_\alpha = C_1$); and O_{II}, 36*f* ($G_\alpha = C_1$). The Na^+ ions compensate for the framework charge, fill all cavities of the *A* type, and occupy the 6*b* positions ($G_\alpha = C_{3i}$). The *B* cavities correspond to the 18*e* positions ($G_\alpha = C_2$) and alternate with the P^{5+} ions.

We can assume that Fe^{3+} impurity ions in the $NaZr_2(PO_4)_3$ structure occupy the Zr^{4+} positions arranged similarly to the Fe^{3+} ions in the $Na_3Fe_2(PO_4)_3$ structure [3]. In the $NaZr_2(PO_4)_3$ structure (Fig. 4), there are two magnetically related Zr^{4+} positions with the coordinates ($x = 0$, $y = 0$, $z = 0.64568$) and ($x = 0$, $y = 0$, $z = 0.85432$). In order to assign the spin-Hamiltonian tensor to one of these positions, the crystal-field tensor V_4^{44} was calculated using the point-charge model for the [ZrO_6] octahedron. In the coordinate system ($X_0 \parallel L_2$, $Y_0 \parallel P$, $Z_0 \parallel L_3$), the ξ, η, and ζ principal axes of the cubic components of the fourth-rank spin-Hamiltonian tensor B_4 and the fourth-rank crystal-field tensor V_4^{44} for the Zr^{4+} position with the coordinates ($x = 0$, $y = 0$, $z = 0.64568$) are determined by the following matrices of the direction angles.

B_4	X_0	Y_0	Z_0
ξ	118.68	47.3	123.82
η	143.44	94.85	53.87
ζ	69.34	43.11	54.18

V_4^{44}	X_0	Y_0	Z_0
ξ	117.91	48.01	125.26
η	144.43	94.06	54.74
ζ	69.80	42.28	54.74

(2)

Good agreement between the direction angles of the ξ, η, and ζ principal axes (the differences do not exceed 1.5°) for these tensors and the insignificant deviation from cubic symmetry $d_4(B_4, O_h) = 0.57 \times 10^{-2}$, $d_4(V_4^{44}, O_h) = 0.38 \times 10^{-2}$ confirm that Fe^{3+} ions occupy the Zr^{4+} positions in the $NaZr_2(PO_4)_3$ structure. The existence of six symmetry-related spectra is associated with the fact that the compensator ion is not located on the triple axis of the substituted position. The mobility of the Na^+ compensator ion suggests that similar ions are located in the *B* cavities in the structure. The coordinates of the compensator ions in the *B* cavities were refined by minimizing the sum of the squares of the deviations of the corresponding elements of the normalized crystal-field tensor V_2^{44} from the elements of the spin-Hamiltonian tensor B_2: $\sigma^2 = \sum_{M=-L}^{L}[B_{LM} - V_{LM}^{44}(S_L(B_L)/S_L(V_L^{44}))^{1/2}]^2$. The crystal-field elements were calculated with due regard for the contribution from the ions in the coordination sphere 35 Å in radius. The elements of the spin-Hamiltonian tensor correspond to the compensator ion with the coordinates ($x = -0.3062$, $y = -0.2336$, $z = 0.7319$) in the *B* cavity with the center ($x = -0.30736$, $y = -0.30736$, $z = 3/4$). In this case, the discrepancy factor was determined to be $\sigma^2/S_2(B_2) = 0.01$ and the matrices of the direction angles of the *X*, *Y*, and *Z* principal axes of the spin-Hamiltonian tensor B_2 and the crystal-field tensor V_2^{44} are in reasonable agreement:

B_2	X_0	Y_0	Z_0
X'	44.03	134.0	90.33
Y'	46.28	44.44	83.54
Z'	94.25	94.87	6.47

V_2^{44}	X_0	Y_0	Z_0
X'	44.95	134.44	95.44
Y'	45.07	45.79	82.98
Z'	91.12	98.82	8.89

The local compensator ion only weakly disturbs the crystal field at the Zr^{4+} position. In order to confirm this assumption, we calculated the direction angles of the L_3 principal axes of the maximum invariant components with symmetry $G_S = C_3$ ($\alpha, \beta, \gamma = 0$) and the parameters d_4 characterizing the deviation from symmetry C_3 of the spin-Hamiltonian tensor B_4 and the crystal-field tensor V_4^{44}. The results of calculations are presented in the following tables:

B_4	α, deg	β, deg	γ, deg	$d_4 \times 10^{-2}$
L_3	124.87	68.94	0	0.48
L_3	135.46	1.56	0	0.03
L_3	65.49	108.97	0	0.52
L_3	184.56	108.48	0	0.54

V_4^{44}	α, deg	β, deg	γ, deg	$d_4 \times 10^{-2}$
L_3	125.22	70.67	0	0.30
L_3	145.68	0.15	0	0.01
L_3	65.15	109.53	0	0.25
L_3	185.23	109.61	0	0.27

It can be seen from these data that the L_3 principal axes of the maximum invariant components with symmetry $G_S = C_3$ for the spin-Hamiltonian tensor B_4 and the crystal-field tensor V_4^{44} only slightly deviate from the [0001] axis in the crystal and are characterized by insignificant deviation from symmetry C_3.

DISCUSSION OF THE RESULTS AND CONCLUSIONS

Analysis of the spin-Hamiltonian and the crystal-field tensors conclusively demonstrates that Fe^{3+} impurity ions substitute for Zr^{4+} ions with local charge compensation and lowering of position symmetry. The Na^+ compensator ions are located in cavities of the *B* type and weakly disturb the crystal field in the substitution region. Since Fe^{3+} impurity ions are randomly distributed in the structure, we can make the inference that compensator ions are mobile under the crystal-growth conditions. The fact that Fe^{3+} impurity ions occupy positions of one regular system of points indicates the absence of a statistical distribution of Na^+ ions in *B* cavities at a low concentration of Fe^{3+} ions. The multiplicity $K_M = 6$ and the arrangement of symmetry-related Fe^{3+} EPR spectra correspond to the space group $D_{3d}^6 - R\bar{3}c$ of the $NaZr_2(PO_4)_3$ crystal and confirm that $Na_{1+x}Fe_xZr_{2-x}(PO_4)_3$ solid solutions at low concentrations *x* have a structure similar to the $NaZr_2(PO_4)_3$ structure [18].

According to the intersection of the groups $C_3 \cap C_2 = C_1$ of the Zr^{4+} positions and *B* cavities, the substitution region $Fe^{3+} + Na^+ \longrightarrow Zr^{4+}$ has symmetry C_1. Therefore, it can be expected that the Na^+ compensator ion should be displaced from the symmetry axis and the *B* cavity center (determined as the center of gravity of the ten O^{2-} ions forming the cavity). This displacement

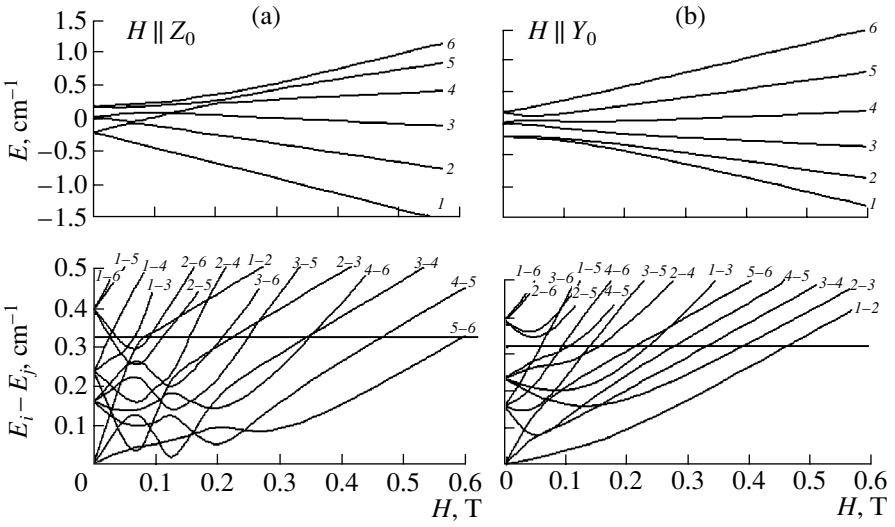

Fig. 3. Energy levels E_i and their differences ($E_i - E_j$) as functions of the magnetic field for the $NaZr_2(PO_4)_3$ crystal: (a) $H \parallel Z_0$ and (b) $H \parallel Y_0$. The line corresponds to the operating frequency ν = 9.4 GHz.

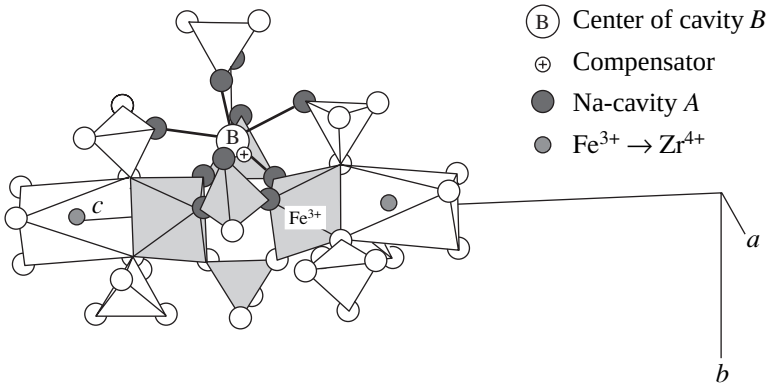

Fig. 4. Positions of the ions forming the crystal framework and the cavities in the $NaZr_2(PO_4)_3$ structure. Shaded octahedra and tetrahedra make up an M_2T_3 lantern. Closed circles indicate the O^{2-} ions forming the cavity *B*.

is 0.77 Å in the direction of the Fe^{3+} impurity ion. The displacement direction forms an angle of 10.3° with the vector connecting the *B* cavity center and the Zr^{4+} position (Fig. 4).

The distance between the Na^+ compensator ion and the Fe^{3+} impurity ion (3.13 Å) is considerably smaller than the distance from the Zr^{4+} position to the *B* cavity center (3.60 Å). This finding is in agreement with the fact that the distances between the dopant and Na^+ ions in the $Na_3Zr_{0.5}Co_{0.5}FeP_3O_{12}$ and $Na_3Zr_{0.5}Fe(II)_{0.5}Fe(III)P_3O_{12}$ compounds are shorter than the Zr^{4+}–Na^+ distance in the $NaZr_2(PO_4)_3$ crystal [19].

However, the distance between the Na^+ compensator ion and the nearest vertex of the $[ZrO_6]$ octahedron (1.85 Å) differs substantially from the sum of the Na^+ and Zr^{4+} radii (2.34 Å). Such a shortened distance is most likely associated with disregarding the displacement of other ions in the substitution region.

As follows from the direction angle matrices (2), the coordination polyhedron of the impurity ion can be determined using the model of point charges corresponding to the first coordination sphere. However, a comparative analysis of the invariant sums of the B_4 and V_4^{44} tensors for different structures, as well as of the systems of principal axes and the ratios of the principal components of the B_2 and V_4^{44} tensors, requires the inclusion of the contributions from more distant charges and the compensator ion. In $ZnSeO_4 \cdot H_2O$ crystals, the inclusion of the contribution from hydrogen ions of the $[Zn(H_2O)_6]$ octahedron to the tensor V_4 leads to satisfactory agreement of the aforementioned topological characteristics of the Mn^{2+} spin-Hamiltonian tensor B_2 and the crystal-field tensor V_2^{44} [6]. The heterovalent substitution $Fe^{3+} \longrightarrow Ge^{4+}$ in $Li_2Ge_7O_{15}$ crystals [7] is accompanied by the local compensation $OH^- \longrightarrow O^{2-}$, and good agreement between the systems of the principal axes of the tensors B_2 and V_2^{44} can be achieved only when the contribution of H^+ compensator ions is taken into account. By generalizing these data, we can argue that the point-charge model for the crystal field adequately describes the main orientational properties of the crystal structure and the spin-Hamiltonian tensors B_2 and B_4 depend quadratically on the crystal-field tensor V_4. At the same time, the tensor B_2 depends linearly on the noncubic elements of the tensor V_4.

Parameters B_{LM} of spin Hamiltonian (1), initial splittings Δ_i ($\times 10^4$ cm^{-1}) of the ground state of Fe^{3+} ions, and quantities S_L ($\times 10^8$ cm^{-2}) in the coordinate system ($X_0 \| L_2$, $Y_0 \| P$, $Z_0 \| L_3$) for the $NaZr_2(PO_4)_3$ single crystal

M, *q*	B_{2M}	b_2^q	B_{4M}	b_4^q
0	−486.597	−595.957	−4.025	−14.432
1	−55.055	330.330	0.204	−6.543
−1	60.834	365.004	0.227	7.280
2	−3.547	−10.641	0.163	3.696
−2	−118.682	356.046	−0.188	4.263
3			5.571	−472.715
−3			−1.487	−126.176
4			−0.174	−5.220
−4			−0.155	4.650

Δ_1 = 2336.5	S_2 = 278423.7	ε* = 7.7 (mT)	
Δ_2 = 1581.7	S_4 = 83.02	*N* = 139	*k* = 20

g tensor $g_{ij} = g_{ji}$

2.00593	0.00102	−0.00034
	2.00539	−0.00019
		2.00512

* $\varepsilon = \sqrt{\sum_{i=1}^{N} \Delta H_i^2/(N-k)}$ is the root-mean-square deviation, and b_2^q stands for the Stevens notation [17].

The invariant S_4 of the spin-Hamiltonian tensor B_4 for Fe^{3+} ions in the $NaZr_2(PO_4)_3$ crystal (table) appears to be unexpectedly close to values characteristic of the tetrahedral environment [7]. Such a small difference cannot be explained only by the Zr–O distances (2.0472, 2.0681 Å) in the $[ZrO_6]$ octahedron in the $NaZr_2(PO_4)_3$ structure. In the $CaCO_3$ calcite, an $[CaO_6]$ octahedron with a Ca–O distance of 2.3598 Å is characterized by the invariant $S_4 = 325 \times 10^{-8}$ cm^{-2} [8]. An increase in the value of S_4 with an increase in the *Me*–O distance is inconsistent with the concept regarding the decrease in the crystal field with an increase in the distance from a field source. A similar contradiction is observed when the invariant $S_4 = 369 \times 10^{-8}$ cm^{-2} [20] for $[TiO_6]$ octahedra characterized by the mean distance $\langle$Ti–O$\rangle$ = 1.977 Å in $KTiOPO_4$ crystals is compared with the invariant $S_4 = 448 \times 10^{-8}$ cm^{-2} [8] for Fe^{3+} ions in $[MgO_6]$ octahedra having the distance Mg–O = 2.0839 Å in the $CaMg(CO_3)_2$ dolomite structure. In order to resolve this contradiction, we examined the mutual arrangement of anion and cation coordination polyhedra with respect to central ions.

The maximum invariant $S_4 = 4735 \times 10^{-8}$ cm^{-2} [21] is observed upon substitution of Fe^{3+} ions for Al^{3+} ions in $[AlO_6]$ octahedra with the mean distance $\langle$Al–O$\rangle$ = 1.9109 Å in $YAlO_3$ crystals having the perovskite-type structure. In these crystals, O^{2-} and Y^{3+} ions comprise the three-layer closest packing; form octahedral and cubic environments of the substitution position, respectively; and make contributions of the same sign to the tensor V_4. The octahedral anion and cubic cation environments are dual. In $Y_3Al_5O_{12}$ garnet, the spin Hamiltonian of Fe^{3+} ions substituting for Al^{3+} ions in $[AlO_6]$ octahedra with an Al–O distance of 1.937 Å is characterized by the invariant $S_4 = 1266 \times 10^{-8}$ cm^{-2}. The substitution octahedron appears to be inside the strongly contracted and substantially elongated octahedra, whose vertices are occupied by Al^{3+} and Y^{3+} ions, respectively. Such an arrangement of cations and anions around the substitution position leads to a decrease in the invariant S_4 as compared to that for $YAlO_3$ crystals. In the $NaZr_2(PO_4)_3$ crystal, the second coordination sphere is formed by the octahedron composed of P^{5+} pentavalent ions. This results in a considerable weakening of the crystal field at the substitution position.

In the $KTiOPO_4$ structure, four vertices of the $[TiO_6]$ octahedron are represented by vertices of four $[PO_4]$ tetrahedra and the other vertices are occupied by "free" O^{2-} ions. In the $NaZr_2(PO_4)_3$ structure, the vertices of the $[ZrO_6]$ octahedron are formed by vertices of six $[PO_4]$ tetrahedra. The calculation of the crystal field with allowance made for the contribution from all the surrounding tetrahedra leads to the ratio $S_4(V_4^{44}, KTiOPO_4)/S_4(V_4^{44}, NaZr_2(PO_4)_3) = 4.6$, which virtually coincides with the ratio between the invariant sums $S_4(KTiOPO_4)/S_4(NaZr_2(PO_4)_3) = 4.4$ for the spin-Hamiltonian tensors B_4. For the $YAlO_3$ and $Y_3Al_5O_{12}$ compounds, similar calculations result in the ratio $S_4(V_4^{44}, YAlO_3)/S_4(V_4^{44}, Y_3Al_5O_{12}) = 4.4$, which is close to the experimental ratio $S_4(YAlO_3)/S_4(Y_3Al_5O_{12}) = 3.7$.

The point charges identical in sign at the vertices of a regular cube and a dual octahedron make the contributions opposite in sign to the tensor V_4. When the charges at the vertices of the cube differ in sign from those of the octahedron, the contributions from the fields of these environments to the tensor V_4 coincide in sign. It is known [22] that, in BaF_2 crystals, an F^- compensator ion located on the triple axis of the $[GdF_8]$ cube with an impurity ion $Gd^{3+} \longrightarrow Ba^{2+}$ leads to an increase in the invariant S_4 of the Gd^{3+} spin-Hamiltonian tensor as compared to a similar invariant without local charge compensation. In CaF_2 crystals, the F^- compensator ion in an $[GdF_8]$ cube neighboring along the quadruple axis results in a considerable decrease in the invariant S_4. A comparison of the above data makes it possible to draw the conclusion that the invariant sum S_4 is governed not only by the effective charges and *Me*–O distances in the first coordination sphere but also by the mutual arrangement of the first and second coordination spheres.

ACKNOWLEDGMENTS

This work was supported by the Ministry of Education of the Russian Federation, project no. E02-9.0-86.

REFERENCES

1. H. Hong, Mater. Res. Bull. **11**, 173 (1976).
2. V. V. Ilyukhin, A. A. Voronkov, and V. K. Trunov, Koord. Khim. **7**, 1603 (1981).
3. A. K. Ivanov-Shits and I. V. Murin, *Solid State Ionics* (S.-Peterb. Gos. Univ., St. Petersburg, 2000) [in Russian].
4. B. E. Sheetz, D. K. Agrawal, E. Brewal, and R. Roy, Waste Manage. Res. **14**, 15 (1994).
5. V. A. Efremov and V. B. Kalinin, Kristallografiya **23** (4), 703 (1978) [Sov. Phys. Crystallogr. **23** (4), 393 (1978)].
6. V. M. Vinokurov, A. R. Al-Soufi, A. A. Galeev, *et al.*, Appl. Magn. Reson. **7**, 323 (1994).
7. A. A. Galeev, N. M. Khasanova, A. V. Bykov, *et al.*, Appl. Magn. Reson. **11**, 61 (1996).
8. N. M. Khasanova, N. M. Nizamutdinov, V. M. Vinokurov, and G. R. Bulka, Kristallografiya **33** (5), 891 (1988) [Sov. Phys. Crystallogr. **33** (5), 527 (1988)].
9. A. K. Przhevuskiĭ, Opt. Spektrosk. **53** (4), 697 (1982) [Opt. Spectrosc. **53** (4), 414 (1982)]; Opt. Spektrosk. **53** (5), 837 (1982) [Opt. Spectrosc. **53** (5), 499 (1982)].

10. N. M. Nizamutdinov, N. M. Khasanova, A. A. Galeev, *et al.*, Kristallografiya **34** (4), 893 (1989) [Sov. Phys. Crystallogr. **34** (4), 536 (1989)].
11. V. A. Il'in and É. G. Poznyak, *Analytic Geometry* (Nauka, Moscow, 1981) [in Russian].
12. Yu. I. Sirotin and M. P. Shaskolskaya, *Fundamentals of Crystal Physics* (Nauka, Moscow, 1979; Mir, Moscow, 1982) [in Russian].
13. A. B. Bykov, L. N. Dem'yanets, S. N. Doronin, *et al.*, Rost Kristallov **16**, 44 (1986).
14. R. V. Galiulin, Kristallografiya **23** (6), 1125 (1978) [Sov. Phys. Crystallogr. **23** (6), 635 (1978)].
15. R. V. Galiulin, *Lectures on Geometrical Foundations of Crystallography* (Chelyabinsk Gos. Univ., Chelyabinsk, 1989) [in Russian].
16. G. Bacquet, J. Dugas, C. Escribe, *et al.*, J. Phys. C: Solid State Phys. **7**, 1551 (1974).
17. C. Rudowicz, Magn. Reson. Rev. **13**, 1 (1987); **13**, 335 (1988).
18. Takashi Asai, Kazuaki Ado, Yuria Saito, *et al.*, Solid State Ionics **35** (3–4), 319 (1989).
19. Hiroyuki Kageyama, Nagao Kamijo, Takashi Asai, *et al.*, Solid State Ionics **40–41** (1), 350 (1990).
20. N. M. Nizamutdinov, N. M. Khasanova, G. R. Bulka, *et al.*, Kristallografiya **32** (3), 695 (1987) [Sov. Phys. Crystallogr. **32** (3), 408 (1987)].
21. V. A. Akkerman, G. R. Bulka, D. I. Vaĭnshteĭn, *et al.*, Fiz. Tverd. Tela (St. Petersburg) **34**, 743 (1992) [Sov. Phys. Solid State **34**, 398 (1992)].
22. I. I. Antonova, N. M. Nizamutdinov, R. Yu. Abdulsabirov, *et al.*, Appl. Magn. Reson. **13**, 597 (1997).

Translated by O. Borovik-Romanova

Crystallography Reports, Vol. 50, No. 5, 2005, pp. 836–842. Translated from Kristallografiya, Vol. 50, No. 5, 2005, pp. 900–907.

PHYSICAL PROPERTIES OF CRYSTALS

Characteristic of Spontaneous Polarization in $Pb_5Ge_3O_{11}$ Crystals

Yu. V. Shaldin, A. A. Bush**, S. Matyjasik***, and M. Kh. Rabadanov***

** Shubnikov Institute of Crystallography, Russian Academy of Sciences, Leninskiĭ pr. 59, Moscow, 119333 Russia*

e-mail:graimo@aha.ru

*** Moscow State Institute of Radio Engineering, Electronics, and Automation (Technical University), pr. Vernadskogo 78, Moscow, 119454 Russia*

**** International Laboratory of High Magnetic Fields and Low Temperatures, Gajowicka 95, Wroclaw, 53-421 Poland*

Received May 13, 2004

Abstract—The temperature behavior of the spontaneous polarization of lead tetragermanate, a uniaxial ferroelectric, is studied in the range from 4.2 to 300 K. The results obtained along with the data from the literature make it possible to reconstruct a complete pattern of the behavior of $P_s(T)$ both in the vicinity of the phase transition and at lower temperatures. In the range from 290 K to T_C, the crystal behavior is found to change from the dipole type ($\beta = 1/2$) to the pseudoquadrupole type ($\beta = 1/4$). This specific crossover manifests itself in the change in the behavior of $P_s^{1/\beta}$ as a function of $(T_C–T)$. In the low-temperature range, weak anomalies in the dependence $P_s(T)$ are found, which point to the occurrence of contributions from the dipole moments of separate structural fragments of Ge_2O_7 and GeO_4, which have internal degrees of freedom and are weakly bound to the dynamics of the crystal lattice. © *2005 Pleiades Publishing, Inc.*

INTRODUCTION

In the most general form, the spontaneous polarization in noncentrosymmetric crystals was considered for the first time in [1–3]. Unfortunately, the results of the theoretical calculations for such a complex dynamic system as pyroelectric do not allow one to indicate unambiguously the directions of experimental investigations. Some advances have been made within the framework of the crystallophysical approach [4], which allows one to single out individual macrofragments responsible for the appearance of spontaneous polarization in the most general sense of this term. These macrofragments are mesotetrahedra, which are built from individual structural elements and obey the symmetry conditions of the object as a whole. It is beyond question that this approach makes it possible to pass from the consideration of the displacements of individual atoms to the analysis of the distortion of mesoscopic formations upon phase transitions and to the estimation of their contribution to the total spontaneous polarization. In connection with this, experimental investigations of the spontaneous polarization in the entire range of occurrence of the polar state and interpretation of these investigations in an effort to determine the contributions from multipole moments are moved to the forefront.

The experimental data available so far point to a considerable scatter in the spontaneous polarization P_s from ~1 C/m^2 (e.g., in $LiNbO_3$ and $LiJO_3$) to 10^{-4} C/m^2 (in $Li_2Ge_7O_{15}$), thus allowing one to doubt the universal character of the appearance of the polar state in crystals. Therefore, the investigation of the particular features of the spontaneous polarization in both proper and improper ferroelectrics (or pseudoproper ferroelectrics) is an important problem.

In our opinion, α-$Pb_5Ge_3O_{11}$ (PGO) single crystals exemplify a rare crystalline medium whose transition to the polar phase is accompanied by interesting gyroanisotropic phenomena [5–10]. Such an unusual combination of physical effects have given impetus to numerous experimental investigations of the physical properties of PGO [10–17] and its structural features [18–22]. Analysis of experimental data on the temperature behavior of the spontaneous polarization [4, 5, 10–14, 23], as well as on gyrotropic [7, 10, 14], piezoelectric [12], nonlinear optical [11, 13], pyroelectric [28, 31], and dielectric [24–27] properties, indicates that, within measurement error, no marked anomalies occur in the range from 300 K to the phase-transition temperature. Virtually no data on low-temperature investigations are available.

The authors of [23] attempted to attribute the particular feature in the temperature behavior of the square of the spontaneous polarization at 420 K to a structural phase transformation. In our opinion, these attempts do not stand up under scrutiny since any monotonic dependence (which $P_s(T)$ usually is) can be approximated with confidence in a finite temperature range by a chain function. There are no data about the structure of this crystal both above and below 420 K that can cast doubt

on this statement. The occurrence of anomalies in the dependence $P_s(T)$ in the range of lower temperatures is equally controversial.

In our opinion, two circumstances determine permanent interest in PGO. The first one is purely cognitive and consists in that the rather small spontaneous polarization of PGO (about 0.05 C/m^2) does not fit in with the empirical rule for oxygen–tetrahedral ferroelectrics [32]: $P_s \sim T_C^{1/2}$. The second circumstance is purely practical and determined by high values of the pyroelectric coefficient at room temperatures [9, 33]. Such an unusual combination of relatively low values of the spontaneous polarization and record-high values of the pyroelectric coefficient stimulates further experimental investigations on the elucidation of the nature of spontaneous polarization in lead tetragermanate. Therefore, the experimental investigation of the particular features of the spontaneous polarization in the entire range of occurrence of the polar state in PGO is moved to the forefront. A quasi-static method [34], which allows one to study changes in the spontaneous polarization in a wide temperature range, is most appropriate for these investigations.

This paper is devoted to the study of the temperature dependence of the spontaneous polarization of PGO crystals of high perfection in the range from 4.2 to 300 K and to the elucidation of the particular features of the structure of these crystals by the modified quasi-static method and with consideration for all known data on the spontaneous polarization (in the range above 300 K). The mesoscopic formations in the form of tetrahedra built from Pb atoms and coordinated GeO_4 tetrahedra that we singled out in the motif of the PGO structure allow us to assign lead tetragermanate to the class of so-called pseudoproper ferroelectrics, whose spontaneous polarization results from multipole interactions.

CRYSTALLOPHYSICAL (NONCENTROSYMMETRIC) PARAMETERS AND PGO STRUCTURE

It is agreed [22] that PGO crystals belong to the class of uniaxial ferroelectrics, undergoing a phase transition from the polar ($P3$) to the nonpolar ($P3/m$) phase at 450 K. Both crystalline phases are described by noncentrosymmetric point groups and, therefore, one can define a polar tensor of the third rank for this class of compounds. According to the symmetry conditions, this tensor can be decomposed into tensor subspaces of vectors ($L = 1$), pseudodeviators ($L = 2$), and septors ($L = 3$) (according to Schouten's notation [35]), where L is the tensor rank. Then, it is easy to verify that, for all the crystals with point symmetry group 3, the components of the two-vector (P_3(I), $-P_3$(II)), pseudodeviator ($Q_{11}^* = Q_{22}^* = -1/2\,Q_{33}^*$), and septor ($S_{121}, S_{212}, S_{131}$) subspaces differ from zero, whereas, for the high-temperature phase, only the components of the septor S_{121} and S_{212} are nonzero. Consequently, the phase transition at $T_C = 450$ K should be characterized by a multipole order parameter when it is necessary to take into account multipole interactions. Considering the tensor quantities introduced as crystallophysical parameters determining the deviation of PGO from the nonpolar phase [4], we can describe the properties of the nonpolar phase in terms of the invariants introduced. Therefore, it is not surprising that only the crystallophysical parameters that are transformed as tensor quantities with the weights $L = 2.3$ will contribute to the spontaneous polarization. This gives rise to a very difficult problem concerning the experimental detection of the contributions from multipole moments to the total polarization.

It is obvious that the problem of separation of the contributions to P_s from the multipole moments can be solved either if these contributions are comparable with the value of the spontaneous polarization itself or if one can choose an appropriate sample orientation.

In [32], an empirical rule has been established for polar oxygen-containing crystals that relates the spontaneous polarization and the phase-transition temperature. Lead tetragermanate with $P_s = 4.8 \times 10^{-2}$ C/m^2 does not fit into this Procrustean bed, thus forcing us to search for reasons for such a deviation in the particular features of its structure (Fig. 1).

In such a complex dynamic system as a crystalline medium, it is not surprising that the multipole moments will contribute to the total spontaneous polarization of all the pyroelectrics. Thus, the expression for the total spontaneous polarization in PGO,

$$P_s^\Sigma = P_s + m_{333}^*: Q_{33}^* + g_{3113}: S_{113} + o(\varepsilon), \qquad (1)$$

does not contradict the symmetry considerations and reflects also the contributions from pseudoquadrupole and octupole moments of the crystalline structure. Here, $P_s = P_3(\mathrm{I}) - P_3(\mathrm{II})$. The proportionality coefficients in (1) are tensor quantities of the $3/m$ point group of the nonpolar phase: $m_{i(jk)}^*$ is the pseudotensor of the third rank, symmetrical with respect to the permutation of the last two indices, and g_{3113} is the coefficient of the tensor of the fourth rank, symmetrical with respect to the permutation of the last three indices. In some cases, e.g., in pseudoferroelectric $Li_2Ge_7O_{15}$ [36], the main contribution is made by the multipole moments, a phenomenon which does not contradict the results of the structural studies.

Since the spontaneous polarization in PGO is relatively low as compared to other oxygen-containing compounds, it seems that an explanation for this deviation (because clear theories are unavailable) can be found by analyzing the structural features of PGO. In both the polar and the nonpolar phases of this compound, one can single out macroscopic fragments in the form of mesotetrahedra formed by two Pb atoms and

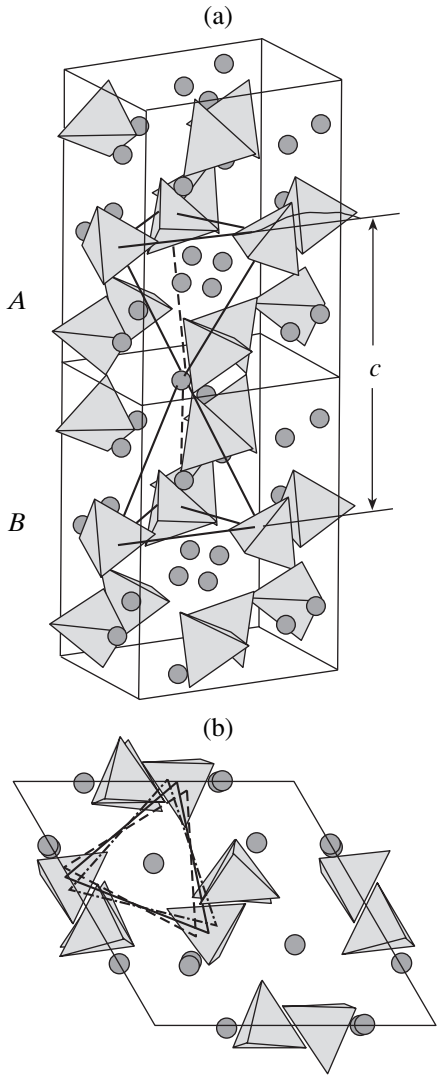

Fig. 1. (a) Fragment of the PGO structure combined from mesotetrahedra of the *A* and *B* types and (b) its projection onto the (0001) plane. The turns of the bases of the mesotetrahedra in the course of the crystal repolarization are shown schematically by the dashed lines.

three single GeO_4 tetrahedra. In the nonpolar phase, both mesotetrahedra are completely equivalent (Fig. 1a). According to the data of diffraction experiments, upon transition to the polar phase, the bases of the mesotetrahedra are rotated with respect to each other in the (0001) plane, which induces a dipole moment along the third-order symmetry axis. Such a deformation of the PGO structure arises owing to anomalous behavior of oxygen atoms from single tetrahedra, as is revealed in [21]. The contribution from the lead atoms, the nonequivalence of the positions of which can be attributed only to a change in their nearest oxygen environment, should be very small. The validity of this statement (see Fig. 2) follows from comparison of the particular features of mesotetrahedra in PGO and $LiTaO_3$ [37], whose P_s, equal to about 0.5 C/m^2, is one

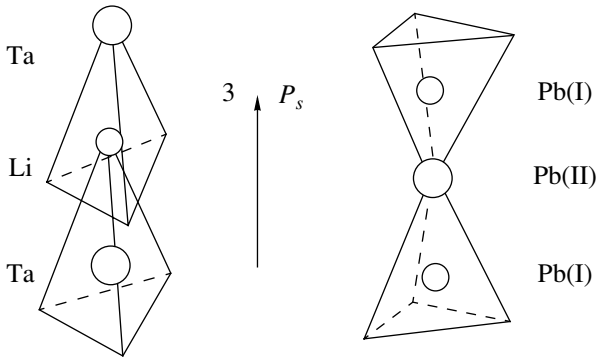

Fig. 2. *A* and *B* mesotetrahedra in the $LiTaO_3$ and $Pb_5Ge_3O_{11}$ structures.

of the record-high values of this parameter. Thus, we can assume that the multipole moments of the main motif of the PGO structure make the major contribution to the spontaneous polarization of this crystal. It is also not improbable that, under these conditions, the contributions to P_s from the local dipole moments of both single GeO_4 and twinned Ge_2O_7 tetrahedra can manifest themselves with decreasing temperature. It follows from the structural studies [21] that such single and twinned GeO_4 tetrahedra have their own internal degrees of freedom, which are characterized by the ordering of oxygen atoms with decreasing temperature and all the consequences ensuing from this.

EXPERIMENTAL

Single PGO crystals were grown by the method of solution–melt crystallization [38]. The phase composition of the samples and their orientation with respect to the polar axis were determined with a DRON-4 X-ray diffractometer and a POLAM L-213M polarization microscope. The powder diffractogram of the single crystals grown and the parameters of a trigonal unit cell (a = 10.224(3) Å, c = 10.664(3) Å) calculated with this diffractogram agree sufficiently well with the data of [15–18]. An examination of the optical homogeneity of the samples in polarized light showed that some samples were perfect. From these samples, we chose a single crystalline plate with an area of 13.4 mm^2 and a thickness of 0.62 mm, which was oriented with respect to the c axis with an accuracy of ~30′. The sample was poled at room temperature with a field of $\pm 2 \times 10^3$ V/cm, created by a Keithly 222 current power supply. The electrodes were made of a current-conducting silver paste, and the current leads were fixed with the same paste. According to the measurements, the resistivity at 295 K exceeded 10^{11} Ohm cm. The hysteresis loop, studied at an electric-field frequency of 0.01 Hz, was practically rectangular in shape (Fig. 3). This result indicates that the PGO sample chosen for the measurements was of high quality.

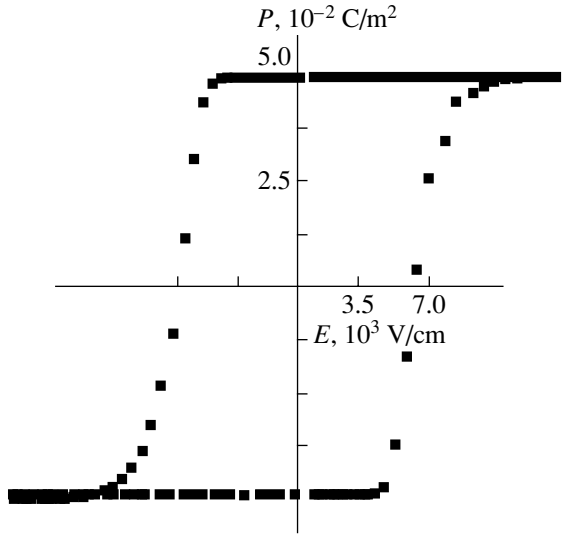

Fig. 3. Hysteresis loop of $Pb_5Ge_3O_{11}$ in a quasi-static electric field.

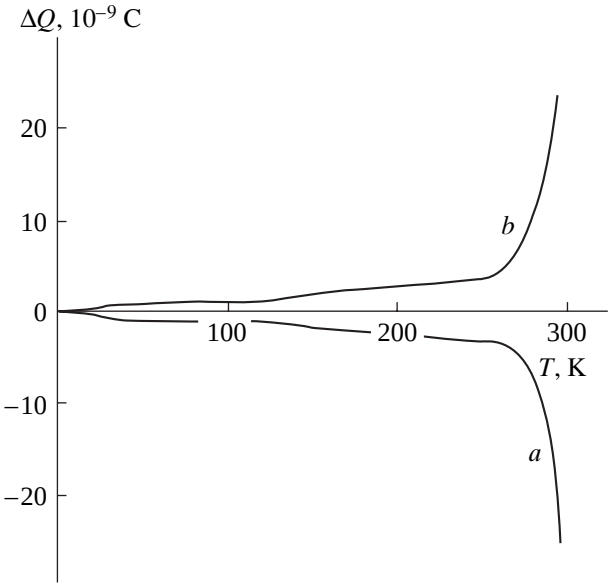

Fig. 4. Temperature dependence of the charge of a PGO sample polarized by electric fields of the two opposite polarities: (*a*) +*E* and (*b*) –*E*.

The temperature dependence of $P_s(T)$ in the range from 4.2 to 300 K was measured using a continuous-flow helium cryostat. The sample was clamped in a crystal holder placed at the end of a coaxial line. A Cemox-1050CD thermometer was fixed to the crystal holder at a middle level of the sample. To control the temperature of the sample, a coil was wound on the crystal holder, which was connected to a stabilized power supply of the type mentioned above. In the course of the measurements, the temperature was maintained with an accuracy of ±0.001 K. The charge arising on the surface of the sample with a change in the temperature was measured by a Keithly 617 universal electrometer. The presence of a digital output in the electrometer significantly simplified the experimental data processing. The temperature dependences of the charge of the monodomain PGO sample experimentally determined for the two opposite polarities of the electric field are shown in Fig. 4.

As the temperature of the sample was decreased to 4.2 K, the sample was short-circuited and then connected to the electrometer input to monitor the zero drift of the measuring system for some period of time. The time interval during which the sample was maintained at helium temperature was determined by the possibility of approximating the zero drift of the system with a linear relationship. In the course of the experiment, the temperature of the sample was varied according to the same time relationship. For our sample connected to the electrometer input through the coaxial line, the zero drift of the entire measuring system was less than 10^{-14} A m/s.

All the measurements were performed in the course of increasing the temperature of the sample and using two opposite polarities of the field. The results obtained were independent of the polarity of the sample (within the measurement error of ±10% and corresponded to its mechanically free state. The whole measurement cycle, including the cooling of the sample, holding at liquid helium temperature, and the measurement process itself, took 4–5 h.

The exit of the sample from liquid helium is a very delicate process and is accompanied by generation of an additional charge due to a temperature gradient. This introduces the major measurement error, which distorts the real temperature dependence of the spontaneous polarization mainly in the range up to 10 K.

RESULTS AND DISCUSSION

The results of the processing of the experimental data that describe the temperature dependence of the change in the spontaneous polarization in PGO crystals,

$$\Delta P_s(T) = P_s(T) - P_s^0 \qquad (2)$$

with respect to P_s^0 at $T \sim 0$ K are shown in Fig. 5. In this dependence, one should distinguish three characteristic temperature ranges: from 4.2 to 30 K, between 30 and 120 K, and from 120 to 250 K. In the first range, the behavior of ΔP_s is typical of all the pyroelectrics; i.e., it can be approximated within the framework of the Debye–Einstein model. The temperature changes of ΔP_s in the other two ranges are very similar, though not

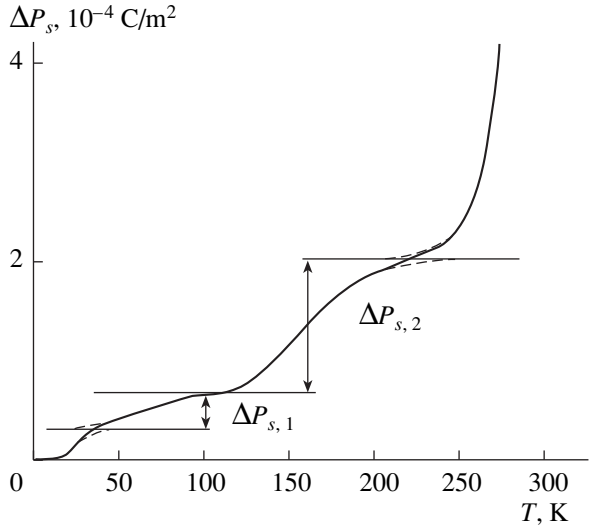

Fig. 5. Temperature dependence of the change in the spontaneous polarization of PGO. $\Delta P_{s,1}$ and $\Delta P_{s,2}$ are the contributions from relaxors of the two types.

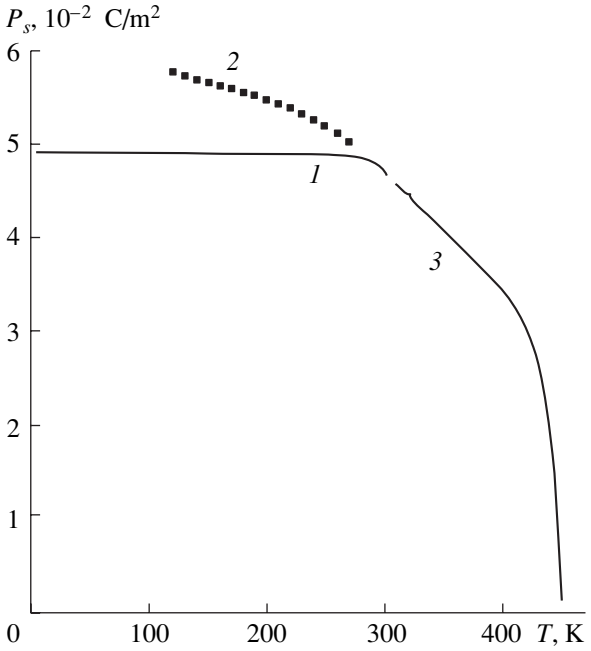

Fig. 6. Temperature dependence of the spontaneous polarization in PGO obtained by normalization of ΔP_s to P for the measurement data obtained: (*1*) in the charge mode and (*2*) in the current mode. For comparison, curve *3* shows the data of [10] on direct measurements of the spontaneous polarization.

quite usual. The data on the dielectric hysteresis measured at a field frequency of 0.01 Hz (see Fig. 3) make it possible to determine the spontaneous polarization of PGO at T = 300 K, which proved to be equal to $(4.8 \pm 0.5) \times 10^{-2}$ C/m^2. This estimate is consistent with the measurement data of other authors [10, 14, 23], thereby allowing us to plot the dependence $P_s(T)$ describing the behavior of the spontaneous polarization of PGO in the entire range of occurrence of the polar state (Fig. 6). Since this dependence (shown by the solid curve) is very atypical for classical ferroelectrics, we performed control measurements of ΔP_s using the same sample but applying a different poling scheme: the sample was heated to $T > T_C$, the field of the above-specified strength was applied, and then the sample was cooled (Fig. 6, curve *2*). A different behavior observed at $T <$ 270 K indicates that the thermodynamic state of the sample changes owing to multiple repolarizations after recording the hysteresis loop.

The smallness of the spontaneous polarization and the unusual temperature dependence give grounds to believe that physically this difference is associated with the smallness of dipole–dipole interactions in comparison with the characteristic energy responsible for the phase transition in lead tetragermanate. Something similar was also observed in other polar compounds of complex composition [36, 39, 40].

The small contribution from dipole–dipole interactions to the order parameter of such compounds can be associated both with insignificant structural distortions of the initial phase and with an anomalously small charge of the soft mode. Turning again to the analysis of the PGO structure, we note that the closeness of the dipole-moment magnitudes in both separated mesotetrahedra *A* and *B* is determined only by the distribution anisotropy of the valence electrons of the lead atoms Pb(I) and Pb(II) due to the different oxygen environment [21]. In this situation, it is not excluded that the phase transition is initiated by multipole interactions; i.e., the contribution to the total spontaneous polarization from the last two terms in (1) considerably exceeds that from the first term. If this assumption holds true, then, upon approximation of the temperature dependence of the order parameter (here, P_s), the critical index β should change. Figure 7 shows the results of treatment of the data on the temperature dependence of the spontaneous polarization in PGO obtained in [10] (which, in our opinion, are the most reliable) in the coordinate system $P_s^{1/\beta} - (T_C - T)$, where β = 1/2 and 1/4. In the temperature range from T_C to $(T_C - 50)$ K, the dependence $P_s^{1/\beta}$ obeys a linear relationship:

$$(P_s)^4 \sim (T_C - T). \quad (3)$$

One can show that later measurement data on P_s [14], as well as the coefficients of the gyration tensor g_{33} [10, 14] and of the nonlinear optical susceptibility d_{333} [13], obey the same law in this temperature range. With a further increase in the temperature, the multipole behavior of PGO changes to the dipole one with β = 1/2 (Fig. 6). The occurrence of the crossover indicates above all that, under conditions of a sharp decrease in the intensity of the multipole interactions, the Lorentz component of the dipole–dipole interaction plays an increas-

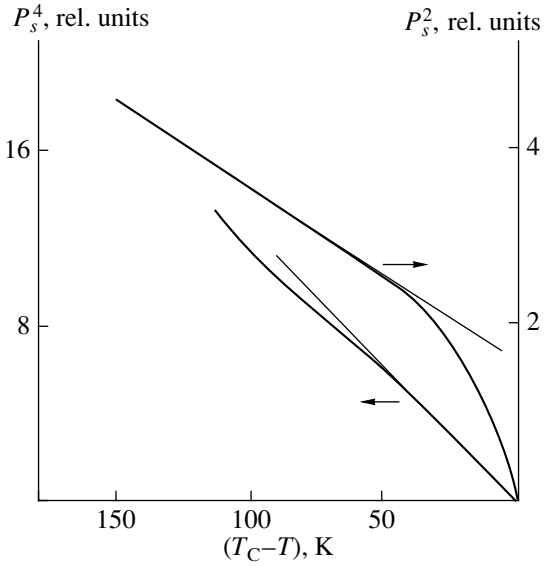

Fig. 7. Approximation of the dependence $P^{1/\beta}(T)$ (β = 1/2, 1/4) as a function of $(T_C - T)$.

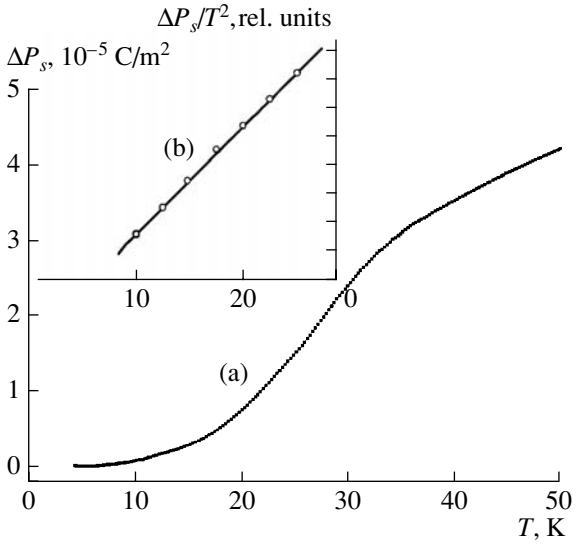

Fig. 8. Temperature dependence of the change in the spontaneous polarization of PGO in the low-temperature range: (a) ΔP_S is plotted as a function of T and (b) $\Delta P_S/T^2$ is normalized to T^2.

ingly important role. Therefore, there is reason to believe that the critical index $\beta = 1/4$ corresponds to the two-dimensional order parameter, described by the coefficients of the second-rank pseudotensor Q_{33}^*.

As was already noted, the experimental technique that we modified allows detection of several anomalies in the behavior of the spontaneous polarization of lead tetragermanate in the low-temperature range. Thus, in the range of helium temperatures below 30 K, the behavior of ΔP_s (Fig. 8) obeys a T^3 power relationship, which disagrees with the theory of [1], predicting that, under the approximation of a continuous anisotropic medium, this dependence should be of the T^4 type. This discrepancy can be primarily associated both with the strong anisotropy in PGO and with the contribution (in terms of the Einstein–Born model) from the Einstein term with the low-frequency characteristic mode ν_E = 32.5 cm^{-1} [41].

The two other particular features are identical and differ only in the value of the contributions: 4.2 and 13.0 (in units of 10^{-5} C/m^2). In the first approximation, their behavior with temperature can be described by the Langevin function

$$\Delta P_s = \sum N_i d_i (\coth d_i E_i^1/kT_i - kT_i/d_i E_i^1). \quad (4)$$

Consequently, we can state here that there are some physical mechanisms that are in no way related to the dynamics of the noncentrosymmetric lattice. It seems that the main motif of the PGO structure contains structural formations of two different types, which have dipole moments and are weakly bound to the lattice. These formations can be considered as certain relaxors of the Debye type. Then, in formula (4), N_i, d_i, and E_i are, respectively, the concentration, dipole moment, and local field of the ith relaxor. According to the data of [24–27], the temperature dependence of the dielectric permittivity in the above-mentioned ranges is also somewhat relaxed in character, with the maximal values of ε_{33} being observed at 106 and 243 K. Therefore, in PGO, there are two ranges of the Debye relaxation with corresponding relaxation times, which should be taken into account in experimental study of the pyroelectric effect by dynamic methods.

For structural elements acting as relaxors, the formations GeO_4 and Ge_2O_7 should be taken. Having dipole moments (the tetrahedra are distorted [21]), these structural elements can align along local fields. Under the condition that the thermodynamic potential of PGO should be minimum, the contribution to the spontaneous polarization from the relaxors is opposite in sign to that of P_s. The first feature, $P_{s,1}$ should be attributed to the contribution from the twinned Ge_2O_7 tetrahedra, whose dipole moments are directed opposite to each other and, therefore, should be partially compensated. The second feature, $P_{s,2}$ is determined by the contribution from the single GeO_4 tetrahedra. Upon transition to the polar phase, these tetrahedra are strongly distorted, which is accompanied by a change in their orientation along the third-order axis [21]. As the temperature decreases, the dipole moments of these tetrahedra align along the polar direction in such a way as to satisfy the condition of the minimum of the thermodynamic potential of the mechanically free PGO crystal.

CONCLUSIONS

Our investigation of the spontaneous polarization in PGO, along with the data previously obtained in [5, 9,

12, 13], allowed us to restore the pattern of behavior of this physical quantity in the entire range of occurrence of the ferroelectric state of this crystal. From the crystallophysical point of view, the analysis of the PGO structure indicates that, along the polar direction, there occur continuous chains consisting of mutually bound mesotetrahedra of the two types, which ensure the ferroelectric ordering of lead tetragermanate. The smallness of the dipole moments of the mesotetrahedra, which results from the smallness of the effective charge of the bond Pb(I) and Pb(II), determines all the specifics of the transition from the dipole behavior ($\beta = 1/2$) to the pseudoquadrupole one ($\beta = 1/4$) against the background of considerable multipole moments. The occurrence of such a crossover is a very nontrivial result, indicating that there are still unknown possibilities for the behavior of complex polar crystals.

ACKNOWLEDGMENTS

We are grateful to S.Dasko for his help in measuring the PGO hysteresis loop.

This study was partially supported by the Russian Foundation for Basic Research, project no. 05-02-16794.

REFERENCES

1. M. Born, Rev. Mod. Phys. **17** (2-3), 245 (1945).
2. R. A. Cowley, Adv. Phys. **12** (2), 421 (1975).
3. P. Grout, N. March, and T. Trorp, J. Phys. C: Solid State Phys. **8** (6), 2167 (1975).
4. Yu. V. Shaldin, Fiz. Tverd. Tela (Leningrad) **19** (6), 1580 (1977) [Sov. Phys. Solid State **19**, 922 (1977)].
5. H. Iwasaki, K. Sugii, T. Yamada, and N. Niizeki, Appl. Phys. Lett. **18** (10), 444 (1971).
6. S. Namamatsu, H. Sujiama, and K. Dei, J. Phys. Soc. Jpn. **31** (2), 616 (1971).
7. H. Iwasaki, K. Sugii, N. Niiseki, and H. Toyoda, Ferroelectrics **3** (2–4), 157 (1972).
8. G. Jones, N. Shaw, and A. Vere, Electron. Lett. **8** (14), 345 (1972).
9. H. Iwasaki, Sh. Mijasawa, H. Koizumi, *et al.*, J. Appl. Phys. **43** (12), 4907 (1972).
10. N. Uchida, T. Saku, H. Iwasaki, and K. Onuki, J. Appl. Phys. **43** (12), 4933 (1972).
11. T. Yamada, H. Iwasaki, and N. Niizeki, J. Appl. Phys. **43** (3), 771 (1972).
12. R. Miller, W. Nordland, and A. Ballman, Ferroelectrics, No. 7, 109 (1974).
13. R. Newnham and L. Gross, Endeavour **23** (1), 18 (1974).
14. M. V. Pentegova, V. D. Sal'nikov, and Yu. Ya. Tomashpol'skiĭ, Kristallografiya **19** (4), 820 (1974) [Sov. Phys. Crystallogr. **19**, 507 (1974)].
15. S. Yu. Stefanovich, V. V. Chechkin, V. D. Sal'nikov, *et al.*, Kristallografiya **21** (3), 540 (1976) [Sov. Phys. Crystallogr. **21**, 300 (1976)].
16. A. A. Bush and Yu. N. Venevtsev, Kristallografiya **23** (1), 203 (1978) [Sov. Phys. Crystallogr. **23**, 110 (1978)].
17. Y. Iwata, H. Koizumi, and N. Koyano, J. Phys. Soc. Jpn. **35** (1), 314 (1973).
18. Y. Iwata, N. Koyano, I. Shibuya, and N. Niizeki, J. Phys. Soc. Jpn. **35** (4), 1269 (1973).
19. M. Kay, R. Newnham, and R. Wolfe, Ferroelectrics **9** (1–2), 1 (1975).
20. Y. Iwata, J. Phys. Soc. Jpn. **43** (3), 961 (1977).
21. Y. Iwata, N. Koyano, and I. Shibuja, Ann. Res. Reactor. Inst. Kyoto Univ **3**, 86 (1973).
22. A. A. Bush and Yu. N. Venevtsev, *Single Crystals with Ferroelectric and Related Properties in PbO–GeO_2 System and Their Possible Applications* (NIITÉKhIM, Moscow, 1981) [in Russian].
23. V. A. Vazhenin, V. B. Guseva, V. Ya. Shur, *et al.*, Fiz. Tverd. Tela (St. Petersburg) **43** (10), 1875 (2001) [Phys. Solid State **43**, 1952 (2001)].
24. A. A. Bush and Yu. N. Venevtsev, Izv. Akad. Nauk SSSR, Neorg. Mater. **17** (2), 302 (1981).
25. V. N. Gavrilov, É. V. Zolotoyabko, *et al.*, Fiz. Tverd. Tela (Leningrad) **25** (10), 10 (1983) [Sov. Phys. Solid State **25**, 4 (1983)].
26. E. L. Rumyantsev, V. A. Vazhenin, and M. S. Gol'dshteĭn, Fiz. Tverd. Tela (Leningrad) **21** (12), 2522 (1979) [Sov. Phys. Solid State **21**, 1457 (1979)].
27. V. V. Dem'yanov and V. D. Sal'nikov, Fiz. Tverd. Tela (Leningrad) **16** (12), 3623 (1974) [Sov. Phys. Solid State **16**, 2353 (1974)].
28. G. Burns, F. Dacol, and W. Taylor, Phys. Rev. B **28** (5), 2531 (1983).
29. R. Watton, Ferroelectrics **14**, 719 (1976).
30. V. A. Borisenok, E. Z. Novitskiĭ, L. A. Shuvalov, *et al.*, Kristallografiya **28** (6), 1154 (1983) [Sov. Phys. Crystallogr. **28**, 678 (1983)].
31. J. Ghulghule and A. Katpatal, J. Phys. Chem. Solids **60**, 425 (1999).
32. S. Abrahams, S. Kurts, and P. Jamienson, Phys. Rev. **172** (2), 551 (1968).
33. *Handbook on Light Detectors*, Ed. by L. Z. Kriksunov and L. S. Kremenchugskiĭ (Tekhnika, Kiev, 1985) [in Russian].
34. M. E. Lines and A. M. Glass, *Principles and Application of Ferroelectrics and Related Materials* (Clarendon Press, Oxford, 1977; Mir, Moscow, 1981).
35. J. A. Schouten, *Tensor Analysis for Physicists* (Clarendon Press, Oxford, 1959; Akad. Nauk SSSR, Moscow, 1965).
36. Yu. V. Shaldin, S. Matyyasik, and M. Kh. Rabadanov, Kristallografiya **48** (2), 347 (2003) [Crystallogr. Rep. **48**, 315 (2003)].
37. Yu. V. Shaldin, Opt. Spektrosk. **72** (4), 913 (1992) [Opt. Spectrosc. **72**, 492 (1992)].
38. A. A. Bush and Yu. N. Venevtsev, Kristallografiya **30** (2), 349 (1985) [Sov. Phys. Crystallogr. **30**, 202 (1985)].
39. Yu. Shaldin, R. Poprawski, and S. Matyjasik, Solid State Commun. **68** (5), 487 (1988).
40. R. Poprawski, Yu. Shaldin, and S. Matyjasik, J. Mat. Sci. and Eng. C. **13** (1–2), 203 (1987).
41. A. A. Bush and E. A. Popova, Fiz. Tverd. Tela (St. Petersburg) **46** (5), 875 (2004) [Phys. Solid State **46**, 902 (2004)].

Translated by V. Rogovoĭ

Crystallography Reports, Vol. 50, No. 5, 2005, pp. 843–848. Translated from Kristallografiya, Vol. 50, No. 5, 2005, pp. 908–914.

LIQUID CRYSTALS

Domain Structure of a Nematic-Liquid-Crystal Layer in Low-Frequency Couette Flow

E. N. Kozhevnikov

Samara State University, ul. Akademika Pavlova 1, Samara, 443011 Russia

e-mail: kozhev@ssu.samara.ru

Received September 24, 2004

Abstract—The spatially periodic structure arising in a homeotropic nematic-liquid-crystal (NLC) layer in low-frequency Couette flow is described theoretically. The analysis of this phenomenon is based on the hydrodynamic equations for NLCs, from which a self-consistent system of equations is selected for perturbations of hydrodynamic variables: the steady-state angle of the molecule rotation, the liquid flow, and the velocity of oscillating vortex flows. The formation of the periodic structure is explained by the phase delay of the velocities of the vortex oscillating flows forming in the deformed structure with respect to the shear velocity in the Couette flow. It is shown that at low frequencies this difference in the velocities is caused by the orientational waves near the layer boundaries. In the case of fixed orientation of molecules at the boundaries, the dependence of the threshold shear amplitude on the frequency and layer thickness is given by the relation $u_{th} \sim (\omega h^2)^{-1/4}$. The influence of the conditions for the molecule orientation at the layer boundaries on the above phenomenon is analyzed. © *2005 Pleiades Publishing, Inc.*

The deformation of a nematic liquid crystal (NLC) under periodic shear results in a change in its optical properties. This effect can serve as a basis for the development of acousto-optic sensors, laser modulators, etc. [1, 2]. The response of liquid-crystal layers to periodic shear is quite diverse and requires adequate theoretical description. At low shear amplitudes, NLC molecules oscillate about their initial equilibrium positions. An increase in the amplitude may lead to the formation of a spatially modulated structure, observed optically as domains. In this case, vortex motions of the liquid arise in the layer, while the molecules oscillate about a new equilibrium direction, which changes periodically along the layer. The geometry and the threshold characteristics of the domains are diverse. They depend on the initial orientation of the sample and the polarization and frequency of the shear and are sensitive to electric and magnetic fields. For elliptical in-plane motion of the boundary plates, roll domains are formed [3–6]. Their orientation and the threshold of their formation depend on the ellipticity of the plate motion. Theoretically, the phenomenon disappears when switching to plane shear. The influence of viscous waves on a homeotropic NLC layer subjected to a perpendicular applied electric field results in the formation of a cellular domain structure. In each cell, the director, deflected from the initial orientation, slowly rotates. This rotation gives rise to the formation and growth of disclinations [7].

An effect of plane periodic shear on homeotropic and planar nematic layers in the absence of fields may also produce a domain structure [8–16]. Attempts to analyze this phenomenon theoretically were made in a number of studies.

The formation of a spatially modulated structure in a homeotropic NLC layer under periodic shear at high and low frequencies was considered in [17, 18] on the basis of the multimode analysis. However, excessive simplifications of the initial equations in these studies lead to a theoretical picture of the effect that is inconsistent with experimental results. The formation of the domain structure in a homeotropic NLC layer under periodic shear produced by the in-plane motion of one boundary plate was described theoretically in [19]. The appearance of the domain structure is explained by the phase delay of the liquid velocity in the vortex flows with respect to the shear velocity in Couette flow; the delay due to the inertia of the medium is also considered. The results obtained in [19] for frequencies higher than 200 Hz agree with the experimental data [8–10]. In particular, the theory predicts the dependence of the threshold shear amplitude U_{th} on the frequency ω and the layer thickness h in the form $U_{th} \sim (\omega h^2)^{-1}$. However, at lower frequencies the theory disagrees with experimental results. The calculation [11] of the threshold of the phenomenon for the planar orientation involves the same simplifications as in [19] and yields comparable results. At low frequencies, these results also disagree quantitatively with experimental data.

Experimental study of the domain structure in the NLC layer at frequencies <200 Hz [12, 13] showed both qualitative (the dependence of the threshold on the frequency and the layer thickness) and quantitative discrepancy with the results of the theoretical analysis presented in [11, 19]. In these studies, a computer simulation of the domain structure was performed using the multimode Galerkin method. The threshold of the for-

1063-7745/05/5005-0843$26.00 © 2005 Pleiades Publishing, Inc.

mation of domains and their spatial period were determined numerically. Inertial effects were neglected. A relation was found between the threshold amplitude of the shear gradient in the layer $u_{th} = U_{th}/h$ and the shear frequency and the layer thickness in terms of the scaling combination $\omega\tau$, where $\tau = \gamma_1 h^2/K_{33}$. It was also shown that the dependence $u_{th}(\omega\tau)$ is described in plane by a curve common for NLC layers of any thickness. This result contradicts the experimental data reported in the same publications [12, 13], which indicate that the curves $u_{th}(\omega\tau)$ in plane are significantly displaced with a change in the layer thickness. The calculated curve does not fit any individual experiment carried out at a fixed layer thickness. Therefore, the result of the computer simulation of the domain structure in the NLC layer in a low-frequency Couette flow is inconsistent with experimental results. The physical mechanism of the domain formation was not analyzed in the above studies.

Thus, the nature of the domain structure formed in a homeotropic NLC by low-frequency shear remains unclear and the corresponding theoretical description of this phenomenon is lacking. In this study, we consider the processes leading to the formation of a spatially modulated structure in an NLC layer in low-frequency Couette flow. This phenomenon is analyzed on the basis of the hydrodynamic equations in which the quadratic terms proportional to the product of the molecule rotation angle and the liquid velocity are retained. The occurrence of the domain structure is shown to be due to the delay of the vortex flows in the layer with respect to shear in Couette flow. At low frequencies the delay is determined by the action of elastic torques in the orientational waves near the boundary plates. The influence of the boundary conditions for the molecule orientation on the phenomenon under study is taken into account.

Let us calculate the effect in the case of a finite orientation energy of molecules at the NLC layer boundaries, restricting ourselves to the one-constant approximation for the Frank elastic energy. The equations describing the rotation of molecules and their motion in an NLC have the form [20, 21]

$$\gamma[\mathbf{N} - \hat{V}\cdot\mathbf{n} + (\hat{V}\mathbf{n}\cdot\mathbf{n})\mathbf{n}] - [\mathbf{h} - (\mathbf{h}\cdot\mathbf{n})\mathbf{n}] = 0,$$

$$\rho\dot{V} = -\nabla P + \nabla\hat{\sigma}.$$

Here, $\mathbf{n}$ is the director specifying the direction of the molecule alignment, V is the liquid velocity, $\hat{V}$ is the deformation-rate tensor, $\mathbf{N} = \dot{\mathbf{n}} - \frac{1}{2}(\mathrm{curl}\mathbf{V}\cdot\mathbf{n})$ is the rotational velocity of molecules relative to the surrounding liquid, ρ is the density, P is pressure, $\hat{\sigma}$ is the viscous-stress tensor, γ is the rotational-viscosity coefficient, and $\mathbf{h}$ is the Frank elastic force

$$\mathbf{h} = \nabla_i\frac{\partial g}{\partial(\nabla_i\mathbf{n})} - \frac{\partial g}{\partial\mathbf{n}}.$$

Here, g is the bulk density of the Frank elastic energy. In the one-constant approximation, g has the form

$$g = \frac{1}{2}K_{33}\sum_i(\nabla n_i)^2, \quad i = x, y, z;$$

where K_{33} is the Frank elastic constant. Setting small viscosity coefficients α_3 and α_1 to zero, we get $\gamma = \alpha_5 - \alpha_6$. In this case, the components of the viscous-stress tensor take the form

$$\sigma_{ij} = \alpha_4 v_{ij} + \alpha_6(v_{ik}n_k n_j + v_{jk}n_k n_i) + \gamma v_{km}n_k n_m n_i n_j - h_i n_j.$$

Let us consider now the domain formation in the shear plane, which is specified by the shear direction (X axis) and the normal to the layer (Z axis). Assuming that molecules rotate in the XZ plane and all variables are independent of the coordinate Y, we find that $V_y = 0$. Such a distribution of the molecule orientation in domains follows from the estimations of the structure stability with respect to the random deviation of molecules from the shear plane [19]. We assume that the shear deformation in the layer is produced by the in-plane motion of the upper ($Z = h/2$) boundary plate with the frequency ω and the shear amplitude U_0, while keeping the lower ($Z = -h/2$) boundary plate at rest:

$$U_x|_{Z = h/2} = u_0 h\sin\omega T,$$

$$U_x|_{Z = -h/2} = U_z|_{Z = -h/2} = U_z|_{Z = h/2} = 0.$$

Here $u_0 = U_x/h|_{Z = h/2}$ is the dimensionless shear deformation of the NLC layer and T is time.

We assume that the shear amplitudes are small: $u_0 = U_x/h|_{Z = h/2} < 1$. Then, the angles θ of the deviation of molecules from the z axis are also small. This allows us to linearize the equations of motion with respect to the angles and set the director components to be $n_x \approx \theta$, $n_z \approx 1$.

In what follows, we go over to the dimensionless coordinates $x = X/h$, $z = Z/h$, time $t = \omega T$, and the dimensionless velocities $v_k = V_k/(\omega h)$. Retaining the terms proportional to the product of the angle θ and the velocity $\mathbf{v}$ in the equations of motion, we obtain the follow-

ing system of equations for θ, v_x, and v_z:

$$\begin{gathered}\partial_t\theta - \varepsilon\Delta\theta - v_{x,z} = -\theta_x v_x - \theta_z v_z - 2\theta v_{zz},\\ (\eta\sigma^2\Delta\partial_t - \hat{D})v_x + \varepsilon\Delta\partial_z^3\theta\\ = [\partial_z(\partial_z^2 - \partial_x^2)(v_{z,z}\theta) - 2\partial_x\partial_z^2(v_{xz}\theta)]\\ + \eta\sigma^2\partial_z[\Delta v_z v_{1x} - v_z v_{x,z^2}],\\ \operatorname{div}\mathbf{v} = 0,\end{gathered} \tag{1}$$

where $\hat{D}$ is the differential operator

$$\hat{D} = \eta\Delta^2 + \partial_z^2\partial_x^2,$$

ε and σ are the dimensionless parameters that determine the dependence of the effect under study on the NLC layer thickness h and the shear frequency ω in terms of the scaling parameter ωh^2

$$\varepsilon = \frac{K_{33}}{\gamma\omega h^2},\quad \sigma^2 = \frac{\rho\omega h^2}{\eta} = \frac{\lambda}{\varepsilon},\quad \lambda = \frac{\rho K_{33}}{\gamma\eta} \sim 10^{-6},$$

and $\eta = (a_4 + a_6)/\gamma$ is the dimensionless viscosity in the viscous wave propagating along the crystal axis.

The hydrodynamic variables will be represented by the expansions

$$\mathbf{v} = u_0(\mathbf{v}_1 + \mathbf{v}') + u_0^2\mathbf{v}_2,\quad \theta = u_0(\theta_1 + \theta') + \theta_2,$$

where the subscript 1 indicates the hydrodynamic variables characterizing the external action, the subscript 2 indicates the steady-state part of the perturbations, and the prime stands for the oscillating part. The appearance of the nonzero steady-state angle θ_2 in the solution to the hydrodynamic equations implies the crystal transition into a new orientation state.

Further, we extract from system (1) the equations for the external action

$$\begin{gathered}(\sigma^2\partial_t - \partial_z^2)v_{1x} - \frac{\varepsilon}{\eta}\partial_z^3\theta_1 = 0,\\ \theta_{1,t} - \varepsilon\partial_z^2\theta_1 - \partial_z v_{1x} = 0,\\ \theta_1 \pm \delta\theta_{1,z}\big|_{z=\pm1/2} = v_{1x}\big|_{z=-1/2} = 0,\\ v_{1x}\big|_{z=1/2} = \cos t;\end{gathered} \tag{2}$$

the equations for the oscillating variables

$$\begin{gathered}\partial_t\theta' - \varepsilon\Delta\theta' - \partial_z v_x' = -\theta_{2,x}v_{1x},\\ (\eta\sigma^2\Delta\partial_t - \hat{D})v_z' - \varepsilon\Delta\partial_z^2\partial_x\theta' = \partial_x^2\partial_z(\theta_2 v_{1x,z}),\\ \operatorname{div}\mathbf{v}' = 0,\\ \theta' \pm \delta\theta'_{,z}\big|_{z=\pm1/2} = v_z'\big|_{z=\pm1/2} = v'_{z,z}\big|_{z=\pm1/2} = 0;\end{gathered} \tag{3}$$

and the equations for the steady-state variables

$$\begin{gathered}\frac{\varepsilon}{u_0^2}\Delta\theta_2 + \partial_z v_{2x} = \langle\theta'_{,x}v_{1x} + 2\theta_1 v'_{z,z} + \theta_{1,z}v_z'\rangle,\\ \hat{D}v_{2x} - \frac{\varepsilon}{u_0^2}\Delta\partial_z^3\theta_2 = -\partial_z(\partial_z^2 - \partial_x^2)\langle v'_{z,z}\theta_1\rangle\\ + \partial_x\partial_z^2\langle\theta' v_{1x,z} + \theta_1 v'_{x,z} + \theta_1 v'_{z,x}\rangle\\ - \eta\sigma^2\partial_z[\langle\Delta v_z' v_{1x}\rangle + \langle v_z' v_{x,z^2}\rangle],\\ \operatorname{div}\mathbf{v}_2 = 0,\\ \theta_2\big|_{z=\pm1/2} = v_{2x}\big|_{z=\pm1/2} = 0,\quad \int_{-1/2}^{1/2} v_{2x}dz = 0.\end{gathered} \tag{4}$$

Here, $\delta = K_{33}/Wh$, W is the density of the surface orienting energy, and the angle brackets denote averaging over the oscillation period. With respect to the steady-state rotation angle θ_2, which varies slowly throughout the layer thickness, the molecules are assumed to be strongly oriented at the layer boundaries. (This corresponds to the actual inequality $\delta \ll 1$.) The oscillating angles θ_1 and θ' contain terms that vary rapidly in orientational waves. Thus, the orienting energy is assumed to be finite in the boundary conditions for these quantities.

Steady-state stresses and torques, which destabilize the initial structure, contain averaged terms of the form $\langle v'_{x,z}\theta_1\rangle = \langle v'_{x,z}u_{1x,z}\rangle$ and are nonzero if the liquid velocity v_x' in the oscillating flows is phase-delayed with respect to the liquid velocity v_{1x} in Couette flow. This delay is related to the inertial properties of the medium, the effect of elastic torques on the director in thin (of the order of magnitude of the wavelength of the orientational wave) boundary layers, and the effect of bulk elastic torques. Simple estimations of the threshold shear amplitude in these cases yield, respectively, the following dependences: $u_0 \sim \sqrt{\varepsilon}/\sigma \sim \omega^{-1}$, $u_0 \sim \varepsilon^{1/4} \sim \omega^{-1/4}$, and $u_0 \sim 1$. Thus, the inertia of the medium and the elastic torques manifest themselves at higher and lower frequencies, respectively. We restrict ourselves to the frequencies

$$\omega < \left\{\frac{\eta^2 K_{33}}{\gamma\rho h^6}\right\}^{1/3}$$

(in this case, $\sigma^4 < \varepsilon$) and ignore inertial terms in the equations of motion. Oscillating perturbations contain both smooth (slowly varying throughout the layer thickness) terms and terms rapidly varying throughout the length of the orientational wave. In the equations for smooth variables, the quantities of the order of magnitude $\varepsilon^{1/2} \ll 1$ are retained, while the terms of higher-order smallness are neglected. In the steady-state equa-

tions, we will only consider a smooth dependence of perturbations on the z coordinate because the consideration of rapid changes in the steady-state variables in the boundary layers only slightly affects the result.

In the above approximation, the solution to Eqs. (2) for an external action takes the form

$$v_{1x} = (z + 1/2)\cos t, \quad \theta_1 = \sin t.$$

Assuming the perturbations to be periodic along the layer, we set θ_2, v_{2x}, $v_z' \sim \cos kx$, and $\theta' \sim \sin kx$. The complex velocity of the oscillating vortex flows v_z' is represented in the form $v_z' = v^*\cos kx$, where $v^* = (v_c + iv_s + v^{(i)})\exp(-it)$, v_c, and v_s are real smooth functions of z and $v^{(i)}$ is a rapid function of z generated by the orientational waves near the layer boundaries.

Let us transform the equations for the steady-state variables by eliminating the angles θ' and θ_1 and their time derivatives. Neglecting the terms of the order of smallness ε, we obtain the following equation for the steady-state angle of molecule rotation

$$\frac{\varepsilon}{u_0^2}\Delta\theta_2 + v_{2x,z} = \partial_z^2\langle \mathrm{Re}\, v_z' u_{1x}\rangle.$$

Introducing the function $w = v_{2x} - \partial_z\langle \mathrm{Re}\, v_z' u_{1x}\rangle$, we recast this equation into the form

$$\frac{\varepsilon}{u_0^2}\Delta\theta_2 + w_z = 0. \tag{5}$$

Because of the boundary conditions for v_z' and v_{2x} in systems (3) and (4), the function w satisfies the conditions

$$w|_{z=\pm 1/2} = 0; \quad \int_{-1/2}^{1/2} w\,dz = 0 \tag{6}$$

and can be regarded as the reduced flow velocity.

In the equation for the steady-state flow in system (4), we transform the convective term using the second equation of system (3):

$$-\eta\sigma^2\partial_z\langle \Delta v_z' v_{1x}\rangle = \partial_z\langle(\eta\sigma^2\Delta\partial_t v_z')u_{1x}\rangle$$
$$= \partial_z\langle u_{1x}\hat{D}v_z'\rangle + \varepsilon\langle u_{1x}\Delta\partial_z^2\theta_{,x}'\rangle + \langle\partial_x^2\partial_z(\theta_2 v_{1x})u_{1x}\rangle.$$

Then, discarding the inertial terms containing powers of σ and the terms of the order of ε, we extract the following equation for w:

$$(\hat{D} + \partial_z^4)w = -[(4\eta + 1)\partial_z^4 + 4\eta\partial_x^2\partial_z^2]\langle v_z' u_{1x,z}\rangle$$
$$= -\frac{1}{2}[(4\eta + 1)\partial_z^4 + 4\eta\partial_x^2\partial_z^2]v_s\cos kx. \tag{7}$$

In the case under consideration, the phenomenon is determined by the right-hand side of Eq. (7) and occurs only at $v_s \neq 0$, i.e., when the velocities in the vortex flows are delayed from the velocity of the boundary plate displacement.

Neglecting first the boundary effects, we find from the first equation of system (3) the angle $\theta' = (u_{z,zz}/k + ik\theta_2 u_0)\exp(-it)$ slowly varying with the z coordinate. On supplementing θ' with the term $\theta^{(i)}$ generated by orientational waves, the complex angle θ^* can be represented in the form $\theta^* = (u_{z,zz}/k + ik\theta_2 u_0 + \theta^{(i)})\exp(-it)$.

Let us extract from system (3) the equations for the rapid perturbations $\theta^{(i)}$ and $v^{(i)}$

$$\partial_t\theta^{(i)} - \varepsilon\partial_z^2\theta^{(i)} + \frac{1}{k}\partial_z^2 v^{(i)} = 0,$$
$$v^{(i)} = -\frac{\varepsilon k}{\eta}\theta^{(i)}. \tag{8}$$

In solving Eqs. (8), the constants of integration are determined from the boundary conditions for the total angle θ^* of the molecule rotation. After appropriate transformations, the velocity v^*, required for further calculations, takes the form

$$v^* = \left\{ v_c + iv_s - i\frac{1 + (1 + i)\delta q}{2q^2(1 + \eta)(1 + 2\delta q + 2\delta^2 q^2)}\right.$$
$$\times[\partial_z^2(v_c + iv_s)\big|_{-1/2}e^{(i-1)q(z+1/2)} \tag{9}$$
$$\left. + \partial_z^2(v_c + iv_s)\big|_{1/2}e^{-(i-1)q(z-1/2)}]\right\}e^{-it}.$$

Here, $q = \sqrt{\eta/[2(1 + \eta)\varepsilon]}$ is the wave vector in the orientational waves.

The velocity v^* and its derivatives with respect to z become zero at the layer boundaries.

$$v^*|_{\pm 1/2} = v_{,z}^*|_{\pm 1/2} = 0.$$

Substituting expression (9) for v^* into these conditions and neglecting the terms of the order of $q^{-2} \sim \varepsilon$, we bring the boundary conditions for the functions v_c and v_s to the form

$$v_c + iv_s|_{\mp 1/2} = 0,$$

$$\partial_z(v_c + iv_s) \pm i\frac{A}{2q(1 + \eta)}\partial_z^2(v_c + iv_s)\Big|_{\mp 1/2} = 0,$$

where

$$A = A(\delta q) = \frac{1 + 2\delta q}{1 + 2\delta q + 2\delta^2 q^2}.$$

The slow velocity is then represented by the sum

$$v^* = \tilde{v}_c + i\tilde{v}_s - i\frac{A}{2q(1+\eta)}[\partial_z^2(v_c + iv_s)\big|_{-1/2}(z+1/2)(z-1/2)^2 - \partial_z^2(v_c + iv_s)\big|_{1/2}(z-1/2)(z+1/2)^2], \quad (10)$$

in which the functions $\tilde{v}_c$ and $\tilde{v}_s$ vanish at the layer boundaries together with their derivatives.

Substituting v^* from (10) into the second equation of system (3), separating the real and imaginary parts in this equation, and neglecting the terms of the order of q^{-2}, we obtain the following equations for $\tilde{v}_c$ and $\tilde{v}_s$:

$$\hat{D}\tilde{v}_c \approx k^2\theta_{2,z},$$
$$\hat{D}\tilde{v}_s = \frac{A}{2q(1+\eta)} \times \{v_{c,zz}\big|_{-1/2}[\eta k^4(z+1/2)(z-1/2)^2 - k^2(1+2\eta)(6z-1))] - v_{c,zz}\big|_{1/2}[\eta k^4(z-1/2)(z+1/2)^2 - k^2(1+2\eta)(6z+1))]\}. \quad (11)$$

The function v_s, entering Eq. (7) for w, is determined by solving system (11)

$$v_s = \tilde{v}_s - \frac{A}{2q(1+\eta)}[\tilde{v}_{c,zz}\big|_{-1/2}(z+1/2)(z-1/2)^2 - \tilde{v}_{c,zz}\big|_{1/2}(z-1/2)(z+1/2)^2]. \quad (12)$$

It follows from Eqs. (5), (7), and (11) and expression (12) that

$$u_0 = \text{const}(qA)^{-1/2}. \quad (13)$$

In this relation, the constant and the period of the domain structure are determined by the solution to this system. The solution was found numerically using the Galerkin method. To this end, the z-dependence of the angle θ_2 was represented by a sum of the trigonometric functions $\sin(2j\pi z)$ and $\cos(2j-1)\pi z$ ($j = 1, 2, 3, \ldots, N$), while the z dependence of the velocities w, v_c, and v_s was represented by a sum of the Chandrasekhar functions

$$\text{Ch}_j = \frac{\cos(l_j z)}{\cos(l_j/2)} - \frac{\cosh(l_j z)}{\cosh(l_j/2)},$$
$$\text{Sh}_j = \frac{\sin(m_j z)}{\sin(m_j/2)} - \frac{\sinh(m_j z)}{\sinh(m_j/2)},$$

in which the numbers l_j and m_j correspond to zero values of the derivatives at $z = \pm 1/2$. The threshold amplitude $u_0 = u_0(k)$ was found from the solvability condition for the system of equations for the coefficients in the expansions of θ_2, w, $\tilde{v}_c$, and $\tilde{v}_s$; the wave vector k at the effect threshold minimizes the value of u_0. The number of terms in the expansions was chosen taking into account the specified calculation accuracy: at $N \geq 4$ the calculation error became less than 5%. The viscosity η was set equal to that of MBBA liquid crystals: $\eta = 0.4$ [21]. The calculated value of the wave vector was $k = 4.4$, which gives the domain width $d \approx 0.7h$. This value is independent of the frequency and the layer thickness and changes only slightly with the crystal viscosity. At $k = 4.4$, the constant in formula (13) is 4.7. Then, the dimensionless threshold shear amplitude u_{th} is given by the formula

$$u_{th} = 4.7\left\{\frac{1 + 2\delta q + 2\delta^2 q^2}{q(1+2\delta q)}\right\}^{1/2}. \quad (14)$$

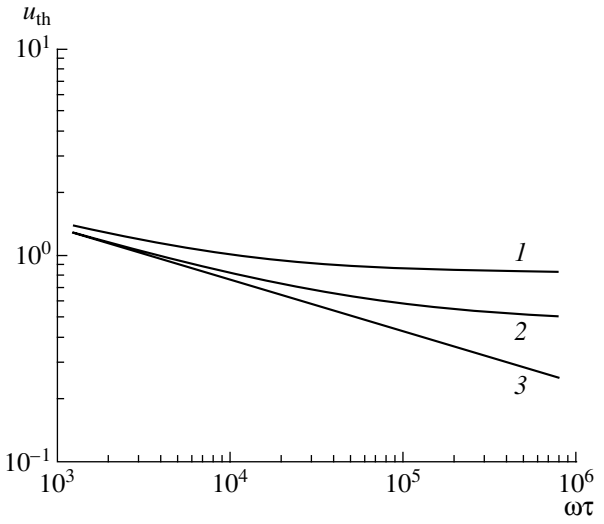

Dependence of the effect threshold on the reduced frequency at δ = (*1*) 0, (*2*) 0.01, and (*3*) 0.03.

At large values of the energy W and the layer thickness or at sufficiently low frequencies, when the condition of strong orientation of molecules at the layer boundary ($q\delta \ll 1$) is valid, the threshold amplitude is $u_{th} = 4.7q^{-1/2}$, while its dependence on the frequency and the layer thickness is determined by the relation $u_{th} \sim (\omega\tau)^{-1/4}$, where $\tau = \gamma h^2/K_{33}$ is the characteristic time of the distortion relaxation in NLC layers. In this case, the calculation shows that the dependence of the threshold amplitude on the frequency and the layer thickness is expressed in terms of the scaling combination $\omega\tau$. On going from the strong orientation of NLC molecules at the boundaries to the weak orientation, the scaling in the dependence of the threshold amplitude on $\omega\tau$ disappears. Indeed, a decrease in the orienting energy and the layer thickness or an increase in the frequency up to the values at which $\delta q \gg 1$ result in the frequency-independent threshold amplitude u_{th} =

$4.7\sqrt{K_{33}/Wh}$. When the value of $\omega\tau$ is fixed, the threshold shear amplitude must decrease with an increase in the layer thickness, approaching a minimum at $\delta q \ll 1$. The condition of the scaling violation in the form $\delta q \approx \sqrt{\omega\eta\gamma^2 K_{33}/W^2} \geq 1$ is independent of the NLC layer thickness and is only determined by the frequency ω of the plate displacement. For a MBBA nematic crystal ($K_{33} \approx 10^{-6}$ dyn, $\eta = 0.4$, $\gamma = 0.78$ P [20, 21]) and a typical value of the orienting energy $W \sim 10^{-3}$ erg cm^{-2}, the scaling is violated at frequencies $f > 1$ Hz. The results obtained shown in Fig. 1, where the dependences $u_{th} = u_{th}(\omega\tau)$, plotted according to (14) for different values of $\delta = K_{33}/Wh$, demonstrate the scaling violation with an increase in the frequency.

It is worth noting that the dimensionless hydrodynamic equations for NLCs, describing the effect of the oscillatory Couette flow on a nematic layer (and being, generally, nonlinear in θ and **v**), contain the frequency ω and the layer thickness h expressed only in terms of the parameters $\varepsilon = 1/\omega\tau$ and $\sigma^2 = \lambda\omega\tau$. For a strong orientation of molecules at the layer boundaries, when $\delta = 0$, the structure of the equations ensures the scaling dependence of the threshold shear amplitude on the frequency and the layer thickness ($u_{th} = u_{th}(\omega\tau)$) for all frequencies and threshold amplitudes, including the values $u_{th} \gg 1$ at low frequencies. The scaling violation in the experiment should indicate either a weak orientation of the molecules at the layer boundary or the difference between the configuration of the initial flows and the Couette flow configuration.

Let us compare the calculation results with the experimental data of [12, 13]. The latter show no scaling in the formation of the domain structure. Thus, along with the oscillatory shear, an additional external factor must be present in the experiment. This factor was ignored in the interpretation of the data obtained in [12, 13]. The increase in the experimental threshold shear amplitude with an increase in the layer thickness at a fixed value of $\omega\tau$ indicates that the scaling violation in the experiment carried out in [12, 13] is not related to weak anchoring energy and requires separate consideration.

The adequacy of the theory developed is qualitatively confirmed by the fact that the experimental dependence of the threshold amplitude on ω disappears with an increase in frequency for small layer thicknesses (30–50 μm) [12, 13], for which this dependence is close to the calculated one. The domain dimension $d = 0.7h$, found above, is somewhat less than the experimental value $d_{exp} \approx h$. At frequencies satisfying the condition $\omega\tau > 5 \times 10^3$, the theoretical values of the threshold amplitude, provided that the orientation of molecules at the boundaries is strong, are close to the values of u_{th} obtained by computer simulation in the cited publications. At lower frequencies, formula (14) predicts a smaller value of the threshold amplitude as compared with the numerical and experimental results of [12, 13]. This difference is caused by the linearization of the hydrodynamic equations with respect to the angle θ_1 performed in our study. However, this linearization is allowed only for small displacement amplitudes and cannot be used at $\omega\tau < 5 \times 10^3$. Nonlinear effects at low frequencies and the inertia of the medium at high frequencies, as well as additional factors affecting the domain formation, require a separate analysis, which is beyond the scope of this study.

ACKNOWLEDGMENTS

This work was supported by the Russian Foundation for Basic Research, project no. 04-02-17454.

REFERENCES

1. A. P. Kapustin and O. A. Kapustina, *Acoustics of Liquid Crystals* (Nauka, Moscow, 1986) [in Russian].
2. G. N. Yakovenko, Akust. Zh. **40**, 851 (1994) [Acoust. Phys. **40** (5), 754 (1994)].
3. E. Gyuon and P. Pieranski, J. Phys. Colloq. France **36**, 201 (1975).
4. P. Pieranski and E. Gyuon, Phys. Rev. A **9**, 404 (1974).
5. E. Dubois-Violette and F. Rothen, J. Phys. France **39**, 1039 (1978).
6. E. Guazelli and E. Guyon, J. Phys. France **43**, 915 (1982).
7. V. K. Kondratenko, M. M. Fardzitov, and A. N. Chuvyrov, Fiz. Tverd. Tela **17**, 795 (1975) [Sov. Phys. Solid State **17**, 506 (1975)].
8. G. N. Belova and E. I. Remizova, Kristallografiya **31**, 517 (1986) [Sov. Phys. Crystallogr. **31**, 304 (1986)].
9. G. N. Belova and E. I. Remizova, Akust. Zh. **31**, 289 (1985) [Sov. Phys. Acoust. **31**, 171 (1985)].
10. G. N. Belova and E. I. Remizova, Kristallografiya **30**, 343 (1985) [Sov. Phys. Crystallogr. **30**, 198 (1985)].
11. S. J. Hogan, T. Mullen, and P. Woodford, Proc. R. Soc. London A **441**, 559 (1993).
12. T. Börsönyi, A. Buka, A. P. Krekhov, and L. Kramer, Phys. Rev. E **58**, 7419 (1998).
13. A. P. Krekhov, T. Börsönyi, P. Tótch, *et al.*, Phys. Rep. **337**, 171 (2000).
14. O. S. Tarasov, A. P. Krekhov, and L. Kramer, Kristallografiya **44**, 1121 (1999) [Crystallogr. Rep. **44**, 1050 (1999)].
15. O. S. Tarasov, A. P. Krekhov, and L. Kramer, cond-mat/0205399 (2002), Vol. 1.
16. A. P. Krekhov and L. Kramer, Phys. Rev. E **53**, 4925 (1996).
17. I. A. Chaban, Akust. Zh. **24**, 200 (1978).
18. I. A. Chaban, Akust. Zh. **31**, 132 (1985) [Sov. Phys. Acoust. **31**, 77 (1985)].
19. E. N. Kozhevnikov, Zh. Éksp. Teor. Fiz. **91** (4), 1346 (1986) [Sov. Phys. JETP **64**, 793 (1986)].
20. P. G. de Gennes, *The Physics of Liquid Crystals* (Clarendon Press, Oxford, 1974; Mir, Moscow, 1977).
21. M. J. Stephen and J. P. Straley, Rev. Mod. Phys. **46**, 617 (1974).

Translated by A. Zolot'ko

Crystallography Reports, Vol. 50, No. 5, 2005, pp. 849–853. Translated from Kristallografiya, Vol. 50, No. 5, 2005, pp. 915–919.

SURFACE AND THIN FILMS

Effect of the Sign of Misfit Strain on the Formation of a Dislocation Structure in SiGe Epitaxial Layers Grown on Si and Ge Substrates

V. I. Vdovin*, M. G. Mil'vidskiĭ, and T. G. Yugova****

** Institute of Chemical Problems for Microelectronics, Bol'shoi Tolmachevskiĭ per. 5, Moscow, 119017 Russia*

*** State Institute of Rare Metals, Bol'shoi Tolmachevskiĭ per. 5, Moscow, 119017 Russia*

e-mail: icpm@mail.girmet.ru

Received August 5, 2004

Abstract—Comparative analysis of the specific features of the formation of a dislocation structure in the single-layer epitaxial heterostructures $Si_{1-x}Ge_x$/Si and $Ge_{1-y}Si_y$/Ge is performed. It is ascertained that, at a relatively low lattice mismatch between an epitaxial layer and a substrate, the sign of misfit strain at the interface significantly affects the processes of defect formation. The most probable reasons for the observed phenomena are analyzed with allowance for the specific features of the state of the ensemble of intrinsic point defects in epitaxial layers subjected to elastic strains of a different sign. *© 2005 Pleiades Publishing, Inc.*

INTRODUCTION

The effect of the sign of misfit strain on the processes of formation of a dislocation structure in epitaxial heterostructures was first revealed in the study of highly lattice-matched heterostructures of quaternary III–V solid solutions grown on substrates of corresponding binary compounds [1, 2]. It was found that, at a deviation from isoperiodicity at the interface (at low misfit strains) when tensile stresses are present in the epitaxial layer, the generation of misfit dislocations begins at a lower misfit strain as compared to the case of compressive stresses in the epitaxial layer [1–3].

An attempt was made in [4] to realate this phenomenon to the effect of the sign of misfit strain on the motion of 30° and 90° partial dislocations formed as a result of the dissociation of 60° misfit dislocations. However, this approach has not been developed.

To investigate this phenomenon in more detail, we used epitaxial heterostructures based on SiGe solid solutions grown on Si and Ge substrates. The tetrahedral radius of the Ge atom greatly exceeds that of the Si atom (1.58 and 1.17 nm, respectively). Therefore, introduction of Ge atoms into Si leads to an increase in the lattice constant of the epitaxial layer of the solid solution in comparison with the lattice constant of the Si substrate; i.e., $Si_{1-x}Ge_x$/Si epitaxial layers grow under the conditions of compression. In contrast, introduction of Si atoms into Ge leads to a decrease in the lattice constant of the epitaxial layer in comparison with the Ge substrate; i.e., $Ge_{1-y}Si_y$/Ge epitaxial layers are subjected to tensile stresses.

Much attention has been given to the regularities of formation of a dislocation structure in SiGe epitaxial heterostructures (see, for example, [5–16]). $Si_{1-x}Ge_x$/Si heterostructures have been studied most thoroughly. Unfortunately, comparative analysis of the specific features of defect formation in $Si_{1-x}Ge_x$/Si and $Ge_{1-y}Si_y$/Ge heterostructures aimed at establishing a possible effect of the sign of misfit strain at the interface and the substrate plasticity on the formation of a dislocation structure has not been carried out. In this study, we tried to some extent to gain insight into this problem.

EXPERIMENTAL

Layers of $Si_{1-x}Ge_x$ solid solutions were grown on Si(100) substrates by molecular-beam epitaxy with a solid Si source and a gaseous Ge source at 700°C. Layers of $Ge_{1-y}Si_y$ solid solutions were grown on Ge substrates by hydride vapor-phase epitaxy at 600°C. These growth techniques were described in [5, 7], respectively. The Si substrates were dislocation-free, and the dislocation density in Ge substrates did not exceed 10^3 cm^{-2}. The epitaxial layers were grown at a relatively low layer/substrate lattice mismatch ($|f| \le 10^{-2}$).

Fairly high growth temperatures and relatively large thicknesses of grown layers (which, under the given growth conditions, significantly exceed not only the critical thickness h_{cr} of misfit-dislocation generation but also the critical thickness h_{FR} of misfit-dislocation multiplication by the Frank–Read mechanism) make it

possible to perform comparative analysis of the results obtained for the heterostructures under consideration.

Structural investigations were performed by chemical etching of angle laps of heterostructures in combination with interference optical microscopy and transmission electron microscopy (TEM). We studied the regularities of changes in the linear densities of misfit and threading dislocations in the epitaxial layer and dislocations in the near-interface substrate region (substrate dislocations) at a change in the solid-solution composition. The dislocation densities in the epilayers and substrates was determined from the density of dislocation etch pits revealed in $Si_{1-x}Ge_x$/Si heterostructures in an etchant based on HF and CrO_3 and in $Ge_{1-y}Si_y$/Ge heterostructures in an etchant based on $K_3Fe(CN)_6$ and KOH. The linear density of misfit dislocations was measured from TEM images of longitudinal cuts of heterostructures in the interface region.

RESULTS AND DISCUSSION

We reported the results of our previous investigations of the structural features of $Si_{1-x}Ge_x$/Si and $Ge_{1-y}Si_y$/Ge heterostructures in [5, 7], respectively. Comparison of these results shows that general regularities in the formation of a dislocation structure in both cases are observed. These regularities manifest themselves in the presence of characteristic extreme points on the experimental dependences of the densities of misfit, threading, and substrate dislocations on the solid solution composition, reflecting the specificity of the processes of nucleation, motion, and multiplication of dislocations in the heterostructures under study as the lattice mismatch between the substrate and epitaxial layer increases. At the same time, the heterostructures under study show some quantitative differences in the observed concentration dependences.

Establishing these differences, it should be taken into account that, in the case we are considering, $Si_{1-x}Ge_x$ epitaxial layers were grown on Si(100) substrates, whereas $Ge_{1-y}Si_y$ layers were grown on Ge(111) substrates. Under these conditions, at the same lattice mismatch at the interface, the effective shear stresses acting in the easiest slip planes and determining the regularities of the nucleation and motion of dislocations in the heterostructures, τ_{eff}, are significantly different. The value of τ_{eff} is found from the expression [17]

$$\tau_{eff} = \cos\lambda\cos\varphi\varepsilon 2\mu(1+\nu)/(1-\nu), \quad (1)$$

where μ and ν are, respectively, the shear modulus and the Poisson ratio in an isotropic solid; ε is the two-dimensional elastic strain in the film, arising because of the difference in the lattice constants of the substrate (a_s) and the layer (a_l), which is determined by the composition of the solid solution (the parameter x or y),

$$f = (a_l - a_s)/a_s; \quad (2)$$

λ is the angle between the Burgers vector and the perpendicular (lying in the interface plane) to the line of intersection of the dislocation-slip plane and the substrate surface; and φ is the angle between the slip plane and the normal to the interface. The quantity $\cos\lambda\cos\varphi$ is referred to as the Schmid factor, which is equal to 0.418 and 0.27 for the substrate orientations (100) and (111), respectively. Therefore, to reveal the specific features of the dislocation-structure formation, one has to compare the dependences of the densities of misfit, threading, and substrate dislocations on τ_{eff}. The corresponding results are shown in Figs. 1–3.

The data shown in Figs. 1 and 2 indicate that the generation of misfit dislocations and, genetically related to them, threading dislocations in the epitaxial layer in a $Si_{1-x}Ge_x$/Si heterostructure, in which the epitaxial layer is subjected to compression strains, begins at much larger values of τ_{eff} than in $Ge_{1-y}Si_y$/Ge heterostructures, where the epitaxial layer is tensile strained. A similar regularity is also observed for the dislocation multiplication by the Frank–Read mechanism: in $Si_{1-x}Ge_x$/Si heterostructures this process begins at values of τ_{eff} exceeding those for the $Ge_{1-y}Si_y$/Ge heterostructures by almost a factor of 2 (Figs. 2, 3). At the same time, the density of threading and substrate dislocations at extreme points of $Si_{1-x}Ge_x$/Si heterostructures is higher in comparison with $Ge_{1-y}Si_y$/Ge heterostructures (Figs. 2, 3).

As follows from our previous data [6, 8], at a small layer/substrate lattice mismatch ($|f| \le 1.5 \times 10^{-3}$), the specific features of the dislocation structure of the heterostructures under study are mainly determined by the generation of misfit dislocations at heterogeneous sources. With a further increase in the mismatch ($1.5 \times 10^{-3} \le |f| \le 10^{-2}$), the dislocation-structure formation is determined to a large extent by the misfit-dislocation multiplication by the modified Frank–Read mechanism, whose intensity first increases and then decreases with an increase in x and y. At sufficiently large mismatches ($|f| > 10^{-2}$), the features of the dislocation structure are determined by the change in the mechanism of epitaxial growth, i.e., the passage from the layer to the island mechanism of crystallization.

The results of our investigations [6, 8] and the data of [18] suggest that the main centers of heterogeneous dislocation nucleation in SiGe epitaxial layers are fine precipitates formed as a result of spinodal decomposition of the solid solution. Spinodal decomposition occurs on the surface of a growing layer and is accompanied by the formation and subsequent in-growth of microprecipitates enriched in Ge ($Si_{1-x}Ge_x$/Si) or Si ($Ge_{1-y}Si_y$/Ge) into the layer matrix. The presence of misfit strains facilitates the process of spinodal decomposition. As was shown in [18] by the example of microprecipitates enriched in Ge in $Si_{1-x}Ge_x$/Si heterostructures, the microprecipitates formed are platelike.

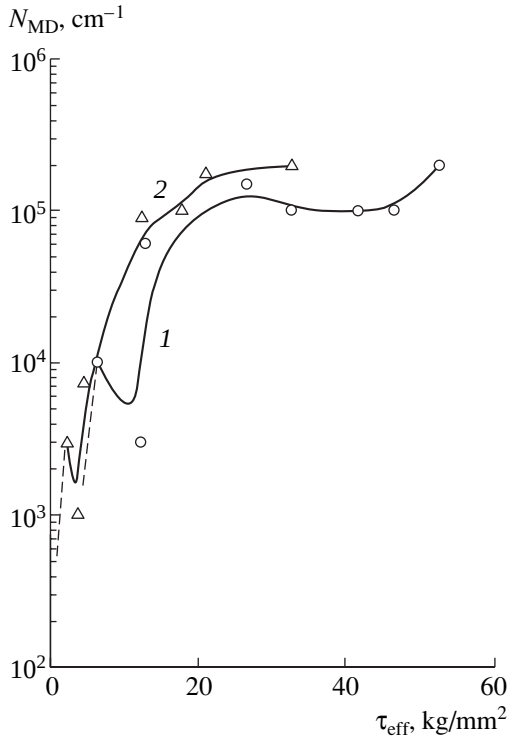

Fig. 1. Dependences of the density of misfit dislocations at the interface in (*1*) $Si_{1-x}Ge_x/Si$ and (*2*) $Ge_{1-y}Si_y/Ge$ heterostructures on the effective shear stress.

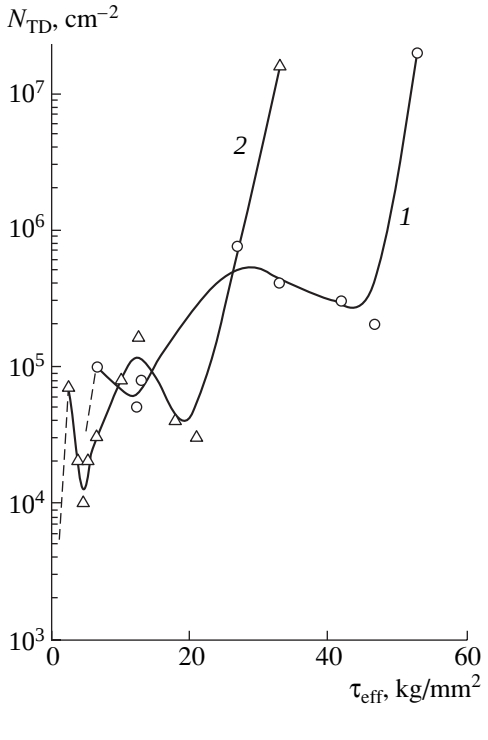

Fig. 2. Dependences of the density of threading dislocations in the epitaxial layers of (*1*) $Si_{1-x}Ge_x/Si$ and (*2*) $Ge_{1-y}Si_y/Ge$ heterostructures on the effective shear stress.

It is known (see, for example, [19]) that the presence of elastic stresses in a crystal lattice leads to a change in the enthalpy of formation of intrinsic point defects (vacancies and interstitials). Elastic compressive stresses decrease the vacancy-formation enthalpy, whereas tensile stresses decrease the interstitial-formation enthalpy. As a result, the equilibrium concentrations of the corresponding defects in an elastically strained lattice increase. In $Si_{1-x}Ge_x/Si$ heterostructures, the epitaxial layer is compressively strained; therefore, the dominant intrinsic point defects in it are vacancies. In $Ge_{1-y}Si_y/Ge$ heterostructures, where the epitaxial layer is tensile-strained, interstitials are dominant in the layer.

Germanium-enriched microprecipitates formed in $Si_{1-x}Ge_x/Si$ have a larger lattice constant in comparison with the solid-solution matrix. In $Ge_{1-y}Si_y/Ge$ heterostructures, where microprecipitates are enriched with Si, the situation is opposite. In both cases, microprecipitates are strained, and additional misfit strains arise at the precipitate/matrix interface, which may lead to the redistribution of intrinsic point defects.

In relatively thick epitaxial layers, when microprecipitates with a lattice constant smaller than that of the matrix are formed, the hydrostatic (dilatation) component of the stress fields should be tensile in precipitates and zero in the surrounding matrix. The situation radically changes when a microprecipitate is located in the immediate vicinity of the free surface of the epitaxial layer (when the distance between the microprecipitate and the surface is either smaller or of the same order of magnitude as the microprecipitate size). Then, owing to the strong screening of the normal component of the microprecipitate stress field by the free surface, the hydrostatic component may become negative in the gap between the microprecipitate and the free surface and positive at the lateral faces of the platelike microprecipitate. Intrinsic interstitials may migrate into these lateral zones. This process is accompanied by the formation of interstitial dislocation loops [20].

Apparently, it is this situation that is implemented in $Ge_{1-y}Si_y/Ge$ heterostructures, since the formation of microprecipitates, as noted above, occurs on the surface of an elastically strained growing layer, and the corresponding migration of intrinsic interstitials, which are dominant in the epitaxial layer, occurs during the subsequent in-growth of microprecipitates into the matrix. In $Si_{1-x}Ge_x/Si$ heterostructures, where the epitaxial layers are compressively strained and Ge-enriched microprecipitates have a larger lattice constant than the matrix solid solution, the opposite situation should be observed. In this case, as a result of the directed migration of vacancies (which are dominant in the epitaxial layer), vacancy dislocation loops are formed at the boundaries between the lateral faces of platelike microprecipitates and the matrix. This is the fundamental dif-

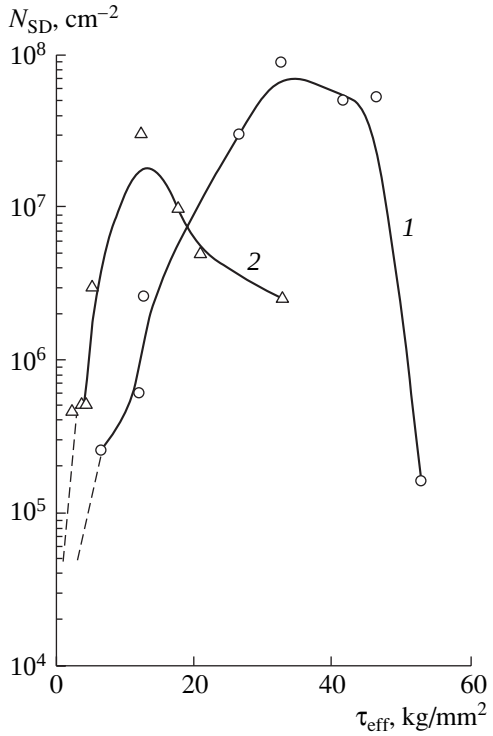

Fig. 3. Dependences of the density of dislocations in the near-interface substrate region in (*1*) $Si_{1-x}Ge_x$/Si and (*2*) $Ge_{1-y}Si_y$/Ge heterostructures on the effective shear stress.

ference in the processes occurring in the heterostructures under consideration.

Within the microscopic theory of dislocation formation in heterostructures [18], when the lattice mismatch at the interface is small and sources of heterogeneous dislocation nucleation in the form of strained microscopic precipitates, coherent with the matrix, are present in the epitaxial layer, the defect formation occurs as follows. When a strained precipitate reaches some critical size, the loss of its coherence with the formation of a stable dislocation loop in its vicinity becomes energetically favorable. The subsequent expansion of the dislocation loop to the critical size and passage to the easiest slip plane lead to the formation of misfit dislocations at the interface. The processes of formation of a stable dislocation loop and its subsequent expansion to the critical size involve intrinsic point defects present in the epitaxial layer. These defects are vacancies in $Si_{1-x}Ge_x$/Si heterostructures, where the epitaxial layers are compressively strained, and interstitials in $Ge_{1-y}Si_y$/Ge heterostructures, where the epitaxial layers are tensile-strained. In both cases, owing to the decrease in the enthalpy of formation of corresponding intrinsic point defects in the elastically strained epitaxial layers, the equilibrium concentrations of these defects are fairly high. Under these conditions, these processes are controlled by the diffusion mobility of the dominant intrinsic point defects. In the Si and Ge lattices, the diffusion mobility of interstitials greatly exceeds that of vacancies. For this reason, at comparable values of the lattice mismatch at the interface, the generation of misfit dislocations in the tensile-strained epitaxial layers in $Ge_{1-y}Si_y$/Ge heterostructures occurs at a much higher rate. This circumstance seems to be the main reason that the generation of misfit dislocations in $Si_{1-x}Ge_x$/Si heterostructures, where the epitaxial layers are compressively strained, begins at larger values of τ_{eff} and their multiplication by the modified Frank–Read mechanism (at comparable misfit strains at the interface) is less intense.

As noted above, the densities of threading and substrate dislocations at the extreme points on their dependences on τ_{eff} for $Si_{1-x}Ge_x$/Si heterostructures exceeds that for $Ge_{1-y}Si_y$/Ge heterostructures. At first glance, this fact contradicts the above-considered phenomena. However, one should take into account that the formation of misfit dislocations, as well as their subsequent, fairly intense multiplication by the Frank–Read mechanism in $Si_{1-x}Ge_x$/Si heterostructures occurs at significantly higher actual misfit strains. It is known (see, for example, [13, 18]) that in both Ge and Si, as well as in epitaxial layers of SiGe solid solutions, the velocity of dislocation motion depends strongly on τ_{eff}: $V_{disl} \sim \tau_{eff}^m$, where the exponent m, according to the data of different authors, changes in the range $1 \le m \le 2$. Thus, the processes of plastic relaxation of misfit strains in $Si_{1-x}Ge_x$/Si heterostructures occur when the velocity of dislocation motion in them exceeds that in $Ge_{1-y}Si_y$/Ge heterostructures. This circumstance is the most likely reason for the high dislocation density at the extreme points of the dependence of the dislocation density on τ_{eff}. The effect of the velocity of dislocation motion also manifests itself in the misfit-dislocation multiplication by the Frank–Read mechanism, which leads to the penetration of dislocations into the near-interface substrate region. In $Si_{1-x}Ge_x$/Si heterostructures, this process is more effective, which leads to deeper penetration of dislocations into the substrate and the formation of slip bands in it [21]. In $Ge_{1-y}Si_y$/Ge heterostructures, slip bands are not observed.

CONCLUSIONS

Comparative analysis of the specific features of formation of a dislocation structure in the single-layer epitaxial heterostructures $Si_{1-x}Ge_x$/Si and $Ge_{1-y}Si_y$/Ge is performed. The effect of the sign of misfit strain on the generation and multiplication of misfit dislocations is established. At a relatively small lattice mismatch between the epitaxial layer and the substrate ($|f| \le 10^{-2}$), the generation of misfit dislocations in $Si_{1-x}Ge_x$/Si heterostructures, where the epitaxial layer is compressively strained, begins at higher misfit strains as compared to $Ge_{1-y}Si_y$/Ge heterostructures, where the epitaxial layer is tensile strained. A similar regularity is

observed for the dislocation multiplication by the modified Frank–Read mechanism: in $Si_{1-x}Ge_x$/Si heterostructures, this process begins at a value of τ_{eff} almost two times higher than in $Ge_{1-y}Si_y$/Ge heterostructures. At the same time, the densities of threading dislocations in the epitaxial layer and the near-interface substrate region at the extreme points of their dependences on τ_{eff} are higher for $Si_{1-x}Ge_x$/Si than for $Ge_{1-y}Si_y$/Ge heterostructures.

The observed differences in the dislocation-structure formation in heterostructures based on SiGe solid solutions are explained with allowance for the specific features of the state of the ensemble of intrinsic point defects in the layers subjected to elastic strains of different signs and for the dependence of the velocity of dislocation motion on the level of actual shear stresses in the system.

ACKNOWLEDGMENTS

This study was supported in part by the Russian Foundation for Basic Research, project no. 02-02-16692.

REFERENCES

1. V. V. Avdeeva, L. M. Dolginov, V. S. Krasil'nikov, *et al.*, Kristallografiya **33**, 712 (1988) [Sov. Phys. Crystallogr. **33**, 418 (1988)].
2. A. É. Bochkarev, L. V. Druzhinina, V. S. Krasil'nikov, *et al.*, Kristallografiya **34**, 176 (1989) [Sov. Phys. Crystallogr. **34**, 101 (1989)].
3. K. Ishida, Y. Matsumoto, and R. Taguchi, Phys. Status Solidi A **70**, 277 (1982).
4. P. M. J. Maree, J. C. Bacbour, and J. F. Van der Veen, J. Appl. Phys. **62**, 4413 (1987).
5. V. I. Vdovin, M. G. Mil'vidskiĭ, T. G. Yugova, *et al.*, J. Cryst. Growth **141**, 109 (1994).
6. T. G. Yugova, V. I. Vdovin, M. G. Mil'vidskiĭ, *et al.*, Thin Solid Films **336**, 112 (1998).
7. V. I. Vdovin, M. G. Mil'vidskiĭ, L. K. Orlov, *et al.*, Kristallografiya **38**, 269 (1993).
8. T. G. Yugova, M. G. Mil'vidskiĭ, and V. I. Vdovin, Fiz. Tverd. Tela (St. Petersburg) **46** (8), 1476 (2004) [Phys. Solid State **46**, 1520 (2004)].
9. R. Hull, J. C. Bean, L. J. Peticolas, *et al.*, J. Appl. Phys. **70**, 2052 (1991).
10. D. C. Houghton, J. Appl. Phys. **70**, 2136 (1991).
11. C. G. Tuppen and C. J. Gibbing, J. Appl. Phys. **68**, 1526 (1990).
12. Y. Yamashita, K. Maeda, K. Fujita, *et al.*, Philos. Mag. Lett. **67**, 165 (1993).
13. R. Hull, J. C. Bean, L. J. Peticolas, *et al.*, Appl. Phys. Lett. **65** (3), 327 (1994).
14. B. W. Dodson and J. Y. Tsao, Appl. Phys. Lett. **51**, 1325 (1987).
15. R. Hull, J. C. Bean, and C. Buescher, J. Appl. Phys. **66**, 5837 (1989).
16. M. V. Mezhennyi, M. G. Mil'vidskiĭ, and T. G. Yugova, J. Phys.: Condens. Matter **14**, 12 997 (2002).
17. Yu. B. Bolkhovityanov, O. P. Pchelyakov, and S. I. Chikichev, Usp. Fiz. Nauk **171** (7), 689 (2001) [Phys. Usp. **44**, 655 (2001)].
18. D. D. Perovic and D. C. Haughton, Inst. Phys. Conf. Ser. **146**, 117 (1995).
19. M. G. Mil'vidskiĭ, N. S. Rytova, and E. V. Solov'eva, in *Problems of Crystallography* (Nauka, Moscow, 1987) [in Russian].
20. M. Yu. Gutkin, I. A. Odiv'ko, and A. G. Sheigerman, J. Phys.: Condens. Matter **15**, 3539 (2003).
21. V. I. Vdovin, Phys. Status Solidi **171**, 239 (1999).

Translated by Yu. Sin'kov

Crystallography Reports, Vol. 50, No. 5, 2005, pp. 854–861. Translated from Kristallografiya, Vol. 50, No. 5, 2005, pp. 920–927.

SURFACE AND THIN FILMS

Investigation into the Structure of Langmuir–Blodgett Films Prepared from Salts of Acetylenic Acids

L. L. Sveshnikova*, I. A. Badmaeva*, K. A. Dembo, and L. G. Yanusova****

** Institute of Semiconductor Physics, Siberian Division, Russian Academy of Sciences, pr. Akademika Lavrent'eva 13, Novosibirsk, 630090 Russia*

*** Shubnikov Institute of Crystallography, Russian Academy of Sciences, Leninskiĭ pr. 59, Moscow, 119333 Russia*

e-mail: janusova@ns.crys.ras.ru

Received December 10, 2004; in final form, March 15, 2005

Abstract—Langmuir–Blodgett films are prepared from lead, cadmium, and copper salts of carboxylic acids, namely, 23-tetracosynoic acid $HC{\equiv}C(CH_2)_{21}COOH$ (with the terminal triple bond) and 2-docosynoic acid $CH_3(CH_2)_{18}C{\equiv}CCOOH$ (with the internal triple bond). The structural transformations in the films during polymerization under exposure to UV radiation are investigated using X-ray reflectomertry. It is found that the X-ray reflectograms of the initial films prepared from salts of both acids exhibit no less than four or five pronounced intense Bragg reflections. This suggests that the initial films have good layer ordering. The bilayer periods for all the films are determined, and the influence of the salt type on the bilayer period is analyzed. It is established that, under exposure to UV radiation, the structural transformations in the films prepared from the salts of 23-tetracosynoic acid occur without substantial disturbances and defects, as can be judged from the absence of significant changes in the location and intensity of the Bragg reflections. An increase in the time of irradiation of the films prepared from the salts of 2-docosynoic acid leads to an increase in the bilayer period. This effect is especially pronounced for the lead and copper salts. However, upon long-term exposure to UV radiation, the salts undergo photolysis, the bilayer period decreases, and the structure of the film begins to break down. © *2005 Pleiades Publishing, Inc.*

INTRODUCTION

Langmuir–Blodgett films are layered structures formed by amphiphilic molecules with different degrees of ordering. Hydrocarbon chains in molecules forming a film can be differently oriented with respect to the normal to the layer plane, depending on the type of molecules and on the preparation technique. Long-chain acetylene derivatives can be formed as ordered multilayers by using the Langmuir–Blodgett method. This provides conditions favorable for topochemical polymerization. In our earlier work [1], the kinetics of photopolymerization in Langmuir–Blodgett films prepared from lead, cadmium, and copper salts of acetylenic acids was investigated using IR spectroscopy and ellipsometry. It was revealed that photopolymerization is accompanied by two competing processes, namely, polymerization (with breaking of triple bonds followed by the formation of a polyene chain) and photolysis of the salt. The character of the polymerization process depends on both the acid and salt types.

The structure of Langmuir–Blodgett films has been studied in a large number of works [2–6]. One of the methods for investigating the structure of multilayer Langmuir–Blodgett films with long periods is small-angle X-ray reflectometry. This method makes it possible to determine the period of layer packing and to construct the electron density profile in the projection onto the normal to the substrate plane.

In this work, we studied the structure of Langmuir–Blodgett films prepared from lead, cadmium, and copper salts of carboxylic acids, namely, 23-tetracosynoic acid $HC{\equiv}C(CH_2)_{21}COOH$ (with the terminal triple bond) and 2-docosynoic acid $CH_3(CH_2)_{18}C{\equiv}CCOOH$ (with the internal triple bond). Moreover, we investigated the transformation of the film structure during polymerization under exposure to UV radiation.

SAMPLE PREPARATION AND EXPERIMENTAL TECHNIQUE

Films were prepared from lead, copper, and cadmium salts of 23-tetracosynoic acid and 2-docosynoic acid according to the Langmuir–Blodgett method. For this purpose, monolayers formed on the surface of an aqueous subphase containing solutions of the lead, copper, and cadmium salts were transferred onto a substrate. Silicon(100) single-crystal wafers served as substrates. The Y-type monolayers were prepared on the substrates under a pressure of 30 mN/m and at a temperature of 18 ± 1°C. The samples under investigation contained 20 to 50 monolayers. Photopolymerization of the Langmuir–Blodgett films was performed in a vacuum chamber with the use of a low-pressure mer-

1063-7745/05/5005-0854$26.00 © 2005 Pleiades Publishing, Inc.

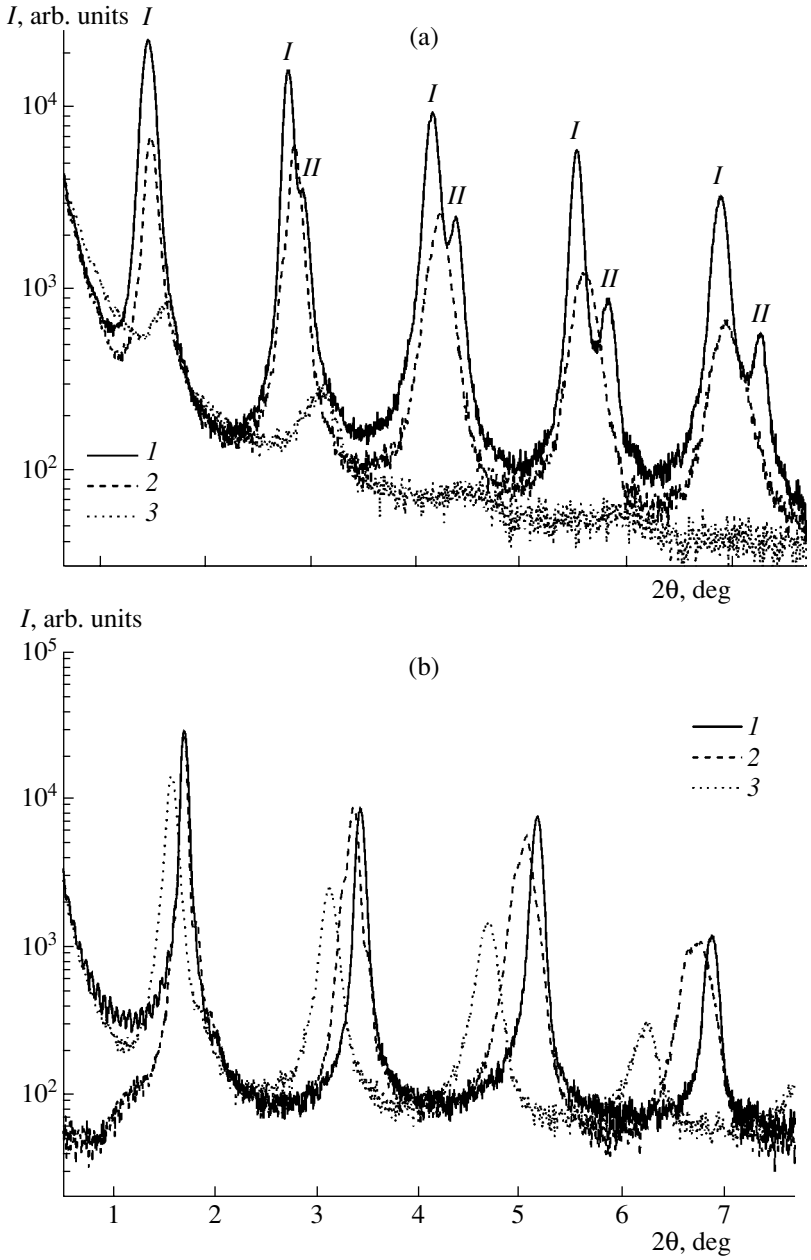

Fig. 1. X-ray scattering curves for films prepared from lead salts of (a) 23-tetracosynoic acid and (b) 2-docosynoic acid: (*1*) the initial film and (*2*, *3*) films exposed to UV radiation for (a) (*2*) 5 min, (*3*) 85 min and (b) (*2*) 80 s, (*3*) 25 min.

cury lamp (radiation power, 1.7 mW/cm^2). The techniques for preparation and photopolymerization of films were described in detail in our previous paper [1].

Before and after polymerization, the film structure was investigated on an AMUR-K small-angle X-ray diffractometer equipped with a linear-response position-sensitive detector. For this purpose, the X-ray intensity distributions upon reflection from the film surface were measured and analyzed according to the special standardized technique [7]. The scattering intensity curves for the samples were measured using CuK_α radiation at a wavelength $\lambda = 1.542$ Å for different glancing angles. The positions of the Bragg maxima in the X-ray reflectograms obtained were determined with a graphic interface of the CAMAC controlling program.

The layer period D in the film was calculated from the formula

$$D = \frac{n\lambda}{2\sin(\theta_n)} \quad \text{or} \quad D = \frac{n2\pi}{(q_z)_n}, \qquad (1)$$

where λ is the wavelength of radiation incident on the sample, n is the reflection order (the number of the chosen Bragg reflection), θ_n is the glancing angle corresponding to the n-order Bragg reflection (the acute angle between the sample plane and the beam incident

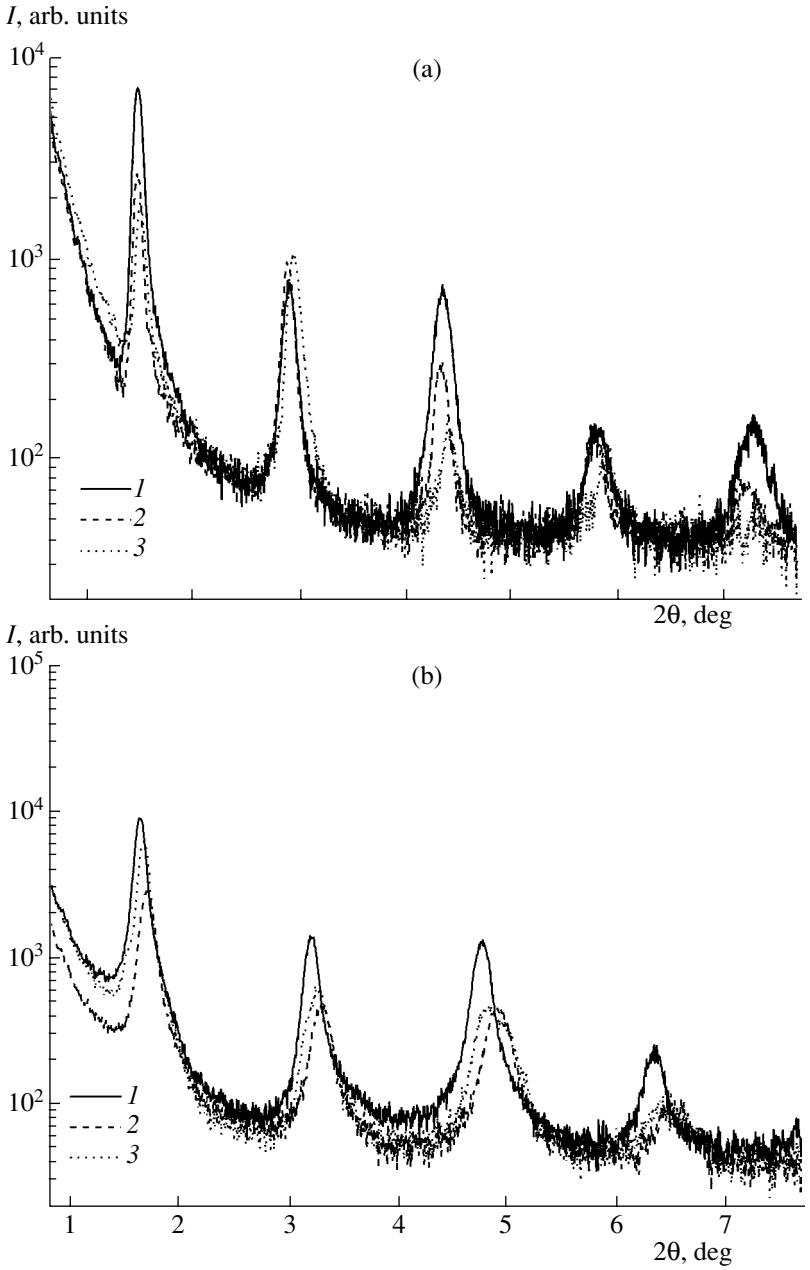

Fig. 2. X-ray scattering curves for films prepared from copper salts of (a) 23-tetracosynoic acid and (b) 2-docosynoic acid: (*1*) the initial film and (*2*, *3*) films exposed to UV radiation for (a) (*2*) 17 min, (*3*) 85 min and (b) (*2*) 70 min, (*3*) 280 min.

on the sample), and $q_z = (4\pi\sin\theta)/\lambda$ is the magnitude of the wave vector expressed in inverse angstroms. This quantity has often been used in reflectometry instead of the angle θ_n and allows one to eliminate the radiation wavelength in formula (1).

Depending on the quality of the film surface and the total film thickness, the measured reflectometric curve can exhibit intensity oscillations due to interference of monochromatic waves scattered from the upper and lower film boundaries (Kiessig oscillations). In the presence of Kiessig oscillations in the X-ray reflectrogram, the total film thickness can be estimated from the relationship

$$L \cong L_n = \frac{\lambda}{2(\sin\theta_{n+1} - \sin\theta_n)} \cong \frac{\lambda}{2(\theta_{n+1} - \theta_n)}. \quad (2)$$

In the case where the positions of Kiessig oscillations in the reflectrogram could not be determined, the total film thickness was estimated from the number of transferred monolayers.

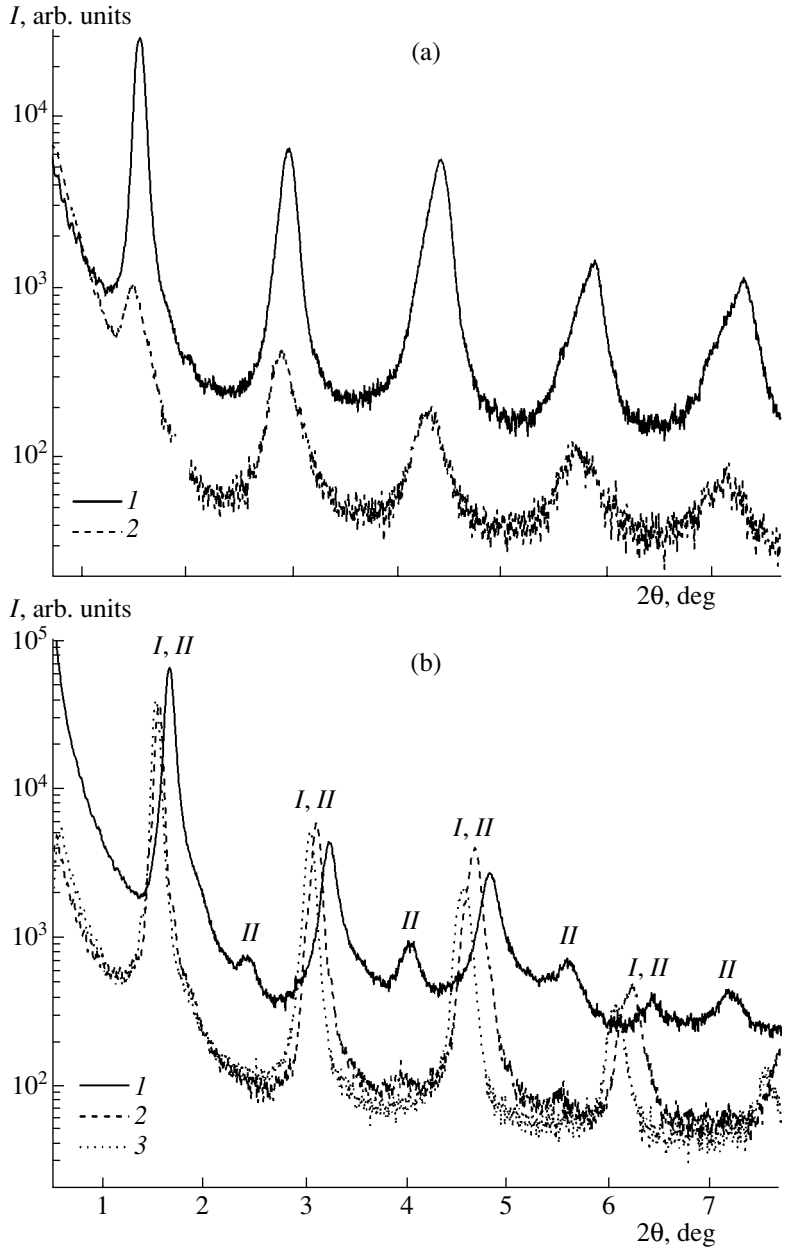

Fig. 3. X-ray scattering curves for films prepared from cadmium salts of (a) 23-tetracosynoic acid and (b) 2-docosynoic acid: (*1*) the initial film and (*2*, *3*) films exposed to UV radiation for (a) (*2*) 195 min and (b) (*2*) 25 min and (*3*) 180 min.

RESULTS AND DISCUSSION

The X-ray scattering curve for the initial Langmuir–Blodgett film prepared from the lead salt of 23-tetracosynoic acid (Fig. 1a, curve *1*) exhibits Kiessig oscillations and two sets, *I* and *II*, each composed of five Bragg reflections with the periods D_I = 64–66 Å and D_{II} = 60 Å, respectively. The intensity of the reflections of set *I* is higher, and, hence, the corresponding molecular packing in the layer occupies a larger region in the film. Set *II* of reflections in the scattering curve for the film can be associated either with the presence of acid molecules unreacted with the metal or with two different conformations of the same molecules. As is known, acid molecules form tilted bilayers and, therefore, their periods are somewhat shorter than those of their salts [8].

Upon exposure to UV radiation for 5 min, the film is polymerized by approximately 80%. As a result, the X-ray scattering curve (Fig. 1a, curve *2*) involves one set of reflections (rather than two sets) with a period D = 61–63 Å. After exposure to UV radiation for 85 min, only two weak broad reflections corresponding to the layer period D = 55–57 Å can be distinguished in the X-ray scattering curve (Fig. 1a, curve *3*). In this

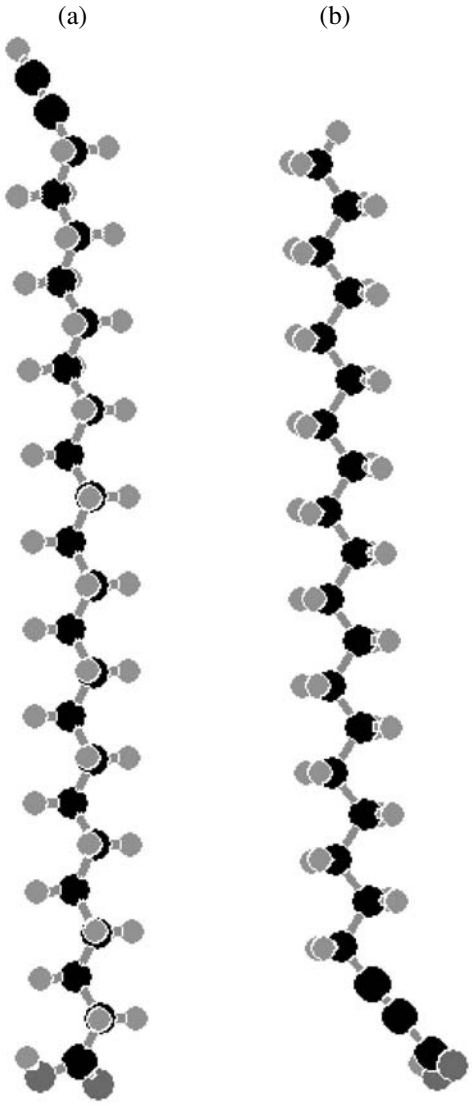

Fig. 4. Spatial structures of (a) 23-tetracosynoic and (b) 2-docosynoic acids.

case, the polymerization and photolysis processes are completed and the layered structure of the film begins to break down.

In the X-ray scattering curve for the initial Langmuir–Blodgett film prepared from the lead salt of 2-docosynoic acid (Fig. 1b, curve *1*), there are four or five pronounced Bragg reflections with a high intensity. The observed Kiessig oscillations indicate that the surface involves sufficiently large flat regions and is characterized by a small roughness parameter. Under exposure to radiation, the intensities of the Bragg reflections do not change significantly and the transformation occurs without substantial disturbances and defects in the film structure and leads to an increase in the layer period. The bilayer period D is equal to 51 Å for the initial sample, 53 Å for the sample exposed for 80 s (Fig. 1b, curve *2*), and 56 Å for the sample exposed for 25 min (Fig. 1b, curve *3*).

The X-ray scattering curves for the initial and irradiated Langmuir–Blodgett film prepared from the copper salt of 23-tetracosynoic acid exhibit pronounced Bragg reflections up to the fifth order. The layer period D for the initial sample is equal to 60 Å (Fig. 2a, curve *1*). After exposure for 70 min, when the film is only half-polymerized, the period increases slightly (Fig. 2a, curve *2*). However, an increase in the exposure time results in a decrease in the period (Fig. 2a, curve *3*). Note that these changes are within the limits of experimental error and, therefore, there is little sense in analyzing the numerical values. It should be noted there is a tendency toward a change in the layer size under exposure to radiation, because, although these changes do not manifest themselves in the first-order reflections, the shifts in the positions of the fifth-order reflections are quite noticeable. Most likely, exposure to UV radiation initially leads to a small increase in the molecular mobility; as a result, the layers are slightly swelled. Long-term exposure leads to the molecular ordering. This, in turn, results in an insignificant shrinkage of layers and is possibly accompanied by the formation of a number of defects, which lead to a smearing of the high-order Bragg reflections.

One more consequence of polymerization consists in redistributing the intensity of the Bragg reflections of different orders. After polymerization for 70 min, the intensities of the odd reflections decrease considerably, whereas the intensities of the even reflections remain identical to those for the initial sample. The redistribution of the reflection intensities can be associated with the change in the electron density in the direction perpendicular to the layer plane, which actually should occur in the course of polymerization. At long exposure times, when the polymerization and photolysis processes are completed, this becomes immaterial because the intensity of the high-order Bragg reflections decreases substantially due to the disturbance of the long-range order.

In the case of the copper salt of 2-docosynoic acid, exposure to radiation leads first to a slight decrease in the bilayer thickness and then to its increase. The bilayer period D is equal to 54 Å for the initial film (Fig. 2b, curve *1*), 52.4 Å for the film exposed for 17 min (Fig. 2b, curve *2*), and 53.2 Å for the film exposed for 85 min (Fig. 2b, curve *3*).

For the Langmuir–Blodgett film prepared from the cadmium salt of 23-tetracosynoic acid, the bilayer period is equal to 60.2 Å for the initial sample (Fig. 3a, curve *1*) and 60.5 Å for the sample exposed for 195 min (Fig. 3a, curve *2*). Note that, after exposure for 60 min, when the degree of polymerization is no more than 0.2, the intensities of the Bragg reflections are close in magnitude and the film structure remains virtually unchanged. Only long-term exposure (for 195 min) results in an increase in the roughness of interlayer

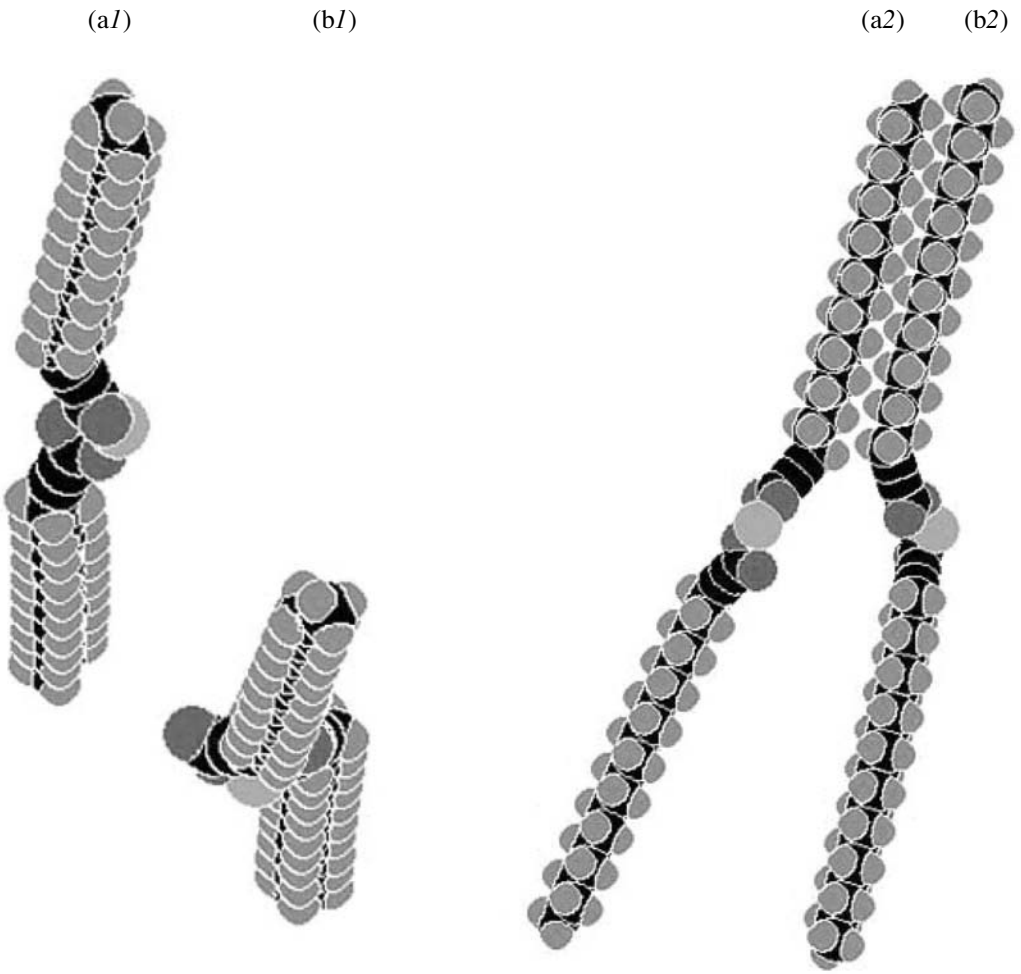

Fig. 5. (*1*) Top and (*2*) side views of two variants of the packing of 2-docosynoic acid molecules around cadmium in a bilayer from the cadmium salt of 2-docosynoic acid according to the computer simulation: (a) the tilted packing and (b) the twisted packing.

boundaries and the deterioration of the long-range order of the layered packing (which leads to a broadening of the Bragg reflections and a considerable decrease in their intensity).

The X-ray scattering curve for the initial Langmuir–Blodgett film prepared from the cadmium salt of 2-docosynoic acid (Fig. 3b, curve *1*) clearly exhibits two different sets of reflections. Set *I* contains four high-intensity reflections corresponding to the layer period D = 54–55 Å. In set *II*, the intensities of the Bragg reflections are substantially lower. The positions of the reflections indicate that they should correspond to the double layer period D = 110 Å. In this case, the first reflection is not observed and all the even reflections coincide with the reflections of set *I*. Therefore, we really observe only the odd reflections (beginning with the third reflection). Exposure of the film to radiation results in a broadening and a shift in the reflections of set *I*, whereas the reflections of set *II* do not shift, decrease in intensity, and gradually disappear (Fig. 3b, curves *2*, *3*).

Since both sets of reflections in the X-ray scattering curve correspond to the layer periods that are multiples of the bilayer size of 55 Å, we can assume the following model of the layer packing. By virtue of steric hindrances, bilayers are packed in the film so that their thickness remains unchanged, whereas layers whose specific features of the structural packing lead to the difference between the electron density profiles alternate with each other. This manifests itself in doubling of the layer period. Let us assume that the structure in which molecules are packed in bilayers in two different ways (for example, one bilayer is vertically located and another bilayer is tilted, or two acetylene tails are extended with respect to the cadmium atom in one bilayer and twisted around this atom in another layer) is energetically favorable. As a consequence, these structural differences lead to a small variations in the layer parameters. In this case, the polymerization under exposure to radiation should enhance the intermolecular interaction in layers as compared to the interlayer interaction of the molecules. In turn, this should lead to

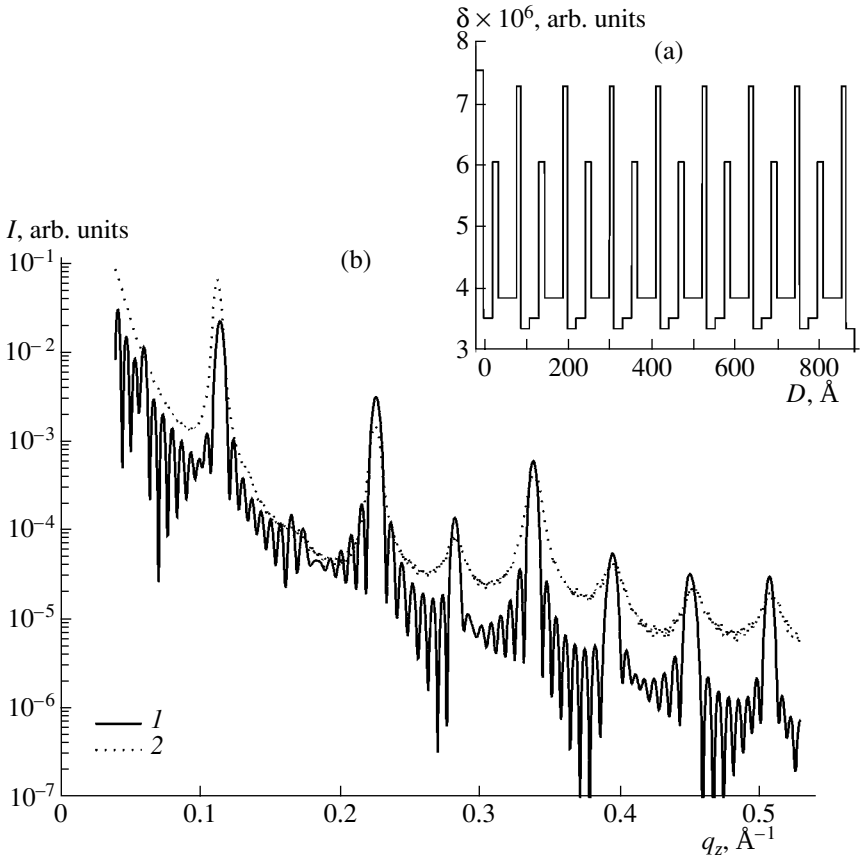

Fig. 6. (a) Model of the electron density profile and (b) the calculated scattering intensity curve (solid line), which reflects the specific features of the Bragg reflections in the experimental scattering curve (dotted line) for the unirradiated sample of the cadmium salt of 2-docosynoic acid.

the equalization of the layer parameters and, hence, to the disappearance of the reflections of set *II*.

In order to verify the proposed hypothesis, the spatial structures of 23-tetracosynoic and 2-docosynoic acids (Fig. 4) were constructed using the molecular dynamics simulation with special computer programs [9]. Furthermore, the possible molecular conformations of the cadmium salt of 2-docosynoic acid were determined by the computer simulation. It was revealed that there are, at least, two allowable variants for the packing of oxygen atoms around the cadmium atoms (Fig. 5). These variants of the packing differ insignificantly in bilayer thickness and electron density. Our situation can occur under the assumption that, after the formation of one bilayer with molecules in the most favorable conformation during the preparation of the Langmuir–Blodgett film, the formation of the next bilayer with molecules in the same conformation is energetically unfavorable.

In addition to the molecular dynamics simulation, in order to confirm the above hypothesis, we attempted to choose the parameters of the model of molecular packing in the layered film so that the scattering intensity curve for this model should qualitatively describe the behavior of the Bragg reflections in the experimental scattering curve. The obtained model (Fig. 6a) and the corresponding scattering intensity curve (Fig. 6b), in our opinion, adequately describe the change in the intensities of the Bragg reflections in the experimental scattering curve and, thus, confirm our assumption regarding the possible molecular packing in the real film.

Analysis of the X-ray reflectograms of the Langmuir–Blodgett films prepared from the salts of acetylenic acids shows that the initial films have a rather good layer ordering and the bilayer periods determined from the small-angle X-ray scattering curves depend on the salt type. The bilayer periods for the Langmuir–Blodgett films prepared from the salts of 23-tetracosynoic acid are almost identical, whereas the period for the films produced from the lead salt of 2-docosynoic acid is smaller than those for the films prepared from the cadmium and copper salts of this acid.

It can be seen from Fig. 4 that the acetylenic acid molecules have different spatial structures. The 23-tetracosynoic acid molecule is represented by the polymethylene chain in which the carbon atoms are bound by single bonds and the carbon atoms bound by the triple

bond lie at an angle to the chain axis. In the 2-docosynoic acid molecule, four carbon atoms at the carboxyl end lie in one straight line and the polymethylene chain forms an angle with this rodlike molecular fragment. The molecules of salts of these acids have the same configuration. In the bilayer packing, spatial structures of molecules are retained.

In the 2-docosynoic acid molecule, the triple bond at the end of the hydrocarbon chain in the α position with the carboxyl group affects the coordination of carboxyl groups by metal ions. It was shown in our earlier work [1] that, in Langmuir–Blodgett films, the lead ion is bonded to two carboxyl groups of neighboring monolayers. However, in films prepared from the cadmium and copper salts, each ion can be bonded to oxygen atoms of four carboxyl groups with the formation of a more symmetric and stable structure as compared to the structure of the lead salt. As a result, the tilt of molecules of the lead salt of 2-docosynoic acid in the layer is larger and the thickness of the monolayer formed by the lead salt is smaller than those in the case of the cadmium and copper salts. Such a molecular configuration can be responsible for the anisotropic optical characteristics of films. This is confirmed by the results obtained in our previous work [10], in which the optical parameters of the films under investigation were determined using ellipsometry at different angles within the model of a biaxial anisotropic film. It was demonstrated that the Langmuir–Blodgett films prepared from the lead salt of 2-docosynoic acid should be considered biaxial, whereas similar films prepared from the cadmium salt of this acid and also the lead and cadmium salts of 23-tetracosynoic acid exhibit a nearly uniaxial anisotropy. The monolayer thicknesses determined from the X-ray data for the salts of 23-tetracosynoic and 2-docosynoic acids are in good agreement with the results of the ellipsometric measurements performed with due regard for the anisotropy of these films [10].

The change in the film thickness during the polymerization is associated with the structural transformations in the layer. Under UV irradiation of the films prepared from the salts of 23-tetracosynoic acid, the intensities of the Bragg reflections change only insignificantly, the transformation occurs without substantial disturbances and defects in the film structure, and the bilayer period remains virtually constant. We can assume that the triple bond at the end of the hydrocarbon chain does not affect the molecular packing in the layer both before and after polymerization. The polymerization of the Langmuir–Blodgett films prepared from the salts of 2-docosynoic acid leads to a change in the tilt angle of polymethylene chains and, hence, to an increase in the bilayer period. Only upon long-term exposure to UV radiation, when the salts undergo photolysis, does the structure of the film begin to break down and the bilayer period decrease.

ACKNOWLEDGMENTS

This work was supported by the Russian Foundation for Basic Research (project no. 01-03-32796) and the US Civilian Research and Development Foundation for the New Independent States of the Former Soviet Union (grant no. CRDF NO-008-X1).

REFERENCES

1. I. A. Badmaeva, L. L. Sveshnikova, S. M. Repinskiĭ, *et al.*, Zh. Fiz. Khim. **75** (12), 2256 (2001).
2. Yu. M. L'vov and L. A. Feĭgin, Kristallografiya **32** (6), 800 (1987) [Sov. Phys. Crystallogr. **32** (6), 473 (1987)].
3. B. K. Vaĭnshteĭn and V. V. Klechkovskaya, Kristallografiya **39** (2), 301 (1994) [Crystallogr. Rep. **39** (2), 256 (1994)].
4. V. V. Klechkovskaya and L. A. Feĭgin, Kristallografiya **43** (6), 975 (1998) [Crystallogr. Rep. **43** (6), 917 (1998)].
5. L. Yanusova, V. Klechkovskaya, L. Sveshnikova, *et al.*, Liq. Cryst. **14**, 1615 (1993).
6. A. K. Khripunov, Yu. G. Balagina, N. D. Stepina, *et al.*, Kristallografiya **45** (2), 352 (2000) [Crystallogr. Rep. **45** (2), 318 (2000)].
7. *GOST* (State Standard) *State System for Ensuring the Uniformity of Measurements*, 2004.
8. G. I. Ivakin, V. V. Erokhin, and V. V. Klechkovskaya, Biol. Membr. **7** (11), 1158 (1990).
9. I. Khmel'kov, Komp'yuterra, No. 8, 3 (2003).
10. I. A. Badmaeva, L. A. Nenasheva, V. G. Polovinkin, *et al.*, Opt. Spektrosk. **96** (3), 486 (2004) [Opt. Spectrosc. **96** (3), 438 (2004)].

Translated by O. Borovik-Romanova

Crystallography Reports, Vol. 50, No. 5, 2005, pp. 862–868. Translated from Kristallografiya, Vol. 50, No. 5, 2005, pp. 928–934.

SURFACE AND THIN FILMS

Surface Matter Waves Caused by the Absorption of Nonrelativistic Particles

R. Ch. Bokun and Yu. V. Kistovich†

All-Russia Research Institute for Physicotechnical and Radiotechnical Measurements, Mendeleevo, Moscow oblast, 141570 Russia

e-mail: richesl@vniiftri.ru

Received September 6, 2004

Abstract—The existence of surface states of nonrelativistic particles at the interface between a vacuum and a layer of a material on a reflecting substrate, which are caused by the absorption in the layer rather than the presence of discrete levels, is established. The wave functions of such states (surface matter waves) are found and the domains of their existence in the complex plane of the "optical" potential (both attractive and repulsive) of the layer are determined. Threshold effects of the count of microparticles at the intersection of the boundaries of these domains are revealed. The spatial characteristics of the surface matter waves are calculated. An example of the layer composition providing the existence of such waves is given for ultracold neutrons. The increase in the loss of trapped ultracold neutrons owing to the excitation of the surface matter waves of these particles in the trap walls is discussed. © *2005 Pleiades Publishing, Inc.*

INTRODUCTION

The localization of an electromagnetic field near surfaces or interfaces in the form of surface electromagnetic waves has been quite thoroughly studied in a wide frequency range (including optical frequencies) in the general case of absorbing media with complex permittivity [1, 2]. At the same time, the generally known data on the surface localization of the wave functions of nonrelativistic particles, which are related mainly to the electronic surface states, were obtained for nonabsorbing media with a real potential of interaction between a microparticle and a medium [3, 4]. Therefore, when a medium is absorbing, a question arises about the conditions of existence and specific features of the surface states of microparticles localized at the vacuum/medium interface. In the general case of an absorbing medium, the wave functions of the surface states of quantum-mechanical particles or, for brevity, surface matter waves, should satisfy the Schrödinger equation with a complex interaction potential in the medium.

The solution to this problem is important in the study of the surface of condensed media using corpuscular radiation effectively absorbed in these media (for example, positrons and slow electrons). The interaction of such particles with a medium can be described by a complex optical potential [5]. This potential is also used for other low-energy particles, in particular, positroniums [6]. In all such cases, consideration of the surface matter waves caused by the absorption may be important. There is much interest in the existence of surface matter waves during the storage of ultracold neutrons (UCNs) in traps. In this case, a constant complex potential can also be applied [7]. The method of storage of UCNs is very promising for various applications in surface physics because UCNs interact only with a thin surface layer of the trap walls. This method has already been experimentally implemented [8]. At the same time, the fact that the measured times of storage of UCNs in traps are much shorter than the calculated values [8, 9] has not been explained yet. This phenomenon may be related to the excitation of surface matter waves of UCNs, which exist only owing to the absorption in the trap walls.

The general conditions of existence of surface electromagnetic waves both at the interface between two media and in layered structures consisting of more than two different media, including absorbing ones, are well known [1, 2]. These conditions can be satisfied, for example, at the vacuum/medium interface, where surface electromagnetic waves generally exist both in the absence of absorption in the medium (Fano modes) and in the presence of absorption (Zenneck modes). Note that the phase velocities of the Fano and Zenneck modes in the interface plane are, respectively, smaller and larger than the speed of light in a vacuum. Therefore, the fields of surface and bulk electromagnetic waves cannot serve as sources for one another in the case of a uniform interface between two media in view of the difference in the components of the wave vectors of these waves in the interface plane. The mutual transformation of surface and bulk electromagnetic waves should also remain forbidden for quantum-mechanical wave functions in the corresponding situation, for example, in planar geometry, where both these waves are formally described by identical equations [10].

† Deceased.

1063-7745/05/5005-0862$26.00 © 2005 Pleiades Publishing, Inc.

Detailed consideration shows that in the planar geometry the Schrödinger equation and the boundary conditions for the wave functions of particles have the same form as in the case of electromagnetic waves of the magnetic type with a transverse electric field. However, it is known that in the case of only two media with a planar interface the fields of transverse electrical waves cannot satisfy the boundary conditions at the interface and do not form surface electromagnetic waves [10]. Hence, surface matter waves do not exist in this case.

In this study, we consider the simplest case of three media (which, however, allows for the existence of surface matter waves): a semi-infinite medium, which completely reflects incident microparticles, is separated from a vacuum by a homogeneous absorbing layer of some thickness. The absorbing layer can be regarded here as a simplified model of a surface transition layer between the vacuum and the bulk structure of the matter (in particular, crystal). In this case, absorption in the layer can be related to the thickness-averaged concentration of impurities absorbing microparticles near the surface. In the case of UCNs, the main absorbing impurity is hydrogen, which is dissolved predominantly near the surface of the trap walls [7]. Previously, we considered an absorbing crystal on a nonabsorbing substrate (without a transition layer) modeled by a one-dimensional (1D) Kronig–Penney lattice potential composed of δ functions [3, 7] with complex coefficients. It was shown in [11] that in this case absorption in the crystal leads to the occurrence of surface waves analogous to Zenneck modes, including substrates with a negative potential, which do not allow for Tamm surface states in a nonabsorbing crystal [3].

In this study, we obtained a solution to the quantum-mechanical problem with a constant complex potential of the layer in the above-described three-media geometry: surface matter waves of a microparticle. The boundaries of the domains of existence of the surface matter waves in the plane of the complex interaction potential for a microparticle having a nonzero mass m and a layer, normalized to $\hbar^2/2ma^2 = E_\infty/\pi^2$, are determined. ($E_\infty$ is the energy of the ground level of the particle in the infinitely deep potential well of width a equal to the layer thickness counted from the well bottom [12]; $E_\infty/\pi^2 = 2.1 \times 10^{-11}$ eV at $a = 1$ μm.) It is noted that some methods of excitation and observation of surface electromagnetic waves can be applied to surface matter waves. It is shown by the example of UCNs that the conditions for the existence of surface matter waves can be implemented in the case of a layer containing isotopes absorbing UCNs, which have already been used in experiments with UCNs [13]. The specificity of the excitation and observation of surface matter waves of UCNs is discussed, as well as the possibility of increasing additional (anomalous) loss during UCN storage due to the excitation of surface matter waves of UCNs in the absorbing surface layer of the trap walls.

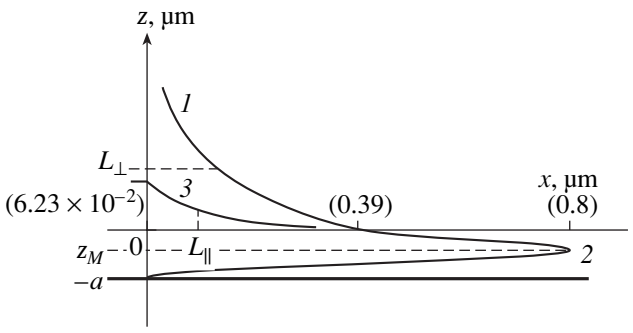

Fig. 1. Surface localization of the probability density $|\Psi_\parallel(x)\Psi_\perp(z)|^2$ in the geometry of an absorbing layer on an reflecting substrate: $|\Psi_\perp(z)|^2$ (*1*) in the vacuum at the localization height $L_\perp = 1.19$ and (*2*) in the layer with a maximum at $z_M = -0.41$, plotted on the x axis, and (*3*) $|\Psi_\parallel(x)|^2$ plotted on the z axis with the decay length $L_\parallel = 16.1$ at $x \geq 0$. The values of $|\Psi_\perp(z)|^2$ and $|\Psi_\parallel(x)|^2$ at the characteristic points are given in parenthesis (in μm^{-1}); all calculations were performed for the potential v_0 in Fig. 2 and $a = 1$.

SURFACE MATTER WAVES IN THE CASE OF ABSORPTION OF MICROPARTICLES IN A LAYER

Let us consider the problem of the surface localization of the wave function of a nonrelativistic particle during its interaction with a planar absorbing layer on a totally reflecting substrate. In this geometry (Fig. 1), the Schrödinger equation for the wave function $\Psi(x, z)$ of the particle has the form

$$\frac{\hbar^2}{2m}\left(\frac{\partial^2\Psi(x,z)}{\partial x^2} + \frac{\partial^2\Psi(x,z)}{\partial z^2}\right) + [E - V(z)]\Psi(x,z) = 0. \quad (1)$$

Here, z is a coordinate along the outward normal to the surface of the absorbing layer with a thickness a; within the layer ($a < z < 0$), the constant complex potential V with real (V') and imaginary ($V'' < 0$) components (the latter is responsible for the absorption) act on the particle; $z \geq 0$ corresponds to the vacuum; $z \leq -a$ corresponds to the totally reflecting medium with an infinite potential; and x is a coordinate along an arbitrarily chosen straight line on the layer surface. Thus, the potential $V(z)$ has the form

$$V(z) = \begin{cases} 0, & z \geq 0 \\ V = V' + iV'', & -a < z < 0 \\ +\infty, & z \leq -a. \end{cases} \quad (2)$$

The boundary conditions for the Schrödinger equation (1) with the potential (2) are as follows: the function $\Psi(x, z)$ and its derivative with respect to z are continuous at $z = 0$ and $\Psi(x, -a) = 0$ owing to the infinite substrate potential. Separating the variables for the lon-

gitudinal and transverse (along the x and z axes, respectively) motions of the particle, we obtain a steady-state solution to Eq. (1) with the potential (2) in the form

$$\Psi(x, z) = \Psi_{\|}(x)\Psi_{\perp}(z)$$

$$= \begin{cases} A\exp(ikx)\exp(i\kappa_0 z), & z > 0 \\ \exp(ikx)[B\exp(i\kappa z) + C\exp(-i\kappa z)], & -a < z < 0 \\ 0, & z \le -a. \end{cases} \quad (3)$$

In formula (3), k is the wave number of the longitudinal motion and κ_0 and κ are the wave numbers of the transverse motion in the vacuum and layer, respectively. Note that in the presence of absorption ($V'' \neq 0$) all these wave numbers are complex. For separable variables x and z, the solution $\Psi(x, z)$ is a product of the wave functions of the longitudinal ($\Psi_{\|}(x)$) and transverse ($\Psi_{\perp}(z)$) motions. In what follows, each of these functions is assumed to be normalized to unity. The function $\Psi_{\|}(x)$ is normalized at the ray $0 \le x < \infty$, where $x = 0$ is the plane in which a surface wave is excited along the x axis, and the function $\Psi_{\perp}(z)$ is normalized at the ray $-a \le z < \infty$ in view of the fact that $\Psi_{\perp}(z \le -a) \equiv 0$ in the substrate with an infinite potential.

If $\Psi(x, z)$ is a surface matter wave, the conditions of its surface localization in the vacuum imply two significant limitations on κ_0: $\mathrm{Re}\,\kappa_0 \le 0$ and $\mathrm{Im}\,\kappa_0 > 0$. The first inequality ensures the absence of a transverse probability flow into the vacuum from the layer containing no sources of particles and the second inequality provides the exponential falloff of the surface matter wave in the vacuum. In contrast to the surface electromagnetic waves at an interface between two media, the surface matter waves considered here decay only at one side from the layer surface: in the vacuum rather than in the layer. Hence, there are no limitations for κ similar to those imposed on κ_0.

After the separation of variables, the Schrödinger equation (1) yields dispersion equations relating the sum of the squared wave numbers in the vacuum and in the layer with the energy E of the particle:

$$k^2 + \kappa_0^2 = 2mE/\hbar^2 \text{ and } k^2 + \kappa^2 = 2m(E - V)/\hbar^2, \quad (4)$$

where m is the particle mass and $\hbar$ is Planck's constant. The homogeneity of the above-stated boundary conditions leads to a uniform linear system of equations for the coefficients A, B, and C in (3). The determinant of this system should be zero if nonzero solutions to the system exist. This requirement gives the following relation between κ_0 and κ at the noted limitations:

$$i\kappa_0 = \kappa\cot(\kappa a), \quad \mathrm{Re}\,\kappa_0 \le 0, \quad \mathrm{Im}\,\kappa_0 > 0. \quad (5)$$

The system of equations (4) and (5) with a given potential V of the layer and the energy E of the particle allows one to find the transverse wave numbers κ and κ_0 and the longitudinal wave number k.

It is noteworthy that the two-dimensional (2D) Eq. (1) with the complex potential $V(z)$ from (2) at $V'' \neq 0$ has a steady-state solution $\Psi(x, z)$ from (3) for the continuous spectrum of real energies E (see below). In contrast, the 1D equation for $\Psi_{\perp}(z)$ obtained from (1) with the same potential (2) and the boundary conditions in the case $\Psi_{\|}(x) \equiv 1$ (for $k = 0$) at $V'' \neq 0$ has no steady-state (with real energies E) solutions. Indeed, in the 1D case, assuming that $k = 0$ in dispersion equations (4) with $V'' \neq 0$, we obtain at real E a real value of κ_0^2 from the first equation and a complex value of κ^2 from the second equation. It turns out that under the condition $\mathrm{Im}\,\kappa_0 > 0$ these values cannot be related by Eq. (5), thus indicating the absence of steady-state solutions to this 1D equation. If the potential $V(z)$ in (2) is real ($V'' = 0$), the 1D equation for $\Psi_{\perp}(z)$ is reduced by replacing the variable $z - r - a$ in the equation for the function $X(r) = rR_0(r)$ of the spherical coordinate $r \ge 0$ (the length of the radius vector); here, $R_0(r)$ is the radial part of the wave function of a particle with a zero orbital momentum in the centrally symmetric field of the short-range potential $(\hbar^2/2m)V(r - a)$ with the cutoff radius equal to the layer thickness a in (2). As a result of this replacement, the boundary conditions for $\Psi_{\perp}(z)$ are transformed into the conventional conditions for $X(r)$ in the case of the above-mentioned potential. The steady-state solutions to $X(r)$ and the conditions for their existence for the real potential $V(r - a)$ are well-known [14]. These conditions imply that the corresponding solutions $\Psi_{\perp}(z)$ to the 1D equation, localized near the interface between the nonabsorbing layer and the vacuum, exist only when the particle has bound states with a discrete spectrum of real energies E for the attractive potential of the layer, in contrast to the 2D case (1) at $k \neq 0$. In the 2D case ($k \neq 0$), it can be seen from Eqs. (4) that k, κ_0, and κ may take complex values at which $\mathrm{Im}(k^2 + \kappa_0^2) = 0$ and $\mathrm{Im}(k^2 + \kappa^2) = -2mV''/\hbar^2 \neq 0$. Thus, steady-state solutions (with real E) to the Schrödinger equation (1) with a continuous spectrum of energies E can exist for the absorbing layer (with $V'' \neq 0$).

However, it is obvious that the conditions $\mathrm{Re}\,\kappa_0 \le 0$ and $\mathrm{Im}\,\kappa_0 > 0$ from (5) are not satisfied at each value of the complex potential V. Equations (4) and (5) allow one to find directly the domains in the plane of the dimensionless complex parameter κa in which these conditions are satisfied. These equations imply the mapping of the complex plane κa to the plane of the normalized complex potential v:

$$v \equiv (2ma^2/\hbar^2)V = -(\kappa a)^2/\sin^2(\kappa a), \quad (6)$$

where V is the potential of the layer with a thickness a from (2). It follows from expressions (5) and (6), which do not contain E, that the domains of existence of surface matter waves in the complex plane v are independent of the energy E of the particle.

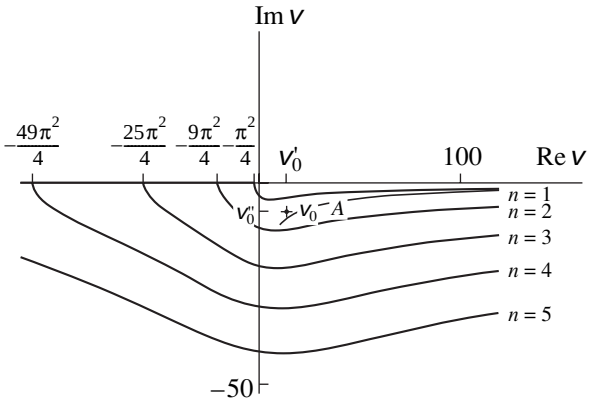

Fig. 2. Domains of existence of $n \geq 1$ surface matter waves below the nth boundary (including the rays $-\infty < \mathrm{Re}\,\nu \leq -(2n-1)^2\pi^2/4$) in the plane of the potential ν; $\nu_0 = \nu'_0 + \nu''_0 i = 13.35 - 7.46i$; A is the asymptotics (7) for $n = 1$.

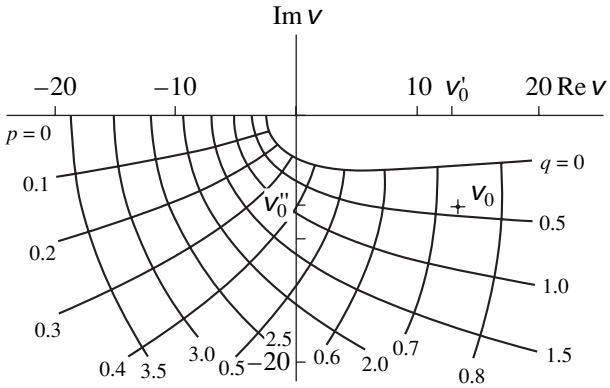

Fig. 3. Isolines of the specified parameters p and q, which determine the characteristics of the surface matter waves in the vacuum in the first domain of existence; $p_0 = 0.74$ and $q_0 = 0.42$ at the point ν_0.

The boundaries of the domains of existence of surface matter waves in the complex plane κa, where the above-mentioned physical limitations on κ_0 are satisfied, were found by numerical solution of Eq. (5). In view of the periodicity of the function $\cot(\kappa a)$, the number of such domains is infinite. They are not overlapped and have closed boundaries, which contain, in particular, straight-line half-intervals $\kappa_n a \leq \mathrm{Re}\,\kappa\, a < \kappa_n a + \pi/2$, where $\kappa_n a = (2n-1)\pi/2$ and $\mathrm{Re}\,\kappa_0 = 0$. The boundaries of different domains of existence of surface matter waves, denoted by the numbers $n = 1, 2, \ldots$ of the half-intervals they contain, are closed in the half-plane $\mathrm{Im}\,\kappa a > 0$ by convex curves at which $\mathrm{Im}\,\kappa_0 = 0$. These curves, including the finite points of the above-defined half-intervals, do not belong to the domains of existence of the surface matter waves. When mapping (6) is performed, the domains of existence of the surface matter waves in the plane κa pass into different domains in the plane ν (see Fig. 2). These domains are unlimited in the plane ν and are partially overlapped, so that the nth domain in the plane ν, obtained by mapping of the nth domain in the plane κa, contains all domains with higher numbers. In the absence of absorption ($\mathrm{Im}\,\nu = 0$), the nth domain is degenerated into a ray $-\infty < \mathrm{Re}\,\nu \leq -(\kappa_n a)^2$ on the semiaxis $\mathrm{Re}\,\nu < 0$, into which the nth half-interval in the κa plane is transformed. Convex segments of the boundaries of the domains of existence in the plane κa pass as a result of mapping (6) to the plane ν into curves going to infinity, asymptotically approaching the semiaxis $0 < \mathrm{Re}\,\nu < +\infty$. Figure 2 shows the asymptotics of this segment of the boundary of the first domain ($n = 1$) at $\mathrm{Re}\,\nu \longrightarrow +\infty$ (curve A). In the general case, at $n \geq 1$, this asymptotic curve has an analytical form

$$\mathrm{Im}\,\nu_n = -[4(n\pi)^2 + 2(n\pi)^{3/2} - 4]/\sqrt{\mathrm{Re}\,\nu_n}, \qquad (7)$$

where ν_n are the points of this curve for the nth domain at $\mathrm{Re}\,\nu_n > 0$.

In experiments with quantum-mechanical particles, counts of the particle detector are generally measured, which gives the value of $|\Psi(x, z)|^2$ from (3) for surface matter waves. Therefore, the calculated values of the factors of this quantity are given in Fig. 1. All noted values were numerically calculated for the dimensionless complex potential ν_0 lying in the first domain of existence of surface matter waves (see Figs. 2, 3).

SPECIFIC FEATURES AND PARAMETERS OF THE SURFACE MATTER WAVES OF MICROPARTICLES

The main specific feature of the surface matter waves revealed by solving the problem under consideration is that they exist, according to Fig. 2, both when the layer potential is attractive, at $\mathrm{Re}\,\nu < 0$, and when the potential is repulsive, at any value $\mathrm{Re}\,\nu > 0$. In the latter case, the absorption in the layer, which is proportional to $|\mathrm{Im}\,\nu|$, should be sufficiently strong to ensure the fall of the potential ν at a specified value of $\mathrm{Re}\,\nu$ at least into the first ($n = 1$) domain of existence of surface matter waves. The physical explanation of the existence of surface matter waves in the case of the absorbing layer potential ($\mathrm{Im}\,\nu < 0$) at arbitrary values of $\mathrm{Re}\,\nu$ is as follows. The absorption in a layer with $\mathrm{Im}\,\nu < 0$ causes a flow of the probability of finding the particle in the vacuum. This flow is directed from the vacuum to the layer through the layer surface at $z = 0$. (This corresponds to problem 7.9 in [12].) At $\mathrm{Re}\,\nu < 0$, the layer attracts the particle and does not counteract the probability flow, which is proportional to $|\mathrm{Im}\,\nu|$. In this case, surface matter waves exist independently of absorption (i.e., including the case when the absorption is absent) in the range $-\infty < \mathrm{Re}\,\nu \leq -\pi^2/4$, which includes the bound states of the particle in the potential well of the

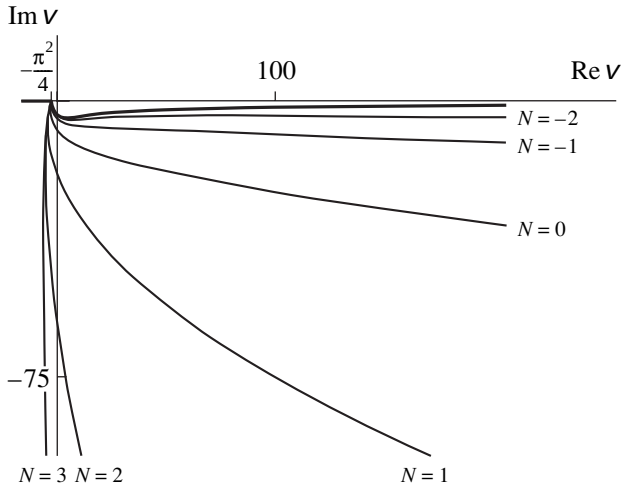

Fig. 4. Boundaries (at specified N) between the domains of existence of fast (to the right of and above the boundaries) and slow surface matter waves with energies $E_N = 10^N(E_\infty/\pi^2)$ in the first domain of existence (the bold boundary).

layer [14]. When $\mathrm{Re}\,\nu > 0$, the layer rejects the particle and counteracts the probability flow from the vacuum. Then, the existence of surface matter waves becomes possible only at sufficiently large values of the probability flow $\sim|\mathrm{Im}\,\nu|$, as in the interval $-\pi^2/4 < \mathrm{Re}\,\nu \le 0$, where, owing to the smallness of $\mathrm{Re}\,\nu$, a discrete level is absent in the potential well of the layer.

Another specific feature of surface matter waves is the large number of domains of their existence in the plane of the potential ν ($n = 1, 2, \ldots$ in Fig. 2). In the domain with $n \ge 1$, n different surface matter waves exist, which correspond to the first n roots $\kappa_j(\nu)$ ($j = 1, 2, \ldots, n$) of transcendental Eq. (6) at a specified value of the dimensionless potential $\nu = \nu' + i\nu''$ (where $\nu' = \mathrm{Re}\,\nu$ and $\nu'' = \mathrm{Im}\,\nu$). Each dependence $\kappa_j(\nu)$ and the dependence $\kappa_{0j}(\nu)$ related to it by Eq. (5) differ from the dependences with $j' \ne j$ and determine the same behavior of the jth surface matter wave in all domains with $n \ge j$ at all points (with the coordinates ν' and ν'') of the plane ν. When the absorption $\sim|\nu''|$ is changed (for example, in the case of surface matter waves of UCNs, by varying the isotopic composition of the surface layer), the boundary of the domain of existence of the nth surface matter wave can be intersected. Each such intersection may lead to the threshold effect: a step in the probability of UCN trapping from a bulk to surface state upon excitation (or quenching) of the nth surface matter wave. This step can be detected by a change in the count of UCNs at changes in the coordinates ν'' and ν' corresponding to the intersection of this boundary, which can be implemented for all boundaries shown in Fig. 2.

Figure 4 shows the curves on which the phase velocity $E/\hbar\,\mathrm{Re}\,k$ of the surface wave along the x axis coincides with the phase velocity $\sqrt{E/2m}$ of the plane de Broglie wave of the particle in free space with the same energy E, specified for each of these curves as $E_N = 10^N(E_\infty/\pi^2)$. (The powers $N = -2, -1, 0, 1, 2$, and 3 are indicated at the corresponding curves.) Here, $\mathrm{Re}\,k$ is obtained for the first surface matter wave in the domain with $n = 1$ from the second equation in (4) after numerical calculation of the root $\kappa_1(\nu)$ of Eq. (6) as a function of ν. The curvilinear boundary of the first domain in Fig. 4 is marked bold. The physical meaning of the curves in Fig. 4 is as follows. In the part of the domain of existence of the first surface matter wave, which is concluded between the bold line and this curve with a definite energy E_N, the phase velocity of this surface matter wave is larger than in the case of a free particle with the same energy. Thus, the surface matter wave is an analogue of the fast surface Zenneck mode in this case. In the rest part of the same domain, the phase velocity of this surface matter wave is smaller than for a free particle with an energy E. Hence, the surface matter wave is an analogue of the slow Fano mode for surface electromagnetic waves.

Let us consider the quantitative characteristics of surface matter waves in the domains of their existence in the complex plane ν. The wave numbers in the vacuum κ_0 and k are more accessible for measurements than the wave number $\kappa_j(\nu)$ in the layer. We find the values of κ_0 and k for the jth surface matter wave by numerical calculations of the jth root $\kappa_j(\nu)$ of Eq. (6) at specified values of ν. Dispersion equations (4) yield $\kappa_{0j}^2(\nu) = \kappa_j^2(\nu) + \nu/a^2$, where the values of $\kappa_{0j}(\nu)$ satisfy the inequalities in (5) at the values of ν from the domains of existence of the jth surface matter wave with $n \ge j$. Then, the values of $\mathrm{Re}\,\kappa_{0j}(\nu)$ and $\mathrm{Im}\,\kappa_{0j}(\nu)$ are determined. For the first surface matter wave, the dimensionless parameters $p(\nu) \equiv -\mathrm{Re}\,\kappa_{01}(\nu)a/2\pi$ and $q(\nu) \equiv \mathrm{Im}\,\kappa_{01}(\nu)a$ are introduced, which determine the wavelength $\lambda_\perp(\nu) = a/p(\nu)$ of the wave function $\Psi_\perp(z)$ from (3) and the localization height $L_\perp(\nu) = a/2q(\nu)$ of the probability density $|\Psi_\perp(z)|^2$ in the vacuum for this surface matter wave. The parameters $p(\nu)$ and $q(\nu)$ give the same wavelength of the wave function $\Psi_\parallel(x)$ and the decay length of the probability density $|\Psi_\parallel(x)|^2$ along the layer surface after the calculation of k from the first equation in (4) at known values of $\kappa_{01}(\nu)$ and the energy E of the first surface matter wave. With accuracy up to the terms of the order of magnitude of $|\mathrm{Re}\,\kappa_{01}^2(\nu)a^2|/(\pi^2E/E_\infty) \ll 1$, the longitudinal wavelength coincides with the Broglie wavelength $\lambda_0 = \pi\hbar\sqrt{2/mE}$ for a particle with a mass m and the same energy E and the longitudinal decay length is equal to $L_\parallel(\nu) = a^2/2\lambda_0 p(\nu)q(\nu)$. Figure 3 shows the isolines $p(\nu) = p = \mathrm{const}$ and $q(\nu) = q = \mathrm{const}$ and the values of p and q calculated numerically for the first surface mat-

ter wave. The data in Fig. 3 make it possible to estimate $p(V)$ and $q(V)$ and the corresponding values of $\lambda_\perp(V)$, $L_\perp(V)$, and $L_\parallel(V)$ at a chosen potential V of the layer. The specific values of $L_\perp = L_\perp(V_0) = 1.19$ μm and $L_\parallel = L_\parallel(V_0) = 16.1$ μm at $a = 1$ μm are indicated in Fig. 1 for the point V_0 with the parameters $p(V_0) = p_0$ and $q(V_0) = q_0$ from Fig. 3. In this case, $\lambda_\perp(V_0) = 1.35$ μm and the longitudinal wavelength of $\Psi_\parallel(x)$ at the energy $E = 8.2 \times 10^{-8}$ eV coincides (accurate to ~0.3%) with the de Broglie wavelength $\lambda_0 = 0.1$ μm, which corresponds to this value of E. The obtained values of the spatial characteristics of the surface matter wave are close to the characteristics of optical surface electromagnetic waves. Therefore, such surface matter waves can be excited and observed by the methods developed for surface electromagnetic waves in the optical range, which use, for example, the frustrated total internal reflection and the diffraction or aperture transformation of bulk waves into surface ones [2].

The interaction of UCNs with a matter is adequately described by the complex potential under any absorption conditions, including the case when the imaginary part of the potential greatly exceeds the real part (as showed experiments with efficient absorbents [13]). Let us show by the example of UCNs, whose minimum wavelengths are close to optical, that the conditions for the existence of surface matter waves of these particles in the geometry under consideration can be implemented by choosing appropriate elemental and isotopic compositions of the absorbing layer and the substrate. We will take for estimation an absorbing layer composed of a mixture of the samarium isotopes ^{152}Sm and ^{154}Sm with natural samarium Sm^{nat} in any ratio and a substrate consisting of the pure isotope ^{154}Sm. The coherent scattering lengths of UCNs by nuclei of isotopes in the mixture will be taken the same as in [13]. The area in the complex plane of the potential V (which is proportional to the scattering length in the mixture) that can be covered by varying a given isotopic composition at $a = 1$ μm is a triangle with vertices at the points $V_{152} = -1.9 \times 10^3$, $V_{154} = 3.03 \times 10^3$, and $V_{nat} = (1.64 - 3.73i) \times 10^3$. These points correspond to 100% contents of ^{152}Sm, ^{154}Sm, and Sm^{nat}, respectively. The noted triangle covers parts of at least 10 domains in which from one to ten surface matter waves of UCNs may exist. As an example, we give the isotopic composition of the layer at the point V_0 in Figs. 2 and 3, where only the first surface matter wave of UCNs may exist: ^{152}Sm (61.1%), ^{154}Sm (38.7%), and Sm^{nat} (0.2%). The substrate potential V_{154} exceeds the layer potential $|V_0| = 15.3$ by a factor of almost 200, which justifies the model of potential (2), infinite in the substrate, in any case, for the layer potential V in the domains with small $n \geq 1$ in Fig. 2, where no more than n surface matter waves can exist.

CONCLUSIONS

The solutions to the 2D Schrödinger equation for microparticles interacting with a complex optical potential of an absorbing layer located on a totally reflecting substrate are analyzed. It is shown that the solutions to this problem in the form of the surface wave functions of the stationary states of the continuous spectrum (surface matter waves localized near the layer/vacuum interface) exist only when absorption occurs in the layer. These waves are an analogue of fast Zenneck modes in the case of surface electromagnetic waves. The boundaries of the domains of existence of different numbers of surface matter waves in the complex plane of the normalized layer potential V are determined. Intersection of each boundary at a variation in the factors determining the values of V may cause a threshold effect: a step of the probability of excitation of surface matter waves at this boundary. This threshold effect primarily makes it possible to establish the existence of surface matter waves in the simplest way: by a sharp change in the count of microparticles. In addition, detecting individual steps at known values of the potential, one can determine the corresponding values of the factors determining the layer potential. For example, in the case of surface matter waves of UCNs, this method can be used to obtain data on the hydrogen concentration in the surface layer (for which only estimates exist [7]) and to solve the general problem of determining the elemental and isotopic composition of a matter near the surface [8], as well as other problems of surface physics [9].

Let us discuss the possibility of occurrence of additional (anomalous) loss of trapped UCNs in the case of excitation of surface matter waves of UCNs in the presence of absorption in the surface layer of the trap walls (without specification of the layer origin). The existence of surface matter waves of UCNs, allowable in the model under consideration, would be an example of the experimentally observed mechanism of localization in the trap walls, which is of great interest for UCN physics [15]. In principle, a surface matter wave of UCNs can be directly observed by measuring the spatial distribution of its density $|\Psi(x, z)|^2$ by a neutron detector with a positional resolution of ~1 μm, which was recently tested in similar measurements of UCNs in the gravitational field of the Earth [16].

Mutual transformations of bulk and surface waves are impossible in the case of a uniform interface between media. However, excitation of surface matter waves of UCNs will occur with a low probability upon scattering of a bulk neutron wave by irregularities (roughness) on the surface of the trap walls, as in experiments with excitation of surface electromagnetic waves [2]. The probability of a subsequent reverse transition of a UCN from a surface to the bulk state upon such scattering will be lower than the probability of excitation of a surface wave because of its decay along the wall caused by the absorption. For this reason, the

excitation of a surface matter wave of a UCN can be considered in the single-scattering approximation without taking into account the reverse transition of the UCN to the bulk state. In this approximation, the excitation of a surface matter wave of a UCN is equivalent to its leakage from the trap bulk with some probability of excitation of a surface matter wave. Thus, the excitation of surface matter waves of UCNs as a result of the absorption, which were not previously taken into account in the consideration of the UCN storage, can make a significant contribution to the additional (anomalous) loss of UCNs in the trap walls. It is noteworthy that surface matter waves of UCNs may exist, as can be seen in Fig. 2, at any real part of the potential of the absorbing surface layer in traps, including the negative real part for a repulsive potential. Hence, the proposed correlation between the anomalous loss of UCNs and the irreversible excitation of surface matter waves, which has a low threshold with respect to the absorption of UCNs in the trap walls, is in agreement with the main experimental data: the generality of manifestation and the weak temperature dependence of the anomalous loss [8, 9].

ACKNOWLEDGMENTS

We are deeply grateful to Academician V.L. Ginzburg for his promotion of the public discussion of this study and interested participation in the discussion. R.Ch. Bokun acknowledges V.I. Morozov and his colleagues for the discussion of the experimental possibilities concerning the subject of the study, V.E. Dmitrienko for reading the manuscript and useful recommendations, and A.V. Kistovich for the help in preparation of the paper for publication.

REFERENCES

1. V. M. Agranovich and V. L. Ginzburg, *Crystal Optics with Spatial Dispersion, and Excitons*, 2nd ed. (Nauka, Moscow, 1979; Springer-Verlag, New York, 1984).
2. G. N. Zhizhin, M. A. Moskaleva, E. V. Shomina, and V. A. Yakovlev, *Surface Polaritions. Electromagnetic Waves at Surfaces and Interfaces*, Ed. by V. M. Agranovich and D. L. Mills (North-Holland, Amsterdam, 1982).
3. S. Davison and J. Levine, *Surface States*, Vol. 25: *Solid State Physics. Advances in Research and Applications*, Ed. by H. Ehrenreich *et al*. (Academic, New York, 1970; Mir, Moscow, 1973).
4. O. Madelung, *Introduction to Solid-State Theory* (Springer-Verlag, Berlin, 1978; Nauka, Moscow, 1985).
5. M. Prutton, *Introduction to Surface Physics* (Clarendon, Oxford, 1994).
6. M. H. Weber, S. Tang, S. Berko, *et al.*, Phys. Rev. Lett. **61**, 2542 (1988).
7. V. K. Ignatovich, *Physics of Ultracold Neutrons* (Nauka, Moscow, 1986) [in Russian].
8. A. V. Strelkov, Usp. Fiz. Nauk **174**, 565 (2004) [Phys. Usp. **47** (5), 511 (2004)].
9. V. K. Ignatovich, Usp. Fiz. Nauk **166**, 303 (1996) [Phys. Usp. **39**, 283 (1996)].
10. L. D. Landau and E. M. Lifshitz, *Course of Theoretical Physics*, Vol. 8: *Electrodynamics of Continuous Media* (Nauka, Moscow, 1982; Pergamon, New York, 1984).
11. R. Ch. Bokun and Yu. V. Kistovich, in *Proceedings of IV All-Union Conference on Coherent Interaction of Radiation with Matter* (Moscow, 1988), p. 314.
12. V. M. Galitskiĭ, B. M. Karnakov, and V. I. Kogan, *Problems in Quantum Mechanics* (Nauka, Moscow, 1981) [in Russian].
13. V. I. Morozov, M. I. Novopol'tsev, Yu. N. Panin, *et al.*, Pis'ma Zh. Éksp. Teor. Fiz. **46**, 301 (1987) [JETP Lett. **46** (8), 377 (1987)].
14. A. I. Baz', Ya. B. Zel'dovich, and A. M. Perelomov, *Scattering, Reactions, and Decays in Nonrelativistic Quantum Mechanics* (Nauka, Moscow, 1971; Israel Program for Scientific Translations, Jerusalem, 1966).
15. E. V. Lychagin, A. Yu. Muzychka, V. V. Nesvizhevsky, *et al.*, Pis'ma Zh. Éksp. Teor. Fiz. **71**, 657 (2000) [JETP Lett. **71**, 447 (2000)].
16. V. V. Nesvizhevsky, Usp. Fiz. Nauk **174**, 569 (2004) [Phys. Usp. **47** (2004)].

Translated by Yu. Sin'kov

Crystallography Reports, Vol. 50, No. 5, 2005, pp. 869–873. Translated from Kristallografiya, Vol. 50, No. 5, 2005, pp. 935–939.

NANOMATERIALS

Microhardness and Fracture Toughness of Y_2O_3- and $Y_3Al_5O_{12}$-Based Nanocrystalline Laser Ceramics

A. A. Kaminskiĭ[1], M. Sh. Akchurin[1], R. V. Gaĭnutdinov[1], K. Takaichi[2], A. Shirakava[2], H. Yagi[2, 3], T. Yanagitani[3], and K. Ueda[2]

[1] *Shubnikov Institute of Crystallography, Russian Academy of Sciences, Leninskiĭ pr. 59, Moscow, 119333 Russia*

[2] *Institute for Laser Science, University of Electro-Communications, Chofu, Tokyo 182, Japan*

[3] *Takuma Works, Konoshima Chemical Co., Ltd., Kagava, Japan*

e-mail: kaminalex@mail.ru

Received December 1, 2004

Abstract—The microhardness and fracture toughness of laser nanocrystalline ceramics based on the cubic oxides Y_2O_3 and $Y_3Al_5O_{12}$ are determined experimentally. It is shown by comparative measurements that the fracture toughness and microhardness of Y_2O_3 ceramics exceed the corresponding parameters of Y_2O_3 single crystals by factors of 2.5 and 1.3, respectively. The fine morphology of grains and grain boundaries in fractures is investigated. It is ascertained that changes in the mechanical properties of the nanocrystalline ceramics under study are related to both the sizes and structure of grains and the structure of grain boundaries. It is suggested that twinning processes determine the mechanisms of formation of nanocrystalline ceramics. © *2005 Pleiades Publishing, Inc.*

One of the most important recent achievements in modern laser materials science is the development of highly transparent nanocrystalline ceramics based on the cubic oxides $Y_3Al_5O_{12}$ and RE_2O_3 (*RE* = Y, Sc, Gd, or Lu), containing ions of trivalent lanthanides (Ln^{3+}) that are responsible for stimulated emission. For a relatively short time, the use of $Y_3Al_5O_{12}$:Nd^{3+} ceramics in lasers operating in the modes of practical importance at different levels of output power showed that these ceramics have begun to compete to a certain extent with $Y_3Al_5O_{12}$:Nd^{3+} single crystals, which are most widely used in quantum electronics and laser engineering (see, for example [1]). Concerning RE_2O_3:Lu^{3+} compounds, we should note that the recently patented ceramic technology [2] also makes it possible to fabricate these laser crystalline materials of high optical perfection and almost any required size on the basis of these compounds. Unfortunately, the known methods of flux growth of RE_2O_3 in the form of large single crystals of laser quality have proven to be inconsistent.

Table 1 shows that the range of known laser VSN (i.e., produced by vacuum sintering and nanotechnological techniques) [2, 3] crystalline ceramics $Y_3Al_5O_{12}$ and RE_2O_3 is sufficiently wide both in the number of different types of ceramics and in the variety of spectral lasing possibilities. Here, it is pertinent to note the main stages in the previous investigations of laser ceramics: 1966 (CaF_2:Dy^{2+} [15]), 1973 (Y_2O_3–ThO_2:Nd^{3+} [16]), and 1995 ($Y_3Al_5O_{12}$:Nd^{3+} [17]). In all these studies, different modifications of the high-pressure sintering method were used, which made it impossible to obtain ceramics with good lasing characteristics.

This study continues our previous investigations of the microhardness and fracture toughness of highly transparent VSN nanoceramics (see, for example, [18]). The purpose is to obtain data that could be used both to estimate the limiting lasing characteristics of VSN nanoceramics and to optimize the process of preparation of nanoceramics with improved optical properties. Here, we also start a detailed study of the fine morphology of grains in VSN nanoceramics. The objects of study are Y_2O_3 ceramics, as well as $Y_3Al_5O_{12}$ ceramics with much smaller grain sizes as compared to the $Y_3Al_5O_{12}$ ceramics investigated in [18].

Microhardness methods (indentation and sclerometry) are widely used to analyze the mechanical properties of crystals, especially brittle ones. Owing to the fast decrease in stress with an increase in the distance from the point of load application and to the presence of a large hydrostatic component, these methods make it possible to induce very high stresses under the indenter tip (of the same order of magnitude as the shear modulus) without catastrophic fracture of a sample, a result which is difficult to obtain by conventional methods (extension, compression, bending, and so on). The use of the indentation and sclerometry methods allowed us to determine the microhardness H and the fracture toughness K_{1C} and to investigate the mechanisms of fracture of the samples under study. The microhardness

Table 1. Laser VSN ceramics and the channels of their spontaneous emission

Ceramics	Sp. gr.[1]	SRS[2]	Ln^{3+} ions and the channels of spontaneous emission		
			Nd^{3+}	Er^{3+}	Yb^{3+}
Y_2O_3	T_7^h	[4]	${}^4F_{3/2} \longrightarrow {}^4I_{11/2}$ [5]		${}^2F_{5/2} \longrightarrow {}^2F_{7/2}$ [6, 7][3]
$Y_3Al_5O_{12}$	O_h^{10}	[4]	${}^4F_{3/2} \longrightarrow {}^4I_{11/2}$ [1][4] ${}^4F_{3/2} \longrightarrow {}^4I_{13/2}$ [8][5]	${}^4I_{11/2} \longrightarrow {}^4I_{13/2}$ [9][6]	${}^2F_{5/2} \longrightarrow {}^2F_{7/2}$ [10]
$YGdO_3$[7]	T_7^h		${}^4F_{3/2} \longrightarrow {}^4I_{11/2}$ [11]		
Sc_2O_3	T_7^h	[9]			${}^2F_{5/2} \longrightarrow {}^2F_{7/2}$ [12]
Lu_2O_3	T_7^h		${}^4F_{3/2} \longrightarrow {}^4I_{11/2}$ [13]		${}^2F_{5/2} \longrightarrow {}^2F_{7/2}$ [14]

[1] Grains are micron-size crystallites.
[2] Stimulated Raman scattering.
[3] Femtosecond lasing with a pulse width of ~430 fs was obtained in [7].
[4] An output power of ~1.5 kW was obtained in [1].
[5] An output power of ~35 W was obtained in [8].
[6] Lasing at a wavelength of 3 μm was excited by Xe-lamp pumping.
[7] $YGdO_3 = (Y_{0.5}Gd_{0.5})_2O_3$.

was estimated by the generally accepted formula

$$H = K\frac{P}{d^2},$$

where P is the load on the indenter; d is the indentation diagonal; and K is the shape factor of the indenter, which is equal to 1.854 for a Vickers pyramid.

The fracture toughness was experimentally determined from the linear sizes of radial cracks (C) arising near the point of load application and estimated by the known formula taking into account the elastic and strength characteristic of a material under study [19]. For the Vickers indenter,

$$K_{1C} = 0.016(E/H)^{1/2}P/C^{3/2},$$

where E is the Young modulus. In calculations, we used the Young moduli of single crystals of yttrium oxide in the [110] direction (E = 170 GPa) and yttrium aluminum garnet in the [110] direction (E = 300 GPa) (i.e., in the directions of maximum hardness).

Mechanical tests of yttrium oxide single crystals were performed in the [111] cleavage plane. Other samples were cut by a diamond saw and then ground and mechanically polished to class 14. Deformation was performed at room temperature by a diamond Vickers pyramid, applying loads in the range 0.1–1 N. Indentation was performed on a PMT-3 microhardness meter and sclerometric tests were carried out on a Martens sclerometer. The load on the indenter was chosen to reliably fix not only indentations but also radial cracks from them. In single crystals, radial cracks can be clearly seen at P = 0.1–0.2 N, whereas in $Y_3Al_5O_{12}$- and Y_2O_3-based ceramics, fracture processes can be reliably fixed only at $P \geq 1$ and ≥0.5 N, respectively. Therefore, the microhardness and the fracture toughness of $Y_3Al_5O_{12}$ single crystals and the corresponding ceramics were measured at P = 1 N, whereas the measurements on Y_2O_3 single crystals and the corresponding ceramics were carried out at P = 0.5 N. Taking into account the sufficiently high homogeneity of the ceramics, 50 indentations were made in each sample in them, as well as in the single crystals. Note that the diagonals of indentations in single crystals were oriented in the [110] direction, i.e., in the direction of maximum hardness. The measurement error did not exceed 3%.

The morphology of fracture surfaces of the samples was investigated by atomic force microscopy (AFM) in the contact mode. A Solver P47 (NT-MDT, Moscow) atomic-force microscope and CSC 37 silicon cantilevers (Mikromasch, Estonia) were used. The samples were fractured as follows: a scratch (stress concentrator) of necessary length was made on the sample surface and then the sample was subjected to three-point bending.

Figure 1 shows the images of indentations on the (111) cleavage plane of an Y_2O_3 single crystal (Fig. 1a) and on the mechanically polished surface of Y_2O_3 ceramics (Fig. 1b), which were made by a diamond Vickers pyramid at room temperature under a load of P = 0.5 N. The indentation-induced cracks in single crystals are much longer and more straight, especially the cracks propagating in the cleavage plane. Apparently, the reason for this phenomenon is that grain boundaries in ceramics serve as stoppers for crack propagation.

The investigations performed showed that the microhardness of Y_2O_3 ceramic samples exceeds that of corresponding single crystals by 30–35%. The crack

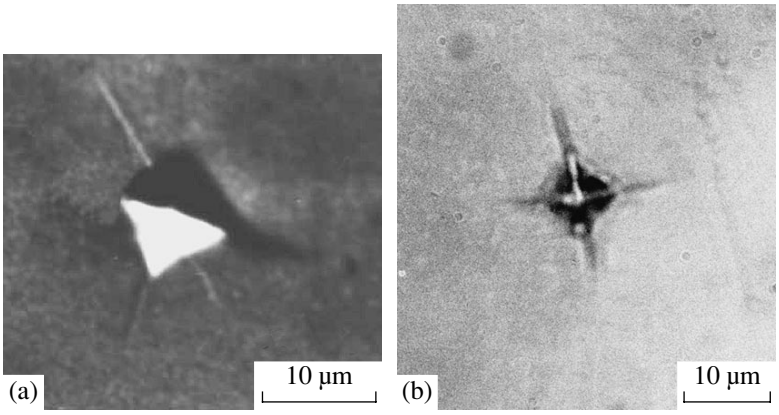

Fig. 1. Microscopic images of indentations in the cleavage planes of (a) Y_2O_3 single crystal and (b) mechanically polished Y_2O_3 ceramics; $P = 0.5$ N.

resistance also significantly increases: the fracture toughness K_{1C} of ceramics exceeds that of single crystals by a factor of about 2.5.

Comparative tests of the ceramics based on yttrium aluminum garnet, with grain sizes of 10–15 μm (samples $Y_3Al_5O_{12}$-1) and 1–2 μm (samples $Y_3Al_5O_{12}$-2), showed that the microhardness of $Y_3Al_5O_{12}$-2 is only slightly higher than that of $Y_3Al_5O_{12}$-1 (by 5–7%), whereas the fracture toughness of $Y_3Al_3O_{12}$-2 is lower than that of $Y_3Al_5O_{12}$-1 by a factor of about 2. Introduction of isomorphically substituting Nd ions into these ceramics somewhat decreases their hardness and the value of K_{1C} (Table 2).

The increase in the microhardness of the ceramic samples with a decrease in the grain size, as well as their higher microhardness in comparison with single crystals, can be explained as follows. It is known that the hardness of crystals is determined by the dispersion work [20, 21]. Relaxation of very high stresses (of the same order of magnitude as the shear modulus) under the indenter tip leads to the decomposition of the crystal structure into nanoblocks. Note that, the harder a material, the smaller the size of the nanocrystallites (grains) formed. It is also known that, with a decrease in the size of crystals (an example is filamentary crystals), their structure becomes more perfect (it is energetically unfavorable for defects to nucleate and exist in small volumes) and their mechanical properties are improved. Therefore, with a decrease in the grain size during conservation of the structure and properties of boundaries, the microhardness of a material increases, a phenomenon which is generally observed in nanocrystalline materials (an analogy of the Petch–Hall effect) [22]. Investigation of the mechanisms of plastic deformation of yttrium oxide single crystals and ceramics showed that, in contrast to garnet samples, in which plastic deformation at room temperature occurs mainly owing to the collective motion of point defects, dislocation slip (mainly in the ⟨110⟩ {100} system) plays an important role in Y_2O_3 [23].

The decrease in the crack resistance of $Y_3Al_5O_{12}$-2, in comparison with $Y_3Al_5O_{12}$-1, can be explained by the fact that the mechanism of intergranular fracture becomes dominant in this case. In $Y_3Al_5O_{12}$-1, cracks nucleate mainly in grains, and boundaries serve as stoppers for their propagation, whereas in $Y_3Al_5O_{12}$-2 cracks predominantly nucleate near boundaries and propagate along them. Figure 2a shows the contact-

Table 2. Microhardness H and fracture toughness K_{1C} of the VSN nanocrystalline ceramics Y_2O_3 and $Y_3Al_5O_{12}$ and the corresponding single crystals

Sample no.	Material	Grain size, μm	H, GPa	K_{1C}, MPa m$^{1/2}$
1	Y_2O_3 ceramics	1–2	~10	~2.5
2	Y_2O_3 single crystal		~7.6	~1.0
3	$Y_3Al_5O_{12}$-1 ceramics	10–15	~16*	~8.7*
4	$Y_3Al_5O_{12}$-2 ceramics	1–2	~16.8	~4.3
5	$Y_3Al_5O_{12}$: Nd^{3+} ceramics	10–15	~15.0*	~5.2*
6	$Y_3Al_5O_{12}$: Nd^{3+} ceramics	1–2	~16.8	~4.3
7	$Y_3Al_5O_{12}$ single crystal		~14.5*	~1.8*

* Data of [18].

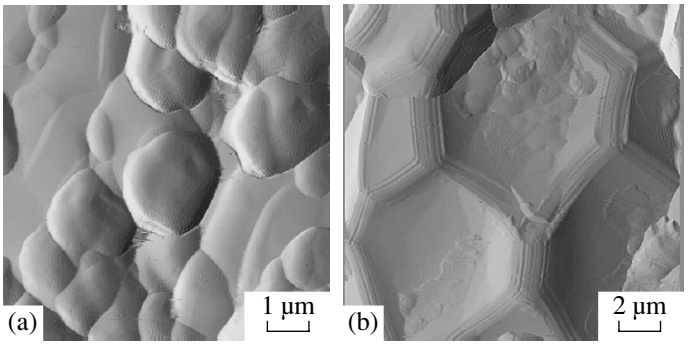

Fig. 2. AFM images of fractures in the $Y_3Al_5O_{12}$ ceramics with grain sizes of (a) 1–2 and (b) 10–15 μm.

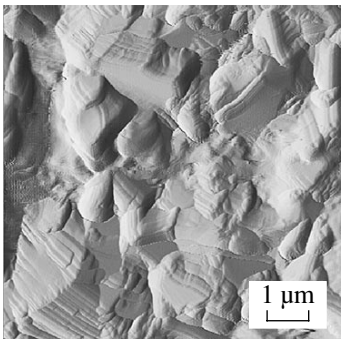

Fig. 3. AFM image of fractures in Y_2O_3 ceramics.

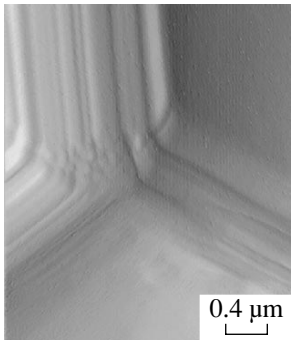

Fig. 4. AFM image of a triple joint in a fracture in the $Y_3Al_5O_{12}$ ceramics with a grain size of 10–15 μm.

mode AFM image of a fracture in an $Y_3Al_5O_{12}$-2 sample. It can be seen that fracture occurs mainly along the grain boundaries (grain relief on the right), although fracture of grains is also sometimes observed (the relatively smooth relief on the left). At the same time, fracture of grains occurs in the $Y_3Al_5O_{12}$-1 ceramics (Fig. 2b). In Y_2O_3-based ceramics, the main fracture mechanism, as in $Y_3Al_5O_{12}$-2, is of the intergranular type. Most grains have a stripe (layered) structure (Fig. 3).

In our opinion, the reason for the decrease in the crack resistance of the ceramics studied with a decrease in the grain size is as follows. The smaller the size of grains, the more perfect their structure is. In addition, as the grain size decreases, stress concentrators are located at grain boundaries, which serve as sinks for point defects. It should be noted that, with an increase in the grain size in ceramics based on yttrium aluminum garnet, the structure of grain boundaries also somewhat changes. They become less uniform and exhibit a stripe structure. Figure 4 shows the AFM image of a triple joint in a fracture in $Y_3Al_5O_{12}$-1. (An enlarged joint image is shown in Fig. 2b, left.) The boundaries show pronounced stripes 100–300-nm wide and 10–15 nm in height; i.e., the boundaries themselves are composites, which impedes their fracture. It should also be noted that triple joints of grains have approximately the same angles (~120°). This indicates grain matching in the (111) planes; i.e., we can speak about the presence of a threefold axis. The minor decrease in the microhardness and crack resistance of the samples doped with Nd ions can be related to the fact that these ions introduce additional stresses into the lattice since their radius exceeds that of isomorphously substituted Y ions.

Sclerometric tests of ceramic samples (scratches were made in radial directions from the center of a circle with a step of 15°) did not reveal the hardness anisotropy, whereas in $Y_3Al_5O_{12}$ single crystals the hardness is maximum in the [112] and [110] directions and in Y_2O_3 single crystals [110] is the direction of maximum hardness [23, 24].

Thus, the investigations performed here showed that a change in the structure of grain boundaries may significantly affect the mechanical properties of the ceramics under consideration, especially the crack resistance. The structure of grain boundaries is of particular interest since most researchers believe that it is the grain boundaries that determine the unique properties (mechanical, optical, electrical, magnetic, and so on) of nanocrystalline materials [22, 25]. We can suggest that the stripe structure of grain boundaries revealed here is related to the twinning processes, which are responsible for the plastic deformation during the ceramic preparation. This suggestion is confirmed by our finding of the existence of a threefold

axis in triple joints (Fig. 4) (since twinning of the cubic crystals $Y_3Al_5O_{12}$ and Y_2O_3 is performed predominantly in the plane (111)). Another confirmation is that twin interlayers do not scatter light beams and improve mechanical properties of some crystals [26, 27]. It should be noted that the observed stripe structure of grain boundaries requires further investigation using high-resolution methods of structural analysis.

ACKNOWLEDGMENTS

This study was supported in part by the Russian Foundation for Basic Research and the Ministry of Education of the Russian Federation; the program of the Presidium of the Russian Academy of Sciences "Femtosecond Optics and Physics of Superstrong Laser Fields"; and the program "21st Century COE Program" of the Ministry of Education, Science, Sport, and Culture of Japan.

The study was greatly facilitated by the cooperation of the authors in the Joint Open Laboratory "Laser Crystals and Precision Laser Systems."

REFERENCES

1. J. Lu, K. Ueda, H. Yagi, *et al.*, J. Alloys Compd. **341** (1), 220 (2002); A. A. Kaminskii, Phys. Status Solidi A **200** (2), 215 (2003).
2. H. Yagi and T. Yanagitani, JP Appl., No. 2003-89578 (2003); JP Appl., No. 2003-128465 (2003).
3. T. Yanagitani and H. Yagi, JP Appl., No. 10-101333 (1998); JP Appl., No. 10-101411 (1998).
4. A. A. Kaminskii, H. J. Eichler, K. Ueda, *et al.*, Phys. Status Solidi A **181** (2), R19 (2000).
5. J. Lu, T. Murai, K. Takaichi, *et al.*, Laser Phys. **11** (5), 1053 (2001).
6. A. Shirakawa, H. Yagi, J. F. Bisson, *et al.*, Opt. Express **11**, 2911 (2003).
7. A. Shirakawa, K. Takaichi, H. Yagi, *et al.*, Laser Phys. Lett. **14** (11), 1555 (2004).
8. J. Lu, J. Lu, A. Shrakawa, *et al.*, Phys. Status Solidi A **189**, R11 (2002); J. Lu, J. Lu, T. Murai, *et al.*, Opt. Lett. **27** (13), 1120 (2002).
9. A. A. Kaminskii, S. N. Bagaev, K. Ueda, *et al.*, Laser Phys. Lett. **2** (1) (2005).
10. K. Takaichi, H. Yagi, J. Lu, *et al.*, Phys. Status Solidi A **200** (1), R5 (2003).
11. J. Lu, J. I. Lu, A. Shirakawa, *et al.*, Laser Phys. **12** (7), 940 (2003).
12. J. Lu, J. F. Bisson, K. Takaichi, *et al.*, Appl. Phys. Lett. **83** (6), 1101 (2003).
13. J. Lu, K. Takaichi, T. Uematsu, *et al.*, Appl. Phys. Lett. **81** (23), 4324 (2002).
14. K. Takaichi, H. Yagi, A. Shirakawa, *et al.*, Phys. Status Solidi A (2005) (in press).
15. E. Carnall, C. E. Hatch, and W. F. Parsons, in *Materials Science Research* (Plenum, New York, 1986), p. 165.
16. C. Greskovich and J. P. Chernoch, J. Appl. Phys. **44** (4), 4599 (1973).
17. A. Ikecui, T. Kinoshita, K. Kamata, and K. Yoshida, J. Ceram. Soc. **78** (4), 1033 (1995).
18. A. A. Kaminskiĭ, M. Sh. Akchurin, V. I. Alshits, *et al.*, Kristallografiya **48** (3), 562 (2003) [Crystallogr. Rep. **48**, 515 (2003)].
19. B. R. Lawn, A. G. Evans, and D. B. Marshall, J. Am. Ceram. Soc. **63** (2), 576 (1980).
20. A. P. Rebinder, Izv. Akad. Nauk SSSR, Ser. Khim. **5**, 639 (1936).
21. M. Sh. Akchurin and V. R. Regel, Chem. Rev. **23**, 59 (1998).
22. F. I. Gusev, Usp. Fiz. Nauk **108** (1), 55 (1998) [Phys. Usp. **41** (1), 49 (1998)].
23. A. A. Urusovskaya, M. Gartmanova, G. G. Knab, *et al.*, in *Actual Problems of Microindentation Physics* (Shtiintsa, Chisinau, 1989).
24. E. A. Stepantsov, M. Sh. Akchurin, and V. G. Govorkov, Kristallografiya **23** (4), 872 (1978) [Sov. Phys. Crystallogr. **23**, 492 (1978)].
25. R. A. Andrievskiĭ and A. M. Gleĭzer, Fiz. Met. Metalloved. **88** (1), 50 (1999); **89** (1), 91 (2000).
26. M. Sh. Akchurin and R. V. Galiulin, Kristallografiya **48** (3), 514 (2003) [Crystallogr. Rep. **48**, 469 (2003)].
27. M. Sh. Akchurin, R. V. Galiulin, and P. P. Fedorov, Vestn. Tambov. Gos. Univ. **8** (4), 549 (2003).

Translated by Yu. Sin'kov

Crystallography Reports, Vol. 50, No. 5, 2005, pp. 874–876. Translated from Kristallografiya, Vol. 50, No. 5, 2005, pp. 940–943.

CRYSTAL GROWTH

Oxygen-Conducting Crystals of $La_2Mo_2O_9$: Growth and Main Properties

V. I. Voronkova, V. K. Yanovskiĭ, and E. P. Kharitonova

Faculty of Physics, Moscow State University, Leninskie gory, Moscow, 119992 Russia

e-mail: voronk@polly.phys.msu.ru

Received November 10, 2004

Abstract—Single crystals of the anionic conductor $La_2Mo_2O_9$ are grown by crystallization from a nonstoichiometric melt. Their polymorphism and domain structure, as well as the temperature dependences of conductivity and dielectric permittivity, are studied. In the temperature range 750–600°C, the conductivity of these crystals is as high as 10^{-1}–10^{-2} Ω^{-1} cm^{-1}. © *2005 Pleiades Publishing, Inc.*

INTRODUCTION

Crystalline materials with high conductivity, related to abnormally high mobility of oxygen anions, are of considerable interest from both scientific and practical points of view. In particular, these materials can be used in fuel cells and similar devices. Such materials are few in number [1]. These are compounds with fluorite (yttrium- and calcium-stabilized ZrO_2 and δ-Bi_2O_3), perovskite (doped $LaGaO_3$), and pyrochlore ($Gd_2Zr_2O_7$, $Gd_2Ti_2O_7$, etc.) structures; bismuth-containing layered perovskite-like compounds (Bi_2WO_6, Bi_2MoO_6, and $Bi_2VO_{5.5}$); and a series of solid solutions based on the latter compound (the BIMEVOX family). Recently, it was demonstrated that lanthanum dimolybdate $La_2Mo_2O_9$ (LM), which was synthesized more than 30 years ago [2–4], also belongs to above-mentioned materials. This compound was recently used to prepare a series of solid solutions with high anionic conductivity (the so-called LAMOX family) by various substitutions [5]. Fournier *et al*. [3] demonstrated that lanthanum dimolybdate has a cubic structure with the unit-cell parameter a = 7.155 Å and undergoes an irreversible phase transition at 572°C. In contrast, Rode *et al.* [4] found that this phase transition is reversible and occurs at 560°C. More recently, Lacorre *et al.* [5] demonstrated that the transformation of the low-temperature α phase to the high-temperature β phase occurs at 580°C, is a first-order phase transition, and is accompanied by an increase in the conductivity by approximately two orders of magnitude. The low-temperature α phase was studied on a high-resolution diffractometer [5, 6]. It was shown that this phase has a monoclinic symmetry described by sp. gr. $P2_1$. Measurements of the temperature dependence of the second-harmonic generation (SHG) intensity [7] confirmed that this phase is noncentrosymmetric. The unit-cell parameter of the cubic phase, determined by Goutenoire *et al.* [6] at 617°C, is 7.2014 Å, sp. gr. $P2_13$. The unit-cell parameters of the low-temperature monoclinic phase are a = 7.1426 Å, b = 7.1544 Å, c = 7.1618 Å, and β = 89.538°. A complex superstructure with the parameters $2a \times 3a \times 4a$ was also established. Data on the preparation of LM single crystals and their properties are lacking in the literature.

The aim of this study was to grow $La_2Mo_2O_9$ single crystals and measure the temperature dependences of their conductivity, dielectric permittivity, and some other characteristics.

SINGLE-CRYSTAL GROWTH AND EXPERIMENTAL TECHNIQUE

The $La_2Mo_2O_9$ compound melts incongruently at 1350–1400°C and shows a narrow crystallization field (3–4 mol % [3] or about 10 mol % [4]). In this study we grew single crystals of this compound by spontaneous crystallization from a nonstoichiometric melt in the La_2O_3–MoO_3 binary system. Our results confirmed the phase diagram of this system that was proposed in [3].

LM single crystals were grown from a melt containing 31 mol % of La_2O_3 and 69 mol % of MoO_3 in accordance with the system studied in [3]. The mixture of the starting reagents of high purity grade was stirred in an agate mortar, placed in platinum or corundum crucibles, heated in a furnace with silicon carbide rods to 1200°C, kept at this temperature for one day, and cooled to 1020°C at a rate of 1 K/h. Next the melt was poured off, and the crucible containing crystals was either cooled at a rate of 50 K/h to room temperature or quenched in air. The LM crystals grew at the bottom of the crucibles. The crystals were then mechanically purified from the residual solvent. The $La_2(MoO_4)_3$ phase generally crystallized in the upper part of the crucibles.

1063-7745/05/5005-0874$26.00

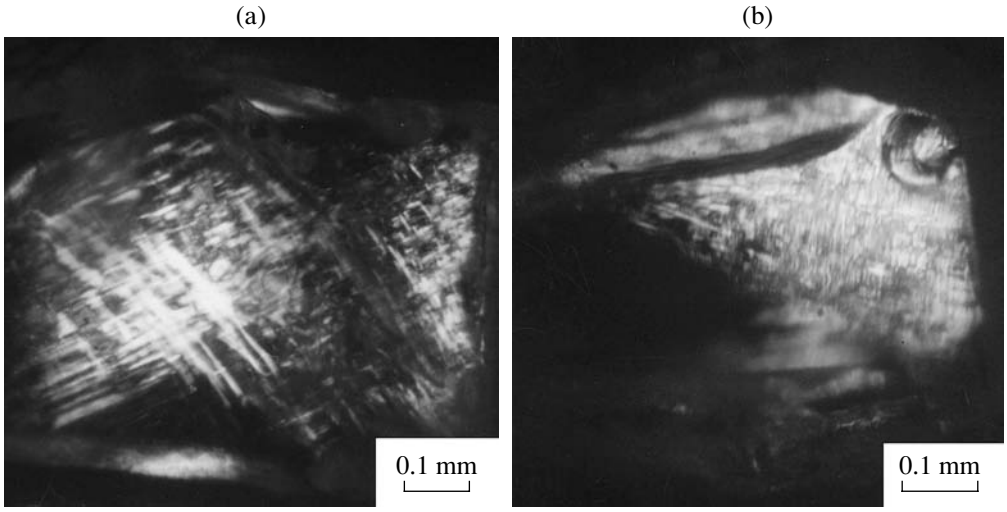

Fig. 1. Domain structure of the $La_2Mo_2O_9$ crystals at (a) room temperature and (b) at a temperature close to that of the monoclinic-to-cubic phase transition.

X-ray powder diffraction analysis of the crystals was carried out on a DRON-2.0 diffractometer (CuK_α radiation). The unit-cell parameters were measured accurate to 10%. Differential thermal analysis (DTA) was performed on a Rigaku Thermoflex scanning calorimeter. The heating and cooling rates were 20 K/min. A piezoelectric test was performed at room temperature by the static method [8, p. 124]. The temperature dependences of the dielectric permittivity and conductivity were measured in the range 25–800°C using a TESLA BM 431E bridge at a frequency of 1 MHz. Polymorphism of the crystals was studied under a MIN-8 polarizing microscope equipped with a heating stage.

RESULTS AND DISCUSSION

The LM crystals obtained by the above-described procedure were transparent, slightly yellowish, and had dimensions about 1–4 mm. X-ray powder diffraction analysis demonstrated that the crystals have cubic symmetry with a unit-cell parameter of approximately 7.17 Å. However, examinations under polarized light showed that the slowly cooled crystals are in fact optically anisotropic and divided into domains in the form of mutually perpendicular stripes (Fig. 1a). The crystals that were quenched from temperatures close to 1000°C remained optically isotropic, which indicates that the high-temperature cubic phase can exist as a metastable phase at room temperature for a long time. Upon heating of polydomain samples on the filament of the heating stage to 580°C, domains disappeared and the crystals became optically isotropic. The boundary between the anisotropic and isotropic phases of one crystal heated to a temperature close to the phase-transition point can be seen in Fig. 1b. These results confirm that the symmetry of the high-temperature phase of LM is cubic, whereas the low-temperature phase has lower symmetry and, according to the results of [6], is crystallized in the monoclinic system. This is a pronounced first-order phase transition, which is apparently associated with substantial structural rearrangements despite that distortions of the crystal lattice of the low-temperature phase are insignificant. DTA study of the crystals showed that the transition is accompanied by a noticeable thermal effect and a substantial temperature hysteresis (as high as 30–40 K).

Figure 2 shows the temperature dependences of the conductivity of an LM single crystal measured at heating and cooling rates of 2 K/min. At 800°C, the conductivity is about 0.1 Ω^{-1} cm^{-1}. At 550°C, the conductivity is about 3×10^{-3} Ω^{-1} cm^{-1}. The activation energy in the high-temperature range is approximately 0.9 eV. The phase transition is accompanied by a diffuse conductivity jump by approximately two orders of magnitude. Measurements of the conductivity for other crystals at 550°C demonstrated that it can be as high as 10^{-2} Ω^{-1} cm^{-1}. These results are in good agreement with those for ceramic samples [5]. However, the phase-transition temperature (580°C) determined in [5] was higher.

Measurements of the temperature dependence of the dielectric permittivity (Fig. 3) confirmed that the LM crystals undergo a phase transition at 500–550°C. This transition is accompanied by a sharp increase in the dielectric permittivity up to 7000, a result which is typical of transitions associated with electric ordering. A further increase in the dielectric permittivity may be related to the increase in the concentration of mobile charge carriers (oxygen anions in the LM crystals).

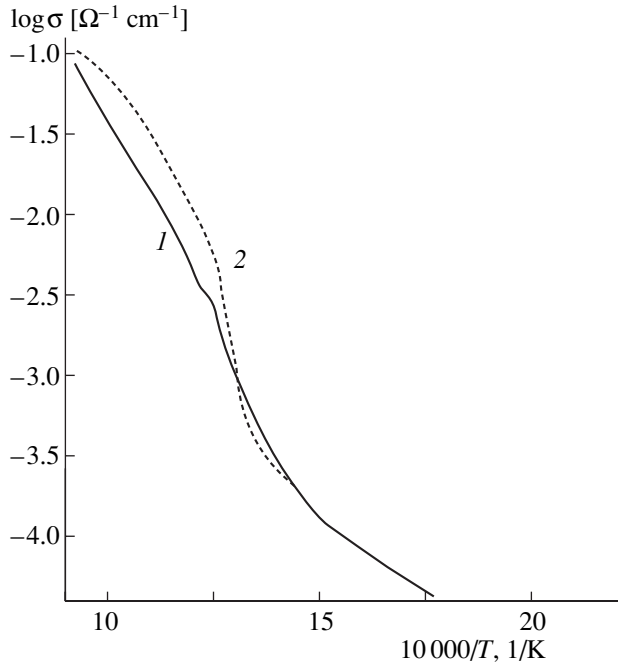

Fig. 2. Temperature dependences of the conductivity of a $La_2Mo_2O_9$ crystal measured upon (*1*) heating and (*2*) cooling at a rate of 2 K/min.

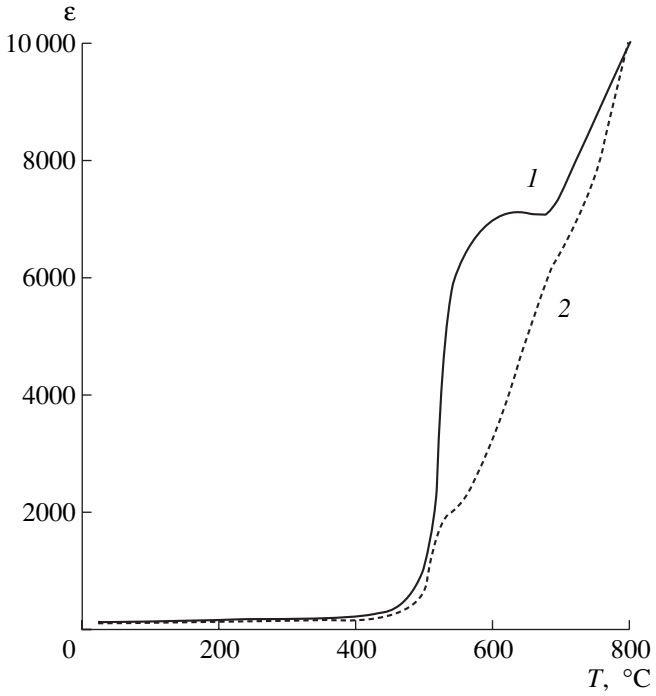

Fig. 3. Temperature dependences of the dielectric permittivity of a $La_2Mo_2O_9$ crystal measured upon (*1*) heating and (*2*) cooling at a rate of 2 K/min.

Piezoelectric tests gave positive results for LM crystals, thus confirming the polarity of their low-temperature phase.

CONCLUSIONS

The study of lanthanum dimolybdate $La_2Mo_2O_9$ single crystals that were prepared by crystallization from a nonstoichiometric melt confirmed the existence of the first-order phase transition from the high-temperature nonpolar cubic phase to the low-temperature polar monoclinic phase at 500–550°C for these crystals. Although this transition is reversible, it is associated with a substantial rearrangement of the atomic structure. This is a pronounced first-order phase transition. The crystals are characterized by high conductivity (up to 10^{-2} Ω^{-1} cm^{-1} at 550°C) due to the anomalously high mobility of oxygen anions in the high-temperature phase. Hence, lanthanum dimolybdate can be considered as a new representative of a specific class of crystalline materials, the so-called ferroelectric–superionic conductors [9].

ACKNOWLEDGMENTS

This study was supported by the Russian Foundation for Basic Research (project no. 04-03-32432) and the program “Universities of Russia” (project no. UR.01.02.491).

REFERENCES

1. P. Knauth and H. Tuller, J. Am. Ceram. Soc. **85** (7), 1654 (2002).
2. E. I. Get’man and M. V. Mokhosoev, Neorg. Mater. **4** (9), 1554 (1968).
3. J.-P. Fournier, J. Fournier, and R. Kohlmuller, Bull. Soc. Chim. Fr., No. 12, 4277 (1970).
4. E. Ya. Rode, G. V. Lysanova, and L. Z. Gokhman, Neorg. Mater. **7** (11), 2101 (1971).
5. P. Lacorre, F. Goutenoire, O. Bohnke, *et al.*, Nature **404**, 856 (2000).
6. F. Goutenoire, O. Isnard, R. Retoux, and P. Lacorre, Chem. Mater. **12**, 2575 (2000).
7. Z. S. Khadasheva, N. U. Venskovskiĭ, M. G. Safronenko, *et al.*, Neorg. Mater. **38** (11), 1381 (2002).
8. *Physics of the Solid State: Special Practical Course*, Ed. by B. A. Strukov (Mosk. Gos. Univ., Moscow, 1983) [in Russian].
9. V. K. Yanovskiĭ and V. I. Voronkova, Fiz. Tverd. Tela (Leningrad) **27**, 2183 (1985) [Sov. Phys. Solid State **27**, 1308 (1985)].

Translated by T. Safonova

Crystallography Reports, Vol. 50, No. 5, 2005, pp. 877–882. Translated from Kristallografiya, Vol. 50, No. 5, 2005, pp. 944–949.

CRYSTAL GROWTH

Growth of α-$NiSO_4 \cdot 6H_2O$ Crystals at High Rates

V. L. Manomenova, E. B. Rudneva, A. É. Voloshin, L. V. Soboleva, A. B. Vasil'ev, and B. V. Mchedlishvili

Shubnikov Institute of Crystallography, Russian Academy of Sciences, Leninskiĭ pr. 59, Moscow, 119333 Russia

e-mail: labsol@ns.crys.ras.ru

Received February 10, 2005

Abstract—The high-rate growth of nickel sulfate hexahydrate $NiSO_4 \cdot 6H_2O$ (α-NSH) crystals up to $120 \times 120 \times 65$ mm^3 in size is described for the first time. The data on the distribution of related impurities in the {011} and {001} growth sectors of α-NSH crystals grown at different rates are reported. The transmission spectra of both growth sectors of these crystals are obtained. The structural quality and the optical properties of rapidly and slowly grown α-NSH crystals are compared. It is established that the {011} growth sector of crystals grown at rates exceeding 5 mm/day shows the best characteristics for application in UV filters. © *2005 Pleiades Publishing, Inc.*

INTRODUCTION

Crystals of nickel sulfate hexahydrate $NiSO_4 \cdot 6H_2O$ (α-NSH) are widely used in optics. These crystals exhibit optical rotatory dispersion in the wavelength range 200–2500 nm [1] and circular dichroism in the visible spectral range [1, 2]. In addition, inversion of the sign of the rotatory power is observed in α-NSH at a wavelength of 503 μm [4]. Crystals of the α-NSH phase are one of the most effective band filters in the solar blind spectral range. Their effectiveness is related to their unusual bandlike absorption spectrum in the range 200–1200 nm, which contains only three transmission bands (peaked at 250, 490, and 880 nm). At the same time, the transmission in the UV region exceeds 80% [4].

The $NiSO_4 \cdot 6H_2O$ compound has two polymorphic modifications: α-NSH and β-NSH. Crystals of α-nickel sulfate hexahydrate $NiSO_4 \cdot 6H_2O$ have a saturated blue-green color. They belong to the tetragonal system with the sp. gr. $P4_12_12$ and unit-cell parameters $a = b =$ 6.780 Å and $c = 18.285$ Å [4]. Figure 1 shows the habit of α-NSH crystals.

Crystals of the β-NSH modification are bright green; they belong to the monoclinic system with the sp. gr. $C2/c$ and unit-cell parameters $a = 9.880$ Å, $b =$ 7.228 Å, $c = 24.130$ Å, $\beta = 9.88°$, and $Z = 8$ [4]. Crystals of the α-NSH phase decompose in air, losing water, even at room temperature [5].

Figure 2 shows three portions of the solubility curves corresponding to the solid phases $NiSO_4 \cdot 7H_2O$, α-$NiSO_4 \cdot 6H_2O$, and β-$NiSO_4 \cdot 6H_2O$ [5, 6]. The point X at a temperature of 31.5°C is the point of the $NiSO_4 \cdot 7H_2O \longleftrightarrow$ α-$NiSO_4 \cdot 6H_2O + H_2O_{liq}$ phase transition [7], and the point Y at 53.3°C is the point of the α-$NiSO_4 \cdot 6H_2O \longleftrightarrow NiSO_4 \cdot 6H_2O$ phase transition. The phase β-$NiSO_4 \cdot 6H_2O$ is stable at temperatures up to 118°C [5].

A number of studies are devoted to the growth of α-NSH crystals from aqueous solutions [4, 8, 9]. Both six-water nickel sulfate $NiSO_4 \cdot 6H_2O$ [4, 9] and seven-water nickel sulfate $NiSO_4 \cdot 7H_2O$ were used as initial raw material for crystal growth [8]. In [4, 9], crystals were grown from solutions of $NiSO_4 \cdot 6H_2O$ of stoichiometric composition. Crystals $65 \times 85 \times 74$ mm^3 in size were grown by the method of decreasing temperature.

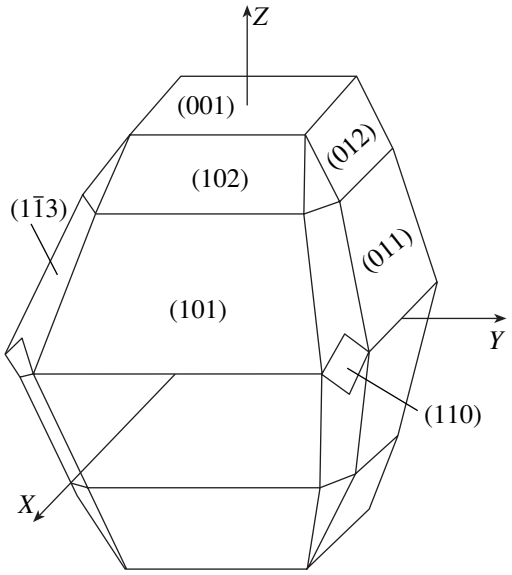

Fig. 1. Habit of an α-NSH crystal [4].

1063-7745/05/5005-0877$26.00 © 2005 Pleiades Publishing, Inc.

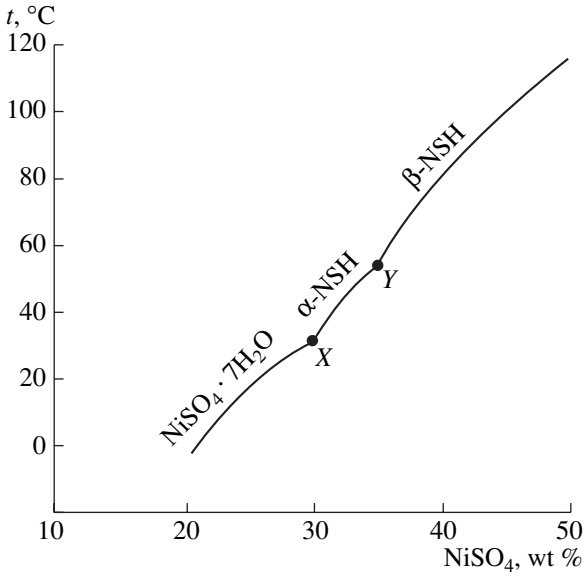

Fig. 2. Solubility of $NiSO_4$ hydrates in water [5].

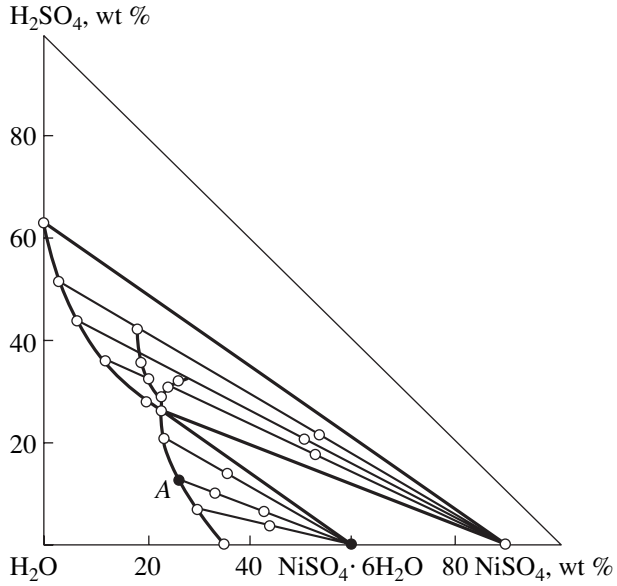

Fig. 3. Phase solubility diagram of the $NiSO_4$–H_2SO_4–H_2O system at 50°C [11].

In [8], on the basis of the analysis of the $NiSO_4$–H_2SO_4–H_2O system, the solution composition corresponding to the point *A* in Fig. 3 (in wt %: $NiSO_4$, 28.00; H_2SO_4, 13.00; H_2O, 59.00) was chosen for the crystal growth. It was shown previously [10] that, to grow crystals of complex compounds, it is reasonable to use mother liquors whose compositions (in wt %) lie on the solubility curve at the maximum distance from the points of invariant equilibria. The composition used in [8] was chosen according to this principle. Crystals up to $53 \times 48 \times 30$ mm^3 in size were grown by the method of decreasing temperature.

In the above-mentioned studies, the crystal growth was performed in the dynamic mode at temperatures from 53 to 32°C; the rate of decrease in temperature of the solutions did not exceed 1 K/day, and the growth rate of α-NSH crystals in the [001] direction was no more than 1 mm/day.

The purpose of this study is to develop a method of rapid growth of large α-NSH single crystals of good optical quality and investigate the transmission spectra, the content of related impurities, and the actual defect structure of the crystals grown.

EXPERIMENTAL

To grow α-NSH crystals, we used hermetically sealed crystallizers with volumes from 1 to 5 l equipped with an automatic cooling system. The temperature in the growth crystallizers was controlled by microcontrollers, which provided an accuracy of maintaining temperature of ±0.02 K. Solutions prepared from seven-water nickel sulfate $NiSO_4 \cdot 7H_2O$ of reagent grade, sulfuric acid H_2SO_4 of high purity grade, and triply distilled H_2O (taken in different ratios) were used as mother liquors. The saturation temperature of the solutions was 48–50°C. Immediately before filtration, the solutions were superheated by 10–15 K above the saturation temperature.

Crystals were grown from aqueous solutions by cooling. The seed crystals (plates in the (001) cut, $8.0 \times 8.0 \times 1.5$ mm^3 in size, cleaved in the (001) cleavage plane) were installed either on immobile platforms (in this case, solutions were stirred by agitators) or on rotating platforms. Stirring of solutions was reversible; the stirring rate ranged from 30 to 60 rpm.

The concentrations of impurities in α-NSH crystals were analyzed by spark mass spectrometry on a JMS-01-BM2 double-focusing mass spectrometer (JEOL, Japan). The mass spectra were recorded on UV-4 photographic plates.

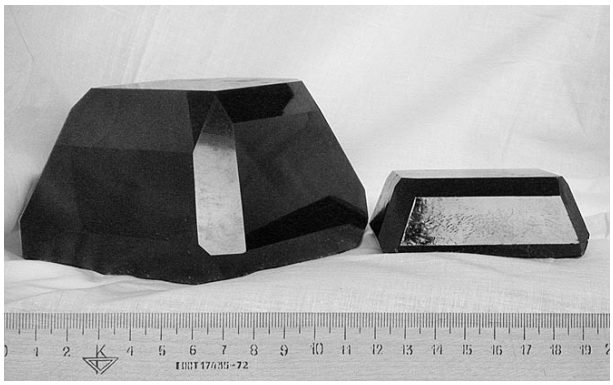

Fig. 4. Rapidly grown α-NSH crystals.

Table 1. Growth parameters for α-NSH crystals grown in different temperature regimes

Crystal	Saturation temperature of solution, °C	Rate of solution stirring, rpm	Average cooling rate, K/d	$R_{[001]}$, mm/d	Growth duration, d	Crystal mass, g	Crystal sizes $x \times y \times z$, mm^3
1	50.5	50	0.6	1.3	27	185	$65 \times 51 \times 35$
2	49.5	60	5	5.5	4	125	$52 \times 52 \times 22$
3	49.0	60	5.5	7	4	190	$63 \times 60 \times 28$

To measure the transmission spectra of the samples studied, we used a SPECORD UV VIS automatic double-beam spectrophotometer, which makes it possible to measure transmission spectra in the range from 185 to 800 nm.

The structure of the crystals grown was analyzed by Lang X-ray topography in Mo$K_{\alpha 1}$ radiation using P-50 photographic plates intended for nuclear study.

RESULTS AND DISCUSSION

Figure 3 shows the 50°C isotherm for the ternary system $NiSO_4$–H_2SO_4–H_2O [12]. Initially, α-NSH crystals were grown from solutions of the same composition as in [8] (in wt %): $NiSO_4$, 28.00; H_2SO_4, 13.00; and H_2O, 59.00 (Fig. 3, point *A* on the solubility isotherm).

However, when attempts were made to increase the rate of growth of α-NSH crystals from the noted solutions by increasing the solution supercooling from 0.3 to 1.6 K (which corresponds to the change in the supersaturation from 0.4 to 1.9%), the crystals grown contained microcracks and inclusions of mother liquor. The supersaturation was calculated by the formula

$$\sigma = \frac{c_r(T) - c_0(T)}{c_0(T)},$$

where $c_0(T)$ and $c_r(T)$ are, respectively, the equilibrium and real concentrations of a solution in molar fractions at temperature *T*.

With a further increase in supersaturation, spontaneous crystallization from solution occurs.

In this context, we carried out a series of experiments aimed at determining the solution composition applicable for rapid growth of α-NSH crystals. As a result, a solution composition was determined that made it possible to reach the supersaturation σ = 4–5.5% without intense nucleation. A series of α-NSH crystals up to $120 \times 120 \times 65$ mm^3 in size (Fig. 4) were grown from solutions of this composition in different temperature regimes. The average cooling rates during rapid growth and slow growth were 5–7 and 0.5–1.5 K/day, respectively. The normal growth rate of faces *R* in the direction [001], $R_{[001]}$, was 5–7 and 1–1.5 mm/day during rapid and slow growth, respectively. Table 1 contains the growth parameters for three crystals grown in 1-l crystallization vessels.

We compared the structural quality and optical properties of rapidly and slowly grown crystals. From the point of view of application of the crystals under study as filters in the mid-UV range, they should have maximum transmission in this wavelength range and minimum transmission in the visible spectral range. To compare the efficiency of UV transmission of different growth sectors of α-NSH crystals, we measured the optical transmission spectra of samples cut from the {011} and {001} growth sectors of the crystals grown at different rates (Fig. 5). (These sectors occupy the major part of a crystal.) All samples were 5-mm-thick plates cleaved in the (001) cleavage plane.

It was found that the {011} growth sector of rapidly grown crystals has the best optical characteristics: its transmittance *T* is 85–86% at λ = 200–370 nm (short-range UV) and relatively low in the visible range. The UV transmittance of the {001} sector of rapidly grown crystals is comparable in magnitude with that of the {011} and {001} growth sectors of slowly grown crystals (*T* ~ 75–77%). In the visible spectral range, the

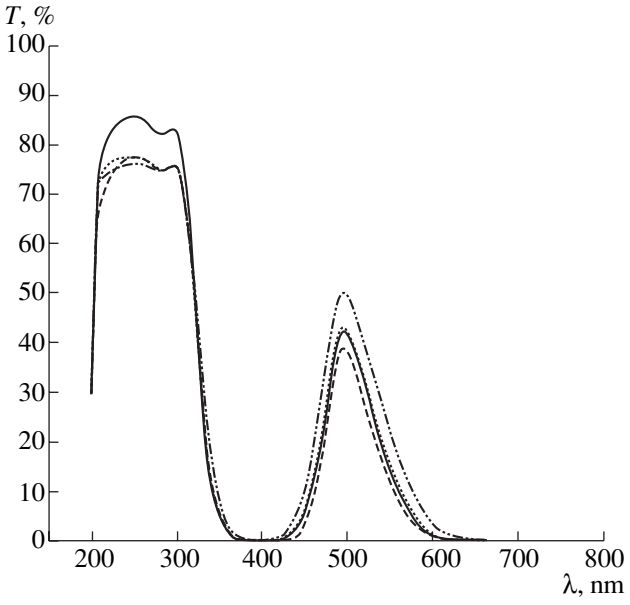

Fig. 5. Spectral characteristics of the {011} and {001} growth sectors of α-NSH crystals grown at different rates: the {001} sector of rapidly (dashed line) and slowly (dash–dotted line) grown crystals and the {011} sector of rapidly (solid line) and slowly (dotted line) grown crystals.

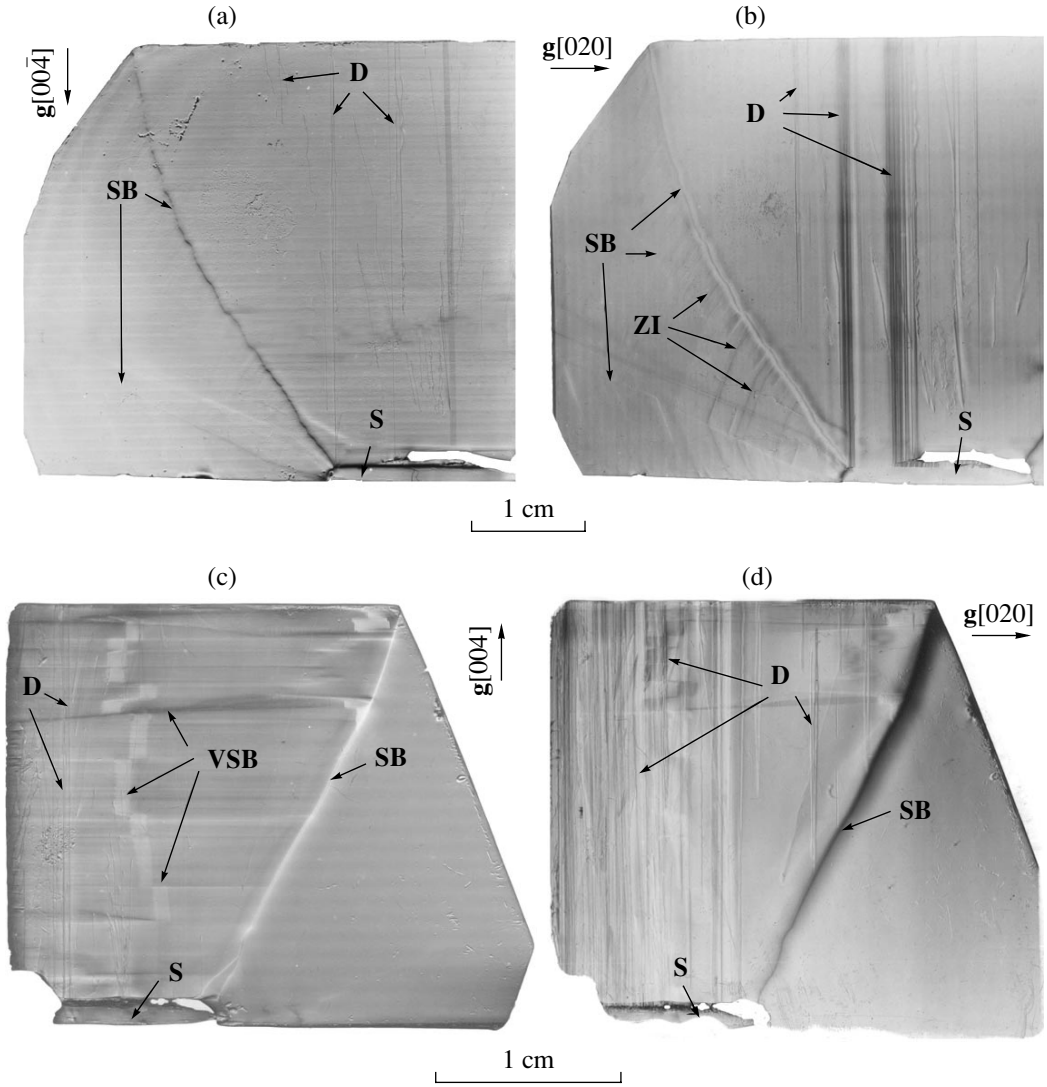

Fig. 6. The X-ray projection topographs of (100) cuts of (a, b) slowly and (c, d) rapidly grown α-NSH crystals. Designations: (S) seed, (SB) sectorial boundaries, (D) dislocations, (ZI) zonal inhomogeneities, (VSB) vicinal sectorial boundary; **g** is the diffraction vector.

transmittances of both growth sectors of slowly grown crystals exceed that of the rapidly grown crystals.

One of possible factors affecting the optical characteristics of crystals is the presence of unintentional impurities. Therefore, we analyzed their content in the crystals grown. The concentrations of most studied impurities, such as Be, Na, P, Sc, Ti, V, Cr, Mn, Ga, Ge, As, Se, Br, Rb, Sr, Y, Zr, Nb, Mo, Ru, Rh, Pd, Ag, Cd, In, Sn, Sb, Te, Cs, Ba, Hf, W, Re, Os, Ir, Pt, Au, Hg, Tl, Pb, Bi, Th, U, and all lanthanides, were below the detection limit ($<1 \times 10^{-4}$ wt %). Table 2 contains the data on the distribution of impurities whose concentration exceeds 1×10^{-4} wt %. Mass-spectrometric analysis shows that the major impurities in the crystals under study are Zn, Co, Cu, I, F, and Cl ($>1 \times 10^{-3}$ wt %). Impurities of Mg, Ca, Fe, Al, Si, and B are present in smaller amounts. The high content of Zn, Co, Cu, Fe, and Mg may be related to the large values of the distribution coefficients of these impurities, which are very likely to exceed unity.

The impurity distributions in α-NSH crystals grown at different rates are different. The data of Table 2 indicate that the maximum content of Zn, Co, Cu, Al, Mg, I, and B is found in rapidly grown crystals; note that in the {001} growth sector the concentrations of Zn, Cu, Al, and B are several times higher than in the {011} sector. For Mg and Co impurities, the situation is directly opposite: their concentrations in the {001} growth sector of the rapidly grown crystals are lower by a factor of 1.5–2.

In slowly grown crystals, the content of related impurities is the same in both growth sectors. Higher concentrations of the halogens Cl and F are observed in

Table 2. Distribution of impurities in α-NSH crystals grown by different methods

Element	Concentration, $\times 10^4$ wt %		
	rapidly grown α-NSH		slowly grown α-NSH
	{011} sector	{001} sector	{001} and {011} sectors
Li	<0.01	<0.01	0.08
B	0.4	1	0.05
Be	<0.005	<0.005	<0.005
F	20	20	30
Mg	10	6	3
Al	0.2	1	<0.07
Si	6	6	3
Cl	7	10	30
K	<0.1	<0.1	3
Ca	0.9	1	0.6
Fe	1	1	1
Co	50	20	10
Cu	10	20	<0.1
Zn	1000	2000	8
I	90	100	3

these crystals in comparison with the rapidly grown ones.

Such a complex redistribution of unintentional impurities in the growth sectors of α-NSH crystals grown at different rates makes it impossible to draw unambiguous conclusions about the effect of specific impurities on the transmission spectra of these crystals.

It is well known that the optical properties of crystals are also significantly affected by their internal defect structure. To compare the quality of rapidly and slowly grown α-NSH crystals, we obtained a series of X-ray projection topographs. The topographs in Fig. 6 demonstrate the typical structure of crystals grown at different rates.

The {011} growth sector of a slowly grown crystal contains distinct stripes of zonal inhomogeneity (Fig. 6b), which may be responsible for the decrease in the transmission of this sector in the visible spectral range in comparison with the {001} sector. A large number of growth dislocations directed from the seed region perpendicular to the (001) face are observed in the {001} growth sector of a slowly grown crystal (Fig. 6b). The presence of one vicinal–sectorial boundary in this sector suggests the presence of only one growth hillock on the surface of the (001) face and, on the whole, is indicative of rather high homogeneity of this sector. Sectorial boundaries, dividing different growth sectors, can be seen in both topographs.

Figures 6c and 6d show the defect structure of the rapidly grown crystals. The image of the sectorial boundary between the {011} and {001} growth sectors has a brighter contrast. On the basis of the change in the contrast at the sectorial boundaries, we may conclude that the lattice parameters in the {011} growth sector are smaller than in the {001} sector. In the {011} sector, there are no growth defects for both reflection vectors. In the {001} sector of a rapidly grown crystal, the concentration of growth dislocations is much higher than in the same sector of a crystal grown at a lower rate. The broken line, corresponding to the vicinal sectorial boundaries, indicates the presence of competing growth hillocks. Under these conditions, the formation of inclusions of the solution [12], which lead to higher scattering of radiation, is very likely. We believe this mechanism to be the most likely reason for the decrease in the transmission of the samples cut from the {001} growth sector. Analysis of the topographs showed that the {011} growth sector of the rapidly grown crystal is more uniform (also compared to the sectors of the slowly grown crystal). This circumstance is, in turn, in good agreement with the obtained maximum values of the transmittance of the {011} sector of the rapidly grown crystals.

CONCLUSIONS

Transparent α-NSH single crystals up to $120 \times 120 \times 65$ mm^3 in size were grown at high rates. (The normal growth rate is up to 7 mm/day.) The transmission spectra of the {011} and {001} growth sectors of crystals grown at different rates were measured. It is shown that the {011} sector in the crystals grown at rates above 5 mm/day has the best characteristics to be used in UV filters. This conclusion is in agreement with the results of the analysis of X-ray projection topographs, which showed a high degree of structural quality of this sector of rapidly grown crystals. A difference in trapping of impurities by {001} and {011} faces during rapid growth is revealed.

ACKNOWLEDGMENTS

This study was supported by the president of the Russian Federation (the program "Leading Scientific Schools," project no. NSh-1954.2003.2).

REFERENCES

1. Ya. O. Dovgiĭ and I. G. Man'kovskaya, Fiz. Tverd. Tela (St. Petersburg) **40** (9), 1608 (1998) [Phys. Solid State **40**, 1460 (1998)].
2. J. R. L. Moxon, A. R. Renshaw, and I. J. Tebbutt, J. Phys. D: Appl. Phys. **24**, 1187 (1991).
3. K. Stadnicka, A. M. Glazer, and M. Koralewski, Acta Crystallogr., Sect. B: Struct. Sci. **43**, 319 (1987).
4. H. Youping, S. Genbo, Y. Xianchum, *et al.*, J. Cryst. Growth **169**, 193 (1996).

5. J. W. Mellor, *A Comprehensive Treatise on Inorganic and Theoretic Chemistry* (Longmans. Green and Co, London; New York; Toronto, 1936), Vol. 15, p. 454.
6. V. B. Kogan, V. M. Fridman, and V. V. Kafarov, *Handbook on Solubility* (Akad. Nauk SSSR, Leningrad, 1961), Vol. 1, p. 358 [in Russian].
7. A. A. Sidel'nikov, A. P. Chupakhin, N. Z. Lyakhov, and V. V. Boldyrev, Dokl. Akad. Nauk SSSR **258** (1), 158 (1981).
8. L. V. Soboleva, E. B. Rudneva, and I. L. Smol'skiĭ, Kristallografiya **43** (4), 756 (1998) [Crystallogr. Rep. **43**, 706 (1998)].
9. S. Genbo, H. Youping, and L. Zhengdong, J. Cryst. Growth **213**, 99 (2000).
10. L. V. Soboleva, Neorg. Mater. **31** (5), 614 (1995).
11. A. W. Babajewa and E. I. Daniluschkina, Z. Anorg. Allg. Chem. **226**, 338 (1938).
12. N. Zaitseva and L. Carman, Prog. Cryst. Growth Charact. Mater. **43**, 1 (2001).

Translated by Yu. Sin'kov

Crystallography Reports, Vol. 50, No. 5, 2005, pp. 883–889. Translated from Kristallografiya, Vol. 50, No. 5, 2005, pp. 950–957.

CRYSTAL GROWTH

Low-Temperature Growth and Doping of InP : S Single Crystals from Melt–Solution in Microgravity

A. V. Kartavykh

Institute of Chemical Problems for Microelectronics,
Bol'shoi Tolmachevskiĭ per. 5, Moscow, 119017 Russia
e-mail: icpm@girmet.ru

Received March 23, 2004

Abstract—The effect of microgravity on the growth of bulk InP:S single crystals from a melt with an initial equilibrium composition (84 at % In, 16 at % P, and ~2.2×10^{18} at cm^{-3} of S) on board the *Foton-11* satellite was investigated. The growth of crystals on board the satellite and on Earth (a reference crystal) was carried out by the traveling heater method. The samples of the grown crystals were investigated by metallography, double-crystal X-ray diffractometry, single- and double-crystal X-ray topography, and secondary-ion mass spectrometry. It is shown that the mass transfer in the melt in microgravity is similar to the diffusion mode. Hence, the mass transfer in the melt results in the following: the formation of a nonstationary boundary layer, depleted in phosphorus; the constitutional supercooling at the crystallization front accompanied with the development of a cellular substructure in the early growth stage; and the hypothetical phase structurization of the transition layer with the formation of In-based associates (clusters), which were found in the grown crystals in the form of spherical defects 10–20 μm in diameter. The coefficients of sulfur distribution $k_0 = 0.274$ and $k_{eff} = 0.43$, the sulfur diffusivity in the melt $D_S = 4.2 \times 10^{-7}$ cm^2/s, and the effective thickness of the transition layer $\delta = 0.07$ cm in terrestrial gravity are determined. The data obtained are necessary to develop a mathematical model of crystallization in zero gravity. © *2005 Pleiades Publishing, Inc.*

INTRODUCTION

The growth of active layers of III–V compounds from nonstoichiometric melt solutions based on the intrinsic low-melting metal component III (III ≡ In, Ga) is successfully used to produce semiconductor devices and optoelectronic structures. Not long ago the principles of liquid-phase homoepitaxy were used to grow bulk single crystals suitable for preparation of high-quality substrates for ion implantation [1]. The potentialities of the traveling heater method (THM) developed for this purpose have a fundamental thermodynamic character and are primarily associated with the relatively low crystallization temperature [1, 2].

At the same time, in comparison with the processes of crystal growth from stoichiometric melts, the crystallization from melt–solution is more difficult and less stable from the point of view of controlling and monitoring. The large slope of the liquidus curves in the temperature–composition phase diagrams indicates the strong dependence of the equilibrium crystallization temperature on the concentration of the component V in the melt. For example, the slope of the liquidus curve dT/dC in the In–InP phase diagram reaches 25–30 K/at % [3]. The component V is crystal-forming, but its concentration in the liquid phase is relatively small (generally ~10–25 at %). During the crystal growth, this component behaves as an impurity with a distribution coefficient $k > 1$, forming a depleted transition layer of melt–solution with a lowered equilibrium crystallization temperature near the phase boundary. Thus, the actual growth kinetics, the structural perfection, and the compositional inhomogeneity of the crystals grown are determined in many respects by the presence of a transition (boundary) layer, the stability of its thickness, the degree of its structural order, and its phase composition.

Since the thickness of the boundary layer and the concentration profile in it are determined in many respects by the intensity of diffusion and/or the convective transport in the bulk of the liquid phase, the processes of crystallization of III–V compounds from melt–solution are extremely sensitive to gravity [4–6]. Along with the dopant inhomogeneity (when a doped melt is used), this sensitivity manifests itself also in the structural perfection of crystals. Therefore, such systems can serve as promising model objects for study of the fundamental regularities of the crystal growth in microgravity (μg) [7–10].

In this paper, we report the results of the investigation of the low-temperature (1143 K) crystallization and doping of InP with sulfur from the liquid phase (In–InP–S melt–solution) carried out on the board of the *Foton-11* satellite. The possibilities of active in situ of the crystallization process on board the satellite are extremely limited. Therefore, the main experimental approach to the solution of the above-stated problem can be the complex investigation of the single crystal samples in order to extract information on the mechanisms of crystallization and the hydrodynamical pro-

1063-7745/05/5005-0883$26.00

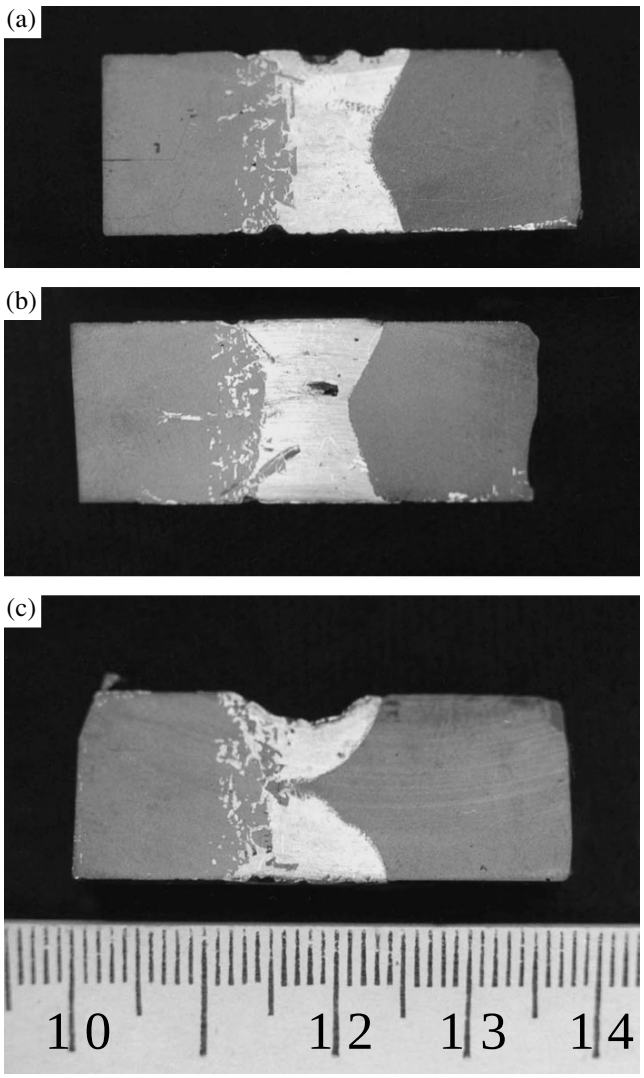

Fig. 1. (a, b) InP samples 1 and 2, respectively, grown in orbit in the Zona-4 growth facility and (c) the terrestrial InP sample 3.

cesses in the liquid phase, which accompany the crystal growth. Particular attention was given to the detection of objective differences between the terrestrial and space samples from the point of view of the uniformity of sulfur distribution and the crystallographic perfection.

EXPERIMENTAL GROWTH CONDITIONS

The objects of study were two InP single crystals grown by the THM in microgravity (samples 1 and 2) and the reference crystal 3 grown horizontally under the same external thermal conditions on Earth. All crystals were obtained using the Zona-4 spaceborn growth facility [11]. The samples processed are shown in Figs. 1a–1c. Each of them is a longitudinal, oriented in the (110) plane, axial cut of the solidified crystallized compound extracted from a hermetic cylindrical quartz cell with an inner diameter of 15 mm. The crystals were doped with sulfur during the growth. An InP:S single crystal (the feed) dissolving in indium melt served as a feed of phosphorus and sulfur. For all samples, a seed with an epitaxial layer (the grown crystal) is on the left and the feed crystal is on the right. In the central part, the region of the indium melt–solution with a metallic luster is pronounced. When ampoules were assembled, a cylinder 8 mm long made of 99.9999% pure indium was placed between the seed and feed crystals. Both these crystals were prepared from InP single crystals grown by the Czochralski method. To unify the boundary conditions and simplify subsequent numerical simulation, all seeds and initial feed crystals were doped with sulfur to the same level: 6.5×10^{18} cm^{-3}.

During the crystallization, the liquid zone moved from the seed to the source (from left to right in Fig. 1), solving the latter. The orientation of the growth plane during the crystallization on the seed was $(111)B \pm 0.2°$ in all cases. As can be seen, the geometry and the thermophysical conditions of the THM are analogous to the conventional floating-zone crystallization in a cell and the physicochemical mechanism of crystallization is similar to the liquid-phase homoepitaxy of very thick layers from a semi-infinite melt–solution with continuous feeding.

The experimental growth conditions were chosen so as to support the melt–crystal system in the state of stationary crystallization with minimum external perturbations. These conditions were facilitated by the low growth rate; small axial temperature gradients (5–10 K/cm); and a low residual gravity (about (3–6) $\times$ 10^{-6} of Earth's gravity [12]), which sharply decreased the intensity of convective flows in the melt on board the satellite. The cyclograms (temperature–time dependences) of the crystallization processes, strictly supported by the programmable unit of Zona furnace, were identical. They can be described as follows:

(i) two-step heating of the indium zone to 1090 K for 1 h and then to the specified crystallization temperature 1143 ± 0.5 K at a rate of 100 K/h;

(ii) isothermal exposure, initial source dissolution, and melt homogenization, all of which occurred over 1 h;

(iii) growth of a crystal (epitaxial layer) during the cell motion through the heater zone with a minimal possible instrumental rate of 0.15 mm/h for 50 h;

(iv) controlled heater cooling to 1040 K at a rate of 100 K/h; and

(v) switching off the heater supply and fast uncontrolled cooling.

Thus, the main difference in the experiments was the difference in the mechanisms of heat and mass transfer in the melt–solution: natural convection is present during the horizontal floating-zone growth under the terrestrial conditions (sample 3), while for the samples 1 and 2, which were grown on board the satellite, the gravitational convection was significantly

reduced and the mass transfer was presumably determined by the prevailing diffusion processes.

The In–InP phase diagram shows that the thermodynamically equilibrium melt–solution contains 84 at % In and 16 at % P (68 at % pure In and 32 at % InP) at the growth temperature [3].

METHODS FOR STUDYING THE GROWN CRYSTALS

To carry out further investigations, each sample was cut in the indium zone, as a result of which the source crystal was separated from the seed part with the grown layer. Furthermore, only the seed parts were treated and analyzed. Residual indium was removed by etching in HNO_3. The crystals were characterized using the following techniques: optical microscopy combined with selective chemical etching; analysis of the rocking curves; single- and double-crystal X-ray topography; and measurement of the sulfur distribution by secondary-ion mass spectrometry (SIMS).

Analysis of the morphology of projection-etch patterns and their microphotographing in polarized light was performed by a Polyvar optical microscope. The metallographic examination of the samples was performed in order to determine the thicknesses of the grown epitaxial layers (crystals) and the sizes of the regions that are of interest for subsequent X-ray and mass spectrometric characterization.

Double-crystal rocking curves were measured on a UARPP-80 X-ray diffractometer in the dispersion mode (*n*; *m*) using Mo$K_{\alpha 1}$ radiation with the wavelength $\lambda = 0.07093$ nm. A perfect Ge(110) crystal was used as a monochromator. The rocking curves were measured for the (440) reflection with a step of 1.5 mm (the distance between the neighboring irradiation spots) along the growth axis.

Single-crystal X-ray topography was carried out using Cu$K_{\alpha 1}$ radiation with $\lambda = 0.15406$ nm. The topographs have negative contrast (defects are brighter). Shaped macroscopic inclusions of the In second phase, which yield no reflections, are dark. The kinematic contrast in the single-crystal mode is formed by structural defects, such as dislocations or In-based microprecipitates, which form elastic stress fields approximately several micrometers in size in the matrix.

Double-crystal X-ray topography was performed for the asymmetric (511) reflection using a perfect Ge(111) crystal as a monochromator and Cu$K_{\alpha 1}$ radiation with $\lambda = 0.15406$ nm. In the double-crystal mode, nonuniform contrast corresponds to areas with different diffraction conditions (different orientations or interplanar spacings). Topographs can also demonstrate extensive matrix areas differing in the magnitude and/or direction of the vector of prevailing elastic stresses.

The axial distribution of sulfur in the samples was determined by SIMS on a PHI-6600 Perkin Elmer spectrometer with a step of 200 μm. A beam of Cs^+ ions was used as a primary one. The size of a single crater formed by ion etching was 1500×50 μm^2. To increase the relative measurement accuracy, the amplitude of the S signal was normalized to the amplitude of the P signal (used as a reference).

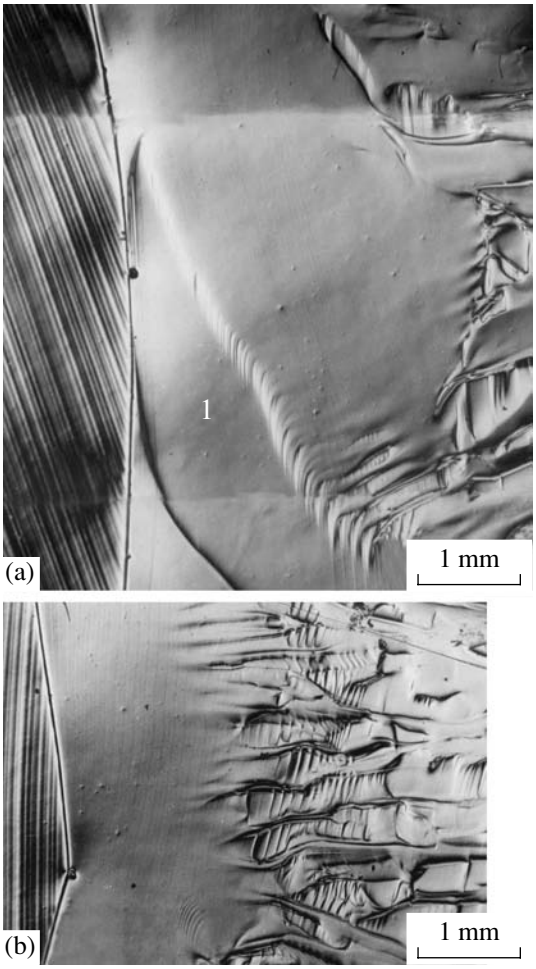

Fig. 2. Central fragments of the panoramic photographs of the epitaxial layers (crystals) after treatment of the samples in the Abrahams–Buiocchi projection etchant (H_2O : CrO_3 : HF = 1 : 1 : 1): (a) sample 3 (1 is the dopant channel occurring owing to the facet effect) and (b) sample 1 (seeds are on the left).

RESULTS AND DISCUSSION

The criterion for choosing the growth rate *f* was the estimate of its maximum allowable (critical) value in the absence of constitutional supercooling at the crystallization front. According to the data of [13], the following approximate estimate can be used:

$$f_{cr} \approx \frac{D_0 \operatorname{grad} T \Delta H (D_p/D_0)}{R(K_0 - 1)T^2}, \quad (1)$$

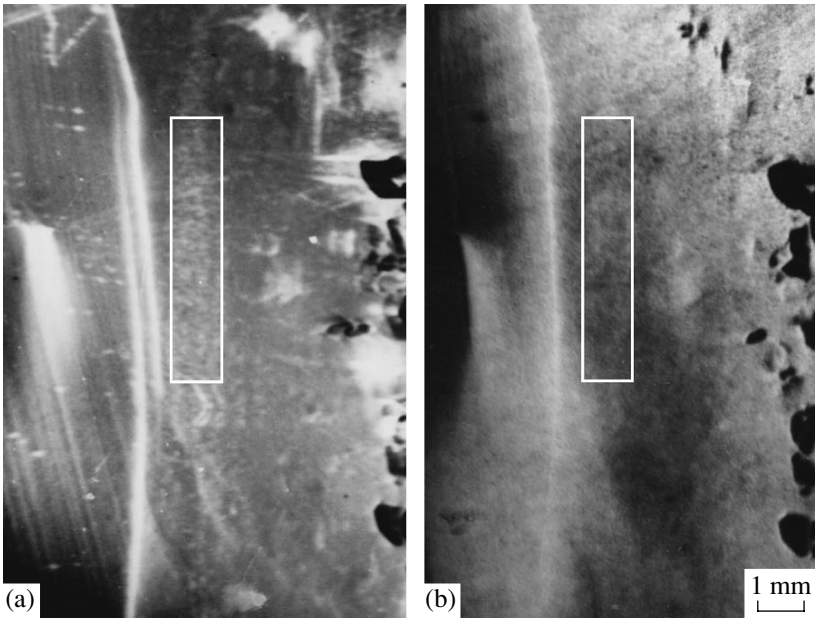

Fig. 3. X-ray topographs of the terrestrial sample 3 measured in the (a) single-crystal and (b) double-crystal modes. The areas of correspondence of the (a) negative and (b) positive contrast, related to the presence of intrinsic microdefects and changes in the lattice constant, respectively, are framed.

where D_0 and D_p are, respectively, the diffusivities of indium and phosphorus in a melt; R is the gas constant; $K_0 \sim 50/16 = 3.1$ is the ratio of the atomic fractions of phosphorus in the solid and liquid phases; ΔH is the enthalpy of phosphorus mixing in the indium melt; the temperature gradient grad $T \sim 10$ K/cm at the crystallization front; and $T = 1143$ K is the equilibrium temperature of the melt solidification. Using the reference data on D_0, D_p, and ΔH [3], we find that $f_{cr} \simeq 0.25$–0.30 mm/h for the stationary diffusion-controlled growth. Similar values were obtained experimentally in [14] on an analogous growth system using the technique of local growth markers.

According to preliminary estimates, the thickness of the grown single-crystal layer in the samples at $f = 0.15$ mm/h should be about 7.5 mm. However, the portion of the grown layer with relatively high structural perfection turned out to be much thinner (Fig. 2). On the left, one can clearly see the metallurgical boundary of the initial crystallization seeding front, which is convex towards the melt–solution. Growth (doping) striations are observed in the seed part. The thickness of the perfect portion of the grown single-crystal layer can be easily estimated: it is ~4 mm in the terrestrial sample (Fig. 2a) and 2–2.5 mm in the μg samples (Fig. 2b). The subsequent morphological instability of the smooth crystallization front leads to the nucleation and development of a cellular substructure. This substructure has a classical form in the μg samples and is indicative of significant constitutional supercooling of the melt–solution as a result of the misbalance of the growth rate and the rate of effective liquid-phase diffusion of phosphorus under the thermal conditions applied. The constitutional supercooling indicates the existence of a boundary layer in the melt, which is depleted in phosphorus and is more pronounced in the μg samples. Further development of the cellular substructure leads to the break of the single-crystal growth. The final portion of the grown layer in the samples has a porous polycrystalline structure with macroscopic second-phase grains based on the solvent (In) captured from the solution. Polycrystalline portions with metallic inclusions can be clearly seen in the longitudinal cuts of all crystallizing systems (to the left of the indium zone in Figs. 1a–1c).

Deterioration of the structural quality of the layers with further growth is confirmed by rocking-curve analysis. The smallest half-widths of the rocking curves (5.3″–7.4″) are observed for single-crystalline seeds. The half-widths obtained for the epitaxial layers in the μg and terrestrial samples are 18″–24″ and 15″–17″, respectively. In the final growth stage, the broadening of the rocking curves rapidly increases with growth time. Thus, there is a significant inhomogeneity in the lattice parameter, which is observed even in the most perfect regions of the layers grown during the first 5–10 h.

Analysis of the X-ray topographs supplements the above data. The topographs obtained in the single-crystal mode demonstrate areas with negative contrast in the form of fairly uniformly distributed bulky clouds. Such areas manifest themselves near the seeding front in the terrestrial sample (Fig. 3a) and, with the largest contrast, in the μg samples (Figs. 4a, 5a). In the double-crystal topographs, they correlate with the positive-

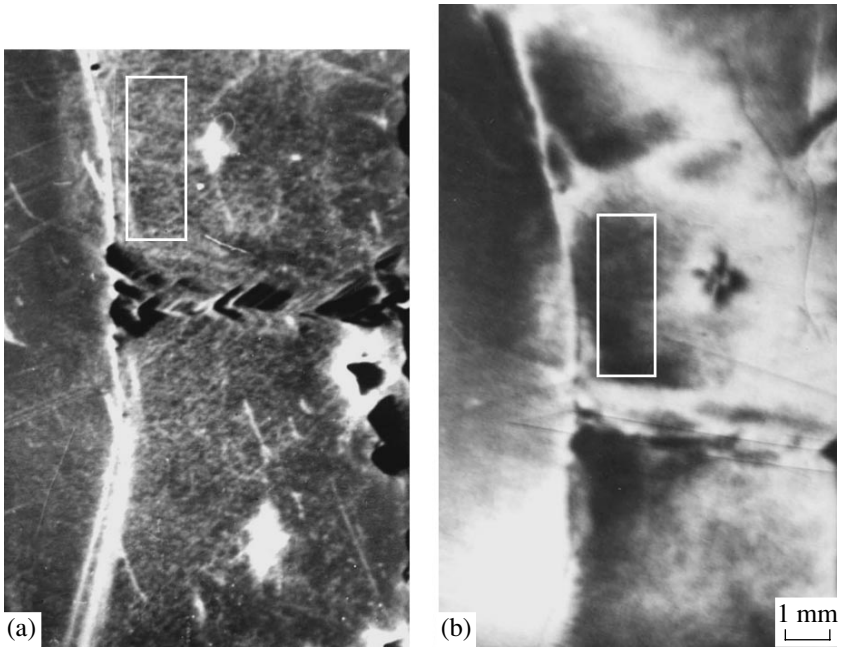

Fig. 4. X-ray topographs of the μg sample 2 measured in the (a) single-crystal and (b) double-crystal modes. The areas of correspondence of the (a) negative and (b) positive contrast, related to the presence of intrinsic microdefects and changes in the lattice constant, respectively, are framed.

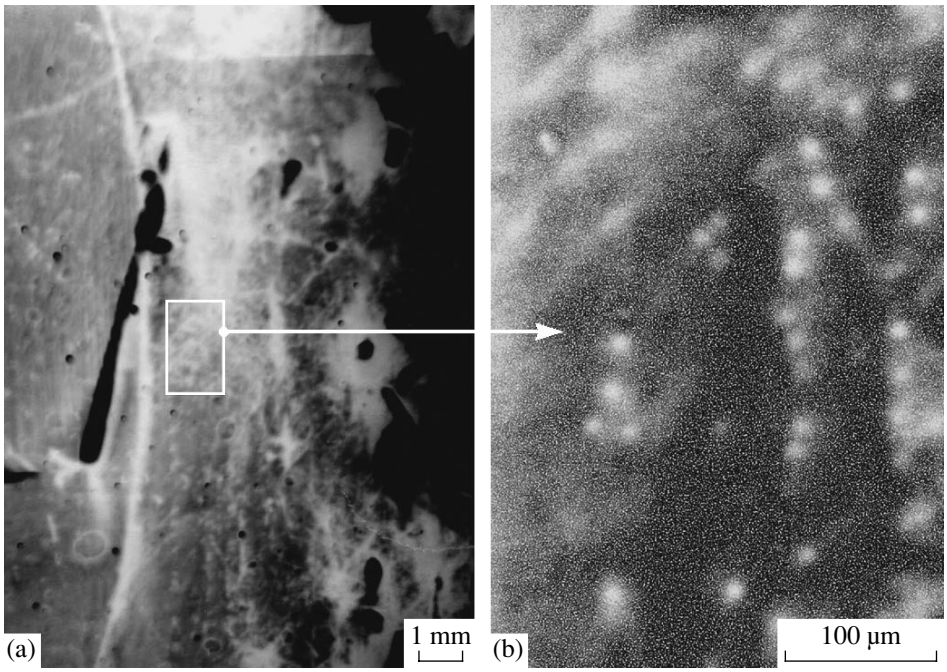

Fig. 5. X-ray topographs of sample 1 measured in the single-crystal mode: (a) general view (the dark crack in the seed was formed at the sample removing from the cell) and (b) "giant" spherical In microdefects revealed near the seeding front.

contrast areas (framed in Figs. 3b, 4b), where the lattice constant differs from that of the matrix. Using ultimate magnification, we managed to resolve the fine structure of such a defect area in sample 1. Along with the fine-grain background, observed also in the terrestrial sample 3, very large (~10–20 μm) microdefects of spherical shape with a density of $\sim 4 \times 10^4$ cm^{-2} in the layer cut were found in the μg sample (Fig. 5b). Similar microdefect structures were found in GaSb single crystals grown in orbit, which were heavily doped with Te [15].

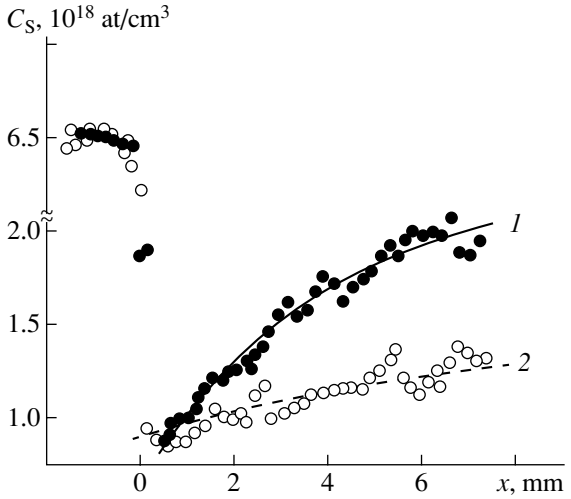

Fig. 6. Axial profiles of sulfur distribution in the epitaxial crystals: (*1*) the distribution in the μg sample 1 and its interpolation by the Tiller diffusion curve and (*2*) the distribution in the terrestrial sample 3 and its interpolation by the Pfann curve.

The similar genesis suggests that we are dealing with specific cluster associates, formed in the stagnant zone of the melt (solution) in the vicinity of the crystallization front under the conditions of strong supersaturation with respect to one of the components (dopants). As can be seen in Fig. 5b, defects tend to form vertical "chains" parallel to the crystallization front; i.e., they are concentrated mainly within the (111) plane. This feature may be in favor of the cluster mechanism of the formation of defects and their incorporation into the crystal lattice immediately during the crystal/melt interface motion. Another possible mechanism of the formation of associates is the decomposition of a supersaturated solid solution and the solid-state diffusion of In atoms to nucleation centers in the absence of effective sinks [16]. However, in this case, a radial depletion region (dark halo) should be observed around each defect serving as a sink, which is inconsistent (Fig. 5b).

Quantitative estimates, which are valuable for subsequent numerical simulation, can be obtained using the axial sulfur concentration (C_S) profiles as additional indicators (tracers) of the mass transfer intensity in the regions of the melt located near the crystallization front. According to the SIMS data, the integral distributions of sulfur within the layers grown on-ground and in the absence of gravity are indeed different. The doping profile in the μg sample 1 (Fig. 6, curve *1*) is adequately described by the pure diffusion Tiller distribution [17]

$$C_S(x) = C_0[1 - (1 - k_0)\exp(-\beta x)], \qquad (2)$$

where $\beta = \dfrac{k_0(f/D_S)}{1 - \exp(-fL/D_S)}$ and L is the thickness of the crystallized layer. The initial sulfur concentration in the liquid zone C_0 can be estimated as 2.2×10^{18} cm^{-3} on the basis of the seed/source doping level and the ratio of the volumes of the initial indium load and the stationary melt–solution zone (Fig. 1). The interpolation parameters for the Tiller curve show the best correlation with the values of the equilibrium coefficient of sulfur distribution $k_0 = 0.274$ and the sulfur diffusivity in the liquid phase $D_S = 4.2 \times 10^{-7}$ cm^2/s, an observation which is in agreement with the data in the literature that were obtained by processing the data obtained in similar experiments in orbit: $k_0 = 0.26 \pm 0.04$ and $D_S = (5 \pm 2) \times 10^{-7}$ cm^2/s [6, 8, 18]. The possibility of interpolating the experimental datapoints by diffusion curve suggests that the effect of residual gravitational convection on board the *Foton-11* satellite on the processes of crystallization and doping was indeed negligible. The profile of C_S in the terrestrial sample 3 (Fig. 6, curve *2*) corresponds to the case of partial convective melt stirring according to the classical Pfann theory for the floating-zone method [19]:

$$C_S(x) = C_0[1 - (1 - k_{eff})\exp(-k_{eff}x/l)], \qquad (3)$$

where l is the length of the molten zone. Interpolation of the experimental curve by formula (3) makes it possible to determine the effective coefficient of sulfur distribution at terrestrial crystallization: $k_{eff} = 0.43$ (beyond the dopant channel). Thus, it is easy to estimate the thickness δ of the boundary (transition) layer, enriched in the dopant, within the Burton–Prim–Slichter theory [20]:

$$\delta = -\frac{D_S}{l}\ln\left[\frac{k_0(1 - k_{eff})}{k_{eff}(1 - k_0)}\right] \approx 0.07 \text{ cm}. \qquad (4)$$

CONCLUSIONS

The fundamental regularities of the effect of microgravity on the crystallization and doping of InP:S single crystals from a nonstoichiometric melt–solution are investigated. It is shown that the mode of mass transfer in the melt on board the *Foton-11* satellite is close to the diffusion mode. The following conclusions can be drawn: (i) a boundary layer depleted in phosphorus is formed; (ii) constitutional supercooling occurs at the crystallization front, which leads to the morphological instability of the smooth phase boundary and early development of a cellular substructure in the grown crystal; and (iii) hypothetical phase structurization of the transition layer occurs with the formation of ordered In-based associates (clusters), observed as spherical defects 10–20 μm in diameter. The following parameters are determined: the sulfur distribution coefficients $k_0 = 0.274$ and $k_{eff} = 0.43$ for InP doping from indium liquid phase, the sulfur diffusivity in the melt $D_S = 4.2 \times 10^{-7}$ cm^2/s, and the effective thickness of the transition layer $\delta = 0.07$ cm under the terrestrial gravity conditions. The experimental data obtained and the numerical estimates will be used for verification and development of the mathematical model of the crystal-

lization processes with consideration for the cluster structure of the boundary layer, proposed in [21, 22].

ACKNOWLEDGMENTS

I am grateful to V.T. Bublik and K.D. Shcherbachev for supplying the results of X-ray diffraction analysis and SIMS study of the samples.

This study was supported by the Russian Foundation for Basic Research, project no. 03-02-16282.

REFERENCES

1. A. N. Danilewsky, S. Lauer, J. Meinhardt, and K. W. Benz, J. Electron. Mater. **25** (7), 1082 (1996).
2. H. Weishart, A. N. Danilewsky, K. W. Benz, and E. Bauser, J. Cryst. Growth **131** (1), 17 (1993).
3. S. S. Strel'chenko and V. V. Lebedev, *Handbook of III–V Compounds* (Metallurgiya, Moscow, 1984) [in Russian].
4. A. N. Danilewsky, St. Boschert, and K. W. Benz, Microgravity Sci. Technol. **10** (2), 106 (1997).
5. St. Boschert, A. N. Danilewsky, and K. W. Benz, J. Cryst. Growth **205** (1), 92 (1999).
6. A. N. Danilewsky and J. Meinhardt, Cryst. Res. Technol. **38** (7–8), 604 (2003).
7. A. N. Danilewsky, S. Lauer, G. Bishopink, and K. W. Benz, Cryst. Res. Technol. **31** (1), 11 (1996).
8. A. N. Danilewsky, J. Meinhardt, and K. W. Benz, Cryst. Res. Technol. **31** (2), 139 (1996).
9. A. N. Danilewsky, G. Nagel, and K. W. Benz, Cryst. Res. Technol. **29** (2), 171 (1994).
10. A. Croell, Th. Kaiser, M. Schweizer, *et al.*, J. Cryst. Growth **191** (3), 365 (1998).
11. I. V. Barmin and A. S. Senchenkov, Fluid Dynamics **29** (5), 620 (1994).
12. V. V. Sazonov, S. Yu. Chebukhov, V. I. Abrashkin, *et al.*, Cosmic Research **39** (4), 419 (2001).
13. M. G. Mil'vidskiĭ, O. V. Pelevin, and B. A. Sakharov, *Physicochemical Principles of Preparation of Decomposing Semiconductor Compounds* (Metallurgiya, Moscow, 1974) [in Russian].
14. A. N. Danilewsky, K. W. Benz, and T. Nishinaga, J. Cryst. Growth **99** (1–4), 1281 (1990).
15. A. E. Voloshin, A. A. Lomov, T. Nishinaga, *et al.*, J. Cryst. Growth **236** (4), 501 (2002).
16. M. G. Mil'vidskiĭ and V. B. Osvenskiĭ, *Structural Defects in Epitaxial Layers of Semiconductors* (Metallurgiya, Moscow, 1995) [in Russian].
17. W. A. Tiller, K. A. Jackson, J. W. Rutter, and B. Chalmers, Acta Metall. **1**, 428 (1953).
18. A. N. Danilewsky, Y. Okamoto, K. W. Benz, and T. Nishinaga, Jpn. J. Appl. Phys. **31** (7), 2195 (1992).
19. W. G. Pfann, *Zone Melting* (Wiley, New York, 1966; Mir, Moscow, 1970).
20. J. A. Burton, R. C. Prim, and W. P. Slichter, J. Chem. Phys. **21** (11), 1987 (1953).
21. A. V. Kartavykh, M. G. Mil'vidskiĭ, V. P. Ginkin, *et al.*, Poverkhnost, No. 6, 91 (2004).
22. V. Ginkin, A. Kartavykh, and M. Zabudko, J. Cryst. Growth **270** (3–4), 329 (2004).

Translated by Yu. Sin'kov

Crystallography Reports, Vol. 50, No. 5, 2005, pp. 890–891. Translated from Kristallografiya, Vol. 50, No. 5, 2005, pp. 958–959.

OBITUARIES

Vladimir Aleksandrovich Koptsik (February 26, 1924–April 2, 2005)

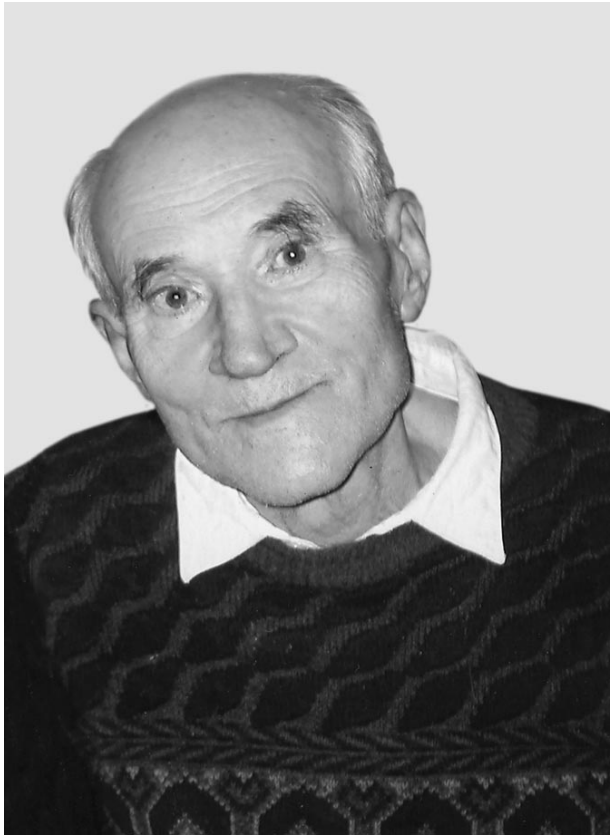

Vladimir Aleksandrovich Koptsik, a leading Russian crystallographer and an expert in symmetry and physics of crystals, died on April 2, 2005.

Koptsik was born on February 26, 1924, in Ivanovo into a family of students. His mother, Aleksandra Ignat'evna Shaposhnikova, was attending Higher Women's Courses at that time. His father, Aleksandr Nikolaevich, a former village teacher in Byelorussia, studied at the Moscow Mining Academy. After graduating, Koptsik's mother worked as a teacher and his father worked as an engineer at an electric-bulb plant in Moscow.

In June 1941, Koptsik finished ninth grade at high school 281 in Moscow. In October and November 1941, he worked on a Komsomol assignment digging antitank ditches near Moscow. From December 1941 to October 1944, he worked as a turner and an operator at a facility for sintering hard alloys at defense plant 632 MPSS in Moscow. In May 1942, he passed examinations for the tenth grade at the Teaching and Consultation Center in Moscow. Then, while working at the plant, he studied by correspondence at the Faculty of Physics of Moscow State University. After finishing three years of study at the Faculty of Physics, in October 1944, Koptsik entered the Department of Geophysics of the Faculty of Geology, Moscow State University, on a full-time basis. He graduated with distinction from the Department of Crystallography and Crystal Chemistry in 1949 and was appointed to the postgraduate course at this department. Koptsik's choice of specialization was affected to a large extent by the lectures of Professor G.B. Bokiĭ on the fundamentals of structural crystallography; the lectures of Professor A.I. Kitaigorodsky on X-ray diffraction analysis of crystals, and, especially, the comprehensive course of lectures on all aspects of crystallography (geometric, physical, and chemical) of Academician A.V. Shubnikov, who supervised Koptsik's diploma work and candidate's thesis.

In 1953, Koptsik was hired at the Faculty of Physics of Moscow State University. Being the closest student and assistant of Shubnikov, he made great efforts to organize the new Department of Crystallography and Crystal Physics (later called the Department of Crystal Physics). He successively worked as an instrumentation assistant, a junior researcher, an associate professor, and a professor. From 1968 to 1974, Koptsik headed the Department of Crystal Physics.

Koptsik began his scientific career in his third and fourth years of University with the investigation of the morphology and the conditions of growth of pyrite and quartz crystals. For this he used the data obtained during his practical training in 1947 and 1948 at the middle Asia and Ural deposits of crystals. In 1949, he defended his diploma on the growth kinetics and physical properties of piezoelectric ammonium dihydrophosphate crystals. With this study, Koptsik began extended research aimed at finding and analyzing new piezoelectric and pyroelectric crystals. The search of new crystals was based on the structural-symmetry criteria formulated by him. As a result, in February 1953, he defended his candidate's dissertation on the growth of resorcin crystals and analysis of their electrical and elastic properties at the Scientific Council of the Institute of Crystallography, USSR Academy of Sciences.

In the 1960s, Koptsik began a cycle of studies on generalized theory of symmetry. He was the first to derive all possible Shubnikov antisymmetry space groups. In December 1963, Koptsik presented this

1063-7745/05/5005-0890$26.00

study at the Scientific Council of the Faculty of Physics, Moscow State University, and defended it as his doctoral dissertation in physics and mathematics. In 1966, his monograph *Shubnikov Groups* was published.

Continuing his studies on symmetry, Koptsik and his students derived point and space groups of colored symmetry and developed their magnetic interpretation. These results were included in the monograph *Symmetry in Science and Art*, published by him and Shubnikov. This cycle of studies was awarded the Fedorov Prize of the Russian Academy of Sciences.

In 1974, Koptsik proposed a new effective approach to the theoretical simulation of the structure and physical properties of real crystals, based on tangling of internal-symmetry groups of structural units (describing their possible physical states) with external-symmetry groups, which describes the short- and long-range order in crystals on the whole. These studies made a significant contribution to the crystal physics of electrically and magnetically ordered crystals and the theory of generalized (colored) symmetry of material (geometrical–physical) spaces having a crystal structure.

What should be noted particularly are Koptsik's studies on the generalization of the Curie principle to the Shubnikov–Curie principle, which supposes a system-stochastic relationship between reasons and consequences, and on the establishment of the principle of nondecreasing symmetry and its transformation into generalized forms of symmetry at phase transitions in crystals.

These and some other new results were included in the second edition of the book *Symmetry in Science and Art* by Shubnikov and Koptsik, published in 2004.

In recent years, Koptsik paid much attention to the problem of inclusion of art analysis in the unified system of natural science knowledge. His considerations on this subject were reported in the large chapter *Approaches of Natural Sciences and Liberal Arts in Culture, Science, and Art* in the monograph *Essays on the Theory of Arts*, written by him, V.P. Ryzhov, and V.M. Petrov and published in 2004.

Koptsik's studies have been highly appreciated by many crystallographers. In 1966, Koptsik was elected a member of the Committee on International Crystallographic Tables of the International Union of Crystallographers and, in 1983, a member of the subcommittee of this union on nomenclature in n-dimensional ($n > 3$) crystallography. In 1996, he was elected a member of the Council of the International Interbranch Association for the Study of Symmetry. Since 1989, he was a member of the editorial board of the international journal *Symmetry: Science and Culture*. Since 1973, Koptsik was a member of the editorial board of the scientific journal *Kristallografiya* (*Crystallography Reports*).

In 1996, Koptsik was awarded the title of Honored Professor of Moscow University and, in 1999, the title of Honored Scientist of the Russian Federation.

Koptsik was the author of more than 300 publications, including four monographs and several textbooks. He edited proceedings of two international conferences. Koptsik supervised 25 candidate's and several doctoral dissertations.

Koptsik devoted his life to science. His name and his deeds will remain in the history of crystallography. Vladimir Aleksandrovich Koptsik, a prominent scientist and a kind, responsive man, will be remembered in the hearts of his students and colleagues.

Translated by Yu. Sin'kov

Crystallography Reports, Vol. 50, No. 5, 2005, p. 892.

ERRATA

Erratum: "Growth and Defect Crystal Structure of CdF_2 and Nonstoichiometric $Cd_{1-x}R_xF_{2+x}$ Phases (R = Rare Earth Elements and In). Part 3. Crystal Structure of As-Grown $Cd_{0.90}R_{0.10}F_{2.10}$ (R = Sm–Lu, Y) Single Crystals" [*Crystallogr. Rep.* 50, 203 (2005)]

E. A. Sul'yanova, A. P. Shcherbakov, V. N. Molchanov, V. I. Simonov, and B. P. Sobolev

On page 205, Table 1, the 9th row from the bottom in the column *R* should read "Diameter of spherical sample, μm" instead of "Radius of spherical sample, μm."

On page 209, the bottom part of Table 2 (for the elements Y, Er, Tm, and Lu), in the second subcolumn of column *R*, the 2nd row should read "$B_{11} \times 10^3$, Å^2" instead of "$B_{11} \times 10^8$, Å^2" and the 4th row should read "$D_{1122} \times 10^8$, Å^2" instead of "$D_{1122} \times 10^4$, Å^2."

On page 209, Table 2, in the second subcolumn of column *R*, the 6th row should read "$C_{123} \times 10^6$, Å^2" instead of "$C_{123} \times 10^3$, Å^2."